

NASA Conference Publication 3161

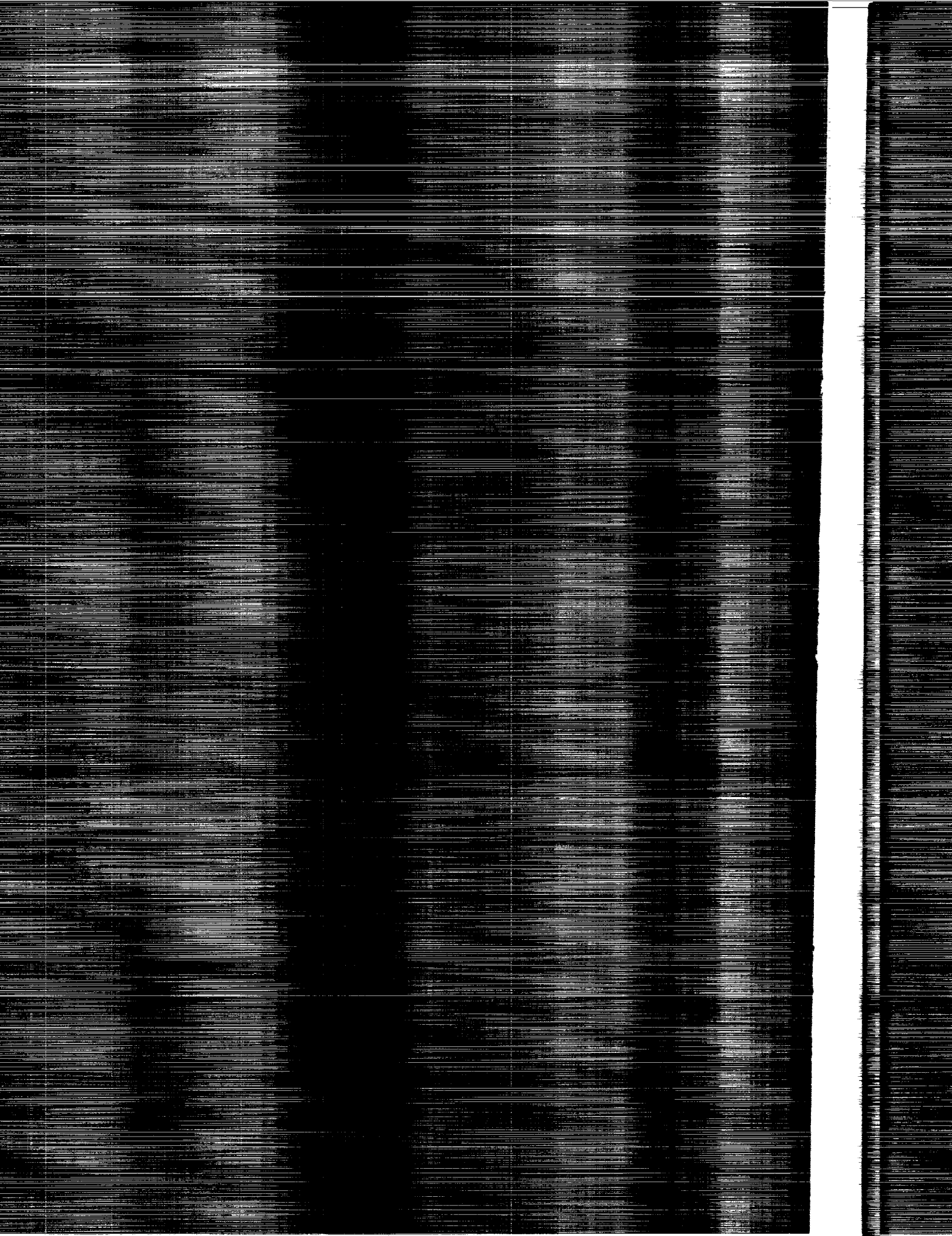
# The 1992 NASA Langley Measurement Technology Conference

*Measurement Technology for  
Aerospace Applications in  
High Temperature Environments*

(NASA-CP-3161) THE 1992 NASA  
LANGLEY MEASUREMENT TECHNOLOGY  
CONFERENCE: MEASUREMENT TECHNOLOGY  
FOR AEROSPACE APPLICATIONS IN  
HIGH-TEMPERATURE ENVIRONMENTS  
(NASA) 435 p

N93-13661  
--THRU--  
N93-13687  
Unclas

H1/35 0121300



*NASA Conference Publication 3161*

# **The 1992 NASA Langley Measurement Technology Conference**

*Measurement Technology for  
Aerospace Applications in  
High Temperature Environments*

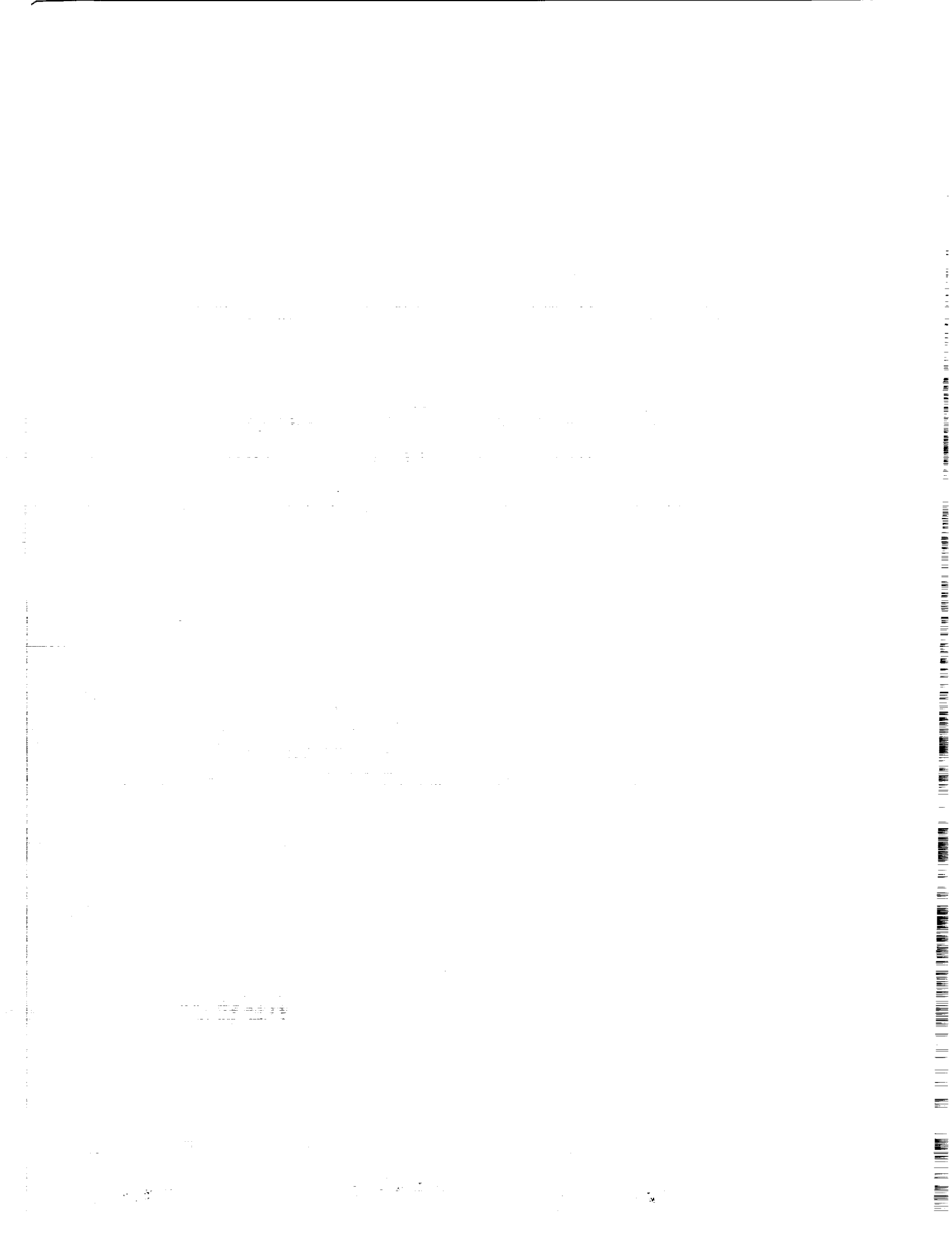
*Edited by  
Jag J. Singh  
and Richard R. Antcliff  
Langley Research Center  
Hampton, Virginia*

Proceedings of a conference sponsored by the  
National Aeronautics and Space Administration, Washington, D.C.,  
the American Institute for Aeronautics and Astronautics, Washington, D.C., and the  
Instrument Society of America, Research Triangle Park, North Carolina, and held at  
Langley Research Center  
Hampton, Virginia  
April 22-23, 1992

**NASA**

National Aeronautics and  
Space Administration  
Office of Management  
Scientific and Technical  
Information Program

**1992**





## Preface

The 1992 NASA Langley Measurement Technology Conference was held at Langley Research Center, Hampton, Virginia, on April 22 and 23, 1992. The Conference was cosponsored by NASA, AIAA, and ISA. The focus of the Conference was measurement technology for aerospace applications in high temperature environments in the areas of pressure, strain/force, temperature/heat flux, and flowfield diagnostics. The Conference was divided into four sessions with each session led by a keynote speaker who described the current status and limitations of the technology in the subject matter of the session. A total of 28 papers by active researchers from the industrial, academic, and Government laboratories were presented at the Conference. These papers are published here in their entirety.

Jag J. Singh  
Technical Program  
Chairman

The 1992  
NASA Langley Measurement Technology  
Conference

Measurement Technology for Aerospace Applications  
in High Temperature Environments

General Chairman: Dr. Frank Allario

Technical Program  
Committee: Dr. Jag J. Singh, Chairman  
Mr. Harlan K. Holmes  
Dr. William L. Sellers, III  
Dr. Richard R. Antcliff  
Mr. Frederick A. Kern  
Mr. Charles G. Miller, III

Administrative Chairman: Dr. Richard R. Antcliff

Conference Secretary: Mrs. Nita W. Langford

Conference Treasurer: Mr. Hector Soto

Certain materials and processes are identified in this publication in order to adequately specify procedures. In no case does such identification imply recommendation or endorsement by the government, nor does it imply that the materials or processes are the only or best ones available for the purpose.

## CONTENTS

<b>Preface</b> . . . . .	iii
<b>Attendees</b> . . . . .	viii
<b>Temperature and Heat Flux Measurements—Challenges for High Temperature Aerospace Application</b> . . . . . Richard D. Neumann	1
<b>High Heat-Flux Measurements and Experimental Calibrations/Characterizations</b> . . . . . C. T. Kidd	31
<b>Time Dependent Heat Transfer Rates in High Reynolds Number Hypersonic Flowfields</b> . . . . . Michael J. Flanagan	51
<b>Heat Flux Microsensor Measurements and Calibrations</b> . . . . . James P. Terrell, Jon M. Hager, Shinzo Onishi, and Thomas E. Diller	69
<b>Thin Film Thermocouples for High Temperature Measurement on Ceramic Materials</b> . . . . . Raymond Holanda	81
<b>Fabrication of Thin Film Heat Flux Sensors</b> . . . . . Herbert Will	97
<b>Gas Temperature Measurements Using the Dual-Line Detection Rayleigh Scattering Technique</b> . . . . . M. Volkan Otugen, Richard G. Seasholtz, and Kurt D. Annen	107
<b>High-Temperature Strain Measurement Techniques: Current Developments and Challenges</b> . . . . . M. M. Lemcoe	127
<b>Skin Friction Measurements in High Temperature High Speed Flows</b> . . . . . J. A. Schetz, T. E. Diller, and A. L. Wicks	171
<b>Palladium-Chromium Static Strain Gages for High Temperatures</b> . . . . . Jih-Fen Lei	189
<b>High Temperature Strain Gage Apparent Strain Compensation</b> . . . . . H. K. Holmes and T. C. Moore, Sr.	211
<b>Elastic and Plastic Strain Measurement in High Temperature Environment Using Laser Speckle</b> . . . . . F. P. Chiang	223
<b>Determination of High Temperature Strains Using a PC Based Vision System</b> . . . . . Stephen R. McNeill, Michael A. Sutton, and Samuel S. Russell	237

<b>Laser-Based Strain Measurements for High Temperature Applications</b> Christian T. Lant	245
<b>Technology Trends in High Temperature Pressure Transducers: The Impact of Micromachining</b> Joseph R. Mallon	251
<b>SiC Device Development for High Temperature Sensor Applications</b> J. S. Shor, A. D. Kurtz, D. Goldstein, and R. M. Osgood	255
<b>Final Report on the Trade-Off Characteristics of Acoustic and Pressure Sensors for the NASP</b> Martin Winkler and Chuck Bush	265
<b>Very High Temperature Silicon on Silicon Pressure Transducers</b> Anthony D. Kurtz, Timothy A. Nunn, Stephen A. Briggs, and Alexander Ned	291
<b>Developments on High Temperature Fiber Optic Microphone</b> Kenneth D. Wright, II and Allan J. Zuckerwar	301
<b>Electron Beam Fluorescence Measurements in the Boeing Hypersonic Shock Tunnel</b> L. L. Price, W. D. Williams, and H. M. Powell	305
<b>Resonance Lamp Absorption Measurement of OH Number Density and Temperature in Expansion Tube Scramjet Engine Tests</b> Walter R. Lempert, Richard E. Trucco, and Robert D. Bitner	321
<b>Visualization of Hydrogen Injection in a Scramjet Engine by Simultaneous PLIF Imaging and Laser Holographic Imaging</b> R. C. Anderson, R. E. Trucco, L. F. Rubin, and D. M. Swain	339
<b>Gas Temperature and Density Measurements Based on Spectrally Resolved Rayleigh-Brillouin Scattering</b> Richard G. Seasholtz and James A. Lock	355
<b>Planar Laser-Induced Fluorescence Measurements of High-Enthalpy Free Jet Flow with Nitric Oxide</b> Jennifer L. Palmer, Brian K. McMillin, and Ronald K. Hanson	375
<b>Planar Laser-Induced Fluorescence Imaging of OH in the Exhaust of a Bi-Propellant Thruster</b> P. H. Paul, N. T. Clemens, and D. B. Makel	387
<b>Exit Plane H<sub>2</sub>O Concentration Measurements Correlated with OH PLIF Near-Injector Mixing Measurements for Scramjet Flows</b> T. E. Parker, M. G. Allen, R. R. Foutter, D. M. Sonnenfroh, and W. T. Rawlins	403

## ATTENDEES

Aeschliman, Dan P.  
Sandia National Laboratories  
Department 1554  
Albuquerque, NM 87185-5800  
(505) 844-0448 FAX:(505) 844-8251

Allario, Frank  
NASA Langley Research Center  
M.S. 117  
Hampton, VA 23665  
(804) 864-6027 FAX:(804) 864-7798

Allen, Mark G.  
Physical Sciences Inc.  
20 New England Business Center  
Andover, MA 01810  
(508) 689-0003 FAX:(508) 689-3232

Anders, Scott G.  
M.S. 170  
NASA Langley Research Center  
Hampton, VA 23665  
(804) 864-8044 FAX:(804) 864-8348

Anderson, Robert  
M.S. 77-1  
NASA Lewis Research Center  
Cleveland, OH 44135  
(216) 433-3643 FAX:(216) 433-8643

Antcliff, Richard R.  
M.S. 235A  
NASA Langley Research Center  
Hampton, VA 23665  
(804) 864-4606 FAX:(804) 864-8315

Atkinson, Bill  
Pratt & Whitney  
400 Main Street, MS 116-01  
East Hartford, CT 06108  
(203) 565-2456 FAX:(203) 565-3086

Auslender, Aaron  
Lockheed, M.S. 168  
NASA Langley Research Center, Hampton, VA  
23665  
(804) 864-6545

Balla, R. Jeffrey  
M.S. 235A  
NASA Langley Research Center  
Hampton, VA 23665  
(804) 864-4608 FAX:(804) 864-8315

Bell, Ron J.  
Thiokol Corp./ Space Operations  
P.O. Box 707 MS L62  
Brigham City, UT 84302-0707  
(801) 863-6469 FAX:(801) 863-4330

Bertelrud, Arild  
AS&M, M.S. 163  
NASA Langley Research Center  
Hampton, VA 23665  
(804) 864-5559 FAX:(804) 851-1826

Blankson, Dr. Isaiah M.  
NASA HQ, Code RN  
Washington, DC 20546  
(202) 453-2743

Blosser, Max L.  
M.S. 396  
NASA Langley Research Center  
Hampton, VA 23665  
(804) 864-5192 FAX:(804) 864-7943

Bogue, Rodney K.  
M.S. D-2205  
NASA Ames Research Center  
Edwards, CA 93523-0273  
(805) 258-3193 FAX:(805) 258-3567

Bowman, Lynn  
Lockheed Eng.  
M.S. 396  
NASA Langley Research Center  
Hampton, VA 23665  
(804) 864-5426 FAX:(804) 864-7943

Briggs, S. A.  
Kulite Semiconductor Products, Inc.  
One Willow Tree Rd.  
Leonia, NJ 07605  
(201) 461-0900 FAX:(201) 461-0990

Britcher, Dr. Colin P.  
ODU  
Dept. ME, M.S. 161  
NASA Langley Research Center  
Hampton, VA 23665  
(804) 683-3720 FAX:(804) 683-5344

Brown, Martha C.  
M.S. 166  
NASA Langley Research Center  
Hampton, VA 23665  
(804) 864-6277

Burner, A. W.  
M.S. 236  
NASA Langley Research Center  
Hampton, VA 23665  
(804) 864-4635 FAX:(804) 864-7607

Bush, Chuck  
Kaman Instrumentation  
1500 Garden of the Gods Rd.  
Colorado Springs, CO 80907  
(719) 599-1814

Camarda, Charlie  
M.S. 396  
NASA Langley Research Center  
Hampton, VA 23665  
(804) 864-5436 FAX:(804) 864-7943

Capriotti, Diago P.  
AS&M  
M.S. 168  
NASA Langley Research Center  
Hampton, VA 23665  
(804) 864-6200

Carraway, Debra L.  
M.S. 234  
NASA Langley Research Center  
Hampton, VA 23665  
(804) 864-4663 FAX:(804) 864-7607

Chiang, Fu-Pen  
Dept. of Mech. Eng.  
State Univ. of New York at Stony Brook  
N.Y., NY 11794-2300  
(516) 632-8311 FAX:(516) 632-8327

Childers, Brooks  
M.S. 236  
NASA Langley Research Center  
Hampton, VA 23665  
(804) 864-4620

Choi, Sang H.  
M.S. 493  
NASA Langley Research Center  
Hampton, VA 23665  
(804) 864-1408 FAX:(804) 864-7730

Comer, William H.  
Calspan Corp.  
(615) 455-4759 FAX:(615) 455-9382

Conway, Bruce A.  
M.S. 235  
NASA Langley Research Center  
Hampton, VA 23665  
(804) 864-4755 FAX:(804) 864-7607

Coyle, Marshall  
UVA  
Aerospace Research Lab  
570 Edgemont Rd.  
Charlottesville, VA 22903  
(804) 982-5360 FAX:(804) 982-5357

Davis, Patricia P.  
M.S. 234  
NASA Langley Research Center  
Hampton, VA 23665  
(804) 864-4724 FAX:(804) 864-8315

Deaton, John  
AS&M, M.S. 231  
NASA Langley Research Center  
Hampton, VA 23665  
(804) 864-4789

DeTurris, Dianne J.  
VPI&SU  
215 Randolph Hall  
Aerospace & Ocean Engineering  
Blacksburg, VA 24061  
(703) 231-3231 FAX:(703) 231-9632

Diller, Tom  
VPI&SU  
Blacksburg, VA 24061  
(703) 231-7198 FAX:(703) 231-9100

Diskin, Glenn S.  
M.S. 170  
NASA Langley Research Center  
Hampton, VA 23665  
(804) 864-6268 FAX:(804) 864-8340

Dziedzic, Bill  
Lockheed  
MS 350  
NASA Langley Research Center  
Hampton, VA 23665  
(804) 864-3754 FAX:(804) 864-8545

Egoavil, Marco  
M.S. 440  
NASA Langley Research Center  
Hampton, VA 23665  
(804) 864-7247

Elgi, Haluk  
Columbia Univ.  
MS 230  
NASA Langley Research Center  
Hampton, VA 23665  
(804) 864-4340

Ellis, Rod  
M.S. 49-7  
NASA Lewis Research Center  
Cleveland, OH 44135  
(216) 433-3340 FAX:(216) 433-8643

Exton, Reginald J.  
M.S. 235A  
NASA Langley Research Center  
Hampton, VA 23665  
(804) 864-4605 FAX:(804) 864-8315

Flanagan, Michael J.  
Ohio State Univ.  
The Aero. and Astro. Res. Lab.  
2300 W. Case Rd.  
Columbus OH 4323  
(614) 292-5515 FAX:(614) 292-5552

Folgman, Tracy  
M.S. 395  
NASA Langley Research Center  
Hampton, VA 23665  
(804) 864-1371

Forman, Bruce  
Bethlehem Steel Co.  
509 E Mosser St., Apt. 18  
Allentown, PA 18103  
(215) 694-7616 FAX:(215) 694-2981

Fralick, Gus  
M.S. 77-1  
NASA Lewis Research Center  
Cleveland, OH 44135  
(216) 433-3645 FAX:(216) 433-8643

Goad, Henry M.  
M.S. 236  
NASA Langley Research Center  
Hampton, VA 23665  
(804) 864-4641 FAX:(804) 864-8559

Goad, William K.  
M.S. 236  
NASA Langley Research Center  
Hampton, VA 23665  
(804) 864-4633 FAX:(804) 864-8559

Goldstein, David  
Kulite Semiconductor  
One Willow Tree Rd.  
Leonia, NJ 07605  
(201) 461-0900 FAX:(201) 461-0950

Gorton, Mark P.  
M.S. 396  
NASA Langley Research Center  
Hampton, VA 23665  
(804) 864-5422

Goss, Larry P., PhD  
Systems Res. Labs., Inc.  
2800 Indian Ripple Rd.  
Dayton, OH 45440-3696  
(513) 252-2706 FAX:(513) 476-4652



Gray, David L.  
M.S. 238  
NASA Langley Research  
Hampton, VA 23665  
(804) 864-4661

Hager, Jon  
Vatell Corp.  
2001 South Main  
Blacksburg, VA 24060  
(703) 951-4004

Hartsley, Frank  
JPL  
4800 Oak Grove Dr.  
Pasadena, CA 91109  
(818) 354-3139 FAX:(818) 354-8153

Heltsley, Fred L.  
Calspan Corp., AEDC  
Arnold AFB, TN 37389-5000  
(615) 454-7364 FAX:(615) 454-6739

Holanda, Raymond  
M.S. 77-1  
NASA Lewis Research Center  
Cleveland, OH 44135  
(216) 433-3738 FAX:(216) 433-8643

Holmes, Harlan K.  
M.S. 238  
NASA Langley Research Center  
Hampton, VA 23665  
(804) 864-4650 FAX:(804) 864-7607

Hoppe, John  
M.S. 236  
NASA Langley Research Center  
Hampton, VA 23665  
(804) 864-4618 FAX:(804) 864-7607

Howard, Floyd  
M.S. 163  
NASA Langley Research Center  
Hampton, VA 23665  
(804) 864-5560

Hunt, L. Roane  
M.S. 395  
NASA Langley Research Center  
Hampton, VA 23665  
(804) 864-1352

Hutcherson, Scott A  
Northrop  
8900 East Washington Blvd.  
Pico Rivera, CA 90660  
(310) 948-7609 FAX:(310) 942-6478

Hwang, In Heon  
Dept. Physics  
Hampton University  
Hampton, VA 23668  
(804) 727-5829 FAX:(804) 727-5188

Jansen, Bernic  
Lockheed Eng., M.S. 165  
NASA Langley Research Center  
Hampton, VA 23665  
(804) 864-6287 FAX:(804) 864-8316

Jarrett, Olin, Jr.  
M.S. 170  
NASA Langley Research Center  
Hampton, VA 23665  
(804) 864-6320 FAX:(804) 864-8348

Jensen, Robin S.  
Thiokol Corp.  
(801) 863-2404 FAX:(801) 863-8823

Joklik, Richard  
N.I.S.T.  
Gaithersburg, MD 20878  
(301) 975-2602

Jones, Gregory S.  
M.S. 170  
NASA Langley Research Center  
Hampton, VA 23665  
(804) 864-1065 FAX:(804) 864-8348

Kahng, S. K.  
M.S. 235  
NASA Langley Research Center  
Hampton, VA 23665  
(804) 864-7533 FAX:(804) 864-7607

Kern, Frederick A.  
M.S. 234  
NASA Langley Research Center  
Hampton, VA 23665  
(804) 864-4615 FAX:(804) 864-7607

Kidd, Carl T.  
Calspan Corp/AEDC Ops.  
ISF/IC2, MS-450  
Arnold AFB, TN 37389  
(615) 454-7432 FAX:(615) 393-3608

Kim, Jong Huy  
Hampton Univ.  
Dept. of Physics  
Hampton, VA 23668  
(804) 727-5814 FAX:(804) 727-5187

Kiss, Laszlo I.  
Sci. Appl.  
Univ. of Quebec  
555 L'Universite'  
Chicoutimi, Quebec, G7H2B1, Canada  
(418) 545-5412 FAX:(418) 545-5012

Kourous, Helen  
M.S. 77-1  
NASA Lewis Research Center  
Cleveland, OH 44135  
(216) 433-6569 FAX:(216) 433-8643

Krauss, Dr. Roland  
UVA  
Aerospace Res Lab  
470 Edgemont Rd.  
Charlottesville, VA 22903  
(804) 982-5350 FAX:(804) 982-5357

Kubendran, Laguduva R.  
Analytical Sciences & Materials, Inc.  
107 Research Drive.  
Hampton, VA 23666  
(804) 865-7093

Lagen, Nick  
Lockheed  
M.S. 165  
NASA Langley Research Center  
Hampton, VA 23665  
(804) 864-6286

Langley, Lawrence W.  
Vatell Corp.  
P.O. Box 66  
Christiansburg, VA 24073  
(703) 961-2001

Lant, Chris  
Sverdrup, M.S. 77-1  
NASA Lewis Research Center  
Cleveland, OH 44135  
(216) 433-6360 FAX:(216) 433-8643

Laufer, Dr. Gabriel  
UVA  
Aerospace Research Lab  
570 Edgemont Rd.  
Charlottesville, VA 22903  
(804) 982-5350 FAX:(804) 982-5357

Lee, Ja H.  
M.S. 493  
NASA Langley Research Center  
Hampton, VA 23665  
(804) 864-1473 FAX:(804) 864-7730

Lei, Jih-Fen  
Sverdrup, M.S. 77-1  
NASA Lewis Research Center  
Cleveland, OH 44135  
(216) 433-3922 FAX:(216) 433-8643

Leighty, Brad  
M.S. 236  
NASA Langley Research Center  
Hampton, VA 23665  
(804) 864-4624

Lemcoe, Dr. M. M.  
PRC/NASA Dryden  
P.O. Box 273  
Edwards, CA 93523-5000  
(805) 258-2189 FAX:(805) 258-3690

Lempert, Walter R.  
Princeton University.  
E-Quad., Rm. D-414  
Princeton, NJ 08544  
(609) 258-2875 FAX:(609) 258-6109

Lesco, Daniel J.  
M.S. 77-1  
NASA Lewis Research Center  
Cleveland, OH 44135  
(216) 433-3728 FAX:(216) 433-8643

Liu, Jin  
Dept. Mech. Eng. of SC  
Columbia, SC 29208  
(803) 777-7617

Lunn, Wayne B.  
United Tech. Corp. Pratt & Whitney  
MS 716-87 Box 109600  
W. Palm Beach, FL 33410-9600  
(407) 796-5500 FAX:(407) 796-4500

Lutes, John E.  
NASA HQ. Code RJ  
Washington, DC 20456  
(202) 453-2825 FAX:(202) 755-4068

Lyons, Valerie  
M.S. 77-10  
NASA Lewis Research Center  
Cleveland, OH 44135  
(216) 433-5970 FAX:(216) 433-8643

MacMillan, Robert C.  
Vibro Meter Corp.  
P.O. Box 2330  
Peachtree City, GA 30269  
(404) 631-0111 FAX:(404) 631-0110

Maddux, Gene E.  
WL/FIBG  
Wright-Patterson AFB, OH 45433  
(513) 255-5159 FAX:(513) 256-1442

Mallon, Joseph R., Jr.  
Nova Sensor  
43517 Ocaso Ct.  
Fremont, CA 94539  
(510) 651-9776 FAX:(510) 770-0645

Mangalam, Siva  
AS&M  
107 Research Drive  
Hampton, VA 23666  
(804) 865-7093 FAX:(804) 865-7309

Martin, Carl J  
Lockheed Eng., MS 396  
NASA Langley Research Center  
Hampton, VA 23665  
(804) 864-5418

McDaniel, Dr. James  
UVA, Aerospace Res Lab  
570 Edgemont Rd.  
Charlottesville, VA 22903  
(804) 982-5350 FAX:(804) 982-5357

McGowan, David M.  
M.S. 396  
NASA Langley Research Center  
Hampton, VA 23665  
(804) 864-4916 FAX:(804) 864-7943

McLeod, Rory  
UVA, Aerospace Research Lab.  
570 Edgemont Rd.  
Charlottesville, VA 22903  
(804) 982-5360 FAX:(804) 982-5357

McNeill, Steve  
University of S. Carolina  
Dept. Mechanical Eng.  
Columbia, SC 29208  
(803) 777-3407 FAX:(803) 777-0106

McWithey, Bob  
M.S. 396  
NASA Langley Research Center  
Hampton, VA 23665  
(804) 864-5417

Melvin, Leland D.  
M.S. 231  
NASA Langley Research Center  
Hampton, VA 23665  
(804) 864-7970 FAX:(804) 864-4914

Menousek, John F.  
McDonnell Douglas  
P.O. Box 516  
St. Louis MO 63166  
(314) 233-3206 FAX:(314) 232-3722

Merski, Ron  
M.S. 408,  
NASA Langley Research Center  
Hampton, VA 23665  
(804) 864-7539

Meyers, James F.  
M.S. 235A  
NASA Langley Research Center  
Hampton, VA 23665  
(804) 864-4598 FAX:(804) 864-8315

Milburn, Daniel J.  
M.S. 222B  
NASA Langley Research Center  
Hampton, VA 23665  
(804) 864-2779 FAX:(804) 864-7731

Miner, Gilda A.  
M.S. 493  
NASA Langley Research Center  
Hampton, VA 23665  
(804) 864-1475 FAX:(804) 864-7730

Mitchell, Gerry W.  
Sandia Natl. Labs  
Org. 6462, P.O. Box 5800  
Albuquerque, NM 87185  
(505) 845-9164 FAX:(505) 845-3117

Moore, Ronald P.  
Kulite Semiconductor Products, Inc.  
One Willow Tree Rd.  
Leonia, NJ 07605  
(201) 416-0900 FAX:(201) 461-0990

Murrow, Hal  
Lockheed Engr. Svs., MS 396,  
NASA Langley Research Center  
Hampton, VA 23665  
(804) 864-5863 FAX:(804) 864-7943

Neumann, Richard  
Univ. of Dayton Research Inst.  
300 College Park  
Dayton, OH 45469-0111  
(513) 229-3846 FAX:(513) 229-4251

Nieberding, William C  
M.S. 77-1  
NASA Lewis Research Center  
Cleveland, OH 44135  
(216) 433-3727 FAX:(216) 433-8643

Northam, G. B.  
M.S. 170  
NASA Langley Research Center  
Hampton, VA 23665  
(804) 864-6268 FAX:(804) 864-8348

Olstad, Stuart J.  
Fluidyne Engineering  
5900 Olson Memorial Hwy.  
Minneapolis, MN 55422  
(612) 544-2721 FAX:(612) 559-6667

Otugen, N. Volkan  
Polytechnic University  
333 Jay Street  
Brooklyn, NY 11201  
(516) 775-4385 FAX:(516) 755-4404

Page, Frank  
Eaton Corp.  
15 Durant Ave.  
Bathel, CT 06801  
(203) 798-3384 FAX:(203) 798-3310

Palmer, Jennifer, L.  
Stanford Univ.  
Bldg. 520, Rm. 521Q  
Stanford, CA 94305-3032  
(415) 723-1295 FAX:(415) 723-1748

Parmar, Devendra S.  
ODU, MS 234  
NASA Langley Research Center  
Hampton, VA 23665  
(804) 864-4744 FAX:(804) 864-8315

Paul, Phillip H.  
Sandia National Laboratories  
Livermore, CA 94550  
(510) 294-1465

Pellett, Jerry  
M.S. 170  
NASA Langley Research Center  
Hampton, VA 23665  
(804) 864-6241 FAX:(804) 864-8348

Porro, Bob  
M.S. 5-11  
NASA Lewis Research Center  
Cleveland, OH 44135  
(216) 433-5921 FAX:(216) 433-8646

Price, Linwood L.  
Calspan Corp. / AEDC  
Arnold AFB, TN 37389-5000  
(615) 454-3732 FAX:(615) 454-6759

Puster, Richard L.  
M.S. 395  
NASA Langley Research Center  
Hampton, VA 23665  
(804) 864-1390 FAX:(804) 864-8193

Rivers, Kevin  
M.S. 396  
NASA Langley Research Center  
Hampton, VA 23665  
(804) 864-5428

Rizzi, Stephen  
M.S. 463  
NASA Langley Research Center  
Hampton, VA 23665  
(804) 864-3599

Rosasco, Dr. Gregory J.  
NIST  
Bldg. 221, B312  
Gaithersburg, MD 20899  
(301) 975-4813 FAX:(301) 926-5002

Rothgeb, Timothy M.  
Lockheed Eng., M.S. 396  
NASA Langley Research Center  
Hampton, VA 23665  
(804) 864-5415 FAX:(804) 864-7943

Ruf, Edward G.  
Lockheed Eng., M.S. 168  
NASA Langley Research Center  
Hampton, VA 23665  
(804) 864-6356 FAX:(804) 864-6243

Russ, Courtney E, Jr.  
M.S. 236  
NASA Langley Research Center  
Hampton, VA 23665  
(804) 864-4639 FAX:(804) 864-7607

Saliga, Debi M.  
Lockheed Engineering  
NASA LaRC, MS 165  
Hampton VA 23665  
(804) 864-6645 FAX:(804) 864-8316

Scotti, Steve  
M.S. 396  
NASA Langley Research Center  
Hampton, VA 23665  
(804) 864-5431 FAX:(804) 864-7943

Seasholtz, Richard G.  
M.S. 77-1  
NASA Lewis Research Center  
Cleveland, OH 44135  
(216) 433-3754 FAX:(216) 433-8643

Sellers, William L., III  
M.S. 170  
NASA Langley Research Center  
Hampton, VA 23665  
(804) 864-2224

Shearin, W. Albert  
M.S. 222B  
NASA Langley Research Center  
Hampton, VA 23665  
(804) 864-2776 FAX:(804) 864-7731

Shepp, Allan  
Aspen Systems, Inc.  
184 Cedar Hill St.  
Marlborough, MA 01752  
(508) 481-5058 FAX:(508) 480-0328

Shideler, John L.  
M.S. 396  
NASA Langley Research Center  
Hampton, VA 23665  
(804) 864-5430

Singh, Jag J.  
M.S. 235  
NASA Langley Research Center  
Hampton, VA 23665  
(804) 864-4760 FAX:(804) 864-7607

Smigay, Steven A.  
Unified Industries Inc.  
7530 Fullerton Court  
Springfield, VA 22153  
(703) 569-0670 FAX:(703) 569-5760

Smith, M. W.  
M.S. 170  
NASA Langley Research Center  
Hampton, VA 23665  
(804) 864-6261 FAX:(804) 864-8348

Spuckler, Chuck (Charles)  
M.S. 5-11  
NASA Lewis Research Center  
Cleveland, OH 44135  
(216) 433-2167 FAX:(216) 433-8643

Stouffer, Scott  
M.S. 170  
NASA Langley Research Center  
Hampton, VA 23665 (804) 864-1347

Tabibi, Bagher M.  
Hampton Univ. , MS 493  
NASA Langley Research Center  
Hampton, VA 23665  
(804) 864-1479

Terrell, Jim P.  
Vatell Corp.  
2001 S. Main St.  
Christiansburg, VA 24073  
(703) 951-0769

Thornton, Aimee  
GWU/JIAFS, M.S. 168  
NASA Langley Research Center  
Hampton, VA 23665  
(804) 864-6245 FAX:(804) 864-6243

Trucco, Richard  
General Applied Science Labs.  
77 Raynor Ave.,  
Ronkonkoma, NY 11779  
(516) 737-6100 FAX:(516) 737-6121

Tseng, Ting  
PRC, Inc.  
POB 273  
Edwards, CA 93523  
(805) 258-3764 FAX:(805) 258-3690

Van Vesslem, Peter  
Eaton Corp.  
15 Durrant Ave.  
Bethel, CT 06801  
(203) 796-6119 FAX:(203) 796-6313

Vause, Frank  
Lockheed Eng., MS 396  
NASA Langley Research Center  
Hampton, VA 23665  
(804) 864-5414

Venkateswaran, S.  
Lockheed Eng.  
144 Research Dr.  
Hampton, VA 23666  
(804) 864-1370

Walsh, Michael J.  
M.S. 163  
NASA Langley Research Center  
Hampton, VA 23665  
(804) 864-5542

Watson, Ralph  
M.S. 163  
NASA Langley Research Center  
Hampton, VA 23665  
(804) 864-5723

Waters, Allen  
M.S. 396  
NASA Langley Research Center  
Hampton, VA 23665  
(804) 864-3118 FAX:(804) 864-7493

Welch, Chris  
NESB (William & Mary) MS 231,  
NASA Langley Research Center  
Hampton, VA 23665  
(804) 864-4797

Wernet, Mark P.  
M.S. 77-1  
NASA Lewis Research Center  
Cleveland, OH 44135  
(216) 433-3752 FAX:(216) 433-8643

West, James W.  
M.S. 236  
NASA Langley Research Center  
Hampton, VA 23665  
(804) 864-4836

Will, Herbert A.  
M.S. 77-1  
NASA Lewis Research Center  
Cleveland, OH 44135  
(216) 433-3741 FAX:(216) 433-8643

Williams, W. Dan  
M.S. 77-1  
NASA Lewis Research Center  
Cleveland, OH 44135  
(216) 433-3725 FAX:(216) 433-8643

Winkler, Martin  
Kaman Instrumentation  
1500 Garden of the Gods Rd.  
Colorado Springs, CO 80906  
(719) 599-1645

Wright, Kenneth  
M.S. 238  
NASA Langley Research Center  
Hampton, VA 23665  
(804) 864-4665 FAX:(804) 864-7607

Yu, Dong  
Titan Corp.  
1950 Old Gallows Rd.  
Vienna, VA 22182  
(703) 883-9423

Zaman, Khairul  
M.S. 77-1  
NASA Lewis Research Center  
Cleveland, OH 44135  
(216) 433-5888 FAX:(216) 433-8643

Zambrano, Charlie  
Pratt & Whitney  
400 Main Street, MS 116-01  
East Hartford, CT 06108  
(203) 565-2456 FAX:(203) 565-3086



TEMPERATURE AND HEAT FLUX MEASUREMENTS -  
CHALLENGES FOR HIGH TEMPERATURE  
AEROSPACE APPLICATION

Richard D. Neumann  
University of Dayton  
Research Institute  
300 College Park  
Dayton, OH 45469-0111, USA

**Thesis Statement**

The fundamental problem is that you and I would like to hear broad, sweeping universal truths about this subject, thermal sensors, but it is dominated by the details of the particular application.

These details involve the materials system complexity; the characteristics of those materials in which measurements are made; the presence, if any, of sub-surface cooling and the comparative use of "add-on" or "build-in" thermal sensors which infer heating rates by either understanding the thermal capacity of a material or the rate at which heat conducts through that material.

**INTRODUCTION  
AND BACKGROUND**

The measurement of high temperatures and the inference of heat transfer data is not strictly a problem of either the high temperatures involved or the level of the heating rates to be measured at those high temperatures. It is a problem of duration during which measurements are made and the nature of the materials in which the measurements are made. Thermal measurement techniques for each application must respect and work with the unique features of that application.

In the past 30 years, high heat flux has successfully been measured on a number of high temperature flight test systems. Among these programs were (1) the NASA "FIRE" program, (2) the NASA "RE-ENTRY F" program and the (3) the NASA SPACE SHUTTLE program. The table below lists the peak measured

heating rates on these vehicles, the flight duration of the experiment, and the peak wall temperature achieved on the sensor.

Flight Vehicle	Peak Heating Rate ( <i>Btu/Ft<sup>2</sup>Sec</i> )	Peak Measured Temperature (°F)	Test Duration (Sec)
Space Shuttle Forebody	16.2	2015 °F	1200
Space Shuttle Flap	26.9	2311 °F	1200
FIRE	1100.0	2440 °F	25
Re-entry F	545		3.2

Each of these was a unique experiment with quite different test goals. As a result, many of the flight-measurement features differed in detail from experiment to experiment.

The Space Shuttle, a lifting body, generated data for the longest duration with the substantial surface wall temperature. The other experiments, while measuring higher heating rates at comparable surface temperatures, obtained these data during far shorter test durations.

Matthews et al <sup>1</sup> discussing the need for high temperature heat flux gages stated that...

...Reliable heat flux gages are currently limited to relatively low operating temperatures, and gages that can operate at temperatures of 2000°F and above are required to measure the heat delivered to a structure during ground and flight testing.

In spite of this, flight tests have generated reliable heat flux data at surface temperatures substantially greater than 2000°F. Admittedly, in each case the thermal instrumentation was well integrated into the thermal protection system in a manner which allows the efficient inference of heat transfer from temperature measurements. The basic thermal instrumentation on the Space Shuttle, for example, was a single platinum thermocouple placed near the surface of the tile, as shown in figure 1, with the surface temperature and the heat flux inferred from this thermocouple through the use of a thermal model. In both FIRE and RE-ENTRY "F" in-depth temperature plug gages, shown in figures 2 and 3, were used

to define heat transfer. This instrumentation initially inferred heating through the temperature drop between adjacent thermocouples in the plug although post test analyses suggested that for the short test durations, multiple gages placed in depth were not required and a single thermocouple defining the heat capacity of the surface material would suffice.

Why would a quote in 1991 argue with successes of the past 30 years? The problem is NOT that heat transfer cannot be deduced at high operating temperatures but that either heat transfer cannot be deduced at high temperatures for more general applications or the problem lies in the definition of the term "heat flux gage". Each of the cases just discussed was carefully crafted from the materials viewpoint, from the test duration viewpoint and from the instrumentation viewpoint to facilitate measurements.

Matthews continues by saying that:

... (Heat flux) gage design emphasis is placed on COMPATIBILITY ISSUES associated with integrating the gage within the structure...and minimizing the gage's influence on the surrounding material response, particularly in actively-cooled structures.

This statement is a key. For each example case, the instrumentation and materials in which it was placed were thermally compatible. Compatibility issues define whether a commercially-available add-on thermal sensor or a built-in thermal sensor should be used in a specific application and whether accurate heat flux can be deduced at all. The corollary is that NOT ALL STRUCTURES CAN BE INSTRUMENTED TO DEDUCE HEAT TRANSFER today. That is the basis of Matthew's comments and a substantial challenge for the measurement community. A more correct interpretation of Matthew's statements, which I might offer, would be...

Significant deficiencies exist in deducing heat transfer from temperature measurements on ARBITRARY MATERIALS and DURING ARBITRARY TEST PERIODS and these problems are made worse by the selection of "add-on" rather than "design-in" thermal sensors. Examples of successful high temperature, high heat flux measurements are the result of careful, integrated designs where the instrument, the flight vehicle and the test acquisition phase of the flight have been properly selected to achieve successful data.

Several concepts have been briefly introduced and these concepts require further discussion.

## THERMAL GAGES AND HEAT FLUX GAGES: AN OPERATIONAL DEFINITION

In this paper, thermal gages are instruments that measure temperature. They include thermocouples, resistance thermometers and fiber-optic based temperature measurements. Heat flux gages are self-contained instruments that use thermal measurements, with a thermal model, to infer causal heat flux.

### ADD-ON VS DESIGN-IN HEAT FLUX GAGES

Heat flux is deduced through thermal models which interpret the measured temperature on or in the structure in terms of the heating that caused those measured temperatures. In so doing, the process must not alter the thermal character of the surface being measured. Heat flux gages are highly localized embodiments of those thermal models, concepts committed to hardware. A cross-section of heat flux gages for low and high temperature applications are defined in the tables below.

Dimensions of Low Temperature Heat Flux Sensors

Heat Flux Sensor Type	Typical Diameter (Ins.)
Thin Film resistance Thermometer *	0.0030 x 0.200
Schmidt-Boelter Gage	0.250
Coax Gage *	0.0150
Plated Thermocouple Gage *	0.008 x 0.008

\* Requires proper materials to form a valid thermal model  
-----

Dimensions of High Temperature Heat Flux Sensors

Heat Flux Sensor Type	Typical Diameter (Ins.)
Water-cooled Gardon Gage *	0.0625
High Temperature Gardon Gage *	0.250
Vatell Gage	0.100 x 0.125
In-depth Thermocouple Gage *	0.125

\* No surface thermocouple measurement

It is possible that heat transfer can be deduced through add-on, commercial heat flux sensors but it is also possible that heat flux must be deduced by distributing thermal sensors within the structure of the hardware being measured and using that hardware as the "heat flux gage" itself. In the Space Shuttle example the TPS material had thermal sensors imbedded in it and the material with the imbedded thermal sensors became the heat transfer gage. For the FIRE and RE-ENTRY "F" examples either the beryllium structure could be thought of as having thermal sensors imbedded in it or the thermocouple plug could be thought of as a thermally transparent add-on heat flux gage.

There were also add-on heat flux gages used on the Space Shuttle in the external tank<sup>2</sup> and added to the orbiter heat shield<sup>3</sup>. These examples are discussed in appendix A. In both cases, the metallic add-on heat flux gages were poorly integrated into the insulative TPS material of the Space Shuttle and the resulting heat transfer "measurements" were of an unacceptable quality.

Thermally incompatible heat flux sensors present two very different problems which must be addressed: 1) the sub-mold-line transfer of heat between the parent structure and the sensor which may destroy the "assumed" thermal model and 2) surface boundary layer distortion of CONVECTIVE flow over the structure housing the heat transfer gage. This distortion is caused by the step function change in the wall boundary condition with no corresponding change at the "edge" of the boundary layer. Since the surface is heated by the gradient of the static temperature distribution through the boundary layer, the sensed heat flux is sensitive to wall temperature disturbances. This is a FLOW FIELD-INDUCED phenomena present in a convective flow which has a developed boundary layer but not in a radiative calibration rig or on the stagnation point of a model placed in a convective flow. The aerodynamic problems of temperature mismatch were discussed both by Carnahan<sup>4</sup> and Praharaj<sup>5</sup>. Both of these problems can be addressed through well-defined numerical techniques which correctly model the flow. The material mismatch problem is found in all high temperature or long time applications of thermal instrumentation.

Both adding-on thermal instruments or designing-in those instruments are potentially acceptable techniques within limitations defined by the specifics of the experiment. The details of the specific application may dictate one technique over the other. In either case, the basis of heat flux measurement must be respected. Clearly, in the case of the add-on gages for the Space Shuttle application, the gages were not well thermally integrated into the TPS system and the

measured results were, as a consequence, not representative of the structure with no instrument installed.

#### **Thermal Gage Location Within the Structure:**

The inference of heat transfer requires the precise placement of thermal gages with the structure to be measured. Large gradients of temperature are present within the structure and imprecisely located thermal sensors reflect inaccuracy in the inferred heating rates. Knowledge of thermal sensor location is far more precise in add-on heat gages than in design-in heat gages. The instrument vendor precisely locates these sensors and calibrates the heat gage to assure they are properly located. This is not the case for design-in heat sensors for which thermal sensors are placed within a structure either during or after the fabrication process. Examples abound of poor data generated as a result of thermal gages imprecisely located within the structure or of shifting within that structure during the process of a test. One such example is, again, the Space Shuttle instrumentation shown in figure 1. In this case, the platinum thermocouple was placed within the soft, insulative tiles during the fabrication process without strict quality controls on the installation process<sup>6</sup>. The result was some ambiguity concerning the actual in-depth placement of the thermocouple wire during the installation and later during the flight-to-flight refurbishment of the tiles containing the thermal gage. Hodge initially identified the problem which is most acute in short duration flight maneuvers and defined a very sophisticated software tool to understand it<sup>7</sup>. Similar studies were conducted by Jones et al<sup>8</sup>. Figure 4 from their paper indicates that the accurate location of thermocouples was required to match heating rate data deduced from thermocouples with heat transfer data deduced from calorimeter gages. In-situ calibration of test hardware containing design-in heat gages is extremely important as well as the collateral use of parameter estimation techniques to generalize that calibration information. The paper by Kipp and Eiswith<sup>9</sup> proposed in situ calibration of instrumentation that is as true today as it was a decade ago.

#### **THERMAL CAPACITY VS CONDUCTION RATE HEAT FLUX INSTRUMENTS**

Although aerodynamic heating is numerically computed from the slope of the static temperature in the boundary layer near the wall boundary condition, aerodynamic heating is experimentally inferred though its influence on the structure as shown in figure 5. The numerist worries only about fluids assuming a perfectly responding structure but the experimentalist worries about both questions of materials response as well as questions of the boundary layer fluid.

As noted earlier by example, successful instruments can be based either on the premise of capturing the heat pulse within the structure or determining the rate of heat transfer through the structure. The Shuttle, because of its insulative tile thermal protection system, essentially captured the heat pulse within the tiles; whereas, the FIRE and RE-ENTRY "F" programs were instrumented with gages capable of either capturing the heat pulse or measuring the rate of heat transfer through the structure. Heat capacity gages are indirect measures of heat transfer requiring a sometimes complicated thermal model to interpret measured temperature in terms of causal heating rates. Heat conduction rate gages are direct reading gages creating a temperature-difference signal proportional to causal heat transfer rates. This is, of course, an idealized description of the problem assuming only a direct relationship between causal convective heating to the surface and conductive dissipation of that heating within the structure, a classic low temperature application.

At high temperatures, the causal convective heating may be dissipated either through internal dissipation, ideally one-dimensional conduction into the skin of the flight vehicle or re-radiated back to space (or other structural elements if you are really unlucky). As the surface temperature of the structure increases, more of the heat radiates (as the 4th power of the wall temperature) and correspondingly less conducts inward. At some point during the flight operation of an uncooled surface, almost all of the heat is re-radiated away from the surface. In the limit, rate gages define zero heat transfer THROUGH the surface although substantial surface heating to the surface is still occurring. In this limiting case, the sole index of heat flux is through a surface temperature measurement that is used to infer heating through calibration of the emissivity of the surface material. On the Space Shuttle, this situation occurred rapidly as shown in figure 6.

Rate gages, while direct reading, may not always measure the total heat load to the surface. All high temperature rate gages must measure not only the rate of heat transfer through the structure but also the absolute level of temperature at the surface. Some do not and others accomplish this only through calibration. Measuring both rate and level requires additional channels of information compounding the difficulty of the measurement process. Finally, heat capacity gages require a larger volume of structure for dissipation as the test duration increases and/or the thermal conductivity of the structural material increases. It is not always possible to capture the heat pulse within a structure and for those cases where it is not, rate gages may be a better choice.



## **SUB-SURFACE COOLING**

Actively cooled materials are feasible and of increasing interest. While cooling reduces the material surface temperature (and the heat re-radiated to space from an instrumentation perspective), cooling also provides an additional heat loss mechanism. Heat capacity measurements, in this environment, require that the heat loss to the coolant be measured. Direct reading heat-rate measurements applied in this environment require that all possible heat paths be measured and that direct measurements be made within the thickness of the panel being cooled and within the portion of that cooled panel at which the temperature gradient (due to conduction) is linear. These thickness dimensions can be very small, challenging the design and integration of thermal instruments.

## **WHAT IS MEASURED AND WHAT IS CALIBRATED OUT**

### **Re-radiation:**

Not all the elements of aerodynamic heating can be measured with either thermal capacity or heat rate sensors. One element that requires calibration is surface re-radiation. The heating due to radiation follows the equation

$$\dot{q}_{\text{radiation}} = \epsilon \sigma T_{\text{wall}}^4$$

Evaluating radiation from the wall is inherently inaccurate resulting in an error of +/- 10% or more in heating rate. The emittance measurement has experimental scatter and the surface temperature measurement converted to a digital signal has experimental scatter whose magnitude depends on the type of thermal sensor used and the quality of the data train (from sensor to digital output). Further, the measured temperature is raised to the 4th power compounding the error and finally, the measured temperature may not be the actual surface temperature but a sub-surface measurement that must be related to surface conditions either numerically or through calibration techniques.

### **Chemical Energy:**

Another increment of heating that normally requires calibration is that associated with incomplete recombination of dissociated boundary layer flow. Static temperature increases through the shock system about the vehicle and the deceleration of the flow in the boundary layer may dissociate the air. Low density flows, which limit energy transfer in the gas, may lock in the stagnation region chemical activity that

sweeps over the surface. If this occurs, the catalytic character of the surface material and that of the thermal gage placed in that material may recombine the dissociated flow. This catalytic character must be calibrated. Upstream history effects are important as well as the local conditions at the instrument in question. Calibration of the surface catalyticity is possible to accomplish but surface aging as the flight surface is repeatedly flown is also important.

Our flight experience with catalytic surfaces is through the Space Shuttle flights. The non-catalytic nature of the Shuttle tile coating (a glassy material) was noted to reduce the measured heating rate up to 60% of a fully catalytic wall<sup>10</sup>. It has been noted that the sudden release of chemical energy over a catalytic gage placed in a non-catalytic surface results in a temperature rise greater than the equilibrium value that would be present for an entirely catalytic surface and gage<sup>11</sup>. Evidence of aging phenomena was also noted and reported by Jones<sup>12</sup> who noted a 20% increase in heating from flight 2 to flight 5 of the Space Shuttle due to either catalysis or emissivity changes.

This situation argues for in-situ calibration of thermal sensors on flight vehicles, yet another measurement challenge. In-situ calibration is more important for thermal sensors which are designed-in to the structure rather than added-on to the structure.

#### **THERMAL MODELS AND THEIR IMPORTANCE:**

Heat transfer is inferred by strategically placed temperature measurements through the use of a thermal model of the temperature dissipation. We implicitly use thermal models while we tend to forget the approximations that limit their application. Whether the causal relationship is seemingly trivial, a 1D conductive flow through the structure defining the flow within a so-called heat gage, or whether it is complicated, full 3D time varying dissipation through a built-up structure, the process is conceptually the same. This paper will not discuss thermal models and their limitations but even a cursory review of the literature demonstrates the problems which are continuing today.

#### **THE SIMILARITIES AND DIFFERENCES BETWEEN GROUND TEST AND FLIGHT APPLICATIONS**

While this paper deals with flight measurements. The reader might deduce that either high temperature measurements are not made on the ground or that the instrumentation and techniques for ground-based measurements are solved or are the same as for flight. None of this is the case.

Ground test applications cover a spectrum of thermal and heat transfer needs and goals. Aeromechanic testing is generally at low temperatures because of experiment design. High temperature ground test goals are structural and propulsion development. While the structural testing uses materials and structural concepts in common with flight goals, the propulsion testing may present ground test unique instrumentation problems. Propulsion tests focus on defining propulsion efficiency without the added cost and complexity of using flight-weight structural materials. This is accomplished by fabricating the model structure out of heat-sink copper. The challenge is to "measure" the highly non-uniform surface heat transfer within highly-conductive copper. A particular concern is the measurement of localized heating peaks within copper structures. These peaks create lateral heat conduction paths that may well invalidate the installed instrumentation.

Another application of ground-test experimentation that has been often proposed is the need for a pre-flight operational validation of flight instrumentation in ground test facilities. While on the surface this appears to be useful, the practical aspects of the problem for high temperature instrumentation make such a test of questionable technical value. Some of these technical issues involve:

1. Defining the radiation environment between the "model" surface and the test-peculiar surroundings.
2. Incorporating sufficient structure about the instrument to correctly simulate the flight structure at flight-simulated test conditions.
3. Generating a clean, simulating test flow without the presence of test-induced contaminants.

Other technical solutions - primarily analysis techniques - should first be investigated and discarded as inappropriate.

### **The Complexity of the Materials System:**

In past examples the instrumented materials system was homogeneous and thick enough to capture the thermal pulse for the duration of the flight experiment. The instrumentation of such systems presents no significant technological instrumentation problems. Instrumentation problems arise when systems goals of weight-efficiency conflict with the test goals to measure temperature and to infer heat flux on those materials. To illustrate, Figure 7 from a paper by Grallert and Keller<sup>13</sup> shows the unit weight of various TPS materials as a function of the wall temperature of that material. Representative metallic TPS candidates are lighter than the

ceramic tiles of the Space Shuttle program as the surface temperature increases. The metallic concepts are superior at high surface temperatures but the challenge is to install thermal sensors within or onto these "...thin metallic foils..." and to infer heat transfer rates from those thermal measurements.

Figure 8 shows both the stiffened heat shield (the ceramic shingle design) that is being considered for the Hermes system and the metallic multiwell concept. The material of the structures as well as the thickness of the typical surface layer are shown. Recalling the dimensions of thermal sensors previously presented, installing any thermal sensor is difficult enough but inferring heat flux through thermal sensor measurements while not altering the thermal character of the surface being measured is certainly a challenge for high temperature aerospace application.

Apart from the thicknesses of the materials, the materials selected conduct heat across the section and radiate that heat both inward and back to space. Finally, the material fabrication process, particularly for coated molybdenum will make bonding of gages to coated materials impossible.

Seven advantages are noted for these advanced material systems which are indicative of advanced materials thinking; instrumentation installation is not one of them. Complex material systems are certainly a challenge to instrument if they can be instrumented at all.

#### **CHALLENGES FOR HIGH TEMPERATURE AEROSPACE APPLICATIONS**

I see several contemporary challenges in the development of measurement technology. These challenges will now be discussed in order.

**Challenge 1:** To capture the character and localized peak values within highly nonuniform heating regions

The characteristics of highly non-uniform heating regions are (1) localized peaks in the imposed heating to the surface, (2) incomplete knowledge of the location of heating peaks due to real gas effects and (3) high thermal gradients along the surface of the material driven by the gradients in imposed heating.

Both ground test and flight test measurements are concerned first with identifying the level of the peak and secondarily defining the structure of the interaction. Either fields of individual point sensors are applied to define peaks by capturing the heating pulse whose location is guided by our incomplete knowledge of the distribution, or survey testing is applied to map the entire interaction process in sufficient detail. Errors in the measurement process are not random but of a bias which produces lower data than actually present. These errors are due to (1) the size of the heat sensor being substantially larger than the spike in heating being measured, (2) the thermal model relating measured temperature to the imposed heating is incomplete and ignores characteristic temperature gradients along the surface or (3) the measurement span of the temperature sensor is inadequate to the measurement (significant for survey testing techniques).

The challenges that I observe are to: (1) develop a compatible system between the types and locations of physical sensors (thermal or heat transfer sensors) and the thermal model that uses these data to define a heat transfer distribution. In the case of highly peaked distributions, the resulting thermal model may be applied to a single sensor or to a sensor field as a group. The need is to define temperature gradients along the surface as well as through the material system; (2) to create thermal and heat transfer sensors that are properly scaled to the characteristic dimensions of the peaked interaction, which implies very small sensors as well as tightly packed thermal sensors; (3) to efficiently manage the volume of data extracted from a field of either isolated sensors or temperature maps produced by various survey techniques; and (4) to broaden the temperature span of survey techniques. The last two items will be discussed in later sections of this paper.

**Challenge 2:** To manage large volumes of thermal instrumentation in order to efficiently derive critical information

On the ground and in flight substantial amounts of raw data are generated that must be managed in acquisition, storage and manipulation. Both the volume and complexity of test data are increasing today. Single test runs can acquire over 100 million data elements. These large volumes of data must be reduced in an efficient but complete manner. This challenge considers the efficient transformation of data into information.

## Ground Test:

Survey sensing techniques now produce digital data that both increase the effective numbers of sensed points and multiply the volume of data to be manipulated. Each "frame" of data can deliver 262 thousand data values, and frames of data must be taken rapidly and sequentially to accurately map the test surface. Video refresh rates of 30 to 60 frames per second are commercially available and the test duration of 1 to 10 seconds is typical. Each run then can generate as many as 100 million data values. Admittedly, a small percentage of these values merit full reduction and much can be gleaned from even a partial reduction of these data but the information contained in these data may require a rather sophisticated reduction for complex interacting flows. Consider, for example, the evaluation of conduction losses along the surface caused by highly non-uniform heating of less than perfect insulators; the required information is captured in the data but the computational effort to reduce the data is not trivial. Numerical analyses by Dorignac and Vulliemre<sup>14</sup> demonstrate that these problems exist even for ideal test surfaces and must be considered in the data reduction and analysis.

Initial, zero order, data reduction of ideal insulative surfaces approximates the actual data reduction equation with a 1D closed form relationship. Using this technique, each data run requires about 4 minutes of computation on an Intel 80386 based machine. Balageas<sup>15</sup>, who has written extensively on survey techniques at ONERA, points out that:

" The snare to be avoided, and it is not a small one, is to keep from being swamped by the flood of data generated by this technique. Processing methods will have to be developed that are thrifty in computational time and memory space, but sophisticated enough that what is of interest can be distinguished from what is secondary or even useless, with user-friendly graphic postprocessing".

## Flight Test:

Managing large volumes of high-frequency flight data with reasonable downlinks requires on-board information processing. This was observed over a decade ago by Galleher<sup>13</sup> who stated that

"...as flight performance measurements become more demanding...more and more on-board processing and data compression techniques will have to be devised

that are acceptable to both system designers and experimenters..."

This paper quote referred to the flight test of BMO's **Advanced Maneuvering Reentry Vehicle, AMARV**, on which 60, in-depth thermocouple plugs (similar to those on the FIRE and RE-ENTRY F programs were used. In each of these plugs 3 to 4 high-temperature Tungsten 5% Rhenium/ Tungsten 26% Rhenium thermocouples were placed.

**Challenge 3:** To accommodate thermal sensors into practical flight structures

Our history is rooted in the thermocouple measurement of temperatures within blocks of material. Our future requires the use of whisker-like sensors to define heat transfer within shim stock. Wind tunnel heat transfer, in the past, was inferred using "thin skin models" having backface mounted thermocouples. Today we can directly measure temperature gradients within that thin skin.

The challenge is to develop more highly integrated sensors into increasingly complex and non-uniform structures without disturbing the natural heat paths of these material systems. The challenge is to transform measurements from add-on to designed-in and, in so doing, to approach the concept of a smart skin.

**Challenge 4:** To broaden the capabilities of thermal survey techniques to replace discrete gages in flight and on the ground

Thermal survey techniques have been used for 30 years to observe heat patterns on the ground and in flight. Initial wind tunnel applications of temperature paint were made in the mid 1960's. Flight test examples are documented on the X-7A<sup>16</sup> and the X-15 flight programs (figure 9) where shock interactions and boundary layer transition were observed. The reasons for those survey techniques of the 1960's still exist and although the quality and sophistication of techniques have improved, there are several challenges which remain.

Survey techniques encompass older irreversible temperature



sensitive paints and newer reversible surface coatings such as thermographic phosphors and infrared (IR) measurements. The newer survey techniques generate large amounts of data that must be acquired, stored and reduced. A challenge is the ability to handle those data efficiently. On the positive side, the effective gage density is increased by a factor of 500 and all that data is "recorded" even though only a fraction may initially be reduced.

Recall that these survey techniques measure surface temperature and not heat flux. Heat flux is derived by a thermal model which relates measured surface temperatures to the causal aerodynamic heating. Ideal thermal models are designed on the basis of one-dimensional dissipation of aerodynamic heating with the structure. More general applications of this technique will require multi-dimensional inverse analysis which is more computationally intensive.

#### GROUND TEST APPLICATIONS:

There are several un-resolved needs for survey testing in ground tests facilities. Two examples are: (1) the need to define the complex boundary layer transition front on 3D models during both aerothermodynamic studies and the longer duration studies of overall forces and moments; (2) the need to more-fully understand the complexities of internal flows dominated by shock interactions. The challenges are to broaden the range of temperature response, eliminate false signals and manage the volume of derived test data.

The range of heat transfer measurable with survey techniques is limited. These techniques are only partially useful in hypersonic facilities. The limitations of the techniques can be observed in the measurement of shock interaction regions where high gradients and an order of magnitude variation occurs between the peak heating and the undisturbed heating level. Survey techniques with limited band-width bias the heating in interaction regions to lower peak heating than are actually present. <sup>17\*</sup>

#### Transition Front Measurements:

While the accuracy of CFD techniques at high Reynolds numbers critically depends on defining the transition front as an experimental input and while that front is difficult to predict for highly three-dimensional flows, few, if any experimental studies map transition fronts as an input to CFD validation. Most force and moment studies measure only gross vehicle forces and never provide the instrumentation to state whether the boundary layer is laminar, turbulent or, most likely, some of each. Matthews et al <sup>1</sup> observes that:

---

\*To be published

"...unfortunately, the ability to predict the boundary layer state accurately - laminar versus turbulent - continues to elude the aerodynamicist".

The fundamental technology exists to observe the state of the boundary layer. The challenge is to implement that technology in the required production test facilities.

#### Internal, Shock Interaction Flows:

There are internal flows dominated by shock interaction processes. In none of these can the thermal effects be adequately defined through any practical number of discrete thermal sensors. Survey techniques are required to satisfactorily measure the thermal loads. This poses the challenge of placing the survey sensor within the restricted passage being measured and the challenge of managing the difficult, technique-peculiar errors involved in these measurements.

#### FLIGHT APPLICATIONS:

The most striking, modern application of survey techniques applied to flight vehicles is/was the use of an infrared (IR) sensor installed on the vertical tail of the Shuttle vehicle, Columbia. The overall features of this technique, its placement on the Shuttle and the views from the infrared camera are shown in figure 10.

Originally conceived in the 1970's and conceptually simple in design, this experiment has been difficult to install in the orbiter and successfully use to generate complete data. The specific technical difficulties encountered have been defined as the following:

- A protective plug over the windows that wouldn't jettison when required
- Inadequate cooling of the windows as heating levels increased during re-entry into the sensible atmosphere.
- Erratic operation of the camera scanning mechanism.
- Massive amounts of raw data that require efficient reduction

Figure 11 demonstrates the high temperatures that occur on the observation windows, temperatures that can only be numerically deduced from an extrapolation of inner pane measurements through the use of thermal modelling techniques, a supplementary challenge in thermal measurements.

Apart from these technical issues, there is a more difficult

and fundamental challenge: the interaction between the inevitable "tweaking" of a complex experiment such as this and the operational imperatives of a schedule-driven, multi-goal flight vehicle such as the Space Shuttle.

The problems are not fundamental in nature but true engineering problems of creating a flight test measurement system that works.

**Challenge 5:** To provide supporting instrumentation conduits which connect the measurement points to the thermally controlled data acquisition system

Data acquisition requires hardware from the surface measurement point back to an environmentally stabilized location on the vehicle where data transmission or on-board recording can be accomplished.

A significant challenge in making flight measurements is in implementing this chain of hardware. The material systems of the flight vehicle as well as the duration of the flight are important considerations. The Space Shuttle, by virtue of its cold structure concept, attained a benign thermal environment within inches of the point of measurement, but other possible flight configurations may not. Hot structures would create a far more difficult thermal instrumentation situation.

The X-20A (Dyna Soar), a hot structure flight vehicle concept, required 3700 feet of 1800 deg F wire and connectors to connect the 750 sensors to be placed on each flight test system. The wire of that day consisted of inconel tubing 0.090 ins OD, magnesium oxide electrical insulation inside the sheath and two electrical connectors.

These high temperature conduits can include simple thermocouple leads, regulated power lines and, possibly, fiber-optic lines. Hellbaum<sup>18</sup> proposed "...platinum films laid down on a substrate of alumina..." to define transition for flights at lower Mach numbers. Platinum films are powered resistance thermometers that require a constant current flow through the measurement film. Similarly, high temperature microphones and photodiodes were suggested for this function. Each of these gage types is electrically-powered and the difficulty of delivering that power increases as the temperature of these conduits increases.

In the 1990's these lines may include fiber-optic bundles connected to surface temperature sensors or fiber optic conduits to interrogate or observe the thermal characteristics

of a remotely located surface of interest.

Apart from conduits there is also a need for high temperature connectors to facilitate instrument replacement as well as in-line amplifiers to boost signal strength, regulators to provide precise power to surface measurements and even cooled lens systems to direct the images remotely sensed.

All of these problems are accentuated if flight duration increases and/or thermal conductors are selected as material systems. The Space Shuttle was one model of TPS and not the unique technology demonstration for future systems which must be instrumented.

**Challenge 6:** To develop a class of "vehicle tending" thermal sensors to assure the integrity of flight vehicles in an efficient manner

There have been consistent thermal problems over the past 30 years caused by uncontrolled internal flow due to leakage of boundary layer air through the flight structure. Flight configurations are not the homogeneous structures but are mechanically built-up of many separate elements held firmly in place with Sauerizen (R) or similar indispensable materials. They present many possible internal flow paths which are driven by large hypersonic pressure differences. McBride, 1983<sup>19</sup> and 1986<sup>20</sup>, termed this flow "sneak flow" as he outlined Space Shuttle experience. He concluded (1) sneak flow is important for any reusable thermal protection system (TPS) large or complex enough to require interfaces and (2) it is difficult to make quantitative predictions of sneak flow effects. Because the problem is severe and the analysis is complex, because every hypersonic flight system has demonstrated sub-surface heating and the best "sensor" to date is a discolored surface, the challenge is to create a new class of vehicle tending thermal sensors.

Vehicle-tending thermal "gages" are a new class of sensors which do not produce a point measurement of either temperature or heating rate but develop a sense of leakage through regions which, ideally, would have none. These developmental sensors monitor the health of joints and gaps determining the severity of imperfect seals.

The X-15 nose wheel door created a gap that allowed hot, boundary layer air to enter the wheel well and destroy the instrument lines located there. Figure 12 is a photograph of

that situation. The X-15 only flew at Mach 5. Figure 13 from McBride indicates the Space Shuttle penetrations including doors, gaps and coves that all could produce potentially serious sub-mold-line flows. These regions are caused by the aero-thermo-elastic effects of hypersonic flight which cannot be simulated in ground tests. They are driven by pressure differences across the produced gap and require an understanding and modeling of the sub-surface flow paths.

McBride, 1983<sup>19</sup> observed that "...penetration thermal instrumentation (on the Space Shuttle) was only adequate. More sensors were required at difficult-to-predict environment locations. Available DFI (developmental flight instrumentation) should have been more concentrated. MORE EXTENSIVE USE OF PASSIVE TEMPERATURE-SENSITIVE DEVICES COULD HAVE BEEN MADE." Of the approximately 6000 recorded measurements (about 2000 of them temperature) available on the orbital flight test orbiter, 627 were dedicated to TPS elements BUT ONLY 90 OF THOSE ARE STRICTLY RELATED TO PENETRATIONS. Table I of AIAA 83-1486 outlines in greater detail the TPS penetrations and their instrumentation.

These regions are characterized by a large seam on the vehicle which could leak at any location on that line or in that region. While point sensors could be placed in such regions, the question is where to place them and what kinds of data are required from them to define leakage.

What we require is an overall impression of whether leakage occurred and whether that leakage was significant. The challenge is to develop a sensor that achieves these goals rather than to measure temperature. The challenge is to produce better coverage with fewer sensor assignments.

One conceptual recommendation is to use ablative (or phase change) overcoat surrounding a distributed sensor. The sensing surface would create a signal proportional to the amount of the overcoat removed as a result of the temperature exceeding a defined threshold level. Perhaps an ablative coating could be applied over a fiber optic bundle through which light is being transmitted and received. In a sense, this is another application of a smart skin. This technique was also discussed by Measures, 1989<sup>21</sup>.

#### CONCLUSIONS:

The conclusions I draw from this material are:

1. The discussion of high temperature, high heat flux

measurements is contingent upon the details of the experiment proposed. Those details are (1) the type, complexity and dimensions of the material system (2) the duration of the flight experiment and (3) the selection of "add-on" or "design-in" heat gages for those measurements.

2. The technical challenges in those heat flux measurements are fundamentally two: (1) the construction of ever smaller physical thermal sensors and (2) the development of efficient inverse thermal models that relate those thermal measurements to causal heat transfer.

3. Six areas of technical challenge have been postulated. These treat the heat flux measurement problem in a broader context, the delivery of information on thermal questions to a customer. They are intended to start a discussion concerning thermal measurement technology.

Finally, a conclusion implicit in this review paper is that thermal instrumentation is an enabling technology that makes possible both flight test and ground test programs. Instrumentation should not be an after-thought of a larger systems-related program or relegated to the catalog purchase of "proven" devices (proven on the last flight vehicle). If considered early and funded adequately, instrumentaton can enable tests otherwise impossible and/or reduce the cost of even routine tests substantially. More and more temperature measurements must be designed into the developing structural component and must be considered as an integral part of that development process.

## Appendix A Add-On Thermal Gages Applied to the Space Shuttle Hardware

### A. Space Shuttle External Tank

Commercially available Schmidt-Boelter and "pill-type" heat flux sensors were installed in the insulative foam surface of the external tank. These metallic gages present a non-uniform surface temperature to the boundary layer, the gages being relatively cold and the surrounding insulator being hotter. Praharaj<sup>1</sup>, reviewing the experience, noted that severe temperature mismatch was present producing "...a large measurement error in a convective flux environment...". "...The underprediction of these island measurements was 100% or more in the peak heating region...". He further notes that these effects can be "...successfully factored out of the flight data in undisturbed regions..." but that "...temperature mismatch effects in the interference regions

are not dealt with in the existing literature and consequently were not factored out of the flight measurements...". Praharaj further notes that "...the choice of sensors for future space vehicles must consider this effect (temperature mismatch) and efforts must be made to reduce the temperature mismatch effects on the measurements...". Finally, Praharaj notes that "...temperature along with heat flux should be measured so that one can be derived from the other. This would help eliminate erroneous readings in a much easier fashion..."

The analysis of undisturbed temperature mismatch used by Praharaj was due to Westkaemper<sup>22</sup> following the expression:

$$\frac{\bar{h}(W, L)}{h(W, 0)} = F(L/W) \frac{(T_{w_1} - T_0)}{(T_{w_2} - T_0)} + H(L/W) \frac{(T_{w_2} - T_{w_1})}{(T_{w_2} - T_0)}$$

where:  $F(L/W) = \frac{5 [1 - (L/W)^{0.8}]}{4 (1 - L/W)}$

and:  $H(L/W) = \frac{5 (L/W)^{0.8}}{4 (1 - L/W)} [(W/L)^{0.9} - 1]^{8/9}$

where: L is the running boundary layer distance to the gage  
W-L is the gage width dimension  
 $T_{w_1}$  is the wall temperature of the surrounding material  
 $T_{w_2}$  is the gage surface temperature  
 $T_0$  is the recovery temperature

#### B. Space Shuttle Orbiter

Little has been written concerning the use of Schmidt-Boelter gages on the orbiter. Figure A-1 is a sketch of the installation. The sketch pre-dates the flight and may not represent actual flight hardware. Figure 4 of this paper shows data from these gages and indicates that problems exist with these gages relative to imbedded thermocouples to which they are compared.

#### C. General Comments:

Hornbaker and Rall<sup>23</sup> presented an excellent review article on this phenomenon as on many aspects of thermal instrumentation. The reader would do well to review this and the several other review papers which were written by these authors.

## APPENDIX B

### A REVIEW OF THERMOSENSING ELEMENTS AND THEIR USE IN AEROSPACE APPLICATIONS

The standard thermo-sensing elements used to measure temperatures were/are wire thermocouples. There are a series of these thermocouple material combinations available with which to measure temperatures at different temperature levels. Table II from Moffat <sup>24</sup> shows representative material pairs:

Material Designation	Temperature Limit, deg R	Output, mv/ 100 deg F
Chromel-Alumel	2290	2.20
Platinel	2650	2.20
Platinum-Rhodium	3730	0.43
Tungsten-Rhenium	4630	0.76

Note that Tungsten/Rhenium thermocouples must be placed in an inert atmosphere. "The main problems were centered around embrittlement of the Tungsten leg (of the thermocouple) and oxidation".

Tungsten thermocouples have been successfully used in high temperature flight tests by applying sheathed configurations.

High temperature gages also suffer from a progressive de-calibration (of the thermocouple) with time due either to changes in the composition of the material or changes associated with grain growth and the annealing out of the residual cold work from fabrication".

The progressive oxidation problems are eliminated through sheathing the thermocouple in a protective material. Very small sheathed thermocouples are currently available with outside diameters as small as 0.008 ins (0.2mm). One concern with thermocouple sheathing is understanding precisely the location of the thermocouple junction within the sheath. This problem, annoying for the measurement of temperature, is a critical deficiency when sheathed thermocouples are a part of a built-in heat transfer measurement system.

As small as these devices have become, the general rule of thumb is that the thermocouple assembly should have an outer diameter roughly 20% of the thickness of the material into which it is placed to avoid excessive conduction down the thermocouple wires. That would place the minimum material thickness at 0.040 inches or greater, far thicker than



anticipated applications shown by Grallert and Keller.

This problem can be circumvented by: (1) avoiding the problem by using a non-conductive thermo-sensor material (such as a fiber-optic-based thermal sensor) (2) integrating the sensor into the thermal analysis of the material, either directly through an inverse technique containing the actual structure elements that are approximately through correction factors developed to account for conduction losses down the wire.

As the temperature to be measured increases, the selection of thermocouple materials decrease as well as the output sensitivity of available thermocouple materials.

Newer thermocouple configurations are plated rather than wire. The output sensitivity of these plated thermocouples is about half that of the corresponding wires. Techniques are, in principle, available to plate extremely small and thin single and multiple thermocouples on "selected" substrate. Plated thermocouples have been studied by several groups; the Vatell heat flux gage is one attempt to use this technology in a fabricated heat gage. The major challenge is broadening the domain of applicability of these plated thermo-sensors.

#### REFERENCES

1. AIAA Paper 91-1441
2. AIAA Paper 84-1750
3. ISA Paper "The Development and testing of Development Flight Instrumentation for the Space Shuttle Thermal Protection System", ISBN 87664-407-8
4. Aerotherm Corp. Report 75-135, 1975
5. NASA CR 179074
6. NASA CP 2283
7. AIAA Paper 83-0482
8. AIAA Paper 84-1763
9. ASME Paper 81-ENAs-13
10. AIAA Paper 84-0224
11. AIAA Paper 82-0944
12. AIAA Paper 87-1508
13. AIAA Jour. Aircraft, V 28, Nr. 6, pp 410-416
14. Rech. Aerosp. 1991-1, pp 67-71 (English Version)
15. Rech. Aerosp. 1991-4, pp 51-68 (English Version)
16. WADD TR 60-567, p 239
17. ASD TR 92-xxx
18. AIAA Paper 88-4651A
19. AIAA Paper 83-1486
20. AIAA Paper 86-1261
21. "Smart Skins with Nerves of Glass", Progress in Aerospace Sciences, V 26, pp 289-351
22. Jour. Aero. Sci, 11/61, pp 907-908
23. ISA Preprint 8.3.63
24. Moffat, R.J., International Heat Transfer Conference, 1982

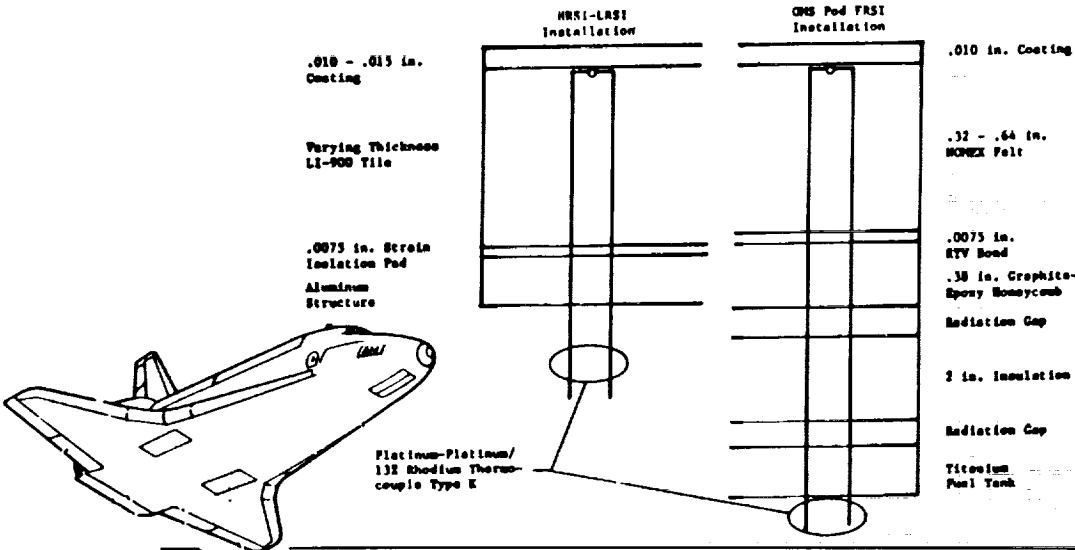


Figure 1, Space Shuttle Thermal Instrumentation

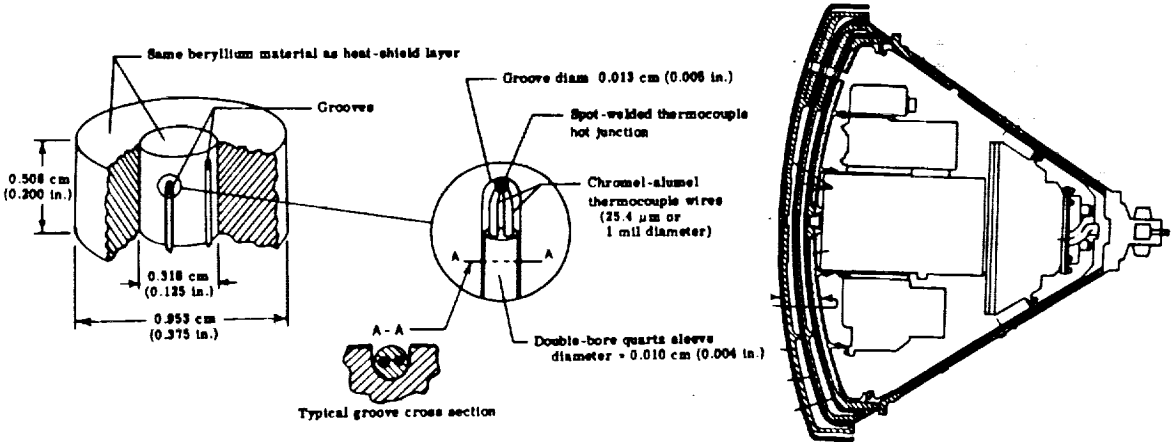


Figure 2, NASA FIRE Project Thermal Instrumentation

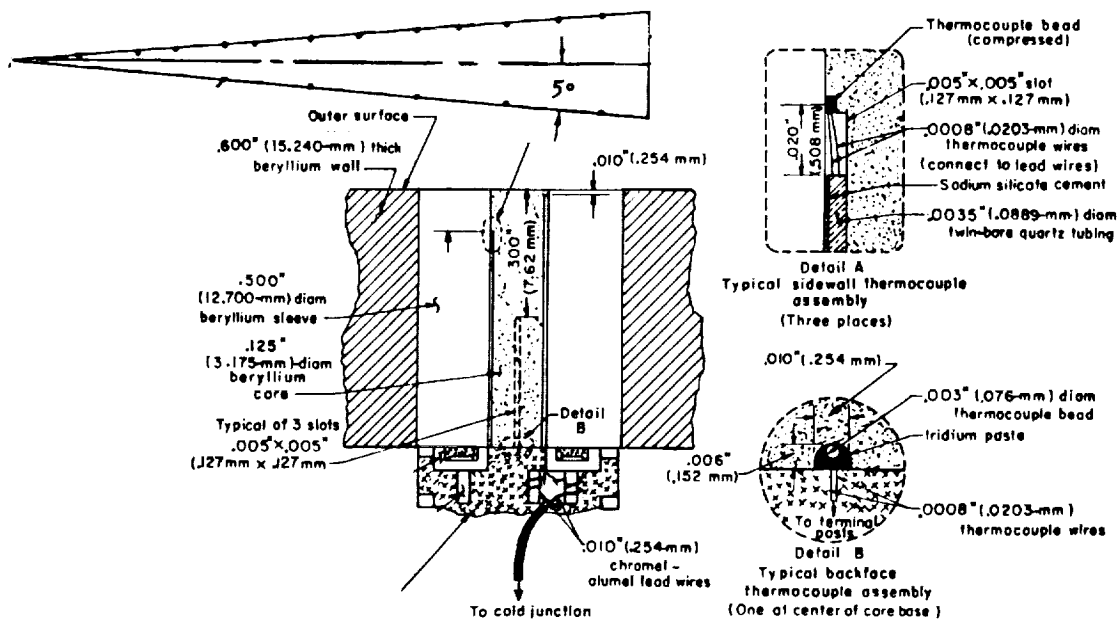


Figure 3, NASA Re-entry "F" Project Thermal Instrumentation

Gross difference is due to uncertain depth of thermocouple below the outer mold line.

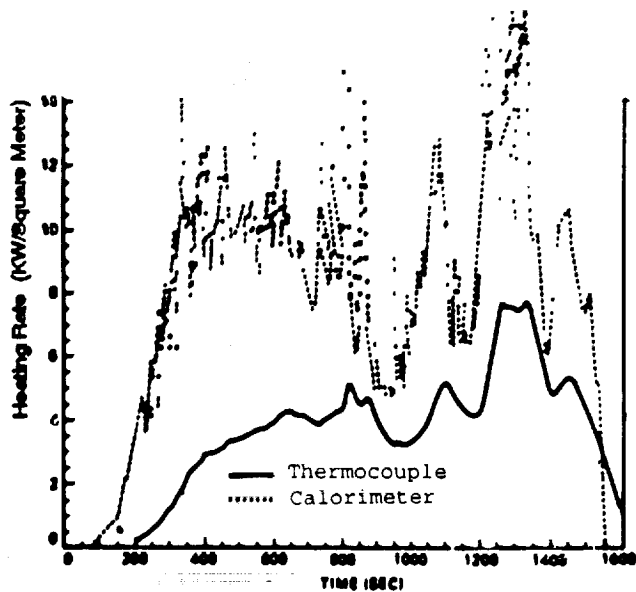


Figure 4, Difference Between Calorimeter and Thermocouple-Based Heat Transfer Inference

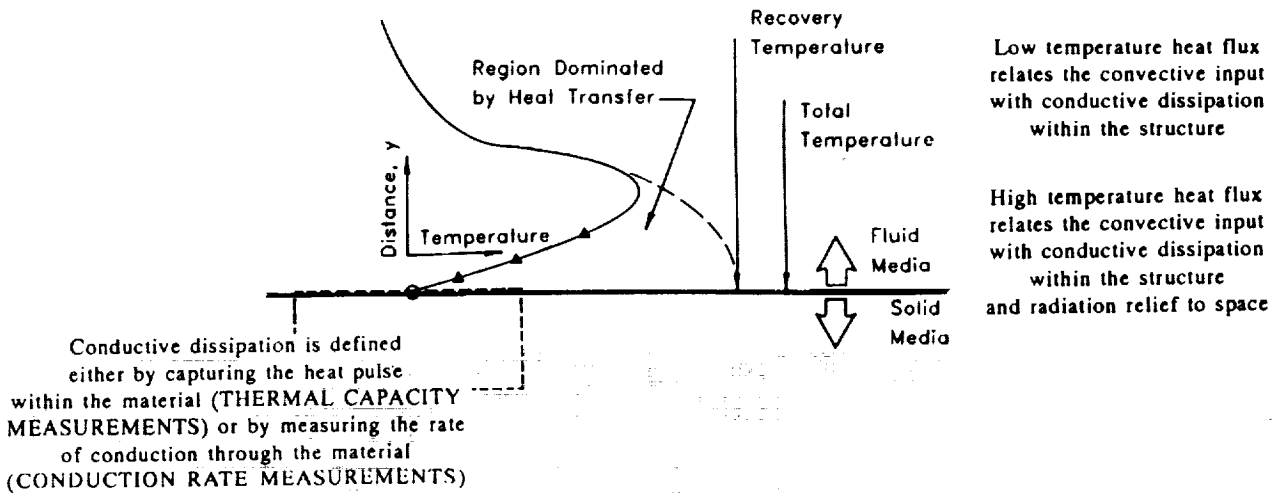


Figure 5, The Process of Heat Transfer Rate Inference

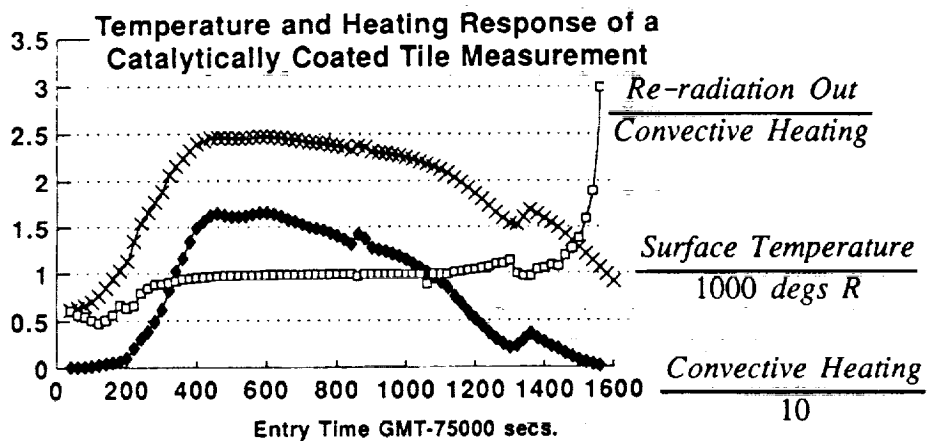


Figure 6, Temperature and Heating Response of a Catalytically Coated Tile Measurement on the Space Shuttle

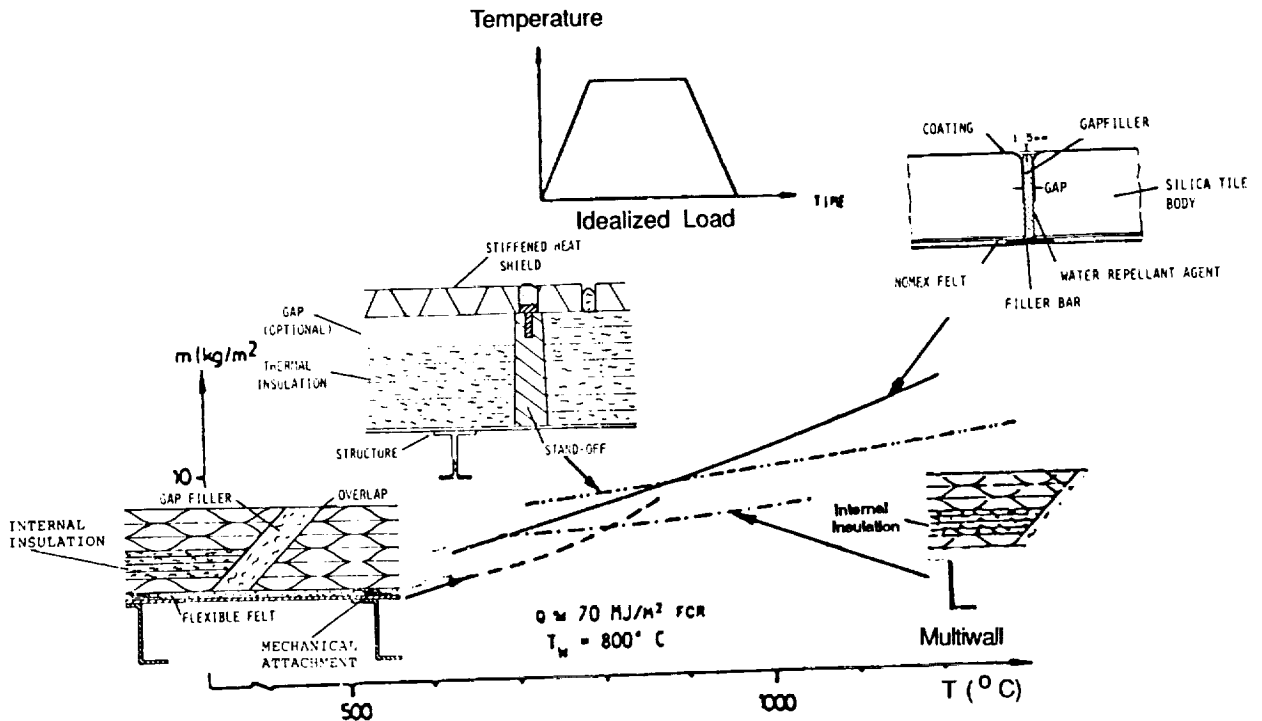


Figure 7, Trend of TPS Mass Per Area vs Temperature for Representative TPS Candidates from Gallert and Keller

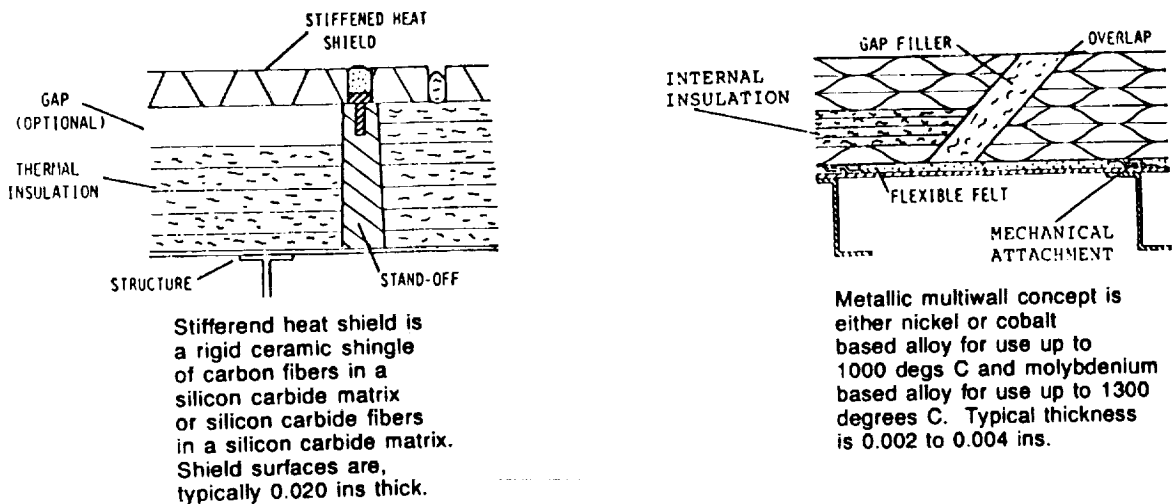


Figure 8, Details of the Scale of Proposed TPS Systems from Gallert and Keller

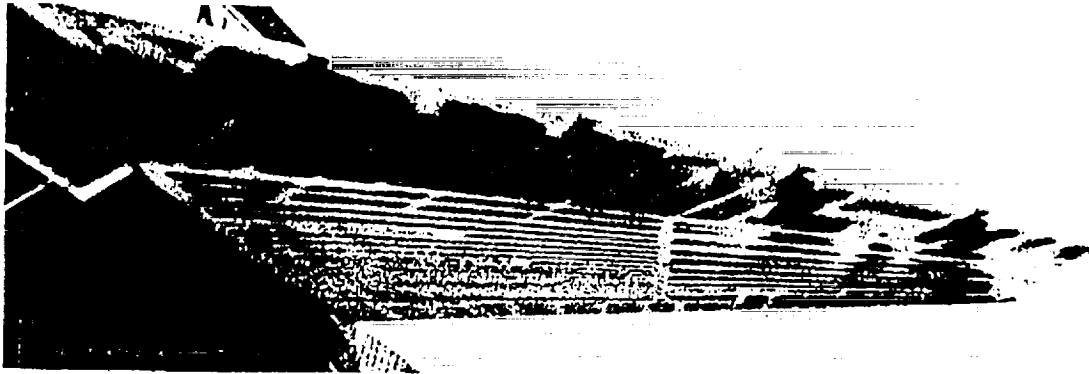


Figure 9, Early Use of Temperature Sensitive Paint on the X-15

(Original figure unavailable)

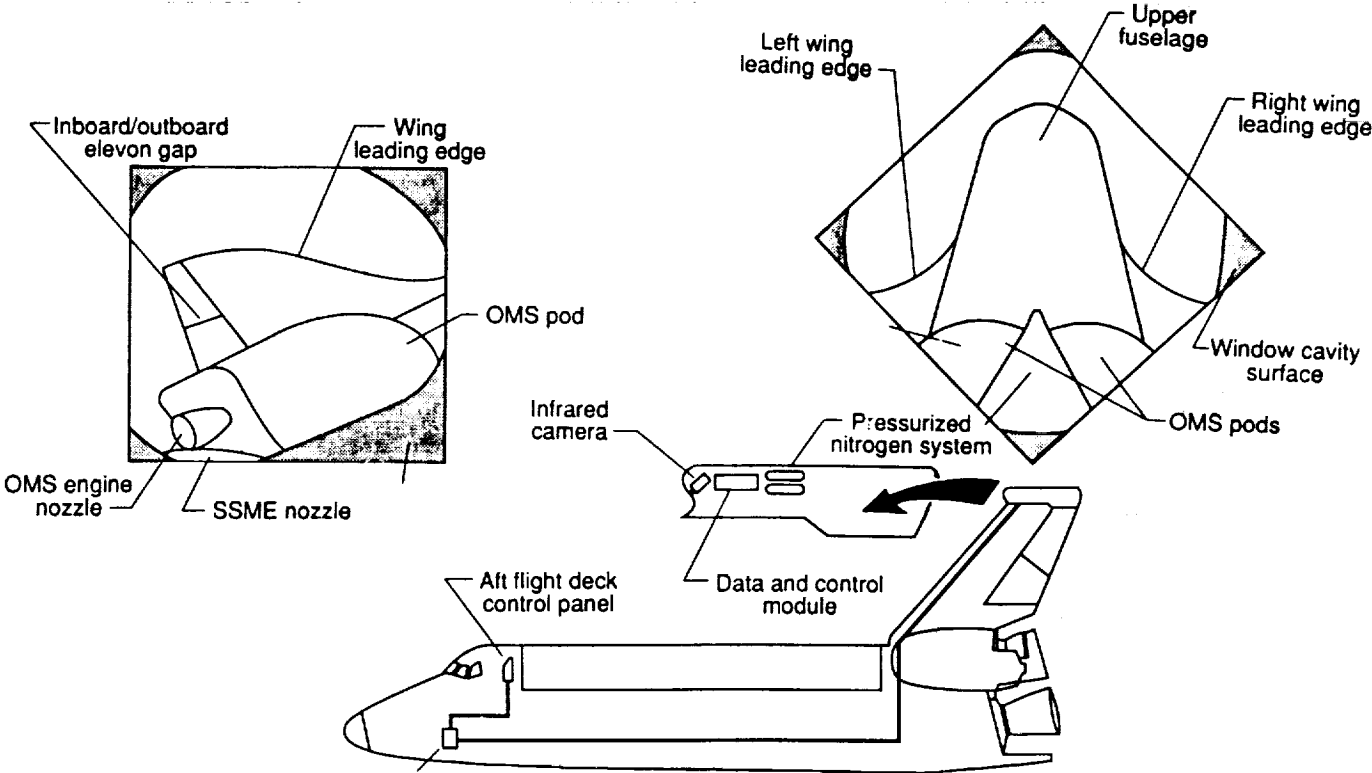


Figure 10, Overall View of the IR Flight Experiment on the Space Shuttle Flight Vehicle, Columbia

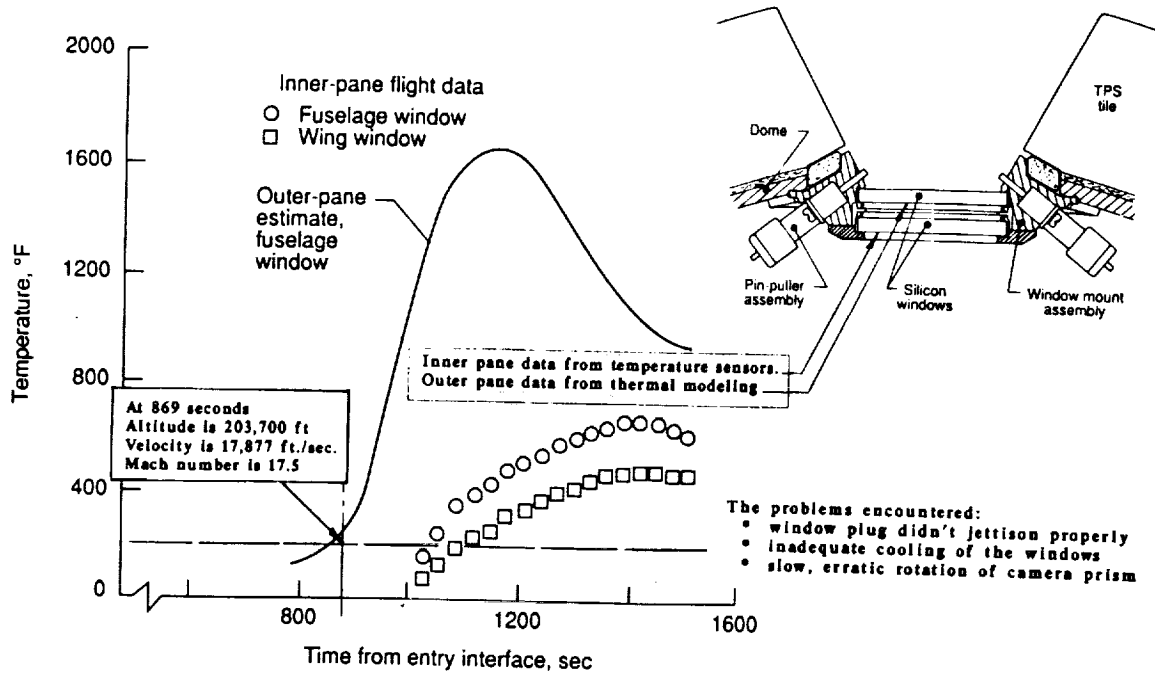


Figure 11, Discussion of the Problems in the IR Flight Experiment

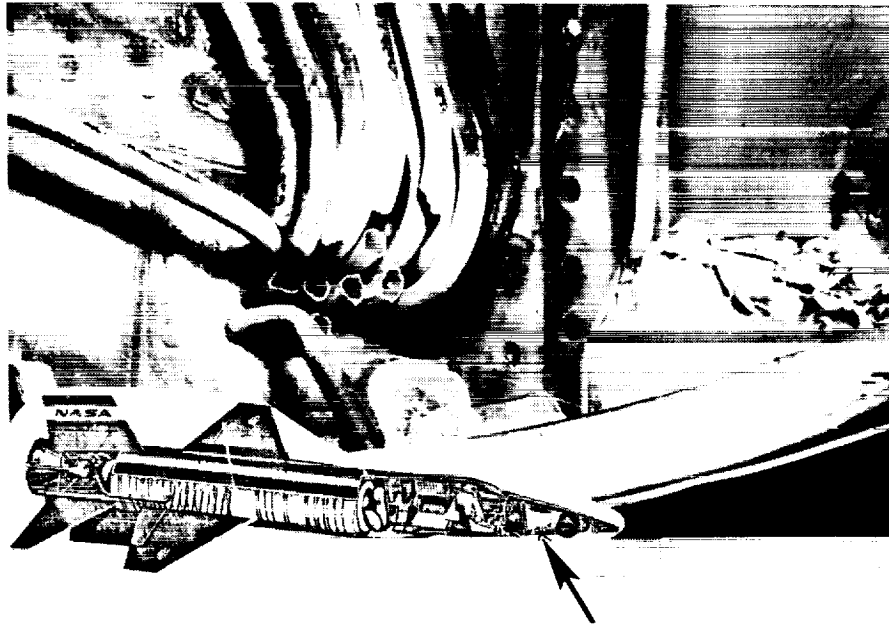


Figure 12, Example of "Sneak Flow" in the X-15 Nose Wheel Cavity

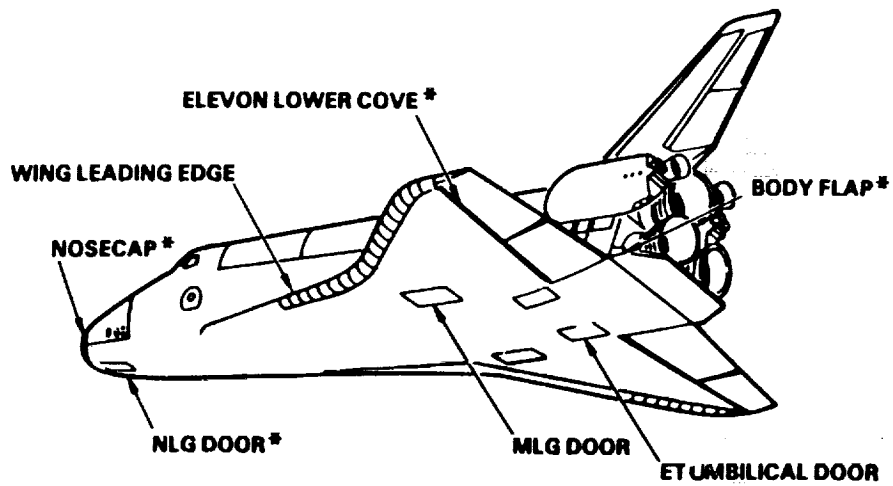


Figure 13, Penetrations on the Space Shuttle Orbiter



HIGH HEAT FLUX MEASUREMENTS AND EXPERIMENTAL CALIBRATIONS/CHARACTERIZATIONS\*

C. T. Kidd\*\*

Calspan Corporation/AEDC Operations  
 Arnold Engineering Development Center  
 Arnold Air Force Base, Tennessee 37389

ABSTRACT

Recent progress in techniques employed in the measurement of very high heat-transfer rates in reentry-type facilities at the Arnold Engineering Development Center (AEDC) is described. These advances include thermal analyses applied to transducer concepts used to make these measurements; improved heat-flux sensor fabrication methods, equipment, and procedures for determining the experimental time response of individual sensors; performance of absolute heat-flux calibrations at levels above 2,000 Btu/ft<sup>2</sup>-sec (2.27 kW/cm<sup>2</sup>); and innovative methods of performing in-situ run-to-run characterizations of heat-flux probes installed in the test facility. Graphical illustrations of the results of extensive thermal analyses of the null-point calorimeter and coaxial surface thermocouple concepts with application to measurements in aerothermal test environments are presented. Results of time response experiments and absolute calibrations of null-point calorimeters and coaxial thermocouples performed in the laboratory at intermediate to high heat-flux levels are shown. Typical AEDC high-enthalpy arc heater heat-flux data recently obtained with a Calspan-fabricated null-point calorimeter installed in a generic flow-field probe model are included.

NOMENCLATURE

- a Radius of null-point cavity, in.
- b Distance from front surface of null-point calorimeter to the null-point cavity, in.
- C<sub>p</sub> Specific heat capacity, Btu/lb-°F
- d Diameter of null-point cavity, in.
- K Thermal conductivity, Btu/in.-sec-°F
- k Thermal diffusivity, in.<sup>2</sup>/sec
- L Length of null-point calorimeter, in.

- l Distance from top surface of semi-infinite solid, or thickness of finite thickness slab, in.
- q̇ Calculated or measured heat flux or heat-transfer rate, Btu/ft<sup>2</sup>-sec
- q̇<sub>0</sub> Constant heat flux or heat-transfer rate, Btu/ft<sup>2</sup>-sec
- R Radial distance from axial centerline of TRAX analytical model, in.
- r Radial distance from axial centerline of null-point cavity, in.
- T Temperature, °F
- T<sub>b</sub> Temperature on axial centerline of null point, °F
- T<sub>s</sub> Temperature on surface of null-point calorimeter, °F
- t Time, sec
- x Distance in axial direction from bottom surface of finite thickness slab, in.
- Z Distance in axial direction of TRAX analytical model, in.
- ρ Density, lb/in.<sup>3</sup>

Subscripts

- b At null-point surface
- s Surface conditions
- o Initial conditions

INTRODUCTION

Recent national test programs such as the National Aero-Space Plane (NASP) have demonstrated the requirement to measure very high heat flux, possibly as high as 80,000 Btu/ft<sup>2</sup>-sec (90.8 kW/cm<sup>2</sup>). Aerospace simulation facilities such as high-enthalpy arc-driven wind tunnels have been used to produce reentry-type aerothermal test environments.

\* The research reported herein was performed by the Arnold Engineering Development Center (AEDC), Air Force Systems Command. Work and analysis for this research were done by personnel of Calspan Corporation/AEDC Operation, operating contractor for the AEDC aerospace flight dynamics facilities. Further reproduction is authorized to satisfy needs of the U. S. Government.

\*\* Principal Engineer, Member ISA.

Probably the most important parameter to be considered in reentry is the stagnation point aerodynamic heating rate. Heat flux in these facilities can exceed 25,000 Btu/ft<sup>2</sup>-sec (28.4 kW/cm<sup>2</sup>) and pressures can reach 160 atm. The experimental determination of these heat-flux levels has always presented a difficult challenge to the measurement engineer. Measurement of heat flux at the stagnation position of simple test model configurations (usually sphere cones) is required to determine the facility flow conditions, since stagnation temperature measurements are not possible with conventional intrusive probes because of the extremely high temperatures (7,500° F) in the flow field. The test environment is usually so harsh that very few of the commonly used discrete heat-flux transducers can survive even short exposures in the test medium. Even the more rugged sensors often experience surface ablation before a meaningful measurement can be made. Exposure times of 50 to 100 msec are typical. This leaves the measurement engineer few practical choices in the development of an effective transducer for this application.

The transducer most commonly used to measure high heat-flux levels in high pressure, arc-heated flow-field environments is the null-point calorimeter.<sup>1-4</sup> Other devices such as coaxial surface thermocouples,<sup>5-8</sup> Gardon gages,<sup>9</sup> and slug calorimeters<sup>10</sup> have been used with varying degrees of success. Each of these has shortcomings which limit their effectiveness in this measurement application. The null-point concept has been used extensively in this application because of its relatively simple principle of operation, adequate time response, and time to burnout. In 1977 the American Society for Testing and Materials (ASTM) officially adopted the null-point calorimeter as a "Standard Method for Measuring" in this application and reapproved this method in 1990.<sup>11</sup> The first application of the null-point calorimeter in an arc-heated flow field involved installing the device in the stagnation position of a probe model such as a sphere-cone and locating the probe on the axial centerline of an arc jet.<sup>2</sup> The nosetip was often protected by a Teflon® cap which was ablated away in a fraction of a second after the arc was ignited. This method had several obvious deficiencies which included the following:

1. Measurements were made at only one location in the flow field;
2. The probe could only be used for one run because of severe nosetip ablation and ultimate destruction; and
3. Significant differences in the indicated heat-flux levels from different null-point calorimeters were commonplace.

As early as 1971, Kennedy, et al.,<sup>3</sup> began using a swept technique for heat-transfer measurements in the Acurex/Aerotherm arc facility. This technique involved installing one or more null-point probe models on a rake and sweeping them through the arc-heated flow field at a rate slow enough to allow the sensor to make accurate measurements, yet fast enough to prevent model ablation. This method has the advantages of measuring the heat-flux profile across the entire jet and preserving the probe/sensor for repeated measurements. Nearly every arc facility making heat-flux measurements with null-point calorimeters has adopted the swept probe method.

Although used by many experimenters and having been developed a relatively long time, the operating principles and the effects of variations in physical dimensions are not well understood in the aerothermodynamic test community. This paper provides comprehensive thermal analyses of the null-point calorimeter concept with emphasis on the effects of variations in the physical dimensions. Some of the common prevailing perceptions about null-point calorimeters are shown to be incorrect. Laboratory experimental data which complement the thermal analyses are shown.

A common misconception prevalent among null-point calorimeter users and suppliers is that it is not possible to provide meaningful experimental time response and calibration data at heat-flux levels close to the measured values in the laboratory. There are only two known commercial sources of null-point sensors, and neither provides meaningful transient time response or calibration data. Since the time response of null-point calorimeters is marginal for arc facility heat-flux measurement applications, an experimental determination of this parameter is essential for accurate measurements. Methods have been developed at the AEDC to provide these data on a routine basis in the laboratory. The experimental apparatus/system which was developed to provide these data is described in this paper and graphical illustrations of typical experimental data are also included.

A unique method of providing run-to-run calibrations and characterizations of null-point sensors in the test area through the facility data acquisition and processing system has been developed and implemented. Experimental data from this system are also included in this paper.

Another sensor extensively used in high heat-flux measurement applications is the Chromel®-constantan coaxial surface thermocouple. Although the coaxial thermocouple has very fast time response,

excellent durability, and contourability, this sensor has one limiting factor which precludes its use in very high heat-flux measurement applications. The value of the lumped thermal parameter of interest (primarily thermal conductivity) of Chromel and constantan is only about 20 percent that of copper. This causes the surface temperature of the coaxial thermocouple to rise almost five times faster than a copper null-point sensor. This is a detriment in very high heat-flux measurement applications because of its shorter time to burnout (ablation). However, the Chromel-constantan sensor can be used in slightly higher ( $\approx 2,200^{\circ}\text{F}$ ) temperature environments than copper ( $\approx 2,000^{\circ}\text{F}$ ) materials. Chromel-constantan sensors can normally be used in applications involving stainless steel materials.

In the aerothermodynamic test community, increasing demands are being made to obtain more heat-transfer data in each succeeding wind tunnel test. Normally, these are low to intermediate ( $< 1,000$  Btu/ft<sup>2</sup>-sec) measurement applications. This often translates into leaving the test article in the tunnel flow for longer periods of time. As a result of this practice, surface temperature data are obtained with coaxial surface thermocouples for periods of time which exceed the limits defined by semi-infinite solid restrictions. Therefore, another method of data processing must be used. One of these is a one-dimensional finite difference heat conduction code developed by E.O. Marchand<sup>12</sup> for calculations on a finite length body. This heat conduction code is being investigated at the AEDC as a possible replacement for the semi-infinite equations under appropriate test conditions. This paper contains limited results of analytical evaluations of the finite difference code in heat-transfer measurement applications.

### NULL-POINT CONCEPT

Figure 1 is a sketch of the null-point concept of heat-flux measurement. The sketch is a physical illustration of a thermal mass of length  $L$  with a flat bottom cylindrical hole of radius  $a$  drilled from the backside of the mass to within a distance  $b$  of the front surface. The location  $0, b$  on the radial centerline of the cylindrical cavity is defined as the null point. A transient backside temperature  $T_b(0, b, t)$  measured at the null point is assumed to be identical to the surface temperature history  $T_s(r, 0, t)$  on the outside surface of the same thermal mass in the absence of the cavity. Therefore,

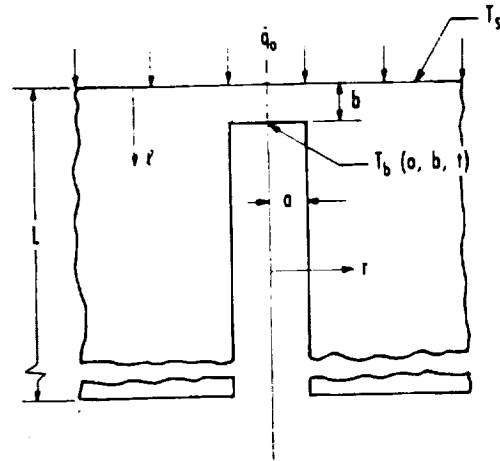


Fig. 1. Concept sketch of null-point calorimeter.

the temperature history measured at the null point could be inserted into a one-dimensional inverse heat conduction equation for a semi-infinite solid to determine the heat-transfer rate at the surface of the solid.

### PRACTICAL IMPLEMENTATION OF CONCEPT

A section view sketch of a null-point calorimeter showing all important components and the physical configuration of the sensor is shown in Fig. 2. The outside diameter is 0.093 in., the length is 0.40 in., and the body material is oxygen-free high conductivity (OFHC) copper. Temperature at the null point is measured by a 0.020-in.-diam ANSI type K stainless steel-sheathed thermocouple with 0.004-in.-diam thermoelements. Although no thermocouple attachment is shown, it is assumed that the individual thermocouple wires are in perfect contact with the backside of the cavity and present no added thermal mass to the system. Note that the null-point body has

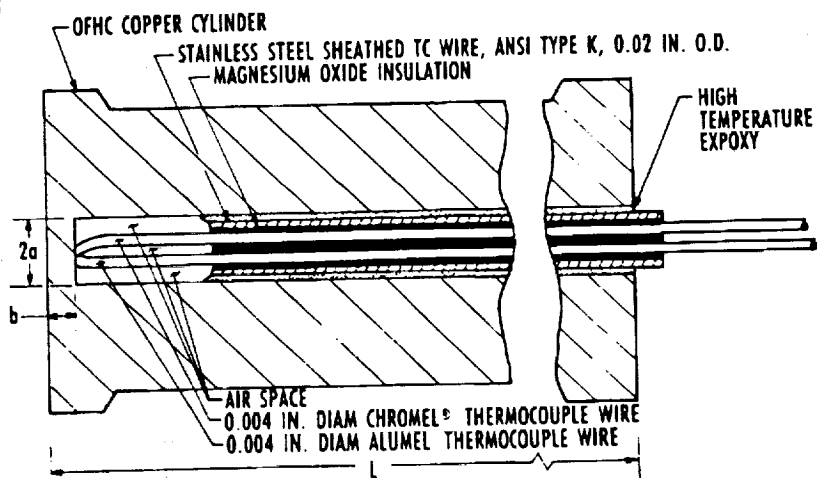


Fig. 2. Section view of null-point calorimeter assembly no scale.

a slight chamfer at the top and bottom which creates an effective circumferential dead air space along the length of the cylinder to enhance one-dimensional heat conduction and prevent radial heat conduction. For aerodynamic heat-transfer measurements, the null-point sensors are generally pressed into the stagnation position of a sphere cone model.

### THERMAL ANALYSIS

Results of thermal analyses presented in this paper were obtained with a finite-element heat conduction code called TRAX<sup>13</sup> which is used to perform transient analyses on axisymmetric bodies. Many heat-transfer problems can be geometrically configured by axisymmetric bodies, thus providing the capability for performing the analyses in three dimensions. This analytical method is practically implemented by designing a plane geometry matrix which simulates the aerodynamic configuration of interest, consisting of a number of finite elements. These elements are usually, but not exclusively, rectangles with nodal points specified at each of the four corners. Constant heat flux, heat-transfer coefficient, and temperature boundary conditions can be specified between any two nodal points on the analytical model. Different time steps can be specified in

the same problem, and different boundary conditions and thermal properties may be specified for each time interval. A tabulated temperature history at each nodal point on the analytical model is provided by the TRAX computer program.

The finite-element model used to represent the null-point calorimeter in this paper is shown by the block diagram in Fig. 3. This geometry has 793 finite elements and 879 nodal points. This block diagram sketch is not to scale. Finite-element numbers are shown within the blocks and nodal point numbers are shown on the sides of the blocks. Because of space limitations and clarity in presentation, only a small number of the finite elements, nodal points, and dimensions are illustrated on the block diagram in Fig. 3. The axisymmetric model is achieved by rotating the plane geometry sketch around the axial centerline shown on the left-hand side of the sketch. Note the "open window" beginning with nodal points 313 to 315 near the top of the model and ending with nodal points 807 to 809. This window represents the circumferential dead air space on a null-point calorimeter installation. All material to the right side of the air space is considered to be model material, also OFHC copper. The physical dimensions of the null-point cavity shown in Fig. 3 are considered by

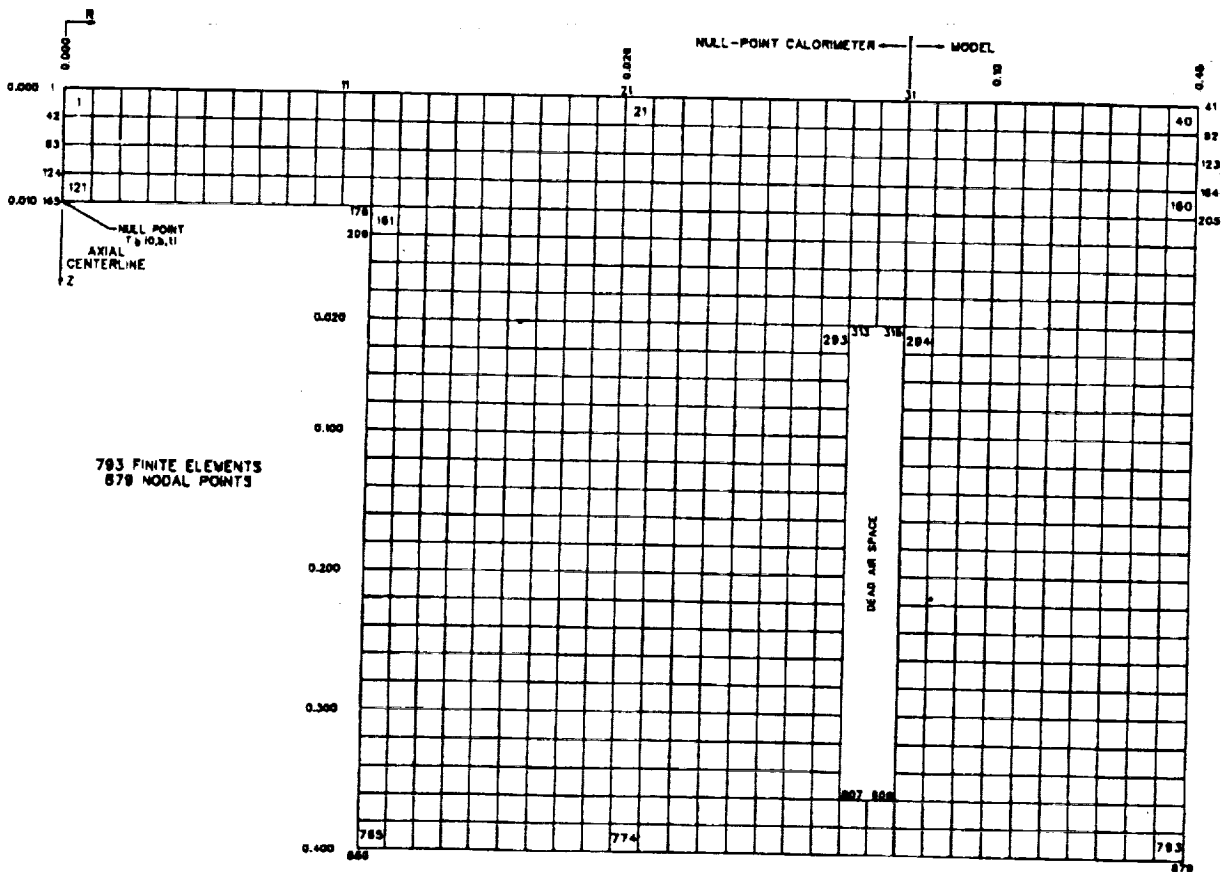


Fig. 3. TRAX model of null-point calorimeter.

some<sup>2,11</sup> to be the ideal geometry with the parameter  $a/b = 1.1$  ( $a = 0.011$  in. and  $b = 0.10$  in.). Note the dimensions shown on the perimeter of the sketch. These dimensions are frequently changed to show the effects of geometrical changes.

**Effects of Changes in Dimensional Parameters** — According to the majority of analysts and/or experimenters quoted in the open literature,<sup>2, 3, 11</sup> the optimum value of the ratio of null-point calorimeter cylindrical cavity radius  $a$  to the copper thickness above the cavity is stated to be between 1.0 and 1.1. Analytical results presented in this paper do not support that position. First, a statement defining the term "optimum" with regard to the performance of the sensor is needed. An optimum value of the parameter  $a/b$  is defined as a value which yields the fastest time response to a step heat-flux input and maintains a constant value of indicated  $\dot{q}/\text{input } \dot{q}$  ( $\dot{q}/\dot{q}_0$ ) after the initial time response period. The analytical results do not necessarily have to give a value of  $\dot{q}/\dot{q}_0 = 1.0$ , since this difference can be experimentally calibrated in the laboratory.

Figures 4 and 5 show analytical time response data for several null-point calorimeter geometries. In both illustrations, the radius  $a$  of the cylindrical cavity is held constant and the thickness  $b$  of the copper above the cavity is varied. A timewise temperature history  $T(t)$  at the back centerline nodal point (#165, see Fig. 3) was calculated by the TRAX program. Data were computed at 0.0002-sec intervals. The timewise temperature history at this nodal point was input to the numerically represented one-dimensional inverse heat conduction equation shown as Eq. (1),

$$\dot{q}(t) = \frac{2(\rho C_p K)^{\frac{1}{2}}}{\pi^{\frac{1}{2}}} \left[ \sum_{i=1}^n \frac{T_i - T_{i-1}}{(t_n - t_i)^{\frac{1}{2}} + (t_n - t_{i-1})^{\frac{1}{2}}} \right] \quad (1)$$

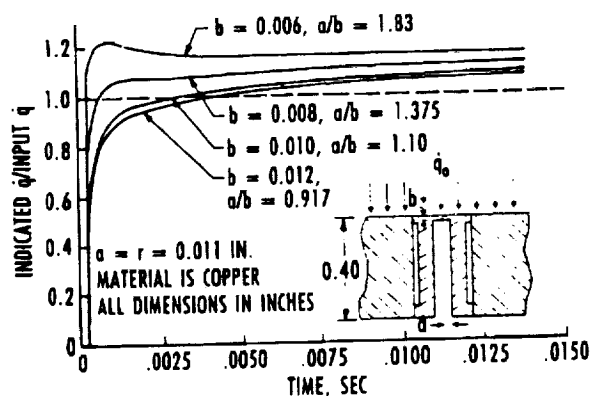


Fig. 4. Null-point calorimeter analytical time response data.

where  $\rho$ ,  $C_p$ , and  $K$  are the density, specific heat, and thermal conductivity, respectively, of the OFHC copper casing. Equation 1 is a short-form version of the Cook and Felderman equation<sup>14</sup> developed by Don Wagner of Sverdrup Technology in 1974. Figure 4 illustrates the time response of a null-point calorimeter of radius  $a = 0.011$  in. as the copper thickness  $b$  is varied from 0.006 to 0.012 in. in 0.002-in. increments. This resulted in a variation in  $a/b$  from 1.83 to 0.917. From the data illustrated on Fig. 4, it is apparent that the greater thicknesses generally result in slower time responses. It is also apparent that the indicated  $\dot{q}/\text{input } \dot{q}$  ( $\dot{q}/\dot{q}_0$ ) asymptotes are above 1.0 even for the lower values of  $a/b$ . The illustration of the case for  $a/b = 1.375$  ( $b = 0.008$  in.) seems to be optimum in that the time to 95 percent of full scale is reached in less than 1 msec and the asymptote for  $\dot{q}/\dot{q}_0$  approaches 1.1. The case for  $a/b = 1.83$  ( $b = 0.006$  in.) results in a 23-percent overshoot of  $\dot{q}/\dot{q}_0$ , tapering down to an asymptote of 1.15. Even though a fast response is realized with this configuration, the overshoot should be avoided, since it indicates an unrealistic value of  $\dot{q}/\dot{q}_0$  at the beginning of the process. Although not illustrated as in this paper, this type of overshoot has been reported by other analysts.<sup>2</sup>

Figure 5 is an illustration of null-point calorimeter time response data when the radius is held constant at a value of  $a = 0.00825$  in. and the thickness  $b$  is allowed to vary from 0.002 to 0.010 in. The optimum value of  $a/b$  shown on Fig. 5 occurs at the same  $a/b$  ratio as it did on Fig. 4; i.e.,  $a/b = 1.375$ . When the value of  $a/b$  was increased to 4.0, as shown on Fig. 5, this produced a very high value of  $\dot{q}/\dot{q}_0$  early in the run time. This thermophysical phenomenon is caused by a thin copper foil above the null-point cavity. This type of overshoot has been observed with a small number of commercial units in laboratory experiments and in units fabricated by Calspan to intentionally

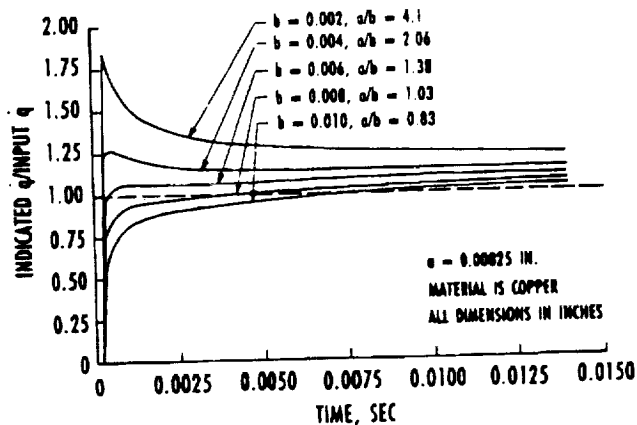


Fig. 5. Null-point calorimeter analytical time response data.

exhibit this type of behavior. Laboratory experimental data which show this effect are presented in the Experimental Considerations section.

Based primarily on a time response criterion, it appears from the analytical data presented in this paper the optimum value of the ratio of the cylindrical cavity radius to the thickness above the cavity ( $a/b$ ) is 1.375. This value is slightly higher than reported by other analysts.

**Effect of Locating the Temperature Sensor Off the Axial Centerline** — The data obtained from thermal analyses performed on the null-point concept shown to this point assume that the temperature sensor was located on the axial centerline of the cylindrical cavity. This section is concerned with the effect of locating the temperature sensor off the axial centerline. Figure 6 shows that placement of the temperature sensor at a location of up to  $r_0/a = 0.5$  will cause an error of less than 3 percent. This result is usually acceptable and adds credibility to the null-point concept in that a strict centerline location of the thermoelements is not essential to obtain high-quality data.

**Effective Run Time** — Effective run time is an important parameter when the null-point calorimeter is used for heat-flux measurements. Since the inverse heat conduction relationship for a semi-infinite solid is used to obtain data from the null-point sensor, the semi-infinite solid limitations apply in data processing. These limitations primarily involve the length of the null-point calorimeter and the time over which data are to be obtained. An exact temperature history calculated from the relationship for a solid of finite length<sup>15</sup> was inserted into the numerical heat-flux solution for a semi-infinite solid to produce the normalized error curve shown in Fig. 7. This relation-

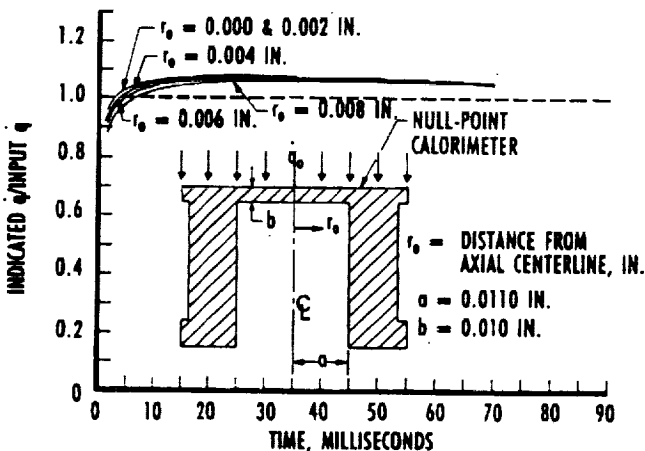


Fig 6. Effect of locating temperature sensor off axial centerline.

ship was developed by the author and has been reproduced by others.<sup>6,7</sup> Figure 7 illustrates that the following relationship [Eq. (2)] must be true to ensure that the error in indicated heat flux does not exceed one percent:

$$\frac{L}{(kt)^{1/2}} \leq 1.8 \quad (2)$$

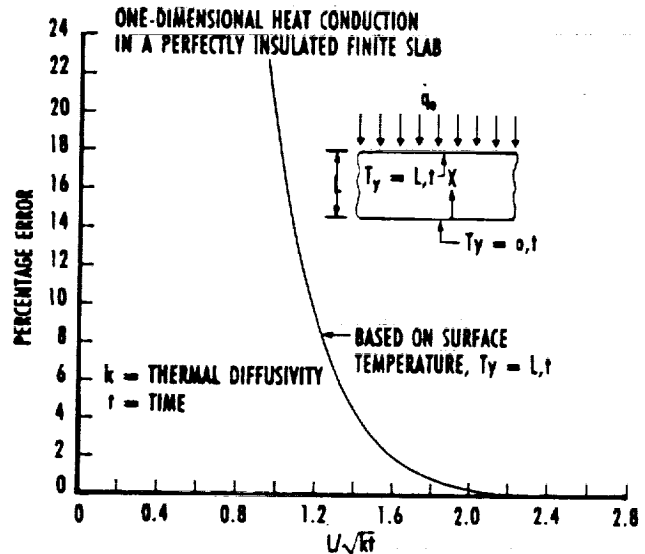


Fig. 7. Errors in indicated heat transfer rate incurred by assuming semi-infinite solid behavior for a finite length slab.

where  $L$  is transducer length,  $k$  is thermal diffusivity, and  $t$  is time from initial heating. For a copper null-point calorimeter of length,  $L = 0.4$  in., the effective run time is 0.28 sec. This result is substantiated by the TRAX heat conduction code as shown in Fig. 8. Although the normalized value of indicated  $\dot{q}/\text{input } \dot{q}$  is 1.07 rather than 1.0, the reader can see that the value reaches 1.08 in less than 0.30 sec.

**Effects of Variations of Thermal Properties with Temperature** — The value of the lumped thermal parameter of copper is not a strong function of temperature. In fact, the value of  $(\rho C_p K)^{1/2}$  of OFHC copper increases only 5 percent over 1,000°F.<sup>16</sup> Thermal properties of OFHC copper are well documented and data from different sources are in good agreement. Because the  $(\rho C_p K)^{1/2}$  parameter of copper is relatively constant over a wide temperature range, most experimenters use the room temperature value of the parameter in processing data from null-point calorimeters. However, the variation in the lumped thermal parameter, as obtained from reliable handbook data, can easily be programmed into appropriate data processing relationships.

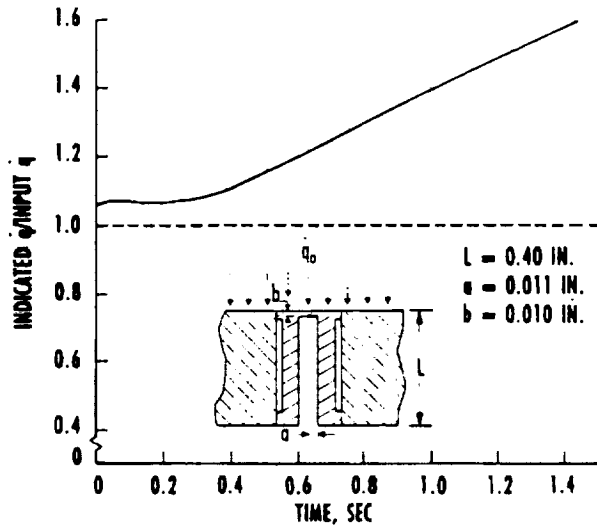


Fig. 8. Effect of heating null-point calorimeter past semi-infinite solid run time.

### COAXIAL SURFACE THERMOCOUPLE

#### DESCRIPTION

A coaxial surface thermocouple begins with a small diameter thermoelement wire coated with a thin ( $\leq 0.0005$  in.) layer of special ceramic insulation (usually MgO) which is capable of withstanding temperatures up to  $3,000^{\circ}\text{F}$ . This inner wire with insulation is swaged into an outer tube of another compatible thermoelement material. The final assembly is effected by drawing the three-component unit (wire, insulation, and tube) down from an initial outside diameter of about 0.125 in. to a final diameter as small as 0.015 in. The coaxial thermocouple assembly is completed by attaching thermocouple lead wires to the coaxial thermoelements and slipping a transition fitting with high-temperature potting over the lead wires. This operation requires special equipment and "hands-on" experience. This applies to thermocouple materials, body length and diameter, lead wires, and transition fitting. Finally, the hot junction is completed by abrading the center conductor and outer tube together with #180 grit emery paper. A sketch of the coaxial thermocouple installation purchased commercially and used at the AEDC is shown in Fig. 9.

The principle of operation of the coaxial surface thermocouple<sup>6,7,8</sup> is similar to that of the null-point calorimeter. In fact, the primary difference is that with the null-point calorimeter an assumption is made that the measured temperature history is the surface temperature; whereas, with the coaxial surface thermocouple, this is a fact. A normal qualifying assumption with the coax TC is that the entire assembly behaves as a homogeneous, semi-infinite solid. This includes the model material as well as the

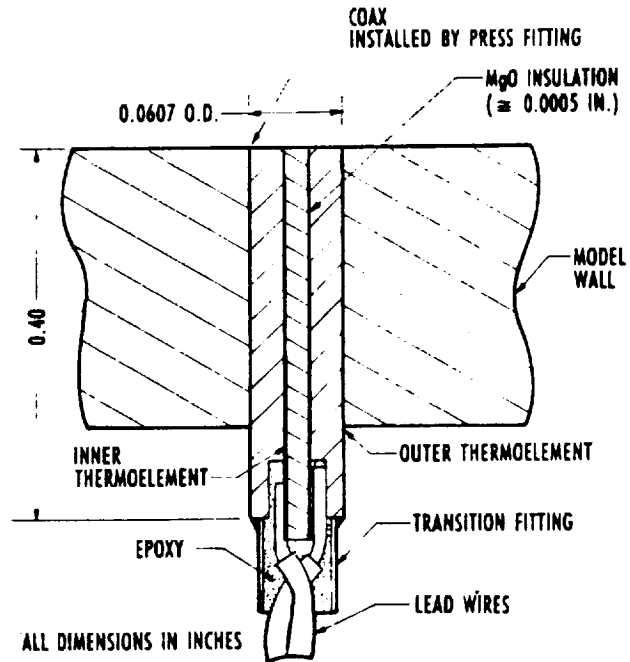


Fig. 9. Sketch of coaxial surface thermocouple installation.

thermoelements. The equation normally used to extract timewise heat-flux data from the coaxial thermocouple was shown earlier in this paper as Eq. 1.

Recently, a finite difference heat conduction code<sup>12</sup> has been used at the AEDC to obtain accurate timewise heat-flux data well beyond the time constraints of semi-infinite solid theory. This analytical code will be briefly described in the next section of this paper. Obviously, [from Eq. (1)] a close match of the lumped thermal parameter  $(\rho C_p K)^{1/2}$  of the thermoelements is necessary so that an analytical scale factor can be assumed for these sensors. Fortunately, there is a commonly used thermocouple pair whose thermoelements have  $(\rho C_p K)^{1/2}$  parameters which, at room-temperature, ambient conditions, are within 1 percent of the same value (see Table 1).

Table 1. Lumped Thermal Property Data for coaxial thermocouple and model materials.

MATERIAL	$(\rho C_p K)^{1/2}$ , $\text{Btu/ft}^2 \text{-sec}^{1/2} \text{-}^{\circ}\text{F}$
CHROMEL	0.410*
CONSTANTAN	0.408
300 SERIES STAINLESS STEEL	0.396

\* ALL DATA OBTAINED AT ROOM TEMPERATURE AMBIENT CONDITIONS.

This thermocouple pair is Chromel-constantan (ANSI type E), which also has a higher thermoelectric sensitivity than any of the common thermocouples.<sup>6</sup> Another requirement is that the model or heat sinking material also have a lumped thermal parameter which matches that of the coaxial sensor materials. This requirement is not hard to satisfy in the majority of cases. Most of the 300-series stainless steels and 17-4 stainless have a lumped thermal parameter less than 10-percent different than the Chromel-constantan coaxial thermocouple. These facts make the coaxial surface thermocouple installed in stainless models a good choice for fast-response wind tunnel measurements.

### DESCRIPTION OF FINITE DIFFERENCE COMPUTER CODE

In the majority of measurement applications involving coaxial surface thermocouples as heat-flux sensors, the transient surface temperature can be input to one of several short-form versions of the well-known numerical integration equation<sup>14</sup> to obtain the timewise heat flux. This numerical equation was developed to apply to transient heat conduction in solid bodies which qualify as semi-infinite in length over the time period of interest. Use of the semi-infinite solid equation is limited to the thermal penetration time defined by Eq. (2) given in a previous section of this paper. To obtain accurate heat-flux data beyond these time constraints, another method of data processing must be used. The method used at the AEDC is a finite difference technique developed by E. O. Marchand<sup>12</sup> for treating transient heat conduction problems in one space dimension. The computer code developed by Marchand employs a fully implicit, finite difference method for heat conduction within a planar body. The finite wall solution has no time limitations inherent in the methodology, but is somewhat more complex mathematically and requires careful analysis of each problem to ensure accurate results.

A computer program which incorporates the finite difference methodology was written to calculate surface heat flux from coaxial surface thermocouple timewise temperature data. This program is quite versatile in its ability to accept a number of nodal points which divide the finite wall into equal segments in the space dimension, and it allows control of the time integration steps. Several test problems which have exact mathematical solutions have been solved with the finite difference computer code with excellent results. Use of this code in this paper will be limited to one analytical problem for demonstration purposes only. For a more thorough use of the code

in a variety of analytical and experimental applications, refer to Refs. 8 and 12.

### THERMAL ANALYSIS OF THE COAXIAL SURFACE THERMOCOUPLE

The first step in the analysis procedure is to construct a finite-element model of the coaxial surface thermocouple system. A computer-generated block diagram of the coaxial surface thermocouple system (including model wall) is shown in Fig. 10. This is an axisymmetric scale model, but the scale is different in the axial and radial planes. The model is defined by 472 finite elements and 523 nodal points. Because of space limitations, only a few of the nodal points and finite elements are shown on the block diagram. Most of the finite elements are shown within the blocks, and the nodal points are shown on the edges of the blocks.

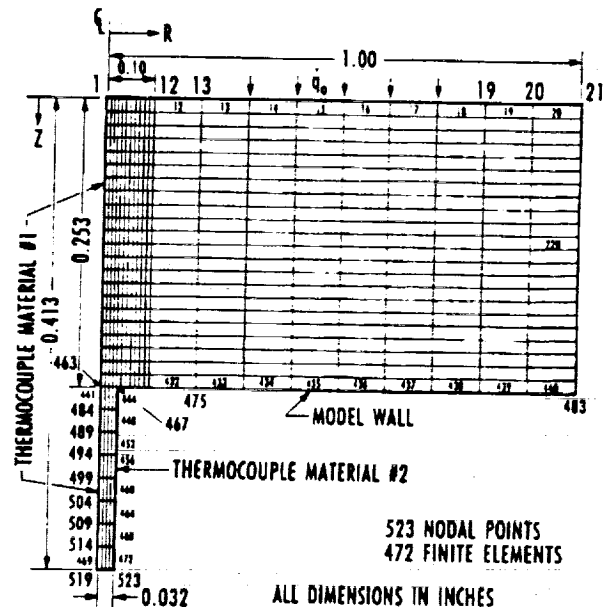


Fig. 10. Trax model of coaxial surface thermocouple system.

TRAX analytical model dimensions can be changed to illustrate the effects of varying the physical configuration of the coaxial TC system. The case for the length of the coaxial sensor being equal to the model wall thickness is accomplished by merely removing finite elements 441-472 (see Fig. 10). The analytical data presented were obtained with a constant and equal heat flux being applied at each nodal point on the top surface of the coaxial TC system (nodal points 1-21). Although the TRAX analytical model shown in Fig. 10 was constructed as a three-material system, all materials were assumed to have the same thermal properties (Chromel) to



eliminate the effects of different material properties from the results shown in this study.

**Analytical Data** — Figure 11 is a graphical illustration of the coaxial TC analytical data to be considered in this documentation. The overall system diameter (model and coaxial sensor) is 2.0 in. The coaxial wire diameter is 0.064 in., which closely approximates the actual commercial coaxial sensor diameter of 0.0607 in. presently used at the AEDC. The model wall thickness for all cases shown on Fig. 11 is 0.253 in. and the coaxial wire length is 0.413 in. This is an ideal example to illustrate the objective of this documentation. The length of the commercial coaxial surface thermocouples presently being purchased is about 0.40 in. Normally, the desired wall thickness is at least 0.375 in., but some model walls are closer to 0.250 in. With an input heat flux of 1.0 Btu/ft<sup>2</sup>-sec applied between each nodal point on the model surface and considering adiabatic boundary conditions on all other surfaces, a transient temperature history was generated at 0.10-sec intervals at each nodal point on the TRAX model over a total time period of 10 sec. The TRAX temperature history at nodal point #1 was input to the normal semi-infinite solid data reduction equation [Eq. (1)] shown in a previous section of this paper. The resulting normalized timewise data are shown on the upper curve on Fig. 11. Obviously, using the semi-infinite solid equation for a finite thickness slab yields significant errors (+27 percent in indicated heat flux at a time duration of 8 sec). Of course, these data are consistent with the predicted errors shown on Fig. 7.

The same temperature history was input to Marchand's one-dimensional finite difference code. This code was formulated with ten nodes and 0.10-sec integration time steps. These results are shown

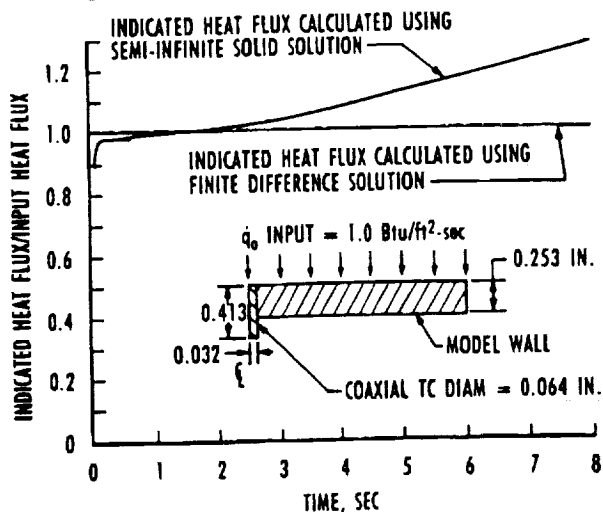


Fig. 11. Timewise coaxial to heat-flux data obtained with different data reduction methods.

by the lower curve on Fig. 11. The normalized timewise data (Indicated Heat Flux/Input Heat Flux) showed a consistent and negligible error through the entire run time of 10 sec. For a much more extensive analytical treatment of this problem, including effects of physical dimensional changes and longer run times, refer to Ref. 8.

## FABRICATION

Although the design of null-point calorimeters and coaxial surface thermocouples is relatively simple with the aid of modern analytical heat conduction codes, the practical implementation of these designs, i.e., fabrication, has always been and remains a difficult task.

## NULL-POINT CALORIMETERS

At the time of this writing, there are only two known commercial sources of null-point calorimeters, although there used to be at least four sources. Reasons for the decline of commercial null-point sensor vendors include the following:

1. there is not a high-volume demand for these sensors at this time,
2. the fabrication process used by the commercial vendors is difficult to control,
3. none of the commercial sources had an experimental facility in which the important performance parameters—primarily time response and calibration—could be determined, and
4. reliability of completed sensors was poor.

All commercial sources of null-point calorimeters use the same basic fabrication technique. The components and construction details of a null-point calorimeter are illustrated in Fig. 2. An OFHC copper cylinder 0.093 to 0.125 in. diam by about 0.40 in. long serves as the calorimeter case. A small ( $\approx 0.025$  in. diam) flat bottom hole is drilled from the back end of the cylinder to within about 0.010 in. of the front surface. In most null-point calorimeters, a 0.020-in.-diam stainless steel thermocouple wire is used as the temperature sensor. The thermocouple type is ANSI Type K (Chromel<sup>®</sup>-Alumel) and the thermoelements are #38 AWG (0.004 in. diam). Attachment of the individual thermocouple wires in the bottom of the null-point cavity is normally done by vacuum brazing. The braze alloy generally used is NIORO which melts at 1,750°F and is composed of 82-percent gold (Au) and 18-percent nickel (Ni). To avoid altering the operating characteristics of the null-point calorimeter, a very small amount of braze alloy must be used.

Actual thermocouple wire attachment must be done in a vacuum oven/furnace because copper oxidizes at 750°F at atmospheric conditions. The inability to control the amount and location of the braze alloy is the primary reason that attachment of the thermocouple by brazing has proved to be an unreliable method.

A null-point calorimeter fabrication method developed by Calspan/AEDC personnel yields a high degree (80%) of reliability at a fraction (25%) of the cost of commercial units. All sensor components are shown in Fig. 2. A significant exception to methods used by commercial suppliers is that no braze is used in the fabrication process. Instead, the thermocouple lead wires are attached to the copper null-point body by a thermal fusion process using a miniature oxyacetylene torch. Another important advantage is gained by Calspan instrument technicians fabricating null-point calorimeters at the AEDC. Since there is ready access to an experimental calibration/characterization system, each null-point sensor can be experimentally checked for time response and output (calibration) at different points in the fabrication process. For instance, a unit which exhibits a slow time response can be brought well within acceptable tolerance by merely machining a few thousandths of an inch off the sensing surface.

### COAXIAL SURFACE THERMOCOUPLE

In-house fabrication of coaxial surface thermocouples is not advised, especially for high-temperature operation. Fabrication of high-quality sensors requires specialized equipment and experience. Medtherm Corp. of Huntsville, AL, which is the only reliable source of coaxial thermocouples known to the author, allows the customer to effectively design his own sensor. Calspan/AEDC is currently using a standard size coaxial sensor with a body diameter of 0.0607 in. and length of 0.4 in. which is press fitted into the model/test article surface.

### EXPERIMENTAL CONSIDERATIONS

Although the definition of transient temperature values and/or heat conduction patterns in the null-point calorimeter and coaxial surface thermocouple sensors by analytical means is of considerable interest to the designers/users of these devices, more significant progress has been made in the experimental areas. Because of manufacturers' inability to hold close tolerances in the fabrication of null-point calorimeters, a laboratory experimental characterization/calibration of each sensor before use in an arc facility measurement application is almost essential. Due to the harsh arc facility environment which

occasionally causes damage to the sensor during a facility run, it is advantageous to be able to conduct an *in situ* experimental qualification of the sensor between runs. Time response and sensitivity are the two most important performance parameters to be experimentally evaluated. Recent advances in experimental methods at the AEDC enable these functions to be performed on a routine basis. These experimental methods and a limited quantity of data obtained with these techniques are described.

### EQUIPMENT AND APPARATUS

**Laboratory Data Acquisition and Processing System** — A schematic block diagram and a drawing of the laboratory data acquisition and processing system used to obtain and reduce the transient experimental data are shown in Figs. 12 and 13, respectively. Since the date of last reporting,<sup>4</sup> a new front-end system, a 24-channel Preston GMAD3A-15B multiplexed analog-to-digital converter, has been incorporated into the laboratory data acquisition equipment. The new data acquisition equipment provides higher gains, higher resolution, higher signal-to-noise ratios, and better stability than the old system. Other system components include a DEC PDP-11/73 computer system, two DEC RL02 disk drives, a MDB MLSI-DWQ11 bus interpreter, a DEC UNIBUS expander box, DEC VT220 and VT240 display terminals, and a DEC LA50 printer/plotter. With the incorporation of the new data acquisition equipment, new user-friendly, menu-driven software has been written which establishes the AEDC calibration laboratory as a very versatile high-accuracy unit designed to perform a multiplicity of tasks. Ordinarily, when it is used to obtain sensor time response or calibration data at high heat-flux levels (>1,000 Btu/ft<sup>2</sup>-sec), the system is configured to accept data from four analog channels, at least one of which is routed through a thermocouple reference junction. These data are sampled at rates up to 0.2-msec intervals. The data acquisition system is synchronized with a high-speed shuttering system (described in following section) when obtaining time response data. Processed data in engineering units are available in hard copy tabular format or timewise plots in less than 5 min after the data are obtained.

**High-Level Heat Source** — Arc-heater facility stagnation heat flux can reach 25,000 Btu/ft<sup>2</sup>-sec (28.4 kW/cm<sup>2</sup>) at extreme test conditions; however, the majority of tests are conducted at heat-flux levels considerably lower. A high-level heat-flux source is needed to simulate actual arc facility test conditions in the laboratory. A goal for the laboratory heat source was to produce a heat flux high enough to approximate the medium to lower arc-heater levels.

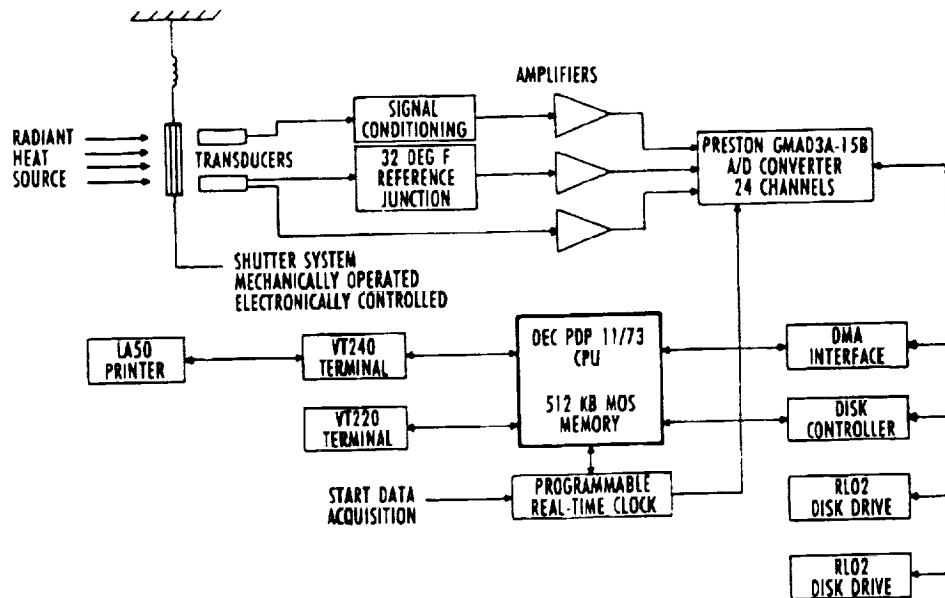


Fig. 12. Data acquisition/processing system block diagram.

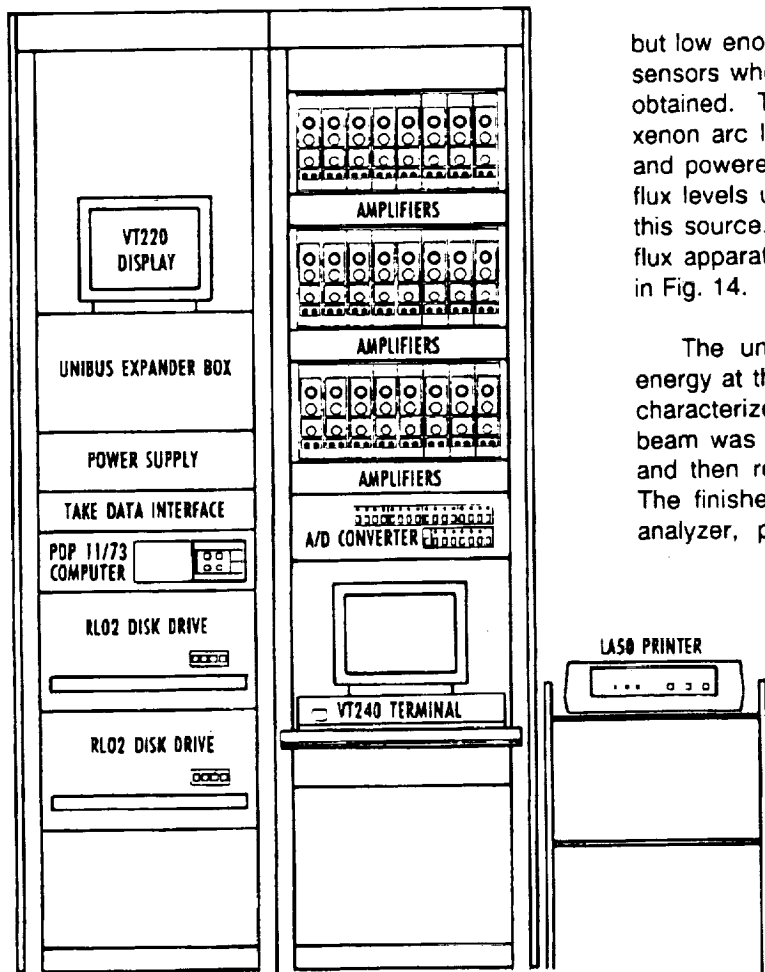


Fig. 13. Pictorial Drawing of thermal measurements laboratory data acquisition system.

but low enough to prevent damaging (by ablation) the sensors when time response and calibration data are obtained. This was accomplished with a 1.6-kW xenon arc lamp focused onto a relatively small area and powered by a pulsed 6-kW power supply. Heat-flux levels up to 2,500 Btu/ft<sup>2</sup>-sec are attainable with this source. A block diagram of the entire high heat-flux apparatus, including support hardware, is shown in Fig. 14.

The uniformity of the focused beam of radiant energy at the focal plane of the arc lamp system was characterized by a photographic technique. The beam was directed onto a scatter plate of mill glass and then reimaged onto film with a pinhole camera. The finished photograph was digitized on an image analyzer, producing a digitized map of normalized radiant intensity as shown by the top two curves on Fig. 15. Pixel-to-pixel resolution was 0.005 in. on the X axis and 0.0061 in. on the Y axis.

Uniformity of the radiant intensity at the focal plane of the arc lamp as shown by the top curves on Fig. 15 was considered unacceptable for performing sensor calibrations with the high heat-flux source. Therefore, it was necessary to develop a method for achieving a better spot size uniformity. This need was met with the effective utilization of a simple optical integrator. The integrator was an aluminum tube with a highly polished inside surface

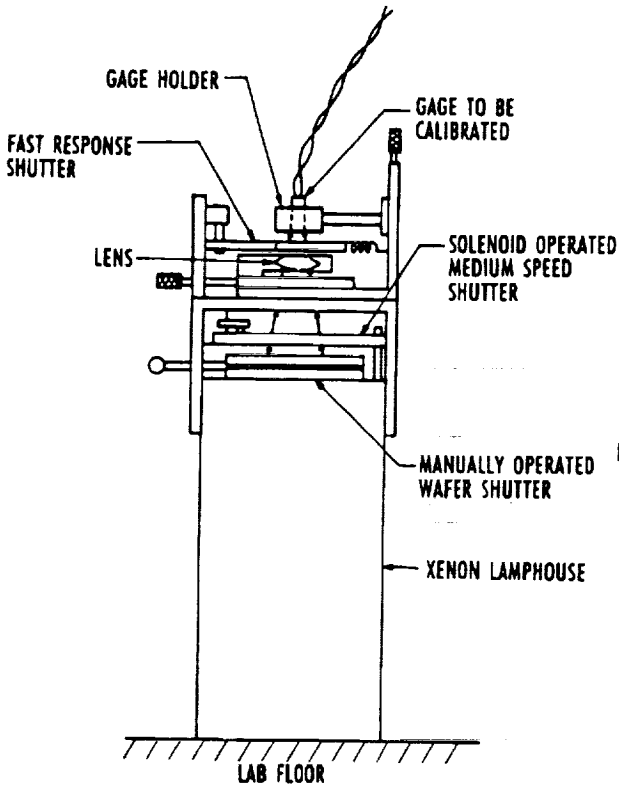


Fig. 14. Block diagram of high heat-flux system.

whose entrance was placed at the focal plane of the calibrator. Plots of the relative intensity in the X and Y axes at the exit plane of the tube are shown on the bottom curves on Fig. 15. As seen from Fig. 15, the magnitude of the radiant heat flux at the exit of the optical integrator is only about 65 percent of the intensity at the focal plane of the lamp system. A computer generated three-dimensional contour map of this intensity obtained with the digitized data from the image analyzer is shown in Fig. 16.

**Shuttering System** — A method of shuttering the high-level radiant heat source was devised to enable the equipment to perform the experimental calibration and time response functions. Three mechanically operated and electronically controlled shutters are used to expose the sensor to the heat source very quickly, but allow the heat source to irradiate the sensor long enough to obtain calibration data. The speed of the high-speed shutter has been experimentally determined to be about 200 in./sec. The fast shutter and the apparatus used to measure the speed are schematically illustrated in Fig. 17. Basically, the shutter consists of a spring-loaded plate with a slot large enough to completely expose the sensor to the heat

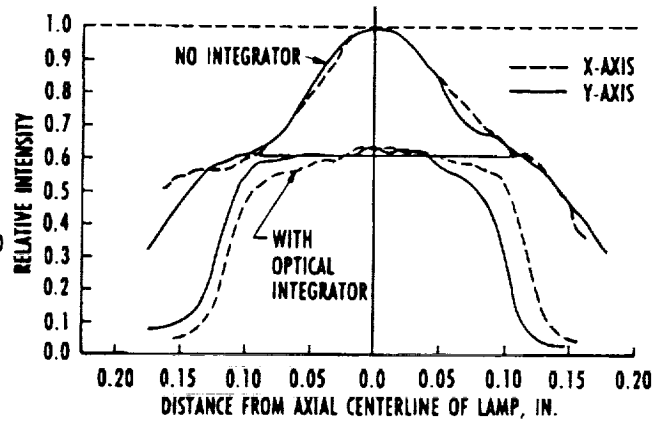


Fig. 15. Uniformity map of high heat-flux source on plane surface at focal point.

source. A 0.5-in.-diam copper sleeve houses a null-point or coaxial thermocouple sensor in the center and two fast response photodiodes whose axial centerlines are located 0.40 in. apart. Sleeves with small (0.013 in. diam) apertures are positioned above both photodiodes. Thus, the leading edge of the shutter opening will completely pass over the heat-flux sensor in less than 0.5 msec. This fast shutter is mechanically stopped with the slot completely open to the sensor. The sensor is shut off from the heat source when the second or middle shutter closes after being open for a time period which can be varied from 100 to 300 msec. Since the analytical data show that the time response of the fastest null-point calorimeter is about 1 msec to 95-percent of full-scale output, the shutter speed is easily fast enough to permit accurate sensor time response measurements.

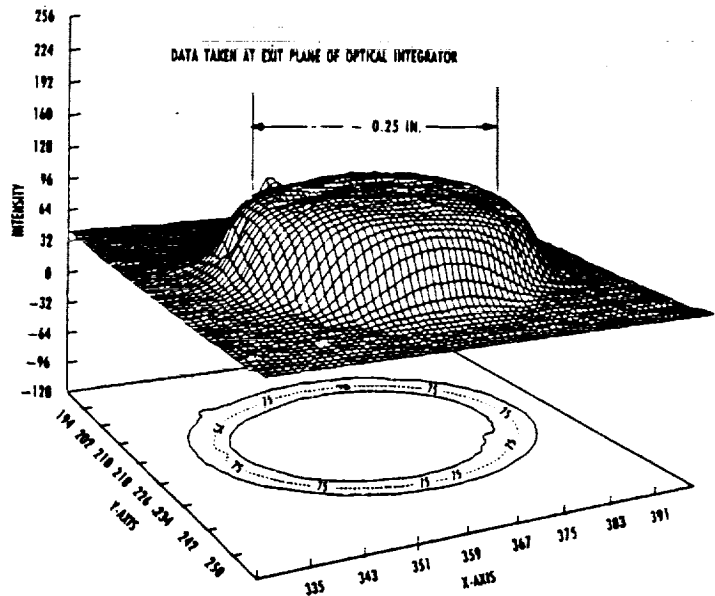


Fig. 16. Three-dimensional intensity map of arc lamp.

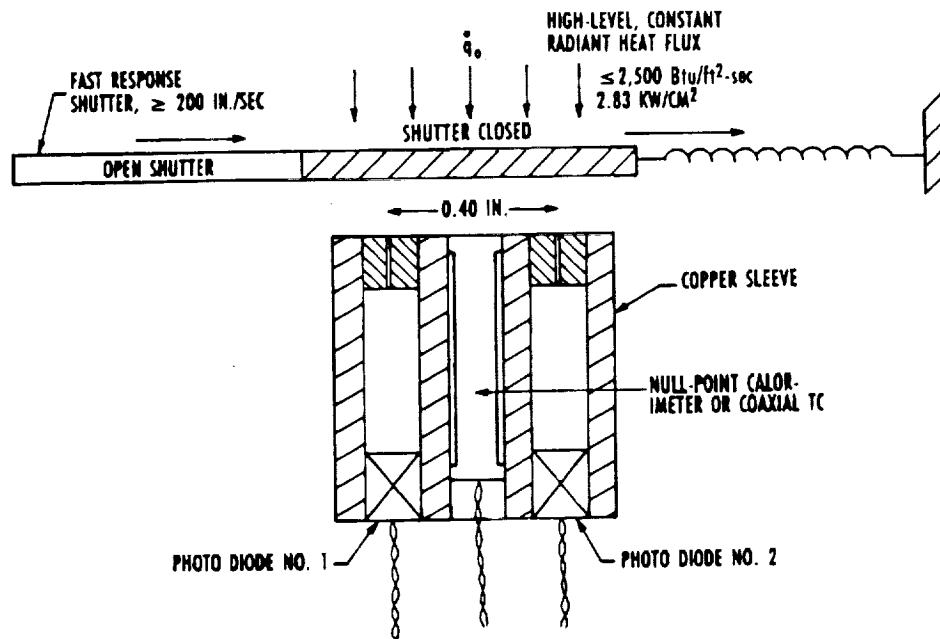


Fig. 17. Calspan/AEDC high heat-flux calibration and time response laboratory hardware.

**Standards** — Two commercial Gardon-type transducers were purchased and adapted to use as standards in the Calspan/AEDC high heat-flux calibration system. These transducers can be operated continuously with water cooling at heat-flux levels as high as 1,000 Btu/ft<sup>2</sup>-sec (1.135 KW/cm<sup>2</sup>). Since these transducers are irradiated for time periods of less than 0.5 sec, water cooling is not necessary. Certified traceability to the National Institute of Standards and Technology (NIST) is accomplished by calibration against a working standard which is calibrated against a transfer radiometer. The transfer standard radiometer is calibrated against a blackbody source whose temperature is measured with an optical pyrometer certified by NIST through application of the Stefan-Boltzmann equation.<sup>15</sup>

**High Absorptivity Sensor Coating** — A thin (<0.0005 in.) coating of high absorptivity must be applied to the sensing surface of each transducer and standard alike to perform accurate heat-flux transducer calibrations. This coating must be capable of withstanding relatively high temperatures (>1,000° F) in this transient measurement application. After screening several candidate coatings, Krylon® High Heat Spray Paint #611250 was chosen as the standard coating in this application because of the ease of application, high temperature capability, high absorptivity, and availability.

## APPLICATIONS

A prevailing misconception regarding null-point calorimeters is that it is not possible to determine the actual time response of the sensors in the laboratory. Commercial suppliers of null-point calorimeters are presently unable to supply time response data with their sensors. Methods for obtaining null-point calorimeter experimental time response data have been developed for use at the AEDC. The experimental data generally complement the analytical data, thereby enhancing the credibility of both methods.

Since the construction of the high heat-flux source, the installation of the fast response shutter, and the integration of the data acquisition and processing system, literally hundreds of runs have been made to experimentally determine the time response characteristics and calibrations of null-point calorimeters and coaxial surface thermocouples. Some of these runs were made at the maximum attainable heat-flux level ( $\approx 2,500$  Btu/ft<sup>2</sup>-sec) of the heat source in its present configuration, but most were made at levels around 1,100 Btu/ft<sup>2</sup>-sec. The data selected for presentation are intended to accentuate the more important aspects of the experimental system, rather than inundate the reader with large quantities of repetitious data. Some of the graphically illustrated data from different sensors are in poor agreement. These data are intentionally shown in this manner to show the poor quality control of some

commercial sensors and the ability of the laboratory experimental methods developed at the AEDC to detect the "bad" sensors before they are installed and used in test programs.

### EXPERIMENTAL DATA

**Experimental Characterization Data** — To illustrate the full extent of the problem which exists with unqualified commercial null-point calorimeters, the experimental data shown on Fig. 18 are offered as an example. These data were obtained from several sensors using the high heat-flux source in 1988, before system upgrades such as fast shuttering, data acquisition and processing improvements, and high heat-flux standards were made. Null-point sensors were intentionally selected to show the large variations which may exist in commercial units. These sensors were not irradiated simultaneously, but rather consecutively on the same day within a 1-hr time period. Indicated heat-flux data should be in good agreement since the heat source has been shown to be quite stable over short (1 to 2 hr) time periods. The solid line represents transient indicated heat-flux data from a null-point sensor installed at the stagnation position of a copper sphere cone model (S/N:0.5-1-17) that was generally accepted as a standard against which other sensors were compared. The other three curves represent data acquired from sensors obtained in 1987 from the same commercial source in a group of about 75 units. Data obtained from sensor designated NPC-042 are in very good agreement with the data from the sensor in the probe model. However, data obtained from null-point calorimeters NPC-047 and NPC-111 are obviously unacceptable.

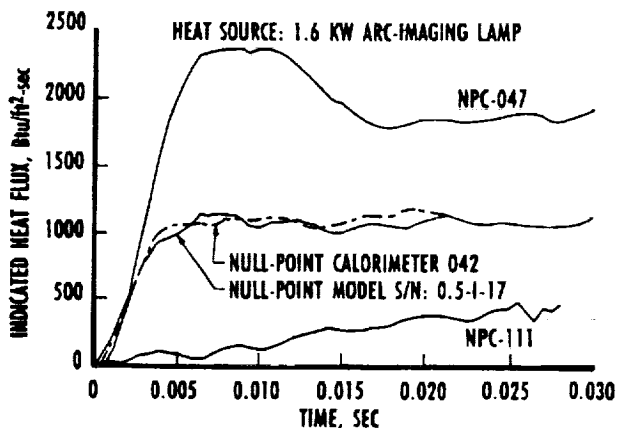


Fig. 18. Null-point calorimeter experimental characterization data.

The sluggish behavior of NPC-111 is caused by either a large quantity of braze in the null-point cavity, or a thermocouple wire attachment being made

near or partially onto the cavity wall. Both problems will cause the sensor to exhibit slow response time and low output. In later years some sensors which exhibited strange behavior have been taken to the X-ray lab at the AEDC to be photographed. Careful examination of the photographs revealed the condition(s) referred to above. X-raying all sensors on a routine basis is time consuming, generally inconclusive, and therefore not cost effective. The transient behavior of NPC-111 is not typical, but has been experienced on a small number ( $\approx$  5 percent) of commercial units. This raises serious doubts about quality control procedures of commercial suppliers.

Analyzing the transient behavior of NPC-047 is more difficult, but a rational explanation does exist. What fabrication feature causes a sensor to initially indicate a heat-flux level more than twice the input level and then decrease to a constant level still well above this level? The only plausible reason is contained in the Analysis section of this documentation and is graphically illustrated by the top curves on Figs. 4 and 5. A reasonable explanation of the behavior of NPC-047 is that the thickness of the copper foil above the null-point cavity is significantly less than the design dimension. This effect is rare and only occurred on one other sensor out of a group of 75 units purchased from this supplier. After Calspan personnel at AEDC perfected the fabrication method now used, several units were intentionally made with a thin foil above the null-point cavity. This same type of behavior was seen in laboratory tests of these units. The data shown on Fig. 18 accentuate the necessity of getting better quality control from the commercial suppliers and performing laboratory experimental tests before wind tunnel use.

**Experimental Time Response Data** — It was accurately stated in earlier sections of this documentation that proper time response is critical for the accurate use of null-point calorimeters in arc facility heat-flux measurement applications. It was shown in the Thermal Analysis and Experimental Considerations sections that null-point calorimeters can respond too quickly, thus indicating a significantly higher level than the actual heat flux incident upon the instrument's sensing surface. And, of course, null-point sensors can easily be too slow for the intended application. Therefore, the capability of performing experimental time response characterizations at high heat-flux levels in the laboratory is of vital importance. The apparatus used at the AEDC for determining time response characteristics of heat-flux sensors was described in an earlier section of this paper. This section will show results of experimental time response characterizations of null-point calorimeters and coaxial surface thermocouples.

Figure 19 shows graphical illustrations of recent experimental time response data obtained from a Calspan/AEDC fabricated null-point sensor. These data were generated by irradiating a single null-point sensor with a high level ( $\approx 1,700$  Btu/ft<sup>2</sup>-sec) constant heat flux from the xenon arc lamp very quickly with the fast shutter and recording the timewise output at 0.2-msec time intervals. The timewise output was converted to a temperature history by applying the fifth-order equations for a Chromel-Alumel thermocouple. As shown on Fig. 19, the null-point cavity temperature increased by nearly 175° F in less than 30 msec. The resulting timewise heat flux on Fig. 19 was obtained by inserting the temperature history into Eq. (1) and applying the room temperature thermal properties of OFHC copper. A time response of 3 to 4 msec is indicated by the timewise heat-flux data. These data represent near optimum sensor behavior. If the copper foil above the null-point cavity was thinner, an operating behavior such as exhibited by NPC-047 in Fig. 18 probably would have resulted. This sensor will be installed at the stagnation position of a high-enthalpy probe model for AEDC arc facility measurement applications. After installation in the probe, the sensor will again be experimentally checked for time response and absolute calibration.

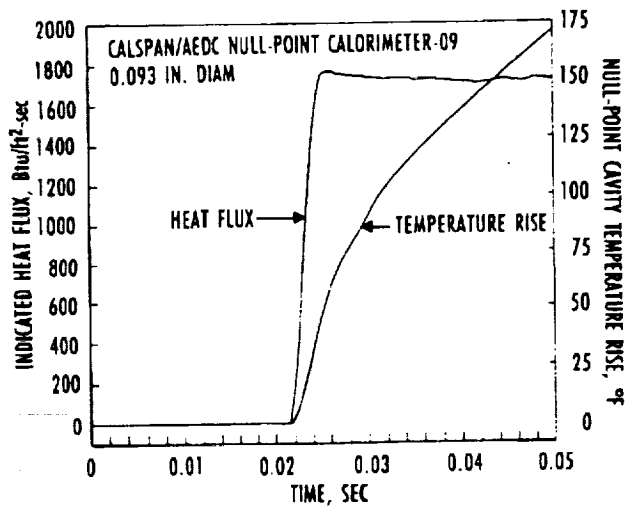


Fig. 19. Null-point calorimeter experimental time response data.

gration technique. It requires about five data points from a perfect temperature history to give an accurate indication of heat flux. Since the raw output data were sampled at 0.2-msec intervals, this accounts for about 1 msec. Normally, it is not necessary to perform time response characterizations on coaxial surface thermocouples for arc facility measurement applications. These data were presented to show the capabilities of the calibration system.

Time response data for a Chromel-constantan coaxial surface thermocouple are shown in Fig. 20 along with output signals from two photodiodes located 0.40 in. apart on either side of the coax TC as shown in Fig. 17. The output signals from the photodiodes indicate the speed of the fast response shutter. The time response of the coaxial sensor is shown to be about 2 msec. Since coaxial TC's have been shown to respond in about 50  $\mu$ sec, the indicated time response is probably a result of the response of the data system and the numerical inte-

**Absolute Calibration Data** - Common practice at most high heat-flux test facilities worldwide is that null-point calorimeters and coaxial surface thermocouples are used without performing absolute calibrations against high heat-flux standards. The justification for this mode of operation is that neither the null-point calorimeter nor the coaxial surface thermocouple are actually heat-flux transducers/gages in the common use of the terminology. These sensors do

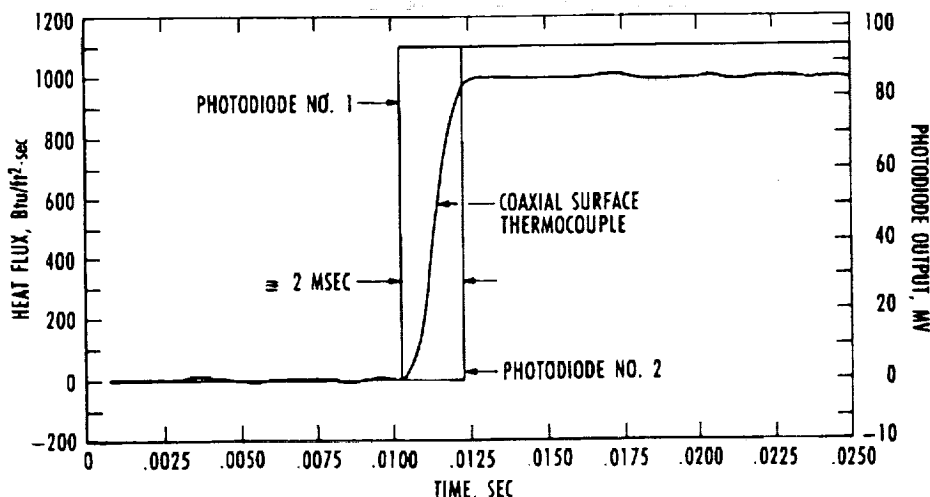


Fig. 20. High heat-flux calibrator time response data.

not provide an output signal directly proportional to the heat flux incident upon the sensing surface. They do provide timewise output signals from common thermocouples which can be accurately processed (converted) into the sensing surface temperature histories. Assuming the sensor behaves as a semi-infinite solid during the time period of interest, the temperature history is input to the numerically represented inverse heat conduction equation [previously shown as Eq. (1)] to obtain transient heat-flux data. Also required for obtaining accurate heat-flux data is a knowledge of the lumped thermal property parameter,  $(\rho C_p K)^{1/2}$ , previously defined in the Analysis section of this documentation. Thermal properties of OFHC copper are known to good accuracy up to temperatures approaching the melting point, 1,981° F. Although not as widely documented as copper, the  $(\rho C_p K)^{1/2}$  parameter of both Chromel and constantan materials is well known from room temperature up to about 1,000° F. However, it is not a strong function of temperature.

If heat-flux measurement applications meet all the criteria outlined in the preceding paragraph, it would appear that absolute calibration of null-point calorimeters and coaxial surface thermocouples would not be necessary. However, results from the Analysis section of this paper show that the performance of null-point calorimeters is quite sensitive to dimensional variations. Therefore, it is advisable to calibrate all null-point calorimeters before installation and use in a facility test program. Conversely, the performance of coaxial surface thermocouples is historically quite stable. Occasional calibration of coaxial TC's can be helpful to check out the system.

#### Laboratory Experimental Calibration Data —

A timewise comparison of indicated heat-flux data from two null-point calorimeters, a Chromel-constantan coaxial surface thermocouple, and one high heat-flux standard gage is shown on Fig. 21. These data were not obtained simultaneously, but rather in consecutive applications of the high-intensity radiant heat source. The calibration heat flux of about 600 Btu/ft<sup>2</sup>-sec was intentionally set lower than maximum to stay within the calibration range of the standard gage. The three transient heat-flux sensors show relatively good agreement with the heat flux indicated by the Gardon type high flux standard. One of the null-point calorimeters was a stagnation sensor installed in a 0.5-in.-diam, 10-deg sphere-cone model. The other null-point calorimeter and the coaxial thermocouple were individual commercial units. Data from the standard gage are shown displaced on the time scale since the time response of the standard is about 50 msec. Because of the slower response of the standard gage and the fact

that the output of the standard is directly proportional to the heat flux incident on the sensing surface, the timewise heat-flux indications from the standard do not contain the spurious noise spikes that are common with the fast response devices. Therefore, if the indicated heat flux is constant in time over a longer time span (0-300 msec), it is appropriate to apply this level over the entire shorter time period experienced in the laboratory calibration of the fast response sensors.

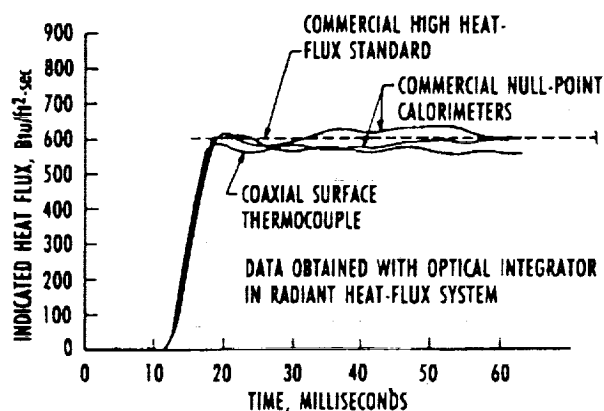


Fig. 21. High heat-flux transducer calibration data.

#### PORTABLE CALIBRATOR (IN SITU OPERATIONS)

Among the more significant recent achievements in arc facility heat-flux instrumentation at the AEDC is the capability to perform *in situ* calibrations of sensors in high-enthalpy probe models at the test site through the facility data acquisition system. This is accomplished by using a portable heat source system which can easily be moved in and out of the test area. This capability has greatly reduced the confusion and speculation with regard to anomalous heat-flux data from similar probes mounted on the same rake. Run-to-run heat-flux probe calibrations/characterizations can now be routinely performed without physically removing the probe from the facility structure (rake). The principal components of the system are a radiant heat source, a power supply, a shuttering mechanism, calibrator attachment hardware, and a standard gage holder.

#### HEAT SOURCE

Serving as the heat source for the portable calibrator is a 200-w tungsten filament lamp with a highly polished ellipsoidal reflector unit housed in a compact 2-in.-diam by 4.0-in.-long cylinder which focuses radiant energy onto a 0.30-in.-diam focal spot about 1 in. from the front end of the cylinder. A power supply which provides electrical power to the lamp from a common 120-VAC, 60-Hz source is included with the system which is a Model 4141 Mini-



Spot Heater manufactured by Research, Inc. A heat source adapter and a high-enthalpy probe holder shown in Fig. 22 were designed, fabricated, and are available for routine use in the calibration of null-point sensors in probes and/or individual sensors. A slot was milled in the probe holder (see Fig. 22) to permit shuttering the lamp and to provide transient data from the sensor. When taking calibration data through the facility data system, the system is actuated by a physical movement of the shutter. In its normal operational mode, the data system is configured to take 1,000 data points at 1-msec intervals. After the timing between the shutter and data acquisition system has been properly established, the number of calibration data points can be significantly reduced by a software change since accurate calibration data can be obtained from 100 to 150 data points.

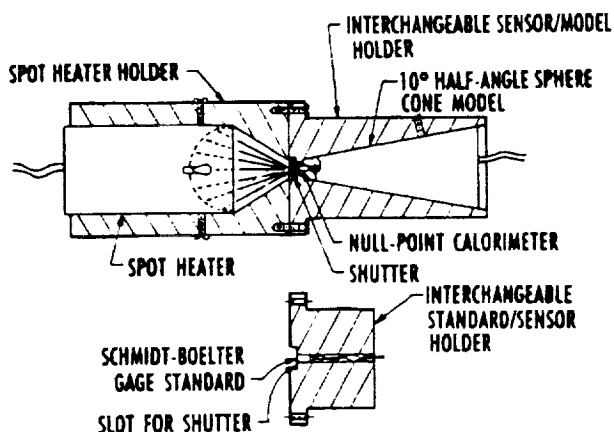


Fig. 22. Sketch of portable calibrator hardware.

An attachment which accommodates a heat-flux standard gage whose calibration is traceable to NIST<sup>17</sup> was designed to fit in exactly the same location (relative to the heat source) as the probe model in the probe holder attachment (see Fig. 22). Since the maximum rated incident heat flux which can be delivered to any surface with this source is only 123 Btu/ft<sup>2</sup>-sec, a high-temperature Gardon gage<sup>18</sup> or a Schmidt-Boelter gage<sup>19</sup> can be used as the heat-flux standard.

## APPLICATIONS

Graphical illustrations of the timewise heat flux measured by null-point calorimeters located at the stagnation position of two different 0.5-in.-diam, 10-deg half-angle sphere cone models on the same rake are shown on Fig. 23. These data were generated by the portable calibrator heat source on consecutive applications. Also shown is a dashed line which represents the heat-flux level indicated by a Schmidt-Boelter gage standard. The probe holder attachment

was removed from the heat source hardware and the standard gage attachment was secured in its place. The output signal from the standard gage was converted to indicated heat flux by a simple direct multiplication of the output signal by the scale factor of the standard. Since the output from the standard gage was constant over a period of several seconds, the output signal can be recorded after the time response requirements of the gage ( $\approx 1$  sec) have been fully met. The measured heat-flux levels from the two probe models are in excellent agreement as well as with the indicated heat flux from the standard gage. Because of the relatively slow shutter speed with this portable source, time response data cannot be obtained with this device in its current configuration. Experimental data shown on Fig. 23 are in exceptionally good agreement. Often, probe models have to be discarded because of poor agreement with standard gages and/or good probes.

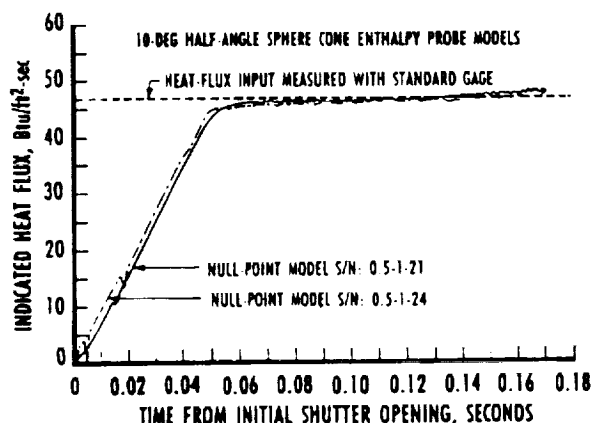


Fig. 23. Null-point calorimeter experimental data obtained with portable calibrator.

## FACILITY DATA

The High Enthalpy Test Unit (HEAT) at the AEDC has two types of arc heaters.<sup>20, 21</sup> Both of these heat a continuous flow of high-pressure air to yield a high enthalpy test jet suitable for ablation testing of advanced nosetip materials and other high-pressure high heating rate tests. The arc heater at the AEDC which produces the highest flow-field enthalpies is of the segmented type and is designated H1.<sup>21, 22</sup> The segmented heater has 200 electrically isolated segments separating the anode (upstream) and cathode (nozzle end) of the heater. Air is injected at the upstream end and distributed through the individual segments to produce a uniform swirl, providing stability for the direct-current arc that heats the air.

Facility data include arc heater voltage and current, cooling water flow rate and temperature rise,

and air pressure and flow rate. These data define arc heater performance. Flow-field data, including heat-transfer rate measurements, are obtained with multiple standard probes that are swept through the flow field at speeds up to 90 in./sec. Flow-field data are nominally recorded at 5,000 points/sec with 1-kHz analog filters. Figure 24 is a graphical illustration of typical temperature and heat flux data obtained recently at the stagnation point of a 0.5-in.-diam, 10-deg half-angle sphere-cone standard probe in arc heater H1. The sensor was a 0.093-in.-diam copper null-point calorimeter fabricated by Calspan personnel at the AEDC. Although the null-point cavity temperature reached about 1,330° R during the run duration, it did not come close to the melting point of copper, which is 2,441° R (1,981°F). However, it should be noted that a coaxial surface thermocouple installed in a stainless steel model would have experienced surface ablation (and ultimate destruction) at this run condition.

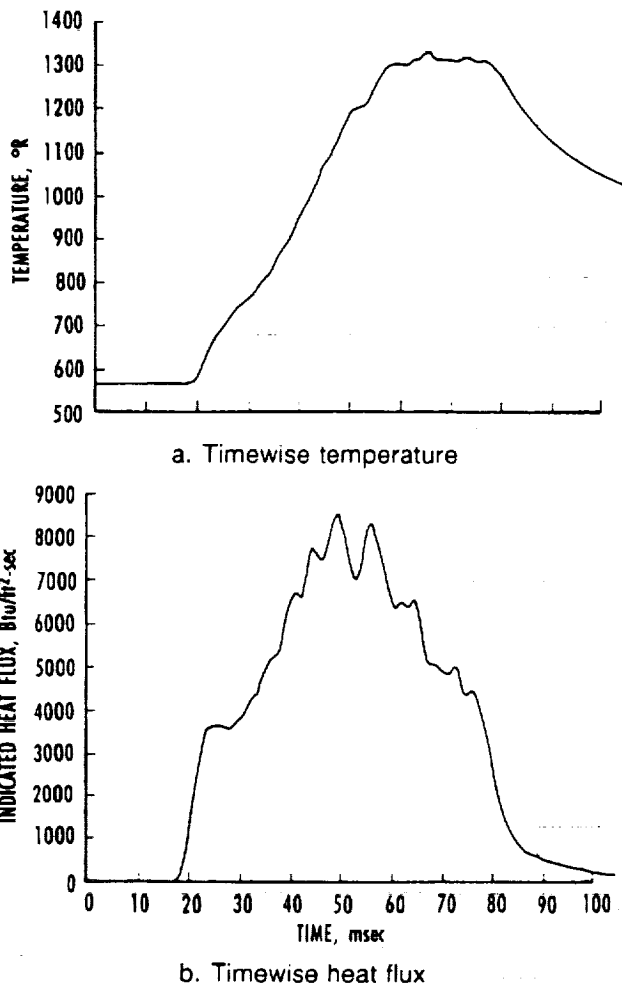


Fig. 24. AEDC arc heater null-point probe data.

The null-point sensor was experimentally tested for time response and calibration in the high heat-flux calibration system (described in earlier sections of this paper) before and after installation in the standard copper probe. This sensor has set a durability record of sorts by surviving over 50 facility "runs" at last count with no apparent detrimental effects. Commercial probe/sensors historically have an inferior performance and survivability record.

## CONCLUSIONS AND RECOMMENDATIONS

To improve the general quality of heat-flux data obtained in high-performance facilities at the AEDC, recent significant achievements have been made in several areas. Accomplishments to date and recommendations for future work are summarized below:

**1. Thermal Analysis** - Before 1990, analytical data which accurately defined the operation of the null-point calorimeter were virtually nonexistent in open literature. In Ref. 4 dated May 1990, the author published extensive analytical data obtained from a finite-element computer code which defined various aspects of null-point calorimeter behavior. Sensing that many users still have only a vague knowledge of the null-point calorimeter concept, some of the more important analytical data were reproduced and expanded upon in this document. Future null-point calorimeter design and fabrication should be influenced by analytical data presented in this paper.

In Ref. 8 also dated May 1990, the author published analytical data dealing with the coaxial surface thermocouple in transient heat-flux measurement applications. Although not as complex a measurement device as the null-point calorimeter, the constraints which apply to the coaxial TC in aerothermal measurement applications are still not well understood by many would-be users. This paper points out that the coaxial TC need not be restricted to semi-infinite solid time limitations.

**2. Fabrication** - It is stated in this document that null-point calorimeters are routinely fabricated by Calspan instrument technicians at the AEDC at a cost of about 25 percent that charged by commercial vendors with a success rate of about 80 percent per unit. This is accomplished by attaching the thermocouple wires in the null-point cavity by thermal fusion.

**3. Laboratory Experimental Methods** - Most suppliers and users of null-point calorimeters consider experimental time response and calibration data to be unattainable in the laboratory. Experi-

mental methods were devised and equipment was designed, fabricated, and assembled which enable these data to be obtained on a routine basis at heat-flux levels exceeding 2,000 Btu/ft<sup>2</sup>-sec (2.27 kW/cm<sup>2</sup>) in the Thermal Measurements Laboratory at the AEDC. Recent data acquisition and processing system upgrades now permit higher quality data to be supplied in a more timely and effective format. This unique (to the AEDC) experimental capability has proved to be most valuable in the calibration and characterization of new sensors and old sensors which have experienced the rigors of arc heater flow-field environments. Future upgrades of these experimental facilities are planned to meet the needs of NASP heat-flux instrumentation calibrations and characterizations.

**4. Portable Calibrator (*In Situ* Operation)** - A portable calibrator which can be transported to the test site to perform *in situ* calibrations of null-point calorimeters through the facility data acquisition/processing system has been developed and effectively used in the AEDC arc heater facilities. This portable heat source can be applied in the test area without removing heat-flux probes from the flow-field rake. This system has been most effective in minimizing the confusion and speculation with regard to transient heat-flux measurements on different probes on a test rake. Although the maximum heat flux which can be attained with this system at present is only 123 Btu/ft<sup>2</sup>-sec, a significant accomplishment has been made in flow-field diagnostic probe qualification methods. It would be desirable to increase the available heat flux to about 1,000 Btu/ft<sup>2</sup>-sec and install a high-speed shutter on the device to enable time response data to be obtained at the test site.

## REFERENCES

1. Beck, J. V. and Hurwicz, H. "Effect of Thermocouple Cavity on Heat Sink Temperature." *Journal of Heat Transfer*, Vol. 82, No. 1, Feb. 1960, pp. 27-36.
2. Howey, D. C. and DiChristina, V. "Advanced Calorimetric Techniques for Arc Plasma Heat Transfer Diagnostics in the Heat Flux Range up to 20 KW/cm<sup>2</sup>." AIAA Paper 68-404, San Francisco, CA, April 1968.
3. Kennedy, W. S., Rindal, R.A., and Powars, C.A., "Heat Flux Measurements Using Swept Null Point Calorimetry." AIAA Paper 71-428, Tullahoma, TN, April 1971.
4. Kidd, C. T. "Recent Developments in High Heat-Flux Measurement Techniques at the AEDC." *Proceedings of the 36th International Instrumentation Symposium*, May, 1990, pp. 477-492.
5. Czysz, Paul and Kendall, David "Testing Technology Advances Associated With Development of an ARC Heated Impulse Tunnel." AIAA Paper No. 66-759, Los Angeles, CA, Sept. 21-23, 1966.
6. Trimmer, L. L., Matthews, R. K., and Buchanan, T.D. "Measurements of Aerodynamic Heat Rates at the AEDC von Karman Facility." International Congress on Instrumentation in Aerospace Simulation Facilities, September 1973.
7. Hedlund, E. R., Hill, J. A. F., Ragsdale, W. C., and Voisinet, R. L. P. "Heat Transfer Testing in the NSWC Hypervelocity Wind Tunnel Utilizing Co-Axial Surface Thermocouples." NSWC MP 80-151, March 1980.
8. Kidd, C. T. "Coaxial Surface Thermocouples: Analytical and Experimental Considerations for Aerothermal Heat-Flux Measurement Applications." *Proceedings of the 36th International Instrumentation Symposium*, May 1990, pp. 203-211.
9. Neumann, R. D. "Aerothermodynamic Instrumentation." AGARD Report No. 761, May 1988.
10. Starner, K. C. "Use of Thin-Skinned Calorimeters for High Heat Flux Arc Jet Measurements." ISA Preprint No. P-11-5 PHYMMID-67, presented at 22nd Annual ISA Conference and Exhibit, September 1967.
11. Standard Method for Measuring, "Extreme Heat-Transfer Rates from High-Energy Environments Using a Transient, Null-Point Calorimeter." ASTM Designation: E 598-77, 1977 (Reapproved 1990).
12. Marchand, E. O. "One-Dimensional, Transient Heat Conduction in Composite Solids." University of Tennessee Space Institute Master's Thesis, August 1974.
13. Rochelle, J. K. "TRAX - A Finite Element Computer Program for Transient Heat Conduction Analysis of Axisymmetric Bodies." University of Tennessee Space Institute Master's Thesis, June 1973.
14. Cook, W. J. and Felderman, E. J. "Reduction of Data from Thin-Film Heat-Transfer Gages: A Concise Numerical Technique." *AIAA Journal*, Vol. 4, Number 3, March 1966.

15. Carslaw, H. S., and Jaeger, J. C. *Conduction of Heat in Solids*. Clarendon Press, Oxford, 1959 (Second Edition).

16. Touloukian, Y. S., ed. "Thermophysical Properties of High Temperature Solid Materials, Volume 1: Elements." Thermophysical Properties Research Center, Purdue University, MacMillan Company, New York, 1967.

17. Kidd, C. T. "Determination of the Uncertainty of Experimental Heat-Flux Calibrations." AEDC-TR-83-13 (AD-A131918), August 1983.

18. Gardon, Robert "An Instrument for the Direct Measurement of Intense Thermal Radiation." *The Review of Scientific Instruments*, Vol. 24, May 1953, pp. 366-370.

19. Kidd, C. T. "A Durable, Intermediate Temperature, Direct Reading Heat-Flux Transducer for Measurements in Continuous Wind Tunnels." AEDC-TR-81-19 (AD-A107729), November 1981.

20. Smith, Richard T. and Folck, James L. "Operating Characteristics of a Multimegawatt Arc Heater Used With the Air Force Flight Dynamics Laboratory 50-Megawatt Facility," AFFDL-TR-69-6, Air Force Flight Dynamics Laboratory, Wright-Patterson Air Force Base, OH, April 1969.

21. Horn, D. D. and Smith, R. T. "AEDC High Enthalpy Ablation Test (HEAT) Facility Description, Development, and Calibration." AEDC-TR-81-10 (AD-A101747), July 1981.

22. Carver, D. B. and Kidd, C. T. "Heat-Transfer Measurement Uncertainty in Arc-Heated Flows." *Proceedings of the 37th International Instrumentation Symposium*, May 5-9, 1991, pp. 951-967.

# TIME DEPENDENT HEAT TRANSFER RATES IN HIGH REYNOLDS NUMBER HYPERSONIC FLOWFIELDS

Michael J. Flanagan  
The Aeronautical and Astronautical Research Laboratory  
The Ohio State University  
Columbus, OH

## ABSTRACT

Time dependent heat transfer rates have been calculated from time dependent temperature measurements in the vicinity of shock-wave boundary-layer interactions due to conical compression ramps on an axisymmetric body. The basic model is a cylindrical body with a  $10^\circ$  conical nose. Four conical ramps,  $20^\circ$ ,  $25^\circ$ ,  $30^\circ$ , and  $35^\circ$  serve as shock wave generators. Flowfield surveys have been made in the vicinity of the conical ramp vertex, the separation point, and the reattachment point. A significant effort was made to characterize the natural frequencies and relative powers of the resulting fluctuations in heat transfer rates. This research effort, sponsored jointly by NASA and the Air Force, was conducted in the Air Force Flight Dynamics Directorate High Reynolds Facility. The nominal freestream Mach number was 6, and the freestream Reynolds numbers ranged from 2.2 Million/ft to 30.0 Million/ft.

Experimental results quantify temperature response and the resulting heat transfer rates as a function of ramp angle and Reynolds number. The temperature response within the flowfield appears to be steady-state for all compression ramp angles and all Reynolds numbers, and hence, the heat transfer rates appear to be steady-state.

## INTRODUCTION

Highlighted by the well-documented in-flight failure of an external support strut on the X-15 flight test vehicle, the problem of shock-wave boundary-layer interactions in hypersonic flowfields has been of interest for almost five decades. In contrast to the so-

called "free-interaction" problem where the impinging shock provides the mechanism for the induced separation, this study is concerned with the separation induced by means of a compression ramp. The resulting interaction between the shock system affects the local flowfield in the interaction region as well as reattachment of the flowfield downstream of the ramp vertex and, hence, seriously effects the overall flowfield structure. With the added intensity of the severe temperature gradients and thin boundary layers that exist at hypersonic flight conditions, an environment is created that is capable of destroying many known materials. The requirements needed to cope with these intense flowfields is currently influencing configuration development as well as defining the focus of basic research efforts in present day aerodynamics.

A region on a hypersonic vehicle that would be particularly vulnerable to dynamic heating due to shock-wave boundary-layer interactions is near control surface hinge points. As the ability to achieve sustained hypersonic flight becomes a reality, the need for maneuverability and acceptable control loads becomes essential. The effects of high-temperature flowfield dynamics within the separated regions caused by the deflection of these control surfaces needs to be understood before any credible system can be designed.

This experimental study investigates the heat transfer rates in the vicinity of a conical ramp in a turbulent, hypersonic flowfield. The results characterize the magnitude, dynamic nature, and characteristic frequencies of the fluctuation levels.

## MODEL DESCRIPTION

Conducted in the Air Force Flight Dynamics Directorate (WL) High Reynolds Facility (HRF) over a period of some four weeks, this test was provided to The Ohio State University (OSU) through a Cooperative Testing Agreement with WL. This Mach 6 facility is capable of producing Reynolds numbers ranging from approximately  $2.0 \times 10^6$  per foot to a maximum as high as  $30.0 \times 10^6$  per ft.

The HRF wind tunnel model is shown in Figure 1. Fabricated from 17-4 PH stainless steel, the model is a cylindrical body 1.558 inches in diameter and 15.1 inches in length. The nose is a  $10^\circ$  cone. Four conical ramps of angles  $20^\circ$ ,  $25^\circ$ ,  $30^\circ$ , and  $35^\circ$  are provided to

act as shock generators. These ramps can be positioned along the body surface from fuselage station (FS) 10.80, referenced from the nose (FS = 0.0), as far aft to FS 14.85.

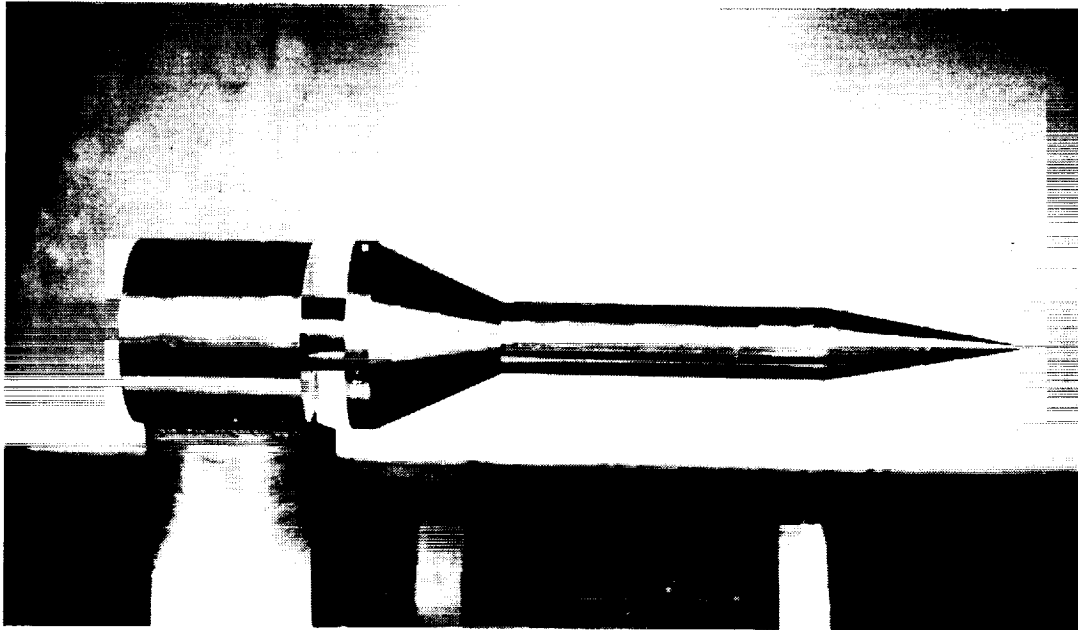


Figure 1. HRF axisymmetric model description

Four coaxial thermocouple gauges are located in a dedicated instrumentation section. These gauges are mounted within the model wall at FS 10.15, 10.35, 10.55, and, 10.75. Additionally, two pressure transducers are mounted within this instrumentation section at FS 10.35 and 10.75 for the simultaneous measurement of pressure fluctuation characteristics. This gauge distribution provides the most economical compromise between data resolution quality (measurement interval along the body) and test time requirements (the number of ramp translation points). This arrangement allows a comprehensive survey of the separation and reattachment regions with the least number of ramp location changes.

Simultaneous measurement of the temperature and pressure data will allow correlations between the characteristic frequencies within the flowfield environment. Once correlated with the pressure data, the frequencies of these temperature data acquired during the test in the HRF can be compared to previous works highlighting shock-wave boundary-layer interactions wherein only pressure data are currently available.

## INSTRUMENTATION SELECTION

Figure 2 provides a graphic representation of the intensity of the temperatures typical of the test environment for this research work. This figure shows the temperature time-history at a point on the model surface during a typical data run in the Air Force Flight Directorate High Reynolds Facility (HRF). Any sensing device used in this environment must be capable of extreme sensitivity in order to detect fluctuations on the order of several percent of the freestream level and still withstand the peak heating rates encountered within the free-jet.

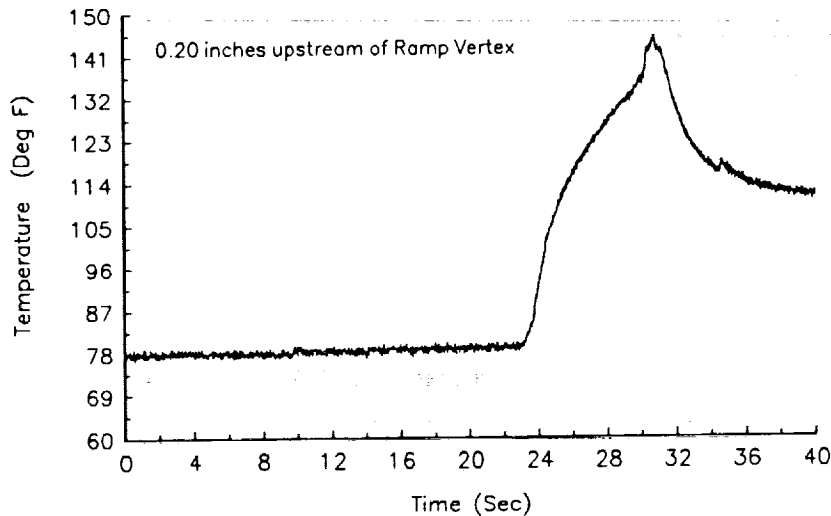


Figure 2. Typical HRF temperature environment :  $Re_{\infty} = 30 \text{ M/Ft}$

Supporting the concerns for gauge selection and survivability issues, References 1 and 2 address the acquisition of time dependent data in a dynamic testing environment. These papers discuss key issues for reliable data acquisition in fluctuating flowfields. With the intense heating rates that exist in hypersonic, high Reynolds number flowfields, these studies combine to suggest a common theme for instrumentation selection. Specifically, the selection of these gauges should be based upon gauge survivability. High frequency response should not be the only primary consideration.



The primary instrumentation for this study is the coaxial thermocouple gauge. Shown in Figure 3, these coaxial gauges can withstand temperatures in excess of 2000° R while still having a dynamic response in excess of 50 kHz. These gauges, described in Reference 3, are more robust than thin-film types, described in Reference 4, and do not introduce the uncertainty of thermal disturbances within the flowfield due to dissimilar thermal properties between the model body and the gauge material or substrate.

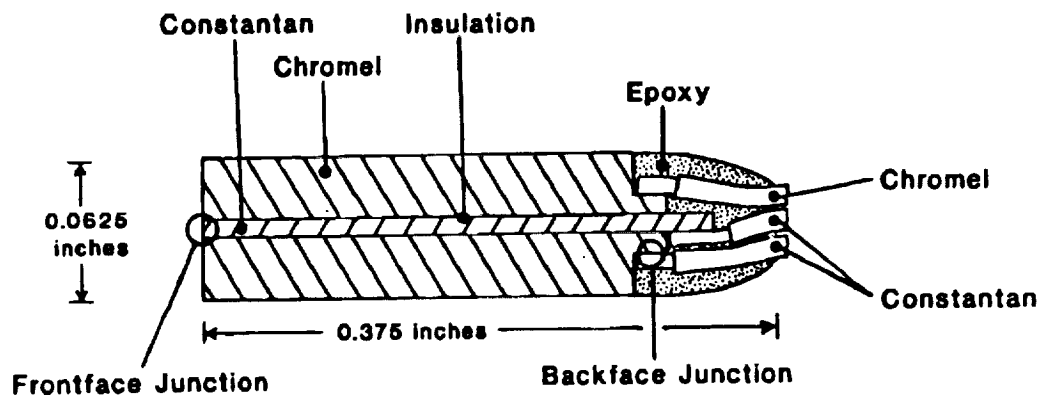


Figure 3. Coaxial thermocouple gauge description

The thermocouple junction is created when, by sanding with 180 grit paper, chromel and constantan slivers are blended in the infinitesimally small region over the insulation separating the two dissimilar metals. The resulting sensing surface resembles an annular ring with dimensions of approximately 0.016 inches for the overall annular ring diameter and approximately 0.0005 inches for the width of the actual sensing ring diameter. This remarkably small size, and hence thermal mass, is the reason for the capability to respond to high-frequency temperature fluctuations.

A preliminary model was constructed as a test-bed for verification of the coaxial gauge response characteristics. This model has a cylindrical body of two-inch length with a hemispherical nose of one inch diameter. The model was sting mounted with one coaxial

thermocouple gauge installed at the nose stagnation point. Experimental data was taken during runs in the OSU 12-inch hypersonic tunnel at Mach numbers of 6, 10, and 12. Comparison runs were made in the WL 20-inch hypersonic tunnel at Mach 12. Figure 4 presents typical test data from the OSU AARL facility. Notice the time delay in response between the front and rear thermocouple junctions.

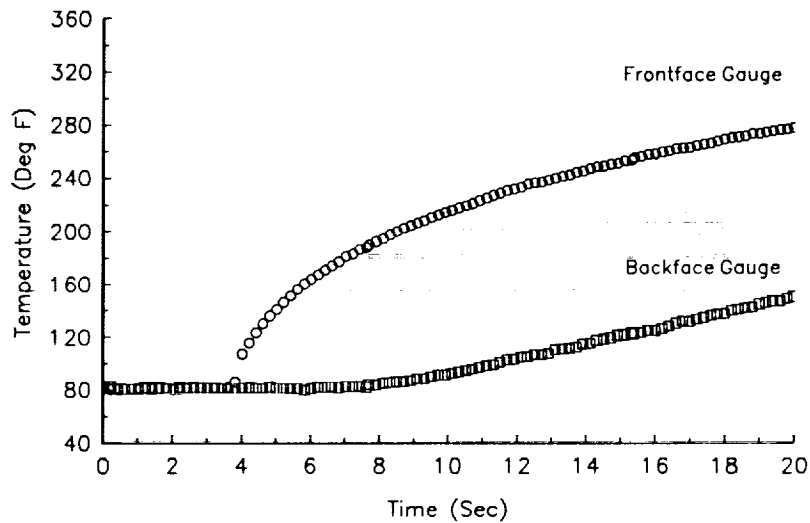


Figure 4. Typical coaxial thermocouple gauge temperature response

The theoretical time-delay in temperature response between the front and rear surface junctions is determined from the thermal characteristics of the gauge material. For purely one-dimensional heat transfer, the time increment for a heat pulse to travel the length of the gauge from the front surface junction to the back surface junction is given by the equation

$$t_D = \frac{0.2L^2}{\alpha} \quad (1)$$

where  $\alpha$  is the thermal diffusivity for a gauge of length (L).

Now for a gauge length of 0.375 inches, this theoretical time delay is approximately 3.7 seconds. Since Figure 4 shows a time delay of approximately 1.7 seconds, it can be

presumed that the heat transfer is not locally one-dimensional. In fact, close inspection of the model reveals that the gauge length is of the same order of magnitude as the model characteristic length, the nose diameter.

Figure 5 shows a comparison between the steady-state heating rates on this model from the two facilities. These heat transfer results are based upon a one-dimensional, semi-infinite slab thermal model. This data reduction method is not consistent with the model design for infinite time as shown in Figure 4; however, for the first few moments, the assumptions should be sufficient for assessing basic, steady-state gauge performance. As the data is valid for approximately the first two seconds of test data, the initial heating gradients and the peak heating rates should be accurate enough for this preliminary gauge evaluation.

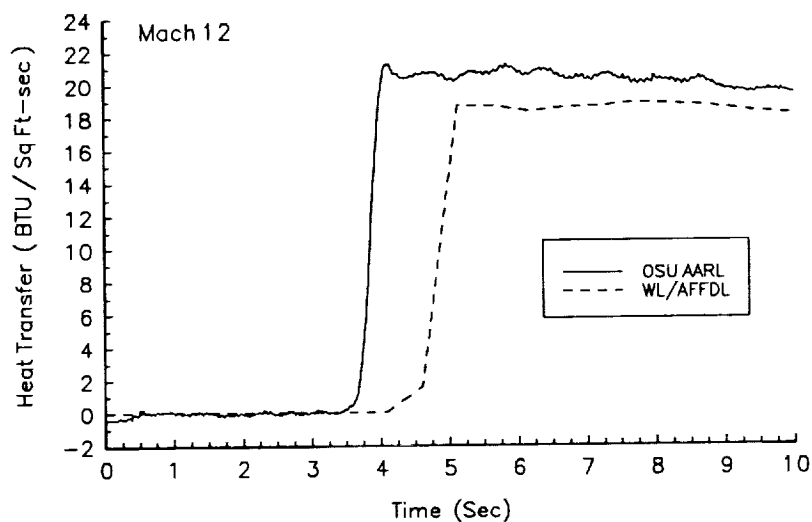


Figure 5. Comparison of stagnation point heating rates

Additional tests were performed to assess the effect of the gauge installation on the output voltage. Figure 6 shows a comparison between voltage output for a freestanding gauge and a gauge mounted within the test-bed model. The model material is 17-4 PH stainless steel. Both gauge arrangements were simultaneously exposed to the same oil bath. The temperature response was recorded. From these data it can be seen that any secondary voltage created from the gauge/model-material interface is insignificant.

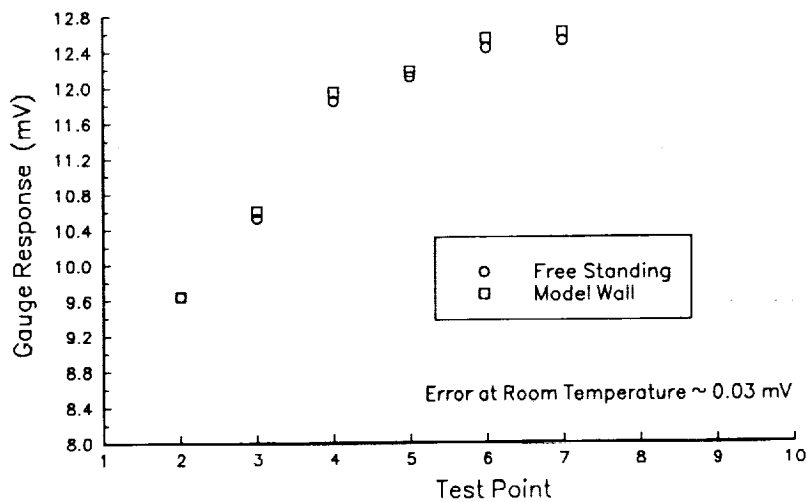


Figure 6. Effect of secondary thermocouple junction on gauge output

The coaxial gauge manufacturer, Medtherm Corp, quotes response times ranging from 100 kHz to 1 MHz depending upon the thermocouple junction treatment (sanded or coated); however, no documentation was made available to the author. Some means to test the high-frequency response characteristics of this gauge design was necessary. With the invaluable assistance of Mr. Greg Elliot, a PhD candidate in at OSU, a temporary test facility was constructed with components adapted from a laser doppler velocimetry (LDV) system at the OSU Aeronautical and Astronautical Research Lab (AARL).

The frequency response of the gauge was tested using a system comprised of a low power (1-watt) laser and a high-frequency chopper. The coaxial gauge, installed in the instrumentation section of the HRF model, was pulsed at frequencies of 20, 40, and 80 kHz. The data was recorded by both the high-speed data acquisition system at AARL and a real-time fast-fourier transformation (FFT) analyzer. The data were reduced to temperature traces and then analyzed both on-line and off-line for frequency content. Figure 7 shows the basic temperature response of the gauge at a pulse rate of 20 kHz. Notice the sinusoidal nature of the test data. The corresponding power spectrum of this data is presented in Figure 8. Notice the dominant peak of energy at 20 kHz. Similar results were obtained at the 40 kHz and 80 kHz pulse rates.

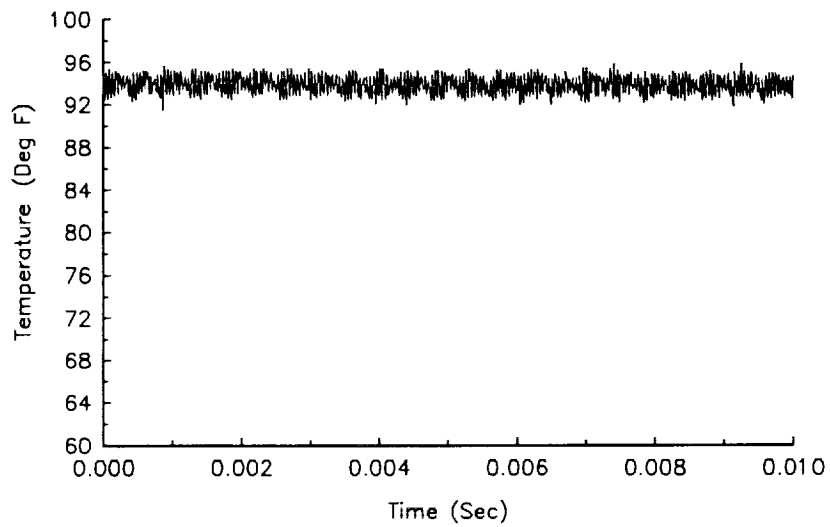


Figure 7. Coaxial gauge response: laser diagnostics at 20 kHz

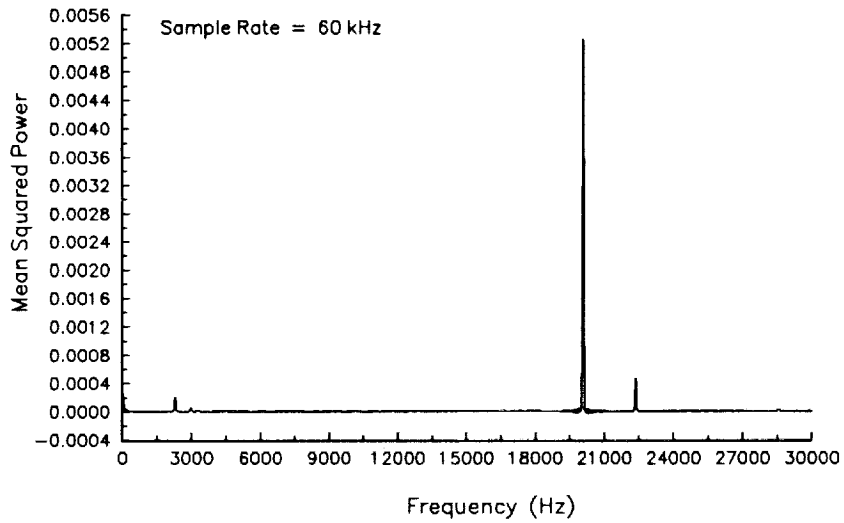


Figure 8. PSD for gauge laser diagnostics: pulse rate at 20 kHz

Based upon the results of these initial laser diagnostic tests, combined with simple bench tests and the gauge/model-material interface analysis, a confidence level was reached wherein it was believed that the coaxial thermocouple gauges would perform as advertized.

## DATA ACQUISITION

For the test in the HRF, the data acquisition system, described in Reference 5, was a 12-bit, 16-channel sample-and-hold and A/D board that was combined with a 25 MHz, Intel 386-based personal computer. This system was created by AARL personnel in order to provide portable, unsteady-data acquisition capability at a remote test facility that did not have that capability.

The data acquisition system was configured with stand-alone filter and signal conditioning equipment that amplified and filtered the signals from the instrumentation prior to sampling by the A/D board. The signal conditioning equipment and the filter units were installed just outside of the tunnel test section. As a result, the amplified and filtered signal could then be sent through shielded cables to the data acquisition computer, located approximately 50 feet from the test section, with less concern for electrical noise<sup>5</sup>.

## DATA REDUCTION

After the acquired temperature data traces are examined, the data are reduced to time dependent heat transfer rates. Spectral analysis is then performed to determine the characteristic frequencies and corresponding power levels of the fluctuations. The heat transfer calculations are based upon the methods presented in References 6 and 7. These methods are currently in use at WL and are the basis for most heat transfer analysis in the Flight Mechanics Group (FLMG). These numerical analysis methods are generally based upon the assumption of 1-D or 2-D conduction paths for boundary conditions that are representative of either infinite, semi-infinite, or finite slab approximations. As the exact characteristics of the heat transfer paths are unknown, evaluation of the model geometry and gauge installation is essential for proper choice of the numerical scheme.

For the axisymmetric HRF model used for this research work, the gauges are located along the body surface. The gauge length is 0.375 inches and the wall thickness is approximately 0.40 inches. The instrumentation section is approximately 11 inches from the nose region and the axisymmetric flowfield should be well established. As the gauge length is of the order of one-fifth of the body diameter, the body is of a homogenous construction of a material with thermal properties close to those of the gauge material, and, as the test times are of the order of 1 second, the assumption that the thermal path could be approximated by one-dimensional conduction into a semi-infinite solid is appropriate.

The relationship between surface temperature and one-dimensional heat conduction into a homogenous semi-infinite solid is given by the equation

$$\dot{q}(t) = \sqrt{\frac{\rho ck}{\pi}} \int_0^t \frac{dT(\tau)}{d\tau} \frac{d\tau}{\sqrt{t-\tau}} \quad (2)$$

where,  $\rho$ ,  $c$ , and  $k$  are respectively the gauge material density, specific heat, and thermal conductivity.

This method, called the direct method, can be used directly on the test data. However, the finite difference scheme is very sensitive to noise in the test data. As this methodology will be applied to high-frequency data, it is possible that the fluctuating components could have the same affect on the numerical scheme as noise. An alternate scheme, referred to as the indirect method, calculates the cumulative heat pulse  $Q(t)$  and then differentiates that pulse with time to obtain  $q(t)$ . The initial calculations for  $Q(t)$  tend to smooth the data and produce a method less sensitive to data noise. This heat pulse,  $Q(t)$ , is calculated from the following equation

$$Q(t) = \sqrt{\frac{\rho ck}{\pi}} \int_0^t \frac{T(\tau)}{\sqrt{t-\tau}} d(\tau) \quad (3)$$

and in finite difference form,

$$Q_n = \sqrt{\frac{\rho ck}{\pi}} \sum_{j=1}^n \frac{(T_j + T_{j-1})(t_n t_{n-1})}{\sqrt{t_n - t_j} \sqrt{t_n - t_{j-1}}} \quad (4)$$

This indirect method provides a more computationally-stable method for calculating the heat transfer rates. However, the intent of this research effort is to detect and analyze the

unsteady nature of the temperature fluctuations. Whether or not the effect of this "smoothing" of the data by this indirect method is significant, specifically, whether or not the indirect method removes any of the measured frequency content, will need to be investigated.

Since the heat conduction can be determined from integration of the heat pulse function  $Q(t)$ ,  $q(t)$  can be computed from the following equation:

$$\dot{q}_n = \left( \frac{1}{40(t_n - t_{n-1})} \right) [-2Q_{n-8} - Q_{n-4} + Q_{n+4} + 2Q_{n+8}] \quad (5)$$

Calculation of the frequency content of the temperature data is accomplished through spectral analysis. Dozens of methods for spectral analysis exist; however, most techniques refer to the methodology proposed by Blackmann and Tukey in Reference 8. Reference 9 is strongly based on the works of Blackmann and Tukey, and forms the basis for the chosen method of data reduction. The details for the mathematical scheme used for this analysis can be found in Reference 10. Generally, frequency content is presented by means of a power spectral density (PSD) plot of energy (in dB) versus frequency. As there is no known means of presenting the energy content of temperature fluctuations in terms of decibels, the spectral analysis methodology chosen for this analysis was selected because the final product is linear with frequency.

## EXPERIMENTAL RESULTS

Initial flowfield data, functions of ramp angle and body Reynolds number,  $Re_b$ , were comprised of schlieren photographs. Studies of these photographs determined the most likely locations of flowfield separation and reattachment as a function of distance from the fixed ramp vertex. Initial ramp locations, determined from these photo surveys, were chosen in an attempt to locate the estimated separation point in the center of the instrumentation section. Following runs would survey both upstream and downstream of this fuselage station in increments of 0.05 inches in an attempt to locate the region of peak temperature and pressure fluctuations. Once the peak location was determined, this separation point was surveyed extensively at different sampling rates and filter settings in an attempt to characterize the nature of the fluctuations.



Figure 9 is an example of a typical turbulent interaction, at a  $Re_b = 21.66 M$ , and shows the size of the interaction region relative to the body diameter of 1.55 inches. This turbulent-type of interaction is characterized not only by a very small separation bubble, generally on order of the boundary layer thickness ( $\delta$ ), but also by a very large separation angle, generally very close in value to that of the conical shock angle.



Figure 9. Schlieren photograph of a typical turbulent interaction

Analysis of the schlieren photographs during the HRF test showed variations of separation bubble size with ramp angle and Reynolds number. Post run analysis of the  $35^\circ$  ramp showed the separation bubble, at  $Re_b = 21.66 M$ , to be of the order of  $10\delta$ . The resulting reattachment point was located approximately  $7\delta$  along the ramp surface downstream from the vertex. As the  $35^\circ$  ramp is approximately 0.4 inches deep at this point, it was possible to mount eight coaxial thermocouple gauges along the ramp surface in an attempt to locate the reattachment point and to characterize the nature of any temperature fluctuations in that vicinity as well.

The temperature data were examined for trends and characteristics indicating some type of flowfield dynamics. Each data trace was further reduced through spectral analysis

techniques and examined for frequency content and the relative power contained in the data signal. Figure 10 shows typical temperature traces for the type of interaction presented in Figure 9. These traces represent temperature time-histories for three body locations in the vicinity of the separation point due to the 30° ramp. These data exhibit similar characteristics upstream, downstream, and in the vicinity of the separation point.

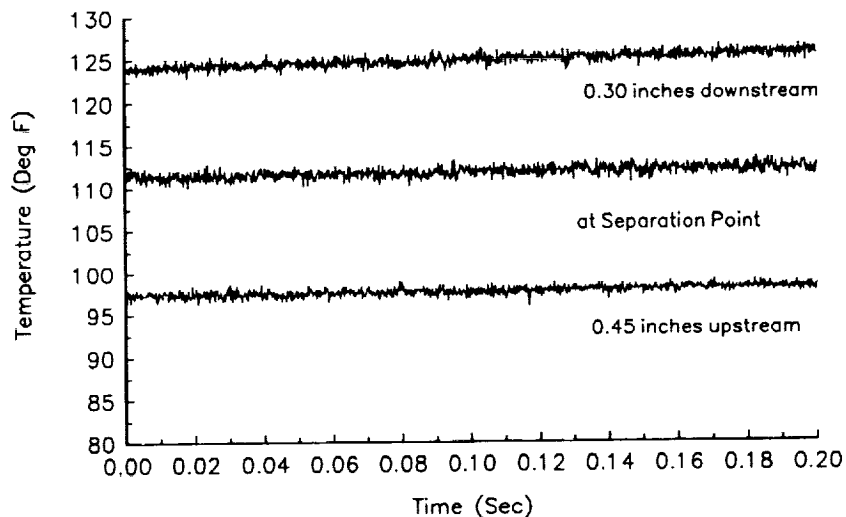


Figure 10. Typical Temperature Response: 30° Ramp at  $Re_b = 21.66 M$

These data show some unsteadiness in temperature response. However, the RMS values are of insignificant magnitude. The magnitude of these fluctuations are approximately 0.5°F in the vicinity of the separation point and approximately 1.0°F in the vicinity of the reattachment point. Comparison of these data to the initial flowfield surveys of the HRF facility shows the ratio of these RMS values to the freestream temperature fluctuation levels to be of the order unity. The absence of any significant time-dependent components in this data, combined with the fact that these trends are repeated for 12 Reynolds numbers ranging from 1.62 to 21.66 M/ft and the ramp angles ranging from 20° to 35°, strongly suggests that the temperature response, and hence, the heat transfer rates, in these interacting regions are steady-state. Furthermore, these same trends were repeated for the data recorded at the reattachment point on the 35° ramp. Although the heating rate at the reattachment point was of the order of 600° F per minute, the temperature response also appears to be steady-state.

Figure 11 presents the results of calculations for the steady-state heat transfer in the vicinity of the separation point on the 30° ramp at  $Re_b = 21.66$  M. These data show an average heat transfer rate of approximately 5.0 BTU/Ft<sup>2</sup>-sec for the two body locations upstream of the separation point and approximately 9.0 BTU/Ft<sup>2</sup>-sec downstream of the separation point. The peak heating spike in the data at approximately 6 seconds is the result of the model insertion through the open-jet wake. Notice the heating rate downstream of the separation point, in the subsonic interaction region, is almost twice the level upstream.

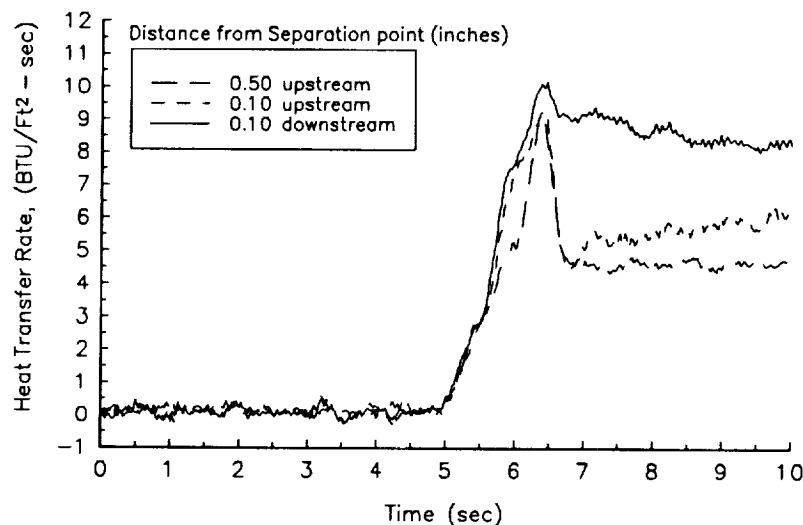


Figure 11. Heating Rate Near Separation: 30° Ramp,  $Re_b = 21.66$  M

Figure 12, in contrast, presents heat transfer data within a laminar-type interaction region for the same model configuration at  $Re_b = 4.33$  M. The term "laminar-type" refers to the shallow interaction angle and large separation bubble as shown in Figure 13. Consider that all of the data from Figure 12 is within the separation bubble. If we take this value to be approximately twice that of the upstream heating levels, as seen in the data trends from Figure 11, the upstream heating rate for this interaction at 4.33 M can be approximated at 0.75 BTU/Ft<sup>2</sup>-sec. This value is of the order of one-eighth the heating rate for the same configuration at  $Re_b$  21.66 M. The ratio of these heating rates gives a result that is consistent with a general comparison between laminar and turbulent flow heating rates in that there is approximately an order of magnitude difference between the heat transfer rates.

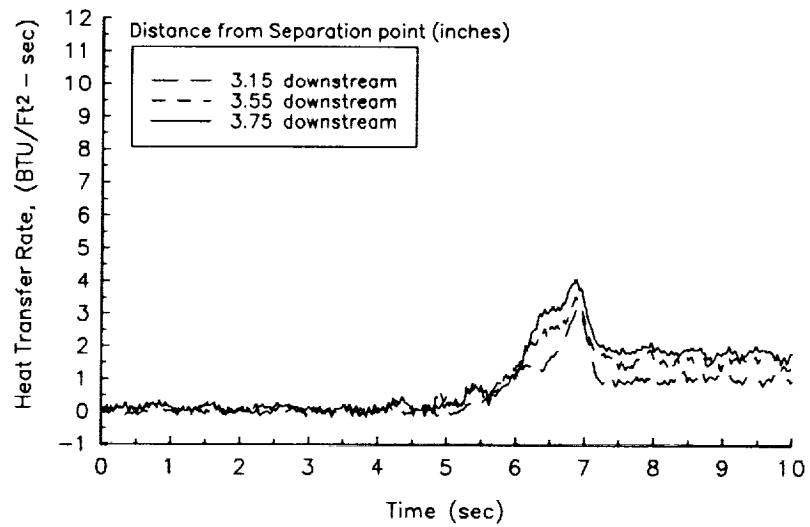


Figure 12. Heating Rate Near Separation: 30° Ramp,  $Re_b = 4.33 M$

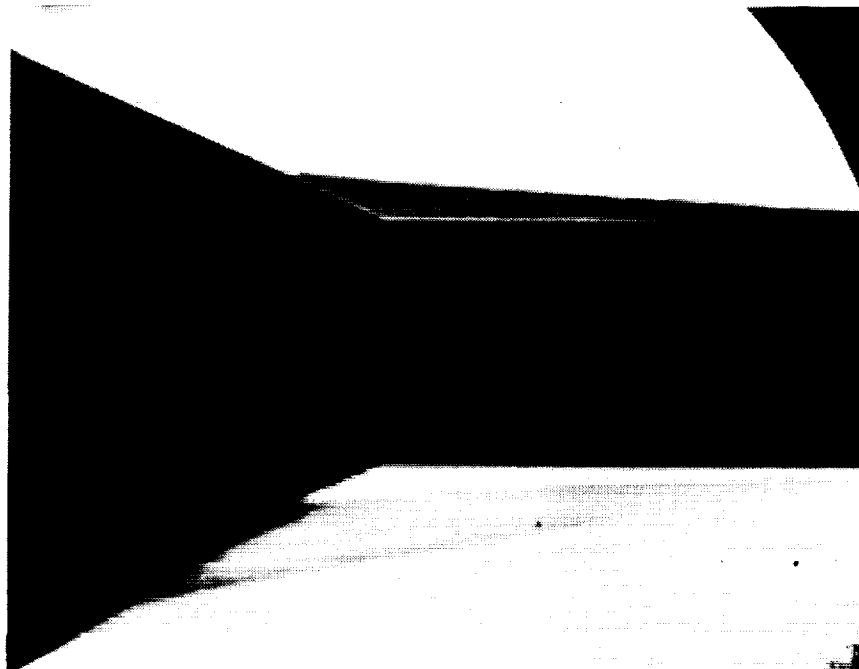


Figure 13. Schlieren photograph of a typical "laminar-type" interaction:  $Re_b = 4.33 M$

The self-consistency of these results validates the steady-state character of the temperature response within the shock-boundary layer region. It is still curious, however, that this interacting flowfield does not exhibit any significant or dynamic fluctuations in temperature. This would seem to indicate that steady-state heat transfer analysis should be sufficient for basic configuration design considerations.

## CONCLUSIONS

These data show some unsteadiness in temperature response at both the flow separation and reattachment locations, however, the RMS values are of insignificant magnitude. Comparison shows the ratio of these RMS values to the freestream temperature fluctuation levels to be of the order unity. The magnitude of these fluctuations are on the order of 0.5°F in the vicinity of the separation point and approximately 1.0°F in the vicinity of the reattachment point. The lack of any significant temperature fluctuations near the separation point is curious as the pressure response at the separation point indicates a dynamic environment oscillating at frequencies in the range of 300 to 400 Hz<sup>10</sup> with RMS pressure fluctuation levels on the order of 10 times the freestream fluctuation levels. More surprising, however, is the lack of any dynamic temperature trends within the vicinity of the reattachment point. The pressure data indicate significant levels of flowfield unsteadiness. This unsteadiness should appear in the vicinity of the reattachment point. The apparent lack of any temperature fluctuations at both the separation and reattachment locations suggests the flowfield environment is not subject to dynamic temperature effects. The heat transfer rates are steady-state.

## ACKNOWLEDGEMENT

The author is deeply indebted to Norm Skaggs and the Air Force Flight Dynamics Directorate for their efforts in providing test time and resources to The Ohio State University through a Cooperative Testing Agreement. This work was supported by the Hypersonic Research and Training Grant administered through NASA and was greatly enhanced by the Air Force Flight Dynamics Directorate at Wright-Patterson AFB.

## REFERENCES

1. Dolling, D.S. and Dussauge, J.P., "Fluctuating Wall-Pressure Measurements," Published as Chapter 8 in the Agardograph "A Survey of Measurements and Measuring Techniques in Rapidly Distorted Compressible Turbulent Boundary Layers," Spring 1988.
2. Owen, F.K., "Measurements of Hypersonic Flowfields," AGARD-FDP-VKI Special Course, Aerothermodynamics of Hypersonic Vehicles, 30 May to 3 June 1988.
3. Neumann, R.D., "Aerothermodynamic Instrumentation," AFWAL Technical Paper, WPAFB, May 1989.
4. Miller, C.G. , "Comparison of Thin-Film Resistance Heat-Transfer Gages With Thin-Skin Transient Calorimeter Gages in Conventional Hypersonic Wind Tunnels," NASA TM 83197, 1981.
5. Flanagan, M.J., "Operation and Design Considerations for Unsteady Data Acquisition with PC-Based Systems in High Reynolds Number Flowfields." AIAA Paper 92-0204. Presented at the 30th Aerospace Sciences Meeting, Jan 92.
6. Burke, G.L., "The Effects of Conduction Heat Transfer on the Temperature Distribution of High Speed Vehicles," AFFDL-TM-73-90-FXG, May 1973.
7. Beck, J.V. and TU, J.S., "IHCP2D: Computer Program for Solutions of General Two-Dimensional Inverse Heat Conduction Problems," AFWAL-TR-88-3111, March 1989. Distribution Restricted.
8. Blackman, R.B. and Tukey, J.W., *The Measurement of Power Spectra*, Dover Publications Inc, NY.
9. Marple, S.L., *Digital Spectral Analysis with Applications*, Prentice Hall Signal Process Series, Prentice-Hall Inc, 1987.
10. Flanagan, M.J. and Hayes, J.S., "Pressure and Temperature Fluctuations in an Axisymmetric Flowfield Due to Shock-Boundary Layer Interactions at High Reynolds Number at Mach 6." AIAA Paper 91-3321.

**HEAT FLUX MICROSENSOR MEASUREMENTS AND CALIBRATIONS**

James P. Terrell and Jon M. Hager  
Vatell Corporation  
Blacksburg, VA

Shinzo Onishi and Thomas E. Diller  
Virginia Tech  
Blacksburg, VA

**SUMMARY**

A new thin-film heat flux gage has been fabricated specifically for severe high temperature operation using platinum and platinum-10% rhodium for the thermocouple elements. Radiation calibrations of this gage were performed at the AEDC facility over the available heat flux range ( $\sim 1.0 - 1,000 \text{ W/cm}^2$ ). The gage output was linear with heat flux with a slight increase in sensitivity with increasing surface temperature.

Survivability of gages was demonstrated in quench tests from  $500^\circ\text{C}$  into liquid nitrogen. Successful operation of gages to surface temperatures of  $750^\circ\text{C}$  has been achieved. No additional cooling of the gages is required because the gages are always at the same temperature as the substrate material. A video of oxyacetylene flame tests with real-time heat flux and temperature output is available.

**INTRODUCTION**

The measurement of high heat flux is a primary concern for the aerospace industry. Existing heat flux sensors lack the reliability and durability needed for use in high temperature, high heat flux environments. These applications include gas turbine blades, hypersonic combustion chambers, rocket nozzles, and atmospheric reentry panels. Harsh environments such as these can produce wall temperatures in excess of  $3,000^\circ\text{C}$ , heat fluxes of more than  $2,000 \text{ W/cm}^2$  and flow speeds reaching Mach 25. These environments may also possess rapid transient processes which require a sensor with fast time response ( $< 1 \text{ msec}$ ).

There are some existing heat flux sensors that have been used for aerospace applications [1]. The high temperature Gardon gages can survive temperatures up to 1000°C and have a time response of 0.2 to 5.0 seconds [2]. Because most Gardon gages have a temperature limit of 500°C, they must be water cooled. Schmidt-Boelter gages normally survive temperatures to 350°C and have a time response  $\geq 0.05$  seconds [3]. Null-point calorimeters are designed for high heat flux measurements ( $> 100 \text{ W/cm}^2$ ) and run times less than 0.5 sec [4]. Heat flux can also be inferred from surface temperature measurements and the substrate thermal properties. Because the measurement depends upon a change in temperature with time, however, the flow conditions must be rapidly changed or the model must be injected into the flow. Jones [5] discusses the required signal processing to extract heat flux from the signal. Temperature measurements using coaxial thermocouples, thin-film resistance elements, and temperature sensitive paints have all been used with some success in impulse facilities. Any one of these gages can only partially satisfy the necessary requirements of the high temperature, high heat flux environments described above.

Heat flux gages often cause the problems of flow field and temperature field distortion. This is especially true for high speed flow and high temperature applications. Flow field distortion can be minimized by fairing the gage surface with its surroundings. In contrast, a distortion free temperature field is difficult to maintain in the presence of a heat flux gage. The distortion is due mainly to the discontinuity of material thermal properties when the flow encounters the gage. For high temperature applications, heat flux gages are often actively cooled to prevent overheating, which creates a cold spot. This will obviously magnify the thermal disruption and alter the heat flux measured. This is a problem with many of the previous measurements in these environments [6].

Layered heat flux gages, as illustrated in Fig. 1, have recently been made with thin film techniques, as first reported by Hager et al. [7]. Called Heat Flux Microsensors, they consist of several thin-film layers forming a differential thermopile across a thermal resistance layer. Because the gages are sputtered directly onto the surface, their total thickness is less than  $2 \mu\text{m}$ , which is much less than previous layered gages. The resulting temperature difference across the thermal resistance layer ( $\delta < 1 \mu\text{m}$ ) is very small even at high heat fluxes. To generate a measurable signal many thermocouple pairs are put in series, as illustrated in Fig. 2. The combination of series thermocouple junctions and thin-film design creates a gage with very attractive characteristics for aerodynamic measurements. It is not only physically non-intrusive to the flow, but also causes minimal disruption of the surface temperature. Because it is so thin, the response time, as reported by Hager et al. [8], is approximately  $20 \mu\text{sec}$ . Unlike the transient thin-film gages, however, the signal of the Heat Flux Microsensor is proportional to the heat flux and gives a continuous measurement. Therefore, it can be used in both steady and transient flows and measures both the steady and unsteady components of the surface heat flux.

A new version of the Heat Flux Microsensor has been developed that has approached meeting the extreme demands exhibited by high temperature, high heat flux environments. These gages use platinum and platinum-10% rhodium as the thermoelectric materials. The melting temperature for platinum is 1700°C and for rhodium, 1900°C. A protective coating of  $\text{Al}_2\text{O}_3$  is



deposited on top of the sensor. The through connection method reported by Hager et al. [9] has survived saturation temperatures to 1000°C. This paper describes the radiation calibrations of these gages at the Arnold Engineering Development Center facility and experimental tests with an oxyacetylene flame and a liquid nitrogen quench.

## MICROSENSOR FABRICATION

Heat Flux Microsensors are fabricated with a thin thermal resistance layer ( $< 1 \mu\text{m}$ ) placed between many thermocouple pairs to create a differential thermopile. The individual voltage outputs of each thermocouple pair are too small to measure, however, many pairs arranged in series elevate the signal to a measurable level. The output voltage of the thermopile is directly proportional to the temperature difference across the thermal resistance layer, which is proportional to the heat flux normal to the surface.

The microsensors are made using thin-film sputtering techniques with stainless steel masks. A separate mask is made for each different layer by cutting with a programmable laser and is aligned one at a time under a microscope until all six layers of the sensor have been completed. Since using the stainless steel masks doesn't require any substrate chemical processing, such as photoresist, the deposition temperature can be increased to 300-400°C. Raising the substrate temperature during deposition reduces the thermal stresses in the film and gives better adhesion of the thin film layers at elevated temperatures. An overlay of the entire pattern is shown in Fig. 3. The surface temperature of the gage is monitored with a platinum thin-film resistance temperature sensor (RTS) located next to the heat flux gage.

A through connection technique has been developed to bring the sensor signal from the material surface through the substrate [9]. This method requires a pin to be inserted after the microsensor is fabricated. The top of the pin is conical in shape to increase the contact area with the hole in the substrate. Matching conical holes are drilled in the substrate before deposition, allowing the metal films to be sputtered down into the holes. Electrical connection between the pin and the film is achieved by compressive contact of the two surfaces. The compressive force is exerted by a miniature push nut encircling the shank of the pin and pressing against the backside of the substrate. A thin protective layer of  $\text{Al}_2\text{O}_3$  is deposited over the gage and the pins for abrasive and chemical protection as well as electrical isolation from the environment. This through connection method has proven to be reliable to over 1000°C. Platinum lead wires are spot welded to the other end of the pins and then connected to their respective twisted pair as part of a four-lead shielded cable.

These gages contribute negligible flow disruption since they are less than  $2 \mu\text{m}$  total thickness. The microsensor fabrication method offers the possibility of preparing a gage directly on the measurement surface or on a plug of the same material. The current gages were deposited on 6.3 mm (0.25 in.) thick, 25.4 mm (1.0 in.) diameter aluminum nitride disks. When gages are deposited on the actual model to be used, or at least the same material, gage thermal disruption

could be virtually eliminated. The small thickness of the gage contributes negligible thermal capacity and affords a high frequency response allowing measurements up to 50 kHz [7].

## MICROSENSOR CALIBRATION

The precision of a heat flux gage measurement is largely based upon the reliability of the calibration. Due to the dependence on independent parameters, such as temperature, it is important to calibrate a gage at or near test conditions. For future success of the Heat Flux Microsensor in extreme environments, there must be a calibration method simulating these high temperature, high heat flux environments. Presently there are very few facilities which can simulate these conditions.

The present gage was calibrated at the AEDC radiation facility, which has the capability to calibrate sensors with heat flux spanning three orders of magnitude. Two of their calibration devices were used for these tests, one for low heat flux (1.0 - 9.1 W/cm<sup>2</sup>) and one for high heat flux (200 - 685 W/cm<sup>2</sup>). Each heat flux range utilized a separate apparatus. The low range calibration method is traceable to NIST [10]. The higher range used a Gardon gage, calibrated by Medtherm, for the standard.

The low heat flux apparatus uses a bank of nine 1,000 watt quartz tube lamps to radiate down through a shutter system. An area of approximately 2.5 cm (1 in.) by 7.5 cm (3 in.) receives radiation uniform to within 1.0%. The gage was mounted in a horizontal aluminum plate along with three Schmidt-Boelter gages used as standards. Because portions of the Heat Flux Microsensor are transparent, the sensors were coated with Krylon Ultra-flat black paint with an emissivity of 0.97. The shutter system allows the lamp bank to preheat to full intensity before the gages are exposed. A single test lasts 10 seconds with data recorded every 0.1 seconds. The data acquisition system was controlled by a microcomputer. A program presented the voltage output of the three standards, their corresponding heat fluxes, and the calculated sensitivity of the Heat Flux Microsensor based on the average heat flux of the three standards. The level of incident heat flux was changed by adjusting the voltage supply to the lamp bank. Several settings were retested to check the repeatability of the tests. The sensitivity of the gage is plotted versus heat flux (Fig. 4) and surface temperature (Fig. 5). The average sensitivity was calculated to be 1.65  $\mu\text{V}/(\text{W}/\text{cm}^2)$  with a standard deviation of 0.13  $\mu\text{V}/(\text{W}/\text{cm}^2)$ .

The high heat flux apparatus radiated upwards using a 1.6 kW Xenon arc lamp focused through a series of shutters. The lamp was capable of producing 2.8 kW/cm<sup>2</sup>. After the radiation passed through the shutter system it was directed through an optical integrator to assure a uniform intensity over the 0.63 cm (0.25 in.) diameter area covering the gage. Unfortunately, the integrator reduced the radiation flux to a maximum level of approximately 700 W/cm<sup>2</sup>. The shutter system consisted of three separate shutters all of which were computer actuated. The shutter system provided radiation protection and allowed evaluation of gage time response. The incident heat flux could be controlled by adjusting the supply voltage to the arc lamp. The small

area of the optical integrator ( $\approx 32 \text{ mm}^2$ ,  $0.05 \text{ in}^2$ ) allowed only one gage to be irradiated at a time. The Gardon gage was placed in the apparatus first to determine the flux level for a 500 msec test. It was then replaced with the microsensor and irradiated with the same voltage setting. The sensitivity of the gage was calculated using the heat flux measured by the Gardon gage,  $q_r$ , the emissivity of the paint on the microsensor,  $\epsilon$ , and the microsensor voltage output,  $q_m$ .

$$S = \left( \frac{1}{\epsilon} \right) \left[ \frac{E_m}{q_r} \right] \quad (1)$$

The resulting gage sensitivities are plotted versus gage surface temperature for four different heat flux levels in figure 6. Because of the high heat flux levels, the surface temperature of the gage rose noticeably even over the short 50 msec time of each test. The temperature dependence of sensitivity is evident over this temperature range. The average sensitivity increase of  $0.44\%/^{\circ}\text{C}$  may be explained by the decrease in thermal conductivity of the thin thermal resistance layer with increasing temperature. When compared with the low heat flux calibrations, the sensitivity at high heat flux is about 20% lower at the same surface temperature. Although this is not a large difference considering the range of almost three orders of magnitude in heat flux, there are several uncertainties in the high heat flux calibrator results. First, the manufacturer's calibration of the Gardon gage standard had to be used because a standard from NIST was not available. Second, the effect of elevated temperatures on the Gardon gage is not known. Third, the emissivity of the paint was assumed to remain constant at 0.97, although its surface finish was noticeably altered after the high heat flux calibrations. Fourth, the spot size of the calibrator was barely larger than the 3 mm by 4 mm size of the microsensor.

Aerodynamic applications for heat flux sensors involve placing the sensor in a flow field. Although the primary mode of heat transfer is often convection, the split between the radiation and convection modes of heat transfer is usually unknown. When radiation is used as the mode of calibrating a heat flux gage, it is usually assumed that convection will cause an identical response from the sensor. To check this assumption, the same gage that was calibrated at the AEDC radiation facility was also calibrated in a convection apparatus at Virginia Tech [9]. The convective heat transfer sensitivity of this gage was found to be  $2.33 \mu\text{V}/(\text{W}/\text{cm}^2)$  with a standard deviation of  $0.05 \mu\text{V}/(\text{W}/\text{cm}^2)$ . This represents a 40% higher sensitivity. Although the Gardon gage used in the Virginia Tech tests was separately calibrated in convection by Diller and Borell [11], there is no NIST traceable standard for convection heat transfer. This is an important issue to resolve in future research.

## HIGH-TEMPERATURE FLAME TESTING

Previous oxyacetylene flame tests were conducted with a platinum RTS protected by a layer of aluminum oxide and silicon nitride [9]. These experiments were continued until failure at approximately  $800^{\circ}\text{C}$ . The latest oxyacetylene flame tests reported here were performed with

several complete Platinum/Platinum-10% Rhodium heat flux gages. The final test for each gage was to destruction to determine the temperature limits of the gage.

The gages deposited on aluminum nitride substrates were mounted in a water-cooled aluminum block to provide a heat sink. The block was positioned at a distance of 15 cm (6 in.) from a standard oxyacetylene torch nozzle, as illustrated in Fig. 7. A wide range of flame adjustments was used to create different temperature and heat flux conditions. Tests were performed with different durations and cooling water flow rates. Fig. 8 shows a typical plot of the measured heat flux as recorded in an accompanying videotape. This test is for a relatively short duration and a low heat flux ( $< 100 \text{ W/cm}^2$ ). The final test in this series was performed by turning off all cooling water and proceeding until failure occurred at approximately  $750^\circ\text{C}$ . Other tests performed at much higher heat fluxes produced failure at approximately  $600^\circ\text{C}$ . The sensitivity of the gages had to be estimated by extrapolating the sensitivity versus temperature curve found from the AEDC radiation calibrations to the measured gage surface temperatures. Because this calibration uncertainty introduces considerable uncertainty into the measurements, facilities for performing heat flux calibrations at elevated temperatures are going to be essential.

### LIQUID NITROGEN QUENCH TEST

A liquid nitrogen quenching experiment was performed to test the thermal shock resistance of the Heat Flux Microsensors. The test was done on an RTS to evaluate the adhesion effects of the thin films when exposed to a temperature shock. Adhesion loss of the thin films has been attributed to differences in the thermal expansion coefficients of adjacent films.

An aluminum nitride disk with an RTS deposited on it was heated to  $580^\circ\text{C}$  in a tube furnace. The disk was removed from the furnace and held in air for 25 seconds. The disk was then placed in the liquid nitrogen with the face of the disk submerged for 25 seconds. Finally the disk was entirely submerged in the liquid nitrogen. These three distinct environments can be seen in Fig. 9, with increasing cooling rates for each subsequent section. The air provided a cooling rate of  $2.4^\circ\text{C/sec}$ . With the disk partially submerged the cooling rate increased to  $4.1^\circ\text{C/sec}$ . While the disk was completely submerged the cooling rate increased to  $5.3^\circ\text{C/sec}$ . This produced very vigorous boiling. The thin-film survived without any detectable damage. Future experiments will include liquid nitrogen tests on a complete gage to demonstrate the ability of the microsensors to measure high negative heat fluxes.

### CONCLUSIONS

High temperature Heat Flux Microsensors have been shown to operate well in several severe environments, typical of the aerodynamic testing conditions now being required of instruments. Radiation calibrations demonstrated good response and repeatability of the sensors.

It has also become clear that high temperature heat flux calibration facilities are needed and that comparison between radiation and convection heat transfer under these conditions is needed.

### ACKNOWLEDGEMENTS

The support of the Air Force in this work is acknowledged. The cooperation and encouragement of Carl Kidd while using the facilities at AEDC is greatly appreciated. The authors also acknowledge the cooperation of the Hybrid Microelectronics Laboratory at Virginia Polytechnic Institute and State University.

### REFERENCES

1. Neumann, R. D., "Aerothermodynamic Instrumentation," in **AGARD Report**, No. 761, 1989.
2. Clayton, W. A., "High Temperature Circular Foil Heat-Flux Gage," Hy-Cal Engineering Report TR-417, Feb. 1980.
3. Kidd, C. T., "A Durable, Intermediate Temperature, Direct Reading Heat-Flux Transducer for Measurements in Continuous Wind Tunnels," AEDC-TR-19-81, Nov. 1981.
4. Kidd, C. T., "Recent Developments in High Heat-Flux Measurement Techniques at the AEDC," ISA Paper No. 90-156, 1990.
5. Jones, T. V., "Heat Transfer, Skin Friction, Total Temperature, and Concentration Measurements," in **Measurement of Unsteady Fluid Dynamic Phenomena**, Hemisphere Pub. Corp., N. Y., 1977, pp.63-102.
6. Neumann, R. D., Erbland, P. J., and Kretz, L. D., "Instrumentation of Hypersonic Structures -- A Review of Past Applications and Needs for the Future," AIAA Paper No. 88-2612, 1988.
7. Hager, J. M., Onishi, S., Langley, L. W., and Diller, T. E., "Heat Flux Microsensors," in **Heat Transfer Measurements, Analysis and Flow Visualization**, Ed. R. K. Shah, ASME, 1989, pp. 1-8.
8. Hager, J. M., Simmons, S., Smith, D., Onishi, S., Langley, L. W., and Diller, T. E., "Experimental Performance of a Heat Flux Microsensor," **ASME Journal of Engineering for Gas Turbines and Power**, Vol. 113, 1991, pp. 246-250.

9. Hager, J. M., Terrell, J. P., Langley, L. W., Onishi, S., and Diller, T. E., "Measurements with the Heat Flux Microsensor," Proceedings of the 37th International Instrumentation Symposium, ISA, Research Triangle Park, 1991, pp. 551-561.
10. Kidd, C. T., "Determination of the Uncertainty of Experimental Heat-Flux Calibrations," AEDC-TR-83-13, August 1983.
11. Borell, G. J., and Diller, T. E., "A Convection Calibration Method for Local Heat Flux Gages," ASME Journal of Heat Transfer, Vol. 109, 1987, pp. 83-89.

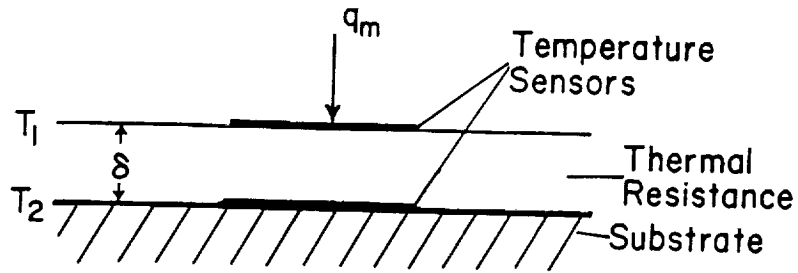


Fig. 1 Layered Heat Flux Gage

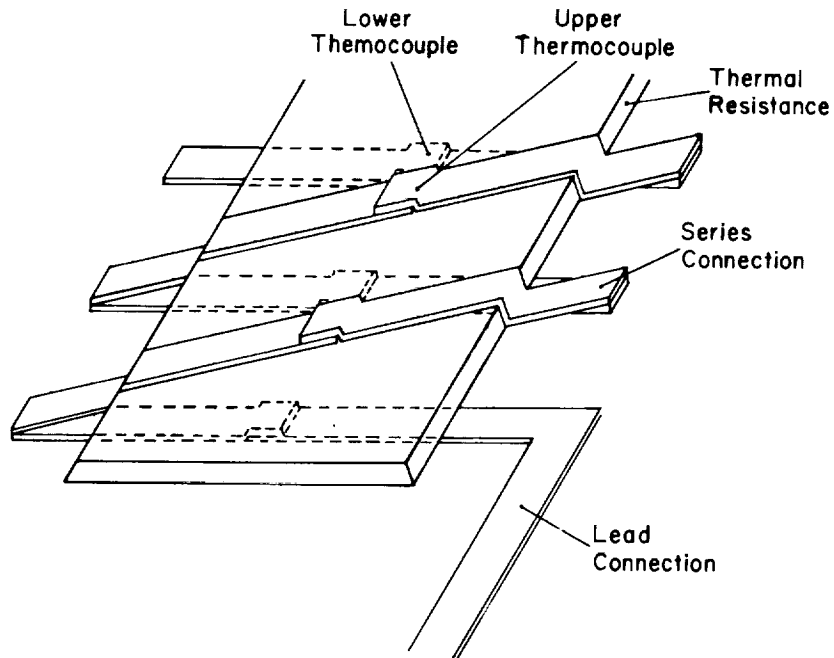


Fig. 2 Detailed Representation of Microsensor

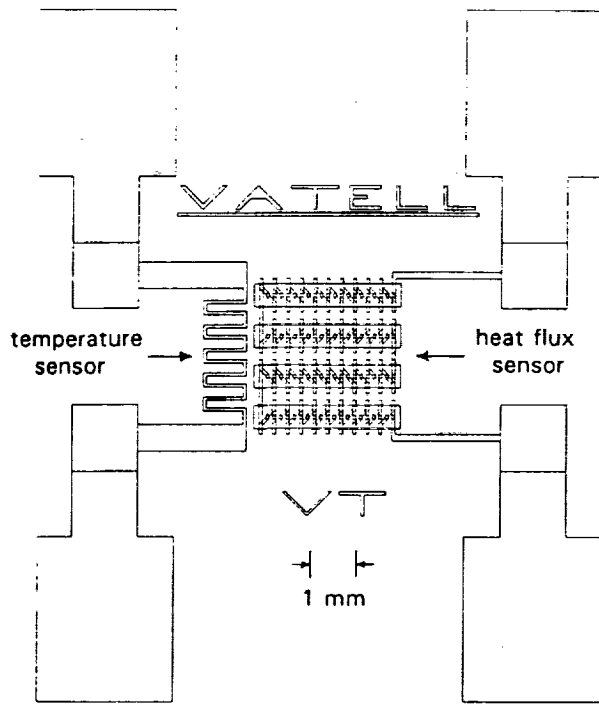


Fig. 3 Heat Flux Microsensor Pattern Overlay

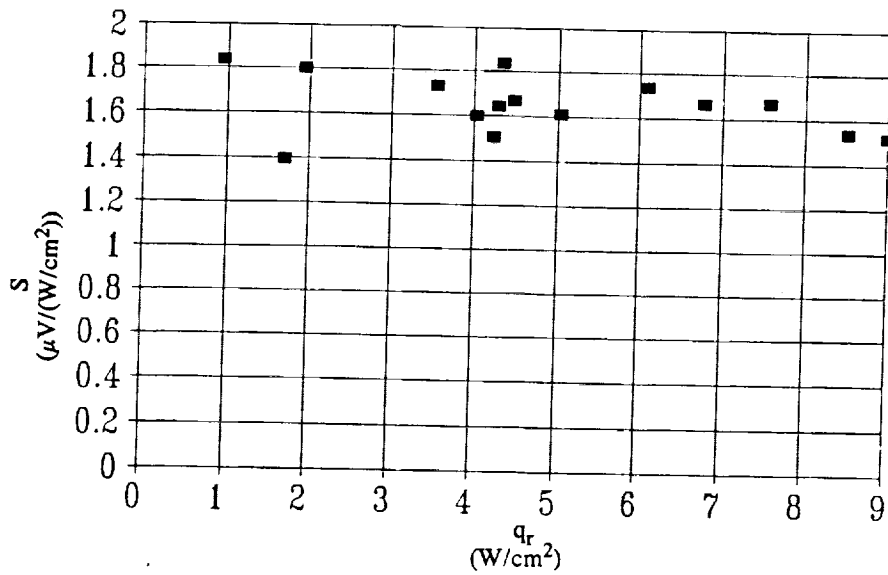


Fig. 4 Low Heat Flux Calibration Tests, Sensitivity Vs. Heat Flux



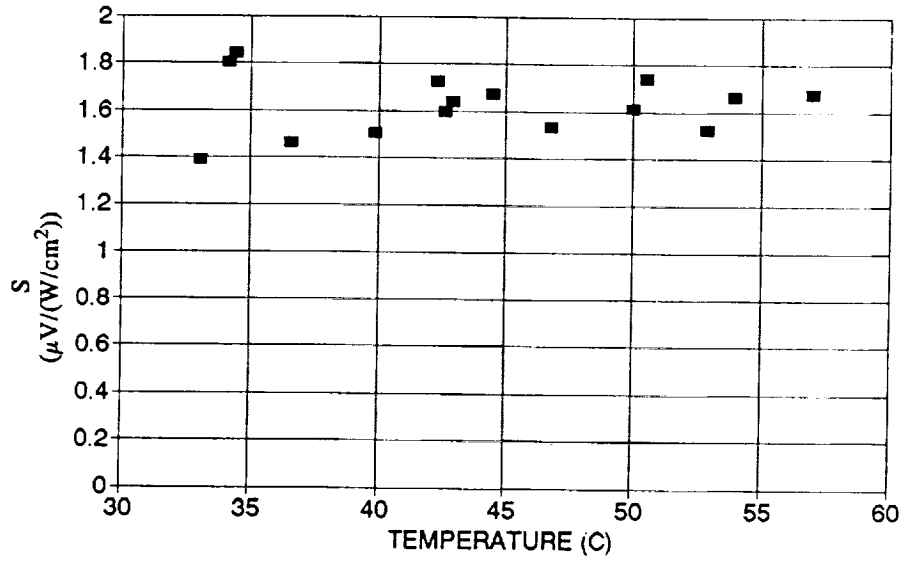
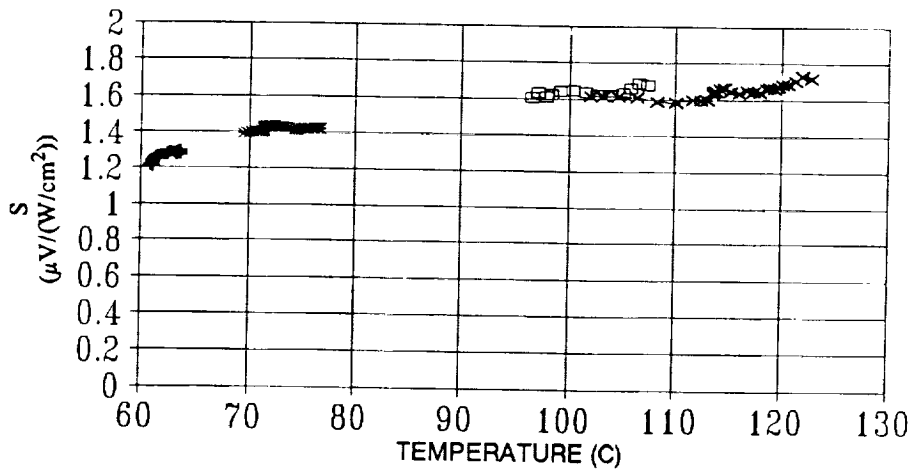


Fig. 5 Low Heat Flux Calibration Tests, Sensitivity Vs. Surface Temperature



+ 201.7 W/cm<sup>2</sup> \* 471.7 W/cm<sup>2</sup> □ 621.9 W/cm<sup>2</sup> —x— 703.5 W/cm<sup>2</sup>

Fig. 6 High Heat Flux Calibration Tests

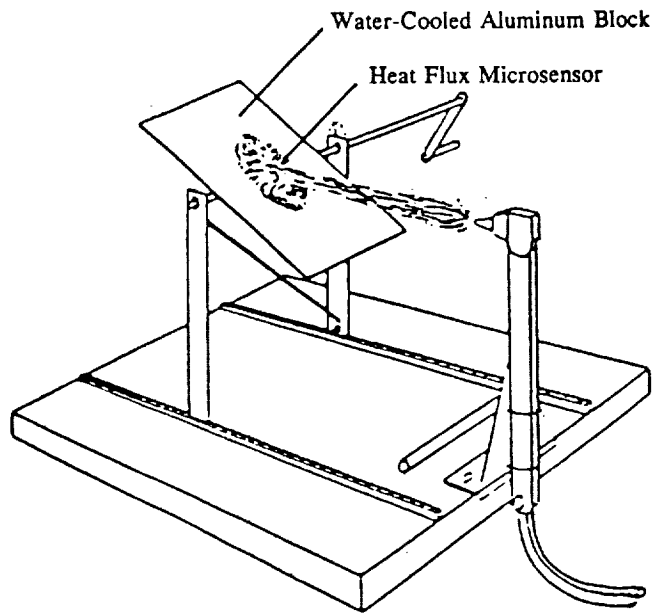


Fig. 7 Oxyacetylene Flame Test Apparatus

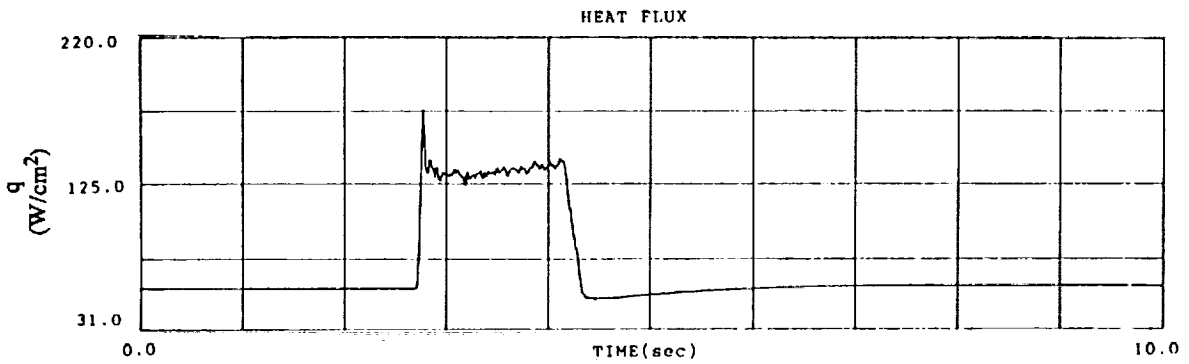


Fig. 8 Sample Oxyacetylene Flame Test

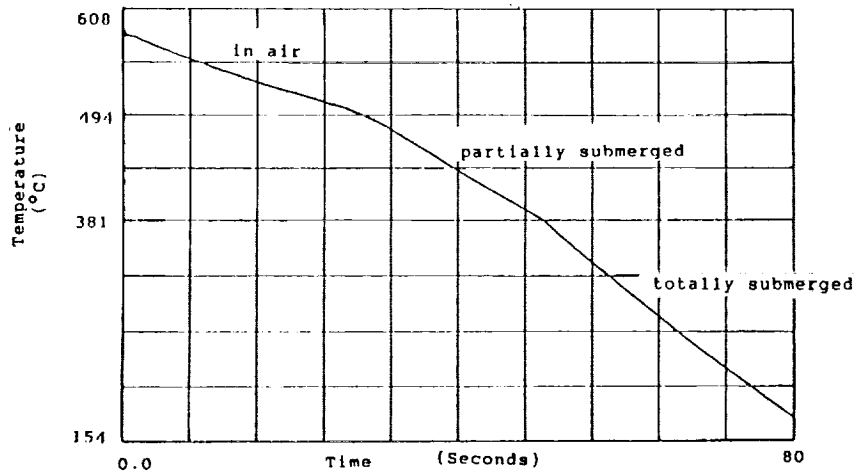


Fig. 9 Liquid Nitrogen Quench Test

THIN FILM THERMOCOUPLES FOR HIGH TEMPERATURE MEASUREMENT  
ON CERAMIC MATERIALS

Raymond Holanda  
NASA Lewis Research Center  
Cleveland, OH

## SUMMARY

Thin film thermocouples have been developed for use on metal parts in jet engines to 1000°C. However, advanced propulsion systems are being developed that will use ceramic materials and reach higher temperatures. The purpose of this work is to develop thin film thermocouples for use on ceramic materials. The thin film thermocouples are Pt13Rh/Pt fabricated by the sputtering process. Lead wires are attached using the parallel-gap welding process. The ceramic materials are silicon nitride, silicon carbide, aluminum oxide, and mullite. Both steady state and thermal cycling furnace tests were performed in the temperature range to 1500°C. High-heating-rate tests were performed in an arc lamp heat-flux-calibration facility.

The fabrication of the thin film thermocouples is described. The thin film thermocouple output was compared to a reference wire thermocouple. Drift of the thin film thermocouples was determined, and causes of drift are discussed. The results of high-heating-rate tests up to 2500°C/sec are presented. The stability of the ceramic materials is examined.

It is concluded that Pt13Rh/Pt thin film thermocouples are capable of meeting lifetime goals of 50 hours or more up to temperatures of 1500°C depending on the stability of the particular ceramic substrate.

## INTRODUCTION

Thin film thermocouples have been available for some time for use on metal parts in jet engines to 1000°C (ref. 1-8). However, advanced propulsion systems are being developed that will use ceramic materials and have the capability of attaining higher temperatures in their operation. Newer thin film thermocouples have been tested on silicon nitride at 1000°C (ref. 9). Additional testing of thin film thermocouples on several ceramic materials up to 1400°C has been performed (ref. 10-11).

The purpose of this report is to describe the effort to develop thin film thermocouples for use on ceramic materials and determine the temperature range and operating conditions for which they are capable of being used. The thin film thermocouples used were Pt13Rh/Pt fabricated by the sputtering process, and the ceramic materials were silicon nitride, silicon carbide, aluminum oxide, and mullite. Both steady state and thermal cycling furnace tests were performed in the temperature range from 1000-1500°C. High-heating-rate tests were

also performed in an arc lamp heat-flux-calibration facility (ref. 12) to 1500°C.

## APPARATUS AND EXPERIMENTAL PROCEDURE

The ceramic materials that were used in this program were silicon nitride, silicon carbide, aluminum oxide, and mullite. Tab. I lists the purity of these materials, the fabrication procedures, and some of the physical properties. The low purity of the silicon nitride is caused by the addition of 13 percent yttria and 3 percent alumina as densification agents for the sintering process. The surface finish is of particular interest because the thin film thermocouple is deposited on the surface of the ceramic materials. Surface finish varied from about .025-.15  $\mu\text{m}$  for the aluminum oxide to about .5-.75  $\mu\text{m}$  for the silicon nitride.

Fig. 1 shows a schematic diagram for the fabrication of thin film thermocouples on ceramic substrates. For the electrically insulating ceramic substrates, the thin film thermoelements are deposited directly on the surface. For the electrically conducting ceramic substrate (silicon carbide), an insulating layer must be deposited between the sensor and the substrate. A two-layer approach was used, starting with a stable, adherent, thermally grown silicon dioxide, followed by a sputter-deposited layer of aluminum oxide of the thickness needed to obtain the required insulation resistance. Each of the two layers was 1-2  $\mu\text{m}$  thick. The thin film thermocouples are Pt13Rh/Pt and are 5-7  $\mu\text{m}$  thick. They were deposited using the RF magnetron sputtering process at a sputtering power of 800 watts and sputtering rate of 5  $\mu\text{m/hr}$ . Substrate heating of about 300°C was used for the Pt and Pt13Rh films, and oxygen-enhanced sputtering of Pt was used for the first .02 $\mu\text{m}$  of deposition to improve film adhesion. Sputtering parameters were chosen based on previous work (ref. 5) and experience at this laboratory.

Fig. 2 is a photograph of the test samples used in these experiments. The ceramic substrates are 15 cm long and 2.5 cm wide, and the thicknesses are 1.5 mm for aluminum oxide, 4.5 mm for mullite, and 6 mm for silicon nitride and silicon carbide. They were cemented to an aluminum oxide support plate using an alumina-based cement with no binders. The thin film thermocouple deposited on the test sample was at least 12.5 cm long with film widths of about 3 mm. Pt13Rh/Pt lead wires were attached to the thin films using the parallel-gap welding process described in detail in ref. 13. These wires were 75  $\mu\text{m}$  in diameter and were routed through ceramic tubing to connectors.

Two ceramic tube furnaces were used in these experiments. The furnaces had a maximum temperature capability of 1300 and 1700°C, respectively. Set-point control of the furnaces was about  $\pm 1^\circ\text{C}$  in the central core of each furnace. Reference thermocouples made from 0.5 mm Type R (Pt13Rh/Pt) material were used to monitor these temperatures. Negligible drift rates for these reference thermocouples were observed throughout the testing; they verified the stability of the furnaces. Thermoelectric potentials were measured with a digital voltmeter with a sensitivity of 1  $\mu\text{volt}$  and an accuracy of  $\pm 0.01$  percent + 5  $\mu\text{volts}$ . Cold junction temperature was recorded but not controlled, and the emf data were corrected to 0°C. Furnace testing of the thermocouples took place in steady state and thermal cycling modes. For steady-state tests, two types of test sample configurations were used. In one configuration, the test sample was only partially inserted into the furnace, resulting in a large temperature gradient along the length of the thin film thermocouple up to a maximum of

about 600°C. This temperature gradient is shown in Fig. 3 as a function of furnace temperature for silicon nitride and silicon carbide test pieces. In the other configuration, the entire test sample and part of the support plate was inserted into the furnace, resulting in a small temperature gradient along the length of the thin film thermocouple up to a maximum of about 100°C. These two test configurations were chosen to evaluate the effect of different temperature gradients on drift rate patterns in thin film thermocouple circuits. The steady-state tests were carried out in the temperature range from 1000-1500°C. Thermal cycling accompanied repeated steady-state tests of a particular test sample.

A total of 15 test samples was fabricated and tested for these experiments. Total test time was about 1000 hours. The lifetime goal of a sensor for advance propulsion system applications was about 50 hours. For laboratory testing, longer lifetimes would be desirable.

High-heating-rate tests were also performed, using an arc lamp heat-flux-calibration facility. Currents of 50-400 amps are generated in the lamp to produce heat fluxes in the range from about 0.1-5 Mw/m<sup>2</sup>.

## RESULTS AND DISCUSSION

The discussion of the results of these tests is divided into three main parts. First, the initial accuracy of the thin film thermocouple, as fabricated, will be discussed. Second, the subject of thermocouple drift will be discussed to illustrate the causes and effects of the change in thermocouple output with time. And last, an analysis will be made of the physical durability of the thin film thermocouples, which includes a discussion of the physical durability of the ceramic materials as well.

### Calibration of Thin Film Thermocouples

A calibration experiment was performed to determine the accuracy of the thin film thermocouple as fabricated by the sputtering process. The thin film thermocouple was fabricated on a silicon nitride substrate in the configuration shown in Fig. 2. A wire thermocouple made from the same 75- $\mu$ m-diameter wire used for the lead wires of the thin film thermocouple was cemented to the back of the test piece directly opposite the thin film thermocouple junction.

The test was performed in the configuration in which the test piece was only partially inserted into the furnace, resulting in the maximum attainable temperature gradient along the length of the thin film thermocouple. In a separate experiment, the value of this temperature gradient was determined as a function of furnace temperature; it is shown in Fig. 3. These data were obtained by cementing an additional wire thermocouple to the back of the test piece opposite the thin-film-to-lead-wire connection.

The calibration test results showed that the thin film thermocouple output was 3 percent less than the wire thermocouple. The result is expressed as percent of the temperature gradient applied to the thin film. The major uncertainty in the experiment is caused by the severe temperature gradient on the test piece and the inability of the cemented

reference thermocouple to indicate the exact test piece temperature at the exact location of the thin film thermocouple junction.

### Causes of Thin Film Thermocouple Drift

Thermocouple drift is defined as a change with time in the voltage vs temperature characteristic of a thermocouple. Suspected causes of thermocouple drift in these thin film thermocouples are oxidation of Rh in the Pt13Rh thermoelement, foreign material at the thin-film-to-lead wire connection, and chemical interaction or diffusion between the sensor and the substrate.

Preferential oxidation of rhodium in the Pt13Rh leg of the thermocouple would cause a change in the Pt/Rh ratio in that leg and result in thermocouple drift. This oxidation rate increases as temperature increases, but there is a conversion of the oxide back to elemental rhodium at a temperature of about 1000°C and above. Oxidation rate is also proportional to the surface area/volume ratio of the thin film sensor and lead wire geometry. The value of this ratio is at least 4 times greater for a 5 μm thin film compared to a 75 μm diameter lead wire. Finally, oxidation rate is dependent on the quantity of oxygen present in the gaseous environment surrounding the thermocouple. In these experiments, ambient air was the environment for all of the thermocouples.

The thin-film-to-lead-wire connection could be a source of thermocouple drift if a foreign material, such as a cement or paste, were introduced into the thermocouple circuit at this point to make the connection. But in these experiments, connections were made using the parallel-gap welding process, which eliminates this source of thermocouple drift.

Thermocouple drift could originate at the substrate-sensor interface if a chemical reaction were to occur at this interface or if diffusion of material into or out of the thermocouple were to occur that would change the thermoelectric characteristics of either thermoelement.

### Results of Thermocouple Drift

Drift-rate data for thin film thermocouples on ceramic materials are shown in Figs. 4 and 5 for steady state tests. The data are plotted as drift rate in °C/hr against the steady state temperature, and each point represents the average drift rate of a steady state test. Also shown on each figure is the temperature gradient across the thin film portion of the thermocouple circuit. In Fig. 4, the tests were performed on silicon nitride and silicon carbide substrates with a large temperature gradient of 500-600°C across the length of the thin film. This was accomplished by inserting only part of the test samples (shown in Fig. 2) into the testing furnace. With the hot junction of the thin film thermocouple at about 1000-1200°C in these tests, the lead wire end of the thin film thermocouple would be about 500-700°C; thus a large portion of the thin film would be in the temperature range where rhodium oxidation occurs. The result is a drift rate of about 0.5°C/hr. In these tests, the region of rhodium oxidation was easily seen by the formation of a dark deposit on the Pt13Rh

thermoelement. Tests were also performed where the temperature gradient along the length of the thin film was only about 100°C (Fig. 5). In these tests, the entire test piece and part of the support plate is inserted into the testing furnace. For a test where the hot junction of the thin film is at 1200°C, the lead-wire end of the thin film would be at about 1100°C; thus only the lead-wire portion of the thermocouple circuit would be in the temperature range where rhodium oxidation occurs. This results in a drift rate of less than 0.2°C/hr for the data in Fig. 5 between about 1000-1200°C. There is no dark deposit on the Pt13Rh thin film thermoelement.

At temperatures greater than about 1250°C in Fig. 5, drift rates rapidly increase as test temperature increases. It is suspected that a sensor-substrate interaction is beginning to occur in this temperature range, either because of a chemical reaction or a diffusion effect. It should also be noted that the drift rate is not the same for each substrate material in this higher temperature range. Auger depth profiling analysis is being used to analyze these effects.

A thermocouple probe was fabricated completely from 75 µm lead wire in order to separately determine lead-wire drift rate. The drift rate was determined at three temperature levels. The drift rate was .03°C/hr at 1150°C, 0.1°C/hr at 1370°C, and 0.3°C/hr at 1500°C. These lead-wire drift rates are tabulated in Fig. 6 along with selected values of the drift rates of the thin film thermocouples on the four ceramic materials. Figs. 4-6 illustrate the complexity of thermocouple drift of thin film thermocouples, which are in actuality composite thin film/lead-wire thermocouple circuits. We can summarize the information contained in Figs. 4-6. Drift rate varies with: the absolute temperature level; the substrate material on which the thin film thermocouple is deposited; the temperature gradient distribution between the thin film and the lead-wire portion of the circuit; and the film thickness and diameter of the thin films and lead-wires, respectively. And for every application, some of these factors could well be different.

Fig. 7 is a plot of drift in °C against time for thin film thermocouples on two test pieces. One test piece was silicon carbide tested at 1100°C for 95 hours with a 500°C temperature gradient across the thin film portion of the thermocouple circuit. In this test, the primary cause of drift was expected to be oxidation of the rhodium in the Pt13Rh leg, and such oxide was visible at the conclusion of the test. It was also expected that the oxide growth rate would follow a parabolic rate law, because of the passivating effect of the rhodium oxide layer; and this in turn would cause a similar functional relationship between temperature drift and time, which can be seen to be the case in Fig. 7.

The other test results plotted in Fig. 7 are for a thin film thermocouple deposited on an aluminum oxide substrate, tested at 1500°C for 20 hours, with a 100°C temperature gradient across the thin film portion of the thermocouple circuit. In these test conditions, the cause of drift was suspected to be sensor-substrate interaction caused by chemical reaction or diffusion. The functional relationship of temperature drift with time is seen to be approximately linear.

### Durability of Thin Film Thermocouples

The four ceramic materials used in this research program exhibited significantly

different characteristics when exposed to high temperatures. The oxide ceramics, aluminum oxide and mullite, showed little visible surface deterioration when exposed to the entire temperature range of these experiments (1000-1500°C). The aluminum oxide was 99.6% pure and the mullite was a 98% pure mixture of aluminum oxide and silicon dioxide (60 to 38 ratio). Despite the lack of visible surface deterioration, the thin film sensors showed a significant increase in drift rate on these substrates above about 1300°C (see Fig. 5), indicating some form of sensor-substrate interaction. Very little degradation of the sensor structure occurred.

The non-oxide ceramics, silicon nitride and silicon carbide, exhibited visible surface changes during these tests. The silicon nitride was fabricated by the hot-pressed method using 13% yttria and 3% alumina as densification agents. It was observed during the testing process that this material formed a complex surface oxide, and that the rate of oxidation increased dramatically at temperatures above about 1250°C. As the oxide formation increased in magnitude, it caused a gradual bubbling and delamination of the thin film sensor material.

The silicon carbide was 99% pure and required an insulating layer to be superimposed between the sensor and the substrate because it is an electrically conducting ceramic. The insulating layer consisted of a thermally grown silicon dioxide layer plus a sputter-deposited aluminum oxide layer. The silicon carbide showed no visible deterioration during testing up to about 1250°C, but above this temperature, the surface morphology began to change to a glassy appearance over a portion of its surface, and other nonuniformities in structure appeared. This change in surface morphology caused delamination of the thin film sensor material to begin.

A total of 15 test samples with thin film sensors were used in these experiments. Thermal cycling accompanied repeated steady-state tests of the same test sample up to a maximum of five cycles. No sensor failures occurred as a result of thermal cycling. Steady state testing of a single test sample occurred for various times up to a maximum of 149 hours. No sensor failures occurred as a result of total test time. The only sensor failures occurred on silicon nitride and silicon carbide substrates and correlated with a deterioration of the ceramic substrate when tested beyond a critical temperature level in the range above about 1250°C.

Photographs of the thin film thermocouple hot junctions were taken at different stages of the testing process (Figs. 8 and 9). Also shown in these figures is the number of hours of testing time and the maximum test temperature of each specimen. Fig. 8 shows the sensors on aluminum oxide and silicon nitride substrates. The sensors on aluminum oxide substrates show negligible degradation up to 1355°C. Oxide formation can be seen on the silicon nitride surface at 1167°C, and a dramatic increase in the magnitude of the oxide formation is seen at 1343°C, causing a bubbling of the sensor material and leading to delamination. Sensors on silicon carbide substrates are shown in Fig. 9. Negligible degradation of sensor films is seen up to 1246°C, but at 1322°C, morphological changes in the substrate have begun to appear, leading to the start of sensor delamination.

Jacobson (ref. 14) discusses the durability of ceramic materials for use in advanced propulsion systems. He points out that the ceramic materials will degrade chemically by oxidation, vaporization, and interfacial reactions. For the oxide ceramics, such as aluminum oxide and mullite, vaporization is the major mechanism. In these experiments, this could lead to a slow, gradual deterioration of the bond between the sensor and the substrate.

For the non-oxide ceramics, such as silicon nitride and silicon carbide, all three



mechanisms of oxidation, vaporization, and interfacial reactions are at work. For silicon nitride, the oxidation of the silicon nitride not only forms an interface at the oxide-substrate boundary, but can lead to a complicated structural interaction with yttria and alumina present as densification agents in the ceramic. This was seen in Fig. 8 to result in the rapid formation of an irregular oxide structure above 1250°C leading to sensor delamination. In the case of silicon carbide, the interfaces were deliberately formed by thermal oxidation and sputtered alumina to form the insulating layer for the sensor. Above 1250°C, the formation of a glassy layer and other irregular structure in the surface layers of the ceramic could be caused by interfacial reactions, phase change, or further oxidation. This leads to a deterioration between the sensor-substrate bond, and eventual delamination.

Lifetime goals for thin film sensors of 50 hours or more are feasible at temperature levels where a particular ceramic substrate is sufficiently stable. Each formulation of a ceramic must be evaluated to determine this limit.

### Heat-flux-calibration Facility Tests

Another aspect of sensor durability is the ability of the sensor to withstand high heating rates accompanied by rapid temperature excursions from room temperature to the maximum operating temperature of the sensors. The arc lamp heat-flux-calibration facility is capable of concentrating a high, known heat flux over a small, well-defined area. Lamp currents from 30-400 amps are used to generate heat fluxes from about 0.1-5 Mw/m<sup>2</sup> over a 1 by 4 cm area. Fig. 10 shows a test piece with a thin film thermocouple deposited on the surface in such a way that the hot junction is at the center of the focal area of the lamp. The test piece is silicon nitride, and a black coating is applied to a portion of the surface to increase the absorption of the radiant energy. A second thin film thermocouple is mounted on the back surface directly behind the front sensor. Fig. 11 shows the temperature rise vs time for the hot-side thermocouple for different lamp currents. Heating rates from about 2-2500°C/sec were generated in these tests. Silicon nitride and mullite were used. Maximum temperature was 1500°C, and maximum  $\Delta T$  across a ceramic was 560°C. No sensor failures occurred during these tests, and a single test piece was subjected to a maximum of 20 test cycles. Note that in these tests the total test time is measured in seconds or minutes rather than hours and therefore the ceramics suffered very little surface degradation.

### SUMMARY OF RESULTS

Pt13Rh/Pt thin film thermocouples were fabricated on ceramic substrates of silicon nitride, silicon carbide, aluminum oxide, and mullite using the sputtering process. They were tested in high temperature furnaces in steady state and thermal cycling modes in the temperature range from 1000-1500°C. The following results were determined:

1. The output of a Pt13Rh/Pt thin film thermocouple was lower than the output of a reference wire thermocouple by 3 percent of the value of the temperature gradient applied to the thin film.

2. A principal cause of thermocouple drift of the thin film thermocouple was determined to be rhodium oxidation of the Pt13Rh thin film thermoelement. A much smaller drift was caused by rhodium oxidation of the lead wire. Rhodium oxidation was confined to that portion of the thermocouple circuit below about 1000°C. Above this temperature the rhodium oxide dissociates. The rhodium oxidation proceeds at an approximately parabolic rate.
3. Above about 1250°C, thermocouple drift increased rapidly. The cause of this drift is presumed to be a chemical reaction or diffusion effect at the sensor-substrate interface.
4. Oxidation of the silicon nitride substrate was visible in tests above 1000°C and increased rapidly above 1250°C. Formation of this surface oxide led to bubbling of the thin film sensor and eventual delamination.
5. No physical change in the appearance of the silicon carbide was seen up to 1250°C. Above this temperature, the surface morphology changed to a glassy appearance accompanied by other nonuniform structural defects. These changes could be caused by interfacial reactions, phase change, or oxidation. The changes caused bubbling and delamination of the sensor to begin.
6. No physical change in the appearance of the aluminum oxide or mullite was seen in the temperature range of these experiments. Thin film sensors on these materials showed very little degradation.
7. Thin film sensors were tested for up to 149 hrs and five thermal cycles in furnace tests without failures attributable to these conditions alone. Lifetime goals for thin film sensors up to 50 hours or more appear feasible at temperature levels where a particular ceramic substrate is sufficiently stable.
8. Thin film sensors on silicon nitride and mullite were tested in an arc lamp heat-flux-calibration facility to a maximum temperature of 1500°C, heating rates from 2-2500°C/sec, and up to 20 thermal cycles, with no sensor failures.

#### ACKNOWLEDGMENTS

The author acknowledges the invaluable assistance of Gerald A. Danzey for the fabrication of the test specimens, and Curt H. Liebert, William T. Dedula, and George W. Readus Jr. for operation of the heat-flux-calibration facility.

#### REFERENCES

1. H.P. Grant, and J.S. Przybyszewski, Thin Film Temperature Sensor. NASA CR-159782, 1980.
2. H.P. Grant, J.S. Przybyszewski, and R.G. Claing. Turbine Blade Temperature Measurements Using Thin Film Temperature Sensors. NASA CR-165201, 1981.
3. H.P. Grant, J.S. Przybyszewski, R.G. Claing, and W.L. Anderson. Thin Film Temperature Sensors. Phase III. NASA CR-165476, 1982.

4. R.C. Budhani, S. Prakash, and R.F. Bunshah, J. Vac. Sci. Technol. A, 4, 2609, 1986.
5. S. Prakash. Thin Film Temperature Sensors for Gas Turbines. Ph.D. Thesis, UCLA, Los Angeles, CA, 1987.
6. J.C. Godefroy, D. Francois, C Gageant, F. Miniere, and M. Portat, in International Conference on Metallurgical Coatings, San Diego, CA, Apr. 7-11, 1986, Paper No. 1986-28, 1986.
7. J.C. Godefroy, C. Gageant, D. Francois, and M. Portat, J. Vac. Sci. Technol. A, 5, 2917, 1987.
8. K.G. Kreider, S. Semancik, and C. Olson. Advanced Thin Film Thermocouples. NBSIR 84-2949, 1984.
9. S. Prakash, R.C. Budhani, and R.F. Bunshah, Mat. Res. Bull., 23, 187 1988.
10. R. Holanda, C. Ho, S. Prakash, and R.F. Bunshah, in NASA Conference Publication 10039, Cleveland, OH, Oct. 31-Nov. 2, 1989, Paper No. 39-1, 1989.
11. R. Holanda, C. Ho, S. Prakash, and R.F. Bunshah, in NASA Conference Publication 10051, Cleveland, OH, Oct. 30-31, 1990, Paper No. 71-1, 1990.
12. C. Liebert and D.H. Weikle. Heat Flux Measurements. NASA TM-101428,1989.
13. R. Holanda, W.S. Kim, E. Pencil, M. Groth, and G.A. Danzey. Attachment of Lead Wires to Thin Film Thermocouples Mounted on High Temperature Materials Using the Parallel Gap Welding Process. NASA TM-102442, 1990.
14. N.S. Jacobson. High-Temperature Durability Considerations for HSCT Combustor. NASA TP-3162, 1992.

TABLE I - DESCRIPTION OF CERAMIC MATERIALS									
MATERIAL	FAB. METHOD	SURFACE FINISH, $\mu\text{m}$	THICKNESS, $\mu\text{m}$	DENSITY, $\text{gm}/\text{cm}^3$	THERMAL COND., $\text{W}/\text{m}\cdot\text{K}$	ELECTR. RES., $\text{ohm}\cdot\text{cm}$	MELTING POINT, $^{\circ}\text{C}$	TCE*, $\alpha$ , $^{\circ}\text{C}^{-1}\times 10^{-6}$	PURITY, %
SILICON NITRIDE	SINTERED	.5-.75	6	3.28	30	$10^{14}$	1900	4	84
SILICON CARBIDE	SINTERED	.25-.5	6	3.1	125	10	2700	4	99
ALUMINUM OXIDE	TAPECAST	.075-.15	1.5	3.9	25	$10^{14}$	2040	8	99.6
MULLITE	HOT-PRESSED	.25-.5	4.5	3.6	4	$10^{14}$	1700	10	98

\* - Temperature coefficient of expansion

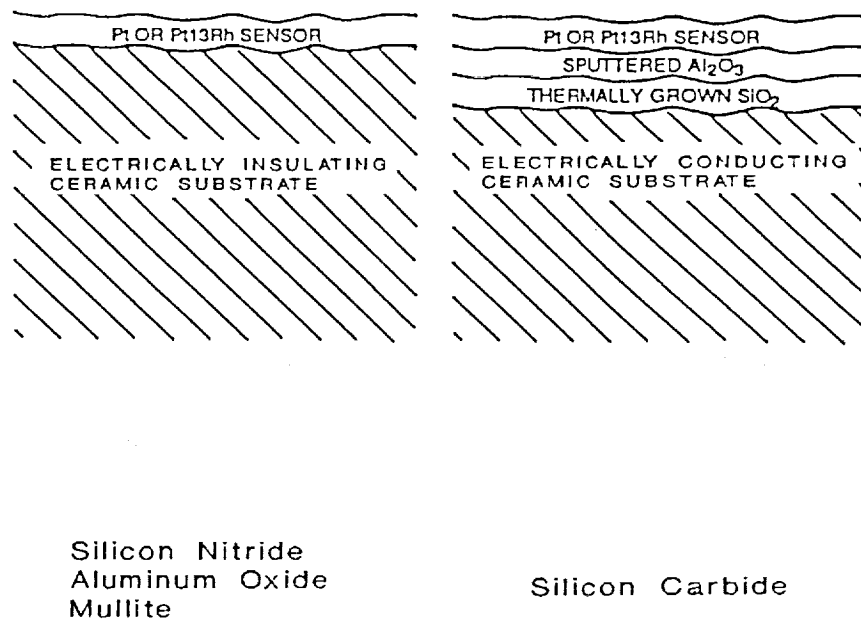


Fig. 1. Schematic diagram of thin film thermocouples on ceramic substrates.

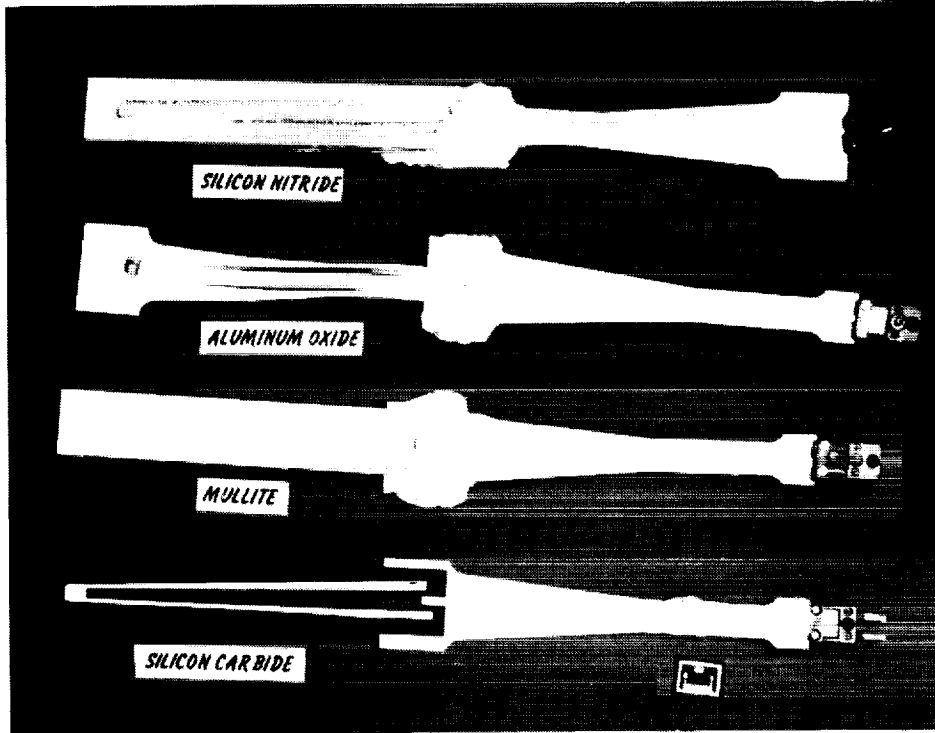


Fig. 2. Thin film Pt13Rh/Pt thermocouples on ceramic materials for high temperature furnace tests.

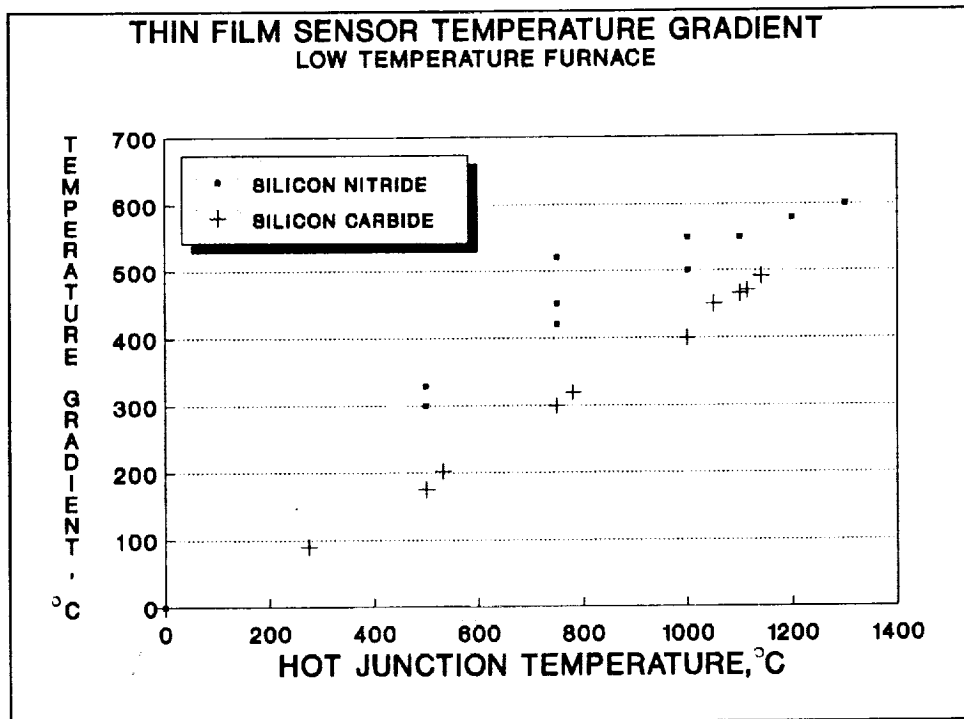


Fig. 3. Measurement of temperature gradient across thin film portion of thermocouple circuit on silicon carbide and silicon nitride substrates- high gradient configuration.

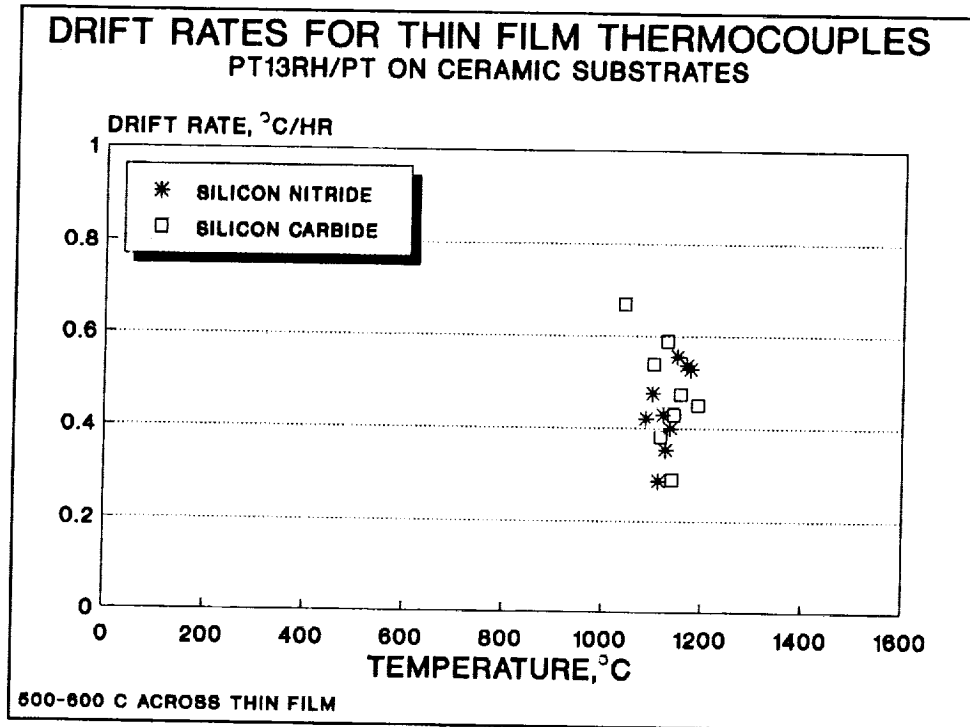


Fig. 4. Drift rates of Pt13Rh/Pt thin film thermocouples on ceramic substrates with 500-600°C temperature gradient across thin film portion of thermocouple circuit.

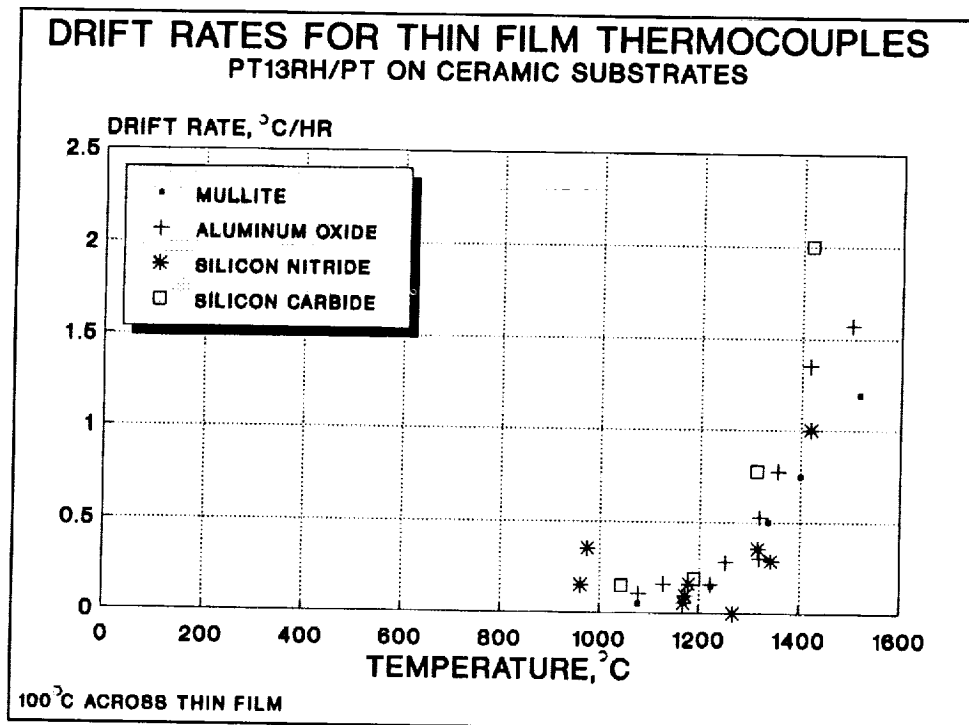


Fig. 5. Drift rates of Pt13Rh/Pt thin film thermocouples on ceramic substrates with 100°C temperature gradient across thin film portion of thermocouple circuit.

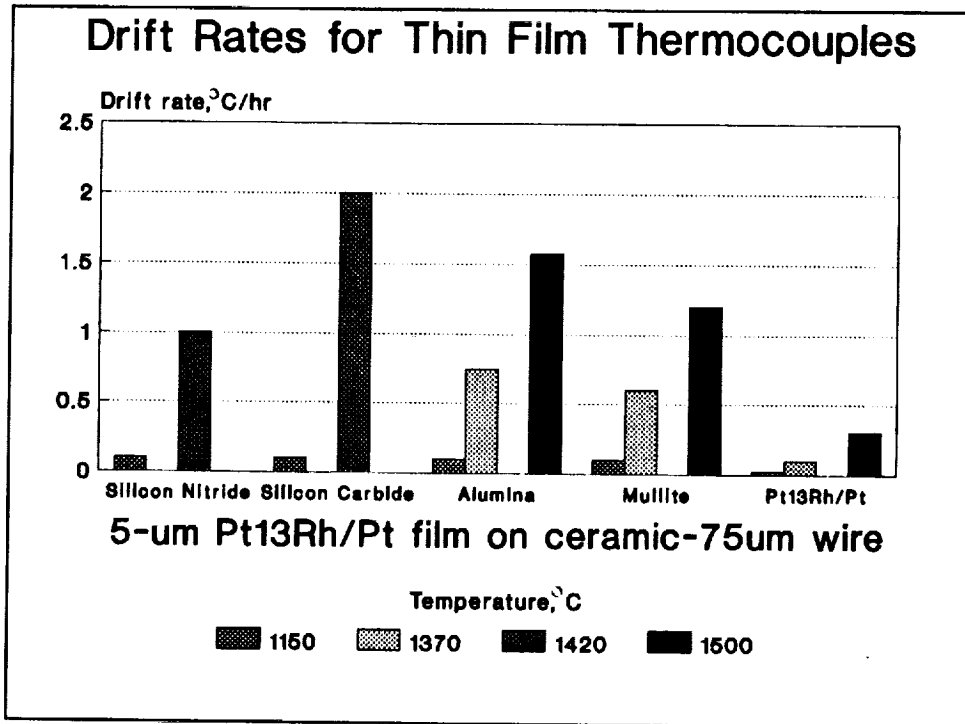


Fig. 6. Drift rates of 5  $\mu$ m Pt13Rh/Pt thin film thermocouples and 75  $\mu$ m lead wires at selected temperature levels.

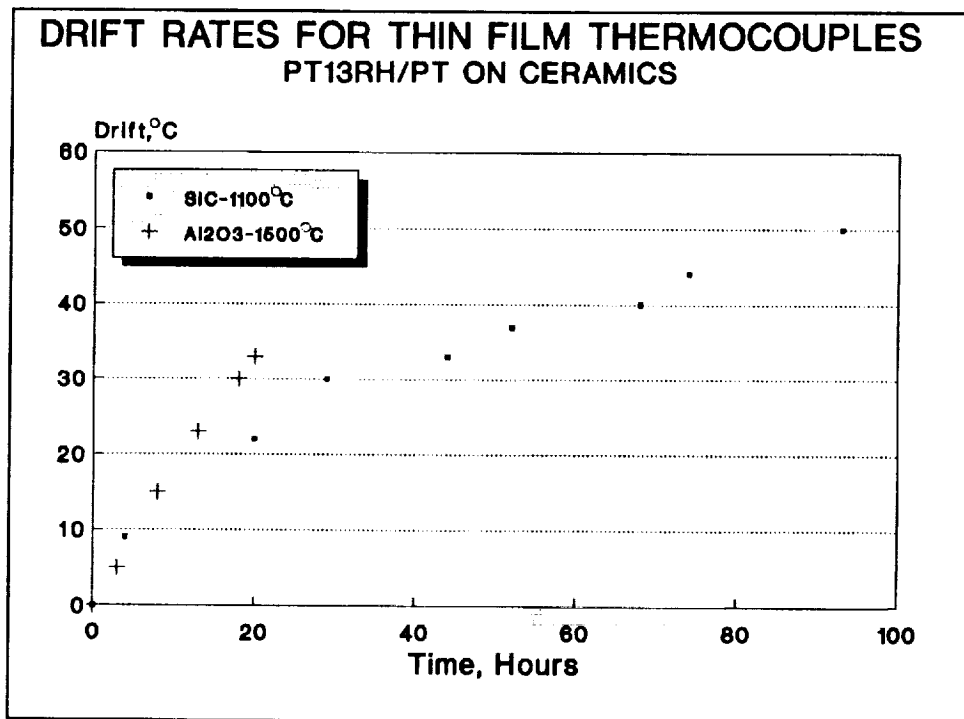
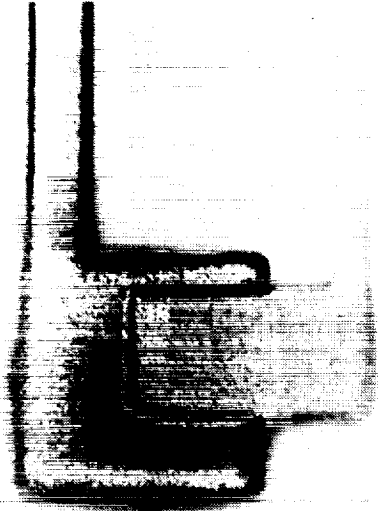
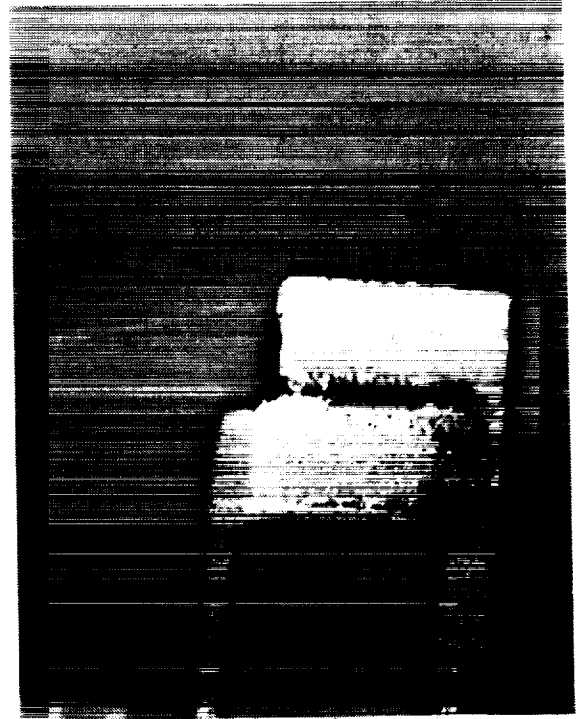


Fig. 7. Comparison of drift rates for Pt13Rh/Pt thin film thermocouples on silicon carbide at 1100°C and aluminum oxide at 1500°C.

ORIGINAL PAGE  
BLACK AND WHITE PHOTOGRAPH



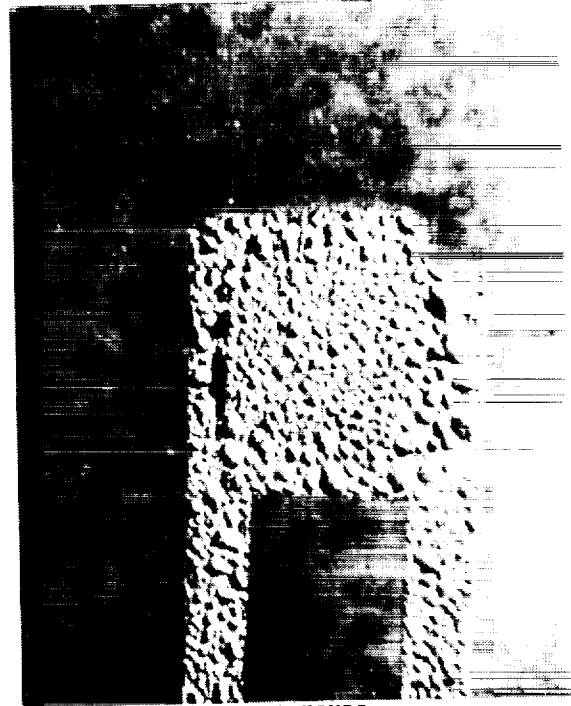
A. ALUMINUM OXIDE SUBSTRATE  
TEST TIME = 38 HOURS  
MAXIMUM TEST TEMPERATURE = 1216°C



B. ALUMINUM OXIDE SUBSTRATE  
TEST TIME = 94 HOURS  
MAXIMUM TEST TEMPERATURE = 1355°C



C. TEST TIME = 149 HOURS  
MAXIMUM TEST TEMPERATURE = 1167°C

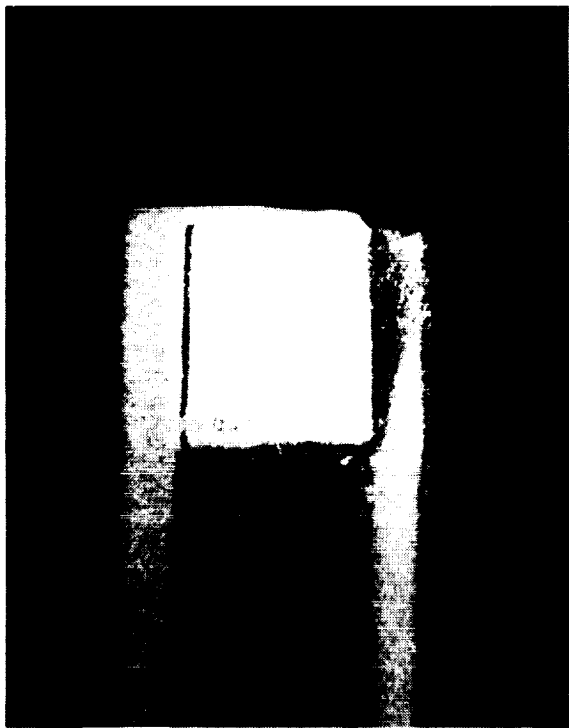


D. TEST TIME = 40 HOURS  
MAXIMUM TEST TEMPERATURE = 1343°C

Fig. 8. Pt13Rh/Pt thin film thermocouple hot junctions on aluminum oxide and silicon nitride at different stages of the testing process.



ORIGINAL PAGE  
BLACK AND WHITE PHOTOGRAPH



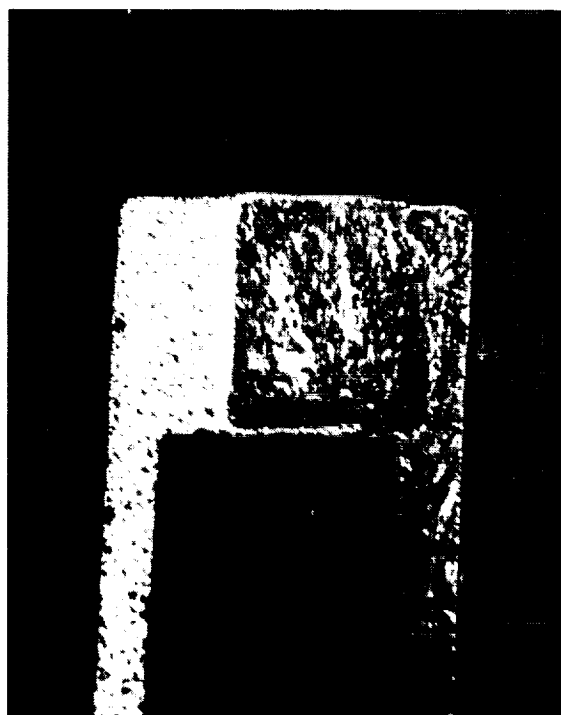
A. TEST TIME = 94 HOURS  
MAXIMUM TEST TEMPERATURE = 1142°C



B. TEST TIME = 93 HOURS  
MAXIMUM TEST TEMPERATURE = 1101°C



C. TEST TIME = 119 HOURS  
MAXIMUM TEST TEMPERATURE = 1246°C



D. TEST TIME = 56 HOURS  
MAXIMUM TEST TEMPERATURE = 1322°C

Fig. 9. Pt13Rh/Pt thin film thermocouple hot junctions on silicon carbide at different stages of the testing process.

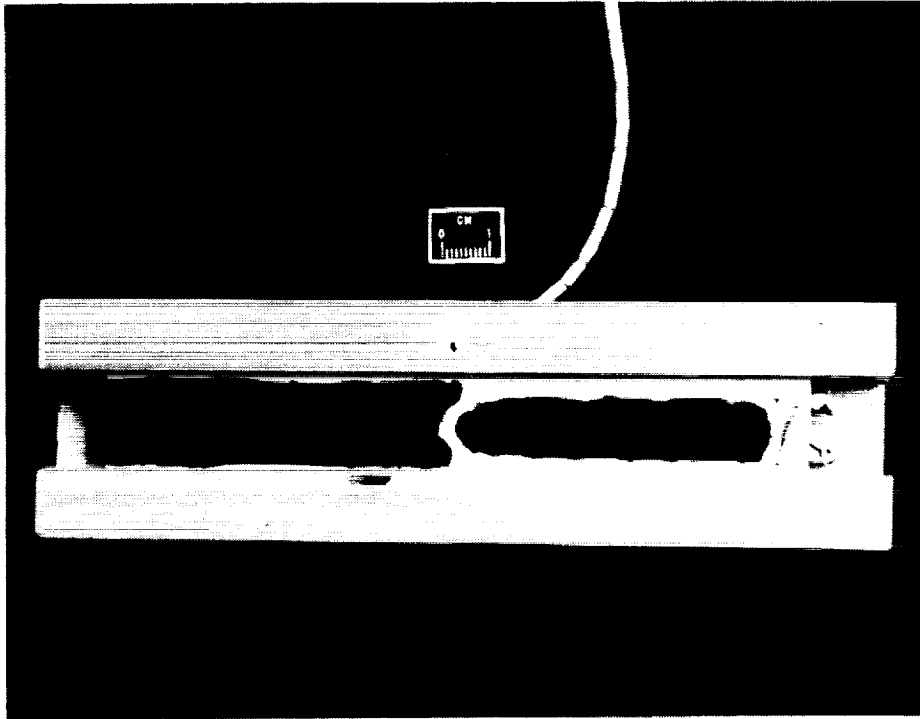


Fig. 10. Pt13Rh/Pt thin film thermocouple on silicon nitride substrate for arc lamp heat-flux-calibrator test.

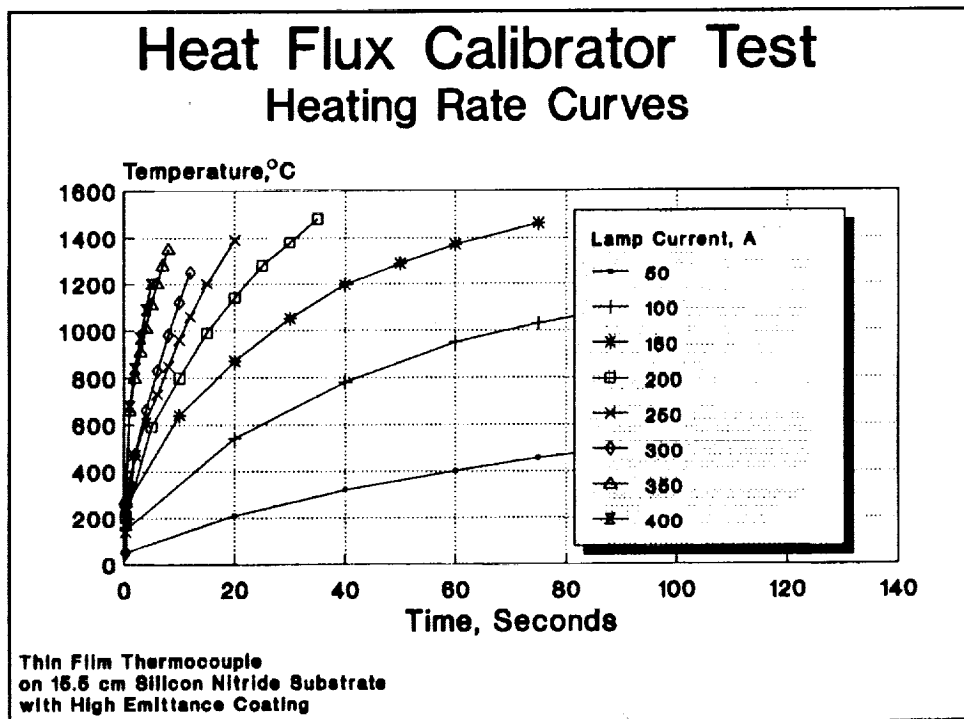


Fig. 11. Heating rate curves for Pt13Rh/Pt thin film thermocouples on silicon nitride substrate in arc lamp heat-flux-calibrator test.

**FABRICATION OF THIN FILM HEAT FLUX SENSORS**

Herbert Will  
National Aeronautics and Space Administration  
Lewis Research Center  
Cleveland, Ohio 44145

**ABSTRACT**

Prototype thin film heat flux sensors have been constructed and tested. The sensors can be applied to propulsion system materials and components. The sensors can provide steady state and fast transient heat flux information. Fabrication of the sensor does not require any machining of the mounting surface. Heat flux is proportional to the temperature difference across the upper and lower surfaces of an insulation material. The sensor consists of an array of thermocouples on the upper and lower surfaces of a thin insulating layer. The thermocouples for the sensor are connected in a thermopile arrangement. A 100 thermocouple pair heat flux sensor has been fabricated on silicon wafers. The sensor produced an output voltage of 200-400 microvolts when exposed to a hot air heat gun. A 20 element thermocouple pair heat flux sensor has been fabricated on aluminum oxide sheet. Thermocouples are Pt-Pt/Rh with silicon dioxide as the insulating material. This sensor produced an output of 28 microvolts when exposed to the radiation of a furnace operating at 1000°C. Work is also underway to put this type of heat flux sensor on metal surfaces.

**INTRODUCTION**

The objective of this work is to research and develop thin film heat flux sensors for application on propulsion system materials and components used in space propulsion system environments. The design and development of space propulsion systems requires an accurate knowledge of the heat loading on all critical propulsion system components. The space shuttle propulsion system makes use of a very reactive fuel and oxidizer system (liquid hydrogen and oxygen). When ignited the components of the engine are highly stressed both mechanically and thermally. The space shuttle main engine high pressure fuel and oxidizer pumps undergo huge temperature variations. The temperatures vary from cryogenic to around 1000°C during start up. This temperature increase occurs in about 1/2 second and results in a very large heat flux. When the engine shuts down a very large reverse heat flux also occurs. The result is cracking of the components and spalling of coatings. Heat flux sensors can be used to monitor the condition of

critical components of an engine during operation. For example, a crack in a blade may cause a drastic change in the heat flux passing through the blade.

Thin film heat flux sensors can be especially valuable for propulsion system components since they can provide heat loading information with minimal perturbation of gas flows. Thin film sensors can provide steady state and fast transient heat flux information. Fabrication of the sensor does not require any machining of the mounting surface.

The approach is to pattern a layer of thin film thermocouples on a substrate, cover it with a thin film insulator, and then pattern another layer of thermocouples on top of the insulator. The two layers of thin film thermocouples are connected together in a thermopile arrangement. This provides a direct measurement of the heat flux by measuring the temperature difference across the insulator. This approach is similar to work done by others<sup>1</sup>.

## THEORY

Heat flux sensors determine heat flux by measuring the temperature difference across a sheet of thermally insulating material. The heat flow per unit time per unit area through an insulating material is expressed as

$$Q = \frac{K(T_1 - T_2)}{t}$$

where  $K$  is the coefficient of thermal conductivity,  $t$  is the thickness,  $T_1$  is the temperature of one face, and  $T_2$  is the temperature of the other face. This equation demonstrates that as the insulating layer is made thicker, the temperature drop becomes larger for a constant heat flux. The larger the temperature drop, the easier it is to measure the temperature difference across the layer.

Most heat flux sensors make use of a single temperature sensor on the upper surface of an insulating layer and a single sensor on the lower surface. The insulating layer is at least several hundred micrometers thick for commercial sensors. The temperature sensor is usually a resistance thermometer or a thermocouple. A schematic diagram of a single thermocouple pair heat flux sensors is shown in figure 1a. The thermocouples are connected in series with similar metal leads connected together. The voltage produced across a pair of thermocouples is proportional to the temperature difference.

Heat flux that is encountered in an engine environment can vary from  $1 \text{ kw/m}^2$  to  $20 \text{ Mw/m}^2$ . For a 10 micrometer thick silicon dioxide insulating layer a temperature difference of  $5.2 \times 10^{-3} \text{ K}$  will be obtained for a heat flux of  $1 \text{ kw/m}^2$ . This small temperature difference is very

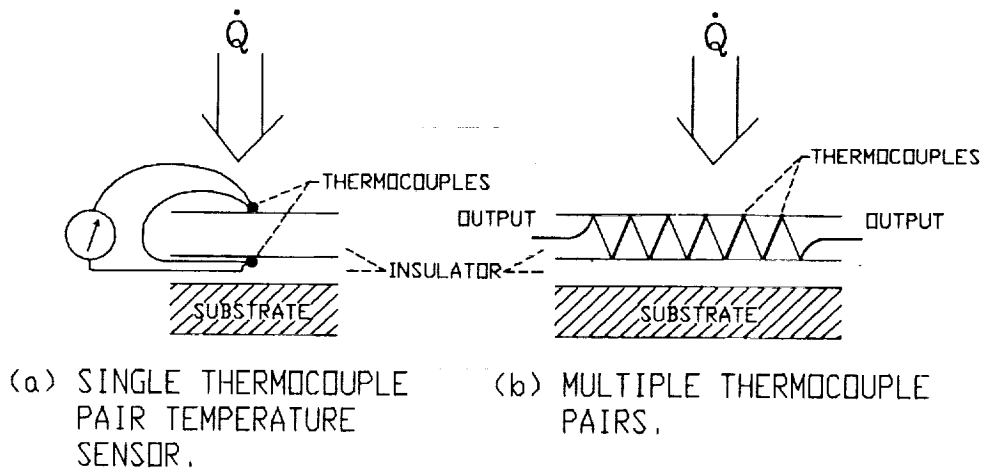


**Figure 1. Schematic diagram of thin film heat flux gage.**

difficult to measure accurately with current temperature sensors. Note that a single thermocouple will generate a microvolt or less for this temperature difference. Typically sensors are constructed with an insulator thick enough to provide a temperature difference that can be easily measured.

### SENSOR DESIGN

The heat flux sensor described here is more sensitive to the temperature difference across an insulating layer. This is done by patterning multiple temperature sensors on the upper and lower surfaces of an insulating layer in a thermopile arrangement.

A schematic diagram of a heat flux sensor with multiple thermocouple pairs connected in series is shown in figure 1b. The number of thermocouple pairs is limited by available space and resolution. The thermocouples are constructed of thin film metals sputter deposited on the upper and lower surfaces of the insulating layer. Upper and lower thermocouple pairs are electrically connected through the insulating layer. The thermocouples are connected so the voltages generated by the pairs add. The resultant output is a voltage signal equal to the number of thermocouple pairs times the voltage output of a single pair.

A three dimensional drawing of a ten thermocouple pair heat flux sensor is shown in figure 2. All the layers are deposited using RF diode sputtering. The thermocouple pairs are sputter deposited onto the insulator surface on the circumference of a small circle. This configuration was chosen so that the sensor measures only the heat flux normal to the surface. The connecting wires are sputter deposited through holes in the insulator on the circumference of a larger circle. This is done so the connecting wires do not disturb the heat flow in the vicinity of the thermocouple junctions.

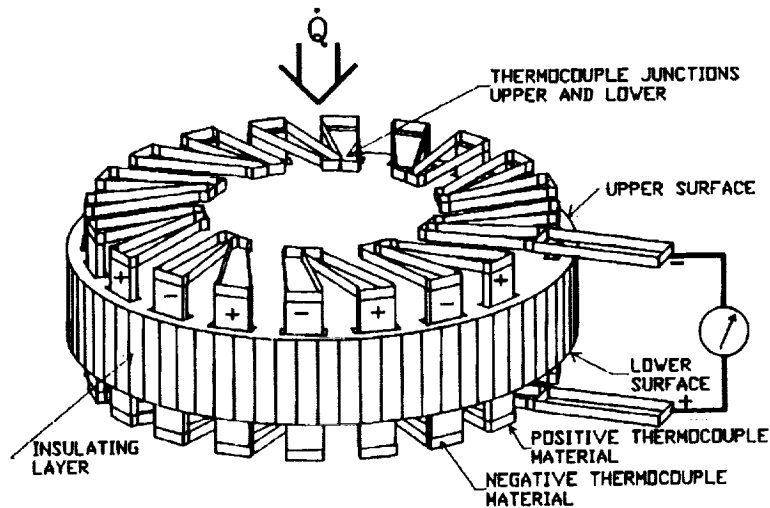


**Figure 2. Three dimensional drawing of thin film heat flux gage. A gage with 10 thermocouple pairs is shown.**

### SENSOR FABRICATION

This high output thin film heat flux sensor can be applied directly to the surface of engine parts. An insulating layer must be deposited first if the surface is a metal.

In order to fabricate a thermocouple two different types of metals must be patterned onto the surface of the substrate. They must overlap one another in only one small area to produce a thermocouple junction. The thermocouples are patterned using a photoresist lift-off technique. Figure 3 displays the steps that are required for the lift-off technique. The substrate is initially coated with an insulating layer (figure 3a). Positive photoresist is applied to the surface and soft baked (figure 3b). The photoresist is then exposed with UV light through a photomask (figure 3c). The photoresist is then processed in a developer to remove the exposed resist. The resist is then dried and hard baked (figure 3d). The next step is to sputter deposit the first metal onto the surface of the sample (figure 3e). This results in the metal covering everything including the areas where the photoresist was developed away. The final step of the lift-off technique is to remove all the photoresist (figure 3f). This also removes the sputtered metal on top of the resist but not in the areas where there was no resist. The result is a metal pattern, on the sample, that is a replica of the photomask.

The process of fabricating a complete heat flux sensor consists of five steps. These five steps are shown in figure 4. The substrate is initially coated with a sputter deposited insulating layer of aluminum oxide. The first step uses the lift-off technique to pattern the first thermocouple layer. The second step also uses the lift-off technique to pattern the second thermocouple layer.

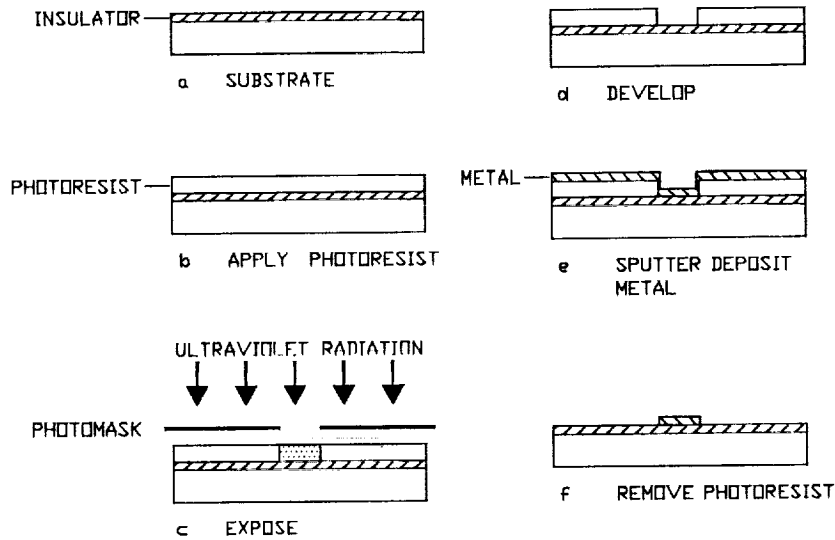


**Figure 3. Diagram of thin film heat flux gage lift-off process.**

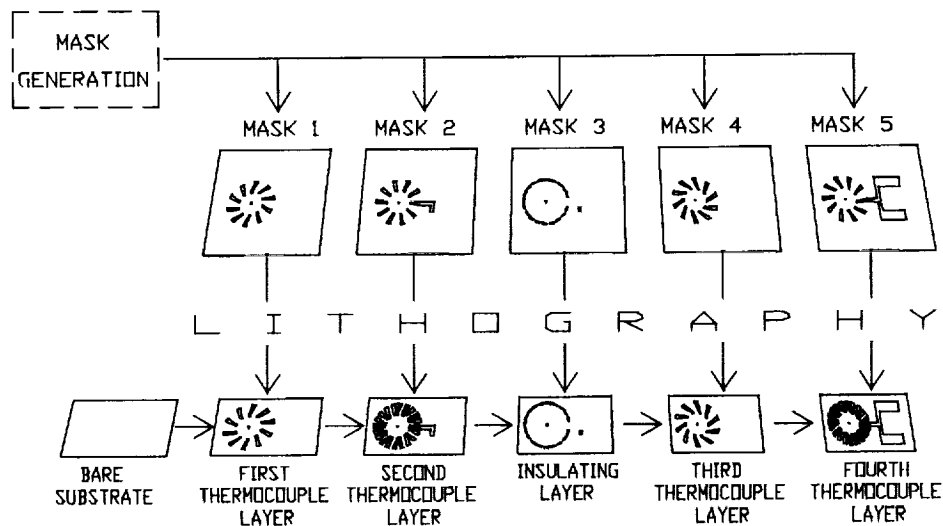


**Figure 4. Processing steps used to fabricate thin film heat flux gage.**

The third step consists of sputtering an insulator (such as  $\text{SiO}_2$ ) over the lower thermocouple layer. The substrate is then coated with photoresist again and exposed with the mask shown in figure 4 (mask 3). The photoresist developer opens holes in the photoresist to expose the insulator for etching. A suitable etchant (buffered HF for  $\text{SiO}_2$ ) is used to etch through the insulator to the underlying thermocouple layer. The final two steps use the lift-off technique again to pattern the upper two thermocouple layers. The result is a completed heat flux sensor with the upper and lower thermocouple layers connected in series through the holes in the insulator.

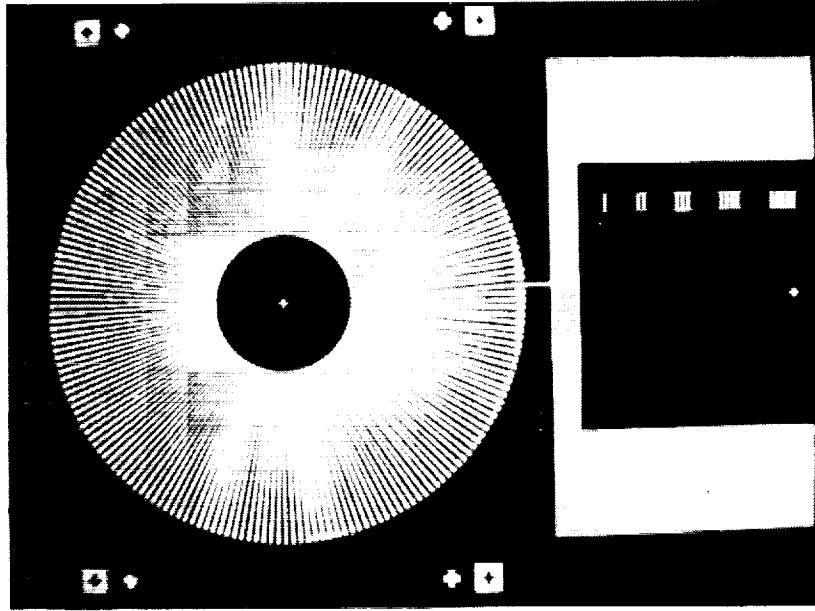


**Figure 5. Photo of complete 100 element thin film heat flux gage.**

## **RESULTS**

A thin film heat flux sensor fabricated on a silicon substrate is shown in figure 5. This sensor is a 100 thermocouple pair heat flux sensor. The thermocouple materials are chromel and alumel. The thermal insulating layer is silicon dioxide. Although the sensor is not without problems, it did work when tested. The resistance of the sensor was 171 ohms across the terminals. The resistance between sensor and substrate was greater than 10 megohms indicating no shorting through the insulator. The measured output using a heat gun as a source of heat was 0.2 to 0.4 millivolts. This heat flux sensor failed after repeated temperature cycling. The failure was an open circuit in at least one of the thermocouple legs. It appears that the failure was at the plated through holes of the thermal barrier layer. This is probably due to damage to the thermocouple metals by the buffered hydrofluoric acid used to etch the holes in the insulator.

In order to correct the open circuit problem it was decided to change the thermocouple materials to platinum and platinum/rhodium. Also it was felt that the current silicon substrate would not survive the high temperatures encountered during testing. As a result, the substrate was changed to aluminum oxide sheet. The pattern for the heat flux sensor was also changed from 100 thermocouple pairs to 20 thermocouple pairs. This was done to make the sensor easier to fabricate on the slightly rougher surface of aluminum oxide.

A 20 element heat flux sensor has been fabricated on a ceramic substrate (aluminum oxide) using Pt and Pt/Rh as thermocouple materials (see figure 6). The thermal insulating layer was 7 microns of silicon dioxide. The thickness of the thin film thermocouples was in the range 0.4 to 0.8 microns. The resistance of the sensor was 1000 ohms across the terminals. The previous



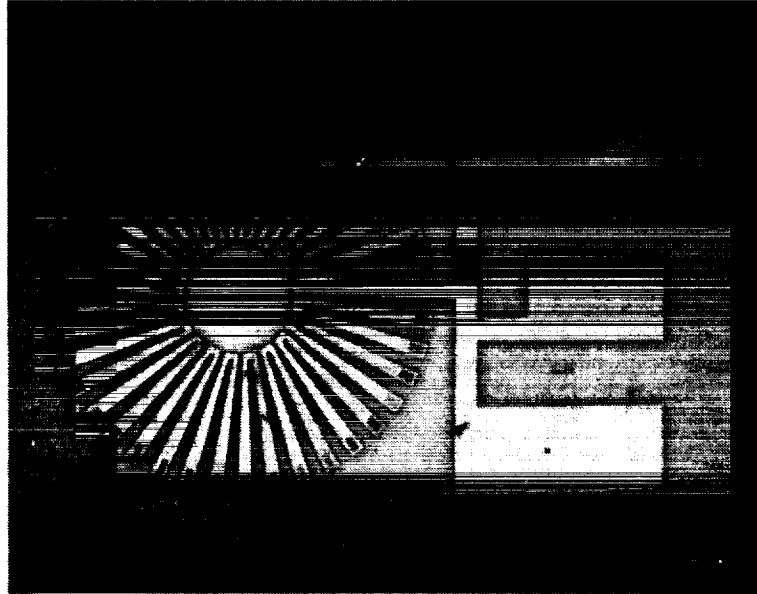


Figure 6. Photo of complete 20 element thin film heat flux gage.

sensors, fabricated on silicon with chromel/alumel thermocouples, failed after one or more temperature cycles. This 20 element heat flux sensor continued to operate after repeated temperature cycling. The calculated output voltage for this sensor as a function of heat flux for two emissivities (1.0 & 0.5) is shown in figure 7. The heat flux sensor was tested by exposing the sensor to the radiation from a furnace operating at 775° C and at 900° C. Black body calculations, using Stefan's law, provided an estimate of the heat flux at each temperature. The output voltage for the sensor as a function of calculated heat flux is shown in figure 7 as two measured data points.

This sensor was also tested in a heat flux calibrator facility using an arc lamp. The sensor had no high emissivity coating since no insulating layer had been put over the top thermocouple layer. The sensor was tested up to a heat flux of 1.5 Mw/m<sup>2</sup>. At this time the sensor broke in half. The voltage output of the sensor was also the wrong polarity indicating reverse heating of the sensor. It is believed the energy of the lamp was absorbed within the aluminum oxide substrate causing non-uniform heating and resulting in the breakage. In the future these sensors will be overcoated with an insulating layer of aluminum oxide followed by a coating of high temperature black paint. The paint will ensure that only the top surface of the sensor is heated.

There is also an additional problem with the use of aluminum oxide as a substrate material. It was found that when photoresist is used on polycrystalline aluminum oxide the exposure time is very critical. The light used to expose the photoresist is reflected off the polycrystalline grains resulting in extreme over exposure of the pattern from underneath. This makes it very difficult to

produce a good photoresist pattern. We have found that this problem can be eliminated by first sputtering 100-200 angstroms of aluminum onto the aluminum oxide surface followed by a few microns of hot (600°C) sputtered aluminum oxide. If any electrical shorting occurs through the sputtered aluminum oxide layer, the problem can be eliminated by heat treating in air at 700°C for 6 hours.

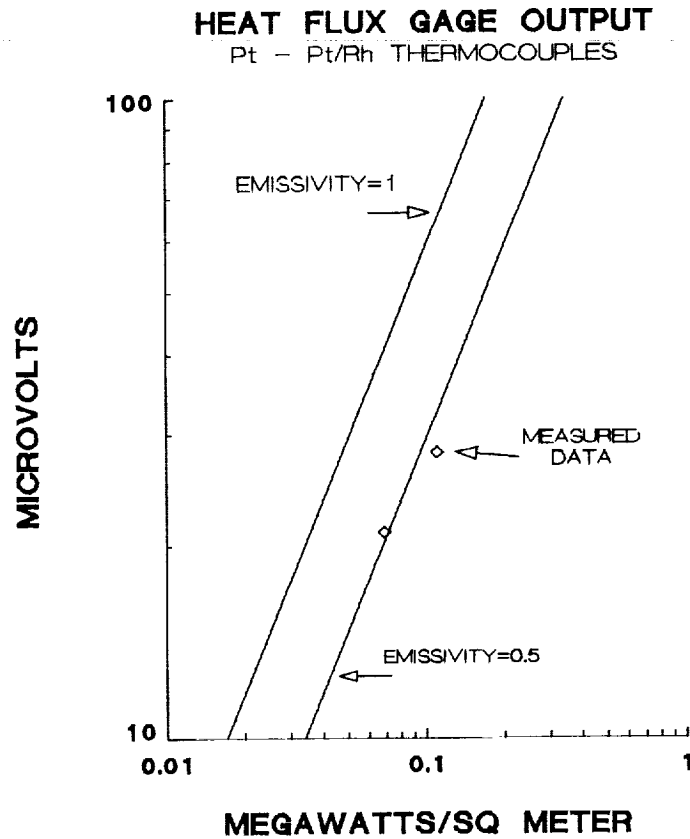


**Figure 7. Calculated output of 20 element heat flux gage. Data points represent measured values.**

### DISCUSSION

The advantage of this heat flux sensor is that it provides a sensor that is minimally intrusive to gas flow, does not require machining of the mounting surface, and provides a relatively large output signal. The output can be ten to ten thousand or more times that of single temperature sensors. This multiplication of the output signal, by adding numerous thermocouple pairs in series, has the result of increasing the signal relative to the noise in the measuring system. This can be especially significant since thermocouple voltages are often in the microvolt range - a range where Johnson noise can easily mask the desired signal.

The heat flux sensor is fabricated from very thin films of metals and insulators. While thin films do not have zero mass, their mass is generally thousands of times less than the part they are

attached to. As a result the time constant, or speed of response, of the sensor will be extremely fast since the output only depends on heating up a film that is a few microns thick. It should be noted that the time constant for the temperature of the top or bottom surface of the heat flux sensor will be fairly slow - depending on the mass of the engine part. However the temperature difference across the sensor will respond very rapidly since this is only dependent on heating the thin film. At this time no calculations or measurements have been done to determine the time response.

The output of the heat flux sensor is a voltage generated by thermocouples. The voltage is linearly proportional to heat flux as was shown in a previous section. Thus heat flux is obtained by multiplying the output voltage by a constant.

The sensor has not been tested at cryogenic temperatures but it is expected to survive temperatures from below liquid O<sub>2</sub> to about 1700°C. The upper temperature is limited by the silicon dioxide insulator. The sensor shown in figure 2 makes use of platinum based thermocouples. As a result this sensor has a low temperature limit of 0°C. The low temperature limit can be extended by using other thermocouple materials. The use of chromel/alumel thermocouple alloys would allow a temperature range of -184°C to +1260°C.

Although the thin film heat flux sensor is difficult to fabricate it can provide the engine designer with much useful information about heat loading on engine components.

## FUTURE WORK

The current work on the heat flux sensor will continue using silicon, aluminum oxide, and MAR-M-200<sup>2</sup> as substrates. The sensors will be tested in a heat flux calibration facility capable of generating heat fluxes in the range of 1 to 5 Mw/m<sup>2</sup>. Fabrication techniques will continue to be refined.

All of the work on thin film heat flux sensors has concentrated on flat substrates. Most propulsion system components are not flat. It is a difficult problem to put a thin film pattern onto curved surfaces. Various methods for solving the curved surface problem are being investigated. One of the methods that will be tried is the use of flexible photomasks. A photomask fabricated on 127 micron (.005") Teflon<sup>3</sup> is shown in figure 8.

# THIN FILM HEAT FLUX

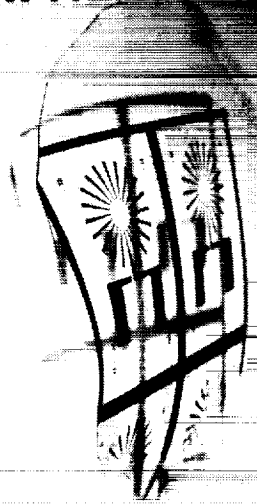


**Figure 8. Flexible photomask fabricated on Teflon<sup>3</sup>.**

## REFERENCES

1. Hager, J.M.; Langley, I.w.; Onishi, S.; Diller, T.E.: "High Temperature Heat Flux Measurements", 29<sup>th</sup> Aerospace Sciences Meeting in Reno Nevada, Jan. 1991, AIAA 91-0165.
2. Sims, Chester T.; Stoloff, Norman S.; Hagel, William C.: "Superalloys II", John Wiley & Sons, 1987, page 108.
3. Teflon - Reg TM E. I. du Pont de Nemours & Co.

GAS TEMPERATURE MEASUREMENTS USING THE DUAL-LINE DETECTION  
RAYLEIGH SCATTERING TECHNIQUE\*

M. Volkan Otugen  
Polytechnic University  
Brooklyn, NY

Richard G. Seasholtz  
NASA Lewis Research Center  
Cleveland, OH

Kurt D. Annen  
Aerodyne Research, Inc.  
Billerica, MA

## SUMMARY

A new laser-induced Rayleigh scattering method is presented for the improved temperature diagnostics of gas flows. In the present technique, the two lines of a copper vapor laser are used to obtain the time and space resolved temperature. A single set of optics is used to form the optical probe and to collect the signal simultaneously from both the 510 nm and the 578 nm lines. The dual-line detection allows for the determination and removal of surface-scattered laser light from a Rayleigh signal thereby improving the applicability of Rayleigh scattering to near wall flows with a high degree of glare. An optical system using the dual-line detection technique is built, calibrated and tested in a hot air jet under various levels of background contamination. The results indicate that highly accurate temperature measurements are possible even when the laser-line background intensity, captured by the collecting optics, is five times that of the Rayleigh signal.

## NOMENCLATURE

- $C$  optical system calibration constant  
 $C'$  surface scattering calibration constant

---

\* Work was undertaken at NASA Lewis Research Center

$I_B$	surface scattered background intensity
$I_L$	laser light intensity
$I_R$	Rayleigh signal intensity
$I_T$	total intensity captured by collecting optics
$I_0$	Incident light intensity
$k$	Loschmidt number
$L$	irradiated length of sample
$n$	gas number density
$P$	gas pressure
$R$	gas constant
$T$	temperature
$\alpha$	gas index of refraction
$\beta$	ratio of surface scattering constants
$\theta$	scattering angle
$\lambda$	wavelength of laser light
$\sigma'$	standard deviation
$\sigma$	Rayleigh scattering cross-section
$X$	mean value

#### Subscripts

1	refers to the 510 nm line
2	refers to the 578 nm line

## INTRODUCTION

Rayleigh scattering is an optical technique which has been successfully used as a temperature and concentration measurement tool in fluid dynamics and combustion research. For example, Graham et al. (1974), Dyer (1979), Pitts and Kashiwagi (1984) and Arcoumanis (1985) measured tracer concentration in non-reacting, binary gas jets while Otugen and Namer (1988) measured temperature in a non-isothermal air jet. The technique has also been applied to simple reacting flows. Bill et al. (1982) and Gouldin and Halthore (1986) measured total gas density while Dibble and Hollenbach (1981) and Namer and Shefer (1985) measured flame temperatures, all in premixed external flames using laser induced Rayleigh scattering. Temperature measurements have also been attempted in combustors (eg. Barat et al., 1991) but these have had limited success due to signal contamination by laser glare. During the last few years, there have been attempts to use Rayleigh scattering for two-dimensional imaging of density and concentration both in subsonic jets (Escoda and Long, 1983) and supersonic wind tunnel

testing (Smith et al, 1989; Shirinizadeh et al., 1991). However, high speed wind tunnel applications for density diagnostics have remained mostly qualitative due to the unwanted scattering of laser light from ice cluster and surrounding surfaces. On the other hand, the application of spectrally resolved Rayleigh scattering as supersonic flow anemometry has been quite successful when the flow velocities are high enough to produce a clearly detectable Doppler shift in scattered signal (Seasholtz, 1991).

A commonly encountered difficulty associated with the Rayleigh scattering technique is the contamination of the relatively low level of Rayleigh signal by the background noise. The two major sources of background noise are the contribution of light from the test environment, which is usually broadband, and the surface scattered laser glare captured by the collecting optics along with the Rayleigh signal. Since the Rayleigh line scattered from the gas molecules in the probe have approximately the same central frequency as the laser beam, surface scattered light cannot be easily discriminated from Rayleigh scattering, especially in low speed flows. In certain applications, particularly in enclosed flows with limited optical access such as combustors, surface scattered glare can become a formidable obstacle. The problem becomes most severe when near forward or near backward collecting angles have to be used, since scattering from surfaces and optical elements are larger at these angles.

In the present study, different methods are used to minimize the effects of both types of background contamination. A pulsed copper-vapor laser with a repetition rate of 6 kHz and a continuous output power of 20 watts is used as the light source. The use of a pulsed source provides a comparatively high level of Rayleigh signal due to the high energy densities at each pulse and greatly suppresses the effect of environmental noise. However, the improved pulse energy does not help increase the ratio of signal-to-background due to laser glare. A new dual-line detection technique is developed to address this problem. The signal is collected from both the 510 nm (green) and the 578 nm (yellow) lines of the copper-vapor laser using one set of collecting optics. The information obtained from both lines is analyzed together at each shot of the laser to determine the laser line background level and to decouple it from the Rayleigh signal. The dual-line detection method eliminates the need for the guesswork in background determination and offsetting and significantly improves the potential of Rayleigh scattering as a reliable quantitative diagnostic tool in high temperature gas flows including combustion.

An optical system at NASA Lewis Research Center is used to test the dual-line detection technique. The dual-line detection Rayleigh (DLDR) system uses a copper-vapor laser as the light source. Optical fibers are used to transmit the laser beam to probe region and the signal to collecting optics. Extensive calibration tests have been performed to characterize the various system parameters. Finally, temperature measurements have successfully been performed in a heated air jet. Results indicate that highly accurate temperature measurements are possible using the dual-line detection in the presence of high level background glare. The method for background determination

is described in the following section.

## DUAL-LINE BACKGROUND DETECTION

Rayleigh scattering involves the elastic interaction of the incident laser light with the gas molecules (Van de Hulst, 1957). The intensity of the scattered light is proportional to the incident laser light intensity, the scattering cross-section of the gas as well as the number density of the gas. Therefore, the technique can be used to measure density directly, or temperature, by invoking the ideal gas law. The intensity of Rayleigh scattered light by a unit volume of gas and an infinitesimal solid angle is given (Jenkins and White, 1981) by

$$I_R = I_o nL\sigma \quad (1)$$

Here,  $\sigma$  is the Rayleigh cross-section of the sampled gas and is a function of the scattering angle,  $\theta$ , wavelength of incident beam,  $\lambda$ , and the index of refraction of gas,  $\alpha$ . For an isotropic molecule, the Rayleigh cross-section can be expressed as follows:

$$\sigma = \frac{4\pi^2}{\lambda^4} \left( \frac{\alpha - 1}{k} \right)^2 \sin^2\theta \quad (2)$$

where  $k$  is the Loschmidt number. For a multi-species gas volume the equivalent (average) cross-section can be found by the weighted average using the mole fraction of each species. Since the Rayleigh cross-section is proportional to -4 power of  $\lambda$ , laser lines with smaller wavelengths will result in a stronger signal for unit incident intensity. For a given experimental condition with a fixed collecting angle and laser line, the Rayleigh scattered light intensity can be written as

$$I_R = I_L C \sigma n \quad (3)$$

Here,  $I_L$  is the intensity of the laser light. The constant  $C$  absorbs all the parameters that are fixed for a given set-up. These parameters include the efficiency of the transmitting and collections optics, quantum efficiency of the photomultiplier, collection angle, solid angle over which signal is collected, amplification of electronic equipment, etc. However, as discussed above, the observed signal contains background due to surface scattered



laser glare as well as the Rayleigh signal so that

$$I_T = I_R + I_B = I_L \sigma n + I_L C C' \quad (4)$$

where,  $C'$  is a constant describing the surface scattering. Thus, the relative signal normalized by laser light intensity is

$$\frac{I_T}{I_L} = C \sigma \frac{P}{RT} + C C' \quad (5)$$

In the above equation, perfect gas law is used. For two line operation, Eq. (5) can be written for lines  $\lambda_1$  and  $\lambda_2$  (with  $\lambda_1 = 510nm$  and  $\lambda_2 = 578nm$ , in the present case) as

$$\frac{I_{T,1}}{I_{L,1}} = C_1 \sigma_1 \frac{P}{RT} + C_1 C'_1 \quad (6)$$

and

$$\frac{I_{T,2}}{I_{L,2}} = C_2 \sigma_2 \frac{P}{RT} + C_2 C'_2 \quad (7)$$

For a given optical geometry and electronics setting the system can be calibrated to obtain the values for  $C_1$ ,  $C'_1$ ,  $C_2$  and  $C'_2$ . This can be accomplished by taking measurements under conditions where the values of  $\sigma$ ,  $P$  and  $T$  are known and either one or a combination of these known quantities is varied. Therefore, a least squares fit of the data with a sufficient number of conditions will determine the constants  $C_1$  and  $C_2$ , which are of importance. Furthermore, the ratio,  $\beta = C'_1 / C'_2$  is also obtained through the calibration process. It is reasonable to expect that the scattering process of light from solid surfaces at different wavelengths may be different. However, since the two beams (lines) from the laser are colinear,  $\beta$  should be a constant for a given system. As discussed later, this point is confirmed through experiments using the present DLDR system. Of course,  $\beta = 1$  would indicate independence of surface scattering from the incident wavelength. With  $C'_1 = C'_2$  and  $C'_1 = \beta C'_2$ , the following is obtained:

$$\frac{I_{T,1}}{I_{L,1}} = \left( \frac{C_1 P \sigma_1}{R} \right) \frac{1}{T} + \beta C_1 C' \quad (8)$$

$$\frac{I_{T,2}}{I_{L,2}} = \left( \frac{C_2 P \sigma_2}{R} \right) \frac{1}{T} + C_2 C' \quad (9)$$

Therefore, this linear system of two equations with unknowns  $1/T$  and  $C'$  yields,

$$T = \frac{\frac{P}{R}(\sigma_1 - \beta \sigma_2)}{\frac{I_{T,1}}{I_{L,1}} \frac{1}{C_1} - \frac{I_{T,2}}{I_{L,2}} \frac{\beta}{C_2}} \quad (10)$$

and

$$C' = \frac{\frac{I_{T,2}}{I_{L,2}} \frac{\sigma_1}{C_2} - \frac{I_{T,1}}{I_{L,1}} \frac{\sigma_2}{C_1}}{(\sigma_1 - \beta \sigma_2)} \quad (11)$$

Equation (10) provides the temperature, decoupled from the background contamination. Obviously, this equation can be re-arranged for density if that property is desired in place of temperature. Equation (11) indicates the normalized background due to surface scattering at the laser lines at each measurement. This information is not related to flow physics; however, in practice, it will be of importance since its magnitude will determine if a particular measurement is reliable once a critical threshold value of signal-to-noise ratio is established from preliminary testing. Although Eqs. (10) and (11) completely decouple background from temperature, in practice, from optical and electronic considerations, there will be a limit on the signal-to-background ratio, specific to a DLDR system, below which an accurate measurement of temperature will not be possible. The present DLDR system was calibrated and tests have been performed to obtain such critical signal-to-noise values.

## EXPERIMENTAL SYSTEM

The optical arrangement for the dual-line detection Rayleigh scattering system is shown in Fig 1. Central to the system is a pulsed copper-vapor laser with a continuous power output of about 20 watts. The laser is normally operated at a pulse rate of 6 kHz with a pulse duration of approximately 36 ns. The output beam contains both 510 nm (green) and the 578 nm (yellow) lines. The relative power of the 510 nm and the 578 nm lines are approximately 60 % and 40 %, respectively. The optical probe and the signal collecting optics are situated on an optical bench with a three-axis traverse capability. The laser is placed on a separate optical table and the output beam is transmitted to the

probe bench through an optical fiber. The beam is coupled into the 400  $\mu\text{m}$  fiber by focusing it with a 150 mm focal length lens. The focussed beam first passes through a 600 0.6 mm pinhole for spatial filtering before reaching the cleaved fiber end. The fiber end is placed slightly beyond the minimum waist diameter location so that the fiber end is protected from burning under high incident laser energies. The transmitting optics are composed of two 150 mm focal length lenses producing a probe waist of about 400  $\mu\text{m}$ . The incident power at the probe is approximately 1.4 watts although variations did occur on a day-to-day basis. The laser light is captured by a beam trap on the opposite side of the Rayleigh probe. Another light trap is situated directly behind the collecting optics to reduce the broadband background captured by the collecting optics. The collecting optics are comprised of two achromat lenses each with a 160 mm focal length and an 80 mm aperture. Therefore, the magnification factor of the collecting optics is unity. The collected signal is coupled into a 200  $\mu\text{m}$  core diameter optical fiber and delivered into a sealed signal box. In the signal box, the total collected signal is collimated and subsequently color separated by a dielectric beam splitter. The green (510 nm) and the yellow (578 nm) signals are shined on two photomultiplier tubes.

Since the copper-vapor laser used has a significant pulse-to-pulse energy variation (up to 5 %), the intensity of the laser from two lines is monitored at each pulse and the signal is normalized by these values as required by Eqs. (8) and (9). This is accomplished by placing a thin glass plate at a small angle in front of the laser beam as shown in Fig. 1 and reflecting approximately ten percent of the beam energy. Some of the reflected laser light is then captured by the open end of a 200  $\mu\text{m}$  core diameter fiber. At the other end of the fiber, this reference intensity is delivered to another box configured very similarly to the signal box. The only difference is that, the signal in the reference box is sensed by photodiodes instead of photomultiplier tubes.

The electronic arrangement for the DLDR system is shown in Fig. 2. The set of four sensor outputs for the two lines; the two signals from the photomultiplier tubes and the two laser reference intensities from the photodiodes are fed into linear gate and hold units on a boxcar averager system as shown. The signals from the photomultiplier tubes are fed directly to the gate integrators without any need for pre-amplification since a fairly strong Rayleigh signal is observed at each pulse of the laser. The timing for the gate generators is provided by a timing module. The timing module, which is a function generator with a TTL output, also provides the trigger pulses for the copper vapor laser and a 16 bit analog-to-digital converter. The trigger pulses to the gate generators and to the A/D converter are appropriately delayed to capture the Rayleigh scattering signal from the probe. The A/D converter is interfaced with an IBM 486 architecture personal computer. At each pulse of the laser, all four signals are gated, integrated, digitized and stored on the hard disk of a computer. Therefore, the system can obtain data at a rate of 6 kHz with a time resolution of about 36 ns. The data acquisition protocol is shown in Fig. 3. Data is post processed after each experiment or calibration on the same personal computer.

## EXPERIMENTAL RESULTS

Preliminary tests were performed first to insure proper operation of the optical and the electronic components of the DLDR system for both the green,  $\lambda_1$  and the yellow,  $\lambda_2$  lines. Temperature was measured in a single, particulate free, heated air jet. For these measurements the dual-line detection feature was not implemented and temperature, independently measured from each laser line, was compared to a thermocouple measurement. Both the environmental background and the laser glare was kept to a minimum. For these measurements, the knowledge of the Rayleigh-cross section was not needed a priori. Each line was calibrated using a reference condition (free air jet at room condition) which is the usual method in the more conventional applications of Rayleigh scattering (eg. Dyer, 1979; Otugen and Namer, 1988). The optical probe was situated on the axis of a jet, approximately 1 mm above the nozzle (10 mm diameter). A chromel-alumel thermocouple with a nominal bead diameter of 1 mm was placed directly above the Rayleigh probe. Readings from both the Rayleigh scattering system and the thermocouple were obtained at various jet temperatures. Figure 4 shows a typical set of results. In the figure, a straight line with a slope of one is also drawn for better comparison. There is good agreement between the thermocouple and the Rayleigh scattering measurements. The slightly higher temperature readings independently obtained by both lines of the Rayleigh system are most likely due to the positioning of the thermocouple relative to the optical probe: The optical probe was slightly closer to the jet exit.

Two separate softwares were developed for the DLDR system: one for calibration and another for actual temperature measurements. The system has to be calibrated each time an experiment is performed since the constants in Eq. (8) and (9) are highly dependent on optical alignment and electronic settings (laser power, pmt sensitivity, electronic gain, gate width on signal integration, etc). Once the calibration procedure is completed, the related constants are put in the data acquisition software. At this point, any change on the electronics setting, including significant electronic drift would invalidate the calibration.

### System Calibration

To qualify the DLDR system, a large set of calibration tests were performed under a diverse set of conditions related to both the optics and the electronics including the laser power, pmt sensitivities, signal gain, etc. Also, different levels of background were allowed to contaminate the signal during these tests to study the behavior of  $\beta$ . The calibration software essentially acquires data from both lines and performs a least squares fit to Eqs. (8) and (9). Values of  $\sigma$ , P and T are provided to the program and

depending on the experimental conditions, either one or a number of these parameters can be varied. In the present, the heated air jet previously mentioned was used. The Rayleigh scattering cross-sections and pressure (atmospheric) were provided to the software as fixed values and the air temperature was the calibration variable. The optical probe was placed at the exit of the jet and the jet temperature was varied. The temperature was monitored by a small-bead, chromel-alumel thermocouple which was placed adjacent to the optical probe.

A set of calibration graphs, performed during a day with various laser line contamination levels are shown in Fig. 5(a-d). The background contaminations were obtained by placing painted (flat black) and non-painted aluminum plates near the Rayleigh optical probe, directly opposite to the collecting optics (Fig. 1). Varying levels of background were obtained by moving the small, flat aluminum plates towards and away from the probe location on a traverse mechanism and allowing the diffuse laser light around the probe location to shine on the plates. The diffuse laser light, surrounding the high intensity beam waist (at the probe) is generated by the focussing lens. The pertinent values of the four constants obtained at each calibration are shown in the figures. The plots for both laser lines are linear confirming Eqs. (8) and (9). Also, for a given laser line, the slope of the plot is fixed for various background levels. Higher levels of background contamination simply lead to larger offset (y-intercept) in the plots. Furthermore, the values of  $C_1$  and  $C_2$  remain essentially constant throughout the experiments. The amount of fluctuation in these values is a measure of the accuracy of the calibration process. However, the most significant result here is the fact that, as postulated,  $\beta = C_1' / C_2'$ , remains nearly constant throughout the calibrations. Higher signal contamination by the surface scattered background leads to larger values of both  $C_1$  and  $C_2$ . However, the ratio  $\beta$  remains nearly constant. The comparatively high value of  $\beta$ , obtained in Fig. 5(d) with the largest contamination level is believed to be related to the photomultiplier noise levels. A slightly higher background level than that corresponding to Fig. 5(d) led to the saturation of both photomultiplier tubes. This set a limit on the total acceptable signal. The results for the calibration constants, obtained for the same day are summarized in Table 1. The average value of  $\beta$  is 0.885 with a standard deviation of about 0.06. Note that these calibration results are obtained with nine data points on each calibration curve. A larger number of data points are likely to lead to lower standard deviation on the constants.

### Temperature Measurements

Next, temperature was measured in a clean (particulate free) heated air jet with co-flow. Figure 6 shows the co-flow jet apparatus. The co-flow was added to the inner jet to prevent the entrainment of particulates from the laboratory environment. Excessive amounts of particulates in the probe region can prevent accurate measurements by contaminating the Rayleigh signal. Only the central jet is heated and jet exit

temperatures in excess of 800 K could be obtained with this jet apparatus. Again, a thermocouple was situated adjacent to the Rayleigh probe, on the downstream side. The thermocouple readings provide a comparison to the DLDR measurements.

Figure 7 shows the calibration results for the experiment. This time, the calibration is performed using 16 points. Since  $C_1$  and  $C_2$  depend on the electronic and optical settings, the current values are different than those previously obtained (Table 1). However, as expected, the value for  $\beta$  is almost identical to the average value previously obtained. In the figure, estimated error bars are also included at selected points.

The temperatures obtained by the DLDR system, approximately 2 mm above the exit plane, are shown in Figs. 8 and 9 for two jet heating levels. The solid line indicates the reading from the thermocouple. For a given heating level of the jet, multiples of DLDR measurements are obtained in the presence of various backgrounds. The background levels were created using the method previously described. For each contamination level, three records of temperature were obtained. Each symbol in the figures represents the average value of a record (5128 samples per record). In these figures, a and b show the same temperature results against the signal-to-background ratio obtained from  $\lambda_1$  and  $\lambda_2$  lines, respectively.  $I_R / I_B$  ratios are obtained in the following manner:  $I_R$  is calculated from Eqs. (8) and (9), including only the first term on the right hand side and using the temperature reading from the thermocouple.  $I_B$  is obtained directly from the measurements using Eq. (11). The agreement between the DLDR and the thermocouple results is quite good. Particularly encouraging is the fact that even with signal-to-background levels as low as  $I_{R,2} / I_{B,2} = 0.2$ , reliable temperature measurements are possible. It should be noted that the lower limit on the signal-to-noise ratio that appears in Figs. 8 and 9 was determined by a practical consideration: beyond a certain position of the scattering surface, the background level increases sharply and saturates either the sensors or the electronic integrators rendering measurements impossible beyond that point.

## CONCLUSIONS

A laser-induced Rayleigh scattering system is developed for gas temperature measurements. A dual-line detection technique is used for the effective detection and removal of the laser line glare from the Rayleigh signal. The technique involves the collection of signal from two lines of a laser. The two linear equations thus obtained are solved simultaneously to give temperature (or density) and the background level. In the present work, a pulsed copper vapor laser is used as the light source. The 510 nm and the 578 nm lines intrinsic to the laser provide the necessary two lines. The use of a pulsed laser greatly reduces the effect of broadband background from the surroundings. Calibration tests and actual temperature measurements also indicate that the dual-line

detection technique can improve the capability of Rayleigh scattering method by greatly reducing the effects of signal contamination due to laser glare. It eliminates the need for background mapping and the associated guesswork typical of Rayleigh scattering measurements in optically non-ideal situations. Accurate temperature measurements were obtained in a heated air jet even when the background level captured by the collecting optics was five times the Rayleigh signal. Using the dual-line detection technique, it is hoped that effective Rayleigh scattering measurements in enclosed test sections (such as in combustors with limited optical access) as well as near walls (such as in boundary layer studies) will be possible. Currently, a second DLDR system, similar to the one discussed here, is being developed which uses an Nd:YAG laser. In this new system, second and fourth harmonics of the laser output will be used as the two detection lines.

### ACKNOWLEDGEMENTS

This work was undertaken while the first author was a summer faculty fellow at NASA Lewis Research Center, Optical Measurement Systems Branch. The support through NASA Grant NAG-3-1301 is also acknowledged.

### REFERENCES

- Arcoumanis, C.: A Laser Rayleigh Scattering System for Scalar Transport Studies. *Exp. Fluids* Vol.3, 1985 pp. 103-108.
- Bill, R. G. Jr., Namer, I., Talbot, L., Robben, F.: Density Fluctuations of Flame in Grid Induced Turbulence. *Combust. Flame*, Vol. 44, 1982 pp.277-285.
- Dibble, R.W.; and Hollenbach, R.E: Laser Rayleigh Thermometry in Turbulent Flows. Eighteenth Symposium on Combustion, 1981. The Combustion Institute pp. 1489-1499.
- Dyer, T. M.: Rayleigh Scattering Measurements of Time-resolved Concentration in a Turbulent Propane Jet. *AIAA J.*, Vol. 17, 1979 pp. 912-914.
- Escoda,C.; and Long, M.B.: Rayleigh Scattering Measurements of Gas Concentration Field in Turbulent Jets. *AIAA J.*, Vol 21, 1983, pp.81-84.
- Gouldin, F.C.; and Halthore, R.N: Rayleigh Scattering for Density Measurements in Premixed Flames. *Exp. Fluids*, Vol. 4, 1986,pp. 269-278.

Graham, S.C.; Grant, A.J.; and Jones, J.M.: Transient Molecular Concentration Measurements in Turbulent Jets. AIAA J., Vol. 12, 1974, pp. 1140-1143.

Jenkins, F.A. and White, H.E.: Fundamentals of Optics, Fourth Edition. London, McGraw-Hill, 1981.

Namer, I. and Schefer, R.W.: Error Estimates for Rayleigh Scattering Density and Temperature Measurements. Exp. Fluids, Vol. 3 1985, pp. 1-9.

Otugen, M. V. and Namer, I.: Rayleigh Scattering Temperature Measurements in a Plane Turbulent Air Jet at Moderate Reynolds Numbers. Exp. Fluids, Vol. 6, 1988, pp. 461-466.

Pitts, W. M. and Kashiwagi, T.: The Application of Laser-induced Rayleigh Scattering to the Study of Turbulence Mixing. J. Fluid Mech. Vol. 141, 1984, pp.391-429.

Seasholtz, R.G.: High Speed Laser Anemometry Based on Spectrally Resolved Rayleigh Scattering. Proceedings of the Annual Conference on Laser Anemometry, August 5-9, 1991, Cleveland, OH.

Shirinzadeh, B; Hillard, M.E.; and Exton, R.J.: Condensation Effects on Rayleigh Scattering Measurements in Supersonic Wind Tunnel. AIAA J., Vol.29, 1991, pp.242-246.

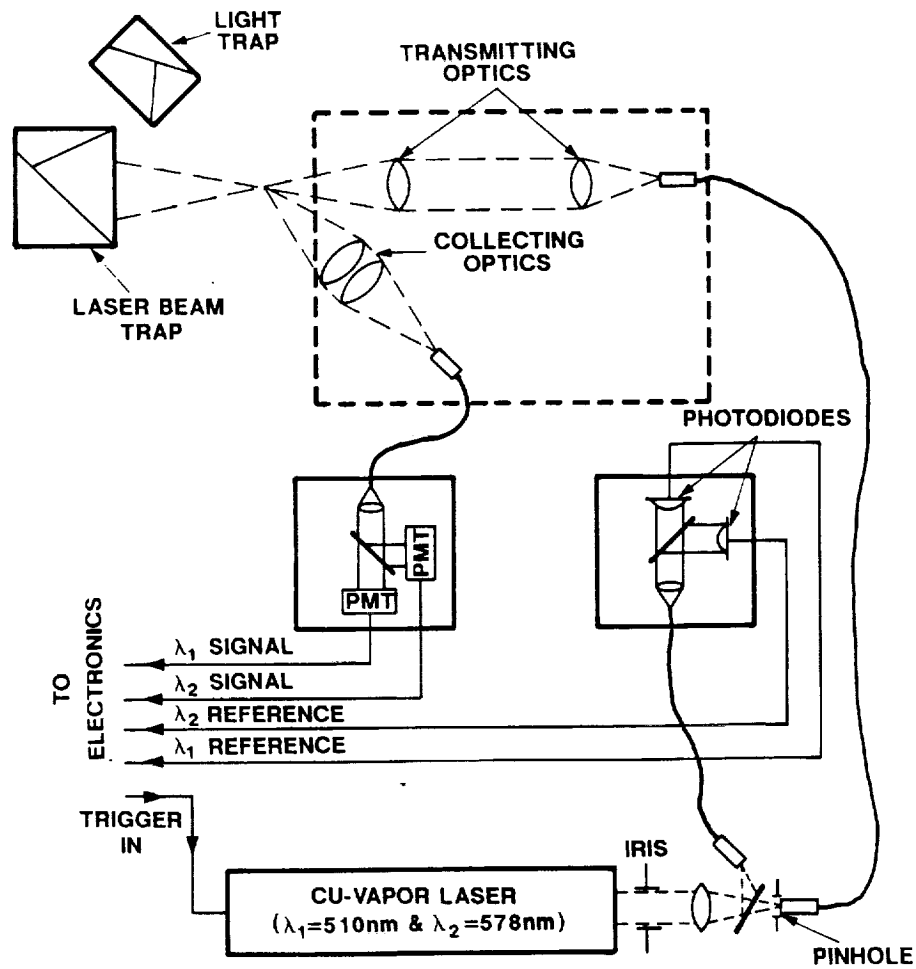
Smith, M.; Smits, A.; and Miles, R.: Compressible Boundary Layer Density Cross Sections by UV Rayleigh Scattering. Optic Letters, Vol. 14, 1989, pp.916-918.

Van de Hulst, H. C.: Light Scattering by Small Particles. Chapman & Hall, London 1957.

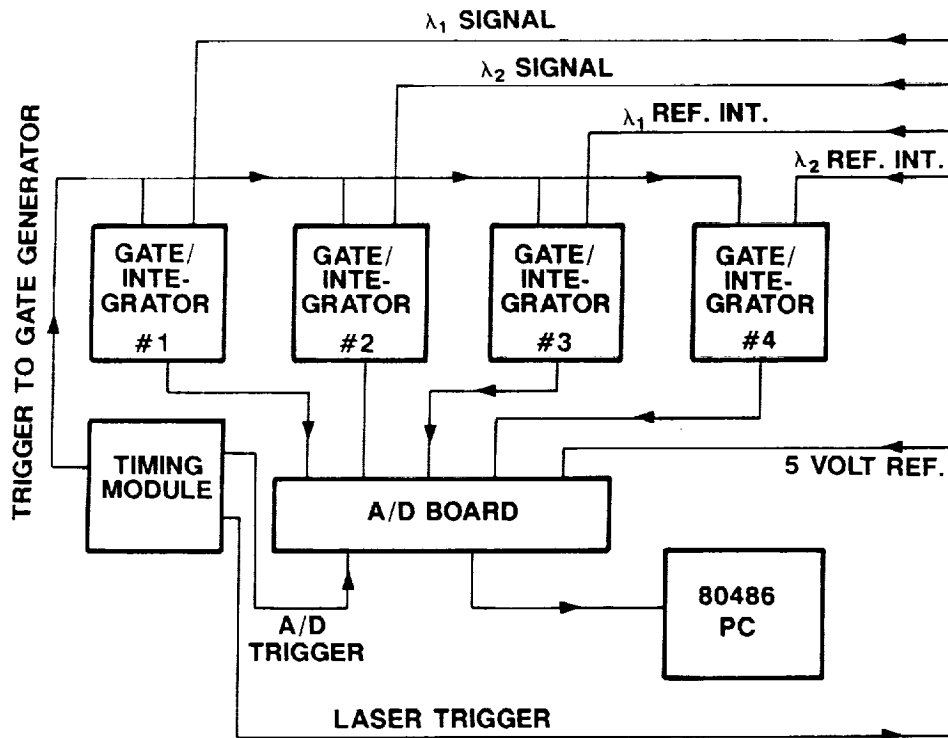


Table 1

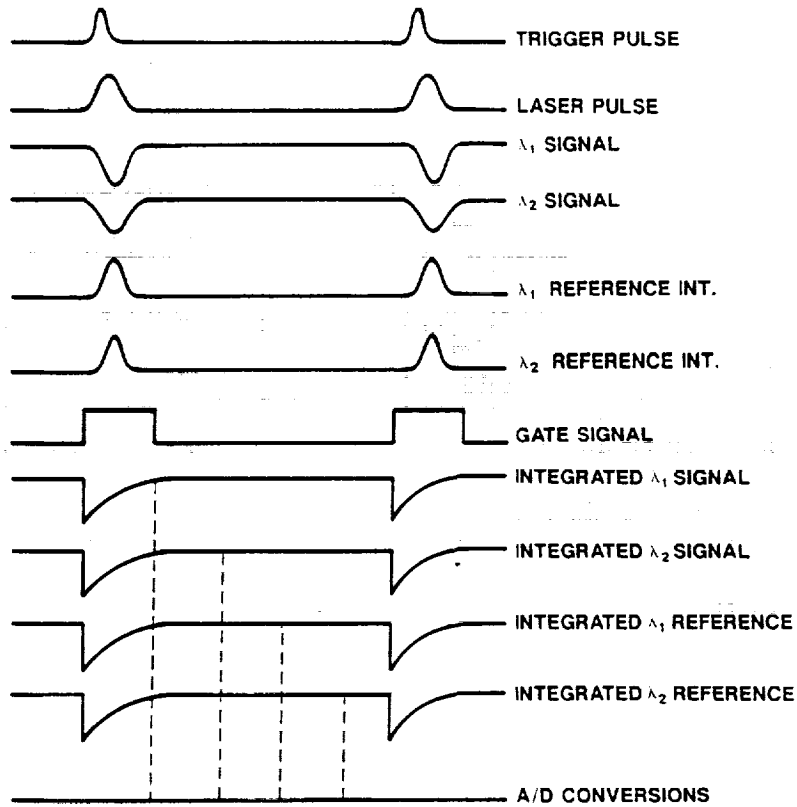
	$\chi$	$\sigma'$	$\sigma' / \chi$
$C_1$	4.4248 E7	0.1545 E7	0.035
$C_2$	1.0479 E8	0.0361 E8	0.034
$\beta$	0.885	0.060	0.068



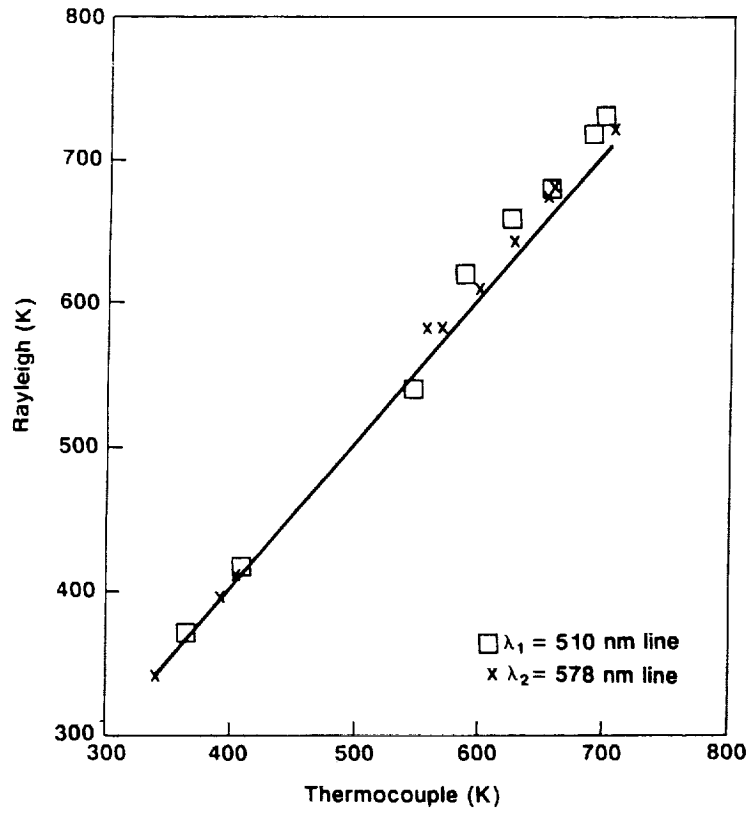
1. Optical arrangement for the DLDR system



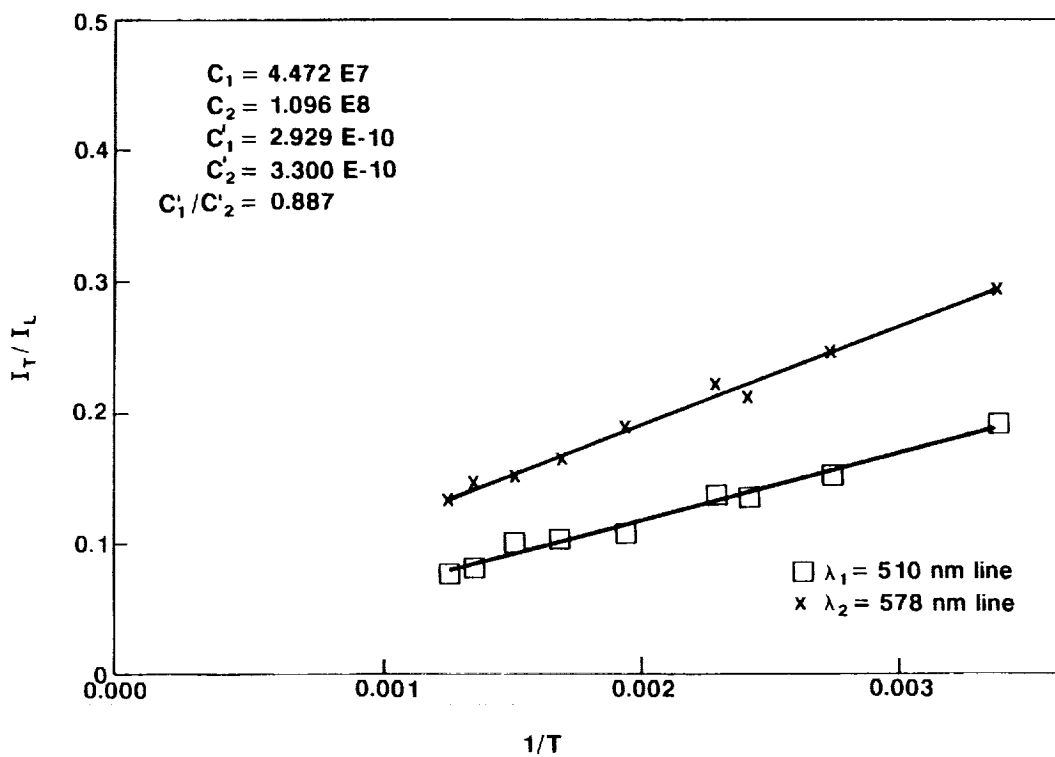
2. Electronic arrangement for the DLDR system



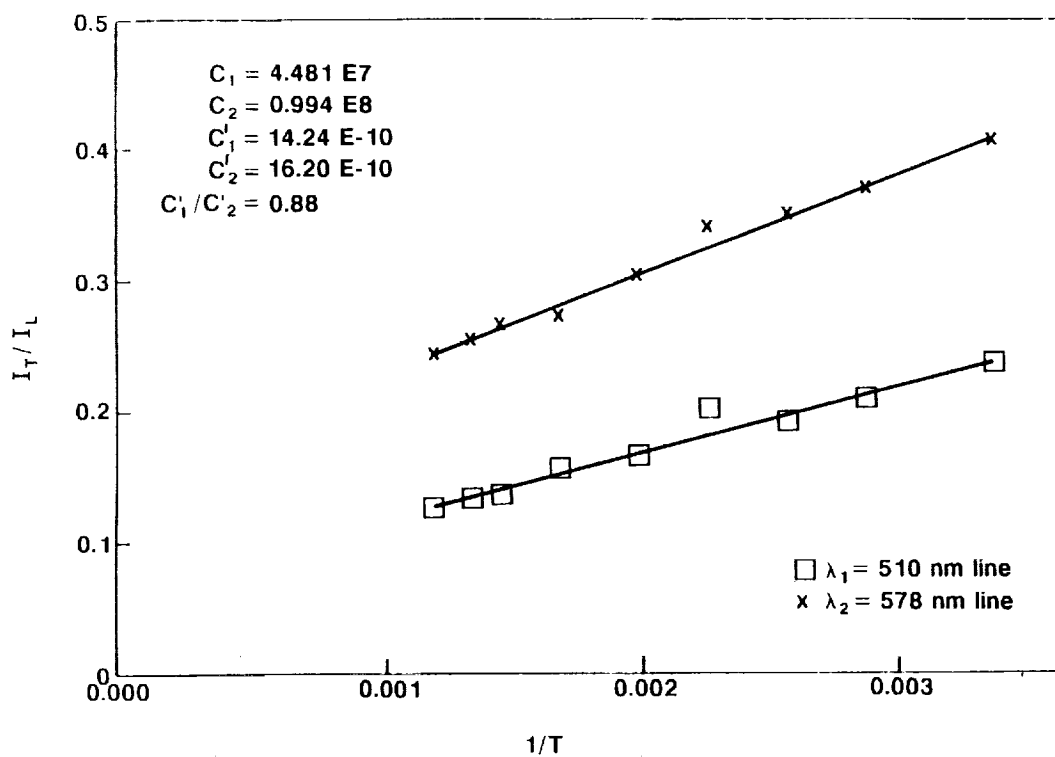
3. Data acquisition procedure



4. Temperature obtained by Rayleigh scattering and thermocouple

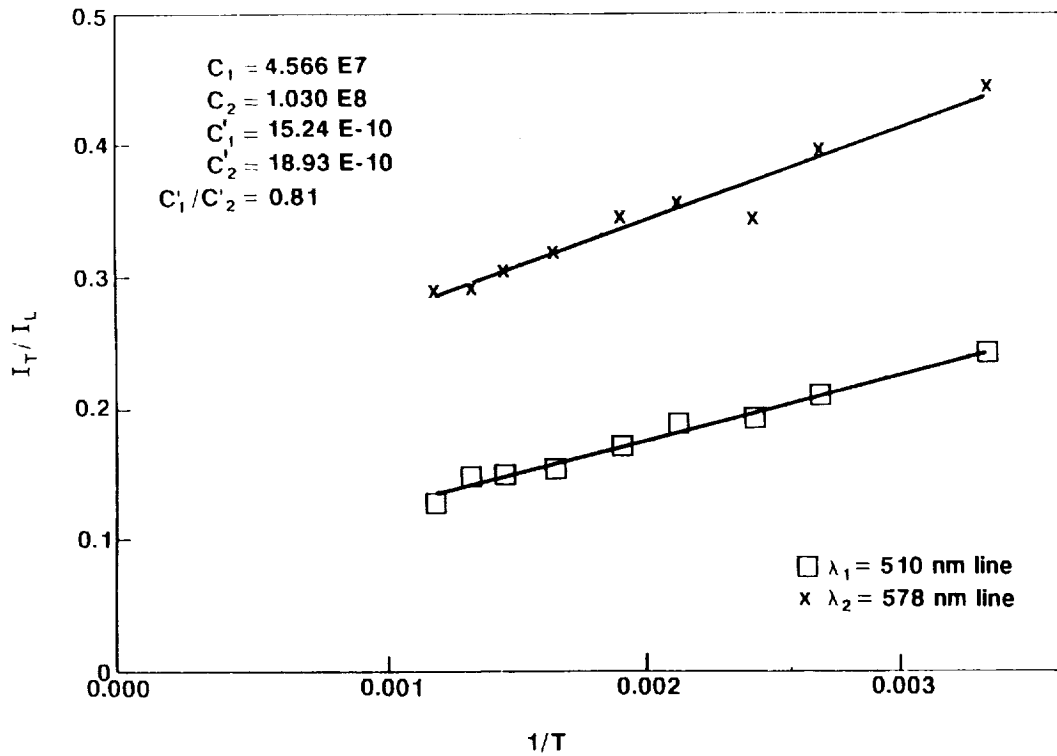


a

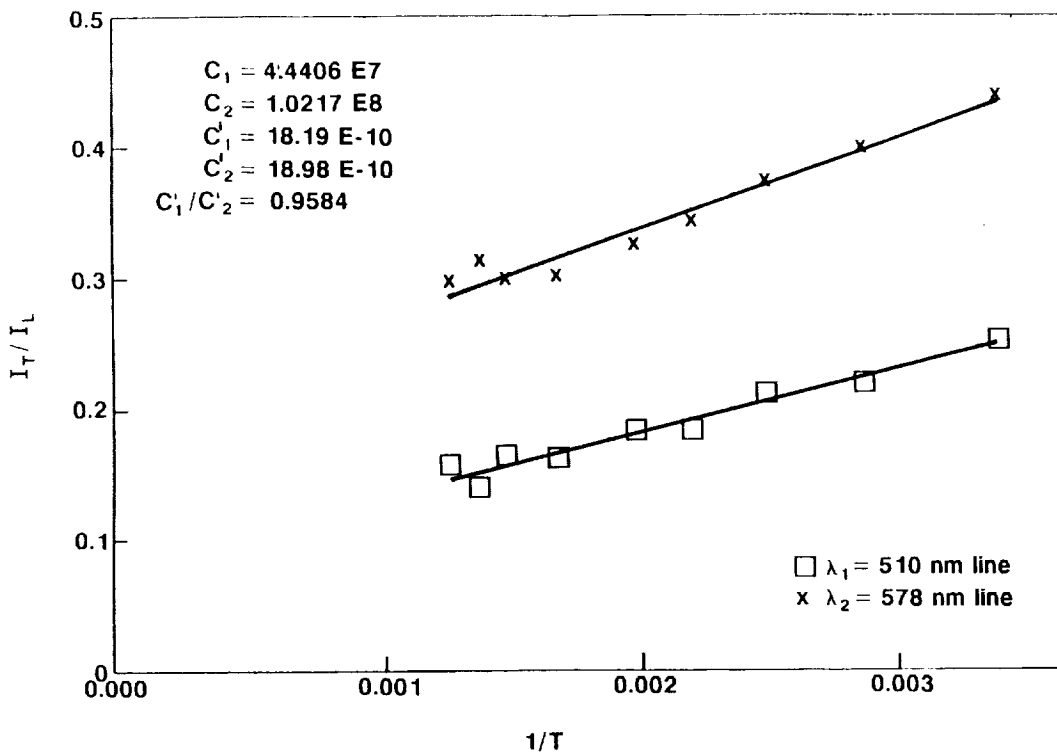


b

5. Calibration curves with various levels of background contamination

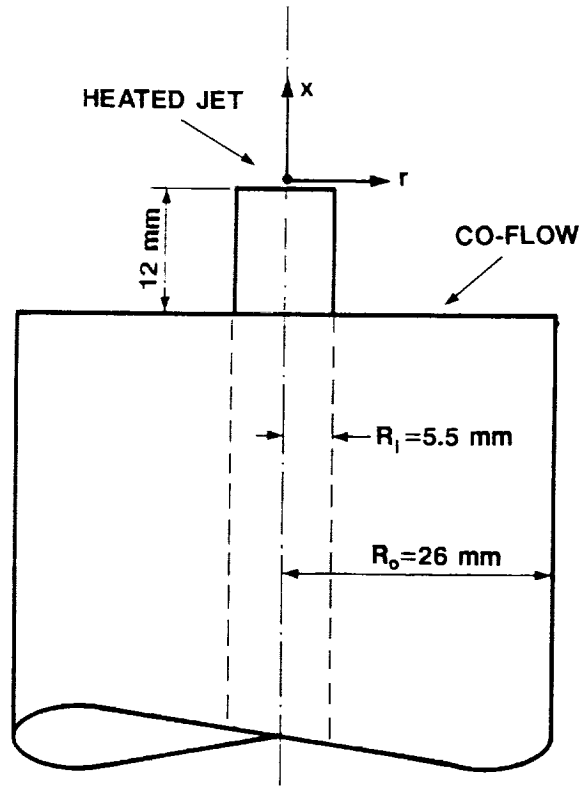


c

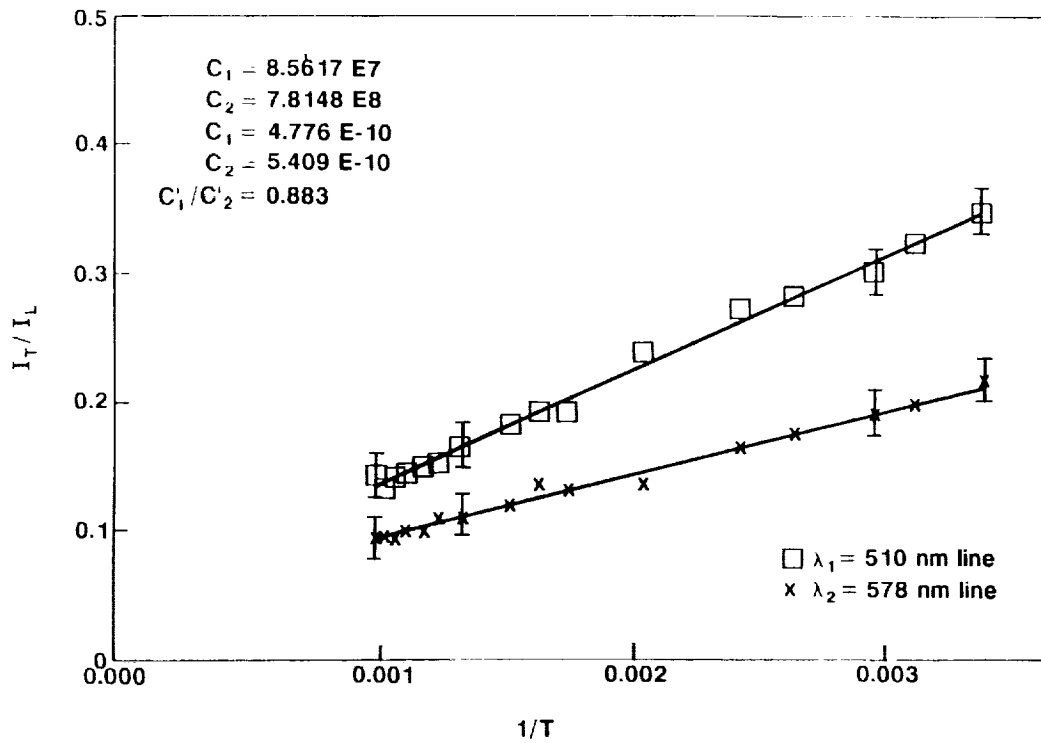


d

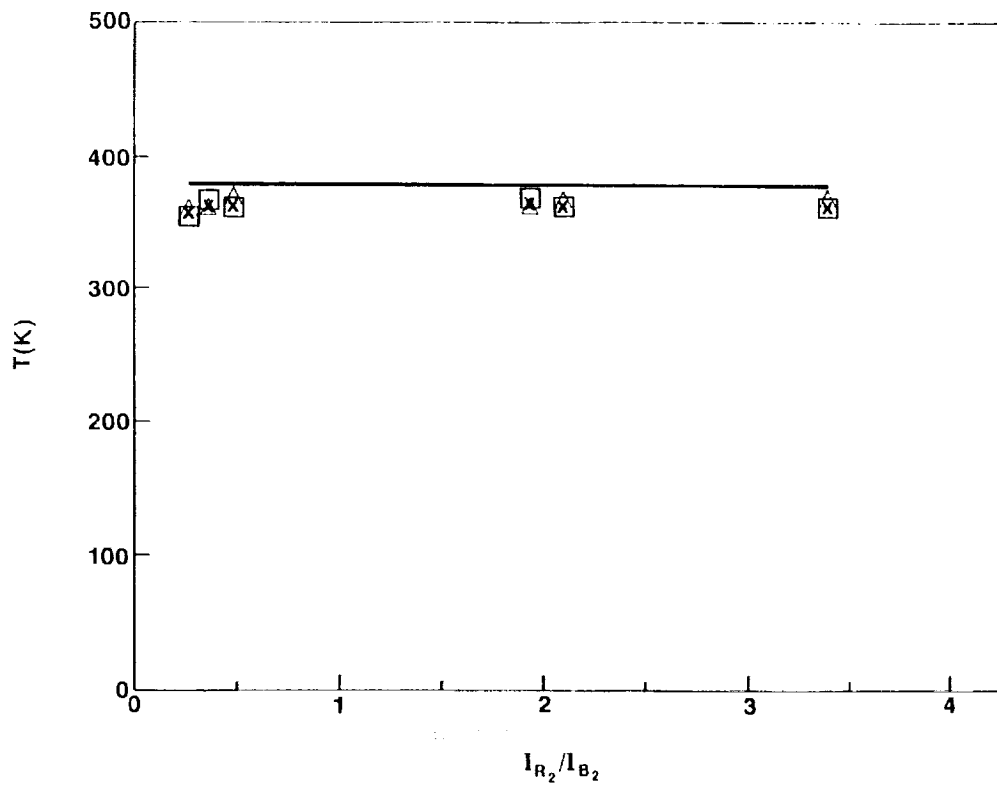
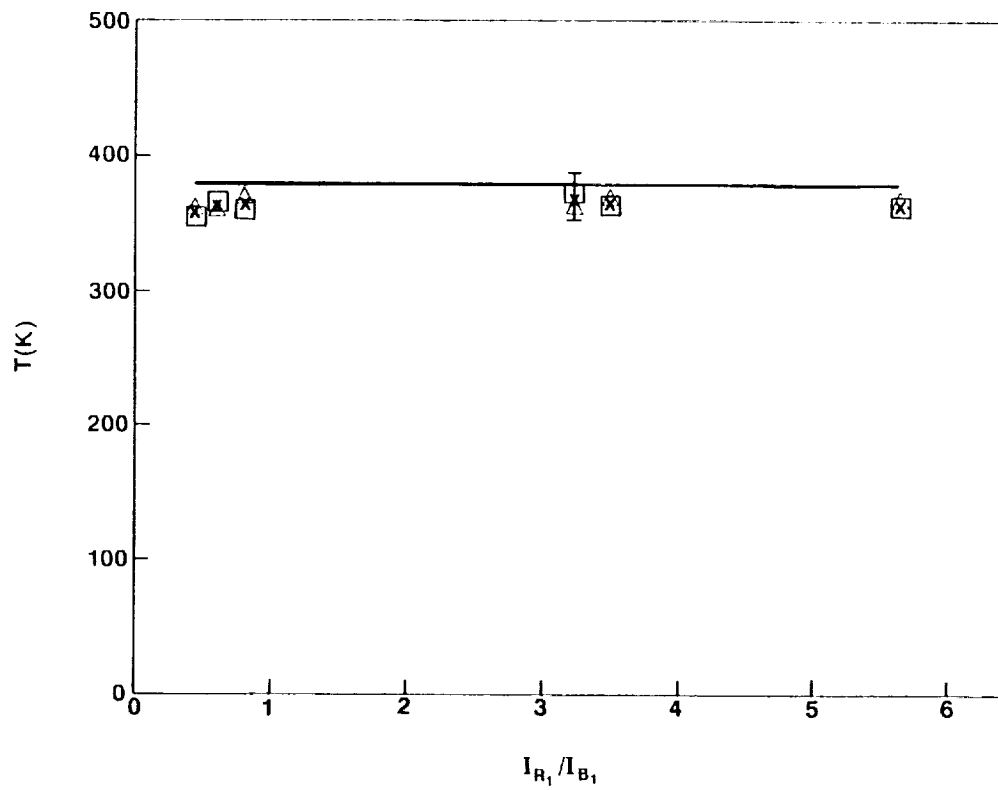
5. Calibration curves with various levels of background contamination (cont)



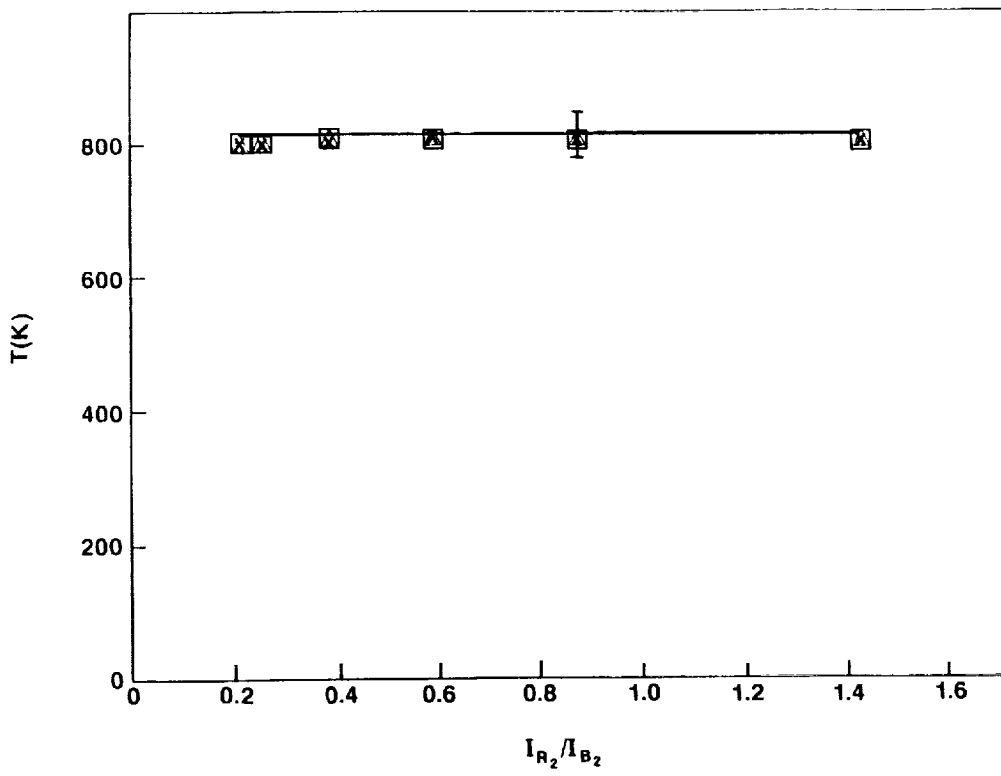
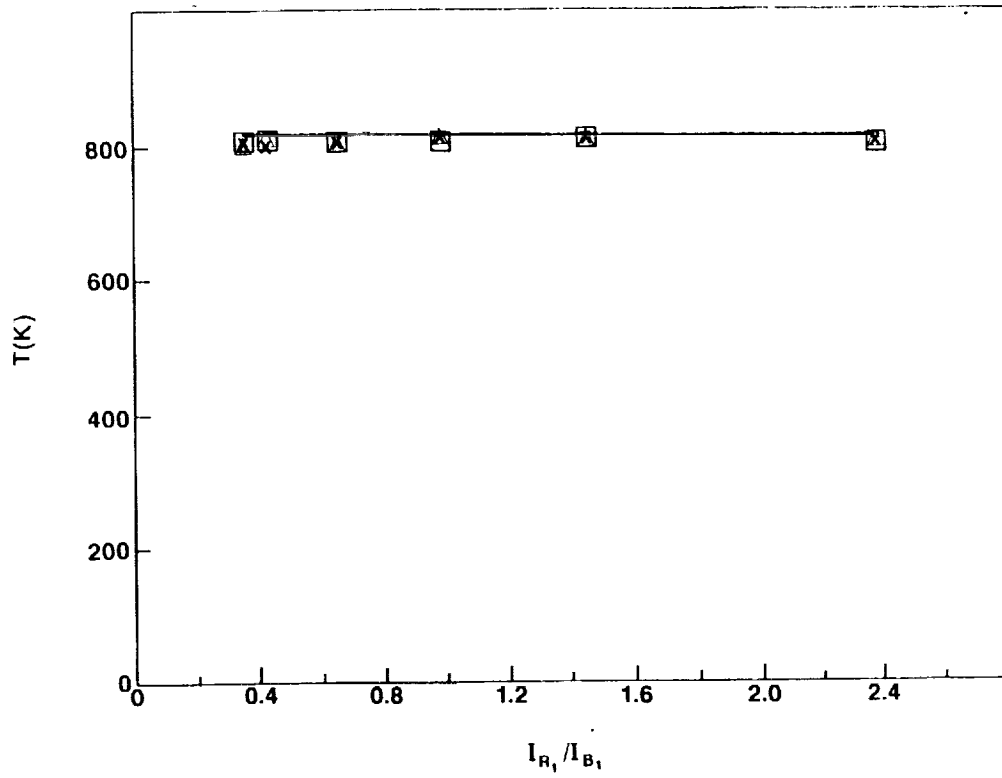
6. Heated jet setup with co-flow



7. Calibration curve for the temperature measurements



8. Jet temperature measured by the DLDR system ( $T_{jet} = 380$  K).



9. Jet temperature measured by the DLDR system ( $T_{jet} = 805$  K).



## ABSTRACT

## High-Temperature Strain Measurement Techniques: Current Developments and Challenges

Keynote Address by

M.M. Lemcoe, Ph.D.  
PRC, Inc., Edwards, CA

Since 1987, a very substantial amount of R&D has been conducted in an attempt to develop reliable strain sensors for the measurements of structural strains during ground testing and hypersonic flight, at temperatures up to at least 2000 deg F. Much of the effort has been focused on requirements of the NASP Program. This presentation is limited to the current sensor development work and characterization studies carried out within that program. It is basically an assessment as to where we are now and what remains to be done in the way of technical accomplishments to meet the technical challenges posed by the requirements and constraints established for the NASP Program.

The approach for meeting those requirements and constraints has been multi-disciplinary in nature. It was recognized early on that no one sensor could meet all these requirements and constraints, largely because of the large temperature range (cryogenic to at least 2000 deg F) and many other factors, including the most challenging requirement that the sensor system be capable of obtaining valid "first cycle data".

Present candidate alloys for resistance-type strain gages include Fe-Cr-Al and Pd-Cr. Although they have superior properties regarding withstanding very high temperatures, they exhibit large apparent strains that must either be accounted for or cancelled out by various techniques, including the use of a dual-element, half-bridge dummy gage, or electrical compensation networks. A significant effort is being devoted to developing, refining, and evaluating the effectiveness of those techniques over a broad range in temperature and time.

In the quest to obtain first-cycle data, ways must be found to eliminate the need to prestabilize or precondition the strain gage, before it is attached to the test article. It should be noted that present NASP constraints do not permit prestabilization of the sensor, in situ. Gages are currently being "heat treated" during manufacture in both the wire- and foil-type resistance strain gages, and evaluation is in progress. In addition, the "gage-on-shim" concept is being revisited. That concept will permit heat treatment of the gage during manufacture, before attachment on the test article. Also, it may permit the individual calibration of each gage regarding gage factor and apparent strain.

Candidate alloys for the NASP include titanium metal-matrix and carbon-carbon composites. Although these materials have very attractive properties at elevated temperatures in terms of strength and weight, they pose significant attachment problems. Methods for making reliable strain gage and thermocouple attachments to them are currently under development. Experience to date indicates that Rokide attachment of the sensor directly to the protective coating is easier than to the base material itself. However, interpreting strain data from gages attached in this way may prove difficult because of possible cracks in the coating that form "islands" and the mobility of those "islands". It is concluded, therefore, that major technical challenges lie ahead as we proceed to meet the stringent strain sensor requirements and constraints of the NASP Program.

## OUTLINE

### I. INTRODUCTION

- CURRENT STATE-OF-THE-ART
  - RESISTIVE STRAIN GAGES
  - CAPACITIVE GAGES
  - CLIP GAGE
  - ELECTRO-OPTICAL METHODS
  - NEED FOR HIGH TEMPERATURE STRAIN MEASUREMENTS
  - NEED FOR RELIABLE ATTACHMENT TECHNIQUES
  - NEED TO REACH TECHNICAL CLOSURE ON CHOICE OF LEADWIRES
- NEED FOR MORE PHYSICAL AND MECHANICAL PROPERTIES DATA FOR NASP CANDIDATE MATERIALS, INCLUDING  $\beta$ 21S TMC
- CRITICALITY OF GAGE LOCATIONS AND ORIENTATIONS, AND HOW DO WE DETERMINE WHERE TO PUT THEM BEFORE GAGING THE TEST ARTICLE?

### II. A MAJOR NASP REQUIREMENT AND CHALLENGE

- GET VALID FIRST CYCLE DATA TO AT LEAST 1500°F
- HOW BIG A TECHNICAL CHALLENGE IS IT?

### III. GAME-PLAN FOR DEALING WITH THIS TECHNICAL CHALLENGE

- CONSIDER USE OF AN EXISTING GAGE IN THE UNTREATED CONDITION THAT HAS ACCEPTABLE PERFORMANCE TO 1500°F
- SUPPRESS THE APPARENT STRAIN
  - USE A REMOTE DUMMY GAGE COMPENSATION SYSTEM
  - USE TEMPERATURE-COMPENSATED GAGES
  - USE GAGES THAT CAN BE HEAT-TREATED DURING MANUFACTURE

USE WELDABLE GAGES (EATON, ETC.) OR SHIM-MOUNTED BCL OR NZ-2104 GAGES THAT CAN BE PRESTABILIZED, PRECONDITIONED, OR PRECALIBRATED PRIOR TO INSTALLATION ON THE TEST ARTICLE OR SPECIMEN

IV. CURRENT ACTIVITIES AT DRYDEN

- A. DEVELOPMENT OF REMOTE DUMMY GAGE TEMPERATURE-COMPENSATION SYSTEMS
- B. DEVELOPMENT OF A DUAL-ELEMENT TEMPERATURE-COMPENSATED GAGE
- C. DEVELOPMENT OF SHIM-MOUNTED GAGES THAT CAN BE PRESTABILIZED, PRECONDITIONED OR CALIBRATED PRIOR TO ATTACHMENT ON TEST ARTICLE OR SPECIMEN
- D. DEVELOPMENT OF AN OPTIMUM WELD SCHEDULE FOR ATTACHING WELDABLE GAGES WITH INCONEL FLANGES (EATON GAGE, ETC.), OR GAGES MOUNTED ON INCONEL SHIMS, TO  $\beta$ 21S TMC
- E. DEVELOPMENT OF OPTIMUM PRESTABILIZATION SCHEDULE FOR BCL GAGES
- F. DEVELOPMENT OF ELECTRO-OPTICAL STRAIN MEASUREMENT SYSTEM (GRANT-CONTRACT TO IIT) FOR STRUCTURAL TESTING TO 2500°F, OR BEYOND
- G. PERTINENT GAGE CHARACTERIZATION STUDIES, INCLUDING A STUDY TO DETERMINE CHARACTERISTICS OF UNTREATED BCL GAGES TO AT LEAST 1500°F
- H. COMPONENT TESTING AND GAGING

V. ON-GOING WORK AT L<sub>6</sub>RC

- Pd-13Cr TEMPERATURE-COMPENSATED GAGE
- GWP 29

VI. ON-GOING WORK AT L<sub>8</sub>RC


- TEMPERATURE-COMPENSATED GAGES
- GAGE ATTACHMENT TECHNIQUES
- GAGE CHARACTERIZATION STUDIES

VII. CONCLUDING REMARKS

 ADHESIVELY BONDED HIGH TEMP. GAGES  
(BLH, MEASUREMENTS GROUP, ETC.)

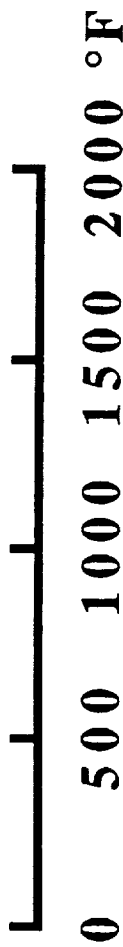
 WELDABLE GAGES (EATON)

 CERAMIC CEMENT (BLH, HITEC, MEII)

 ROKIDED GAGES (BLH, HITEC, MEII)

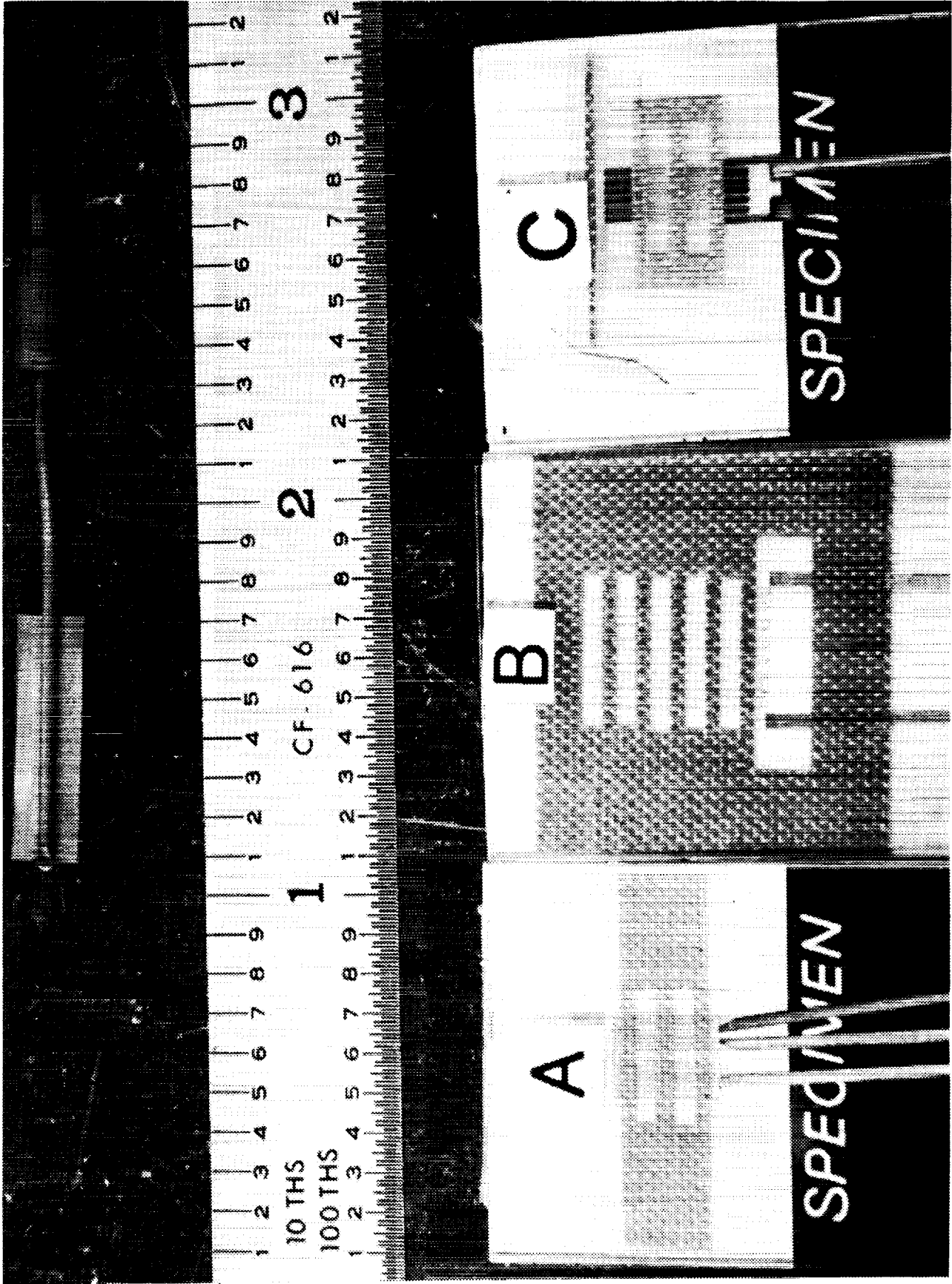
 CAPACITANCE GAGES

 ROKIDED BCL GAGES



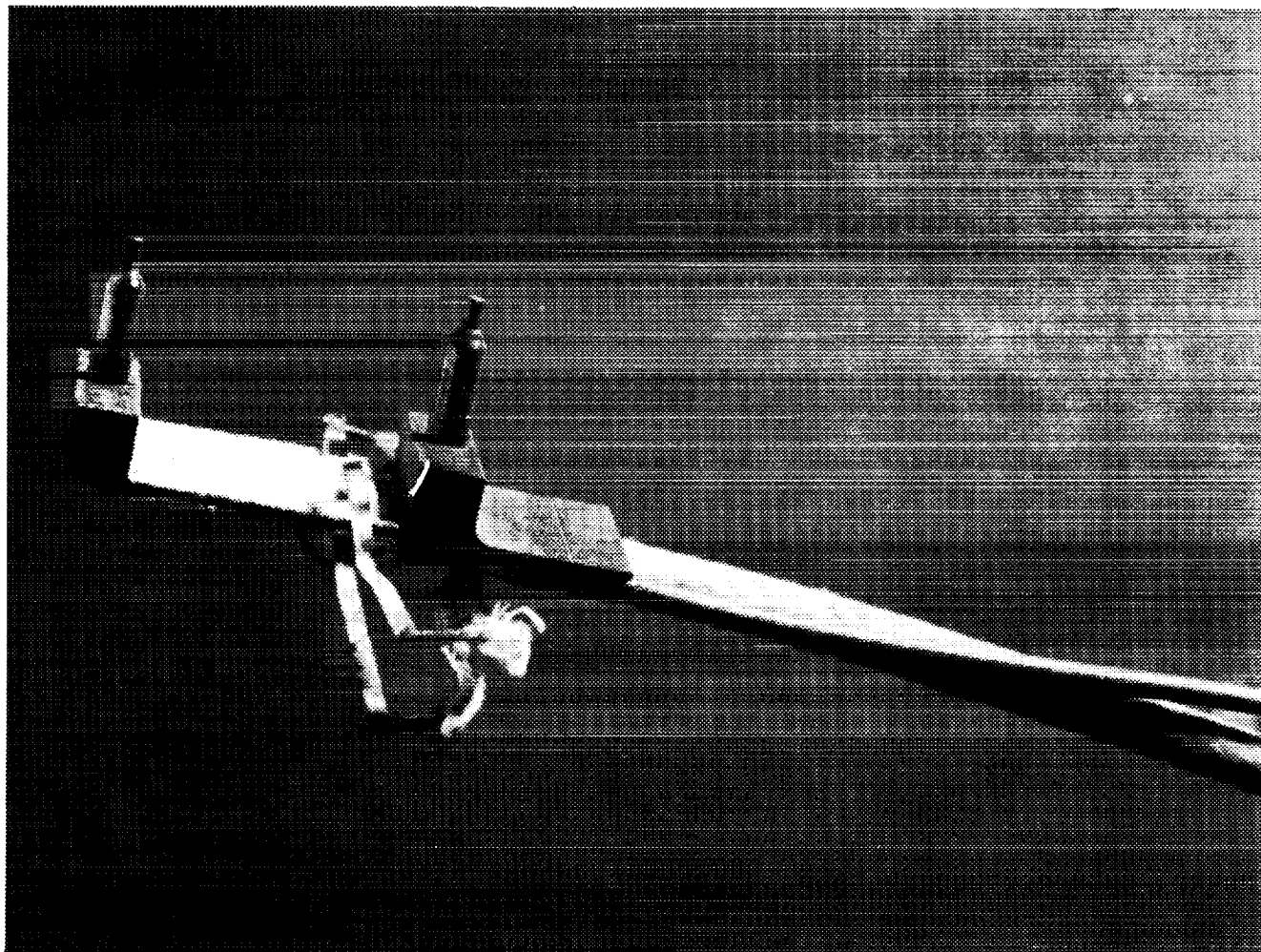
MAX OPERATING TEMPERATURE

STATE OF THE ART OF EXISTING  
ELECTRIC RESISTANCE AND  
CAPACITANCE STRAIN GAGES

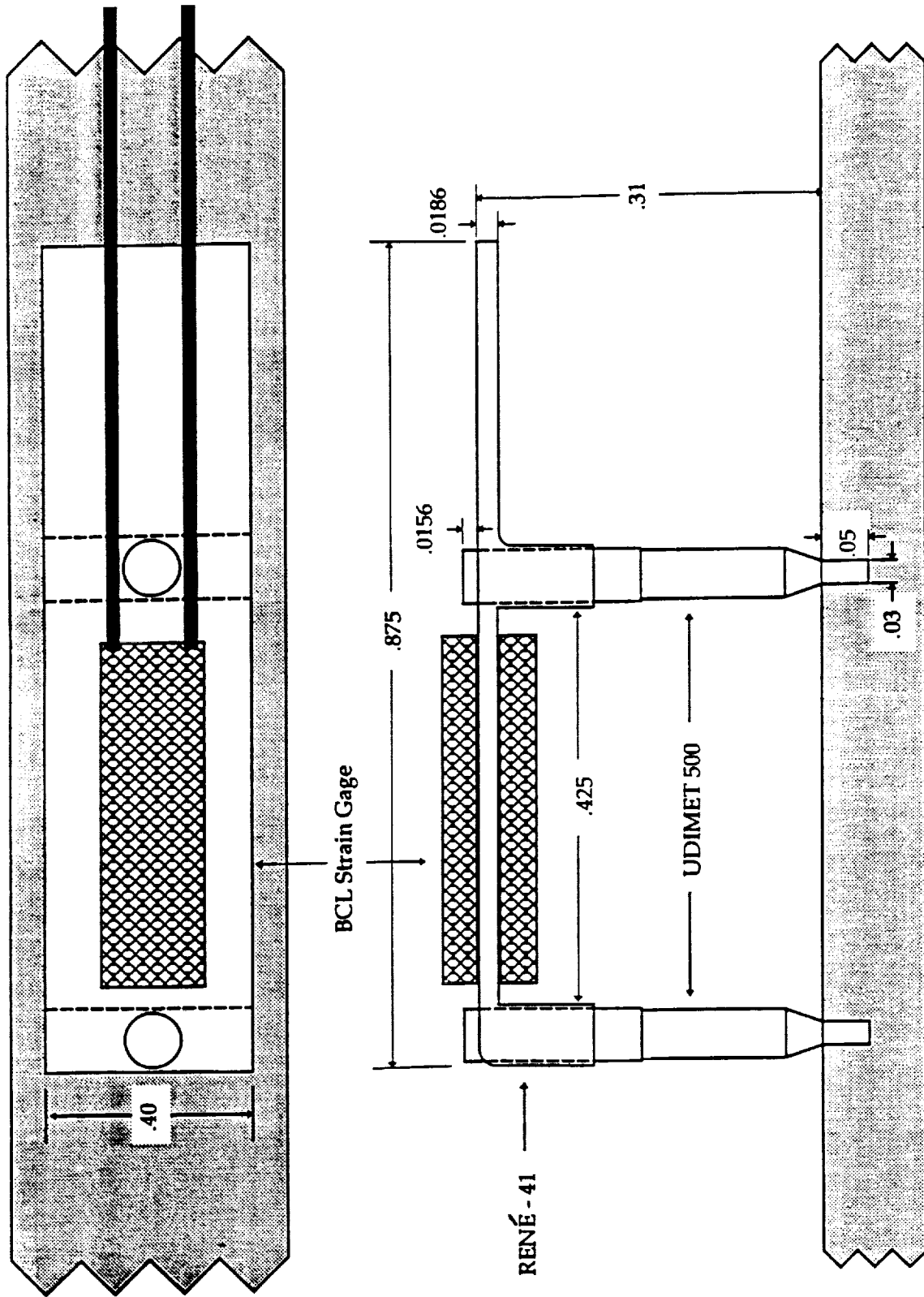


A: Untreated, Temperature-compensated BCL gage; B: Standard, Untreated BCL gage; C: NZ-2104 gage. At top: Eaton SG425 gage with Inconel 600 flange

ORIGINAL PAGE  
BLACK AND WHITE PHOTOGRAPH

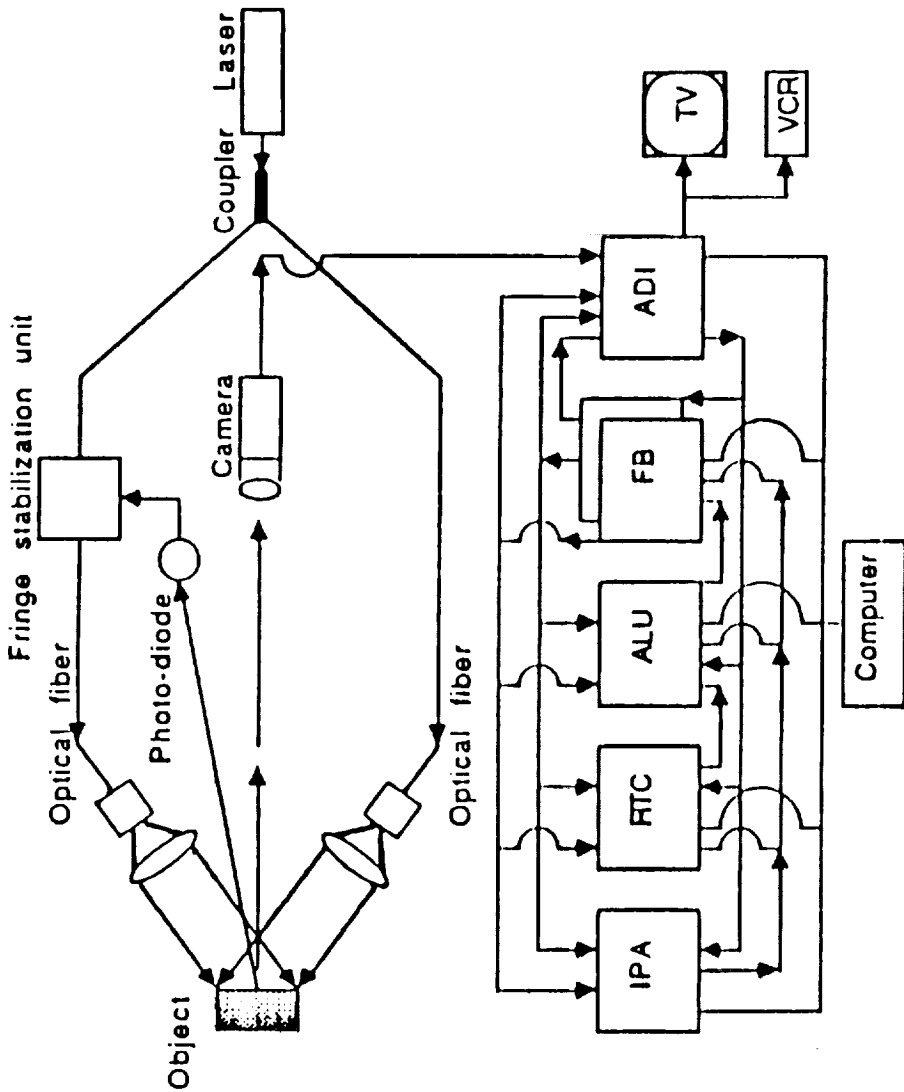


**High-Temperature Clip Gage**



BCL Clip Gage

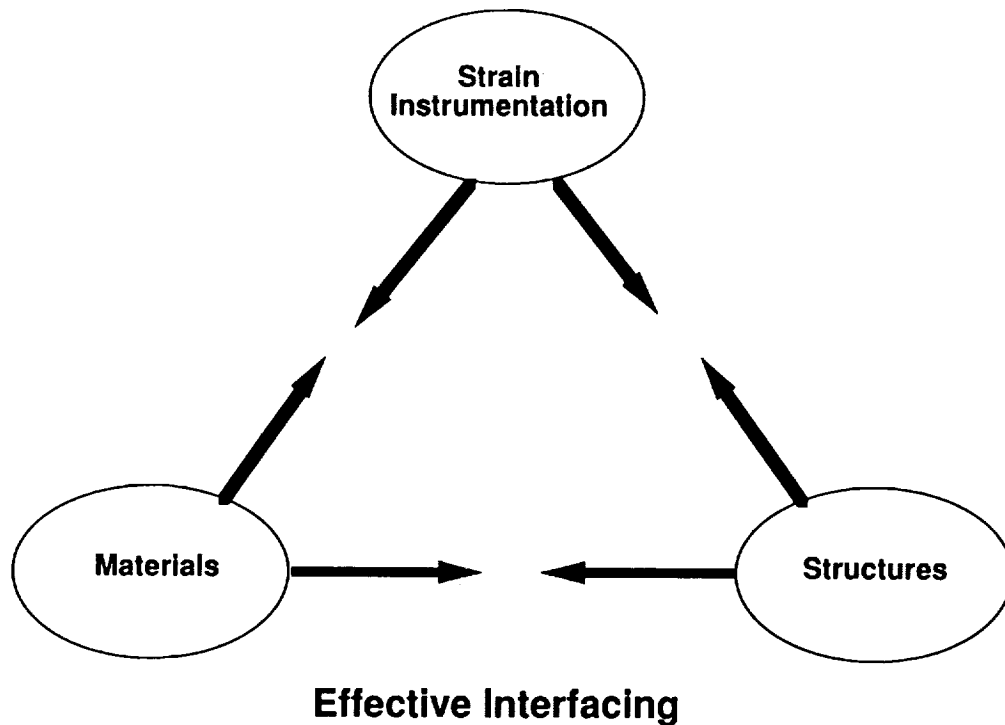




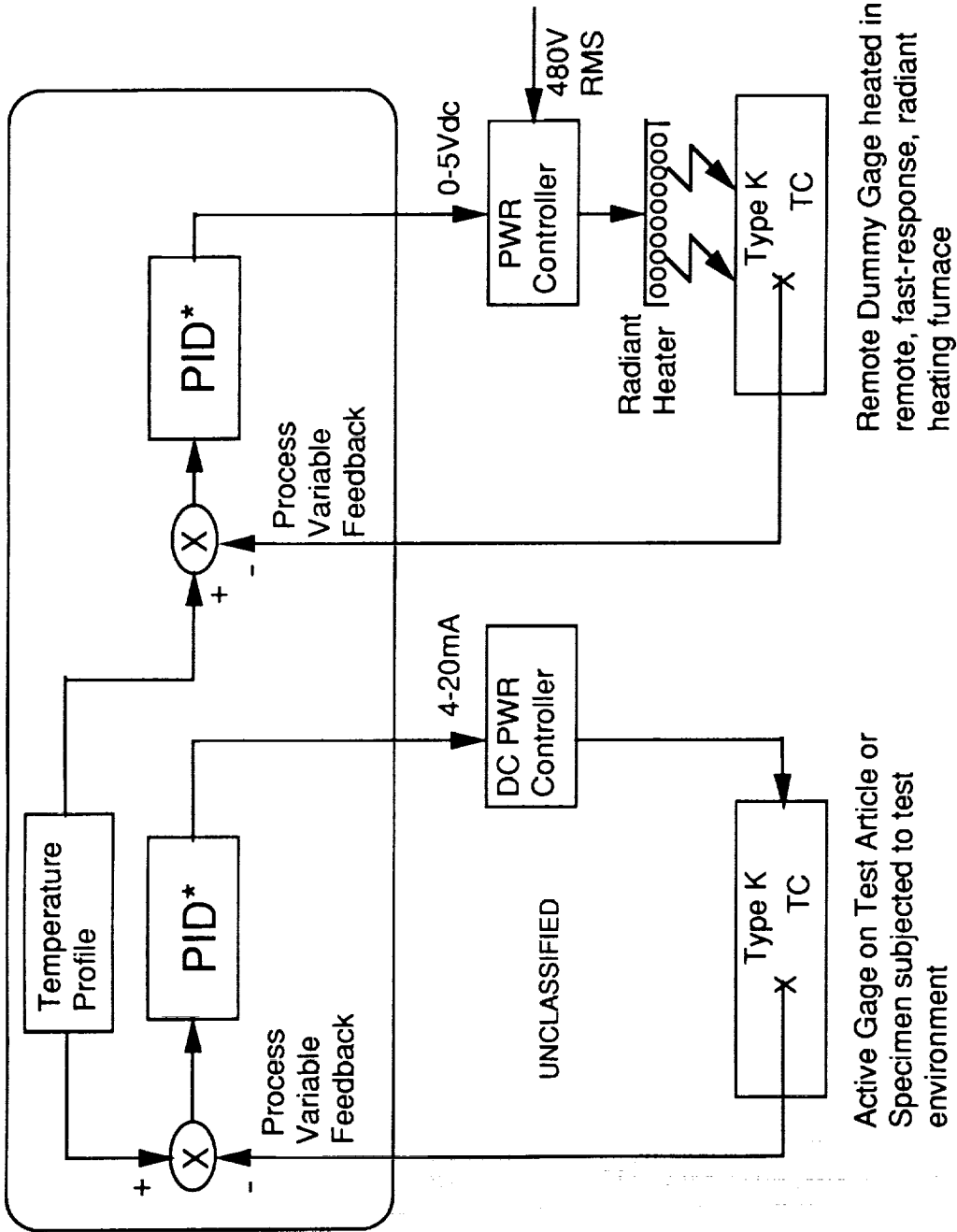
ADI - Analog to digital interface    FB - Frame buffer    ALU - Arithmetic and logic unit  
 RTC - Real time convolver    IPA - Image processor accelerator

Schematic representation of the electro-optical system to measure strains

- **Needs for High Temperature Strain Measurements**
  - **NASP Structural Ground Tests**
  - **NASP Flight Tests**
  - **Validation of finite element computer codes for NASP stress analysis**
  - **Materials behavior studies, including determination of strains resulting from release of residual or fabrication stresses, during and after heating**

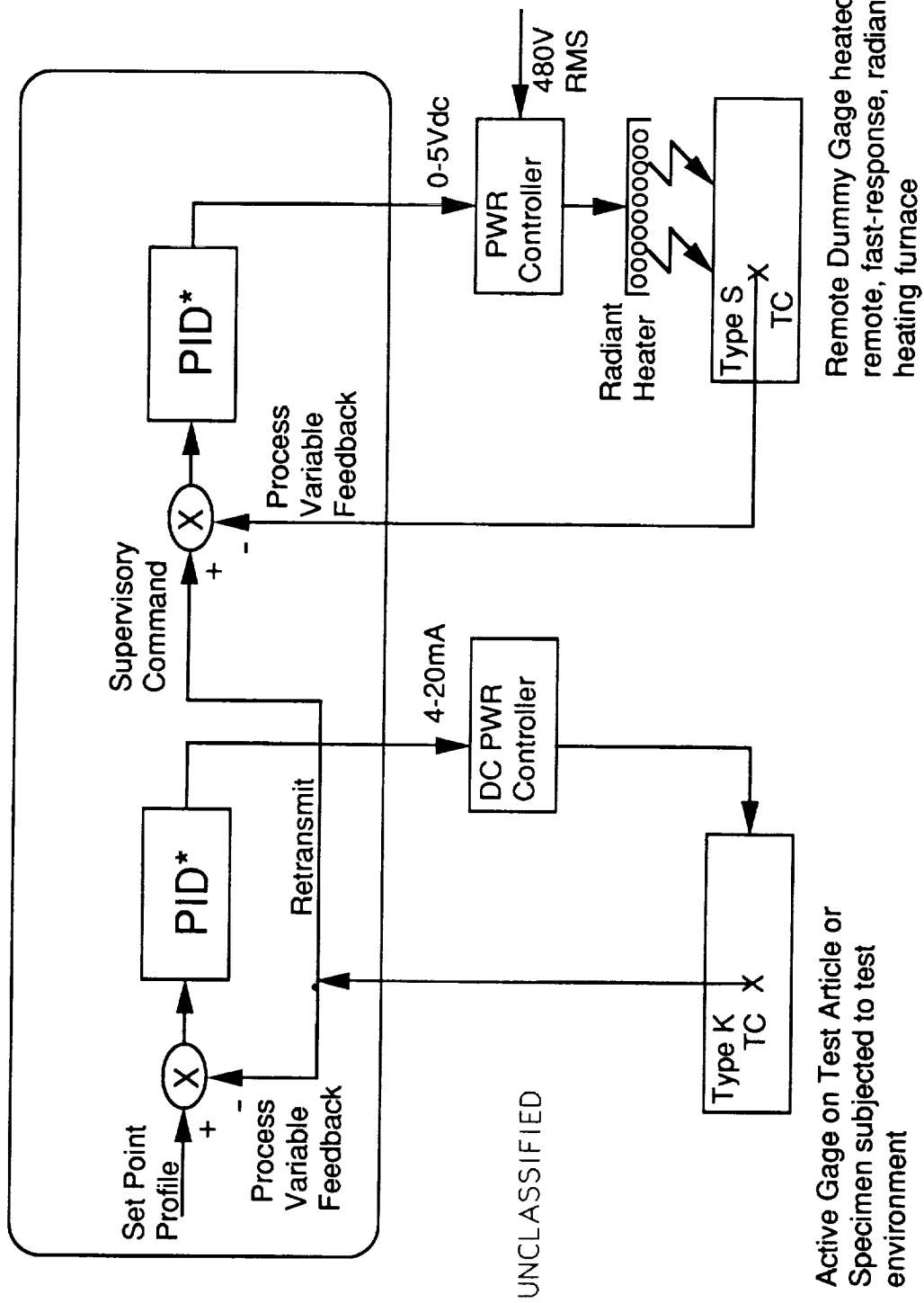


- **Standard Prestabilization-Preconditioning Procedure**
  - **Prestabilize the attached gages for 4 hours (minimum), at a temperature about 25°F above the maximum test temperature, in an air environment**
  - **After prestabilization, precondition the installed gages by subjecting them to 3 thermal cycles from room temperature to maximum temperature, and 3 mechanical cycles at maximum test temperature to a minimum of  $\pm 2000 \mu\epsilon$**



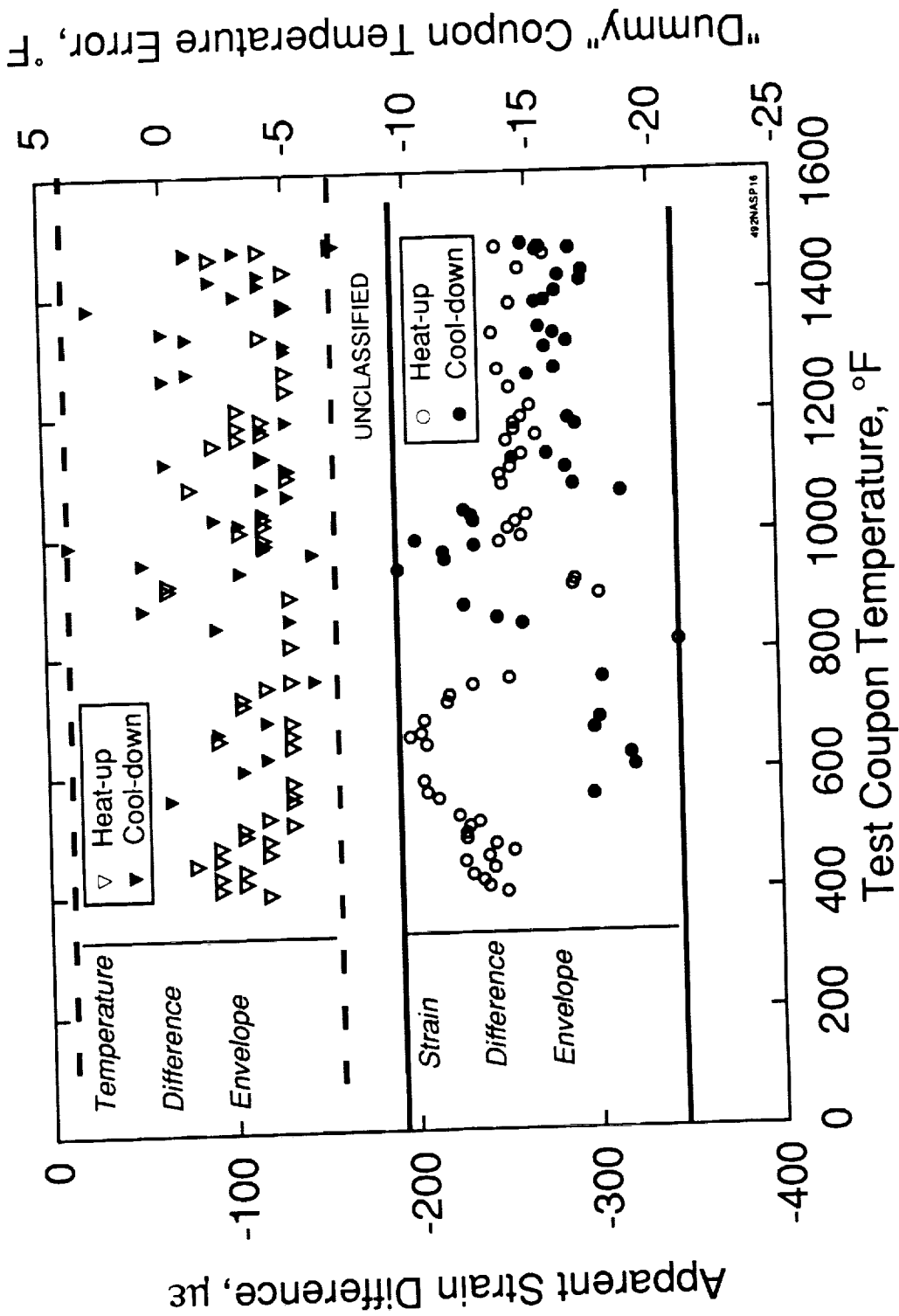
\* - PID: Proportional-Integral-Derivative temperature controllers

## Schematic of Breadboard Electronic Follower/Control System for Remote Suppression of Apparent Strain



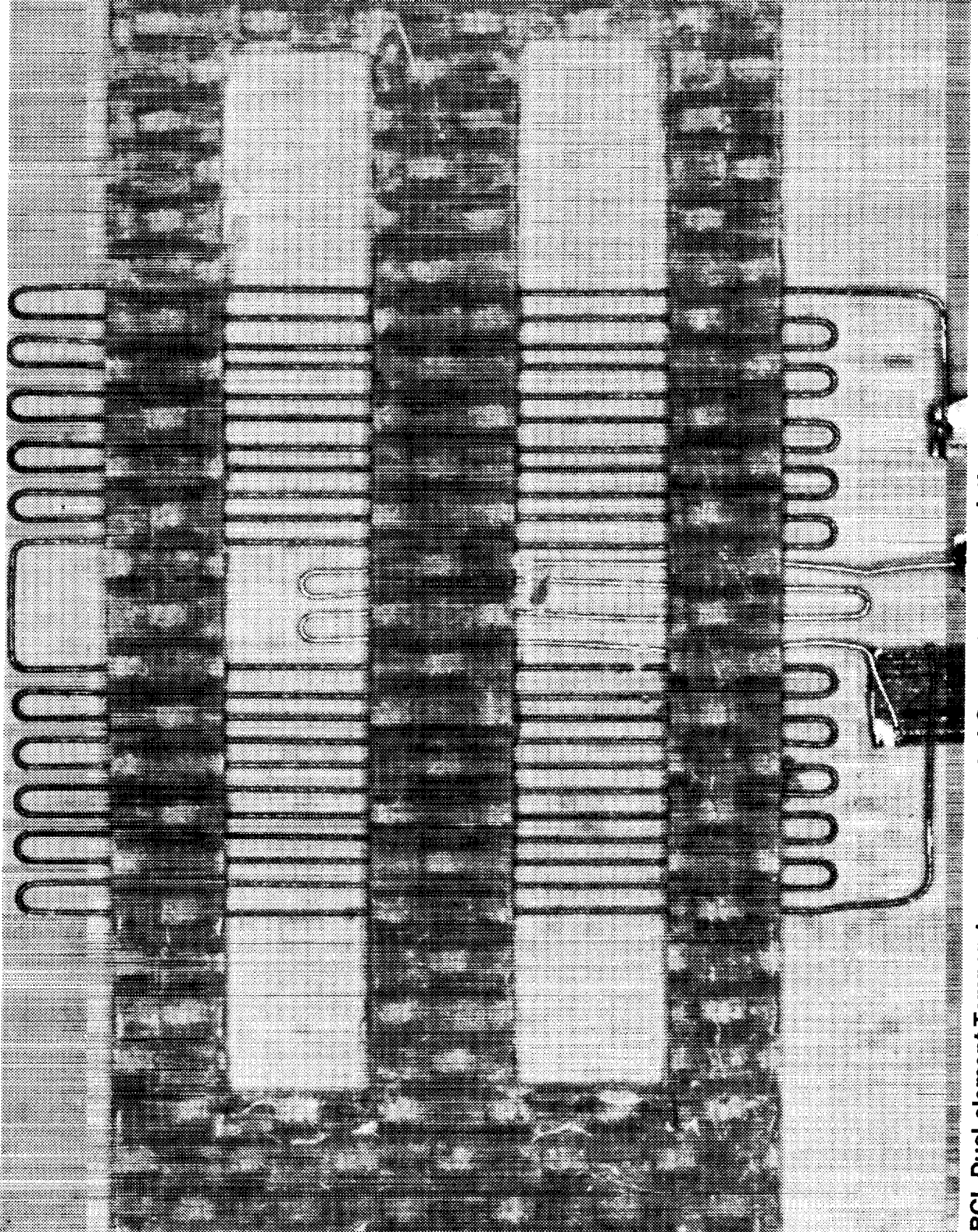
\* - PID: Proportional-Integral-Derivative temperature controllers

## Schematic of Electronic Follower/Control System for Remote Suppression of Apparent Strain

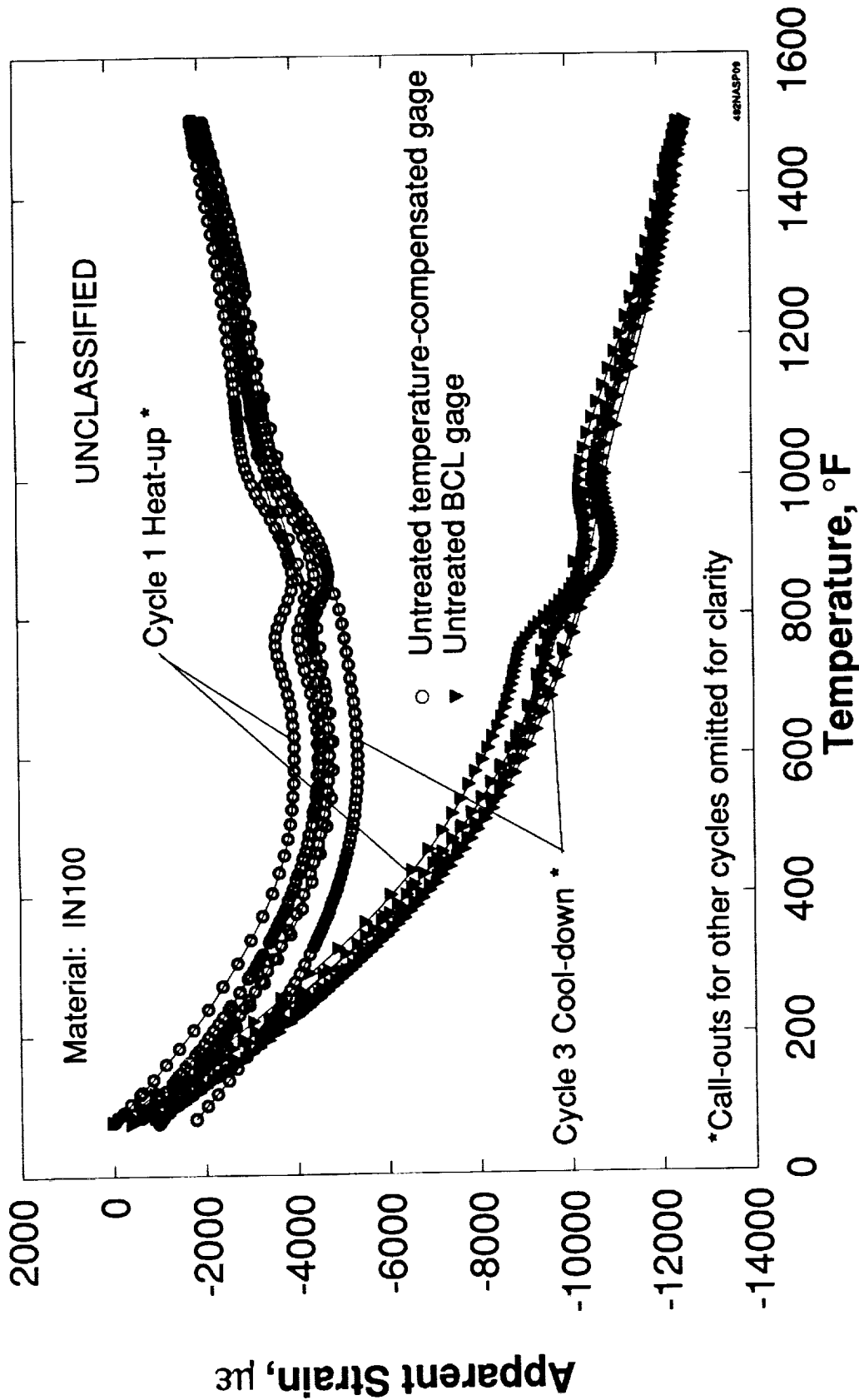


Apparent Strain from an Untreated BCL Active Gage with Remote Dummy Gage. First Cycle Data.

"Dummy" Coupon Temperature Error,  $^{\circ}F$



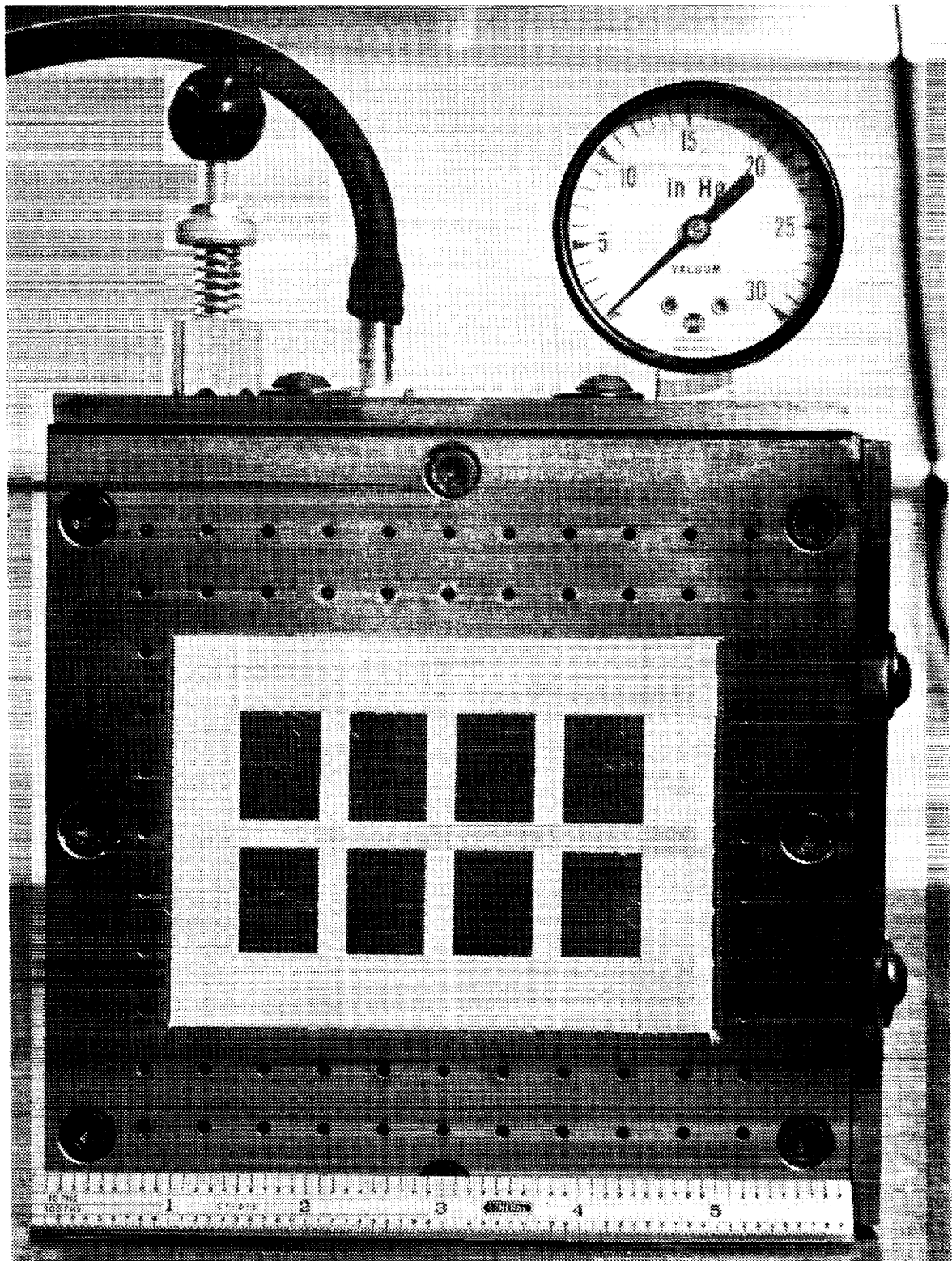
BCL Dual-element Temperature-compensated Gage with central platinum compensating element



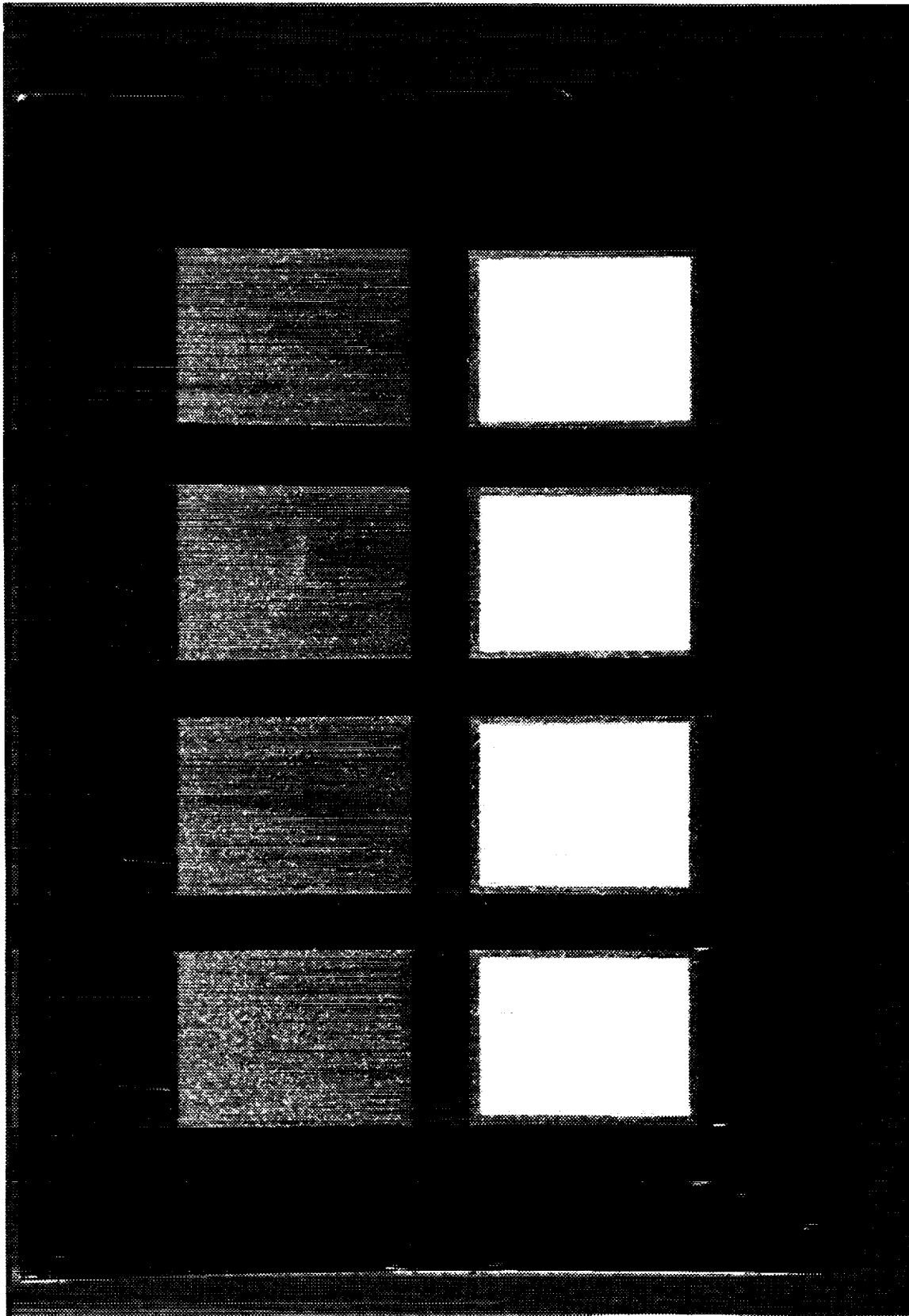
# Apparent Strain of BCL Temperature-Compensated and Standard BCL Untreated gages



ORIGINAL PAGE  
BLACK AND WHITE PHOTOGRAPH

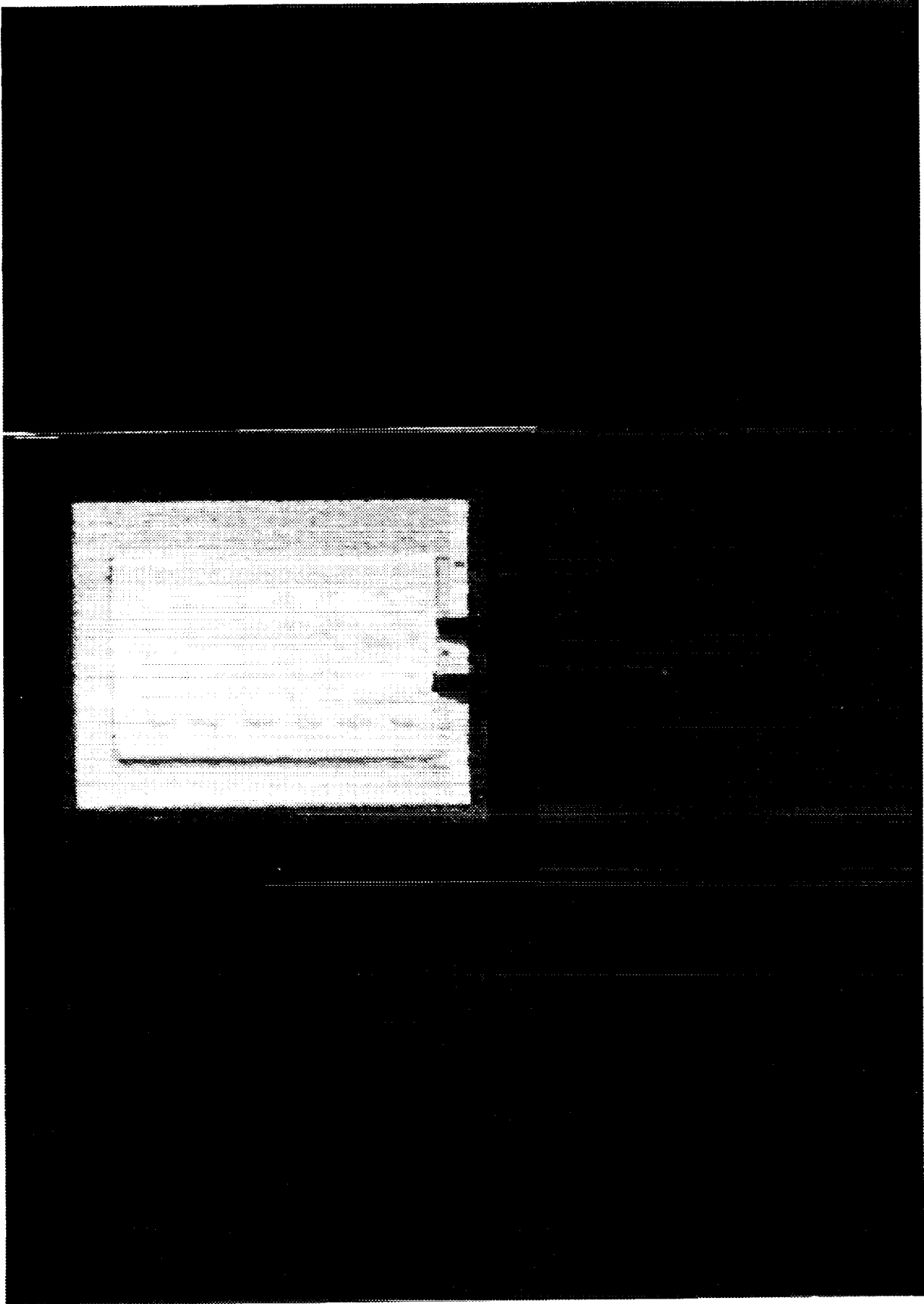


**Vacuum Chuck used to hold Coupon  
flat during spraying**

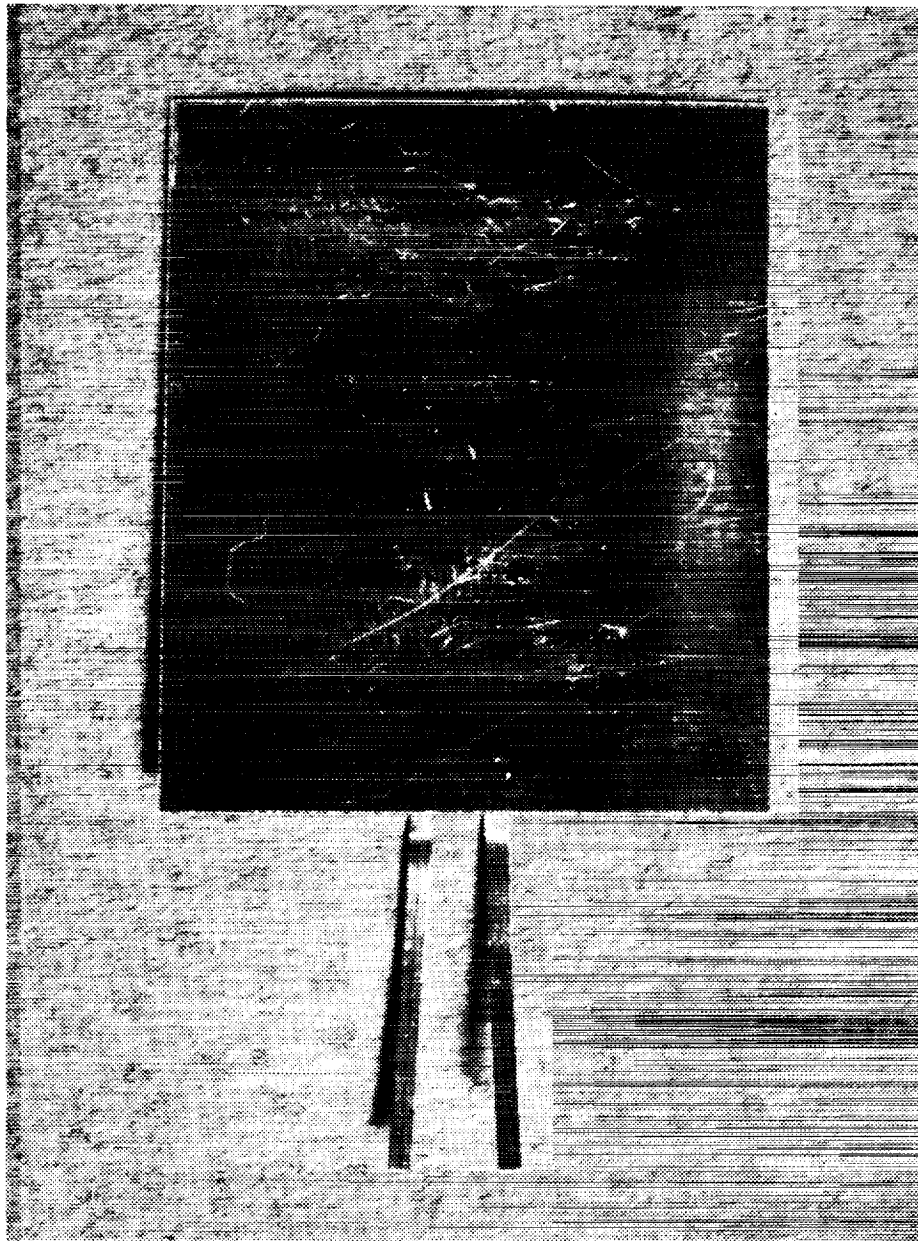


TOP: Plasma-sprayed Precoat of Metco 461 on Inconel 600, 5 mil Shim  
BOTTOM: Rokide Insulating Substrate bonded to Precoat

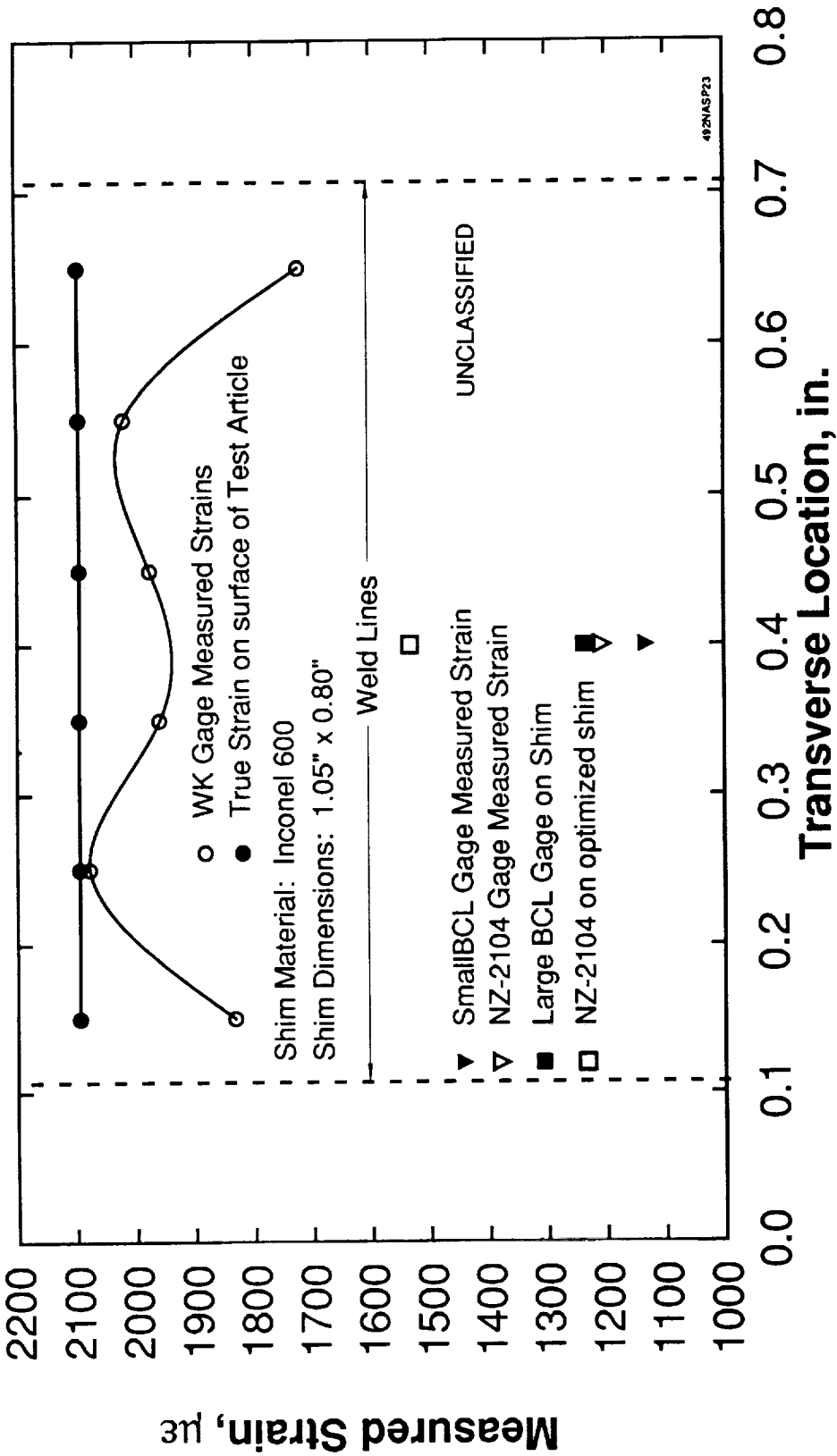
ORIGINAL PAGE  
BLACK AND WHITE PHOTOGRAPH



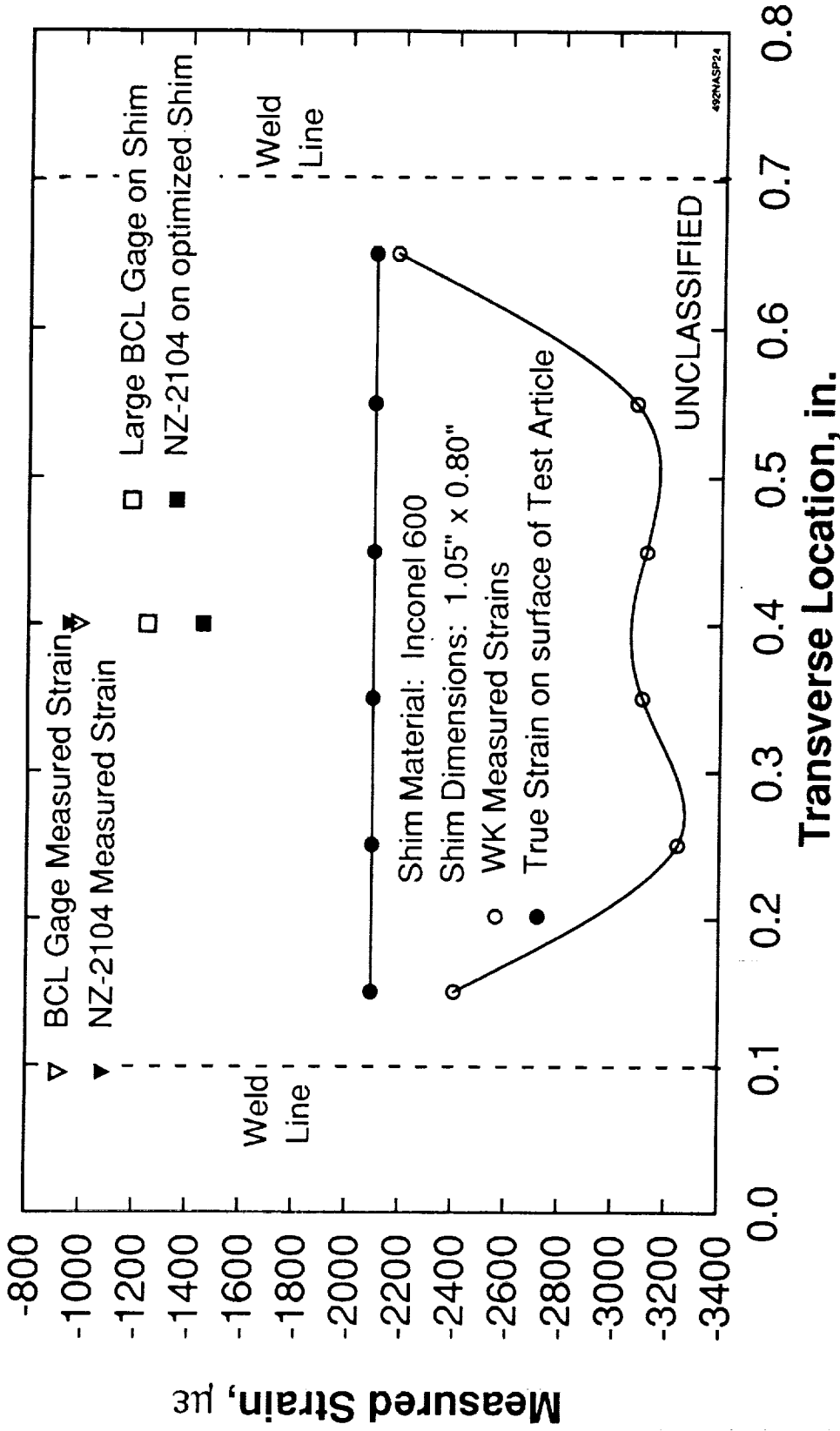
Complete NZ-2104 Gage Installation on Inconel 600 Shim



**Back Face of Shim, after Gage Installatlon**



# Tensile Strain Distribution Across Transverse Section at Centerline of 5 mil Thick Shim



# Compressive Strain Distribution Across Transverse Section at Centerline of 5 mil thick Shim

## BCL-instrumented Shim Fatigue Data

Cycle No.	Maximum Measured Tensile Bending Strain	Maximum Measured Compressive Bending Strain
	$\mu\epsilon$	$\mu\epsilon$
1	1288	-1013
10	1304	-996
20	1304	-972
30	1304	-982
40	1302	-978
50	1302	-972
60	1299	-972
70	1302	-969
80	1300	-967
90	1299	-966
100	1299	-962

All data is at room temperature.  
True Strain on calibration specimen was  $\pm 2095$  microstrain.

## Effective Gage Factors of Shimmed Gages

	Small BCL on Large Shim	Standard BCL on Large Shim	NZ-2104 on Large Shim	NZ-2104 on Optimized Shim
<b>Tension</b>	1.41	1.86	1.53	2.30
<b>Compression</b>	1.30	1.87	1.33	2.18

Nominal BCL Gage Factor is 2.36, nominal NZ-2104 Gage Factor is 2.60.  
Shaded columns indicate latest test data.

		Watt-sec														
		10	15	20	25	30	35	40	45	50						
<b>F</b>	<b>6</b>	Y3	N	Y1	N	Y3	N	Y3	Y3	N	Y1	N	Y3	N	N	
	<b>8</b>	N	N	Y3	N	Y3	Y3	Y1	Y3	Y3	N	Y1	N	Y3	N	Y3
<b>r</b>	<b>10</b>	Y3	N	Y3	N	Y2	N	Y1	Y3	Y2	Y3	Y2	Y3	Y1	N	Y3
	<b>12</b>	N	N	Y3	N	Y3	N	Y3	Y3	Y1	Y3	Y3	Y3	Y1	Y3	Y3
<b>e</b>	<b>14</b>	N	N	N	N	Y3	N	Y3	N	Y1	N	Y3	Y3	Y1	N	Y3

Left-Hand side of box in matrix: Inconel 600, 2.8 mils/ Uncoated β21S TMC  
 Right-Hand side of box in matrix: Inconel 600, 5.1 mils/ Uncoated β21S TMC

All flanges 1.125" x 0.188"  
 Welder: Measurements Group Model P-28  
 Electrode: RWMMA 2; Tip: .027"

Y1 : Very Good weld - Excellent nugget remained after peel test  
 Y2 : Good weld - Satisfactory nugget remained after peel test  
 Y3 : Good weld - Materials welded, but nugget was unsatisfactory  
 N : Not a good weld - Materials did not weld

## Preliminary Inconel 600/β21S Weld—Schedule Data



## IN600 / B21S Weld Joint Peel Test Results

		Flange Material		
		IN600 (2.8)	IN600 (5.1)	B21S (2.5)
Weld Energy	W-s	25	40	15
Electrode Force	lbs	10	10	10
Average Peeling Force	lbs	5.30	7.74	4.62

## IN600 / B21S Weld-Joint Lap-Shear Test Results

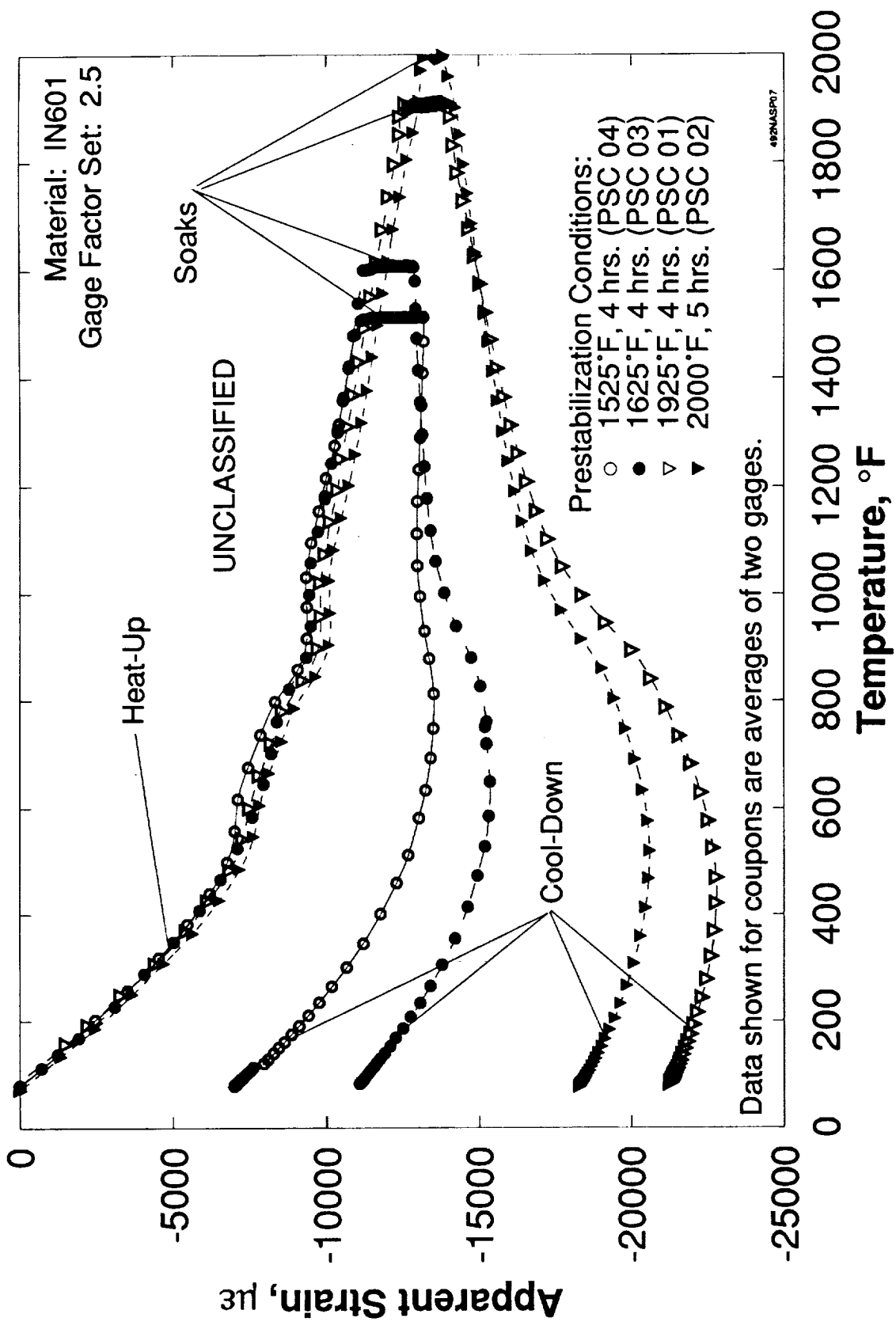
		Flange Material (Thickness, mils)		
		IN600 (2.8)	IN600 (5.1)	B21S (2.5)
Weld Energy	W-s	25	40	15
Electrode Force	lb	10	10	10
Average Breaking Stress	ksi	103.7	94.8	135.9
Average Breaking Strain	$\mu\epsilon$	3344	3057	10650

- NOTES:
- (1) In all cases, the flanges failed before the welds failed.
  - (2) Breaking Strain is calculated using the formula for elastic strain,  

$$\epsilon = \sigma / E$$
 since stress-strain curves beyond the elastic range were unavailable.
  - (3) Numbers after flange material types are thicknesses of flanges.
  - (4) All flanges were spotwelded to a coupon of 65.7 mil thick B21S.
  - (5) All flanges nominally 0.165 in. wide.

Coupon Number	Prestabilization Temperature (°F)	Soak Time (hours)	Test Temperature (°F)
1	2000	5	1900
2	1925	32	1900
3	1925	20	1900
4	1925	8	1900
5	1925	4	1900
6	1525	20	1500
7	1525	8	1500
8	1525	4	1500
9	1225	20	1200
10	1225	8	1200
11	1225	4	1200
12	1625	4	1200
13	1525	4	1200

## BCL Prestabilization Optimization Coupon Testing

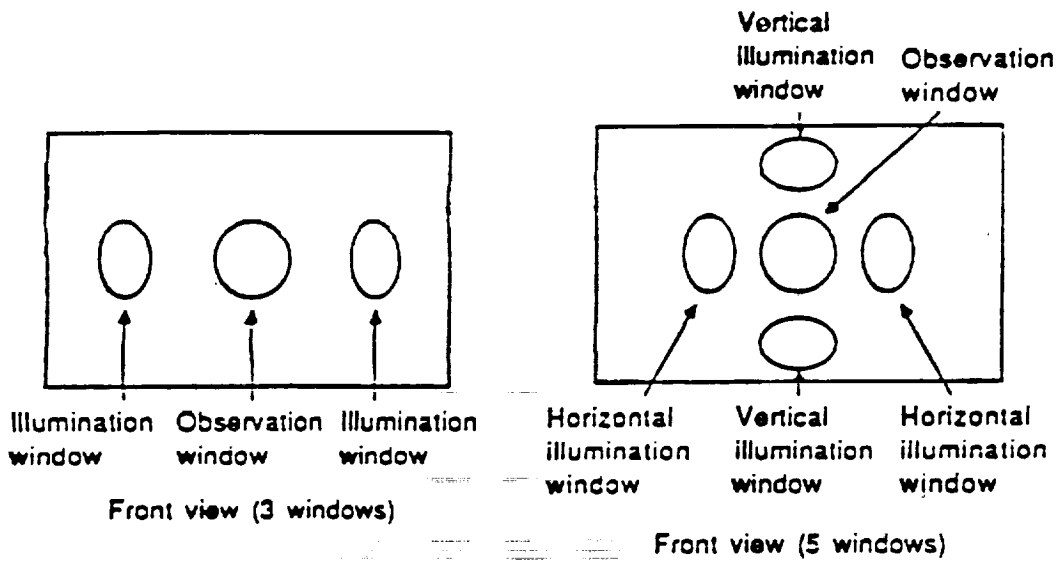
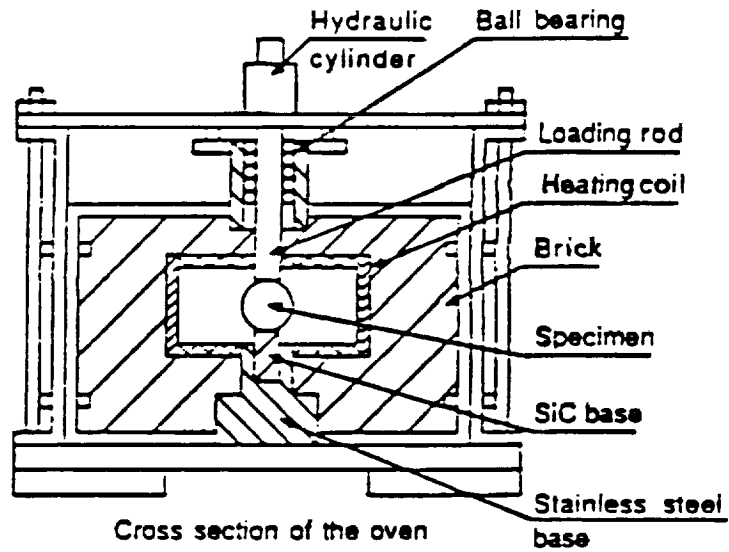


# First Cycle Untreated BCL Gage Apparent Strain During Prestabilization

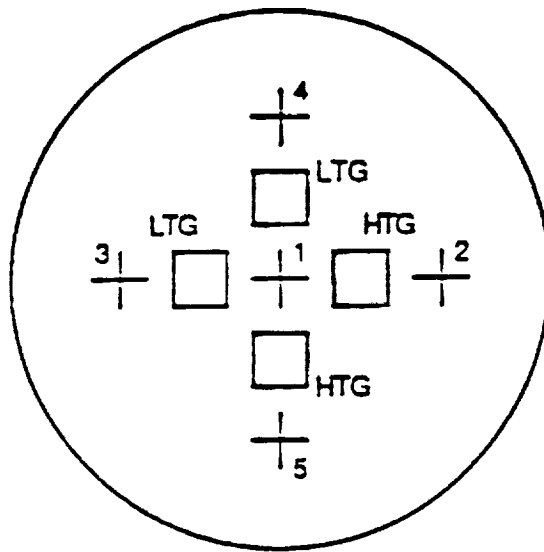
		0-4 hrs.	0 - 20 hrs.	12- 20 hrs.
1525°F	Gage 1	-127.49	-63.65	-34.13
	Gage 2	-111.74	-58.73	-33.55
	Average	-119.62	-61.19	-33.84

		0-4 hrs.	0 - 20 hrs.	10- 20 hrs.
1925°F	Gage 1	-138.58	-71.07	-39.68
	Gage 2	-129.10	-70.05	-41.46
	Average	-133.84	-70.56	-40.57

## First Cycle Untreated BCL Gage Average Drift Rates During Prestabilization



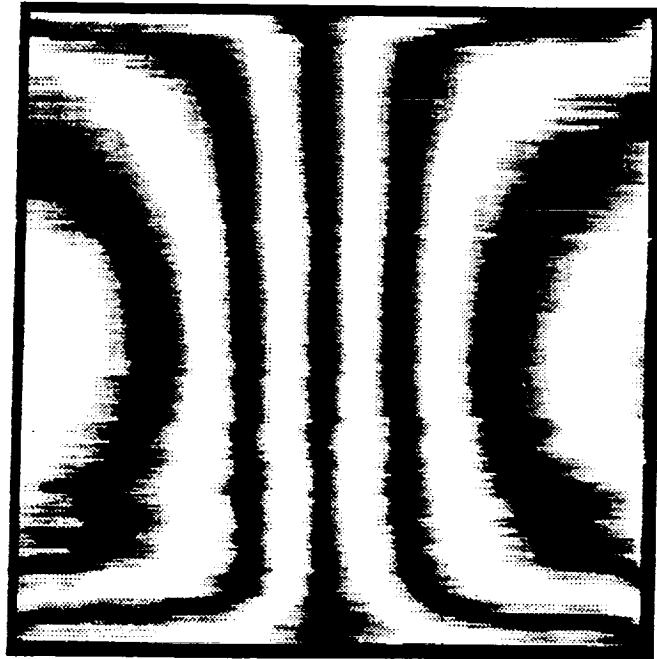
High temperature oven used to test specimens up to 1000°C.



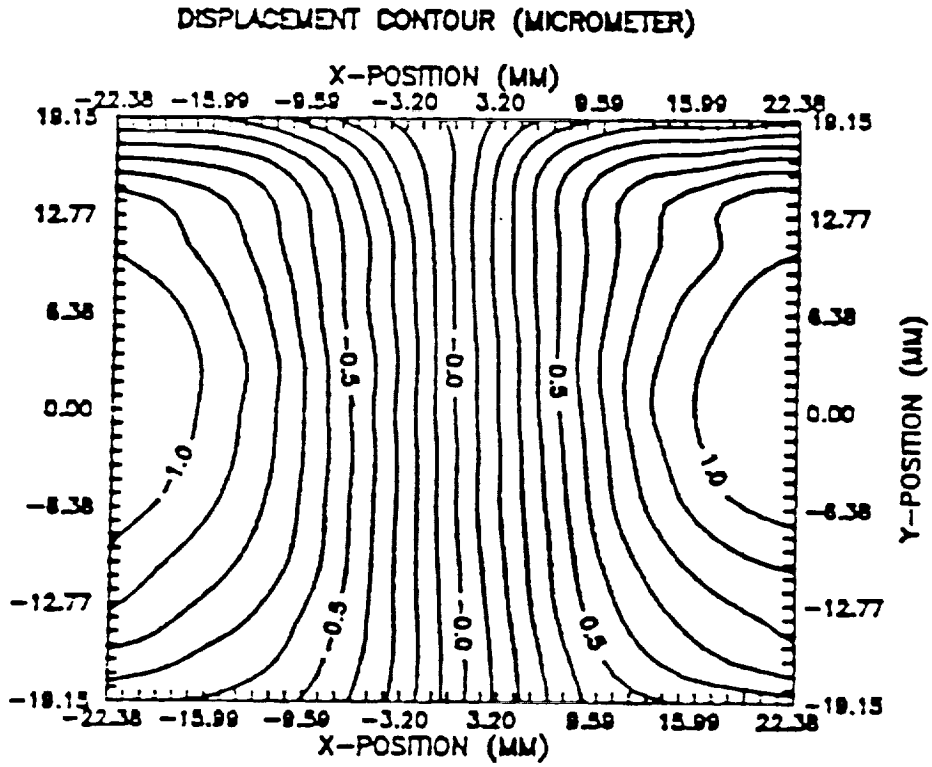
Diameter = 60 mm  
 Thickness = 4.76 mm

LTG - Low temperature gage  
 HTG - High temperature gage  
 1,2,3,4,5 - Thermocouples

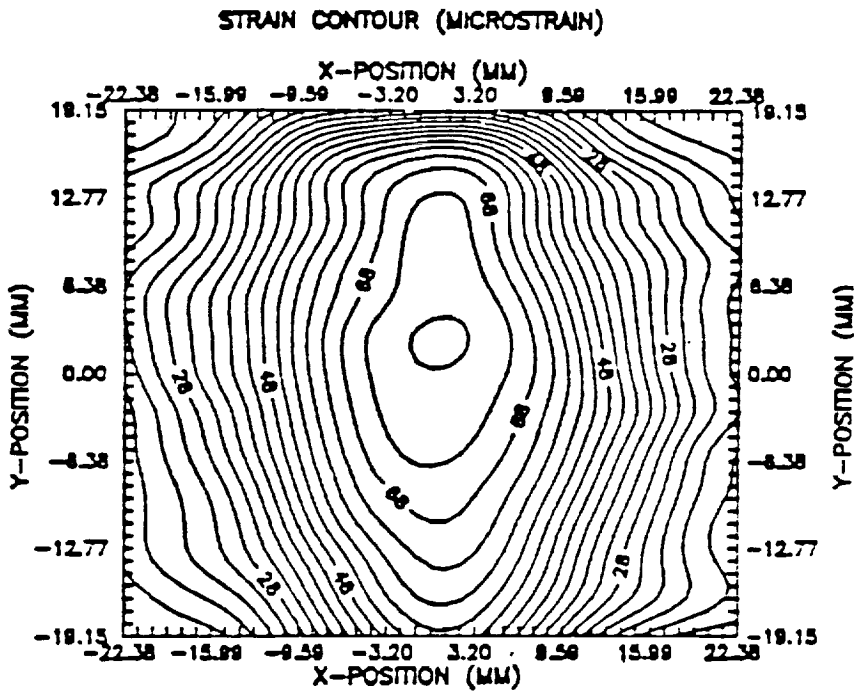
Location of thermocouples and strain gages in the disk specimen



Electro-optical holographic-moire pattern (horizontal displacements) resulting from the phase averaging of 40 patterns recorded at 990°C.

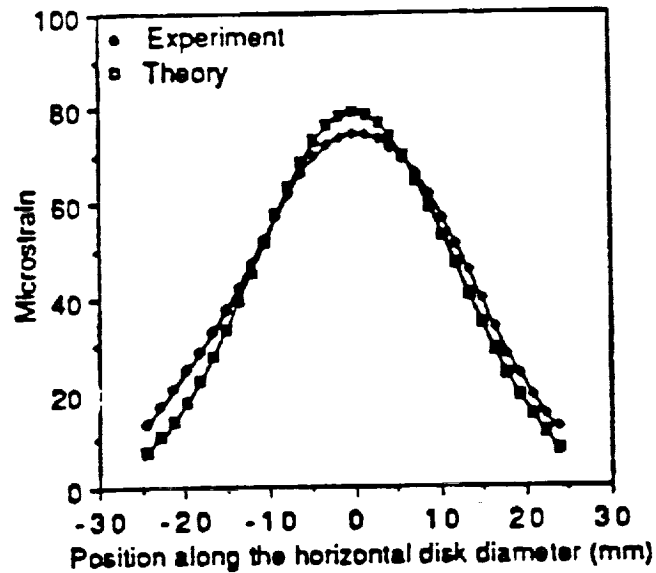


Displacement contours corresponding to the pattern on bottom of page 156.



Strain contours corresponding to the pattern shown on bottom of page 156.

Initial load = 1.744 kN    Elastic Modulus = 186.3 GPa  
 Final load = 5.231 kN    Temperature = 985 C



Comparison of theoretical and experimental results along the horizontal diameter (strains) as shown on bottom of page 157.

### Optical vs. Gage

17.8 KN

### Vertical Illumination and Strains

°C (°F)	Gage #3	Optical	% Difference Gage - Optical
Temp Oven			
23.3 ( 75)	-529 $\mu\epsilon$	-501 $\mu\epsilon$	-5.3%
93.3 (200)	-456 $\mu\epsilon$	-477 $\mu\epsilon$	+4.6%
149 (300)	-496 $\mu\epsilon$	-525 $\mu\epsilon$	+5.7%
205 (400)	-512 $\mu\epsilon$	-487 $\mu\epsilon$	-4.8%
260 (500)	-499 $\mu\epsilon$	-507 $\mu\epsilon$	+1.6%



## Optical vs. Gage

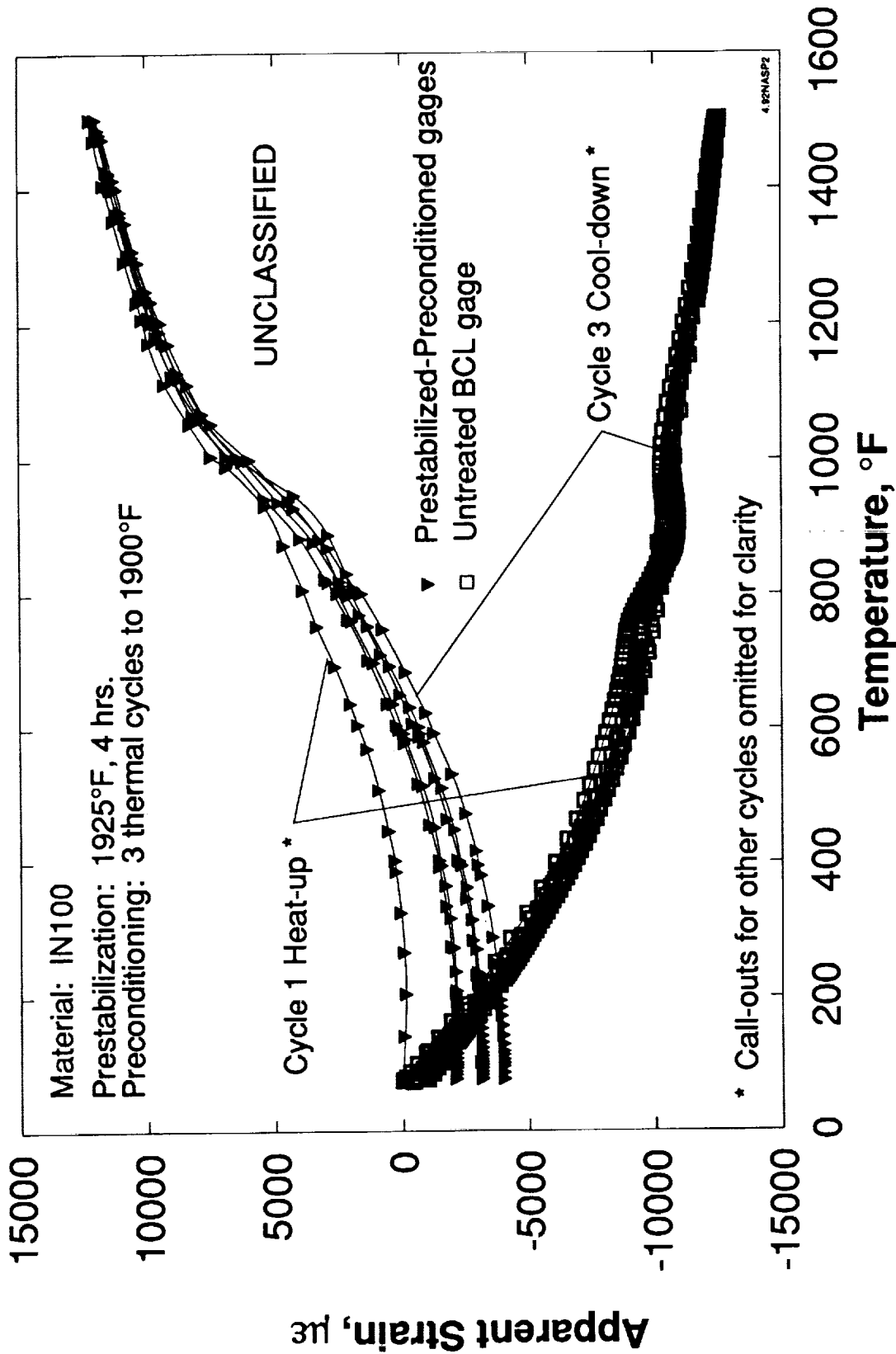
---

20.93 KN  
Horizontal Illumination and Strains

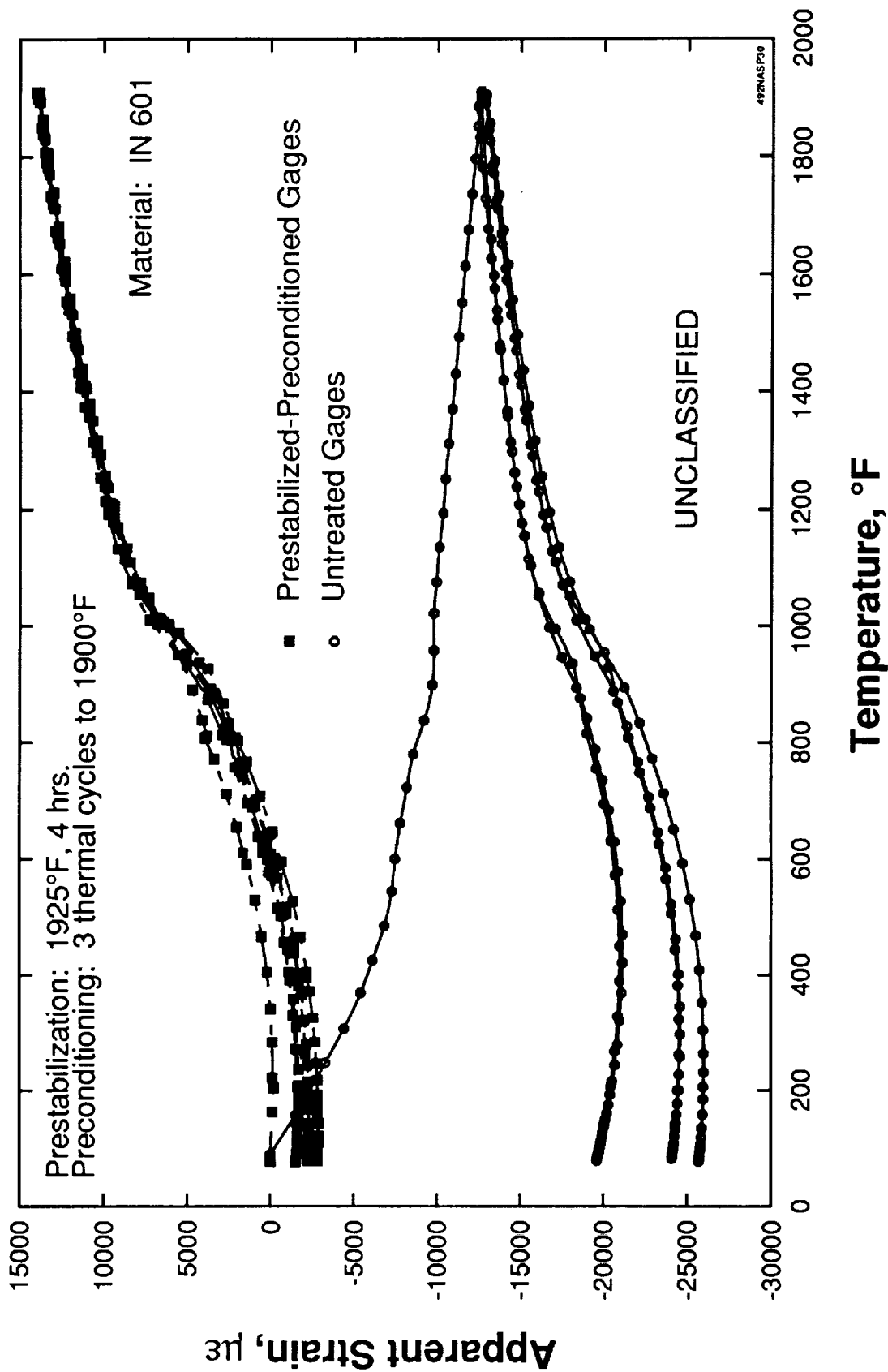
---

°F Temp Oven	Gage #4	Optical	% Difference Gage - Optical
23.3 ( 75)	230 $\mu\epsilon$	243 $\mu\epsilon$	+ 5%
93.3 (200)	212 $\mu\epsilon$	227 $\mu\epsilon$	+ 6%
149 (300)	205 $\mu\epsilon$	221 $\mu\epsilon$	+ 7%
205 (400)	210 $\mu\epsilon$	211 $\mu\epsilon$	+ 0.8%
260 (500)	220 $\mu\epsilon$	216 $\mu\epsilon$	-1.5%

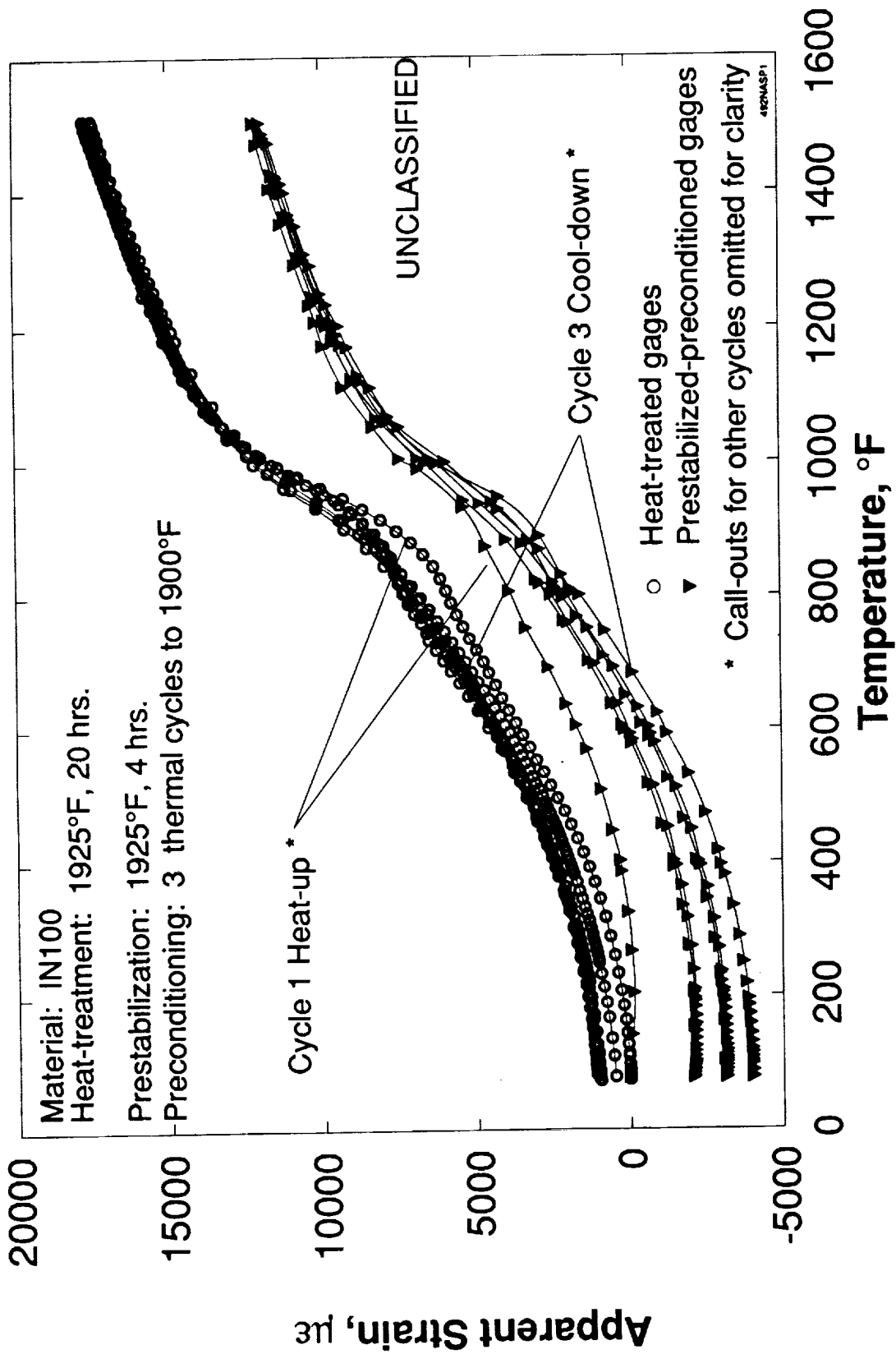
---



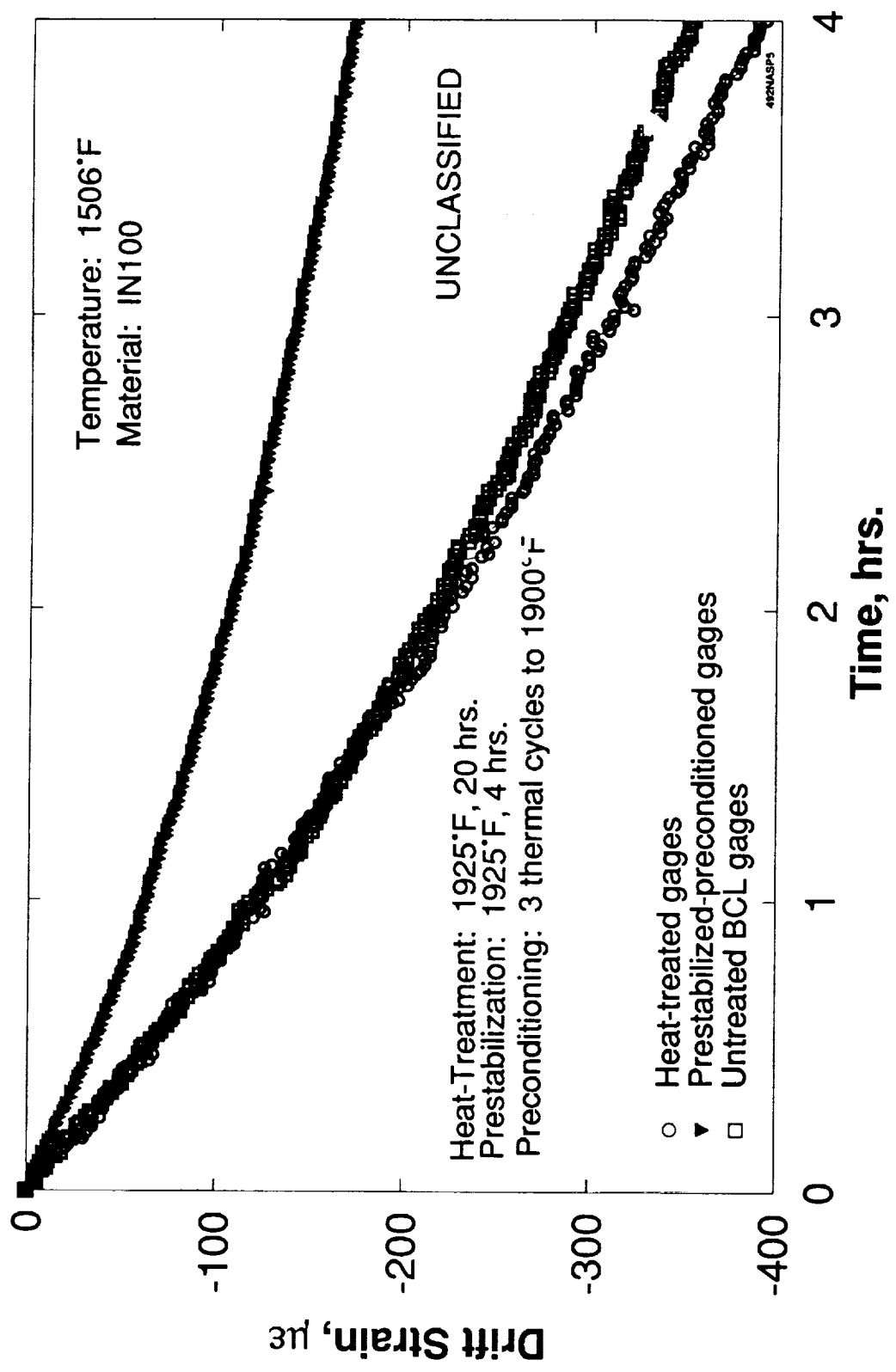
## Apparent Strain of Prestabilized-preconditioned and Untreated BCL Gages



# Comparison of Prestabilized-Preconditioned and Untreated BCL Gage Apparent Strains to 1900°F



# Apparent Strain of Heat-treated and Prestabilized-preconditioned BCL Gages

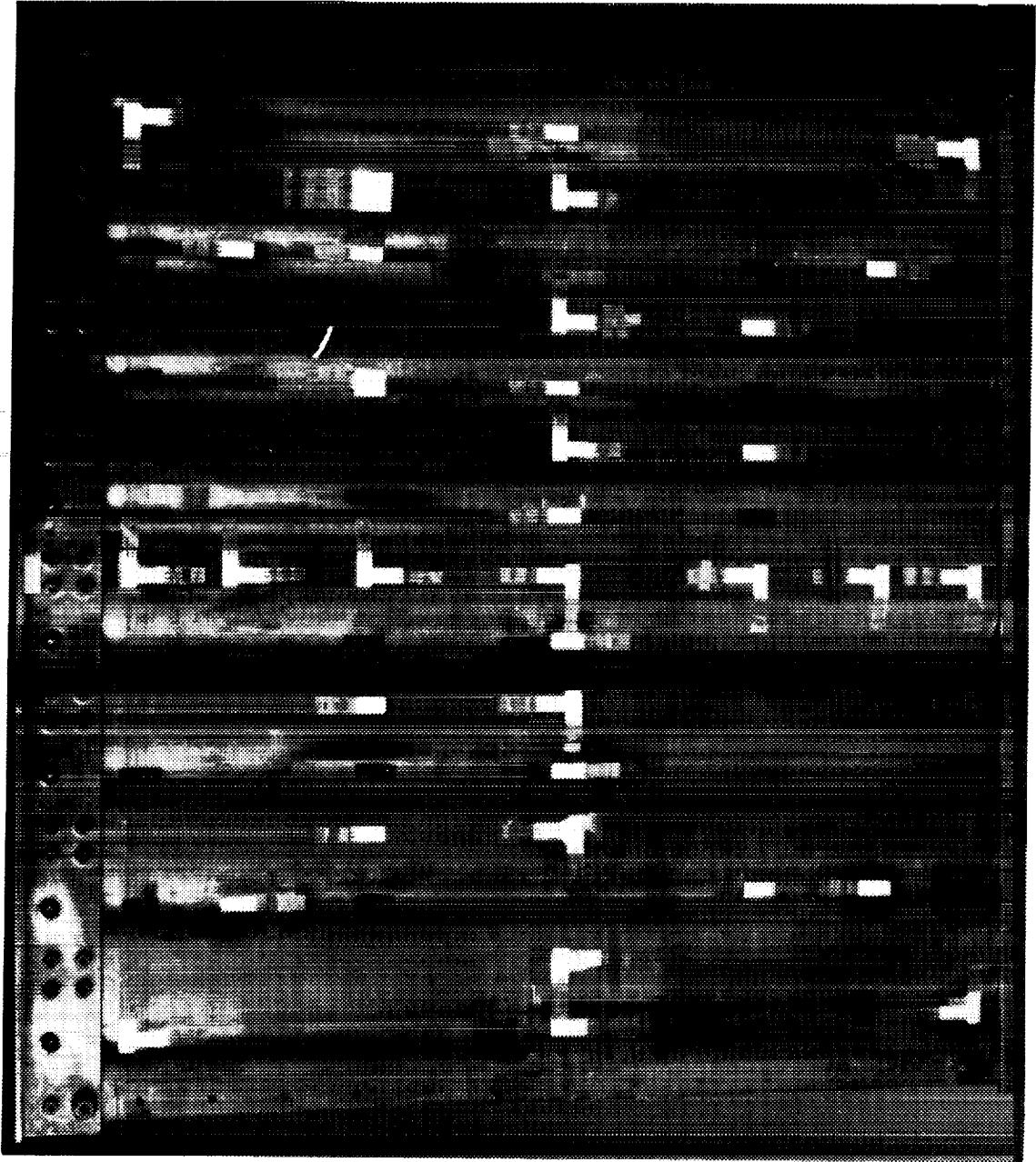


## Drift Strain of Heat-treated, Prestabilized-preconditioned, and Untreated BCL gages

Temperatures, °F	BCL Gage Drift Rates, $\mu\text{E}/\text{hr}$	NZ-2104 Gage Drift Rates, $\mu\text{E}/\text{hr}$
500	25.40	16.33
1050	-26.18	-87.93
1200	-11.63	-80.63
1350	-57.48	-118.13
1500	-148.89	-181.46

Gage Factor Setting was 2.50 for both gage types at all temperatures.  
Values shown are averaged for 1 hour tests.

## Comparison of BCL Gage and NZ-2104 Gage Untreated Gage Drift Rates



**Brazed-Beaded 621S Buckling Panel. Instrumented Skin Side.**

Gage Type	Expected Number of Gages	Maximum Test Temperature
NZ-2104-120L	110	1500 °F
WK-03-250BG-350	57	500 °F
PdCr (Lewis gage)	4	1500 °F
BCL-3	2	1500 °F
Modified Chinese Gage (Tom Moore's 1/2 bridge)	1	1500 °F

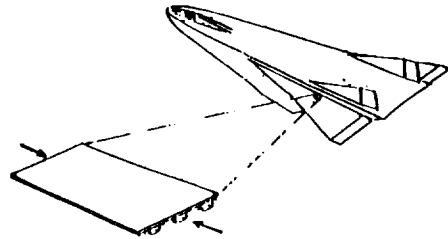
**Gages to be Used on the Brazed, Beaded  
Beta 21S Buckling Panel**



UNCLASSIFIED

## NASP Highly Loaded Stiffeners

- Represents typical mid-plane stiffener and runout region at panel ends

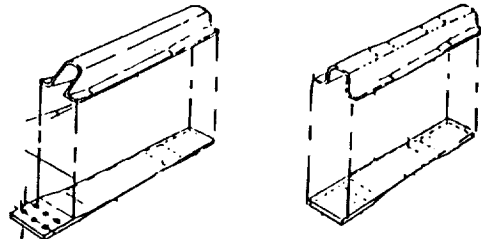


- Test Objectives

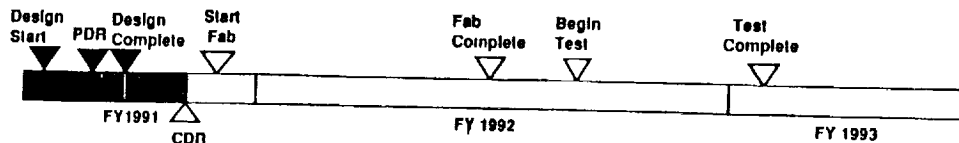
Validate capability of highly loaded, thick ply buildup TMC stiffener attachment and runout through testing of six articles

- Key Requirements

- Design limit loads: 5000 #/in axial compression/tension
- 1500 °F maximum usage temperature
- Thermal-mechanical fatigue



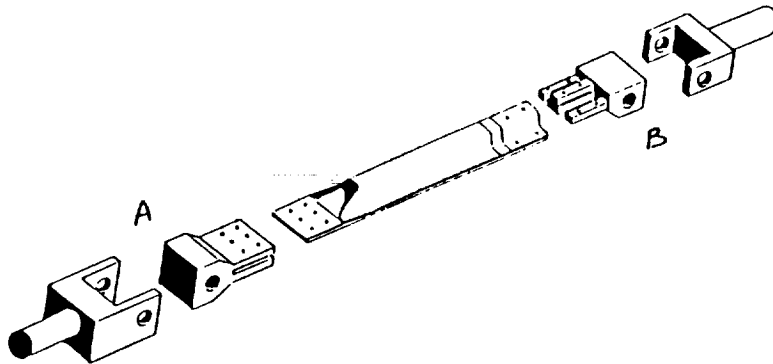
- Major Milestones



## NASP Highly Loaded Stiffeners (U)

### Test Fixture Concept (U)

- (U) Simple supports into uniaxial testing machine
- (U) Radiant quartz lamp heating
- (U) Actively cooled clevises



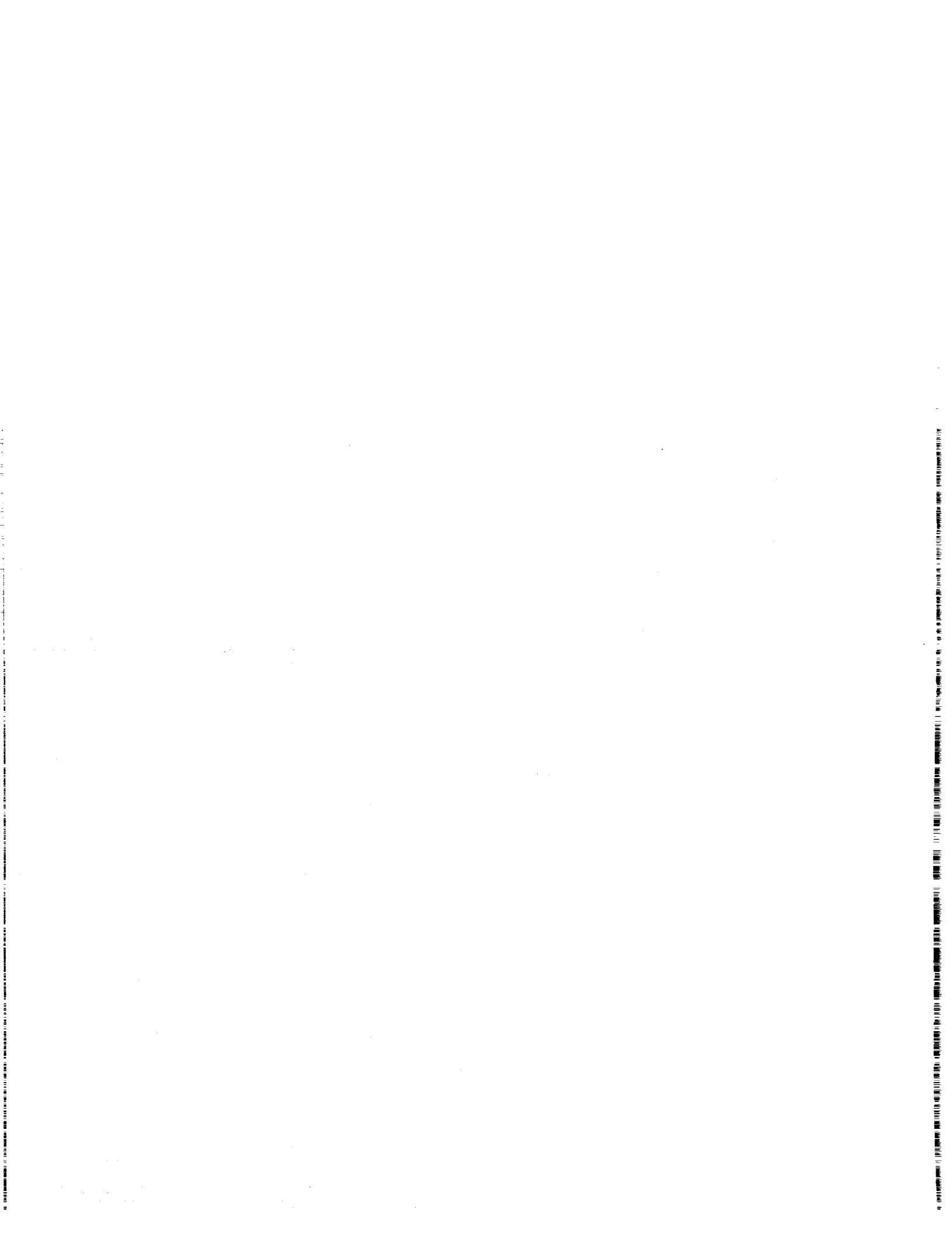
UNCLASSIFIED

## VII. CONCLUDING REMARKS:

BASED ON THE MOST RECENT FINDINGS, IT APPEARS THAT:

- OBTAINING VALID FIRST-CYCLE DATA TO 1500°F MAY BE POSSIBLE, WITH THE BCL GAGE DEPENDING UPON THE OUTCOME OF CHARACTERIZATION STUDIES AND DEVELOPMENTAL ACTIVITIES NOW IN PROGRESS
- FOR STRAIN MEASUREMENTS WITH THE BCL GAGE ABOVE ABOUT 1500°F, PRESTABILIZATION AND PRECONDITIONING WILL BE REQUIRED, UNLESS THE APPARENT STRAIN OR DRIFT IS SUFFICIENTLY SUPPRESSED VIA HEAT-TREATMENT, USE OF TEMPERATURE-COMPENSATED GAGES, OR A REMOTE DUMMY GAGE SYSTEM.
- FOR STRAIN MEASUREMENTS ABOVE 1900°F, IT APPEARS THAT ONLY THE ELECTRO-OPTICAL METHODS HAVE THE POTENTIAL CAPABILITY. HOWEVER, BEFORE THESE METHODS ARE VIABLE FOR GROUND OR FLIGHT TESTING, MORE DEVELOPMENT AND VALIDATION WORK - OFF THE OPTICAL BENCH - NEEDS TO BE DONE UNDER REALISTIC FIELD CONDITIONS, AND ON MATERIALS OF INTEREST TO THE NASP AND OTHER PROGRAMS.
- IT MAY BE POSSIBLE TO PRESTABILIZE, PRECONDITION, OR PRECALIBRATE SHIM-MOUNTED OR WELDABLE TYPE GAGES PRIOR TO INSTALLATION ON THE TEST ARTICLE OR SPECIMEN - SATISFYING THE PRESENT NASP REQUIREMENT THAT NO PRESTABILIZATION BE DONE ON THE TEST ARTICLE.

- **HEAT-TREATED GAGES OR PRESTABILIZED AND PRECONDITIONED SHIM-MOUNTED GAGES, OR TEMPERATURE-COMPENSATED GAGES (DUAL-ELEMENT OR FLOATING DUMMY), OR REMOTE DUMMY GAGE SYSTEMS OFFER A VARIETY OF CHOICES OR COMBINATIONS FOR EFFECTIVE SUPPRESSION OF APPARENT STRAIN. USE OF THE REMOTE DUMMY GAGE SYSTEM OR FLOATING DUMMY GAGE SHOULD ALSO SUPPRESS DRIFT STRAIN.**



# SKIN FRICTION MEASUREMENTS IN HIGH TEMPERATURE HIGH SPEED FLOWS

J. A. Schetz  
Department of Aerospace and Ocean Engineering

T. E. Diller and A. L. Wicks  
Mechanical Engineering Department

Virginia Polytechnic Institute and State University  
Blacksburg, VA 24061

## SUMMARY

An experimental investigation was conducted to measure skin friction along the chamber walls of supersonic combustors. A direct force measurement device was used to simultaneously measure an axial and transverse component of the small tangential shear force passing over a non-intrusive floating element. The floating head is mounted to a stiff cantilever beam arrangement with deflection due to the flow on the order of 0.00254 mm (0.0001 in.). This allowed the instrument to be a non-nulling type. A second gauge was designed with active cooling of the floating sensor head to eliminate non-uniform temperature effects between the sensor head and the surrounding wall. Samples of measurements made in combustor test facilities at NASA Langley Research Center and at the General Applied Science Laboratory (GASL) are presented. Skin friction coefficients between 0.001 - 0.005 were measured dependent on the facility and measurement location. Analysis of the measurement uncertainties indicate an accuracy to within  $\pm 10-15\%$  of the streamwise component.

## NOMENCLATURE

$C_f$	=	skin friction coefficient
$D$	=	diameter of floating head
$G$	=	gap around floating head
$L$	=	lip thickness of head
$P_t$	=	total pressure
$q$	=	dynamic pressure
$T_t$	=	total temperature

$\tau_w$  = wall shear force  
 $\rho$  = density  
 $V$  = velocity

Subscripts:

x = streamwise component  
z = transverse component

## INTRODUCTION

Knowledge of drag resulting from skin friction is important for numerous engineering applications. Before a complete understanding of many flow fields both internal and external can be obtained, an accurate calculation or measurement of skin friction is required. In many combustor testing programs, accurate measurement of skin friction is necessary to correctly determine combustion efficiency. In addition, relatively small amounts of skin friction can seriously limit the available thrust from a scramjet combustor.

The current techniques employed in the measurement of skin friction fit into two general categories, those being either an indirect or direct method. Indirect methods involve measurement of the velocity gradient or heat transfer at the combustor wall. Reference [1] contains a review of many of the strategies adopted in these methods. Uncertainties with these methods can be quite large, especially in a compressible 3-D turbulent boundary layer, because a mathematical model or Reynolds analogy type relation is required to deduce the skin friction. For these reasons and considering that the flow types of interest in these studies are high heat flux and combusting, a direct shear force measurement technique was adopted. Reference [2] presents some limited measurements in a scramjet at the Applied Physics Laboratory. DeTurris, Schetz, and Hellbaum [3] present skin friction measurements in scramjet combustors from several test programs.

A direct force measurement device is a relatively straight forward concept, but when applied to the severe testing environment of a supersonic combustor boundary layer, it can quickly become a difficult and complex engineering problem. A gauge design has been developed for, but not limited to, measurement of skin friction in supersonic combustion boundary layers. This design is comparable, although somewhat improved, to the design of Ref. [3]. Also, in an attempt to further optimize these gauge designs, a technique was developed to thermally match the gauge sensor head to the surrounding combustor wall by internal cooling. These gauges are capable of measuring shear stress in both axial and transverse directions to the flow path, and have been tested in both heated and unheated supersonic flows.

The basic configuration of the skin friction gauges consists of a cantilevered floating element. A history of early direct measurement designs which includes floating element designs is presented by Winter [4]. Skin friction balances that have been developed for supersonic flows

include the efforts of Roensch and Cadwell [5], Allen [6,7], and Voisinet [8]. The balances of these studies were primarily subject to supersonic flows with only moderate total temperatures.

The frictional forces that are a result of the supersonic combusting flow passing tangent to the combustion chamber walls are small in magnitude. However, since the shearing force is being measured over only a small area, it is necessary for the skin friction gauge to be very sensitive. The present designs have the ability to measure forces from a fraction of a gram to over ten grams accurately. The first of the two designs uses a deflection sensing device that was first used by Schetz and Nerney [2] and recently by DeTurrís et al. [3]. This device employs piezoresistive crystal strain gages. This type of strain gage is exceedingly sensitive with gage factors in the area of 150, which is comparative to a gage factor of near 2 for common foil strain gages. This kind of sensitivity enabled the adoption of a non-nulling type design. Several benefits are obtained with a non-nulling design over a self-nulling design. First, the non-nulling design is less complex in that it does not require a series of mechanical linkages which can introduce substantial error in the measurement. Second, the time response of the non-nulling device is superior to that of the nulling device. Since the piezoresistive strain gages have a high gage factor, the cantilevered floating element of the current designs undergo extremely small deflections during a measurement. This renders insignificant any misalignment effects that could cause an errant measurement. One difficulty that is introduced by these crystal strain gages is that they are sensitive to temperature. An active cooling system near the gages was developed to minimize any error introduced by temperature gradients in the strain sensing elements.

Matching the sensing element thermally to the facility is critical to making an accurate skin friction measurement. The gauges have been designed to exactly match the tunnel wall thickness, materials and cooling pattern. This minimizes interference of the gauge with the rest of the wall so that the shear measurement represents the general wall conditions as opposed to only the local conditions proximate to the sensing head. It was determined that a temperature mismatch between the actual floating head of the skin friction gauge and the surrounding wall of the combustion chamber can introduce significant error in the shearing force measurement. An optimized design has been developed that actively cools the floating head of the instrument and retains the benefits of the uncooled head design. This design is needed specifically for high heat flux cases. Because of the importance of the wall heat flux and temperature conditions for proper skin friction measurements, the possibility of making simultaneous measurements of all three quantities has been investigated. This is also useful for considering the application of a Reynolds analogy to these severe flow conditions. A discussion of a thin film heat flux gage is reported in an accompanying paper [9]. This is also a direct reading gage capable of operating at comparable conditions. Future work could incorporate these two sensors into a single gauge.

## DESCRIPTION OF GAUGES

A schematic of the skin friction gauge design which employs the displacement sensitive transducer is shown in Fig. 1. The floating head of this instrument is mounted on a cantilevered

tube which is fit onto the sensing arm of the displacement sensor. The displacement sensor is a commercially available Deflection Sensor Cartridge (DSC) capable of sensing deflection in two orthogonal axes simultaneously. Encapsulated into the DSC are piezoresistive strain gages making it sensitive to very small deflections. Output from the sensor is enhanced by arranging the strain gages into a half Wheatstone bridge. One gage is in tension and one in compression for each axis. Output resolution is also increased by the extension of the effective moment arm on the DSC by the cantilevered tube. Heat transfer through the instrument is a primary concern since the strain gages are temperature sensitive. The outer housing is cooled by a continuous water cooling channel and, in addition, the cantilevered beam surface area is increased with fins. Also, the entire DSC-beam-floating head assembly is immersed in a silicon based heat transfer fluid.

The facilities that these instruments are designed to operate in are inherently crowded on the exterior. This necessitates three basic configuration requirements. First, the gauge must be small. The current gauges in use are all about three inches in length and a half an inch in diameter. Second, the instrument may be required to be mounted in any orientation dependent on the desired measurement location. Due to the presence of the internal heat transfer fluid these gauges operate best when the floating head is oriented either up or on its side with respect to the duct, although inverted operation is possible. Third, these instruments must be rugged. The delicate components of these sensors are enclosed in a metal housing which protects them from ordinary activity around the testing facilities. The strain gages are protected from thermal damage by the cooling system and the DSC cannot be over stressed since the maximum amount the floating head can move is the width of the gap between it and the housing which is far below the maximum allowable deflection for the sensor.

It is possible to introduce misalignment effects due to the tilting of the floating head in a non-nulling type gauge. This effect has become insignificant because of the sensitivity of the piezoresistive strain gages. The gauge is designed with a very stiff beam that will result in only small deflections of the sensing head, but the sensitivity of the DSC is more than adequate to accurately detect the small deflection. The expected maximum deflection of the sensing head is 0.00025 cm (0.0001 in.) which translates into a protrusion of four micro inches into the flow. By itself, this small protrusion should be insignificant, but the floating head geometry is designed to eliminate this type of misalignment effect as well.

Floating head misalignment effects are always a concern with these types of instruments. Allen [6] did a systematic study to identify and minimize these effects by considering specific geometric attributes of the floating head. Those studied were the effects of gap size, lip size, misalignment with the surface by either protrusion or recession, and pressure gradient effects between the top and underside of the floating element. The results of this study were referred to extensively in the design of the current sensor heads. The head for these gauges has a diameter of 0.615 cm (0.242 in.) before tapering to a 0.462 cm (0.182 in.) diameter leaving a thin lip at the flow surface. These dimensions were chosen to minimize the effects of the 0.01 cm (0.004 in.) gap between the head and the surrounding housing. The head also has a small lip at the lower end leaving a 0.0153 cm (0.006 in.) gap between it and the housing.



Allen [6] found that there was no advantage to having as small a gap size as possible. In fact, a skin friction balance is less sensitive to protrusion error with a large gap size. For the DSC gauge design, the gap to diameter ratio ( $G/D$ ) is 0.0165 which is considerably larger than the lower limit suggested by Allen of 0.005. Effects due to the size of the floating head lip must also be considered. Again, Ref. [6] was consulted to choose a lip to diameter ratio ( $L/D$ ) of 0.04. The gap to diameter ratio taken with this lip to diameter ratio combine to produce a design unaffected by gap size and lip protrusion effects.

The heat transfer fluid contained in the cavity serves several purposes. It not only provides thermal protection for the piezoresistive strain elements, but also aids in eliminating the effects due to a possible pressure gradient acting on the top surface of the floating head [3]. Moreover, the fluid produces strong damping to limit errors introduced by facility vibrations and cantilever beam oscillations.

### **Design for NASA Langley Vitiated Air Tunnel**

An assembly drawing for the NASA Langley gauge is shown in Fig. 2. This gauge is similar to that for the same facility in the study of Ref. [3], except that a cooling channel has been added to the top of the outer housing in the area that fits inside of the chamber wall. The outer housing and floating head are constructed of carbon steel to match the tunnel chamber walls. Temperature of the DSC is monitored by a type K thermocouple mounted adjacent to the DSC in the heat transfer fluid. The heat transfer fluid consists of a silicon based oil (1000 centistoke viscosity) which is filled through a small access hole on the side of the outer housing.

### **Design for the GASL Test Series**

An assembly drawing for the DSC based gauge for the first tests conducted at the General Applied Science Laboratory is depicted in Fig. 3. This gauge is constructed of copper to match the chamber walls of the GASL facility. The tunnel walls for this test are 4.76 cm (1.875 in.) thick, therefore the sensor head of the balance was lengthened to 2.54 cm (1.0 in.) to aid in transferring heat from the gauge. The temperature of the DSC was monitored by a thermocouple inserted through an access hole in the housing near the unit. A dummy balance was constructed for these tests which contained a copper/constantan thermocouple on the surface of the sensor head. This dummy balance and the skin friction balance were mounted in an oblong plug which bolted into the tunnel wall. Also, the plug in which both gauges were mounted was fitted with another copper/constantan thermocouple on its surface to measure chamber wall temperature. This complete package enabled the measurement of two skin friction components, sensor head temperature, and combustion chamber wall temperature.

The balance used for the second series of tests at GASL is essentially the equivalent of the one for the first test series with a few exceptions. For this second test series, a balance similar to that of Fig. 3 was inserted into a housing consisting of a circular 1.27 cm (0.5 in.) diameter, 4.76 cm (1.875 in.) long plug with a flange for a bolt circle to secure the unit into the chamber wall. Also, the DSC cooling system pressure was increased to approximately 350 psi (1035 kPa).

### Cooled Sensor Head Design

The basic gauge configuration is shown in Fig 4. The gauge is a non-nulling type similar to the previously discussed designs. The shear sensing head is supported by a quartz cantilevered tube with an outside diameter of 0.062 cm (0.238 in.) and an inside diameter of 0.40 cm (0.157 in.). However, instead of using the Displacement Sensitive Cartridge to measure the sensor head deflection, piezoresistive semiconductor strain gages are mounted directly to the cantilevered quartz tube. At the location of the strain gages, the tube is machined square with an abrasive diamond wheel cutter to provide a secure smooth base to mount the strain gages and insure orthogonality of the measurement axes. This geometry was found effective in providing enough mass flow of cooling fluid to the sensor head and adequate resolution from the strain sensing elements. The sensor head is mounted to the tube which is then mounted into the base with a ceramic-like high temperature cement. This cement has the ability to withstand temperatures up to 2500°F (1650 K) and has a tensile strength of 425 psi (2929 kPa).

The strain gages are piezoresistive semiconductor type gages. These gages provide several advantages over conventional foil gages including higher sensitivity, resistance, and fatigue life, as well as small size. Kulite 750 ohm semiconductor strain gages are used in this instrument. These are ruggedized gages encapsulated into an epoxy/glass matrix with large solder tab terminals. Overall dimensions of each gage are 0.11 cm (0.28 in.) by 0.06 cm (0.14 in.). Four gages are mounted to the quartz cantilevered beam with a thin layer of a high temperature strain gage cement and coated with several layers of both polyurethane and an acrylic for protection from the environment. The gages are arranged in a half Wheatstone bridge, one gage in tension and one in compression for each axis of measurement while the sensor head is displaced. This provides compensation for any axially imposed strain which may arise from an axial force on the sensor head. Bridge completion is accomplished externally with precision resistors and a potentiometer for pretest output balance. The strain gages are powered by a +5 volt regulated DC power supply.

A flow pattern for sensor head cooling is developed through a co-axial tube arrangement. A stainless steel 0.160 cm (0.063 in.) tube is mounted along the centerline of the instrument to provide an inflow passage for the cooling fluid to the back side of the sensor head. Heat transfer calculations were made with a finite element code to determine the optimum thickness of the sensor head. In this calculation the sensor head thickness was varied to determine the thickness that would closely match the sensor head temperature with the surrounding combustion chamber wall. A heat flux that is expected from a scramjet combustor and a convection coefficient which is obtainable with water as the cooling fluid were prescribed as boundary conditions. A sensor head

thickness of 0.083 cm (0.0325 in.) was found to be effective (see Fig. 5). The cooling fluid is exhausted from the instrument by flowing back along the outside of the stainless steel tube and inside of the quartz tube. At the base of the quartz beam the exiting liquid passes through a manifold and out through a 0.317 cm (0.125 in.) copper line. A variable convection coefficient at the sensor head is obtainable by regulating the pressure of the incoming cooling liquid. Tests were conducted, and it was determined that the sensor head cooling system is able to withstand pressures up to 500 psi (3450 kPa). Bench tests showed that the flowing water did not influence the tangential force measurement.

The gage is enclosed by an outer housing constructed of copper as is the floating element sensor head and the cantilever beam base. The gauge is mounted into the test facility with screws through a flange on the outer housing. As with all of the previously discussed designs, the cavity between the beam and the housing is filled with a silicon based heat transfer fluid, primarily in this case for vibration damping and pressure gradient effect minimization. A calculation was performed to estimate the natural frequency of the instrument and was found to be 1.5 kHz. Overall length of the gauge is 8.89 cm (3.5 in.). The sensor head was designed in a similar manner as the previous designs with a slightly larger diameter 0.812 cm (.320 in.) and a 0.013 cm (0.005 in.) gap. Lip size was set at 0.051 cm (0.020 in.).

## EXPERIMENTAL PROCEDURES

Each measurement axis of the DSC forms half of a Wheatstone bridge; the crystal strain gages have a nominal resistance of 1000 ohms. Bridge completion is external to the instrument with 1000 ohm precision resistors and a 500 ohm potentiometer for pre-test output balancing. The DSC is powered by a +6 volt DC power supply. For the most part, data is recorded with a two channel strip chart recorder. At the NASA Langley and GASL tests data were also recorded with a PC-AT based 12 bit, 16 channel A/D card with one multiplexed channel equipped with an electronic ice point to record up to 16 thermocouple inputs. During the second set of tests at GASL, data were also recorded on GASL hardware at a 4 Hz acquisition rate.

### Calibration

The DSC gauge and the cooled-head gauge are calibrated by applying a force in the axis of measurement and recording the output voltage from the wheatstone bridge. A digital voltmeter was used to record a series of data points, and a least squares linear regression was performed on the data yielding a linear calibration curve. In order to apply the force directly to the measurement axis, the gauge is clamped vertical and weight standards are hung by a thin line from the sensor head. This enables the application of the force to be "on-axis," although a slight amount of output is registered by the transverse axis. This transverse output is due to a small tolerance on the orthogonality of the transducer axes. The magnitude of this transverse sensitivity output is less than

5% of the axial output and is accounted for in the data reduction. Figure 6 contains a sample calibration for this type of instrument.

### NASA Langley Scramjet Test Facility

Tests were conducted at the NASA Langley Vitiated Air Test Facility. Vitiated air was expanded to Mach 3.0, and fuel was injected through a perpendicular scheme. Skin friction measurements were recorded near the rear and on the centerline of a 2 degree, 122 cm (48 in.) long diverging duct located just downstream of the fuel injector. Cooling water was supplied at 500 psi (3450 kPa) with nominal tunnel test conditions of  $T = 3000 \text{ R}$  (1667 K) and  $P_t = 500 \text{ psia}$  (3450 kPa).

### GASL Facility and Test Procedures

Tests were conducted at the General Applied Science Laboratory in two separate test series. DSC based gauges were used to measure skin friction in both test series. Some results were obtained with the cooled head skin friction gauge during the last test series. Measurements were acquired in a scramjet combustor model in both the constant area and diverging sections. Nominal combustor entrance conditions include  $M = 3.3$ ,  $T_t = 4000 \text{ R}$  (2222 K), and  $P_t = 800 \text{ psia}$  (5510 kPa). The heat flux in the combustor was estimated at 400 BTU/ft<sup>2</sup>/sec.

## EXPERIMENTAL RESULTS

A small sample of results are presented here, although many test runs were conducted with the DSC based gauge in all of the test facilities. The gauges proved to be reliable over extended periods of operation. Frequency response of these gauges is more than adequate to capture the frequently changing conditions exhibited by the combustors including start and finish of a fuel cycle.

A skin friction coefficient was calculated for all of the tests presented here. The skin friction gauge measures the tangential force due to the flow over the sensor head, which is related to the wall shear,  $\tau_w$ , by the flow wetted area of the sensor head. A skin friction coefficient can be readily calculated by

$$C_f = \frac{\tau_w}{q} \quad (1)$$

where  $q$  is the dynamic head of the flow given as

$$q = \frac{1}{2}\rho V^2 \quad (2)$$

Table 1 summarizes the results obtained with the DSC based gauge from some of the tests. The values of  $q$  used to calculate the skin friction coefficients for the GASL tests are based on flow conditions at the combustor entrance.

A sample result of the output from the NASA Langley tests is depicted in Fig. 7. A streamwise skin friction coefficient ( $C_f = 0.0042$ ) was calculated from an average of the gauge output between 12 and 15 seconds. The transverse or cross-stream measurement is shown to be small compared to that of the streamwise component suggesting a near 2-D flow field at the measurement position.

Figure 8 illustrates both the streamwise and cross-stream wall shear measured for GASL Test Run 112. The friction gauge was located in the side wall of the constant area section of the combustion chamber downstream of a rearward-facing step. An average value of the wall shear at a point with steady fuel conditions was used to calculate a skin friction coefficient. The interval over which the average was taken is indicated on the plot between the vertical dashed lines. For Test 112,  $\tau_w = .11 \text{ lbf/in}^2$  ( $760 \text{ N/m}^2$ ) in the streamwise direction and  $\tau_w = 0.043 \text{ lbf/in}^2$  ( $295 \text{ N/m}^2$ ) for the cross stream component. The streamwise and cross-stream skin friction are listed in Table 1. Shear and friction coefficient values are listed in Table 1, as well. During Test 112, the temperature of the sensor head was recorded as well as the temperature of the combustion chamber wall adjacent to the sensor head (Fig. 9). A temperature difference of up to 400 R (222 K) was obtained during these and other test runs. Considering this temperature discrepancy and its possible effects on the accuracy of the skin friction measurements was a leading factor for designing the cooled head skin friction gauge.

Figure 10 presents data measured for different fuel conditions where the fuel equivalence ratio was ramped from 0.5 to 0.8. These skin friction measurements are based on a combustor inlet reference dynamic pressure. The test runs are representative of data recorded in the constant area section of the combustor. Relatively high values of skin friction are reported for these test cases in the streamwise direction (see Table 1). Cross-stream components for this location can be as much as 35% of the streamwise values.

### Cooled Head Skin Friction Gauge Results

A first test for this type of skin friction gauge was conducted in a cold Mach 3.0 supersonic flow. Output from this test is shown in Fig. 11. This result indicates that the gauge has an excellent time response, apparent by its following of the start of the supersonic tunnel on the left of the figure and unstart of the tunnel on the right of the figure. Output reached a steady constant value which translates into a skin friction of  $C_f = 0.0015$ . A calculation of the skin friction

coefficient based on the boundary layer height measured from a nanoshadowgraph of the measurement position indicates a skin friction coefficient of  $C_f = 0.0014$ .

The gauge was installed into the constant area section of the combustion chamber of the last GASL test series to make a skin friction measurement. Some limited success was achieved. Figure 12 illustrates the output for the streamwise direction of Test 602. An average was taken over the range during which fuel was being injected and a skin friction coefficient was calculated to be  $C_f = 0.0023$ . Table 2 contains the results from this test run as well as Test 601.

## MEASUREMENT UNCERTAINTIES

The largest source of error is due to heating of the DSC or in the case of the cooled head gauge of the strain gages themselves. The manufacturer of the DSC specifies the temperature sensitivity to be 0.02 percent of full scale. Presently the gauge operates at about 2 to 3 percent of full scale, which would magnify this temperature error potential. This results in a requirement of keeping the DSC temperature to  $\pm 2^\circ\text{C}$ . The cooling system integrated into the DSC design has been able to keep the DSC to  $\pm 1^\circ\text{C}$ , which results in an uncertainty less than  $\pm 2\%$ .

Further uncertainties can be due to asymmetric heating of the crystal strain gauges. A zero shift is the result of a temperature change of these elements. If the temperature change is symmetric then the output can be corrected with the known temperature sensitivity. If heating is asymmetric correction is not possible. For the DSC based gauge this error is virtually eliminated by the active cooling system around the housing. In the case of the cooled head gauge this type of system is not as effective. In the future, tests are planned with spray cooling on the outer housing that should reduce these errors.

Pressure gradients in the combustion chamber can result in a moment on the sensing head. Pressure drop in the duct at NASA Langley is approximately 1.5 psi/ft (34 kPa/m). This results in a negligible moment on the balance. Pressure gradients in all tests are assumed small.

Many of the measurement uncertainties with these instruments result in negligible effects. Overall uncertainty is based on the effects of the misalignment, possible zero shift, and calibration concerns. This results in an overall uncertainty of 10-15%.

## CONCLUSIONS

Results of these experiments confirm the validity of a floating element, non-nulling, cantilever skin friction balance design. Accurate measurements were obtained in very high heat flux supersonic environments. Measurements were improved over those previously reported by active cooling of the DSC with continuous high pressure water channels surrounding the balance.

Dual axes measurements indicate nearly 2-D flows in the NASA Langley facility and in the constant area section of the combustor during the early test series at GASL. Results from the later test series at GASL show transverse shear to be up to 90% of the streamwise value in the diverging section of the combustion chamber indicating a highly 3-D turbulent flow.

The design of an active cooling system for the floating element proved to be a feasible design option to further improve the accuracy of these types of non-nulling balances. Encouraging preliminary results from both a cold and high heat flux supersonic flow were obtained. Accuracy will be improved with better control over heating of the piezoresistive strain gages. Ultimately a heat flux sensor could be added for measurement control to precisely match thermal conditions.

### ACKNOWLEDGEMENTS

The invaluable assistance provided by all the involved employees of NASA Langley Research Center and the General Applied Science Laboratory is greatly appreciated. Also acknowledged are the efforts of D. J. DeTurris and K. M. Chadwick (graduate research assistants at Virginia Tech) in obtaining much of the data presented.

### REFERENCES

1. Nitsche, W., Haberland, C., and Thunker, R., "Comparative Investigations of the Friction Drag Measuring Techniques in Experimental Aerodynamics", ICAS-84-2.4.1, 14th ICAS Congress, Sept. 1984.
2. Schetz, J. A., and Nerney, B., "Turbulent Boundary Layer with Injection and Surface Roughness", AIAA Journal, Vol. 15, Sept. 1977, pp. 1268-1274.
3. DeTurris, D. J., Hellbaum, R. F., and Schetz, J. A., "Direct Measurements of Skin Friction in a Scramjet Combustor", AIAA 90-2342, 26th Joint Propulsion Conference, July 1990.
4. Winter, K. G., "An Outline of the Techniques Available for the Measurement of Skin Friction in Turbulent Boundary Layers", Progress in Aerospace Sciences, Vol. 18, 1977, pp. 1-57.
5. Roensch, R. L., and Cadwell, J. D., "Direct Measurements of Skin Friction in a High Reynolds Number Supersonic Blowdown Wind Tunnel", Douglas Paper 1728, Douglas Aircraft Company.

6. Allen, J. M., "Systematic Study of Error Sources in Supersonic Skin-Friction Balance Measurements", NASA-TN-D-8291, Oct. 1976.
7. Allen, J. M., "Improved Sensing Element for Skin-Friction Balance Measurements", AIAA Journal, Vol. 18, Nov. 1980, pp. 1342-1345.
8. Voisinet, R. L. P., "Combined Influence of Roughness and Mass Transfer on Turbulent Skin Friction at Mach 2.9", AIAA 79-0003, 17th Aerospace Sciences Meeting, Jan. 1979.
9. Terrell, J.P., Hager, J.M., Onishi, S., and Diller, T.E. "Heat Flux Microsensor Measurements and Calibrations". NASA Langley Measurement Technology Conference, NASA CP- , 1992.



Test Facility	NASA Langley Batch 5 Run 28	GASL Test 112	GASL Test 564
Mach no.	3.0	3.3	3.3
$P_t$ (psia)	500	800	800
$T_t$ (R)	3000	4000	4000
V (ft/sec)	5000	6300	6300
q (psf)	4100	10700	7800
$\tau_{wx}$ (psi)	0.122	0.11	0.125
$\tau_{wz}$ (psi)	0.032	0.043	0.0535
$C_{fx}$	0.0042	0.0014	0.0023
$C_{fz}$	0.0005	0.0006	0.0010

Table 1 - Summary of the DSC based skin friction gauge results

Test Facility	GASL Test 601	GASL Test 602
Mach no.	3.3	3.3
$P_t$ (psia)	800	800
$T_t$ (R)	4000	4000
V (ft/sec)	6300	6300
q (psf)	7800	7800
$\tau_{wx}$ (psi)	0.160	0.181
$C_f$	0.0029	0.0033

Table 2 - Cooled Head Friction Gauge  
Results

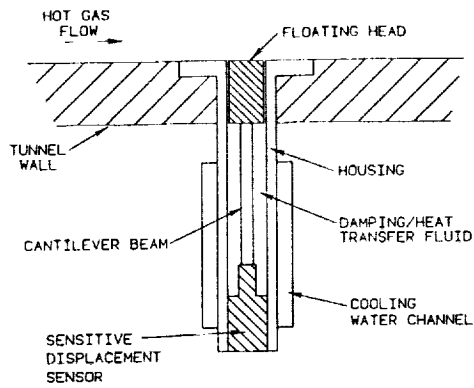


Fig. 1 Schematic of a Skin Friction Balance

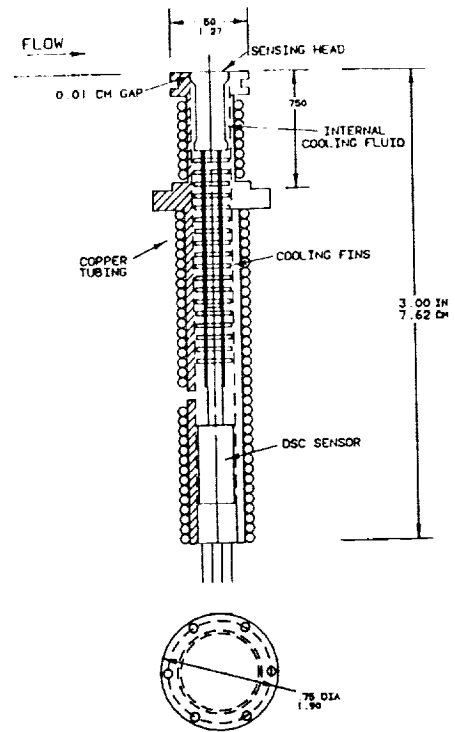


Fig. 2 Schematic of NASA Langley Skin Friction Balance

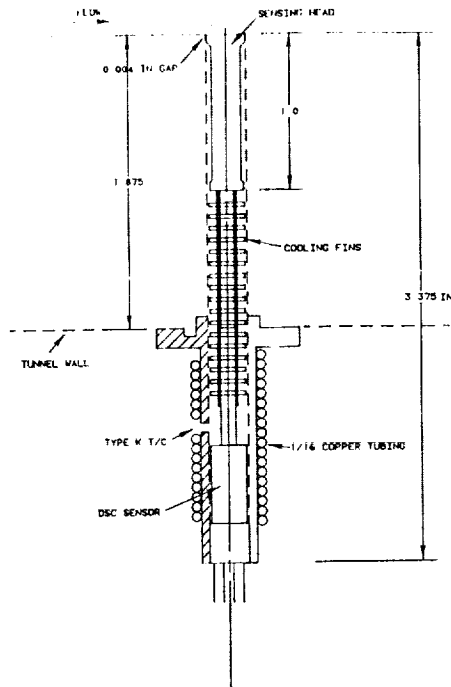


Fig. 3 Schematic of GASL Skin Friction Balance

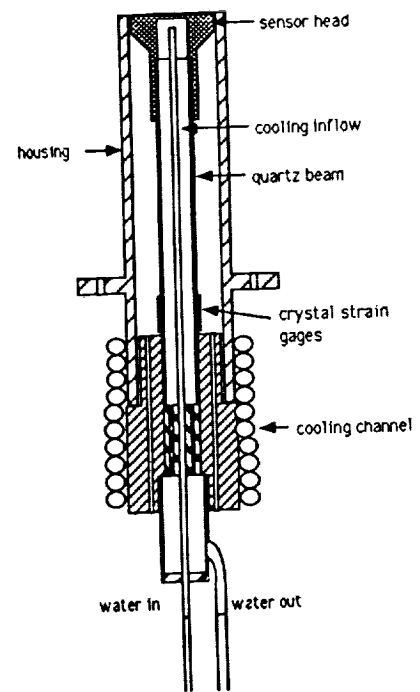


Fig. 4 Cooled Head Skin Friction Balance

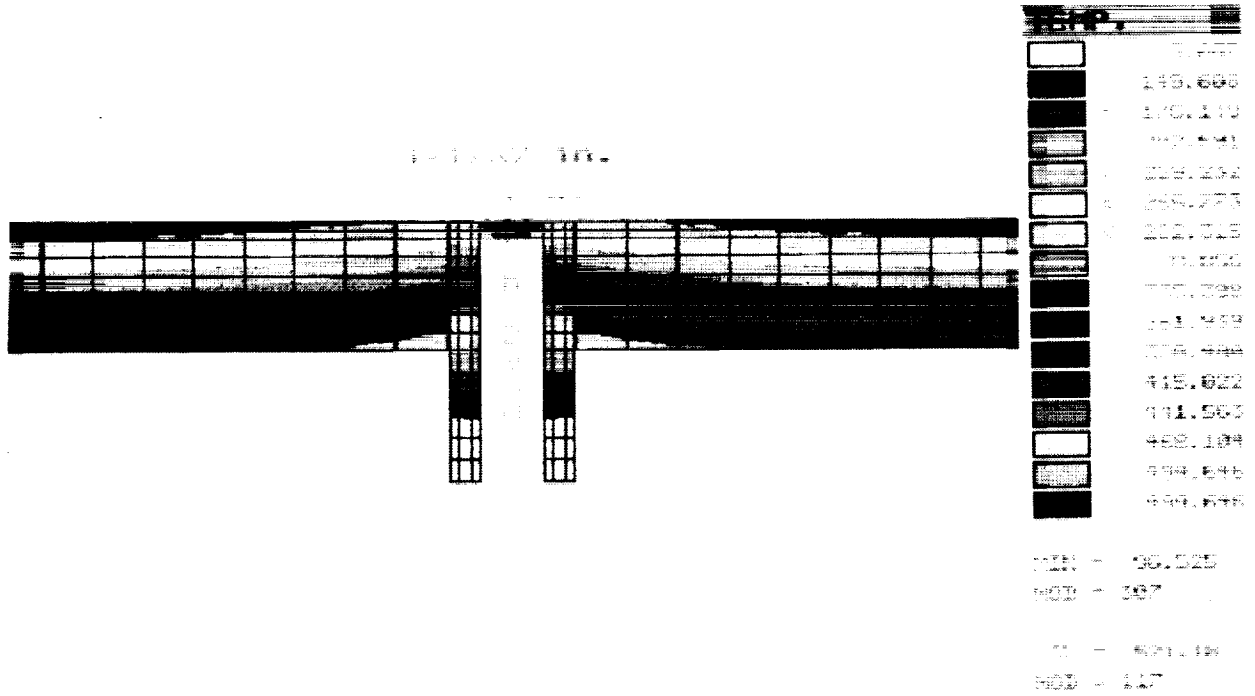


Fig. 5 Cooled Head Heat Transfer Contour

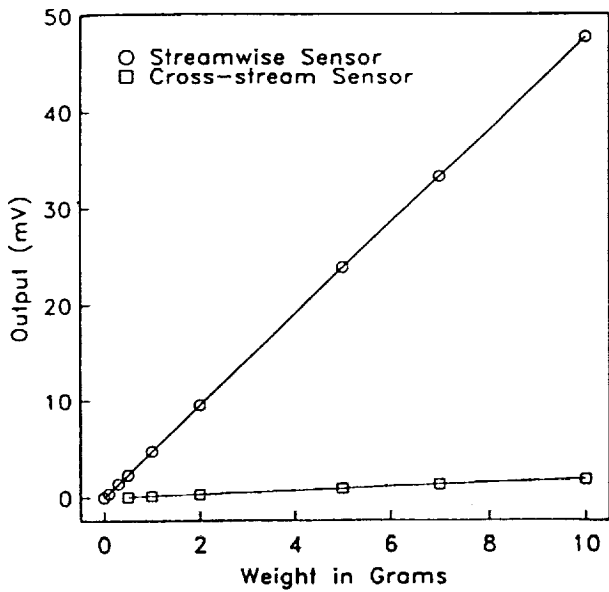


Fig. 6 DSC Balance Calibration

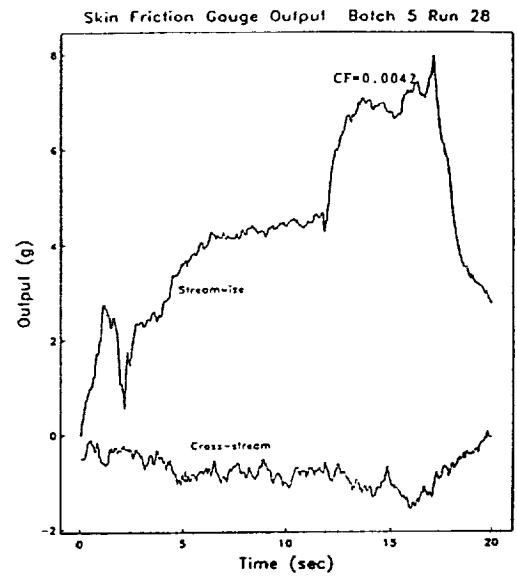


Fig. 7 NASA Langley Test Run 5 Results

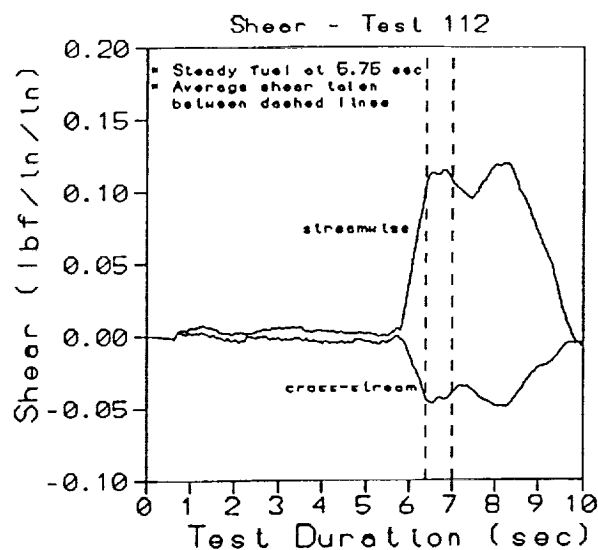


Fig. 8 GASL Test 112 Results

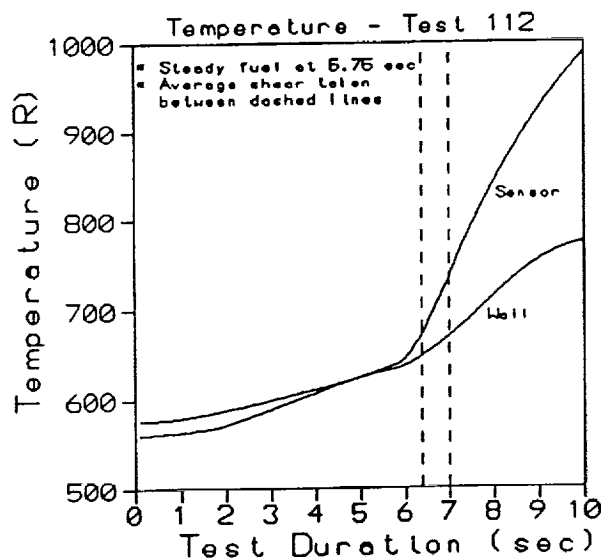


Fig. 9 GASL Test 112 Temperature Mismatch

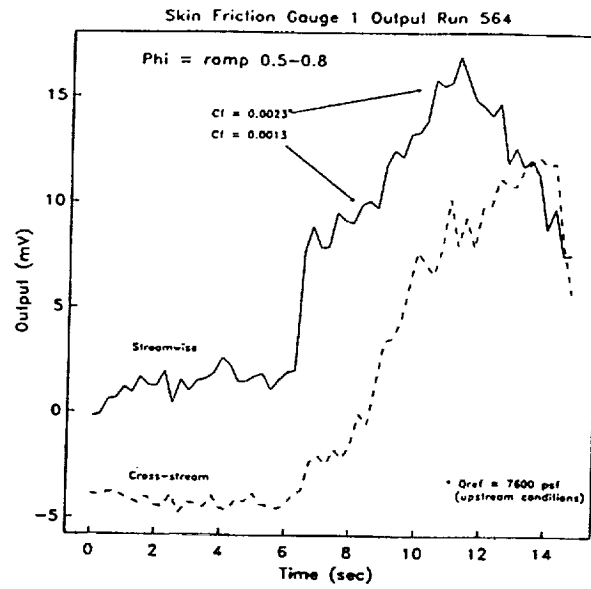


Fig. 10 GASL Test 564 Results

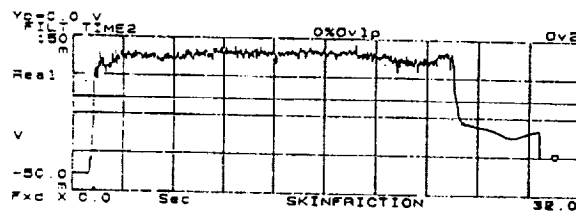
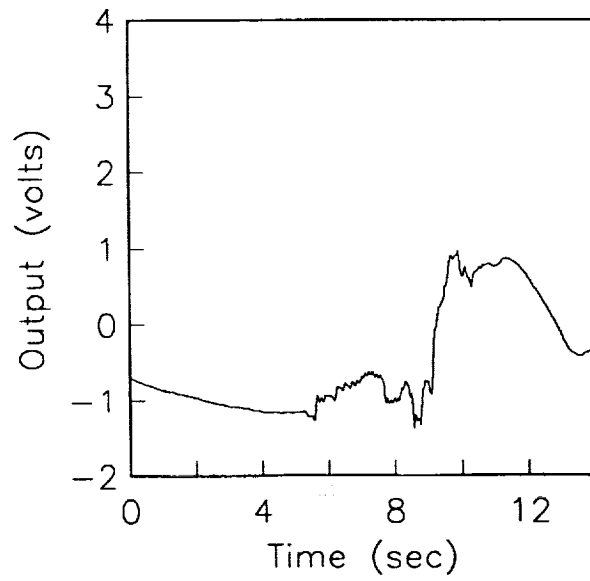


Fig. 11 Cooled Head Balance Cold Supersonic Flow Results



**Fig. 12 GASL Test 602 Cooled Head Balance Results**

**PALLADIUM-CHROMIUM STATIC STRAIN GAGES FOR HIGH TEMPERATURES**

Jih-Fen Lei  
Sverdrup Technology, Inc  
NASA Lewis Research Center Group  
Cleveland, OH

**ABSTRACT**

An electrical resistance strain gage that can provide accurate static strain measurement to a temperature of 1500°F or above is being developed both in fine wire and thin film forms. The gage is designed to be temperature compensated on any substrate material. It has a dual element: the gage element is a special alloy, palladium-13wt% chromium (PdCr), and the compensator element is platinum (Pt). Earlier results of a PdCr based wire gage indicated that the apparent strain of this gage can be minimized and the repeatability of the apparent strain can be improved by prestabilizing the gage on the substrate for a long period of time. However, this kind of prestabilization is not practical in many applications and therefore the development of a wire gage which is prestabilized before installation on the substrate is desirable. This paper will present our recent progress in the development of a prestabilized wire gage which can provide meaningful strain data for the first thermal cycle. A weldable PdCr gage is also being developed for field testing where conventional flame-spraying installation can not be applied. This weldable gage is narrower than a previously reported gage, thereby allowing the gage to be more resistant to buckling under compressive loads. Some preliminary results of a prestabilized wire gage flame-sprayed directly on IN100, an engine material, and a weldable gage spot-welded on IN100 and SCS-6/B21-S Titanium Matrix Composite (TMC), a National Aero-Space Plane (NASP) structure material, will be reported. Progress on the development of a weldable thin film gage will also be addressed. The measurement technique and procedures for using thin PdCr based gage as well as some considerations related to the installation procedures and the lead wire effect will be discussed.

**INTRODUCTION**

An electrical resistance strain gage that can provide accurate static strain measurement to a temperature higher than the limit of the conventional technology is urgently needed for high temperature materials studies and hot structure design validation. A PdCr based strain gage that has shown some promise for high temperature application is being further developed under the support of the National Aero-Space Plane (NASP, X-30) program. Previous results

of a PdCr based wire gage suggested that the apparent strain of this temperature compensated gage is relatively small (within 750 microstrain ( $\mu\text{in/in}$ )) and repeatable (within 100 microstrain between thermal cycles to 1470°F) after the gage is prestabilized on the substrate at 1470°F for 50 hours [1]. This kind of prestabilization process on the test article is not allowed for many practical tests where the first thermal cycle data is needed. A wire gage which is prestabilized before installation on the substrate is therefore required. This paper will present our recent progress in developing a prestabilized wire gage.

The maximum use temperature for a PdCr based wire gage is currently limited to 1470°F due to the presence of the impurities in the PdCr wire, while a sputter deposited PdCr thin film gage has demonstrated the possibility of extending the use of the PdCr based gage to a higher temperature of approximately 1800°F [2]. A weldable thin film gage is being developed for applications where sputtering a thin film gage directly on a large test article, such as the NASP airframe, is impossible. A weldable thin film gage is a thin film gage fabricated on a thin metal shim, which is then transported and installed on the test article by welding. The status of the development of a weldable thin film gage will be reviewed. Some considerations related to the installation of the gage and measurement techniques will also be addressed.

## GAGE FABRICATION AND INSTALLATION

### I. Wire Gage

The PdCr based gage is designed to be temperature compensated on any substrate material. It has a dual element: the gage element is .001" (1 mil) PdCr wire and the compensator element is .001" (1 mil) platinum wire. The Pt compensator is around the periphery of the PdCr gage grid to minimize the effect of the temperature gradient. Fig. 1 shows a wire gage with the high temperature tape frame used for flame spray mounting. The configuration of this gage is similar to that of the previous gage [1] except (1) the PdCr wire is heat-treated (prestabilized) before winding into gages, (2) the spacing between the gage grids is decreased so that the width of a total gage is decreased from 0.42" to 0.16" and (3) the length and therefore the resistance of the platinum compensator is decreased so that the gage is closer to a one-to-one bridge system. The nominal resistances of the gage and the compensator are 120 ohms and 5 ohms, respectively. There are three gage lead wires extended from the gage system with a common lead wire shared by both the gage and the compensator. These gage lead wires are .003" (3 mil) diameter PdCr wire.

The wire gage is mounted on the test article with flame-sprayed powders. A layer of nickel-chromium-aluminide is first applied to the substrate as the bondcoat and then a layer of alumina is applied as the precoat. The gage is then taped down onto the precoat by means of high temperature adhesive strips. A mixture coating of alumina and zirconia which provides oxidation protection for the gage is applied to the open areas between the strips. The strips are then removed and the final alumina mixture overcoat is applied. Since both PdCr and Pt



were found to be very sensitive to impurities such as aluminum and silicon, care must be taken during handling and installation to protect the gage from contamination. The spraying powders need to be pure and the tape residue has to be completely removed. Fig. 2 shows two prestabilized wire gages installed on a 0.125" thick IN100 coupon.

## II. Thin Film Gage

Thin film gages provide a means for minimally intrusive surface strain measurements, and are therefore advantageous for use in harsh testing environments. Fig. 3 shows a compensated thin film gage fabricated on an alumina test bar. The configuration of this thin film gage is similar to that of the wire gage with a Pt compensator located around the periphery of the PdCr gage. This thin film gage is prepared in a Class 1000 clean room by means of sputter deposition, photolithography, and chemical etching techniques. The size of a total gage is approximately 0.19" (5mm) long and 0.17" (4.3mm) wide. PdCr .003" lead wires were attached to the three thin film lead pads by means of parallel gap welding.

## III. Weldable Gage

A .003" thick Hastelloy-X shim is used as the carrier of the weldable gage. The wire weldable gage is fabricated simply by flame-spraying the wire gage onto the shim with the process described earlier. The fabrication process of a thin film gage on the weldable Hastelloy-X shim is similar to that of the gage fabricated on an alumina substrate except a layer of insulating material, alumina, is deposited in between the conductive Hastelloy-X shim and the gage element. This insulation layer has to be able to provide enough resistance to ground up to the maximum use temperature.

The weldable gage can be installed to the test article simply by using a spot-welder. Surfaces of the Hastelloy-X shim and the substrate material need to be cleaned before welding to remove the possible surface oxides. This can be done by sand blasting the surface area with fine grit powders followed by cleaning with alcohol. Since the performance of the weldable gage depends on good welding attachments, it can be applied only to the weldable base materials. In spite of this and other limitations, such as the stiffening effect and the stress concentrations at the welds, the weldable gage offers an advantage when the installation must be done in the test field and flame-spraying or sputter deposition cannot be applied. Fig. 4 shows two weldable wire gages welded on a 0.025" thick SCS-6/B21-S TMC coupon and Fig. 5 shows a weldable thin film gage welded on a 0.125" thick IN100 coupon. The welding energy used in these two cases was approximately 48-50 watts/second.

## IV. Installation of Extended Lead Wires (Trunk Leads) and Thermocouples

The trunk leads which extend from the gage to the measurement system are attached to the gage lead wires by means of spot-welding. Alumina beads are threaded on the trunk leads to provide oxidation protection and to prevent the wires from shorting to each other.

The first two inches of the wires are fixed on the substrate following a "Z" loop for the strain relief, as shown in Figs. 2 and 5. Several lead wire materials, including chromel, Hoskins 875, and platinum, were studied for their suitability for high temperature static strain measurement. The results of this study are discussed in Appendix A. Thermocouples which are needed for monitoring the temperature of the gages and for detecting any temperature gradient across the gage are also spot-welded to the substrate. Accurate temperature measurement is necessary for accurate correction of the apparent strain.

## MEASUREMENT TECHNIQUE AND PROCEDURE

This PdCr based gage provides a unique ability to compensate for temperature effects on materials with a wide range of thermal expansion coefficients by simply varying the resistors of an external circuit (Fig. 6). However, to perfectly compensate for the unwanted temperature induced errors, a pre-calibration process is needed in order to determine the best value of the ballast resistor ( $R_B$ ) [3]. This pre-calibration process should be done at least once for each set of substrate material and lead wires to accommodate for the temperature dependent effects such as the difference in thermal coefficient of expansion between the gage, compensator, and the substrate materials, the change in lead wire resistance, the thermal EMF generated at the junctions of dissimilar materials, and the leakage resistance between the gage and the substrate. This pre-calibration process is best done on the test article if a thermal cycle to the maximum use temperature is allowed. Otherwise, it can be duplicated on a coupon only if the coupon material is the same as that of the test article. Also the lead wire material and its length used in the hot zone must be the same as in the real test. The procedures for this pre-calibration test are described in Appendix B.

Once the value of the ballast resistor  $R_B$  is determined through the pre-calibration process, the wheatstone bridge system shown in Fig. 6 is then balanced at room temperature by adjusting the ratio between the bridge balancing resistor  $R_1$  and  $R_2$  so that  $R_1/(R_1+R_2)=(R_G+r_{lg})/(R_B+R_C+r_{lc}+R_G+r_{lg})$ .  $R_G$  and  $R_C$  are the resistances of the gage and compensator, respectively, and  $r_{lg}$  and  $r_{lc}$  are the resistances of the lead wires connected to the gage and compensator, respectively. The bridge is now ready for apparent strain and mechanical strain measurements. Notice that the accuracy and stability of this measurement strongly depend on the accuracy and stability of the ballast resistor  $R_B$  and the bridge balancing resistors  $R_1$  and  $R_2$ . Precision decade resistors which are temperature insensitive are therefore needed.

## CHARACTERISTICS OF THE GAGE

### A. Wire Gage

The flame-sprayed prestabilized wire gage has been tested on IN100, an engine material, and the weldable wire gage has been evaluated on both IN100 and SCS-β21S TMC, a NASP structure material. Fig. 7 presents typical resistance change versus temperature curves for the effective gage ( $R_G^* = R_G + r_{lg}$ ) and compensator ( $R_C^* = R_C + r_{lc}$ ) of a prestabilized gage during the pre-calibration process. In this case, the gage was flame-sprayed directly on an IN100 coupon with Pt .010" wires used as trunk leads. As shown, both curves are quite linear and repeatable between a heat-up and cool-down cycle to 1450°F. This suggested that this prestabilized gage is stable and repeatable from the very first thermal cycle.

Fig. 8 is the apparent strain vs temperature characteristics of this prestabilized gage during two thermal cycles to 1450°F. As described in Appendix B, the resistance of the ballast resistor used in the wheatstone bridge circuit was calculated from Fig. 7 and was 109.89 ohms. The bridge system was balanced with  $R_1/(R_1 + R_2) = 0.516$ , which was very close to a one-to-one bridge. As shown in Fig. 8, the change in apparent strain of this prestabilized gage is within 1200 microstrain with a repeatability within 100 microstrain between thermal cycles to 1450°F. The magnitude of the apparent strain of this prestabilized PdCr gage, although very small compared to that of the other high temperature strain gages, is large compared to that of the PdCr gage stabilized on the test article. This is because the PdCr wire is oxidized during the prestabilization process and the resistance versus temperature curve of the prestabilized gage is found to be not as linear as that of the gage which is stabilized on the part. Note that the shape of the apparent strain vs temperature curves and the value of the residual apparent strain of a compensated gage simply reflect the nonlinearity of the resistivity versus temperature characteristic of the gage and compensator element. However, the repeatability of the apparent strain of this prestabilized gage is comparable to that of the gage which is stabilized on the substrate. Furthermore, the initial thermal cycle data are meaningful due to their reproducibility from the very first thermal cycle.

There was another prestabilization process explored. The PdCr gage was flattened and heat-treated before the construction of the Pt compensator and the joining of the lead wires. The properties of this type of prestabilized gage were found to be comparable to that of the wire stabilized gage; however, the fabrication of a flattened gage is much more complicated. In addition, the weld joints between the flattened gage wire and the round lead wire were found to be less durable. As a result, the flatten, heat-treated method was abandoned.

Fig. 9 shows the apparent strain vs temperature characteristics of a weldable wire gage during two thermal cycles to 1450°F. The gage is welded on a 0.125" thick IN100 coupon. As can be seen, the characteristic of this weldable gage is similar to that of the gage directly installed on the IN100 (Fig. 8). The reproducibility of the apparent strain of these two types of gages is comparable, while the weldable gage has a slightly larger change in apparent strain in the temperature range. This may have resulted from the difference in the coefficients of thermal expansion between the gage, Hastelloy-X shim, and the IN100 coupon. No delamination of the weldable gage from the substrate is observed after several thermal cycles to 1450°F.

Fig. 10 shows the apparent strain vs temperature characteristics of a weldable gage on a coupon of SCS-6/Beta 21S TMC. This 0.025" thick TMC coupon is 3 plies with a fiber

layup of [0,90,0]. The gage is spot-welded along the top fiber direction as shown in the Fig.4. As shown, the apparent strain of this weldable gage on TMC during the first two thermal cycles to 1200°F (Fig. 10a) is very similar to that of the gages on IN100. This indicates that the PdCr gage is well temperature-compensated both on IN100 and on TMC. However, as the gage and the TMC are exposed to a higher temperature, the repeatability of the apparent strain of the gage between thermal cycles decreases. As seen from Fig. 10b, there is approximately 400 microstrain zero shift at 1300°F between two 1300°F thermal cycles, although the shape of the apparent strain curve is similar to that of the 1200°F thermal cycles. Fig. 10c presents the apparent strain of the gage on TMC during three thermal cycles to 1420°F. As shown, the first cycle data is similar to that of the gage on IN100; however, data for the second and third cycles are not characteristic of the PdCr gage. There is a large drop of the apparent strain at temperatures above 1300°F during the second heat-up cycle while there is a large increase of the apparent strain above 1300°F during the third heat-up cycle. This indicates the substrate material TMC is not stable at temperatures above 1300°F. Exposure to a higher temperature may result in fiber shifting, laminate bending, or other permanent changes in the material. There is no gage delamination from the TMC substrate occurring after these tests; however, the TMC substrate does warp.

The critical compressive strain for a weldable gage to start buckling depends strongly on the width, but not much on the length, of the gage. The narrower the gage is, the higher its critical strain for buckling [4]. Furthermore, the difference in coefficients of thermal expansion between the shim and the test article may either increase or decrease the critical buckling strain. When the thermal expansion coefficient of the shim material is greater than that of the substrate material to which it is welded, an increase in temperature will produce a compressive strain in the shim. This will effectively reduce the critical strain limit for the imposed mechanical strain. For example, the thermal expansion coefficient of the Hastelloy-X and the TMC are approximately 9 and 6 ppm/°F, respectively. Heating to 1200°F will then produce a compressive mechanical strain of 3600 microstrain in the Hastelloy-X shim. Since the gage with a previous design (0.42" wide) has a critical strain for buckling of approximately 1500 microstrain, it would buckle and delaminate from the substrate after the gage is exposed to 1200°F. This is the main reason for decreasing the size of the gage. The gage with this new design (0.16") has a critical strain for buckling of approximately 8000 microstrain and can therefore survive to a much higher temperature without delamination.

It should be noted that since materials like TMC, having a thermal expansion coefficient that is fiber orientation dependent, a weldable gage may be usable along one fiber direction but not along the other direction. Alignment of the weldable gage on the TMC is therefore very important. Values of apparent strain of the gage reported in this paper were calculated assuming a constant gage factor of 1.4. The gage factor characteristic of the prestabilized gage in addition to how well the strain transfers through the weldable gage have yet to be determined.

## B. Thin Film Gage

Fig. 11 presents the change in resistance versus temperature of the effective gage ( $R_G^*$ )

and the compensator ( $R_c^*$ ) of a thin film gage during the pre-calibration process. In this case, the gage was fabricated on an alumina cantilever beam with Pt 0.010" wire used as trunk leads as shown in Fig. 3. Both curves are quite linear and repeatable during heat-up and cool-down cycles to 1850°F. This makes the temperature compensation possible for this thin film gage up to this high temperature. In this case, the gage has been pre-heated at 1850°F for one hour. Fig. 12 presents the apparent strain versus temperature characteristics of the gage during a thermal cycle to 1850°F. As shown, the shape of the apparent strain curve of this thin film gage is similar to that of the wire gage but with a larger apparent strain variation between the heat-up and cool-down cycles. More work is underway to improve the properties of thin film gage. As for the thin film weldable gage, an insulation layer that can provide at least 1 Mohm up to the maximum use temperature (1900°F) is still being developed. As shown in Fig. 5, studies of the gage welded on an IN100 coupon indicated that the attachment of thin PdCr weldable gage on IN100 is durable. No gage delamination from the IN100 coupon occurred after several thermal cycles to 1850°F.

## SUMMARY

The procedures for fabricating a prestabilized wire gage have been established. This prestabilized wire gage can provide meaningful first thermal cycle data. A weldable gage, which can be used in the field where the conventional flame-spray technique installation can not be applied, has also been developed. The apparent strain characteristic of a weldable gage is similar to that of the gage installed directly on the substrate. However, the gage factor characteristic of this weldable gage, in addition to how well the strain transfers through the .003" Hastelloy shim, has yet to be determined. As for the thin film weldable gage, the preliminary results indicated the possibility of extending the use of thin PdCr based gage to approximately 1850°F; work is underway to further optimize and characterize its properties. More gages, both wire and thin film, will be tested in the near future in order to establish a statistical database for thin PdCr based resistance strain gage.

## REFERENCES

1. J.-F. Lei, "A Resistance Strain Gage with Repeatable and Cancelable Apparent Strain for Use to 800°C", NASA Contractor Report 185256, July 1990.
2. J.-F. Lei, "Palladium-Chromium Static Strain Gage for High Temperature Propulsion Systems", The Third Annual Health Monitoring Conference for Space Propulsion Systems Proceedings, p.391-400, Nov. 1991.
3. J.-F. Lei, D. R. Englund and C. Croom, "The Temperature Compensation Technique for a PdCr Resistance Strain Gage", SEM Conference Proceedings, Fall, 1991.

4. F. F. Hines, "Weldable Bonded Resistance Strain Gages", WRS GC Proceedings, May 1960.

## APPENDIX

### A. Trunk Lead Effects

PdCr heavy wires were originally used as trunk leads for this PdCr based gage. However, due to its high cost and limited availability, several alternate lead wire materials were studied. These include chromel (Ni10Cr), Hoskins 875 (Fe22.5Cr5.5Al0.5Si0.1C), and Pt. The values of some of the most important properties of these lead wire materials as well as their relative rankings are listed in Table I. The selection criteria for the trunk leads are (1) the lead material should not react with gage lead, (2) the resistivity ( $\rho$ ), the temperature coefficient of resistivity ( $\alpha$ ), and the product of  $\rho$  and  $\alpha$  of the trunk lead should be small so as not to influence the gage property, and (3) it should have a high melting temperature (M.T.), be oxidation resistant and stable at high temperatures, and undergo no phase transition. Among all the materials studied, Pt has the highest melting temperature, smallest resistivity and the best stability; however, it has a very large  $\alpha$  and product of  $\rho\alpha$  and is expensive. Both chromel and Hoskins 875 wire experience phase transitions in some temperature range, and therefore do not have linear resistance vs temperature (R vs T) curves. However, they have a smaller  $\rho\alpha$  product and are cheaper than Pt. In comparison, Hoskins 875 is a better choice than chromel for static strain measurement because it is more stable at high temperatures and its R vs T characteristic is more repeatable (Fig. A1). However, large diameter wire is needed to minimize the total lead wire resistance. Overall, Pt and Hoskins 875 may replace PdCr as trunk leads when PdCr heavy wires are not available.

Table I. Properties and Relative Ranking of Some Lead Wire Materials. The Lower the Ranking, the Better the Material.

	MT (°F)	$\rho$ ( $\mu\Omega$ -cm)	$\alpha$ ( $\mu\Omega/\Omega/^\circ\text{F}$ )	$\rho\alpha$ ( $\mu\Omega$ - cm/ $^\circ\text{F}$ )	Phase Trans.	Stable	\$
Chromel (Ni10Cr)	2593	70	175	0.012	Yes	3	1
Hoskins 875 (Fe22Cr5Al.5Si)	2770	145	87	0.013	Yes	2	2
Platinum (Pt)	3223	11	1637	0.018	No	1	3
Palladium- Chromium (Pd13Cr)	2372	80	98	0.008	No	2	4

## B. Pre-calibration Procedure

The value of the ballast resistor  $R_B$  required for temperature compensation is

$$R_B = R_C^* (\alpha_C^* - \alpha_G^*) / \alpha_G^*$$

where  $R_C^*$  is the effective compensator resistor, i.e.,  $R_C^* = R_C + r_{lc}$

$\alpha_C^*$  is the effective temperature coefficient of resistance of the effective compensator resistor, such that  $\alpha_C^* = \Delta R_C^* / (R_C^* \Delta T)$ , and

$\alpha_G^*$  is the effective temperature coefficient of resistance of the effective gage resistor, such that  $\alpha_G^* = \Delta R_G^* / (R_G^* \Delta T)$ , where  $R_G^* = R_G + r_{lg}$ .

The values of the  $R_C^*$ ,  $\alpha_C^*$  and  $\alpha_G^*$  are determined during a cycle of heating to and cooling from the maximum test temperature. Data are taken from room temperature to the optimum test temperature in 200°F steps. The oven temperature is stabilized within  $\pm 2^\circ\text{F}$  during the data acquisition process and the substrate is isothermal to within  $\pm 10^\circ\text{F}$  along the gage before the data are recorded.

At each test temperature, the lead wires from the gage system are first connected to the electrical circuit, as in Fig. B1(a), to obtain  $R_G^*$ , and are then connected to the circuit as in Fig. B1(b) to obtain  $R_C^*$ . Two digital multimeters and a thermometer are needed in this process. Based on the obtained  $R^*$  vs temperature (T) data,  $\alpha^*$  values can be obtained by curve fitting.

## PdCr Temperature Compensated Strain Gage

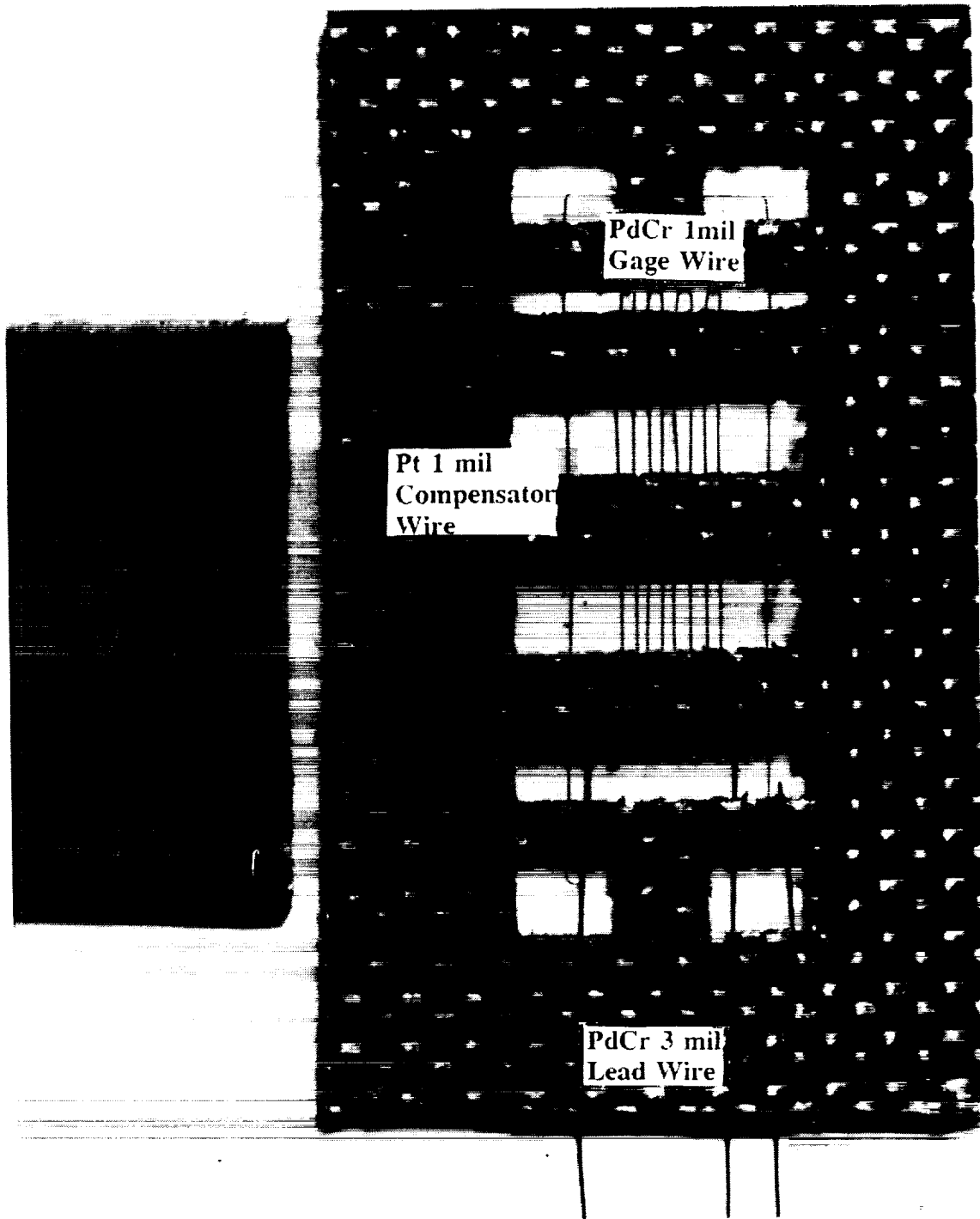


**Fig. 1.** A PdCr/Pt temperature-compensated wire gage with the high temperature tape frame used for flame spray mounting. (The scale is in inches).



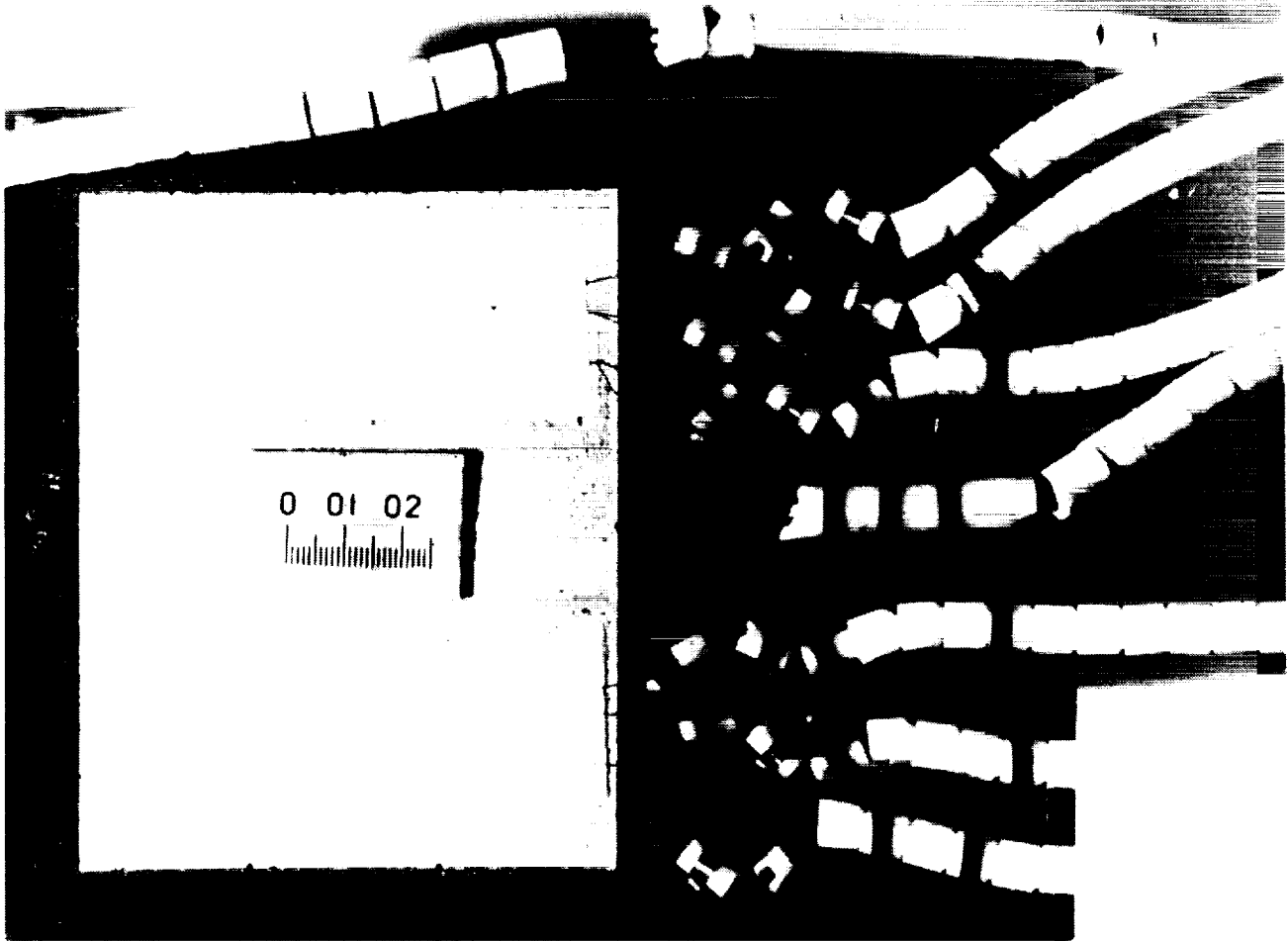


**Fig. 2. Two prestabilized wire gages installed on an IN100 coupon. There are three lead wires extended from each gage. There are also two thermocouples welded on the coupon.**

# PdCr/Pt Thin Film Strain Gage on Alumina Cantilever Bar

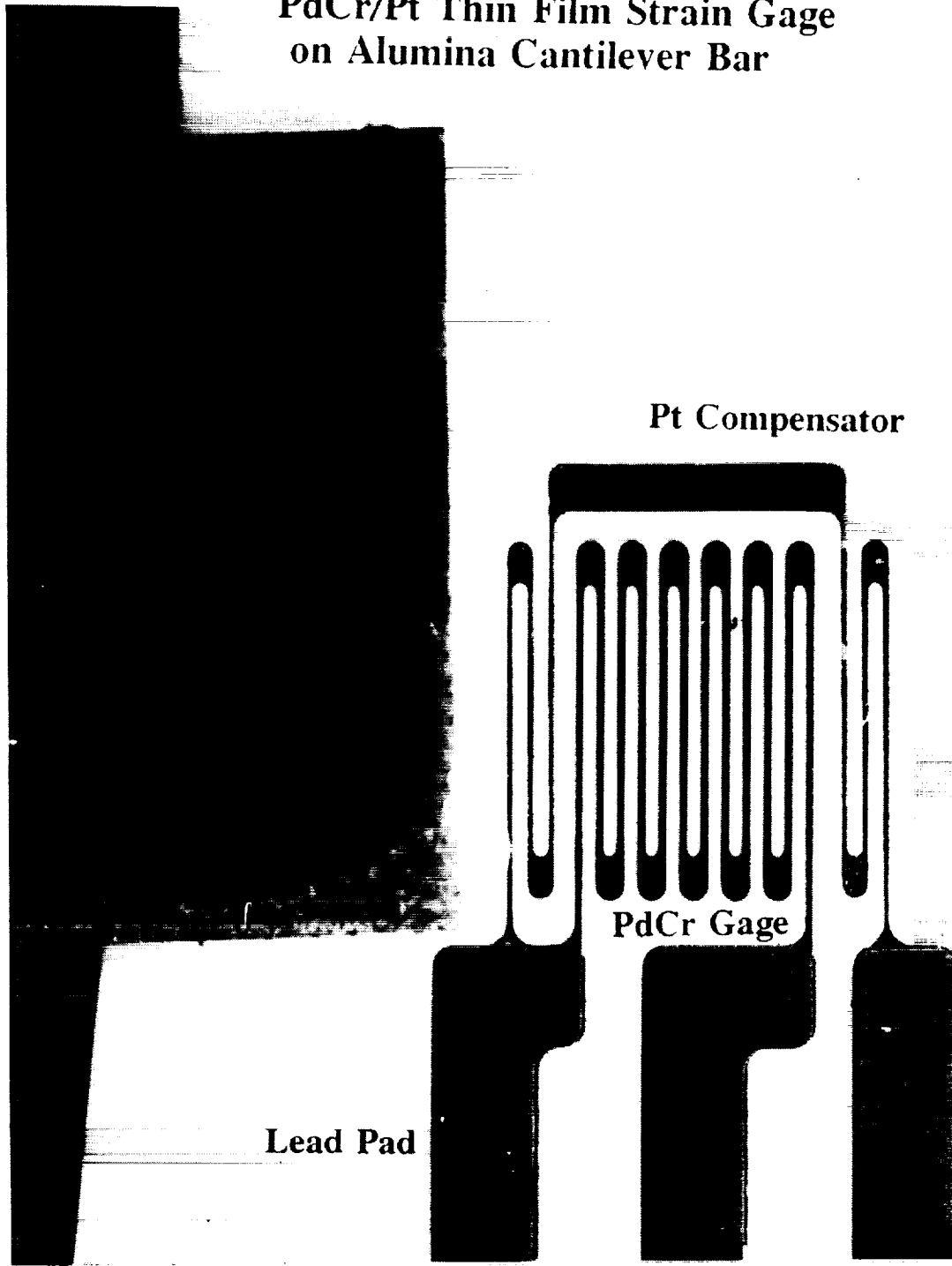
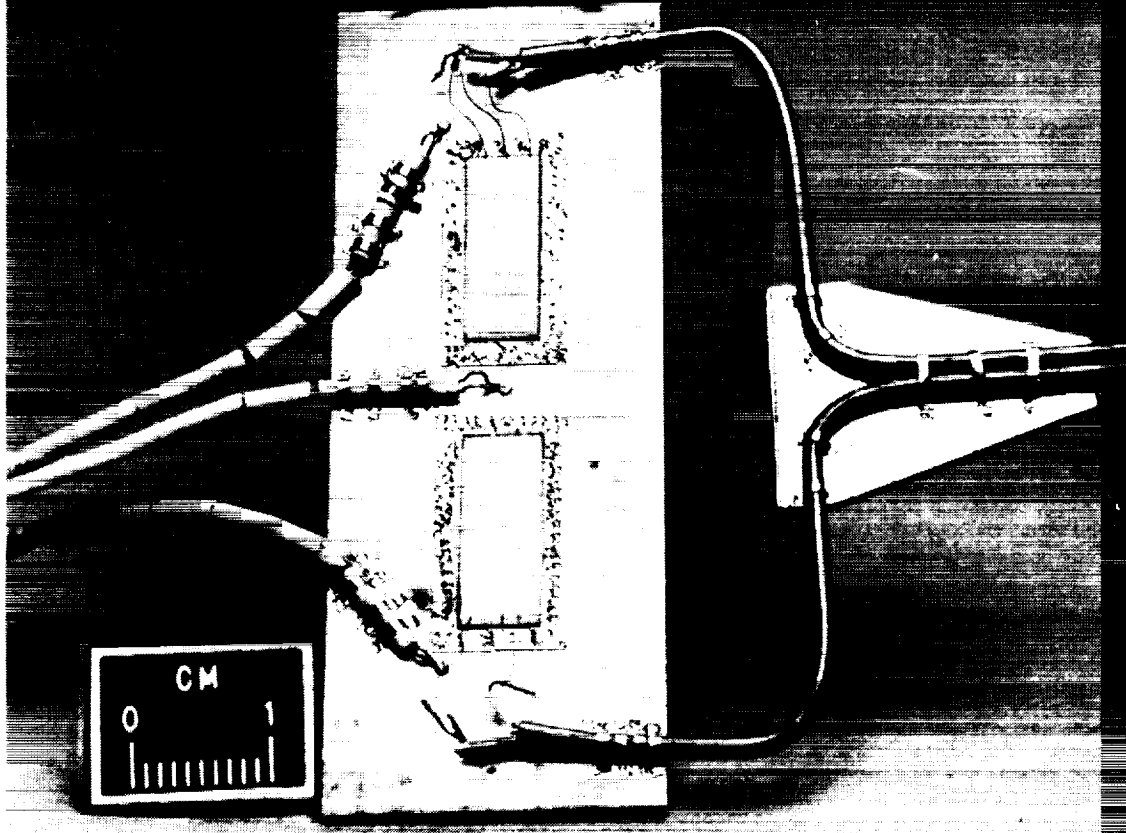


Fig. 3. A PdCr/Pt temperature-compensated thin film gage fabricated on an alumina substrate. (The scale is in millimeters).

ORIGINAL PAGE  
BLACK AND WHITE PHOTOGRAPH

**Two PdCr Weldable Gages Spot-Welded  
on a SCS-6/Beta 21S TMC [0,90,0]**



**Fig. 4. Two weldable wire gages welded on a SCS-6/B21-S titanium matrix composite (TMC) coupon. The gages are welded along the top fiber direction (1). There are three thermocouples spot-welded on the coupon.**

## A PdCr/Pt Thin Film Weldable Gage Spot-Welded on an IN100 Coupon

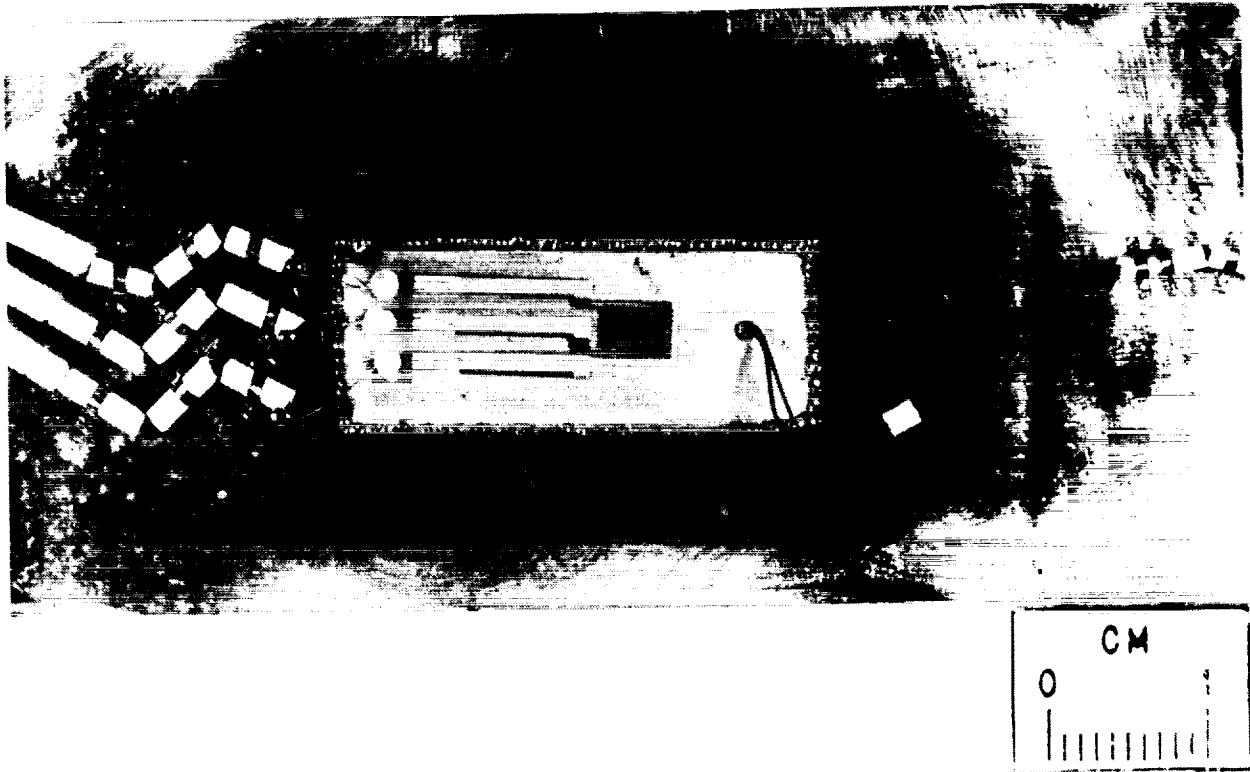


**Fig. 5.** A weldable thin film gage welded on an IN100 coupon. A 0.003" thick Hastelloy-X shim is used as the carrier of the weldable gage. There is also a thermocouple welded on the coupon.

# Strain Gage Measurement Circuit

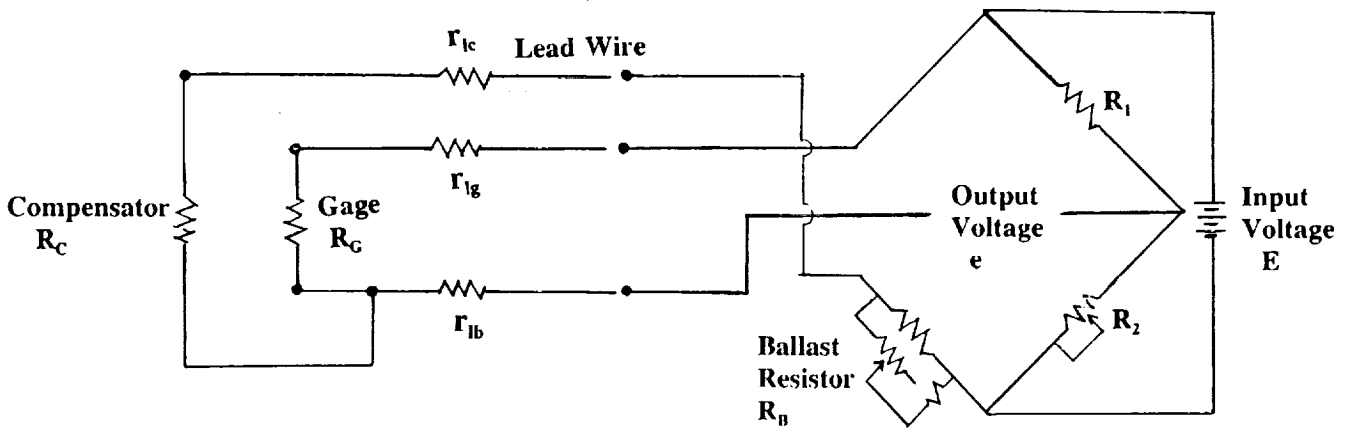
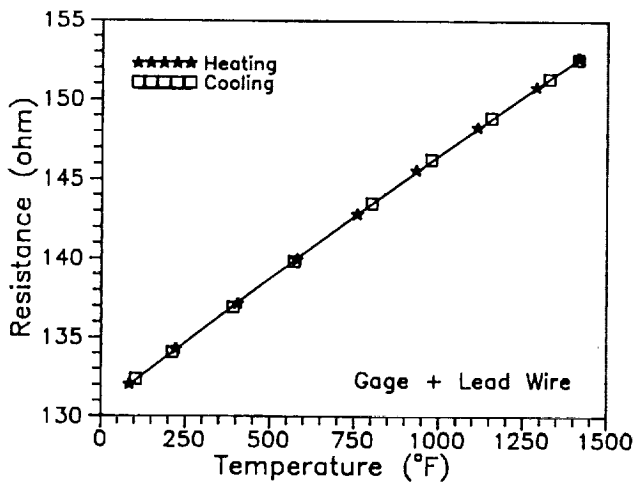
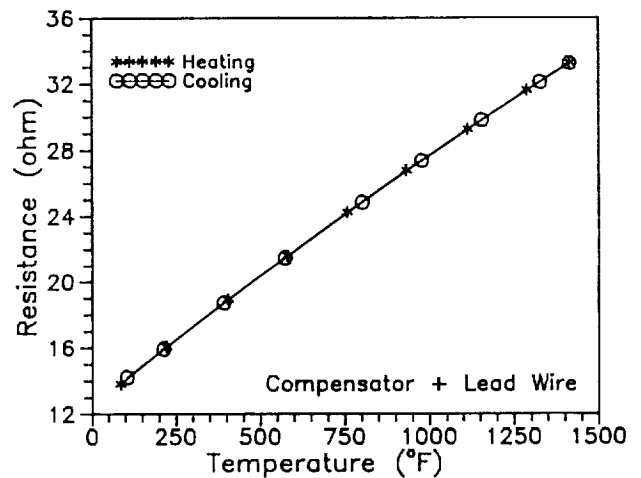


Fig. 6. Strain gage measurement circuit. The value of the ballast resistor,  $R_B$ , needed for temperature compensation is  $R_B = R_C^* (\alpha_C^* - \alpha_G^*) / \alpha_G^*$ , where  $R_C^* = R_C + r_{lc}$ ,  $\alpha_C^* = \Delta R_C^* / (R_C^* \Delta T)$  and  $R_G^* = R_G + r_{lg}$ ,  $\alpha_G^* = \Delta R_G^* / (R_G^* \Delta T)$ .



(a)



(b)

Fig. 7. Resistance vs temperature curves for the (a) effective gage  $R_G^* (=R_G + r_{lg})$  and (b) effective compensator  $R_C^* (=R_C + r_{lc})$  of a prestabilized wire gage during the pre-calibration. Values of  $R_G^*$ ,  $R_C^*$ ,  $\alpha_G^*$  and  $\alpha_C^*$  needed for calculating  $R_B$  are obtained by curve fitting.

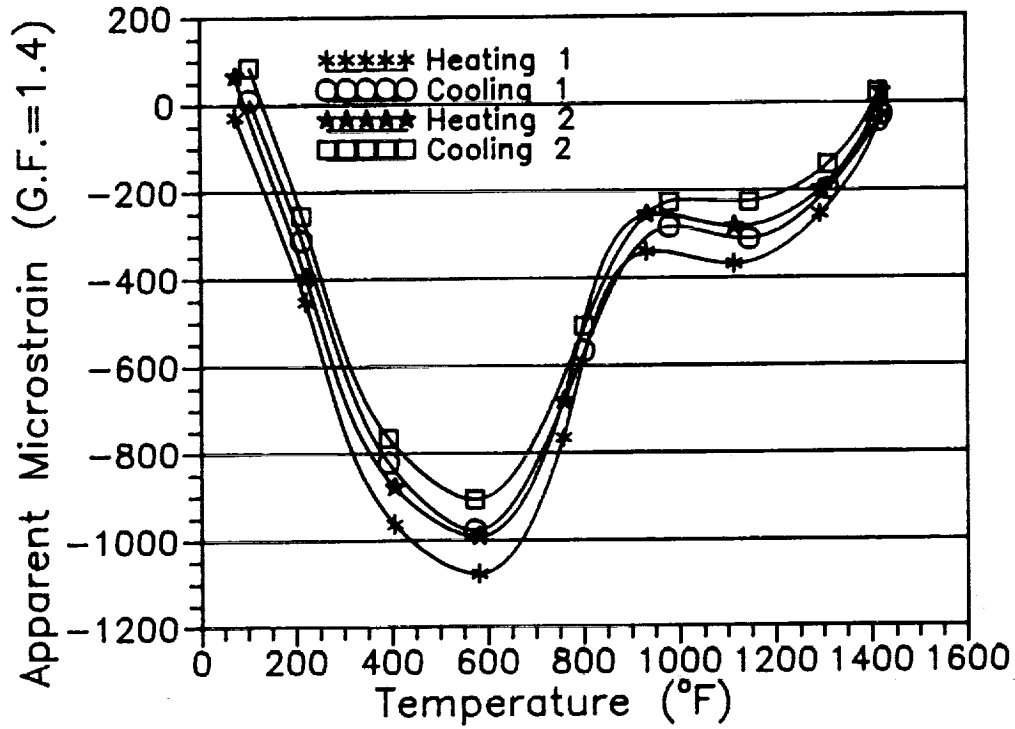


Fig. 8. Apparent strain vs temperature curves of a prestabilized PdCr/Pt wire gage during two thermal cycles to 1450°F. The gage is installed on an IN100 coupon by flame-spray technique. Values of apparent strain of the gage are calculated assuming a constant gage factor of 1.4.

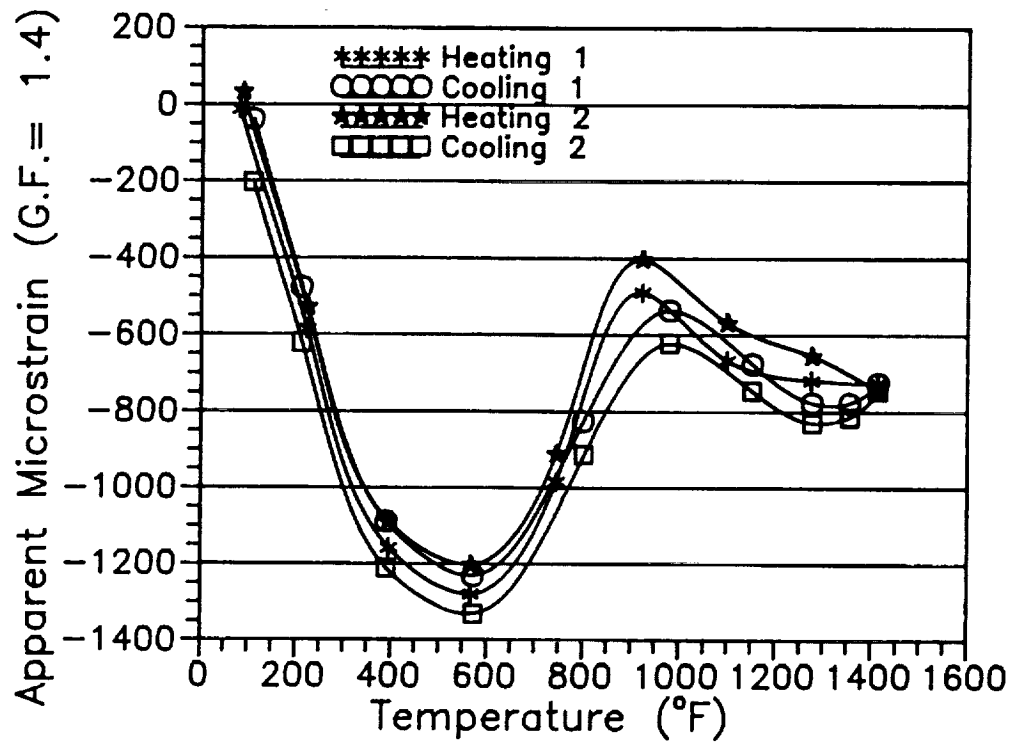
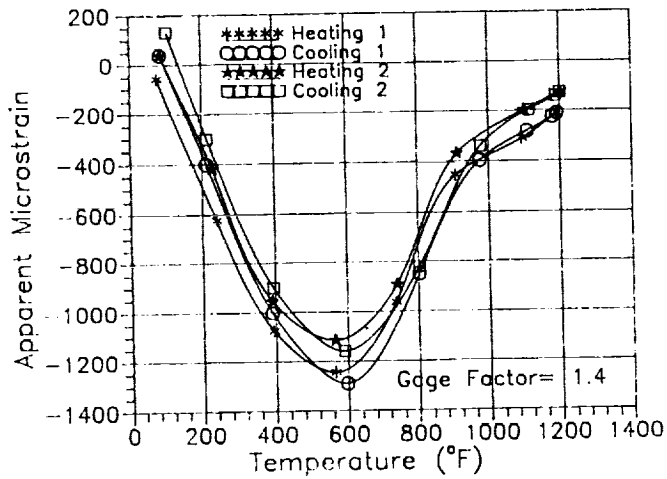
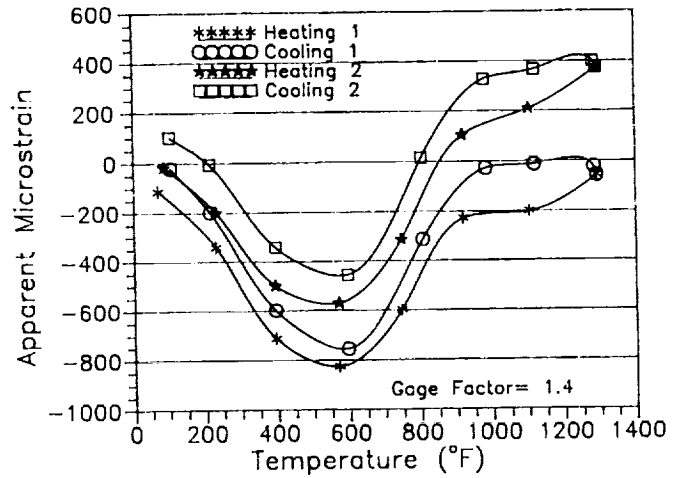


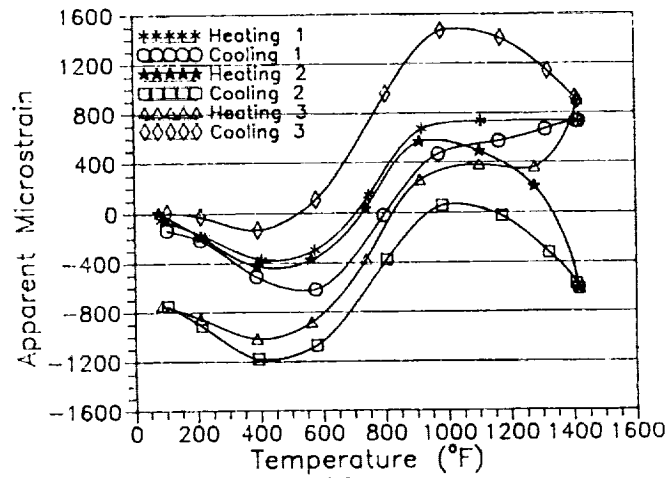
Fig. 9. Apparent strain vs temperature curves of a weldable wire gage during two thermal cycles to 1450°F. The gage is welded on an IN100 coupon.



(a)



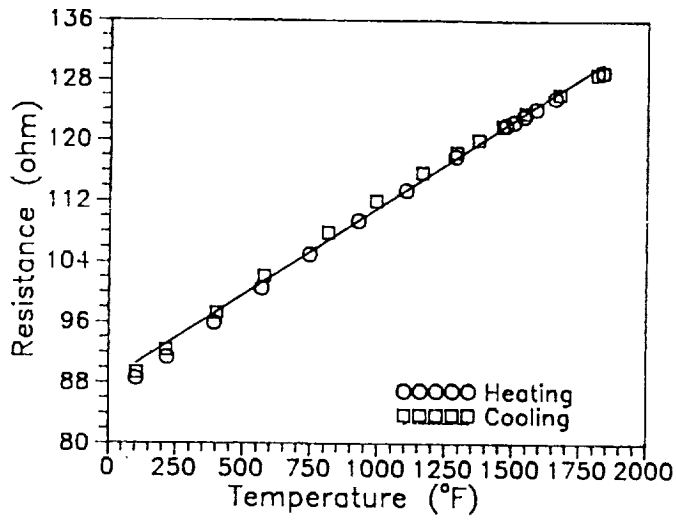
(b)



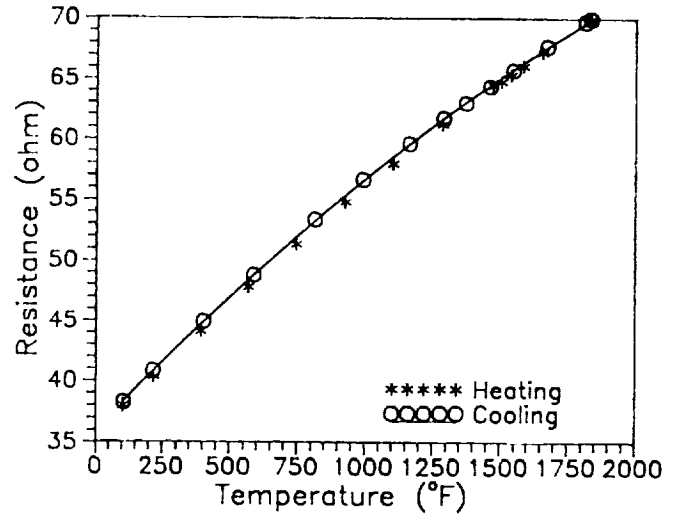
(c)

**Fig. 10. Apparent strain vs temperature characteristics of a weldable wire gage during (a) two thermal cycles to 1200°F, (b) two thermal cycles to 1300°F and (c) three thermal cycles to 1420°F. The gage is welded on a 0.025" thick TMC coupon.**





(a)



(b)

**Fig. 11. Resistance vs temperature curves for the (a) effective gage  $R_C^* (=R_C + r_{lg})$  and the (b) effective compensator  $R_C^* (=R_C + r_{lc})$  of a thin film gage during the pre-calibration process.**

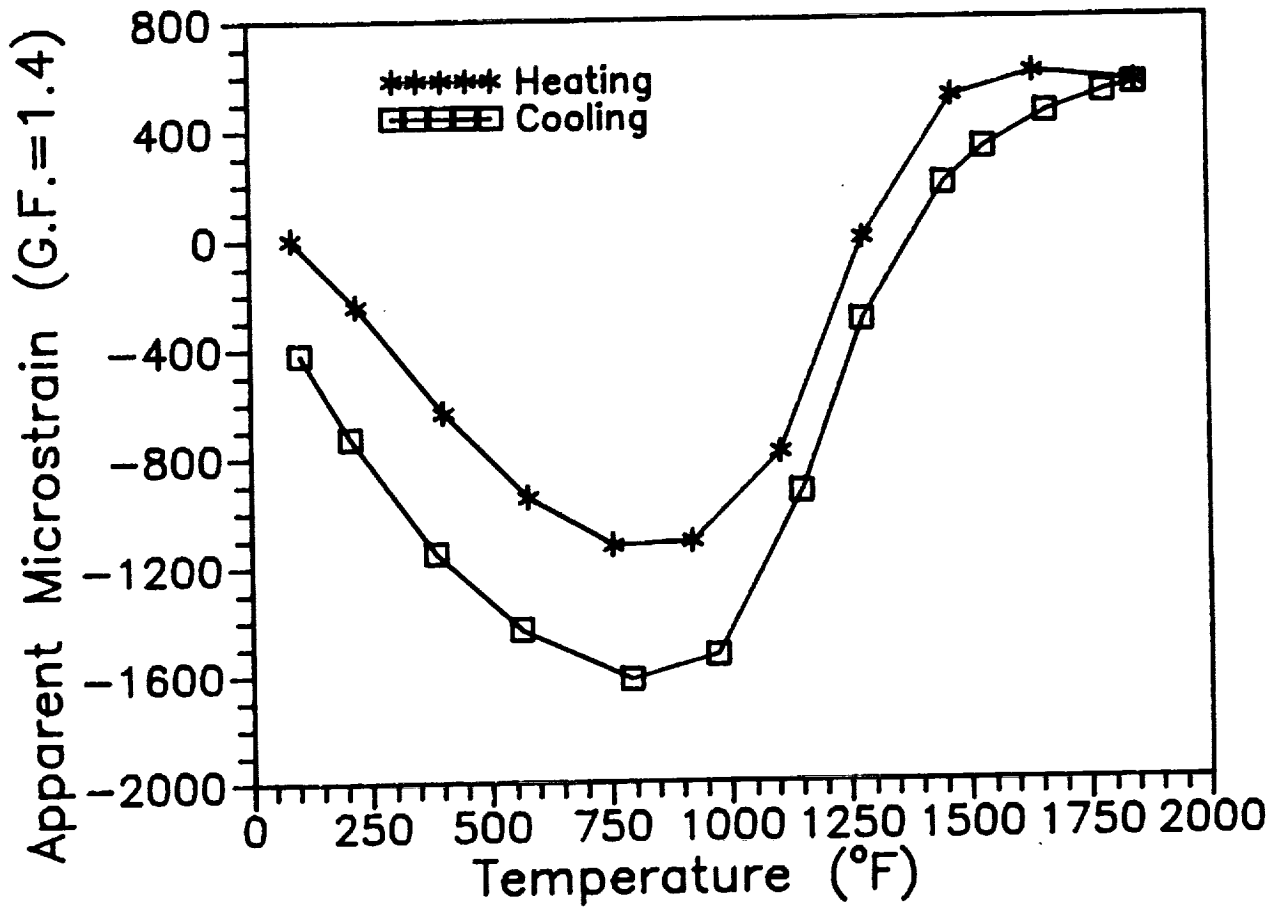


Fig. 12. Apparent strain vs temperature characteristics of a thin film gage during heat-up and cool-down cycles to 1850°F. The gage is fabricated on an alumina cantilever beam. Values of apparent strain of the gage are calculated assuming a constant gage factor of 1.4.

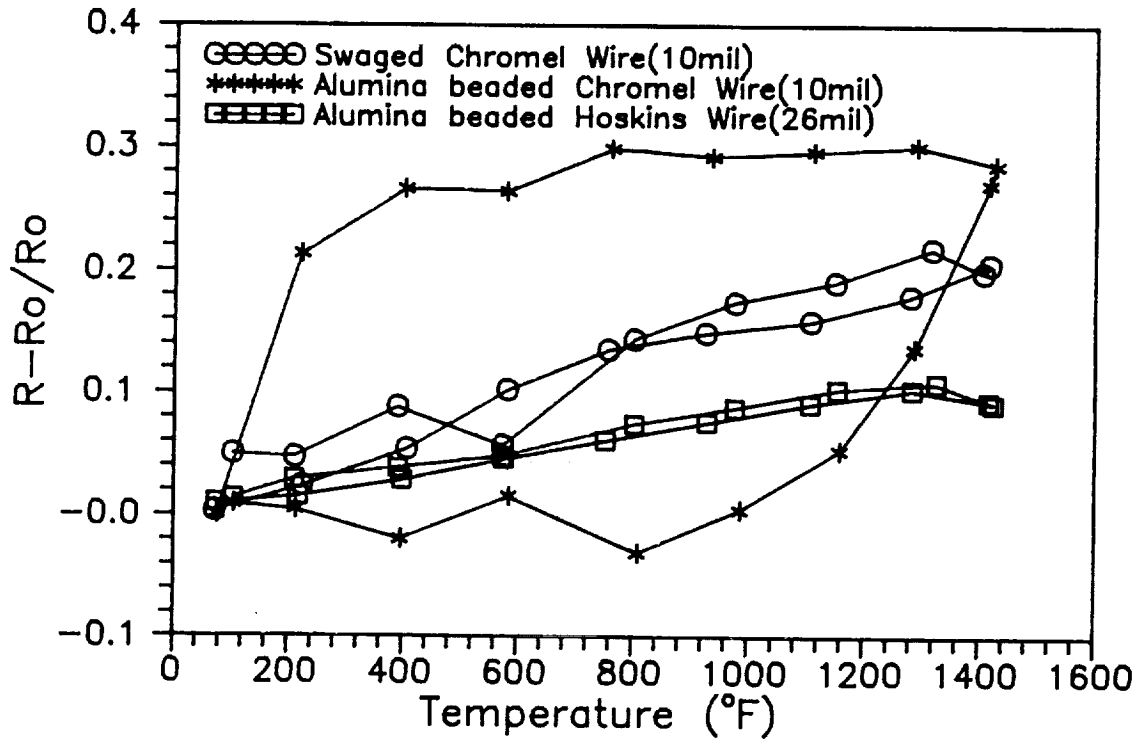


Fig. A1. The change in resistance vs temperature of various lead wires (3mil PdCr gage lead wire with various extended lead wires). Swaged chromel wire has a better oxidation resistance than the alumina beaded chromel wire.

### PRECALIBRATION PROCESS

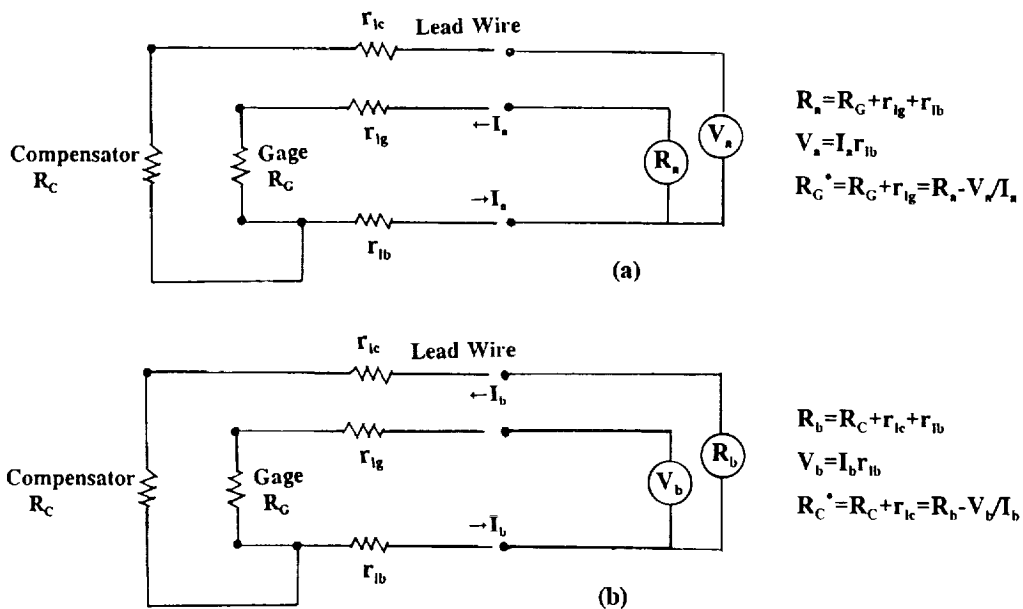
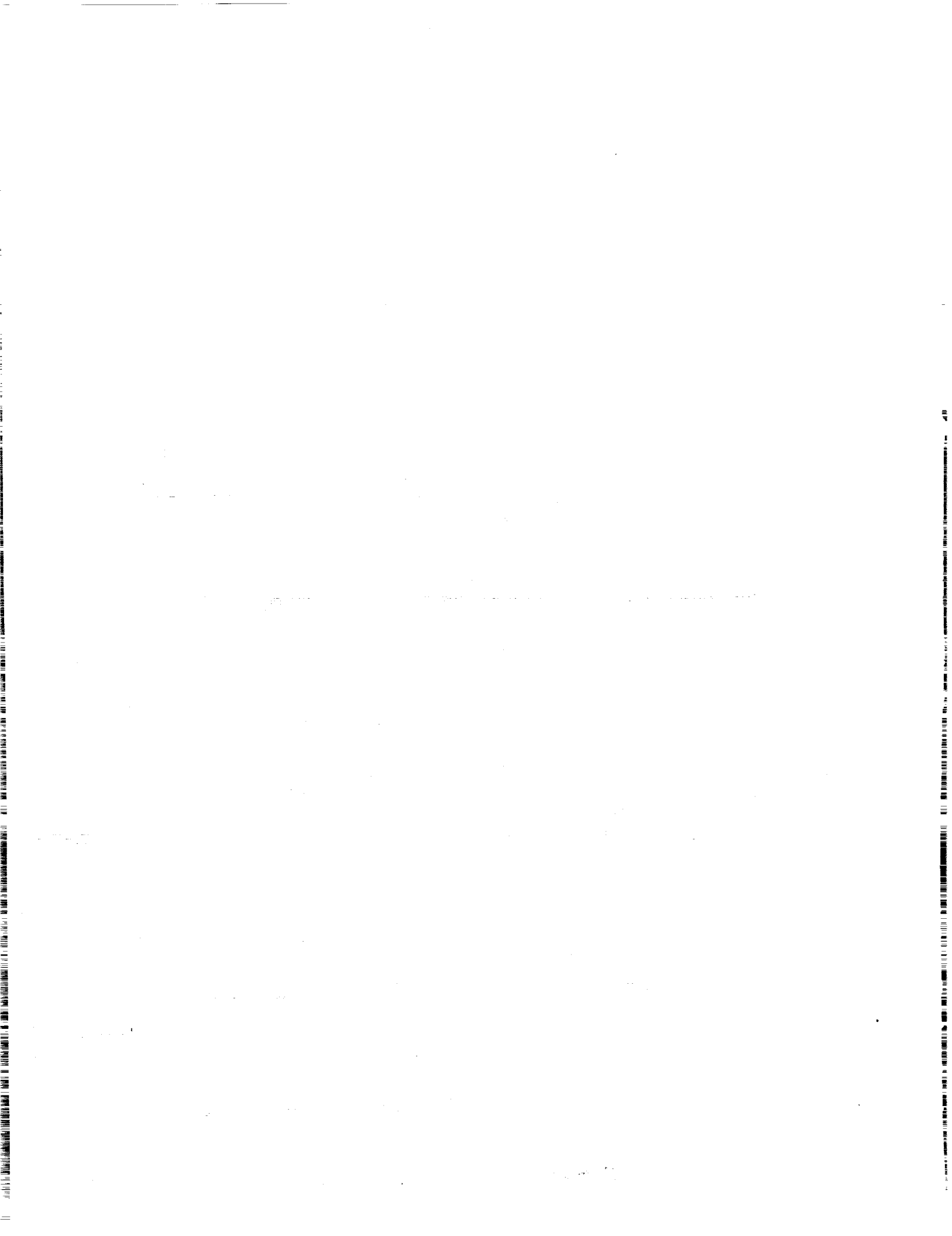


Fig. B1. The electrical circuits used in the pre-calibration process.



# HIGH TEMPERATURE STRAIN GAGE APPARENT STRAIN COMPENSATION

H. K. Holmes, T. C. Moore, Sr.  
NASA Langley Research Center  
Hampton, Virginia

## INTRODUCTION

Once an installed strain gage is connected to a strain indicating device and the instrument balanced, a subsequent change in temperature of the gage installation will generally produce a resistance change in the gage. This purely temperature-induced resistance change will be registered by the strain indicating device as strain and is referred to (in the U.S.) as *apparent strain* to distinguish it from strain in the test part due to applied stress.<sup>1</sup> Apparent strain is caused by two concurrent and algebraically additive effects in the strain gage installation. First, the electrical resistivity of the gage itself is temperature dependent and, secondly, differential thermal expansion between the gage and the substrate material upon which the gage is bonded creates an apparent mechanical strain. Mathematically, the electrical output of an initially balanced Wheatstone Bridge strain indicator is proportional to the strain experienced by the component resistive strain gages. The strain, as seen by any gage, can be expressed as follows:

$$\begin{aligned}\epsilon_{IS} &= \epsilon_{MS} + \epsilon_{App} \\ &= \epsilon_{MS} + \left[ \frac{\beta_G(T)}{F} + (\alpha_S(T, PO) - \alpha_G(T)) \right] \Delta T\end{aligned}$$

$\epsilon_{IS}$	=	Indicated Strain
$\epsilon_{MS}$	=	Mechanical Strain
$\epsilon_{App}$	=	Apparent Strain
$\beta_G(T)$	=	Resistance Change of Strain Gage due to Temperature
F	=	Gage Factor of the Strain Gage Used
$\alpha_S(T, PO)$	=	Coefficient of Expansion of Substrate Material as a Function of Temperature and Substrate Ply Orientation
$\alpha_G(T)$	=	Coefficient of Expansion of Gage as a Function of Temperature
$\Delta T$	=	Temperature Change from an Arbitrary Initial Reference Temperature

The apparent strain, particularly for most currently available high temperature gages, is highly nonlinear, generally non-repeatable, and can exceed the desired mechanical strain by several orders of magnitude. To reduce the apparent strain to an absolute minimum requires the

<sup>1</sup> Technical Note, TN-504, Strain Gage Temperature Effects, Measurement Group, Inc., P.O. Box 27777, Raleigh, North Carolina 27611; 1983.

practitioner to use all the "tricks" in the book and to employ compensation techniques which are highly application-specific.

The most desirable solution for accommodating apparent strain is to employ a gage that has a linear apparent strain relationship as a function of temperature and then employ any additional compensation in the same or adjacent leg of the Wheatstone bridge as required. This installation will most probably require three lead wires from each gage location plus the addition of a precise, probably non-standard, resistance connected in series with the compensation element in order to balance the bridge. If the gage resistance change with temperature is highly nonlinear, one generally ends up only with "end point" compensation, i.e., the bridge is compensated or balanced only at the temperature for which the compensation resistance was determined. Another highly desirable technique for apparent strain compensation is to employ two identical gages with identical mounting procedures which are connected in a "half bridge" configuration where both gages see the same thermal environment but only one experiences a mechanical strain input. Their connection in adjacent arms of the bridge will then balance the thermally induced apparent strains and, in principle, only the mechanical strain remains. Two approaches that implement this latter technique are the subject of this report.

## CO-LOCATED HALF-BRIDGE COMPENSATION TECHNIQUE

### Description

Several popular high temperature strain gages employ various alloys of iron, chromium and aluminum (FeCrAl) whose "apparent strain" output, due to resistance change versus temperature, is the dominant output for these type strain gages. These gages have been typically installed as one arm of a Wheatstone bridge, and when the bonded strain gage is strained (elongated or compressed) the gage resistance changes as a function of the strain. This strain is then converted into an output signal representative of the magnitude of the strain. Unfortunately, the indicated output due to apparent strain resulting from a temperature change is usually far greater than the resistance change generated due to mechanical strains. Additionally, the resistance change is non-linear, non-repeatable, and drifts with time at elevated temperatures.

The compensation concept to be described first is relatively straightforward. If the resistance in adjacent arms of a Wheatstone bridge remains equal to each other, the output remains nulled. Therefore, if a second strain gage, with an identical thermal coefficient of resistance as that of the gage to be strained, was placed in an adjacent arm of the bridge circuit, the output signal would remain nulled even when temperature changes occurred if no mechanical strain was present. An additional condition is that both gages be subjected to the same rate of temperature change. The condition that the second (compensating) strain gage be non-responsive to mechanical strain inputs while subjected to the same temperature environment as the active gage is achieved through installation procedures.

First, an electrically insulating layer of  $Al_2O_3$ , approximately three mils thick and of sufficient area to contain the active and the compensating gage, is applied to the surface to be gaged. The gages are placed on the  $Al_2O_3$  substrate and the active gage is bonded to the substrate using a flame spray system while the compensating gage is only "tack-bonded" at a few points, arranged so that it cannot respond to mechanical strains. Figure 1 is a photograph showing the active gage partially bonded and the compensating gage tack-bonded. This is the only bonding that the compensating gage will receive. Figure 2 shows the active and compensating gage after all flame spraying is completed. Note that the active gage is completely covered while the compensating gage is exposed except for the tack-bonded areas.

ORIGINAL PAGE  
BLACK AND WHITE PHOTOGRAPH

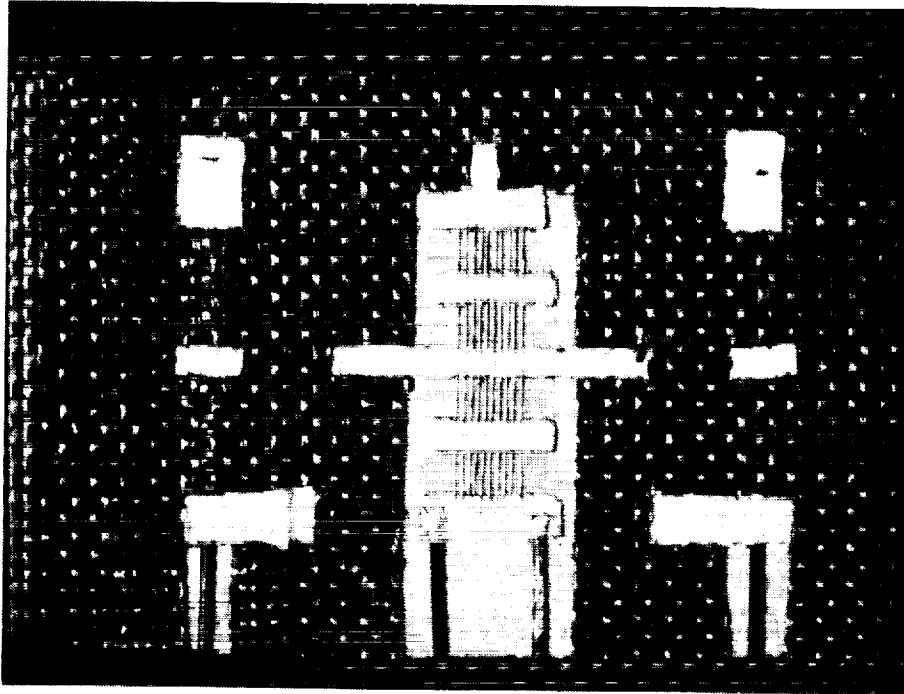


Figure 1. Gages and lead wires tacked in place and active gage ready for attachment.

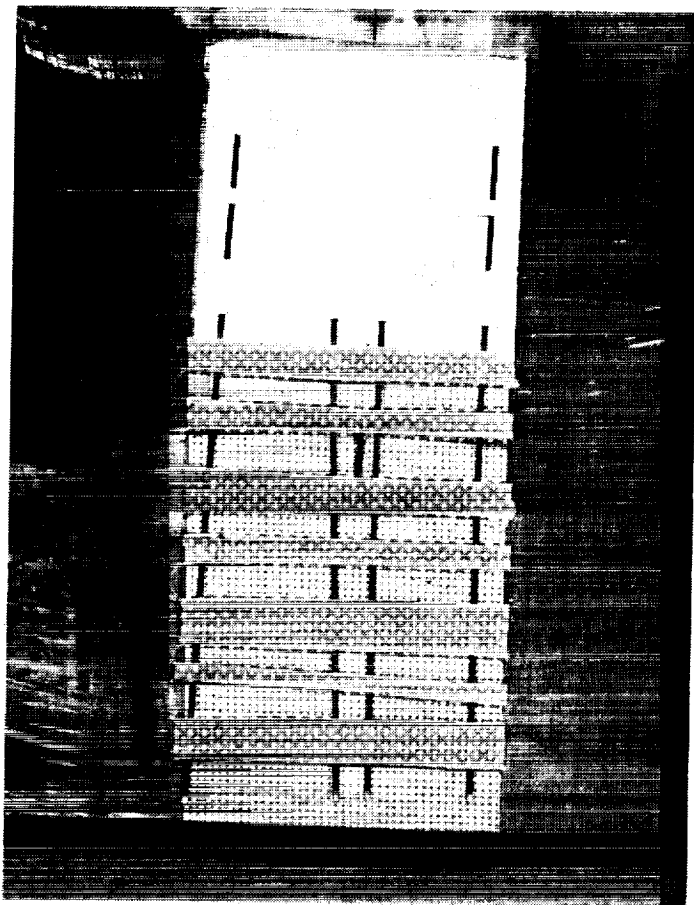


Figure 2. Active gage bonded and compensating gage exposed.

The next step requires the installation of a "thermal blanket" which attempts to maintain isothermal conditions for both gages. The thermal blanket is a sheet of a high temperature woven ceramic cloth which has the top (exposed) surface flame sprayed with a coating of  $Al_2O_3$  while the underside remains soft. This blanket is cut to shape, placed over the active and compensating gages, and then secured to the test article surface either by strapping and spotwelding or bonding with a high temperature ceramic cement. The thermal blanket, shown in figure 3, is ready for installation. Because the inactive (compensating) gage is on the same substrate material and at the same relative height above the test surface as the active gage, and because the surface coating of the thermal blanket cover is of the same material as that used in bonding the active gage, both gages are subjected to the same rate of temperature change even when moderately high heat fluxes are encountered. A photograph of the LaRC developed "compensated high temperature strain gage" is shown wired and ready for testing in figure 4.

### Test Results and Discussion (Co-located Compensation Technique)

Figure 5 shows the typical apparent strains generated by several commercially available high temperature strain gages and compare the apparent strain with two types of compensated high temperature gages. The commercially available single element gages reveal apparent strains 20 to 30 times the magnitude of the compensated gages. The Palladium-Chrome (Pd.-Cr.) compensated gage does an excellent job of correcting for apparent strain and is under development at the NASA Lewis Research Center. It does, however, require a prestabilization period of considerable length at high temperature in order to obtain repeatable apparent strain correction as shown in the plot. The Langley Research Center developed gage requires no prestabilization, and the initial run to  $540^{\circ}C$  generated very small apparent strains and a small zero shift during the cool-down portion of the run as seen in the figure. The dotted line shown for the Langley gage was the second apparent strain run for the gage, but the first excursion extended to  $800^{\circ}C$ . Note the repeatability of the apparent strain with the first excursion to 800 degrees C. Figure 6 shows subsequent apparent strain runs up to  $815^{\circ}C$  ( $1500^{\circ}F$ ) and, again, excellent repeatability was observed as well as small total apparent strains at  $1500^{\circ}F$ .

Beta 21S titanium matrix composite (TMC) is a material of great interest to the NASP program and will require high temperature strain measurements. The Langley developed compensated gage has been installed on several McDonnell Douglas furnished Beta 21S TMC coupons, and test results have been very encouraging. Even though the coefficient of expansion of the compensated gage alloy is not matched to TMC, the gage managed to provide relatively small apparent strains from room temperature to  $1500^{\circ}F$ . More importantly, all of the gages tested generated virtually the same apparent strain slope for all of the coupons tested. Also, exceedingly important for structural testing, the apparent strain curve obtained during the first temperature excursion exhibits very small zero shifts. This allows the test engineer to obtain static strain data during the first heat-up of the test article. Large zero shifts during the first cycle cool-down are routine for all of the commercially available single element high temperature gages.

Figure 7 is a plot comparing the Langley Chinese alloy compensated gage with a popular single element high temperature gage (type NZ-2104). As shown, the Langley gage's apparent strain curve is virtually linear with no zero shift during the cool-down phase of the temperature run, while the NZ gage has a terribly non-linear apparent strain curve and a large zero shift during the cool-down to room temperature. Also, the gage generates a much larger total apparent strain than does the LaRC gage. Three apparent strain runs to  $1200^{\circ}F$  were conducted on this coupon and the Langley gage generated 3805 micro-strain at  $1200^{\circ}F$ , within 1.5 percent, for all three runs. The NZ gage generated strains that varied between 4815 and 6360 micro-strain with zero shifts as large as 1990 micro-strain. The poor apparent strain performance of the NZ gage is typical of high temperature strain gages when no prestabilization of the gage at elevated temperature is allowed prior to testing.



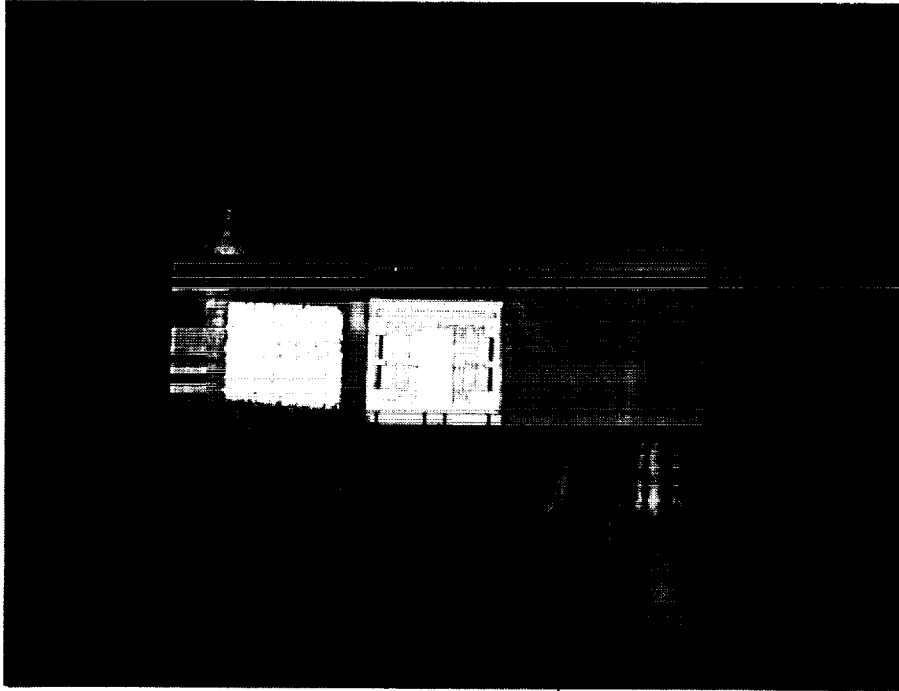


Figure 3. Nextel blanket with Alumina overcoating ready for installation.

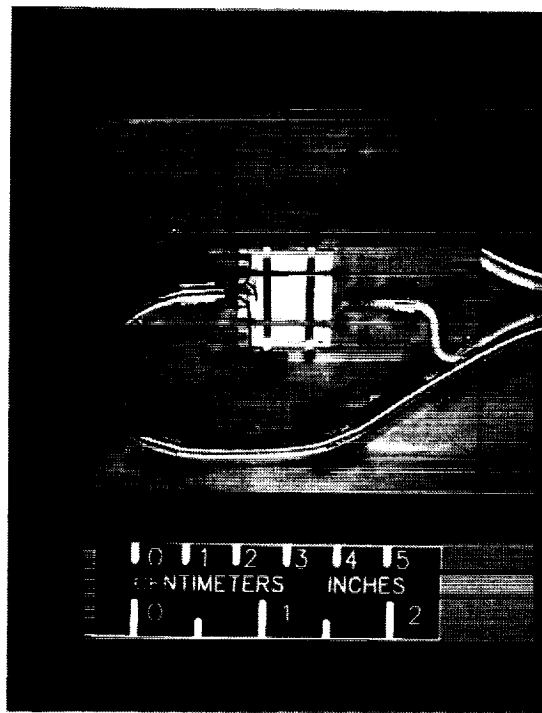


Figure 4. Final assembly. Nextel blanket secured and lead wires attached.

## THERMAL OUTPUT COMPARISONS UNCOMPENSATED VS COMPENSATED

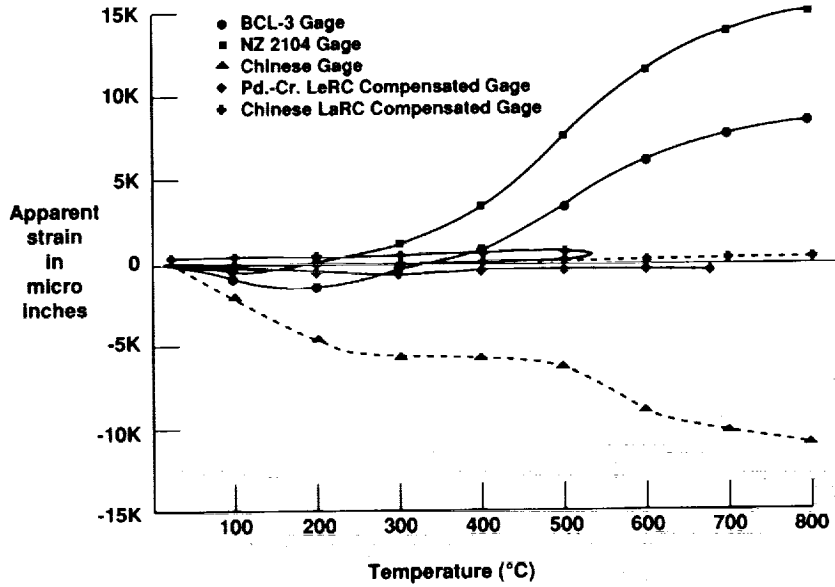


Figure 5. Apparent strain from several gages compared.

## THREE CONSECUTIVE APPARENT STRAIN RUNS TO 1500°F CHINESE ALLOY GAGES

One Active Gage, One Compensation Gage Wired  
Together To Form A Half Bridge

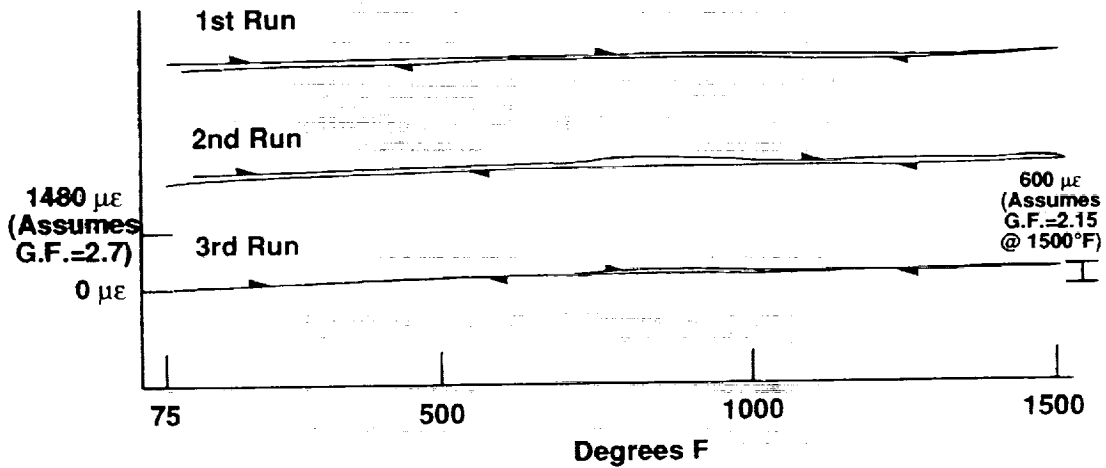


Figure 6. Three apparent strain runs to 1500°F on IN-750 test beams.

LaRC APPARENT STRAIN TEST  
MDLLSS TMC COUPON APPARENT STRAIN TEST

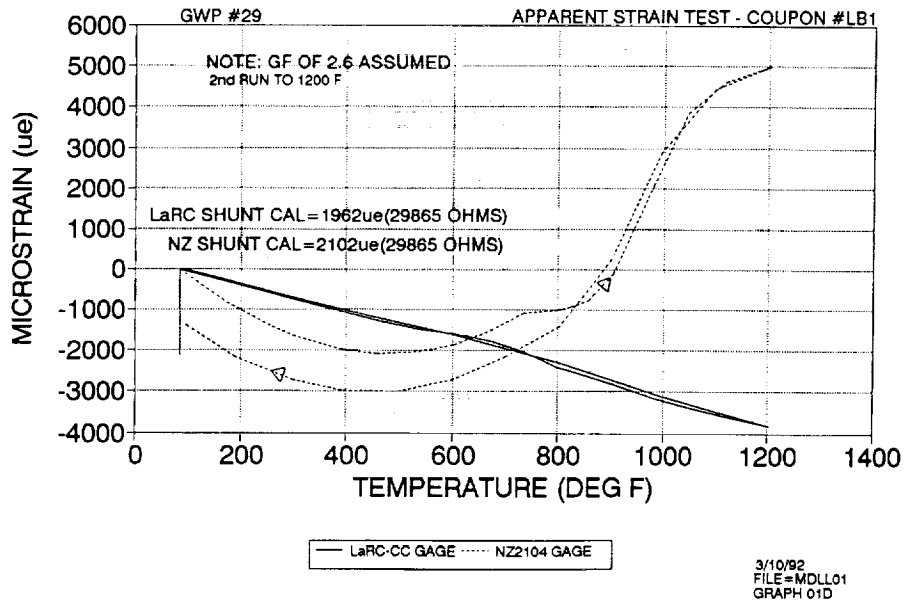


Figure 7. Apparent strain of compensated gage and NZ-2104 gage on TMC coupon.

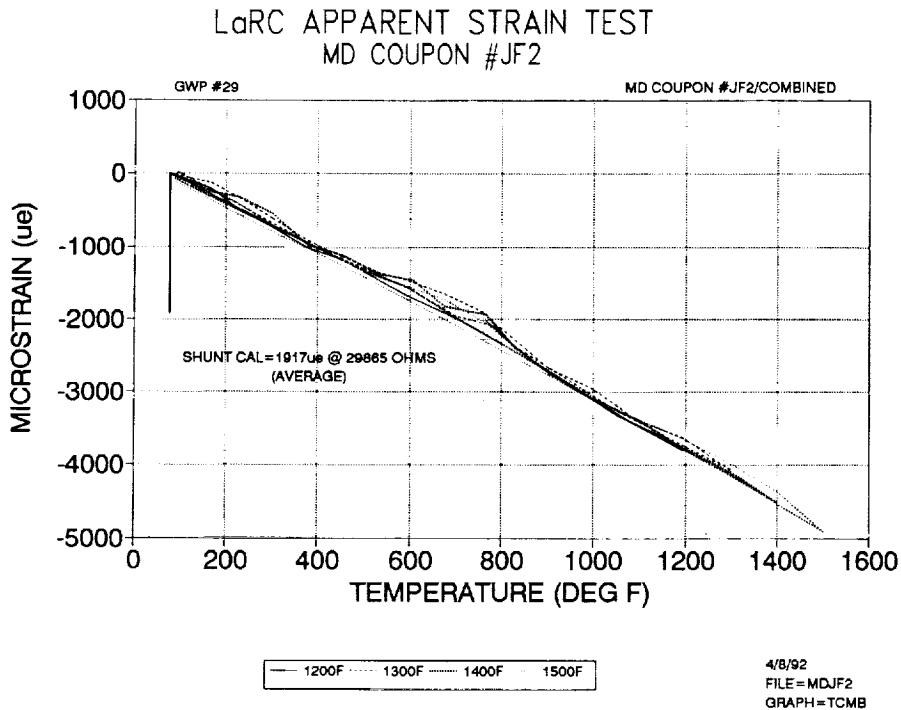


Figure 8. Repetitive apparent strain runs to different T<sub>max</sub> on 2<sup>nd</sup> TMC coupon.

## HIGH TEMPERATURE APPARENT STRAIN COMPENSATION SYSTEM

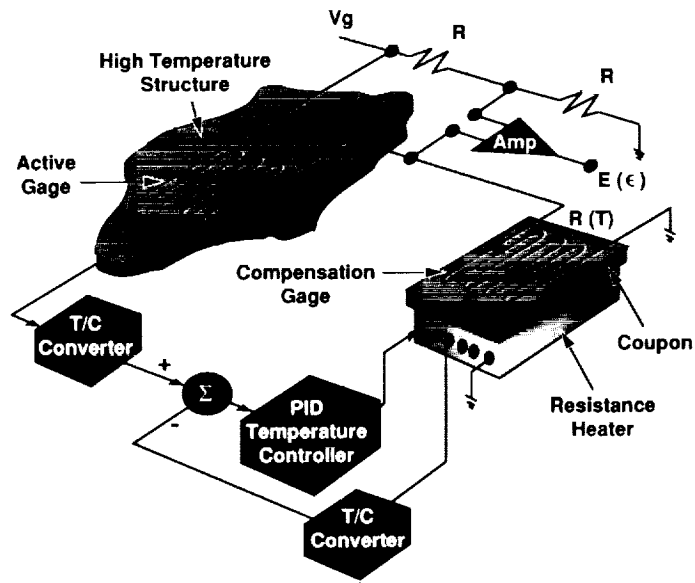


Figure 9. Schematic of remote compensation concept.

Test results from another LaRC compensated gage on a second TMC coupon were also encouraging. A series of apparent strains were conducted with the plots shown in figure 8. Shown is the first temperature excursion to each of four temperatures and the cool-down to room temperature. Note that the slope is virtually the same for all four temperatures, and that zero shifts at room temperature following the cool-down are very small. Even though this second coupon was a 4-ply coupon (the first was a 6-ply), both Langley gages generated 3800 micro-strain at 1200°F on each coupon. This agreement builds confidence in the ability to correct for the thermally induced apparent strain for test articles fabricated of this material.

## REMOTE COMPENSATION TECHNIQUE

### Description

An alternative, somewhat complicated, yet feasible approach to compensating high temperature strain gages is the subject of the balance of this report and is illustrated in figure 9. Conceptually stated, a high temperature strain gage and a thermocouple, located in the closest proximity to the gage, are attached to the structure of interest. The Wheatstone Bridge completion resistors, including the adjacent bridge element, are housed in the signal conditioning and power supply electronics unit. The adjacent arm of the bridge consists of a matched, high-temperature strain gage attached to a coupon having identical material properties as the main structure and similarly oriented with respect to ply orientation, and includes a thermocouple located in the same proximity to the compensation or dummy gage as the first is to the active gage.

Next, a controllable heater element attached to the coupon maintains the temperature of the coupon identical with that of the structure under investigation as measured by the respective thermocouples. With this approach, the apparent strain due to temperature is compensated for by utilizing a "matched" (same temperature coefficient of resistance) gage, and the apparent strain due to differential expansion is compensated by utilizing the same substrate material, ply orientation and mounting techniques. By controlling the temperature of the adjacent bridge element with a PID (proportional plus integral plus derivative) controller, one can maintain temperature control with a zero temperature error.

Figure 10 is a block diagram of a closed loop control system where the reference input is the analog of the measurement gage temperature and the controlled output is an analog of the compensation gage temperature expressed in the z-transform domain. The difference in these two quantities is the error signal which one wants to be zero. The digital controller consists of the necessary sample-and-hold, analog-to-digital conversion, algorithmic processing, amplitude scaling, and digital-to-analog conversion circuitry to control the input to the plant. The plant consists of the necessary heater element, sample material specimen, compensation gage, connecting wiring, mounting materials, and the requisite thermocouple needed to sense the controlled temperature and provide the feedback signal needed to close the loop.

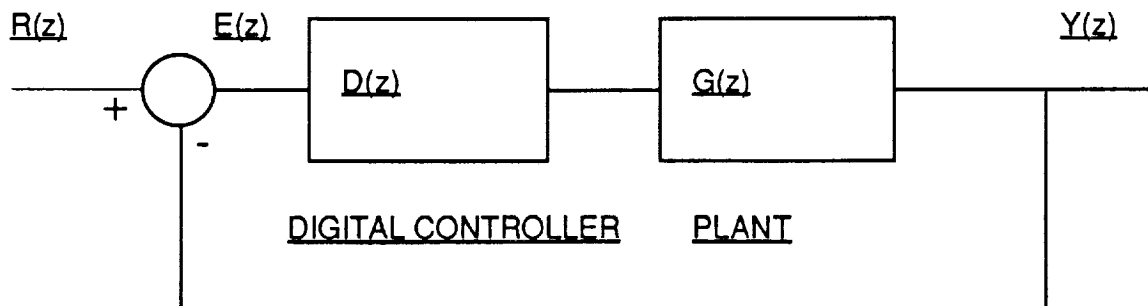


Figure 10 - CONTROL SYSTEM BLOCK DIAGRAM

Figure 11 expands on figure 10 and reveals more detail about the closed loop system as well as details of the Wheatstone bridge which show the measurement resistance  $R(3)$  in one arm of the bridge and the compensation resistor  $R(4)$  in the adjacent arm. Thermocouples provide a measurement of the respective strain gage temperatures and are the reference input and the controlled output signals of the system. The output of the bridge  $E_o$  is dependent only on the mechanical strain seen by the element  $R(3)$  because the temperature induced effects on the measurement gage are compensated by the same temperature induced effects on an identical gage connected in the adjacent bridge arm. Also, from figure 3 one can see the parallel nature of the three control actions, proportional, integral and derivative, which act on the error signal. If proportional control only was used, a non-zero error signal would result because an input is required to maintain an output. Adding the integral control action allows the error signal to be driven to zero, the input necessary to sustain an output is held on the integrator's capacitive feedback element. Derivative control provides a method to control overshoot in the output signal by modifying the rate at which the error signal is allowed to change.

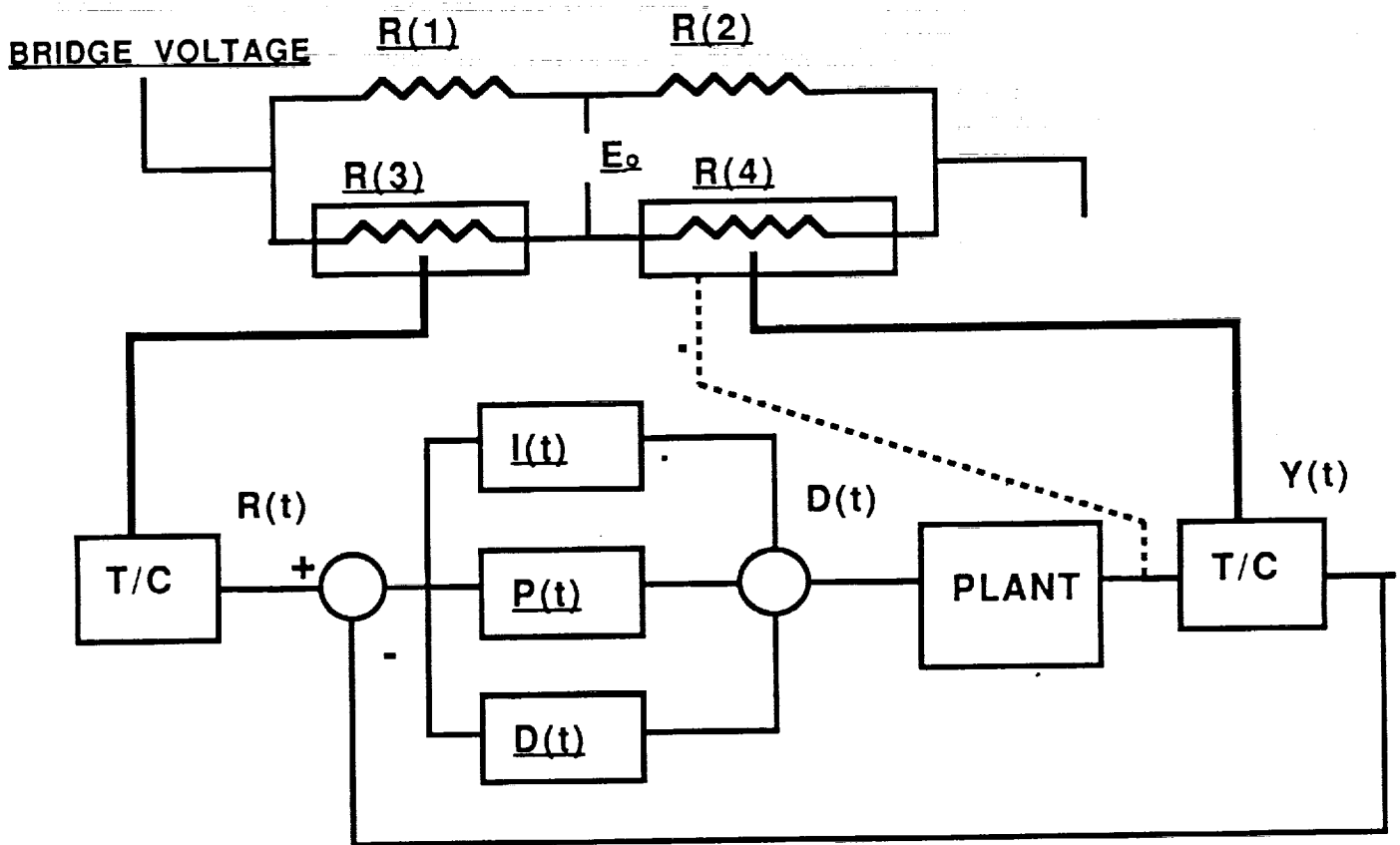


Figure 11 - CONTROL SYSTEM SCHEMATIC INCLUDING EXPANDED DIGITAL CONTROL ELEMENT AND THE MEASUREMENT WHEATSTONE BRIDGE

As can be seen from figures 9 and 10 and the associated text, a concept for compensating a resistance strain gage to eliminate the apparent strain effects resulting from temperature variations has been described. With this method, non-linear effects due to the alloy composition of the gage, coefficient of expansion differences between the gage and substrate and, to a degree, ply orientation of the substrate material have been compensated for by requiring the adjacent bridge arm resistor to exist in an environment controlled to be as close to the measurement gage environment as is possible. With this control, the apparent strain effects are nullified.

## Test Results and Discussion (Remote Compensation Technique)

Preliminary runs were made using NZ-2104 FeCrAl gages, previously utilized in apparent strain studies, mounted on IN-750 test bars. One specimen was placed in a clam-shell oven, destined for use on a tensile test machine, and the second was placed in an aluminum minibox with heat being supplied by a fan driven, electric "paint stripper." The primary purpose of the initial tests was to test the system's ability to control and track temperatures in two separate ovens. The heat-up rate in the clam-shell oven was set to approximately 5°F per minute, and it was found that the controlled specimen tracked the reference specimen within 2 to 2.5°F in both the heat-up and the cool-down phases. The controlled specimen's enclosure was poorly insulated so that control in the cool-down mode was primarily the addition of less heat input in response to a slowly decreasing reference temperature.

During these trials, the two gages were connected in a quarter bridge configuration, and apparent strains showed similar but disparate behavior. When connected in a half-bridge configuration, the apparent strain output was quite low but not as low as was expected. It was hypothesized that the two specimens had not been cycled to the same upper temperatures and thus the metallurgical state of the two gages was dissimilar. The two specimens were then placed in an oven and thermally soaked at 1300°F for two hours.

Figure 12 shows the apparent strain obtained from the two gages in separate ovens but connected in a quarter bridge configuration. One can see the similarity but some definite disparity. The gages were then connected in a half bridge electrical configuration and a test to 550°C conducted with the results as shown in figure 13. It is seen that the residual, or not compensable, apparent strain is approximately 300 micro-strain where the uncompensated, single NZ-2104 gage at these temperatures might have on the order of 4000 to 6000 "apparent" micro strain output.

## CONCLUSIONS

Because the compensated half-bridge approach can be applied at most locations where a quarter-bridge gage has historically been utilized, it should see wide use in high temperature test structures, especially where static strain measurements are a must. The gaging concept has many advantages which included the ability to obtain static strain data during the first temperature excursion due to the gage's half-bridge configuration which cancels the non-linearity and non-repeatability of a single active gage; the ability to minimize the thermal output throughout the temperature excursion as opposed to nulling at one temperature only; and, because of the insensitivity of the inactive gage to mechanical strains, the sensitivity (gage factor) of the bridge circuit will not be compromised. Finally, the precipitous slope and the non-repeatability of the thermal outputs of "hi-temperature" strain gages cause the accuracy of the data to be in question.

The ability to virtually eliminate the thermal output using the active/inactive gage method should dramatically improve data accuracy while alleviating the need to accurately measure the temperature of a single gage when attempting to use a quarter-bridge strain gage circuit. Additionally, the remotely located half-bridge compensation method has the potential to compensate thermal expansion disparities as well as the resistive component. This method has a second possible attribute of being able to selectively switch several active gages to connect with one completion and controlled gage thus obtaining a relatively higher "apparent strain" compensation with less expensive or specialized gages. In this procedure, the task is now to develop a more sophisticated remotely controlled oven so fast transient response can be achieved.

It is apparent from the material presented in this report that two technically viable, straightforward approaches to eliminating or minimizing the effects of "apparent strain" in high temperature strain measurements have been demonstrated.

## APPARENT STRAIN COMPEN. SYSTEM APP. STRAINS FOR INDIVIDUAL GAGES

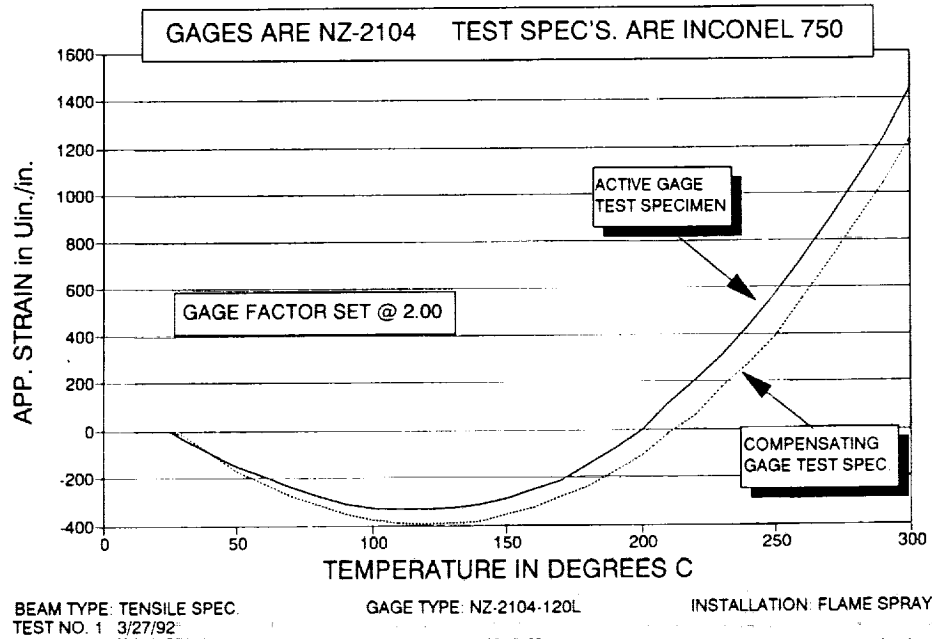


**Figure 12. Apparent strain of two NZ-2104 on Individual IN-750 test beams.**

## APPARENT STRAIN COMPEN. SYSTEM APP. STRAIN AS A HALF-BRIDGE

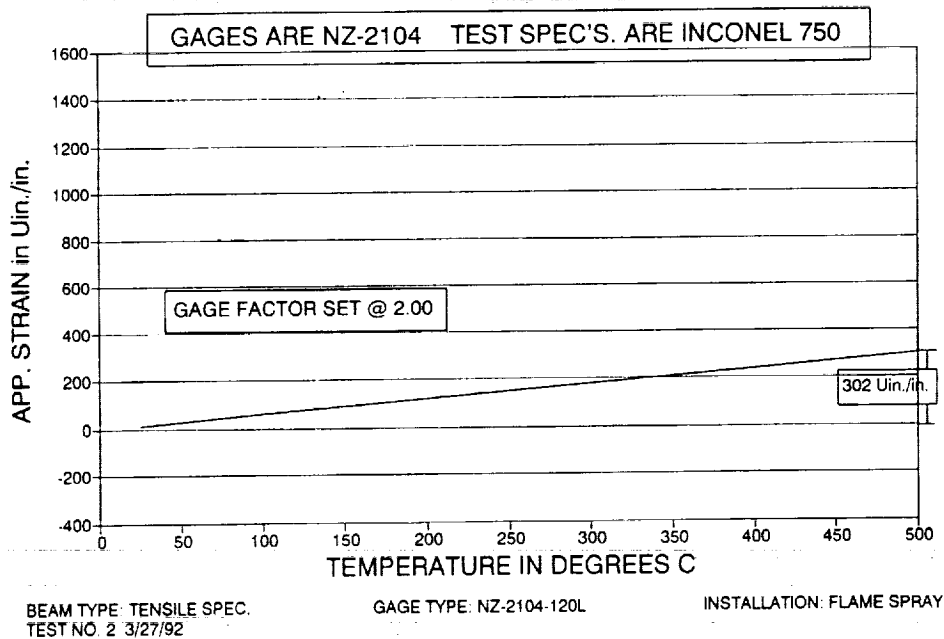


**Figure 13. Apparent strain with the two NZ-2104 gages connected in a half-bridge configuration but in different ovens.**



## Elastic and Plastic Strain Measurement in High Temperature Environment Using Laser Speckle\*

F.P. Chiang

Laboratory for Experimental Mechanics Research  
State University of New York at Stony Brook  
Stony Brook, New York 11794-2300

### SUMMARY

Two laser speckle methods are described to measure strain in high temperature environment and thermal strain caused by high temperature. Both are non-contact, non-destructive and remote sensing techniques that can be automated. The methods have different but overlapping ranges of application with one being more suitable for large plastic deformation.

### INTRODUCTION

In order to measure thermal strain accurately it is paramount that the output of the measuring device not be influenced by temperature. Both mechanical and electrical strain gages require compensation schemes to overcome thermal effect. But compensation becomes difficult if not impossible when temperature extremes or large temperature gradients are involved. The situation becomes worse when the loading is a thermal shock. Optical techniques such as moire or moire interferometry require that a grating or grid be attached to the specimen surface over an area. Although it has been shown [1] that by appropriately mixing a certain ingredient into the photoresist, it can sustain temperatures up to about 560°C, at higher temperatures the grating or grid tends to disintegrate. Holographic interferometry has also been used for measuring thermal strain. However, since it is not easy to apply it to measuring in-plane strain, its application is limited.

In this paper we describe two non-contact, non-destructive and remote sensing methods of thermal strain measurement using laser speckles. In principle thermal strain up to the melting point can be measured without the aid of an auxiliary device. Other than the impingement of photons from a laser beam nothing touches the specimen. Recording can be done remotely using a telephoto lens and data analysis can be computerized.

### LASER SPECKLE TECHNIQUES OF STRAIN ANALYSIS

Two laser speckle techniques are described in this article. Each has its own range of applicability and the two ranges overlap and complement each other. The first technique is the so-called speckle photography or one beam laser speckle interferometry [2,3]. When an expanded coherent laser beam illuminates a specimen surface which is optically rough (i.e.) its RMS roughness is much larger than

\*Work supported by Army Research Office, Engineering Science Division Grant No. DAAL0388K0033

the wavelength of the light from the laser), multiple reflection (scattering) occurs. The reflected wavelets, being still coherent, mutually interfere to form a random interference pattern called speckles. An example of such a speckle pattern after magnification is shown in Fig.1. These are the equivalent optical displacement "gages" that are used for thermal strain measurement. Under the condition of small strain and small displacement these speckles move as if they were physically attached to the specimen surface. When they are recorded on a photographic film via a camera before and after the specimen's deformation, the superimposed speckle pattern is called a double exposure specklegram. The specklegram may be processed either in a pointwise or a full field manner. For pointwise processing, a thin laser beam impinges upon the specklegram as shown in Fig.2. Its far field diffraction pattern is a circular halo modulated by a series of uniformly distributed fringes. It can be shown [3] that the in-plane displacement vector at the probed point can be expressed as follows:

$$\vec{d} = \frac{\lambda L}{S} \vec{i} \quad (1)$$

where  $\vec{i}$  is a unit vector perpendicular to the fringes,  $L$  the distance of the screen from the specklegram where the halo is received,  $\lambda$  the wavelength of the laser light that is used to probe the specklegram and  $S$  is the fringe spacing.

The full field processing technique uses an optical bench as shown in Fig.3. It can be shown [3] that the intensity of the diffraction spectrum displayed at the transformed plane of the first field lens is given by the following equation:

$$I(r_1, r_2) = K \cos^2 k \frac{\vec{d} \cdot \vec{r}}{L} I_s(r_1, r_2) \quad (2)$$

where  $I_s(r_1, r_2)$  is the diffraction pattern of a single exposure specklegram with  $(r_1, r_2)$  being the coordinates of the spectrum plane.  $k(= 2\pi/\lambda)$  is the wave number;  $\vec{d}$  is the displacement vector at a point;  $\vec{r}$  is a position vector at the spectrum plane;  $K$  is a proportional constant and  $L$  is the distance between the specklegram and the spectrum plane. Alternating bright and dark fringes are observed when the following condition is met:

$$\vec{d} \cdot \vec{r} = n\lambda L, \quad n = 0, \pm 1, \pm 2, \dots \quad (3)$$

By placing an aperture at  $\vec{r}$  and reconstructing the specimen image through the second field lens, isothetic (contours of equal displacement component) fringes similar to moire fringes are observed covering the specimen surface and they are governed by the following equation:

$$u \equiv d_x = n\lambda L/|\vec{r}_x| = nP_x, \quad n = 0, \pm 1, \pm 2, \dots \quad (4)$$

$$v \equiv d_y = n\lambda L/|\vec{r}_y| = nP_y, \quad n = 0, \pm 1, \pm 2, \dots \quad (5)$$

where  $\vec{r}_x$  and  $\vec{r}_y$  are the position vectors of the apertures sequentially located along  $r_1$  and  $r_2$  axes, respectively.  $u$  and  $v$  are the displacement components along  $x$  and  $y$  directions, respectively; and  $P_x(= \lambda L/|\vec{r}_x|)$  and  $P_y(= \lambda L/|\vec{r}_y|)$  are the equivalent "pitches" of moire gratings if they were used for the determination of strain. This technique is suitable only for the determination of small strains unless single exposure specklegram and mechanical superposition are adopted. The process has been automated as a result of our recent development of CASI (Computer Aided Speckle Interferometry) [4].

The second laser speckle technique is the so-called LSS (Laser Speckle Sensor). A schematic of this method is shown in Fig.4. A narrow laser beam impinges upon a point on the specimen surface where the strain is to be determined. The specimen surface has to be sufficiently smooth such that its scattering speckle field is fairly restricted. Upon deformation the surface roughens resulting in a more spread out speckle pattern whose autocorrelation function can be used as a means of assessing the underlying surface strain. The quantity that is most sensitive to strain is the coefficient of autocorrelation function of the speckle pattern  $g(i, j)$  defined as

$$C_a[g(i, j), \delta_i, \delta_j] = \frac{\sum_{i=1}^M \sum_{j=1}^N g(i, j) \times g[(i - \delta_i), (j - \delta_j)]}{\sum_{i=1}^M \sum_{j=1}^N g^2(i, j)} \quad (6)$$

where  $\delta_i$  and  $\delta_j$  are shifting distances along  $i$  and  $j$  directions, respectively.

One can use light scattering theory to compute the autocorrelation coefficient for various amounts of plastic strain [5]. An example is given in Fig.5 where a three dimensional view of the laser speckle field at three different levels of plastic strain in a copper alloy specimen is depicted. The corresponding experimental result is shown in Fig.6 and the agreement is quite good. The calculated autocorrelation functions for different levels of plastic strain and for different lag lengths are depicted in Figs. 7 and 8, respectively. It should be noted that the lag length is the shifting "distance" between the speckle field and its image that is used in the calculation of autocorrelation. Since the speckle field denotes the spatial frequency (see Figs. 5 and 6) of the light disturbance from the specimen surface, its dimension is in terms of lines/mm. If the area under the curve of the autocorrelation function is integrated and expressed as a function of strain, the relation can be approximated by a straight line as shown in Fig.9. Thus for plastic shear strain  $\gamma \leq 3.5\%$ , the linear relationship between the integrated autocorrelation coefficient and  $\gamma$  is

$$C_1 = 29.2\gamma - 0.04 \quad (7)$$

with an error band of 10%. For higher strains the relation is no longer linear. The broadening of the scattering speckle field becomes saturated at higher strains. In aluminum specimens we have shown that LSS can be effectively used for strains up to 20%.

## APPLICATION TO THERMAL STRAIN PROBLEMS

Fig.10 shows the  $u$  and  $v$  fields' isothetics representing the thermal strain distributions of an aluminum plate at elevated temperatures. The specimen was a quarter inch thick aluminum plate of about  $2' \times 2'$  in size. It was heated at the left lower corner with a propane torch. This place manifests itself as a dark spot in the pictures, especially at higher temperatures. When the torched place became red-hot at the back side, the flame was extinguished and the plate was allowed to cool naturally by thermal convection. A series of double exposure specklegrams were taken. At near the top of the plate a thermal couple was mounted to monitor the temperature change. (The wiring of the thermal couple is vaguely visible as a vertical line near the top of the picture.) The temperature reading at the time of each exposure was recorded and is indicated in the figure. A 1-joule ruby laser ( $\lambda \simeq 0.69 \times 10^{-6}m$ ) was used to record the specklegrams. It was a pulsed laser with a pulse width of about 60 nsec. The laser only gave a single pulse and needed to be repumped after each firing. The time separation between the two pulses and the resulting temperature difference as

indicated on the picture represent the amount of cooling between the exposures. Since the thermal couple was located far away from the heat source, it is reasonable to expect that the temperature near the heat source was much higher than those indicated on the picture.

The double exposure specklegram was Fourier processed using the full-field processing scheme shown in Fig.3. Filtering apertures were placed at two orthogonal directions to yield the  $u$ - and  $v$ -field fringe patterns, respectively. A qualitative way to read the fringe pattern is as follows. Uniform strain is depicted by uniformly spaced fringes whose spacing is inversely proportional to the local average strain. Thus one can see from the pictures that at the earlier stages of thermal relaxation, the strain distribution is quite nonuniform and the strain is higher. As the convection cooling progresses the fringe becomes less dense (indicating smaller strain) and more uniform (indicating lower strain). A quantitative calculation of strain near the point where the thermal couple was located was carried out and the result is depicted in Fig.11. In the course of about 120 seconds the thermal strain has relaxed from about 0.2% to about 0.02%. The difference between horizontal and vertical normal strains also decreases with time as indicated by the gap between the two data points. A comparison of thermal strain at various temperatures for this material using data from an Alcoa Aluminum Handbook was also plotted. Within the range where comparison can be made the agreement is quite good.

Another example is the application of the laser speckle method to the determination of stress-strain relation at high temperature and high heating rate. Fig.12 is the schematic of a medium strain rate testing machine with a resistance heating attachment. Two types of testing were performed [6]. One was a soaking test at elevated temperature and the other a high heating rate test. In both tests the strain rate was kept at  $10^{-1} \text{ sec}^{-1}$ . Strain gages were mounted on the tensile specimen as a comparison with the laser speckle result. The ruby laser was fired once before the beginning of the test and a second time at an appropriate delay time. A camera was used to record the laser illuminated specimen. The double exposure specklegram was pointwisely processed by probing different points along the axial direction within the gage length of the specimen. The resulting Young's fringes represent the absolute displacement at the probed points between the exposures. Since the strain field is homogeneous within the gage length, the difference in displacement between two probed points divided by the separating distance is nothing but the strain. The results of the soaking test and high heating rate test are depicted in Figs.13 and 14, respectively. As can be seen from the data presented, the difference between the strain gage reading and laser speckle result is only a few percent. We have thus demonstrated the reliability of the speckle method at high temperature tests. At extreme temperatures the strain gage may fail but the laser speckle method will not. It can even be applied to specimens giving off a wide spectrum of radiation which may include the radiation of the laser. However, thermal radiation, being incoherent, does not produce speckles. To prevent thermal radiation from fogging the film, a narrow band ( $10\text{\AA}$ ) interference filter can be mounted on the lens of the recording camera to allow only the laser light to enter the camera.

For tests that are not repeatable, single exposure specklegram at different times can be recorded using a continuously pulsing laser (such as a copper vapor laser) and a high speed framing camera. Two single exposure specklegrams at different instances can be mechanically superimposed to yield the difference between the two stages of loading. However, the strain difference between the two cannot be too large, for otherwise decorrelation of the speckle pattern will result.

When either the strain variation or the absolute strain is large, decorrelation of laser speckle tends

to occur. In such a situation the LSS (Laser Speckle Sensor) technique should be used. The advantages of LSS technique are that only single exposure is required and speckle decorrelation will not affect the result. Currently we are in the process of applying LSS to high temperature testing and the results will be reported in the near future.

## References

1. Burch, J.M. and Forno, C., "High resolution moire photography," *Optical Eng* vol. 21(4), 1982, pp.602-614.
2. Khetan, R.P. and Chiang, F.P., "Strain analysis by one-beam laser speckle interferometry I: Single aperture method," *Applied Optics*, vol. 15(9), 1976, pp. 2205-2215.
3. Chiang, F.P., "A family of 2D and 3D experimental stress analysis techniques using laser speckles," *Solid Mechanics Archives*, vol. 3(1), 1978, pp.1-32.
4. Chen, D.J. and Chiang, F.P., "Computer speckle interferometry," *Proc. Society for Experimental Mechanics 1990 Fall Meeting, 1990.*, pp.49-58.
5. Dai, Y.Z. and Chiang, F.P., "Scattering from plastically roughened surfaces and its application to mechanics," *Optical Engineering*, vol. 30(9), 1991, pp.1269-1276.
6. Emslie, J., Green, J., Chou, S.C. and Chiang, F.P., "The application of laser speckle interferometry to measuring strain and strain rate under dynamic conditions," *Proc. Society of Experimental Mechanics, 1990 Fall Meeting, 1990*, pp.59-66.

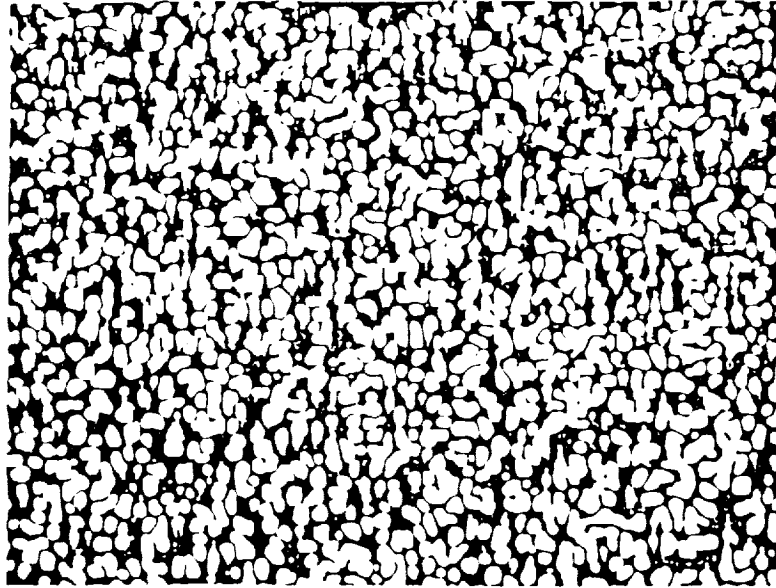


Fig.1 Typical Laser Speckle Pattern

*(Original figures unavailable.)*

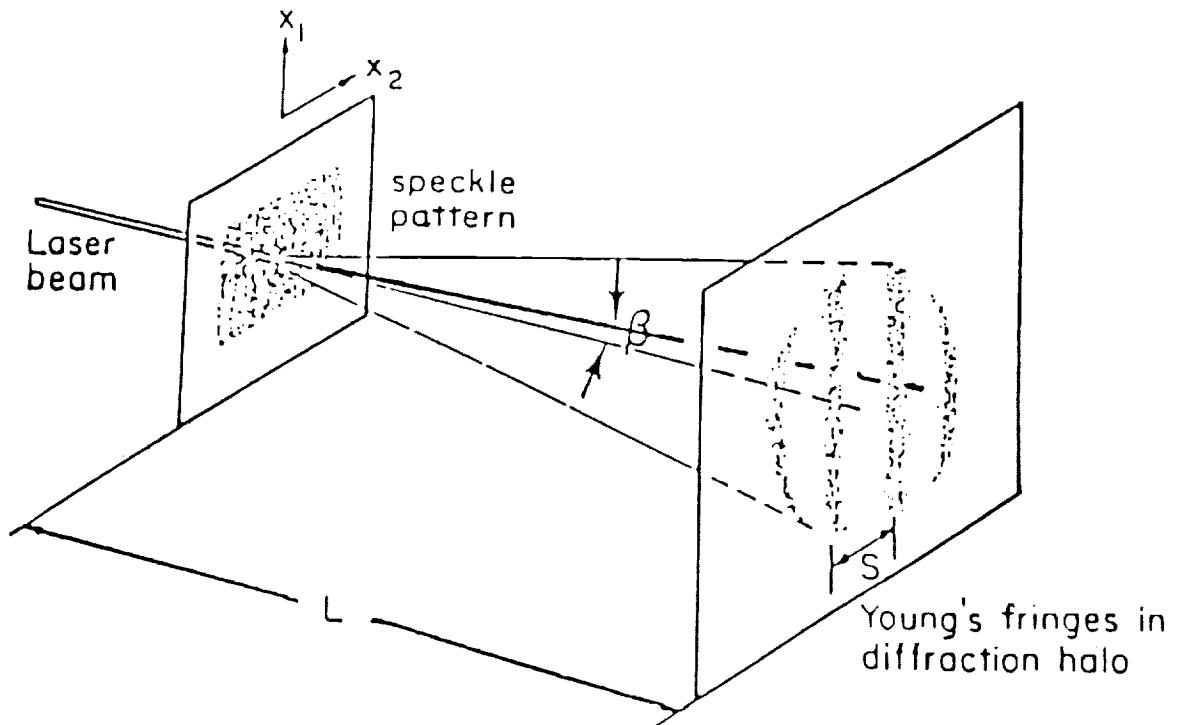


Fig.2 Pointwise Processing of Specklegram

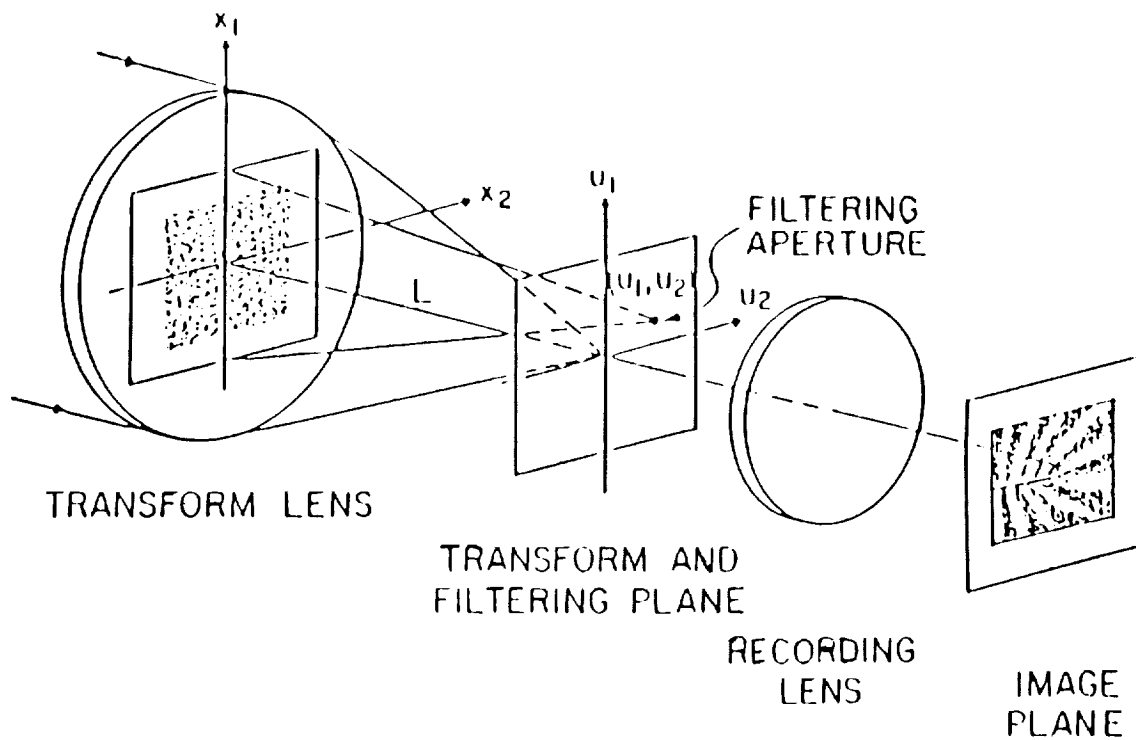


Fig.3 Full-field Processing of Specklegram

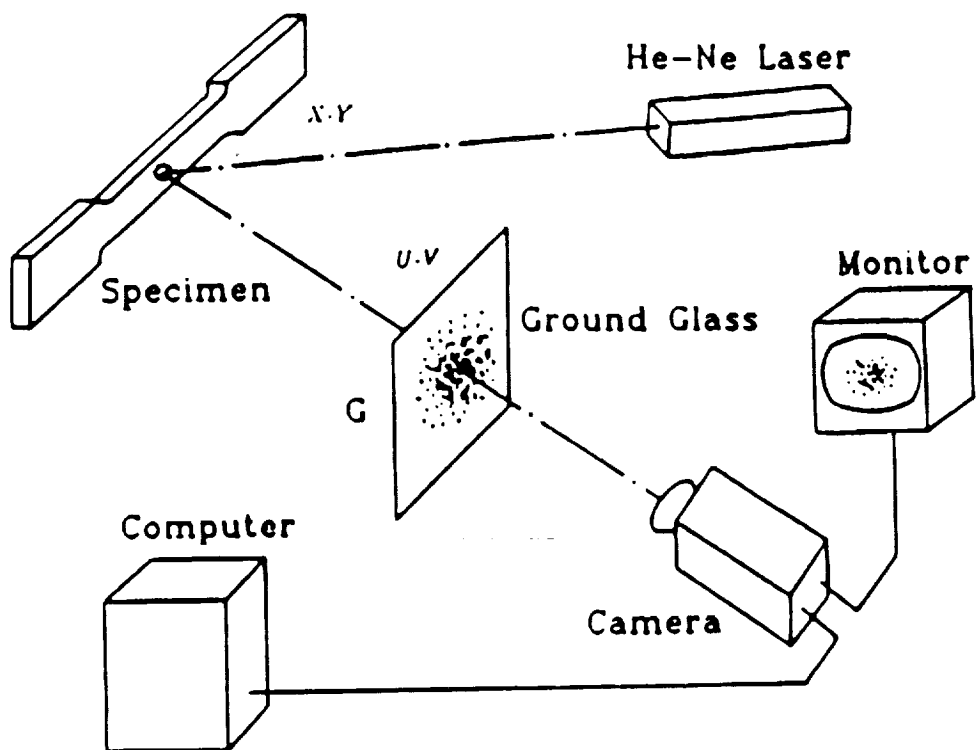


Fig.4 Schematic of LSS (Laser Speckle Sensor)

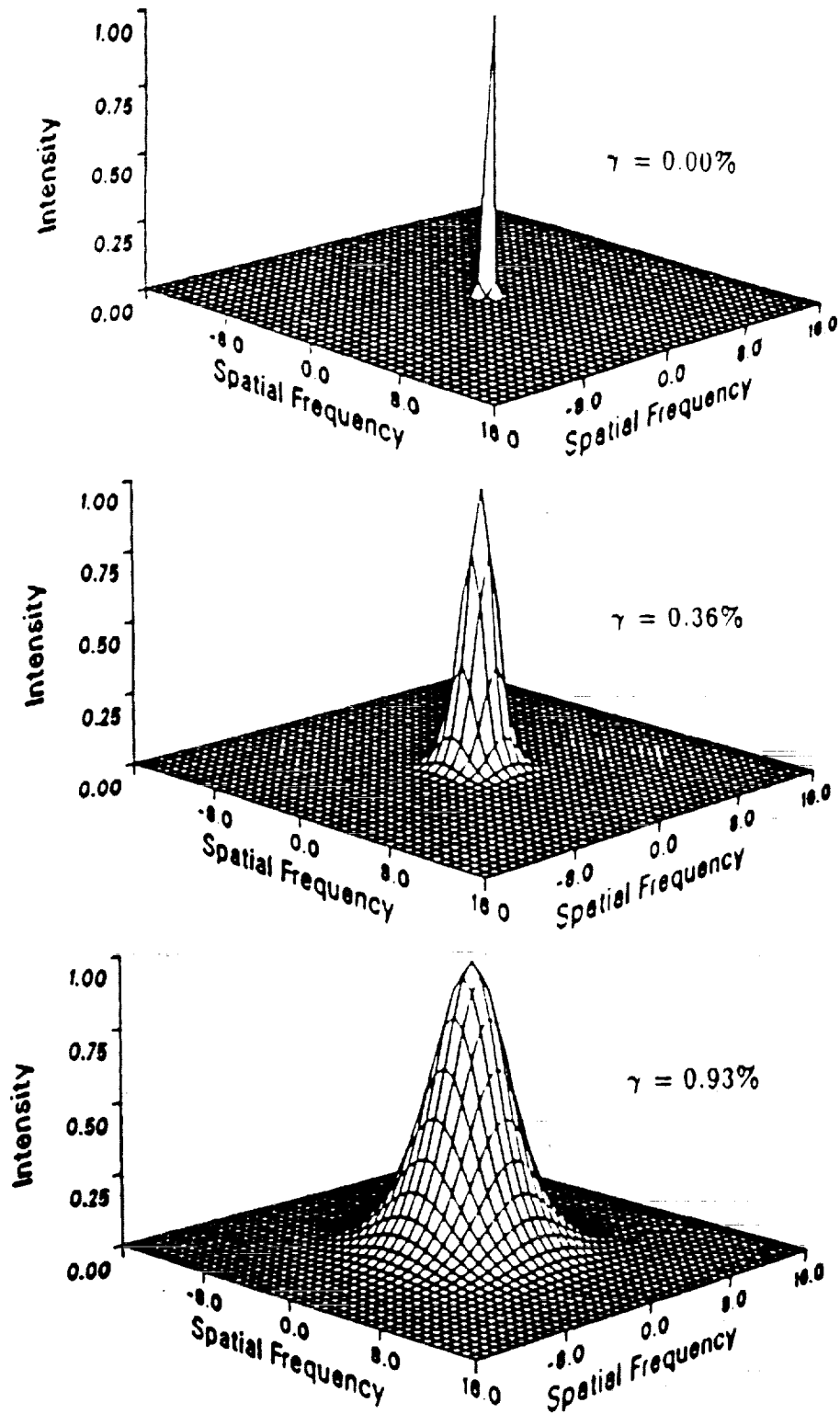


Fig.5 Theoretical Laser Speckle Field at Different Levels of Plastic Strain of a Copper Alloy Specimen



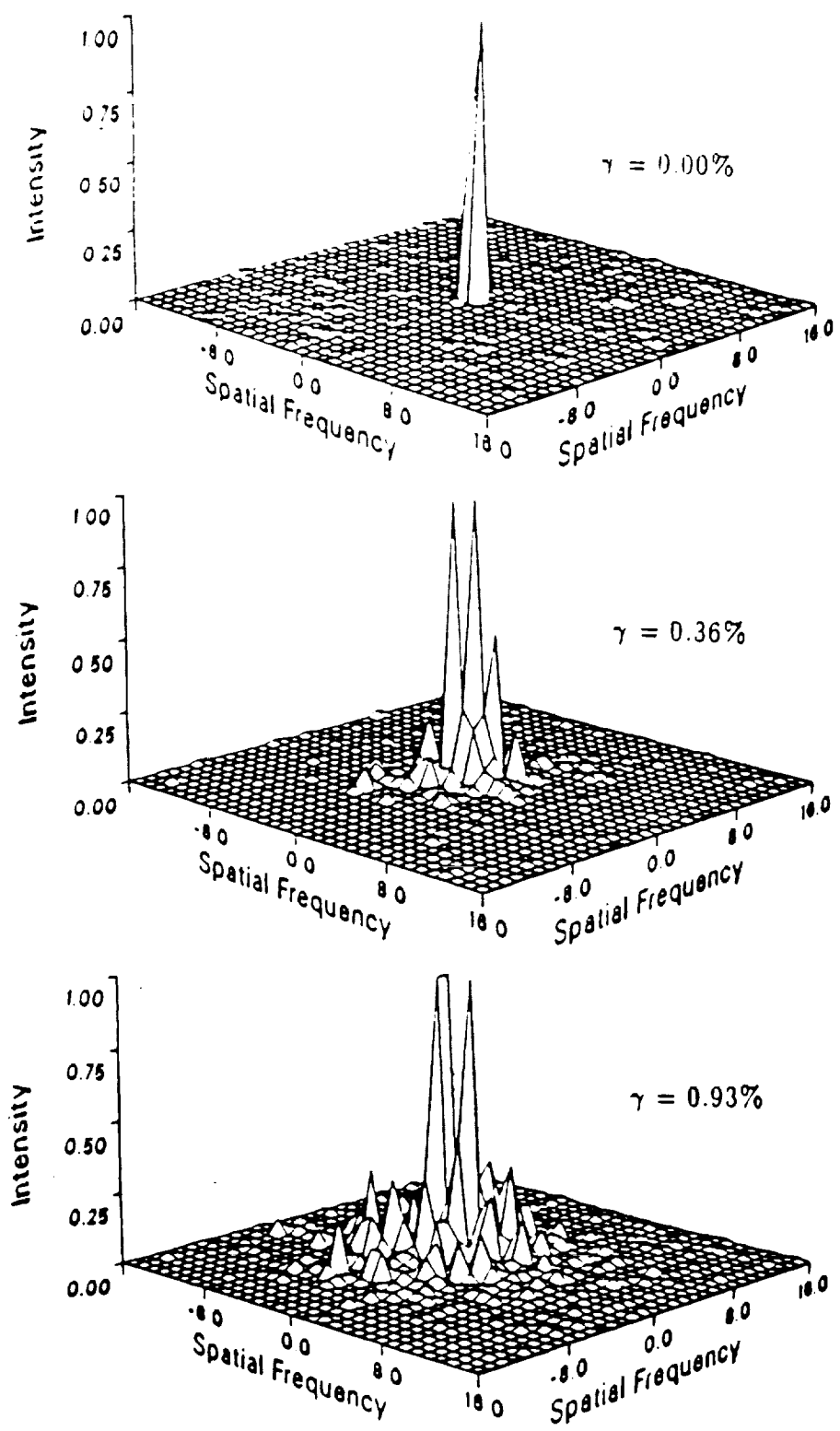


Fig.6 Experimental Laser Speckle Field at Different Levels of Plastic Strain of a Copper Alloy Specimen

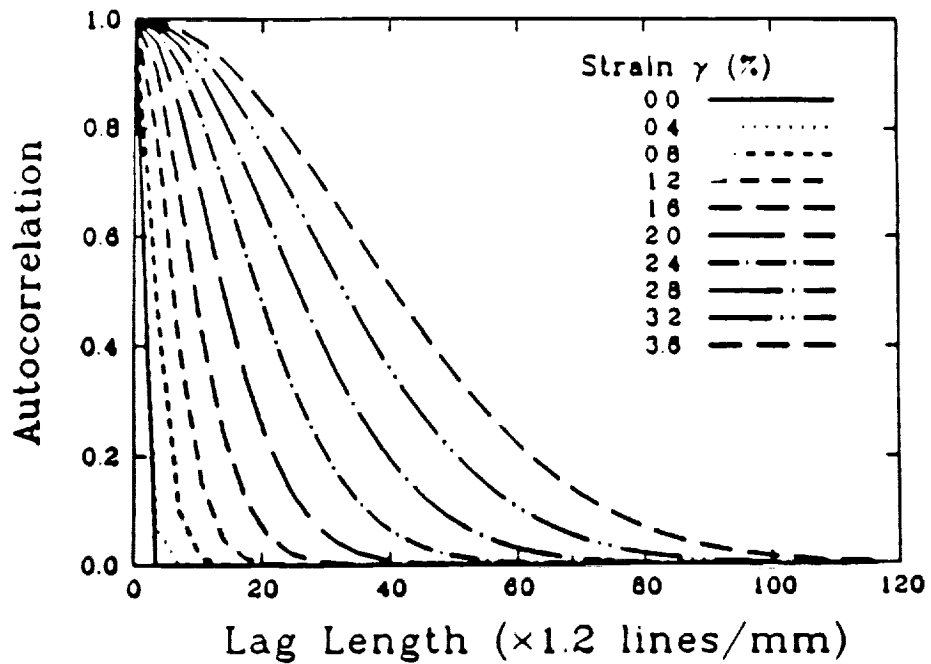


Fig.7 Theoretical Autocorrelation Function of Speckle Pattern at Different Levels of Plastic Strain

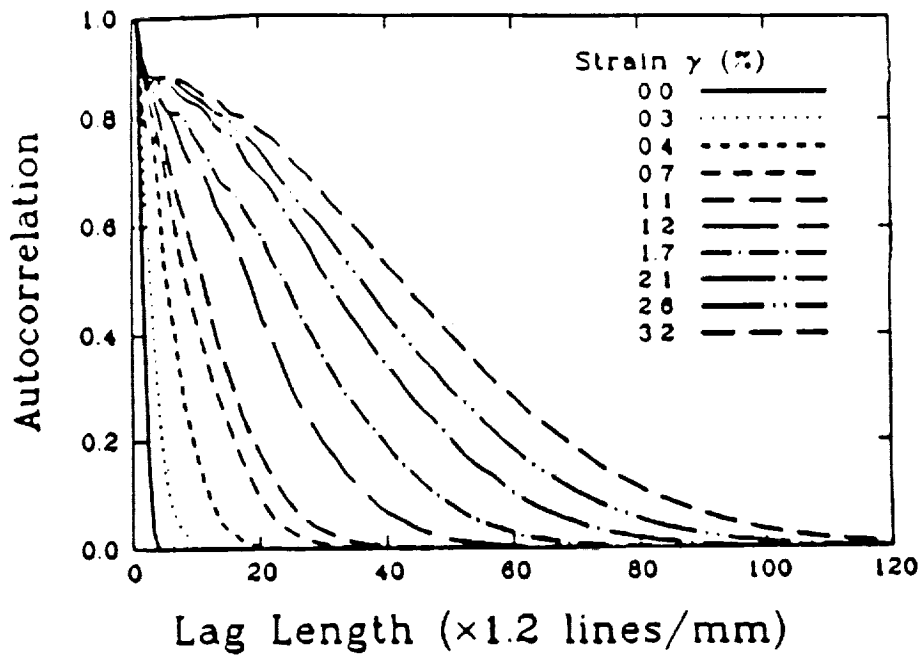


Fig.8 Experimental Autocorrelation Function of Speckle Pattern at Different Levels of Plastic Strain

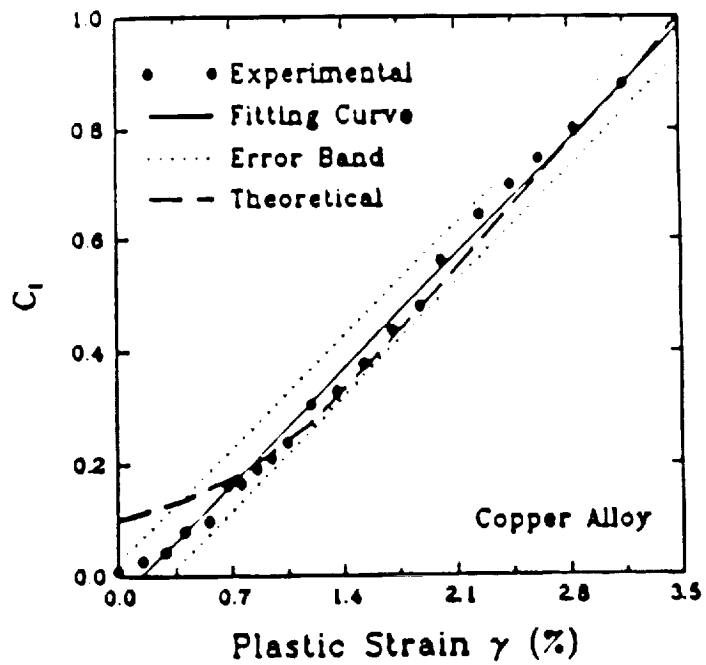


Fig.9 Integrated Autocorrelation Coefficient as a Function of Plastic Strain

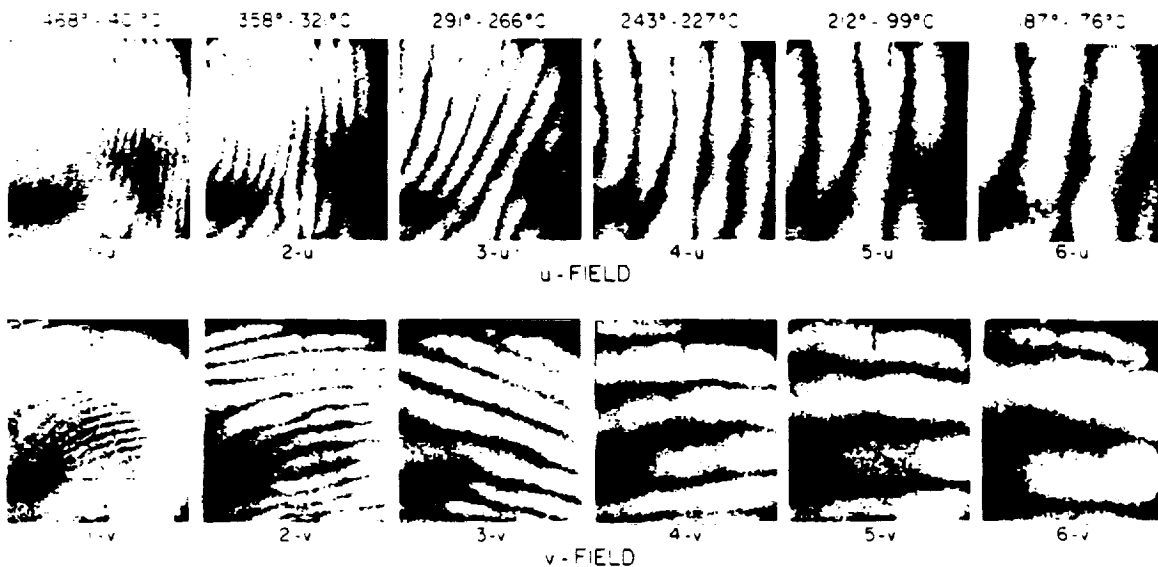
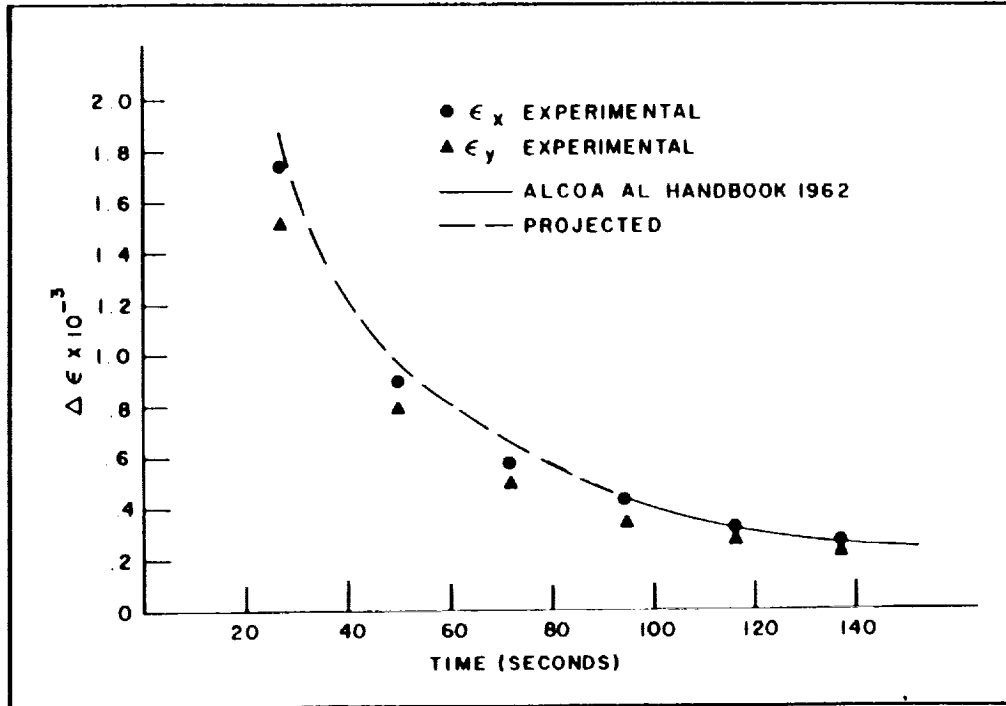
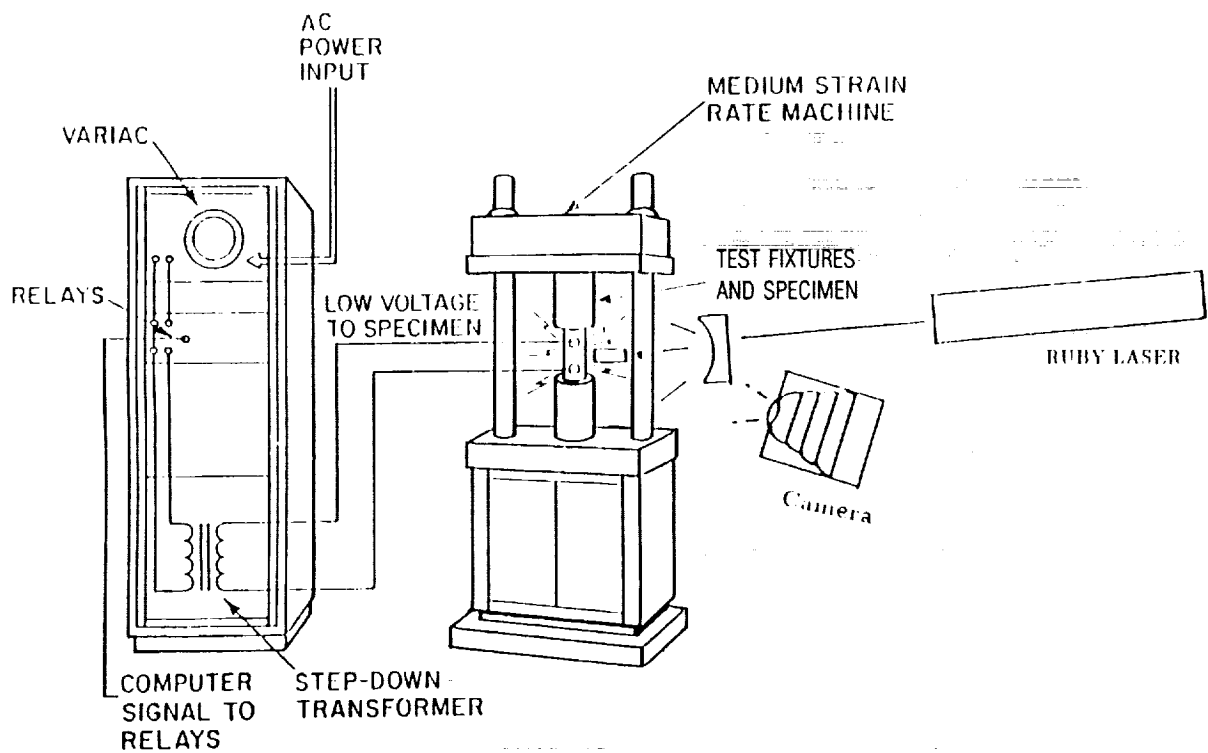


Fig.10 Distribution of Thermal Strain Relaxation of an Aluminum Plate Heated at Lower Left Corner.



**Fig.11 Thermal Strain Relaxation as a Function of Time at a Point near the Thermal Couple**



**Fig.12 Medium Strain Rate Testing Using Laser Speckle Resistance Heating**

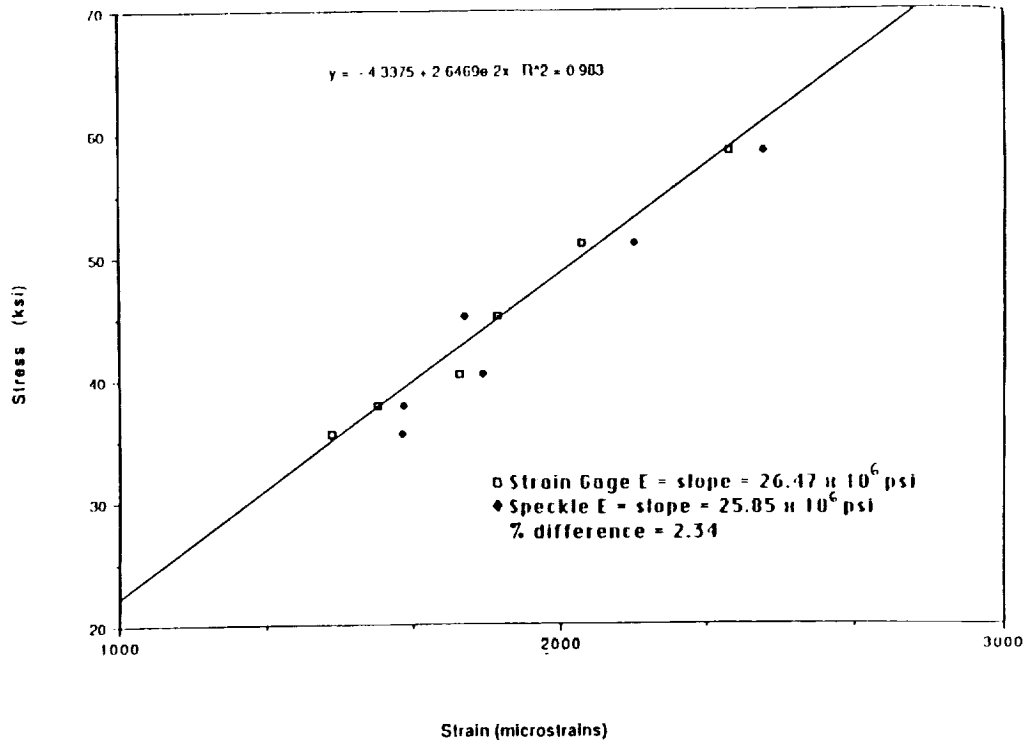


**Fig.13** Results of a Soaking Test at 250°F and  $\dot{\epsilon} = 10^{-1} \text{sec}^{-1}$

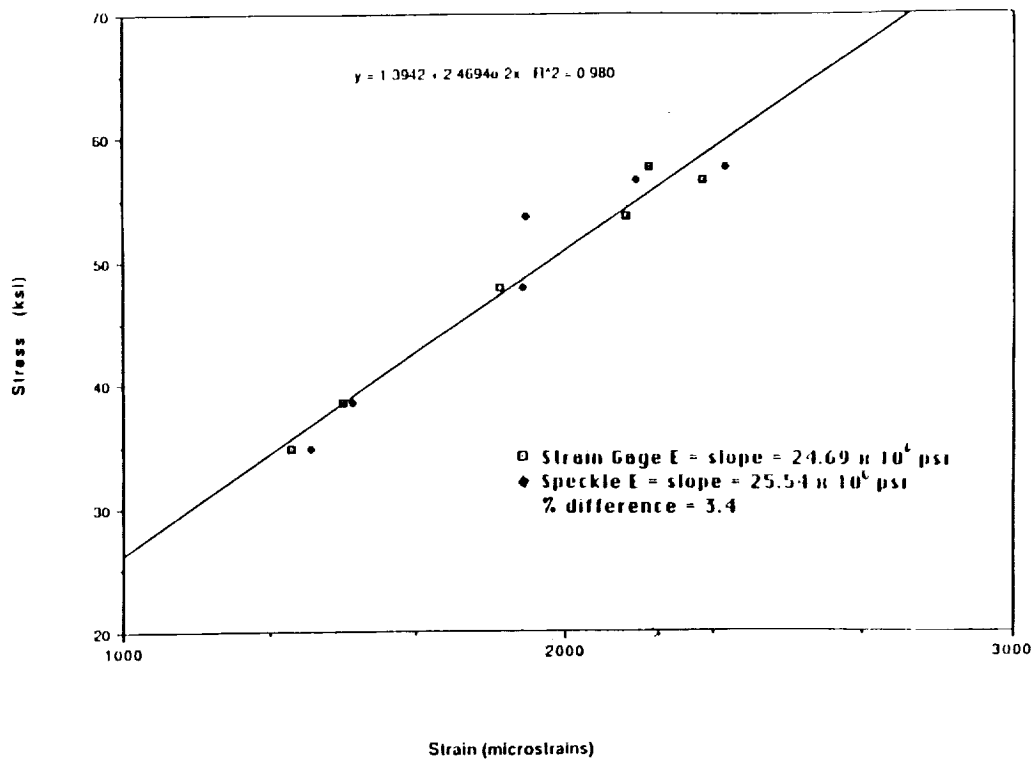


**Fig.14** Results of a High Heating Rate Test at 250°F/sec. and  $\dot{\epsilon} = 10^{-1} \text{sec}^{-1}$



DETERMINATION OF HIGH TEMPERATURE STRAINS USING  
A PC BASED VISION SYSTEM

Stephen R. McNeill  
Michael A. Sutton  
Dept. of Mechanical Engineering  
University of South Carolina  
Columbia SC 29208

Samuel S. Russell  
NASA Marshall Space Flight Center  
Huntsville, AL

## INTRODUCTION

With the widespread availability of video digitizers and cheap personal computers, the use of computer vision as a experimental tool is becoming common place. Theses systems are being used to make a wide variety of measurements that range from simple surface characterization to velocity profiles. The Sub-Pixel Digital Image Correlation technique<sup>[1,2,3]</sup> has been developed to measure full field displacement and gradients of the surface of an object subjected to a driving force. The technique has shown its utility by measuring the deformation<sup>[4,5,6]</sup> and movement of objects that range from simple translation to fluid velocity profiles<sup>[7]</sup> to crack tip deformation of solid rocket fuel\*. This technique has recently been improved and used to measure the surface displacement field of an object at high temperature.

## DIGITAL IMAGE CORRELATION

Sub-Pixel Digital Image Correlation uses a digitized image of a random pattern attached to the surface on an object. The pattern may consist of the natural surface finish, if appropriate, or may be applied using any method which will produce a random "speckle" pattern. A representative pattern is shown in Figure 1. After the object is subject to a driving force a second image is acquired. The movement of the pattern on the surface can be determined by correlating the two image's intensity patterns. Sub-Pixel accuracy is obtained by interpolation between pixel gray levels. Typical accuracy for this technique is  $\pm 0.02$  pixels<sup>[8]</sup>.

The correlation is performed by selecting from the undeformed image a set of neighboring pixels around the point of interest. The subset must be large enough to contain a unique portion of the surface's random pattern. A typical subset size is 20 pixels by 20 pixels. The subset chosen is then compared to subsets of the deformed image to find a match.

---

\* Sutton, M.A., work in progress.

Because the corresponding subset in the deformed image will probably not only be translated but also be deformed, the comparison of the subsets is done by also deforming the original subset to find the match. The deformation across the subset is assumed to be linear. The deforming of the subset is performed using

$$\begin{aligned} x^* &= x + u + \frac{\partial u}{\partial x} dx + \frac{\partial u}{\partial y} dy \\ y^* &= y + v + \frac{\partial v}{\partial x} dx + \frac{\partial v}{\partial y} dy \end{aligned} \quad (1)$$

where  $x$  and  $y$  are the coordinates of a pixel in the subset before deformation,  $u$  and  $v$  are the displacement of the center of the subset, and  $dx$  and  $dy$  are the distances from the center of the subset to the pixel.

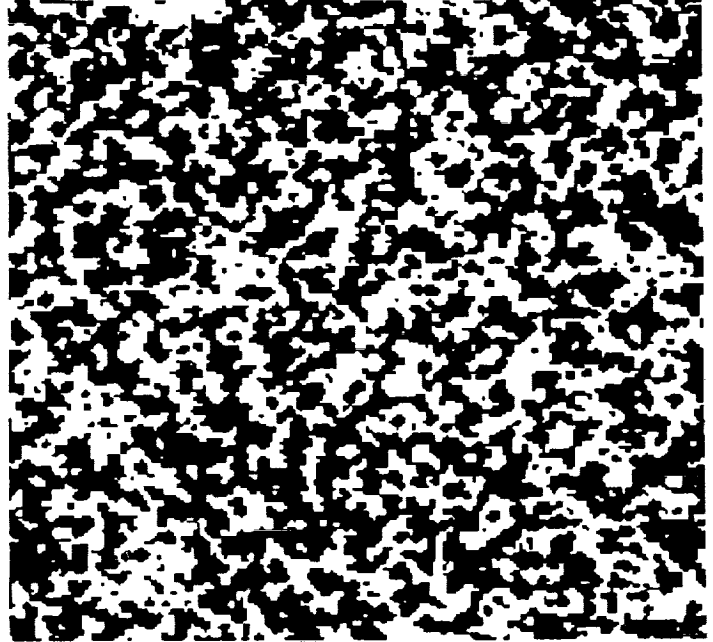


Figure 1. Representative speckle pattern.

The correlation function used is

$$C\left(x, y, u, v, \frac{\partial u}{\partial x}, \frac{\partial u}{\partial y}, \frac{\partial v}{\partial x}, \frac{\partial v}{\partial y}\right) = 1 - \frac{\sum_{i,j=1}^n A(x_i, y_j) * B(x_i^*, y_j^*)}{\sqrt{\sum_{i,j=1}^n A(x_i, y_j)^2 \sum_{i,j=1}^n B(x_i^*, y_j^*)^2}} \quad (2)$$

where  $A(x_i, y_j)$  is the gray level at in the undeformed image at location  $(x_i, y_j)$ ,  $B(x_i^*, y_j^*)$  is the gray level in the deformed image at location  $(x_i^*, y_j^*)$  which was determined by Equation 1, and  $n$  is the subset size.

When the image is digitized each pixel is assigned a single value representing the intensity over a finite area of the sensor. The correlation technique was designed assuming that the gray level value is at the center of the pixel. The mapping of Equation (1) usually maps integer pixel locations of the undeformed image to non-integer locations in the deformed image. To determine the gray level at these non-integer locations bi-linear interpolation is used. The formula for this interpolation is

$$B(x, y) = a_1 + fract(x) * a_2 + fract(y) * a_3 + fract(x) * fract(y) * a_4 \quad (3)$$

where

$$a_1 = B(int(x), int(y))$$



$$a_2 = B(int(x+1),int(y)) - B(int(x),int(y))$$

$$a_3 = B(int(x),int(y+1)) - B(int(x),int(y))$$

$$a_4 = B(int(x+1),int(y+1)) + B(int(x),int(y))$$

*fract(x)* = fractional part of *x*

*int(x)* = integer part of *x*

The correlation used in the work presented here assumes that all motion of the object is parallel to the camera's image sensor. When this is true then the displacement of the subsets from the undeformed image to the deformed image is proportional to the displacement of the object's surface, and the gradient terms are equal to the gradients of the object's surface. When long focal length lenses are used small amounts of movement toward the camera can be tolerated without significant error being introduced. 3-D correlation methods are available<sup>†,‡,§</sup> which can handle large amount of out-of-plane motion.

#### PC IMAGE CORRELATION

The program required to perform sub-pixel correlation is memory and CPU intensive. In the past, the program was run on a VAX 11/780. By running on a machine such as this, there are a host of problems associated with the transferring of the images between the vision system and the computation system. Due to the increase in power and memory capabilities of personal computers, the correlation program has recently been implemented on a PC<sup>||</sup>. By implementing the program on the PC, the system which acquires the images can now be used to correlated them. This allows for ease of implementation and quicker turnaround.

The PC based correlation program runs under Windows 3.0. It was written so that other applications can be run at the same time. It is user friendly with features which allow it to run automatically or on a point by point basis. Images from different sources and different formats can be used. It can display images on the PC monitor (requires a super-VGA monitor card with 1-Mbyte RAM). Two different correlation schemes are available and user selectable.

The processing times for PC based correlation are, of course, dependent on the machine configuration. When running a PC configuration of 486, 33Mhz, 8MegRam, 64K CPU cache, and

---

† McNeill, S.R., Sutton, M.A., Miao, Z., Ma, J., "Automated Measurement of Surface Shape by Computer Vision: Part I", submitted for review to IEEE Transactions on Pattern Analysis and Machine Intelligence, 1992.

‡ McNeill, S.R., Sutton, M.A., Miao, Z., Ma, J., "Automated Measurement of Surface Shape by Computer Vision: Part II", submitted for review to IEEE Transactions on Pattern Analysis and Machine Intelligence, 1992.

§ McNeill, S.R., Sutton, M.A., Ma, J., Miao, Z., "Image Correlation for Determination of 3-D Displacements and Gradients", paper in preparation.

|| Work done on contract by S.R.McNeill Services, NAS8-39030.

64K Disk Cache the correlation time per point is the same as the program used on the VAX 11/780. In addition, due to the nature of the PC, when image correlation is being performed on a large number of points per image, results are obtained faster for the PC than for a multi-user VAX 11/780.

## EXPERIENTIAL DETERMINATION OF HIGH TEMPERATURE STRAINS

One application of the systems described above is in the area of high temperature strain measurement. To test the viability of such a system, an extensive experimental program was initiated and recently completed to quantify thermal strains by computer vision for temperatures from 0 to 1200°F. The experimental setup, shown in Figure 2, included a Lindberg Furnace with radiative heating elements and a central open area 250mm X 250 mm X 200mm. The door of the furnace had a 100mm X 50mm viewing area.

The viewing area contained two thin panes of high quality sapphire glass, with the panes separated by 38mm, to minimize optical distortion. All of the specimens were rectangular thin strips, approximately 25mm X 50mm X 3mm in size. Both

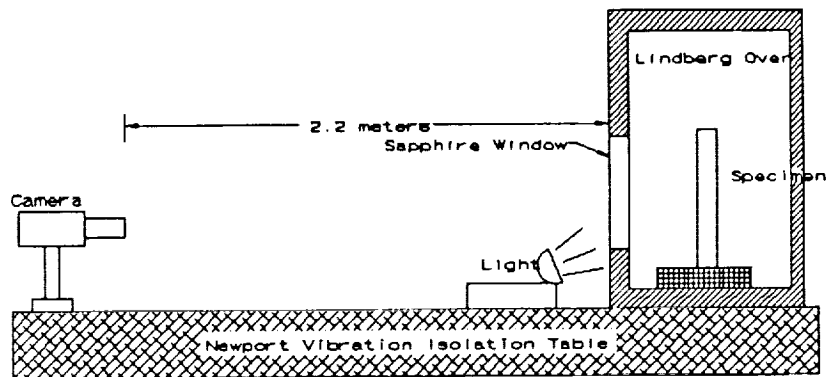


Figure 2 Experimental Setup

aluminum and titanium alloys were used. The surface preparation prior to obtaining the digital images included spray painting each specimen with a random black and white pattern, using high temperature paint. The maximum temperature for the paint is approximately 1200°F. After painting, the specimen was heat cured in the oven to ensure stability of the paint during the tests. For the strain tests, each specimen was placed on a high temperature ceramic stand in the middle of the furnace open area. The stand was used to support the specimen during the test and to minimize out-of-plane motion of the specimen due to expansion of the oven interior. The specimen was illuminated by white light using a fiber optic lamp placed directly outside of the furnace door. A video camera was placed approximately 2.2 meters away with various Nikon lenses used to magnify the image. Typically, the image-camera resolution was 40 pixels per mm on the object surface. The images were obtained during the high temperature test and stored in the computer for detailed analysis after the test was completed.

After several experiments were completed, it was determined that thermal oscillations in the air outside of the sapphire windows were the primary source of noise in the optical images. To reduce this noise, several approaches were tried. The most successful was the use of a steady flow of air over the surface of the sapphire windows. This was accomplished by using a small fan to blow room air over the windows. Images obtained using this procedure at temperatures of 0, 400, 800 and 1200°F were obtained. Results for the displacement field on the specimen surface were determined to be relatively free of large variations due to the thermal convective air currents.

To obtain the surface strain fields, the displacement fields at each temperature were first smoothed<sup>[9]</sup>. By averaging approximately 1000 derivatives of the smoothed displacement fields over the surface of the specimen, and using small strain-displacement gradient theory, the surface strains could be estimated. Results of several tests indicate that (a) the point to point variation in optically measured strain (this is important if the strain field is not uniform) is on the order of 300 microstrain, (b) the average strains, obtained by comparing several composite images obtained at one temperature, vary by 10-30 microstrain, (c) the thermal oscillations in the air outside the window are almost solely responsible for the errors in the strain data and (d) comparison of the optically estimated thermal coefficient of expansion to data obtained from the literature indicates that the optical values are within the scatter in available data.

## EXPERIMENTAL RESULTS

A representative sample of the data obtained is shown in Figure 3 and Figure 4. The  $\pm 0.02$  pixel error can be seen in the data.

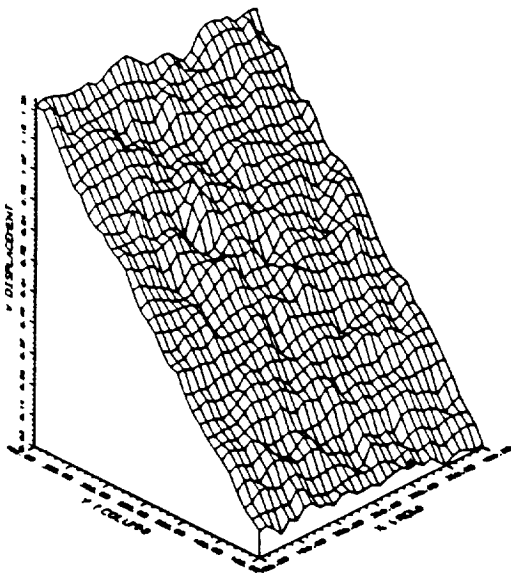


**Figure 3** V-Displacement at 800°F

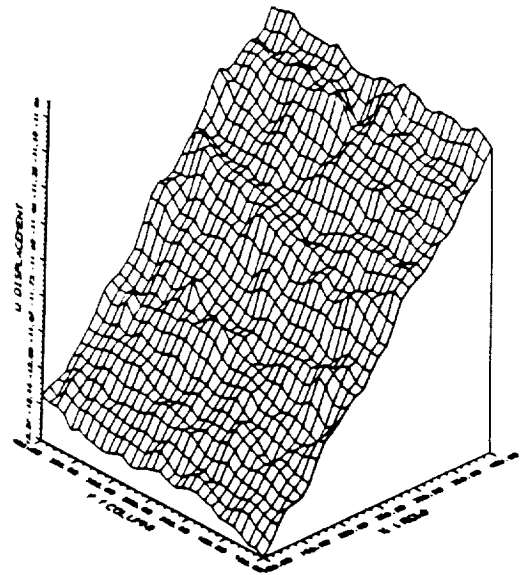


**Figure 4** U-Displacement at 800°F

The data was smoothed and is shown in Figure 5 and Figure 6.

It is emphasized that the images shown in Figures 3 and 4 were obtained using the small fan to "randomize" the effect of the convective currents. If the fan is not used, the effects of these currents can be seen in Figures 7 and 8. Figs. 7 and 8 are correlation results from two images that were taken at the same temperature but different times. If a fan is used to circulate the air then the plots would have been essentially flat.

## SUMMARY

In summary, the development of a PC based Sub-Pixel Digital Image Correlation system has yielded an accurate and easy to use system for the measuring surface displacements and gradients. Experiments have been performed to show the system is viable in use of measuring thermal strain.

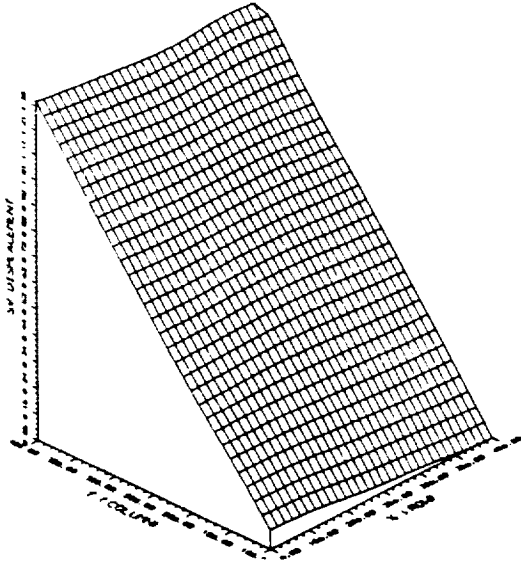


Figure 5 Smoothed V-Displacement at 800°F.

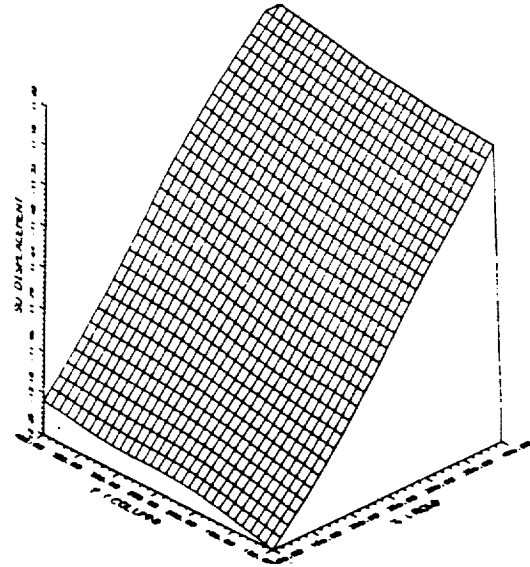


Figure 6 Smoothed U-Displacement at 800°F.

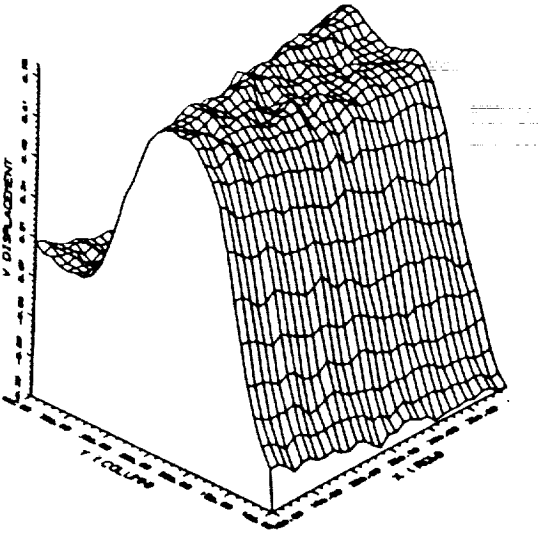


Figure 7 V-Displacements due to convective current.

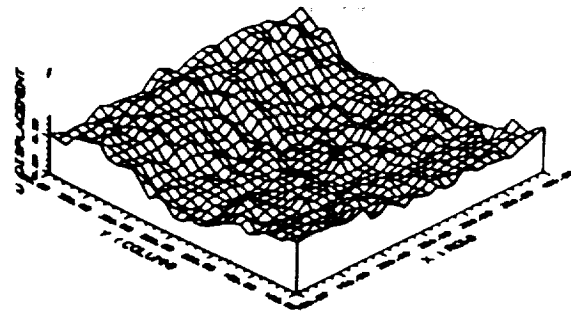
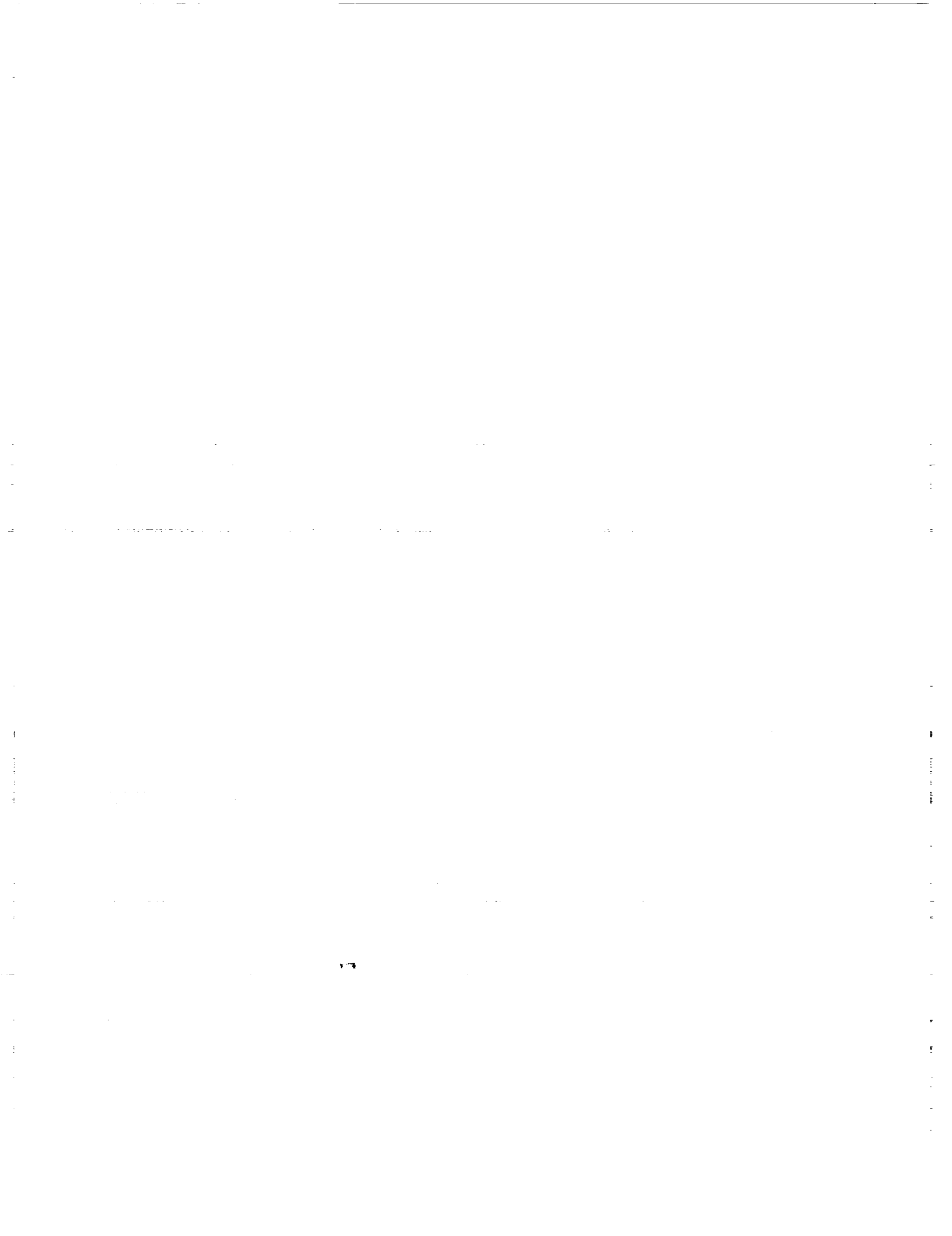


Figure 8 U-Displacements due to convective currents.

## REFERENCES

1. Peters, W.H. and Ranson, W.F. "Digital Imaging Techniques in Experimental Stress Analysis", *Opt. Eng.*, 21, 427-431, May 1982.
2. Sutton, M.A., Cheng, M., Peters, W.H., Chao, Y.J., and McNeill, S.R. "Determination of Displacements Using an Improved Digital Correlation Method", *Computer Vision*, 133-139, Aug. 1983.
3. Bruck, H.A., McNeill, S.R., Sutton, M.A., and Peters, W.H. "Digital Image Correlation Using Newton-Raphson Method of Partial Differential Correction", *Experimental Mechanics*, Vol.29, No.3, pp.261-267, Sept. 1989.
4. Chu, T.C., Peters, W.H., Ranson, W.F., and Sutton, M.A. "Application of Digital Correlation Methods to Rigid Body Mechanics", *Proc. 1982 Fall Meeting of SESA*, 73-77, Nov. 1982.
5. Sutton, M.A., Cheng, M., Peters, W.H., Chao, Y.J., and McNeill, S.R. "Application of an Optimized Digital Correlation Method to Planar Deformation Analysis", *Image and Vision Computing*, 4 (3), 143-150, Aug. 1986.
6. McNeill, S.R., Peters, W.H., and Sutton, M.A. "Estimation of Stress Intensity Factor by Digital Image Correlation", *Eng. Fracture Mechanics*, Vol 28, No.1, 101-112, 1987.
7. He, Z.H., Sutton, M.A., Ranson, W.F., Peters, W.H., "Two-dimensional Fluid-velocity Measurements by Use of Digital-speckle Correlation Technique", *Experimental Mechanics*, Vol 24, No.2, 117-121, 1984.
8. Sutton, M.A., McNeill, S.R., Jang, J., Babai, M., "Effects of Subpixel Image Restoration on Digital Correlation Error Estimates", *Optical Engineering*, Vol.27, No.10, 870-877, 1988.
9. Sutton, M.A., "Full-field Representation of Discretely Sampled Surface Deformation for Displacement and Strain Analysis", *Experimental Mechanics*, June, 168-177, 1991.



# Laser-Based Strain Measurements For High Temperature Applications

Christian T. Lant  
Sverdrup Technology, Inc.  
NASA Lewis Research Center Group  
Brook Park, Ohio 44142

## SUMMARY

The Instrumentation and Control Technology Division at NASA Lewis Research Center has developed a high performance optical strain measurement system for high temperature applications using wires and fibers. The system is based on Yamaguchi's two-beam speckle-shift strain measurement technique. The system automatically calculates surface strains at a rate of 5 Hz using a digital signal processor in a high speed micro-computer. The system is fully automated, and can be operated remotely.

This report describes the speckle-shift technique and the latest NASA system design. It also shows low temperature strain test results obtained from small diameter tungsten, silicon carbide, and sapphire specimens. These specimens are of interest due to their roles in composite materials research at NASA Lewis.

## INTRODUCTION

The NASA Lewis Research Center has been engaged in an ongoing effort to develop a non-contacting optical strain measurement

system. This measurement system is intended for use on test specimens subject to hostile environments, such as those found in earth-to-orbit propulsion systems.

This effort has developed systems that can measure strains along one or two principal axes at a point on a flat test specimen, at high specimen temperatures. Both one-dimensional and two-dimensional strains have been measured beyond 750°C.<sup>1-2</sup> The systems are based on the laser speckle-shift strain measurement technique of Yamaguchi,<sup>3</sup> which utilizes the linear relationship between surface strain and laser speckle shifts in the Fraunhofer diffraction plane. This technique accurately measures surface strains in the presence of rigid body motions of the specimen, and requires no surface preparation. The optical system is very stable and requires no periodic adjustment once initially aligned.

A feasibility study investigated theoretical aspects of using the system on small diameter wires and fibers at high temperatures.<sup>4</sup> Interest in fiber and wire materials research for the development of high temperature composites has led to the current focus of this effort, which is to make real-time uniaxial strain measurements on small diameter specimens.

The current effort advances the state-of-the-art of Lewis' optical strain measurement system, and demonstrates the successful application of the speckle-shift technique to small diameter wire and fiber specimens. Although the system is certainly not restricted to making measurements on wires and fibers, the testing emphasized these specimens to demonstrate measurements on a traditionally difficult application. In the past, strain measurements on these specimens have been made using extensometers, or even visual observation of the movement of flags on the specimen surface. These techniques have suffered from either a long gage length and/or low strain resolution. The optical technique described here features a short gage length ( $< 1$  mm) and a strain resolution of about  $15 \mu\epsilon$ . It requires no surface preparation, and can make measurements at very high temperatures. It is estimated that measurements are feasible on specimens as hot as  $2000^\circ\text{C}$ , under controlled conditions.

The low strain measurement rate of the previous speckle-shift systems (on the order of  $0.1$  Hz) limited the response time of the tests. The previous systems were limited to making strain measurements under strictly static conditions. Higher sampling rates and, therefore, higher computation rates were desired to allow continuous loading of the specimen at higher strain rates. This paper describes a system designed to provide high performance at low cost. The system has achieved a performance increase of nearly two orders of magnitude over the previous system, using modular, off-the-shelf components at a relatively low price.

A high speed digital signal processor (DSP) performs the strain calculations with near-real-time results. The use of a two-dimensional charge-coupled device (CCD) for the detector provides the flexibility of a standard video interface, and reduces decorrelation errors due to rigid body motions when using a two-dimensional specimen.

## Theory

Objective laser speckle patterns, generated by spatially coherent illumination of a rough specimen surface, shift when the surface is strained or when the specimen undergoes rigid body motion. The speckle patterns are recorded on a sensor array, and cross-correlations of the patterns before and after they move are calculated to determine the amount of shift between them (the peak position of the cross-correlation indicates the number of picture elements (pixels) the particular speckle pattern moved). Figure 1 is a schematic of the optical setup. The figure shows a dual beam configura-

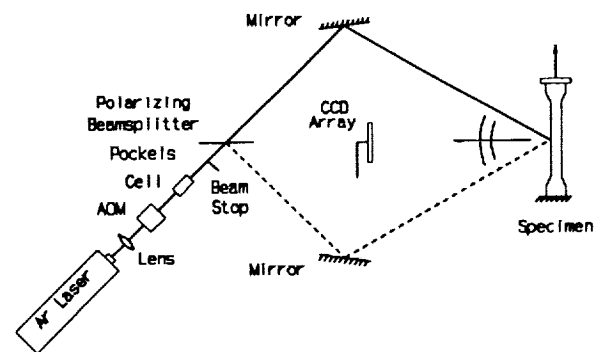


Figure 1: *Optical schematic*

tion, which allows automatic cancellation of rigid body motion. By taking the difference in shifts of the speckle patterns generated independently by two laser beams incident on the specimen from equal but opposite angles, error terms due to rigid body motion are canceled.

The current system measures one-dimensional strain in near real-time on small diameter wires and fibers, as well as extended flat specimens, by using a digital signal processor (DSP) for the calculation intensive cross-correlations. Rigid body motion constraints and decorrelations are reduced by using a two-dimensional CCD array to record an extended speckle pattern. A two-dimensional extended pattern allows off-axis speckle shifts to be tracked dynamically, without irrecoverable decorrelation. While this is important when



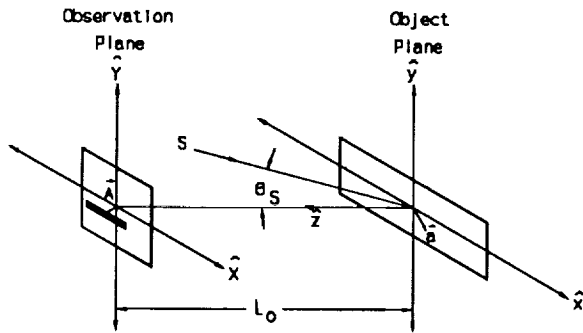


Figure 2: Simplified coordinate system

using flat specimens, however, tests showed that for quasi-one-dimensional specimens (defined roughly as specimens much narrower than the laser spot diameter, such as wires or fibers) the correlations are relatively insensitive to transverse speckle shifts.

Figure 2 shows the simplified geometry of the coordinate system. The specimen is in the  $x,y$  plane, and the sensor is defined to lie in the  $X,Y$  plane. The  $x,y$  and  $X,Y$  planes are separated by a distance  $L_0$  along the  $z$  axis. Deformation of object points on the specimen surface are described by vector  $a(x,y)$ , and the resulting shifts of the speckle pattern are given by vector  $A(X,Y)$ . The shaded rectangle in the figure indicates a one-dimensional reference slice of the speckle pattern (one line of the 2-D CCD array) shifted from the origin by  $A(X,Y)$ . The  $x,z$  plane is the plane of the incident laser beam, which comes from source point  $S$ .

After rigid body motion terms are canceled out of the simplified speckle-shift equations, the surface strain  $\epsilon_{xx}$  in the  $x$  direction can be calculated by the relation

$$\epsilon_{xx} = \frac{-\Delta A_x}{2L_0 \sin(\theta)} \quad (1)$$

where the incident angle  $\theta = |\theta_s|$ , and  $\Delta A_x$  is the difference between speckle shifts from the

two beams

$$\Delta A_x = A_x(\theta_s) - A_x(-\theta_s) \quad (2)$$

The value of  $L_0$  is 577 mm, and  $\theta = 30^\circ$  in equation 1.

## SYSTEM DESIGN

The optical system uses a switched single beam design, for compactness, following the schematic in Figure 1. The argon ion laser beam is diverted into the beam stop by the acousto-optic modulator (AOM) between tests and exposures. The Pockels cell and polarizing beamsplitter form an optical switch, in order to provide two beam paths for the error cancellation. The Pockels cell rotates the polarization of the beam by  $\pi/2$  radians when a high voltage is applied across it; this allows the beam to either pass through the polarizing beamsplitter, or be reflected to the other beam leg. A waist positioning achromatic lens provides a planar wavefront at the specimen surface, in order to maximize error cancellation.<sup>2,3</sup>

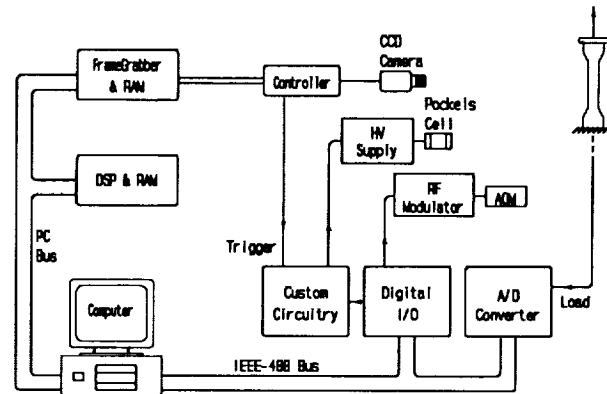


Figure 3: Block diagram of system

The data acquisition system is based on a high performance personal computer (Intel 80486 CPU), with a VGA graphics adapter using a graphics co-processor. This PC is the system controller, synchronizing the video and

load data acquisition with the strain calculations. Figure 3 shows a block representation of the system control paths. The image processing system components (frame grabber and DSP board) plug into the computer's 16-bit I/O bus (ISA PC bus). The computer controls the data acquisition and graphics display while the DSP board correlates the speckle patterns. A simple, custom digital circuit switches the Pockels cell in synchronization with the camera. This synchronization circuit is basically a flip-flop, driven by the RS-170 even/odd field signal supplied by the CCD camera circuitry (labeled "trigger"). The exposures for the two beams are timed for successive video frames, 1/30 second apart. The output of the custom circuit is a line driver that toggles the state of the Pockels cell. The computer has an IEEE-488 bus (GPIB), to which is connected a digital I/O unit, and an analog-to-digital converter (A/D converter). The digital I/O unit controls the state of the acousto-optic modulator by turning on or off the RF signal to the crystal. The A/D converter digitizes the voltage across a load cell connected to the specimen mount.

The fibers and wires are mounted in a custom load rig. The load cell is connected to the fixed specimen grip in the rig. A stepping motor with a fine pitch lead screw moves the other grip along rails, applying a load to the specimen. The resolution of the stepping motor is much finer than the resolution of the load cell, so the loading is essentially continuous.

## RESULTS

Tests of the system demonstrated the performance of the real-time speckle tracking technique, and showed that accurate strain measurements can be made on small diameter specimens. Rigid body motion tests showed that residual error was below the resolution of the system for static tests. The system measured strains at a rate of 5 Hz, which

included speckle data acquisition, image transfer from the frame-grabber to the DSP board, calculation of strain, and updates to the graphics displays.

Figure 4 shows a plot of stress versus strain for a 150  $\mu\text{m}$  (6 mil) diameter sapphire fiber (Saphikon). The solid line indicates a least-squares linear regression of the data. The dashed line indicates the theoretical stress-strain data whose slope represents the published value of Young's modulus for this

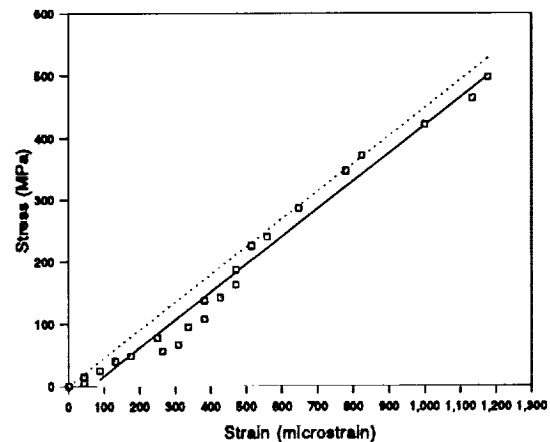


Figure 4: Stress-strain plot for 150  $\mu\text{m}$  diameter Saphikon, at room temperature

material. The measured modulus is 450 GPa (65 Msi), which agrees with the handbook value of modulus to within two significant figures. The RMS deviation of the strain

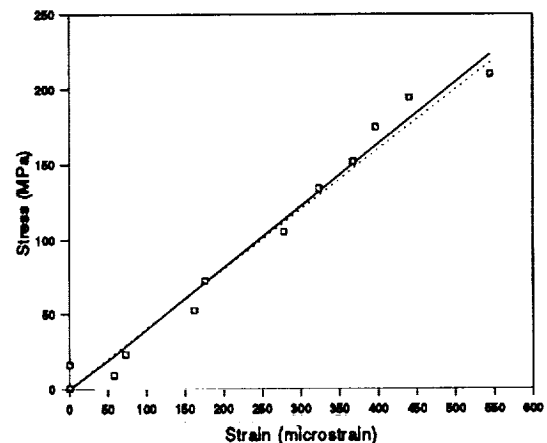


Figure 5: Stress-strain plot for 140  $\mu\text{m}$  diameter SiC fiber, at room temperature

points from the fit is  $50 \mu\epsilon$ . The correlation coefficient of the linear fit is 0.99.

Similarly, figure 5 shows a stress-strain plot of a  $140 \mu\text{m}$  diameter silicon carbide fiber (Textron SCS-6). The measured modulus is 410 GPa (60 Msi) and the handbook value is 400 GPa (58 Msi). The RMS deviation of the strain from the fit is  $25 \mu\epsilon$ . The correlation coefficient of the fit is 0.99.

Figure 6 shows a plot of the stress-strain values measured on a  $76 \mu\text{m}$  (3.0 mil) diameter tungsten-3% rhenium wire specimen. The

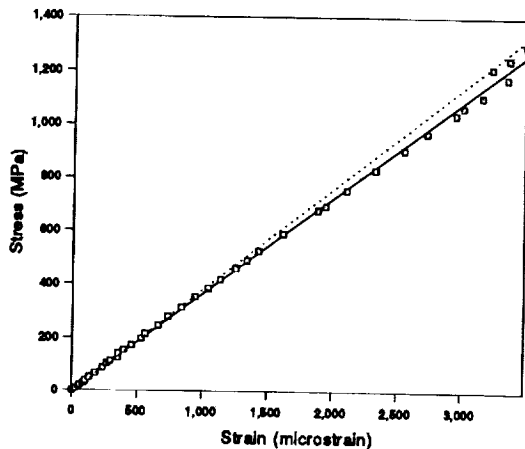


Figure 6: *Stress-strain plot for  $76 \mu\text{m}$  diameter W-3% Re wire, at room temperature*

value of Young's modulus given by a fit of the measured data is 360 GPa (52 Msi) and the handbook value is 380 GPa (55 Msi). The discontinuity in the data at 1200 MPa was caused by a false correlation, such as discussed in the error analysis section, which offset the subsequent strain values by about  $170 \mu\epsilon$ . The RMS deviation of the corrected strain data from the fit is about  $22 \mu\epsilon$ . The correlation coefficient of the fit is 1.0.

## CONCLUSIONS

There are two critical changes implemented in the speckle-shift strain measurement technique that, combined, create a speckle tracking system that greatly increases the usefulness of the technique. A two-dimensional CCD array

camera prevents most off-axis speckle shifts from causing decorrelation, and a DSP-based processing system allows strain to be calculated at a rate near the data acquisition rate. The system has also demonstrated the ability to measure strains on small diameter wires and fibers, with no strain resolution penalty for having very short gage lengths.

## REFERENCES

1. Lant, C.T., Qaqish, W.: "Optical Strain Measurement System Development - Phase I," (Sverdrup Technology, Inc.; NASA Contract NAS3-24105) NASA CR-179619, 1987.
2. Lant, C.T.: "Two-dimensional High Temperature Optical Strain Measurement System - Phase II," (Sverdrup Technology, Inc.; NASA Contract NAS3-24105) NASA CR-185116, 1989.
3. Yamaguchi, I.: "A Laser-speckle Strain Gauge," J. Phys. E. Sci. Instrum., vol. 14, no. 11, Nov. 1981, pp. 1270-1273.
4. Lant, C.T.: "Feasibility Study for the Advanced One-Dimensional High Temperature Optical Strain Measurement System - Phase III," (Sverdrup Technology, Inc.; NASA Contract NAS3-25266) NASA CR-185254, 1990.



## Extended Abstract

# Technology Trends in High Temperature Pressure Transducers: The Impact of Micromachining

Joseph R. Mallon Jr.  
Executive Vice President  
Lucas NovaSensor  
Fremont, NJ 94539

### Abstract

This paper discusses the implications of micromachining technology on the development of high temperature pressure transducers. The introduction puts forth the thesis that micromachining will be the technology of choice for the next generation of extended temperature range pressure transducers.

The term micromachining is defined, the technology is discussed and examples are presented. Several technologies for high temperature pressure transducers are discussed, including silicon on insulator, capacitive, optical, and vibrating element. Specific conclusions are presented along with recommendations for development of the technology.

### Introduction

Silicon high temperature pressure transducers have been available since the late 1960's<sup>1</sup>. Small rugged high temperature pressure probes had a major impact

on flight tests and engine development for the current generation of high performance military aircraft. The development of this technology was made possible by the confluence of a number of factors including

1. The existence of a new, under-exploited technology due to the discovery and elaboration of the Piezoresistive effect in silicon at Bell Labs in the 1950's.
2. Selective funding of semiconductor and silicon sensor research in the 1950's and 1960's.
3. The existence of several entrepreneurial companies that were instrumental in the field.
4. A pressing need for the development of new measurement tools for the development of high performance military aircraft.

The author contends that the 1990's may see the significant development of silicon high temperature pressure transducers as the result of the existence of a similar set of factors. I believe that silicon micromachining will be the fabrication technology of choice for the new generation of such high temperature sensors.

## Micromachined Sensors

Micromachining is the three dimensional sculpting of silicon using the techniques of semiconductor manufacturing. Originally developed as a set of tools for the manufacturing of sensors, micromachining has become a technology in its own right.

Micromachining is expected to become increasingly important as the manufacturing of mechanical systems concentrates on smaller and smaller structures. Proponents of this technology see the dawning of a new age of micro-manufacturing and micro-robotics.

The technology has been very successful in the manufacturing of sensors. Today, over 90% of all pressure sensors representing over half of the industry revenues employ this technology.

Why micromachining for high temperature pressure sensing? It exploits readily accessible university and industrial semiconductor device and process technology research. In last decade, it has become the sensor technology of choice. The technology allows for the production of very small, highly accurate sensors. It employs high temperature fabrication processes and high temperature materials. It is applicable to a variety of sensor modalities. Finally, it is cost effective for complex fabrication sequences.

Many micromachining technologies are relevant to high temperature pressure transducers, but particularly noteworthy is Silicon Fusion Bonding<sup>2</sup>, a new "welding" tool for microstructures. It allows the bonding of silicon wafers with a bond strength which approaches that of silicon. The resulting structure is electrically stable. In fact, active devices such as transistors may be formed across a silicon fusion bonded interface.

Silicon fusion bonding is a high temperature, clean process which is compatible with semiconductor processing. High temperature processing at

temperatures of 1200°C after wafer bonding is possible. This is unique to this wafer lamination technique. Finally, silicon fusion bonding allows the design and fabrication of novel three dimensional structures unobtainable with conventional micromachining techniques.

## Silicon Pressure Sensor Technologies for High Temperature Applications

Fortunately, semiconductor fabrication techniques, which have been exploited by a number of researchers, have resulted in the development of several viable, high temperature sensor technologies exploiting several sensing modalities. These modalities include piezoresistive, capacitive, vibrating element, and thin film strain gage.

Although the initial developers of silicon high temperature pressure sensors investigated and successfully developed several viable piezoresistive technologies, including solder glass bonding of conventional strain gages, by far the most successful technique has been variants of what has come to be called silicon on insulator or SOI technology. The first such technique was originally proposed by Kurtz and Gravel in the mid-1960's and realized by Mallon and Kurtz<sup>3</sup> in the late 1960's. This technique employed a polycrystalline silicon diaphragm and very small bulk silicon strain sensing elements separated by a thin film of quartz. These sensors made possible, for the first time, multiple transducer flight tests of inlet pressure distributions.

Newer SOI technologies have allowed the development of several generations of SOI sensors. Today's sensors exploit the superior properties of single crystal silicon. Kurtz, Weber et al. have developed a sensor based on electrostatically bonding two wafers separated by an intermediate pyrex layer. Wilner employs a high temperature boron oxide-quartz glass to form the bond layer. Petersen, Mallon<sup>4</sup> et al. employ silicon fusion bonding to laminate two wafers.

All three techniques are commercially successful and viable. These sensors operate to about 600°F. The upper limits of SOI technology have not been reached due to a lack of suitable packaging and lead out, but it is anticipated that this technology should be viable to about 1000°F.

SOI technologies draw on the many excellent materials available with semiconductor technology, including the following:

Transducer element:

Silicon, quartz, silicon nitride, silicon oxide, deposited metal films, polysilicon, diamond

Sensor element:

Silicon, silicon carbide, silicon nitride, thin films of metal

Contacts:

Aluminum, platinum, tungsten, platinum silicide, titanium, chrome-gold

Silicon piezoresistive high temperature pressure sensors are ripe for further development. A suitable development path would include:

Package and interconnect development to extend range to 1000°F

Microprocessor compensation

Silicon on sapphire for higher temperatures

Silicon carbide for very high temperatures

Capacitive pressure sensors have been demonstrated in silicon. They have the advantage of being readily micromachined, small and suitable for dynamic measurement. Such sensors sense in a displacement mode and theoretically can produce smaller temperature errors. They have the disadvantages of low capacitance, lead out problems and high signal to noise ratio. Such sensors have the potential for high temperature applications.

A recent demonstration of light emission in silicon has given new impetus toward silicon integrated electro-optics. Micromachining technology is recognized as an adjunct to fiber optic sensors. Such sensors have an outstanding potential for applications in excess of 1000°F.

Another potential technology for very high temperatures is vibrating silicon element pressure sensor technology. These sensors employ a digital sensing mode and are free of analog temperature errors. They are very accurate - 1 to 2 orders of

magnitude better than piezoresistive sensors and can be excited with fiber optics. Some issues limiting relevance for aerospace test applications are: packaging stress and issues concerning dynamic pressure measurement and concentration on known lucrative applications for processing technology.

## Conclusions and Recommendations

Silicon micromachining should be pursued as the base technology for the next generation of pressure sensors. It is of concern that although the U. S. is the leader in micromachining, Germany and Japan are spending several times as much as the U. S. for government funded research in this area.

It is anticipated that silicon micromachining will be the technology employed for the next generation of high temperature pressure sensors. I suggest pursuing a dual strategy:

Extend current SOI technology to 1000°F.

Pursue an alternate technology for operation to 2000°F - Optical, vibrating and/or capacitive.

I further suggest that government funding in this area be increased and that agencies should promote university-industrial joint development.

## Acknowledgment

The author was employed between 1965 and 1992 at Kulite Semiconductor Products where he was responsible, along with Dr. Anthony Kurtz, for that company's silicon technology. During this time Dr. Kurtz was the author's teacher, mentor and collaborator. High temperature sensing was a frequent area of investigation and the author's initial exposure to the field was a result of that collaboration. In 1985 the author founded NovaSensor along with Dr. Janusz Bryzek and Dr. Kurt Petersen. Many of the author's views on silicon micromachining and silicon fusion bonding resulted from this collaboration. Dr. Petersen is the preeminent pioneer in the field of micromachining and introduced silicon fusion bonding to sensors. Joseph Brown and Rose Siemeca were instrumental in the development of silicon fusion bonded high temperature sensors.

## References

---

<sup>1</sup>Kurtz, A. D., "Development and Application of High Temperature, Ultraminiature Pressure Transducers," ISA Silver Jubilee Instrumentation Symposium, October 1970, Philadelphia, PA.

<sup>2</sup>Petersen, K., Barth, P., Poydocki, J., Brown, J., Mallon, J., "Silicon Fusion Bonding for Pressure Sensors," Tech. Digest, IEEE Solid State Sensor Workshop, Hilton Head Island, S.C., June 1988, pp. 144-147.

<sup>3</sup>Mallon, J., Germanton, D., "Advances in High Temperature Pressure Transducers," ISA Silver Jubilee Instrumentation Symposium, October 1970, Philadelphia, PA.

<sup>4</sup>Petersen, K., Brown, J., Vermuellen, T., Barth, J., Mallon, J., Bryzek, J., "Ultra Stable High Temperature Pressure Sensors Using Silicon Fusion Bonding," Sensors and Actuators, A21-A23, 1990 96-101.



SIC Device Development for High Temperature Sensor Applications

J.S. Shor, D. Goldstein, A.D. Kurtz and R.M. Osgood\*

*Kulite Semiconductor Products, Inc, Leonia, NJ*

\*Columbia University  
Microelectronics Sciences Laboratories, NY, NY

Introduction

The two most common measurements of operating parameters in wind tunnels, materials processing, biomedical applications, and aeronautical propulsion systems involve temperature and pressure. As these applications become more advanced, increasing need is developing to measure these parameters in hostile environments, such as high temperatures. For example, in the wake of the current drive to reduce energy costs, commercial airlines are attempting to develop more fuel efficient engines while maintaining or even upgrading the safety factor. This need requires computer control of injection valves, fuel/air ratios and operating parameters within the engines. Therefore, it is essential to monitor pressures in different segments of the engines during flight. Since engine efficiency in turbojet engines is also greater at higher temperatures of the combustion gas, the emphasis has been to increase the operating temperatures of the engines, which can reach temperatures as high as 2000°F in sections of the engines. Thus, highly reliable, durable high temperature sensors are required. Furthermore, in order to develop such engines, test sensors are required to verify existing design codes. This category of sensor must be very precise, but need not last as long as an instrumentation sensor. Wind tunnel testing and instrumentation have similar demands on the measurement of operating parameters such as pressure and temperature. Finally, the materials processing industry also has sensor needs as diverse as the measurement of operating parameters in oil refineries, pipes, heat exchangers, etc. Very often these measurements require sensors that must be durable over a long period of time, while others, such as CVD growth, will only require cheap sensors for a one time use.

Piezoresistive sensors fill many of the requirements of these applications. The wheatstone bridge design allows the simultaneous measurement of both temperature and pressure with a high degree of accuracy. Furthermore, the development of a high temperature piezoresistive transducer involves the fabrication of strain sensing elements on a diaphragm or beam. These strain gauges can also be used for applications where a highly accurate measurement of strain at high temperatures is needed. For example, the outer skins of commercial airliners can reach temperatures as high as 1400°F. In order to design such aircraft, it is important to know the relationship of stress/strain on the frame at these temperatures.

Although silicon transducers have been reported with stable

pressure outputs at high temperatures (see Kurtz et al. in these proceedings), there are fundamental problems with using silicon as a mechanical material at temperatures above 600°C. Namely, silicon begins to undergo plastic deformation under minimal loads at these temperatures, rendering it useless as a sensing element. Furthermore, silicon becomes intrinsic at these temperatures. Thus, in order to make a sensor which will be useful at temperatures of 600°C and higher, a more temperature resistant semiconductor must be used. These problems have motivated our research into SiC.

**Comparison of High Temperature Semiconductors**

Table 1 lists a number of wide band gap semiconductors that are currently being researched, including Si, 3C-SiC, 6H-SiC, Diamond, GaN and GaP. In order for a material to be developed for device applications, it is necessary that the properties of the material be appropriate for the device in question and that the processing

Table 1 Comparison of Semiconductors

Property	Si	GaAs	GaP	$\beta$ -SiC (6H SiC)	Diamond
Bandgap (eV) at 300 K	1.1	1.4	2.3	2.2 (2.9)	5.5
Maximum operating temperature ( °C)	300	460	925	873 (1240)	1100(?)
Melting point ( °C)	1420	1238	1470	Sublimes > 1800	Phase change
Physical stability	Good	Fair	Fair	Excellent	Very good
Electron mobility R.T., cm <sup>2</sup> /V-s	1400	8500	350	1000 (600)	2200
Hole mobility R.T., cm <sup>2</sup> /V-s	600	400	100	40	1600
Breakdown voltage E <sub>b</sub> . 10 <sup>6</sup> V/cm	.3	.4	—	4	10
Thermal conductivity $\alpha_r$ , W/cm-°C	1.5	.5	.8	5	20
Sat. elec. drift vel. v(sat), 10 <sup>7</sup> cm/s	1	2	—	2.5	2.7
Dielectric const., K	11.8	12.8	11.1	9.7	5.5
Relative Z <sub>J</sub>	1	7	—	1100	8100
Relative Z <sub>K</sub>	1	.5	—	6	32

$$Z_J \propto E_b^2 v^2(\text{sat})$$

$$Z_K \propto \alpha_r [v(\text{sat})/K]^{1/2}$$

Table 1: Comparison of high temperature semiconductors (courtesy of J.A. Powell, NASA Lewis)

technology be advanced enough to allow device fabrication. Diamond can only be deposited in a polycrystalline form on non-diamond substrates, and bulk single crystal growth has not been achieved yet; thus diamond technology is too immature at this stage to be practical. GaP has poor physical stability at high temperatures and a melting point which is similar to silicon, which suggests that its mechanical properties will be inappropriate for high temperature sensors. GaN cannot be used for devices at the present time, since p-type conduction and ohmic or rectifying contacts have not been produced in GaN as of yet. However, SiC has excellent electrical and mechanical properties at high temperatures. Its wide band gap will allow p-n junctions to function at temperatures as high as 600°C. SiC has a high thermal conductivity, melting point and thermal stability at temperatures of interest. Furthermore, there is very little deterioration in the mechanical properties of SiC, such as its tensile strength up to 1800°C [1]. Of the high temperature semiconductors mentioned, SiC has the most advanced device technology associated with it\*. For these reasons, it appears that SiC has the best potential for high temperature sensors. In this paper, we will review recent progress made at Kulite in the characterization and processing of 3C-SiC for sensor applications.

### Piezoresistance of 3C-SiC

The piezoresistive properties of SiC have not yet been fully characterized in the literature. There was some early Russian work done on the piezoresistance of  $\alpha$ -SiC, which has a large piezoresistive effect (e.g. high resistivity n-type 6H-SiC has  $\pi_{11} = -142 \times 10^{-12}$  cm<sup>2</sup>/dyne at 273°K [2]). However, there was only one study done on the piezoresistive properties of 3C or  $\beta$ -SiC [3] which reported only the hydrostatic pressure coefficient  $\pi_{11} + 2\pi_{12}$ , but did not examine the two coefficients  $\pi_{11}$  and  $\pi_{12}$  separately.

Epitaxial layers of  $\beta$ -SiC were grown by CVD on silicon substrates at the NASA Lewis Research Center by previously described means [4]. These films were of the (100) orientation and were 10  $\mu$ m thick. The samples were n-type with resistivities ranging between 0.1-1.0  $\Omega$ -cm and carrier concentrations  $\approx 10^{16}$ - $10^{17}$  cm<sup>-3</sup>. The samples were metallized and patterned into narrow rectangular bars with metal contacts at each end. The silicon substrates were then selectively etched leaving thin SiC strips which would be used as strain gauges. Since piezoresistance is a tensor property, several gauge configurations were tested (Fig. 1). By applying a known stress along the axis of the gauges and measuring the change in resistivity, the three piezoresistive coefficients can be calculated. In our experiments, it was more convenient to apply a strain rather than a stress. Hence, the quantity measured was the gauge factor (GF), which is defined as

$$\delta R / \epsilon R \quad \text{where } R = \text{resistance and } \epsilon = \text{strain.}$$

A positive gauge factor corresponds to an increase in resistance

---

\*Proceeding of the Fourth Int. Conf. on Amorphous and Crystalline SiC, Santa Clara Univ., Santa Clara, CA, Oct. 10-11, 1991, to be published by Springer-Verlag.

with tensile strain, while a negative GF signifies a decrease. The gauge factor is related to the piezoresistive coefficients by Young's modulus and dimensional corrections, which are small in this case. The SiC gauges were mounted onto a cantilever beam, and the beam was bent to produce a uniaxial strain. Resistivity changes were measured with applied strain. P-type Si strain gauges of known gauge factor were used as controls in order to determine the experimental error, which is estimated to be within 10%.

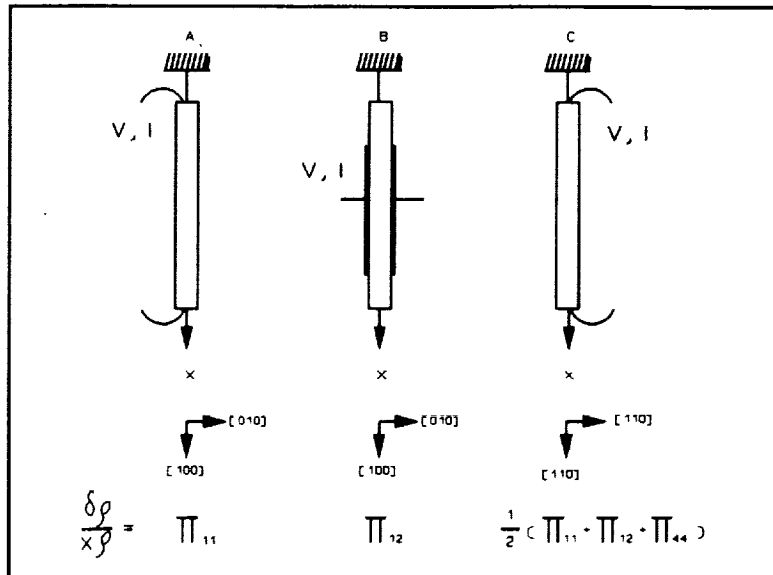


Figure 1: Three configurations used for the measurement of the piezoresistive properties of SiC.

The room temperature gauge factors for  $\beta$ -SiC are listed in Table 2 along with the GF's of n-Si calculated from the literature. Configuration "A" has the largest magnitude, indicating that  $\pi_{11}$  is the largest of the piezoresistive coefficients for both n-SiC and n-Si. There is a small nonlinearity with strain shown by the SiC gauge factors. This effect amounts to 0.4%/100 ppm in configuration "A" with the magnitude of the GF's decreasing with tension and increasing under compression.

There are several theories found in the literature for the mechanism of the piezoresistive effect in semiconductors. In n-type material, the one that applies most often is the electron transfer effect [5]. This theory relates the change in resistivity to a redistribution of electrons among the multivalleys in momentum space. Fig. 2 is a diagram of four of the six multivalleys found in a cubic crystal. In this figure, the multivalley minima are all along a major crystallographic axis,  $\langle 100 \rangle$ . The electron mobility is highly anisotropic within the valleys, but the symmetry of the six valleys causes the net mobility to be uniform. The application of a tensile strain in the  $\langle 100 \rangle$  direction will cause the multivalley minima along the x-direction to rise in energy, while those in the y- and z-directions will drop. This is depicted by the dotted lines. The energy difference will cause a redistribution of the electrons between the potential wells. In a resistivity measurement along the  $\langle 100 \rangle$  direction, more electrons will have mobilities equal to  $\mu_t$  than  $\mu_l$ , hence the piezoresistive effect.

For a lightly doped sample, Boltzman statistics can be used to estimate the value of the change in resistivity for strains applied in different configurations (e.g. Fig. 1). This analysis has been done [5], and the results indicate that for a cubic semiconductor with its multivalley minima in the  $\langle 100 \rangle$  direction,  $\pi_{11}$  will be the largest coefficient with  $\pi_{12} \approx -\frac{1}{2}\pi_{11}$  and  $\pi_{44}=0$ . It is easy to visualize why  $\pi_{44}$ , the shearing coefficient plays no role. A shearing strain is equal to a tension in the  $\langle 111 \rangle$  direction and an equal and opposite compression at  $90^\circ$ , in the  $\langle 11\bar{1} \rangle$  direction. This will cause all of the six multivalleys to deform in the same manner, preserving the crystal symmetry.

Table 2: Room temperature gauge factors of  $\beta$ -SiC

Material	resistivity (ohm-cm)	$GF_A$	$GF_B$	$GF_C$
n $\beta$ -SiC	0.7	-31.8	+19.2	-3.7
n Si	11.0	-133.0	+68.3	-52.0
corresponding piezoresistive coefficients		$\pi_{11}$	$\pi_{12}$	$\frac{1}{2}(\pi_{11} + \pi_{12} + \pi_{44})$

The electron transfer mechanism has been accepted as the primary effect for n-Si, which has its multivalleys in the  $\langle 100 \rangle$  direction and piezoresistive coefficients in accord with the theory. Electron cyclotron resonance experiments on  $\beta$ -SiC [6] have shown that it also has its multivalleys in the  $\langle 100 \rangle$  direction and a large mobility anisotropy exists within the valleys. The data in Table 2 shows that the piezoresistive coefficients of  $\beta$ -SiC follow the theory closely with  $\pi_{12} \approx -0.6\pi_{11}$  and  $\pi_{44} < \pi_{11}, \pi_{12}$ . Thus, it is reasonable to assume that the electron transfer effect is the dominant mechanism for n-type  $\beta$ -SiC, with smaller secondary effects playing a role as well. A more detailed description of the temperature coefficient of gauge factor and the temperature coefficient of resistivity is being published elsewhere.†

The electron transfer mechanism for the piezoresistive effect in semiconductors predicts a  $1/kT$  dependence of the piezoresistive coefficients with temperature [5]. This temperature dependence is most valid at low temperatures and low doping levels. For highly doped semiconductors, both the magnitude of the piezoresistance and its dependency on temperature are reduced. In the case of extreme degeneracy, as is seen in metals, the piezoresistive effect becomes smaller than resistance changes due to deviations in dimensionality of the gauges. However, degenerately doped semiconductors have

†J. S. Shor, D. Goldstein, and A. D. Kurtz, unpublished data.

large gauge factors compared to metals while being significantly more temperature independent than lower doped semiconductors. Therefore, degenerately doped semiconductors are generally more useful as strain sensing elements than low doped materials, since it is easier to achieve a temperature independent output with highly doped gauges.

The temperature variation of gauge factor is shown in Fig. 3, which plots gauge factor for undoped ( $0.2-0.7 \Omega\text{-cm}$ ,  $10^{16}-10^{17} \text{cm}^{-3}$ ) and degenerately nitrogen doped ( $0.02 \Omega\text{-cm}$ ,  $10^{18} \text{cm}^{-3}$ )  $\beta\text{-SiC}$  of configuration "A". Initially, the gauge factor shows a large decrease with temperature, but levels off at  $400^\circ\text{C}$ . This result is similar to the behavior of lightly doped silicon strain gauges which exhibit a large temperature dependence at low temperatures and a reduced temperature dependence at higher temperatures [5]. The gauge factor is much more temperature independent in the case of the degenerate doping level,  $10^{20} \text{cm}^{-3}$ . In fact, most of the temperature variation in the degenerate gauges is due to an increase in the low temperature GF's due to compression caused by mounting. It should be noted that the degenerately doped gauges of Fig. 3 had a very low gauge resistance, and a relatively high contact resistance. Measurements of gauges with Kelvin contacts indicate that the values of the GF's of the degenerately doped gauges of Fig. 3 are reduced by  $\approx 25-40\%$  due to the contact resistance.

All of the doping levels in n-type SiC exhibit a more temperature independent gauge factor at temperatures above  $200^\circ\text{C}$ . At temperatures approaching  $500^\circ\text{C}$ , the gauge factor appears to be almost constant with temperature. This behavior indicates that at even higher temperatures the gauge factor will retain this constant value. The gauge factor of silicon at high temperatures is between 40-60 depending on the doping level, while those of metallic gauges are between 1-2. Since the magnitude of the SiC GF at high temperatures equals 10-15, it appears that n-type  $\beta\text{-SiC}$  has a sufficiently high sensitivity to be useful at temperatures where silicon cannot be used.

#### TCR (Temperature Coefficient of Resistivity) of n-type $\beta\text{-SiC}$

In order to evaluate a piezoresistive sensing material that will be used over a wide temperature range, it is important to

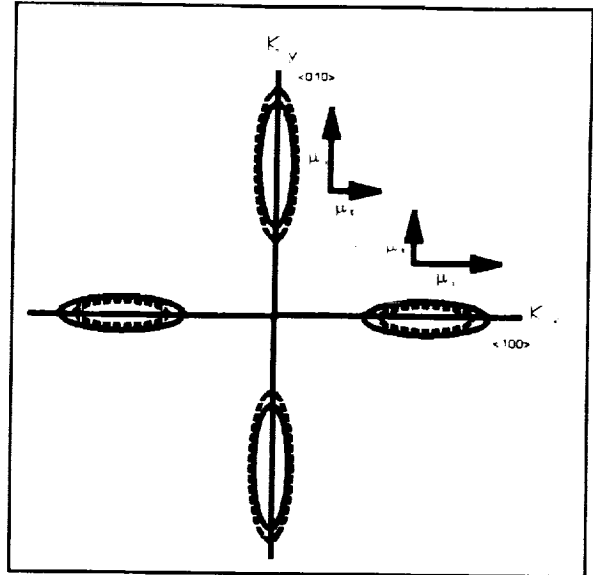


**Figure 2:** Energy surfaces in momentum space. Under zero strain the multivalleys are symmetric (solid lines), while this symmetry is removed under tensile strain in the  $\langle 100 \rangle$  direction (dashed lines).

understand the variation of resistivity with temperature. In Figure 4, the resistance of undoped, lightly doped and degenerately doped gauges is plotted as a function of temperature for the calculation of the TCR, which is defined as

$$TCR = \{R(T) - R(T_{ref})\} / R(T_{ref}) \{T - T_{ref}\}.$$

The TCR reflects both the magnitude and direction of the dependence of resistivity on temperature. In Fig. 4, the resistivity of all three doping levels is plotted against temperature on a semi-logarithmic scale for comparison. Both the undoped and lightly nitrogen doped samples have a negative TCR at low temperatures, representing a decrease in resistance with temperature. At higher temperatures the TCR becomes positive and the resistance increases with temperature. The undoped samples exhibit a positive TCR above  $-50^{\circ}\text{C}$ , and above room temperature the TCR has an approximately constant value of  $0.72\%/^{\circ}\text{C}$ . These characteristics are very similar to those exhibited by silicon samples of similar resistivity. The nitrogen doped samples are less temperature dependent than the undoped ones and have a positive TCR only above  $200^{\circ}\text{C}$ , at which point the resistance increases in a nonlinear manner. The lowest TCR is exhibited by the degenerately doped gauges, which have a positive TCR of  $.04\%/^{\circ}\text{C}$  at all temperatures measured.

In general, at low temperatures (typically  $< 0^{\circ}\text{C}$ ), the resistivity of extrinsic semiconductors will decrease with increasing temperatures due to the ionization of impurities. In this regime, the dominant scattering mechanism, impurity scattering, bears a smaller effect on the resistivity than the carrier generation does. Once the impurities are fully ionized, usually at  $\approx 0^{\circ}\text{C}$ , the resistivity increases due to lattice scattering, which is a larger effect than the thermal electron-hole generation. At very high temperatures, the impurity carriers are swamped by intrinsic carriers, causing the resistivity to decrease once again. This type of behavior is exhibited by  $\beta\text{-SiC}$ . However, the undoped samples appear fully ionized at a much lower temperature than the lightly nitrogen doped samples ( $10^{18}$ ). This effect may be

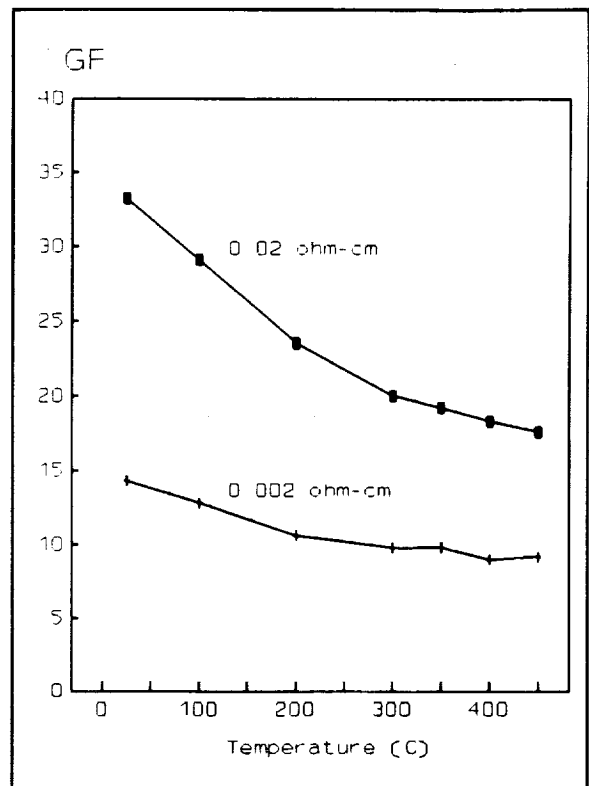


**Figure 3:** Gauge factor vs. temperature for n-type  $\beta\text{-SiC}$  gauges of the "A" configuration (Fig. 1).

explained by the donor mechanisms that control the electrical properties of  $\beta$ -SiC grown on silicon. Photoluminescence measurements [7] have determined that in the nitrogen-doped films, nitrogen is a substitutional donor with an activation energy of 40-54 meV, depending on the doping level. However, in the undoped films the principal donor, which has an activation energy of 18 meV, is not substitutional nitrogen [7]. At this time, the cause of this shallow donor is unknown. Nevertheless, it is possible, that the 18 meV donor, because of its lower activation energy, causes a lower ionization temperature in the undoped samples.

In the case of degenerately doped SiC ( $10^{20}\text{cm}^{-3}$ ), the Fermi level is in the conduction band. Thus, the carriers are fully ionized at all temperatures and the TCR increases due to scattering effects.

Intrinsic carrier generation was not observed in the TCR of SiC up to  $800^\circ\text{C}$ , because of the material's wide bandgap. As with silicon, the TCR of SiC decreases as the carrier concentration is increased. This is due to the effects of statistical degeneracy, which make semiconductors behave more like metals, which generally have very low TCR's.

### Photoelectrochemical Etching and Dopant Selective Etch-Stops in SiC

One of the technological problems for SiC transducers is that the material is chemically inert, making micromachining difficult. There are a number of molten metals and molten salts [1] that attack SiC, but these are impractical for device fabrication due to the high temperatures involved. Device structures have been selectively etched in SiC using Reactive Ion Etching (RIE) [8]. However, the etch rates reported for RIE are too slow for many applications and RIE shows no selectivity between different conductivity types. Recently, we have developed a photoelectrochemical etching technique which has very high etch rates (up to  $100\ \mu\text{m}/\text{min}$ ) and large selectivity between conductivity

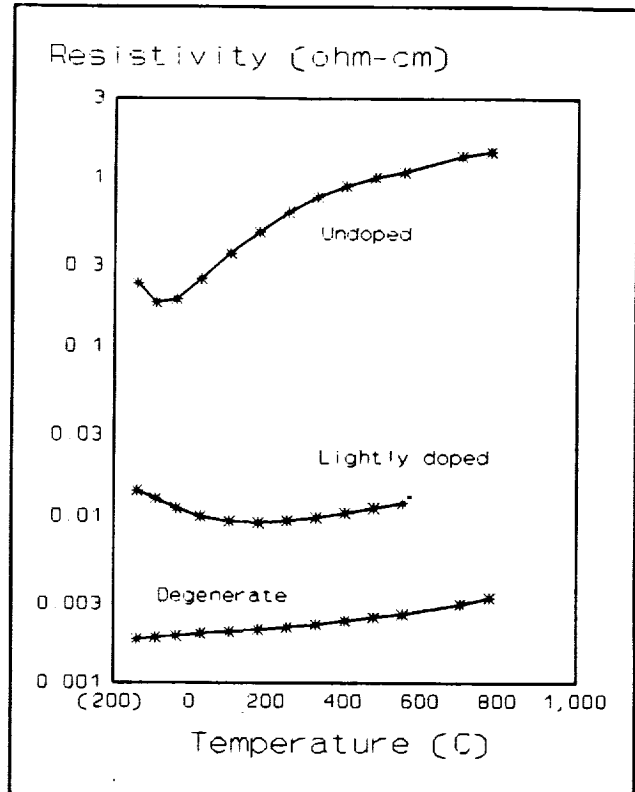


Figure 4: TCR of n-type  $\beta$ -SiC for several doping levels.



types.

The etch rates and process mechanism of SiC PEC etching have been described in an earlier publication [9]. Those results will be summarized here briefly for clarity. Fig. 5 is a diagram of the n-type  $\beta$ -SiC/HF junction, which is similar in its charge transfer and energy band characteristics to a Schottky contact. At equilibrium, the Fermi level of the semiconductor lines up with the redox potential of the solution, which for n-

type material results in upward surface band-bending. Under these conditions, photocarrier generation near the surface will result in hole confinement at the surface, while electrons will be driven into the bulk. The holes that reach the surface are transferred into the solution, causing anodic oxidation of the SiC by  $H_2O$ . The reaction products,  $SiO_2$  and  $CO_2$  are removed from the surface by HF dissolution and bubbling, respectively.

At certain potentials, p- and n-type SiC will exhibit the opposite band bending in HF solutions [10]. Thus, holes can be transported to the semiconductor/solution interface in the case of n-type material, while they will be confined in the bulk in p-type material. Therefore, a potential can be chosen where n-SiC will be etched and p-SiC will not, making dopant selective etch steps feasible.

#### High Temperature Ohmic Contacts for n-type $\beta$ -SiC Sensors

In order to fabricate high temperature sensors and other devices, it is necessary to develop ohmic contact metallizations that can withstand elevated temperatures. A variety of ohmic contact metallizations were investigated with contact resistivity measured as a function of anneal time in air. The metallizations were based on Ti and W ohmic contacts, which have contact resistivities as low as  $10^{-4} \Omega\text{-cm}^2$ . Several of the contact metallizations were stable after 10 hrs. at  $650^\circ\text{C}$ , while one system, based on a Ti ohmic contact, was able to withstand  $> 20$  hrs. at  $650^\circ\text{C}$  with only a 30-40% increase in contact resistivity. Contact resistivity was measured using the four point probe method developed by Terry and Wilson [11] and modified by Kuphal [12].

#### Acknowledgements

We would like to thank J.A. Powell and L.G. Matus of NASA Lewis for providing the SiC samples and for their useful discussions.

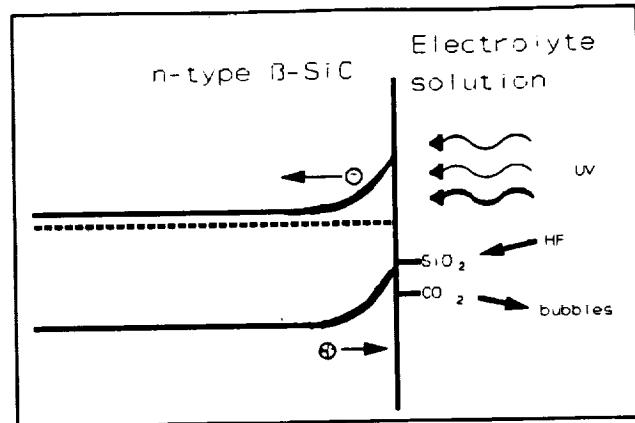


Figure 5: Band diagram of the SiC/HF interface.

## References

1. Silicon Carbide-1973, ed. by R.C. Marshall, J.W. Faust and C.E. Ryan, (Univ. of S. Carolina Press, Columbia, South Carolina, 1974).
2. I.V. Rapatskaya, G.E. Rudashevskii, M.G. Kasaganova, M.I. Iglitskin, M.B. Reifman and E.F. Fedotova: *Sov. Phys. -Solid State* **9**, 2833 (1968).
3. G.N. Guk, N. Ya. Usol'tseva, V.S. Shadrin, and N.K. Prokop'eva: *Sov. Phys. Semicond.* **10**, 83 (1976).
4. J.A. Powell, L.G. Matus, and M.A. Kuczumarski: *J. Electrochem. Soc.* **134**, 1558 (1987).
5. C. Herring and E. Vogt: *Phys. Rev.* **101**(3) 944-961 (1956).
6. R. Kaplan, R.J. Wagner, H.J. Kim, and R.F. Davis: *Solid State Comm.* **55** (1) 67-69 (1985).
7. J.A. Freitas, S.G. Bishop, P.E.R. Nordquist Jr. and M.L. Gipe: *Appl. Phys. Lett.* **52**, 1695 (1988).
8. J.W. Palmour, R.F. Davis, P. Astell-Burt, and P. Blackborow in " Science and Technology of Microfabrication " ed. by R.E. Howard, E.L. Hu, S. Namba and S.W. Pang (Mat. Res. Soc., Pittsburg, 1987) p. 185.
9. J.S. Shor, X.G. Zhang and R.M. Osgood Jr.: *J. Electrochem. Soc.* **139**, 1213 (1992).
10. J.S. Shor, R.M. Osgood Jr. and A.D. Kurtz: *Appl. Phys. Lett.* **60**, 1001 (1992).
11. L.E. Terry and R.W. Wilson: *Proc. IEEE* **57**, 1580 (1969).
12. E. Kuphal: *Solid State Electron.* **24**, 69 (1981).

FINAL REPORT ON THE TRADE-OFF CHARACTERISTICS OF ACOUSTIC AND  
PRESSURE SENSORS FOR THE NASP

Martin Winkler  
Kaman Instrumentation Corporation  
Colorado Springs, CO

Chuck Bush  
Kaman Sciences Corporation  
Colorado Springs, CO

INTRODUCTION

This is the final report of a trade study for the development of pressure and acoustic sensors for use on the NASP. Pressure sensors are needed to operate to 100 psia. Acoustic sensors are needed that can give meaningful information about a 200 dB SPL environment. Both sensors will have to operate from a high temperature of 2000°F down to near absolute zero.

At the start of this study, the performance goals and operating environment shown in Table 1 were given as a starting point. At this time in the study, it is known that many of these goals are unattainable, although they have been useful as guidelines in directing this trade study. Revised goals based on the findings of this study for the acoustic sensor are shown in Table 2.

The most significant compromises are: the smallest size attainable is 0.2 inch diameter; the highest frequency response for the microphone is 12 KHz. The temperature range is 70°F to +2000°F operational and absolute zero to +2200°F survival; linearity, resolution, accuracy and thermal performance are as yet unknown, although revised estimates are as shown in Tables 1 and 2.

SURVEY OF GENERAL PRINCIPLES

Sound is an oscillation in pressure, stress, particle displacement, particle velocity, or density that is propagated in an elastic or viscous medium or material. An acoustic sensor or microphone is a device that measures sound and from which information about sound pressure and frequency are obtained.

Performed under Contract  
For General Dynamics Corp.  
Order No. 4197599  
June, 1991

Table 1. Design Goals For Pressure/Acoustic Sensors

<u>Performance</u>	<u>Original</u>	<u>Revised Cap</u>	<u>Revised Eddy Cur</u>	<u>Revised Fiber Optic</u>	<u>Units</u>
Freq. Resp.	0 to 20K	0 to 5K	0 to 20K	0 to 20K	Hz
Pressure (max)	100	100	100	100	PSI
Accuracy	±0.5	±1	±0.5	±0.5	% of F.S.
Repeatability	±1	±1	±1	±1	% of F.S.
Size (max dia.)	0.125	0.26*	0.26*	.125	in
<u>Environment</u>					
Temperature (min)	-460	-330**	-330**	-330**	deg-F
Temperature (max)	2500	2000**	2000**	2000**	deg-F
Pressure Range	0 to 100	0 to 100	0 to 100	0 to 100	PSI

Acoustic Noise, Mechanical Shock and Thermal Shock goals unrevised.

\*Sensor only--does not include mounting.

\*\*Survival: -460 to 2200°F

Table 2. Revised Design Goals For Acoustic Sensor

<u>Performance</u>	<u>Original</u>	<u>Revised Eddy Cur</u>	<u>Revised Fiber Optic</u>	<u>Units</u>
Freq. Resp.	10 to 50K	10 to 12K	10 to 20K	Hz
Dynamic Range	100-200	100-190	100-190	dB
Linearity	±1	±1****	±1****	dB
Shift of Sensitivity	±1	±2	±1	% of F.S.
Accuracy	1	1****	1****	dB
Size (max dia.)	0.125	0.26*	.125*	in
<u>Environment</u>				
Temperature	-460 to 2500	-330 to 2000**	-330 to 2000**	deg-F
Pressure Range	0 to 100	0 to 100***	0 to 100***	PSI
Duration, Mechanical Shock, and Thermal Shock goals unrevised.				

\*Sensor only, does not include mounting provisions.

\*\*\*Must be vented.

\*\*Operating Survival: -460 to 2200°F.

\*\*\*\*Except for low press. levels.

Pressure is the force per unit area that one object exerts on another. A pressure sensor measures this force generally by changing the pressure to a physical displacement.

The difference between a pressure sensor and an acoustic sensor then is that the acoustic sensor only measures oscillations in pressure, while a pressure sensor measures both changes as well as static conditions.

Usually a diaphragm is used to convert pressure to a displacement which can be detected by a variety of transduction techniques. At the start of this study, a survey of leading researchers and manufacturers led to the elimination of piezo-electric and piezo-resistive transduction techniques from further consideration. Because of the extreme temperature range of this application, only non-contact transduction techniques are evaluated. These are capacitance, eddy-current and fiber optic.

Under this premise then, pressure acts on a diaphragm which is consequently displaced. This displacement is converted into an electrical signal which is proportional to the pressure. When it is required that this device operate over a wide temperature range, the relationship between pressure, diaphragm displacement and electrical signal becomes a variable influenced by temperature and pressure. Minimizing the temperature effect, or at least identifying and quantifying it, is the objective of good extreme environment pressure/acoustic sensor design.

Accounting for temperature transients and gradients along the sensor further complicates the design task. Also, compatibility of materials as well as stability or at least accountability of the changing material properties over a very wide temperature range must be inherent in the well designed pressure/acoustic sensor.

## DIAPHRAGMS

A plain circular diaphragm was selected for this study because of its high natural frequency relative to other pressure sensing devices of equivalent size (Bourdon tube, bellows, convoluted diaphragm). Furthermore, the plain diaphragm is well suited (manufacturable) to small sized sensors (less than 0.25" diameter).

The design formulae for flat circular diaphragms that were used in this trade study are as follows:

$$(T) \quad T_{MAX.} = \frac{3 a^2 p}{4 t^2}$$

$$(Z) \quad Z_{MAX.} = \frac{3 (1-V^2) a^4 p}{16 E t^3}$$

$$(F) \quad F = \frac{2.56 t}{\pi a^2} \sqrt{\frac{g E}{3 M (1-V^2)}}$$

T = MAX. STRESS

a = DIAPHRAGM RADIUS

P = FULL SCALE PRESSURE

t = DIAPHRAGM THICKNESS

Z = MAX. DIAPHRAGM DEFLECTION AT FULL SCALE PRESSURE

V = POISSON'S RATIO

E = YOUNG'S MODULUS

F = RESONANT FREQUENCY

M = SPECIFIC WEIGHT

g = GRAVITATIONAL CONSTANT

The first requirement, or the one that is not compromised, is the pressure range (100 psi pressure sensor, 15 psi acoustic sensor). Then the maximum diaphragm stress for a range of diaphragm diameters and thicknesses is calculated. A graph of stress versus radius for a 0.005" and 0.003" thick diaphragm is shown in figures 1 and 2.

Using the results of the material survey, a practical design limit of 20 KSI at 2000°F is established. This limit means that for a 0.003" thickness, the diaphragm can be no larger than 0.25" diameter, and for a 0.005" thickness, it can be no larger than 0.42" diameter.

Diaphragm center deflection is calculated for the same diaphragm thicknesses over a range of diameters and temperatures for MA 6000. These graphs are shown as Figures 3 and 4. From these graphs, the full scale diaphragm center deflection is determined by adding the maximum diameter requirement of the previous paragraph. The maximum deflection for a 0.003" and 0.005" thick diaphragm is 0.0011" and 0.0002" respectively.

For the three types of transduction techniques discussed, a minimum full scale diaphragm deflection of 0.0003", 0.001" and 0.003" is required for fiber optic, eddy-current and capacitance, respectively. These minimum deflections are based on system level signal to noise ratio and the desired resolution (1 part in 1,000).

A region of feasibility can now be determined as that area bounded by the maximum sensor diameter, the minimum required diaphragm deflection for a particular transduction technique and the deflection versus diameter curve. This region of feasibility for the eddy-current and fiber optic transduction techniques is shown in figures 5 and 6. Because the capacitance technique requires 0.003" deflection, it is not feasible at the diameters and thicknesses considered (up to 0.5" diameter, down to 0.003" thickness).

The resonant frequency for an eddy-current microphone is calculated to be 15 KHz and for the smallest fiber optic sensor, it would be 35 KHz. If the diaphragm is undamped, the useful portion of this frequency range is one third of the resonant frequency. This is approximately 5 KHz for the eddy-current probe and 12 KHz for a fiber optic probe.

## COMPARISON OF TRANSDUCTION TECHNIQUES

### Fiber Optic Sensors

#### Transduction Techniques

Many fiber optic based techniques have been used to sense pressure and acoustic signals. Fiber optic based sensors can offer a number of advantages over other techniques. These include: excellent sensitivity, small size, immunity to EMI, ease of multiplexing, and use in some extreme environments. Not all advantages are available in each of the various techniques. Disadvantages of some fiber optic sensors include: sensitivity to other environmental factors such as temperature and strain, complexity, sensitivity to light from other sources, and fragility.

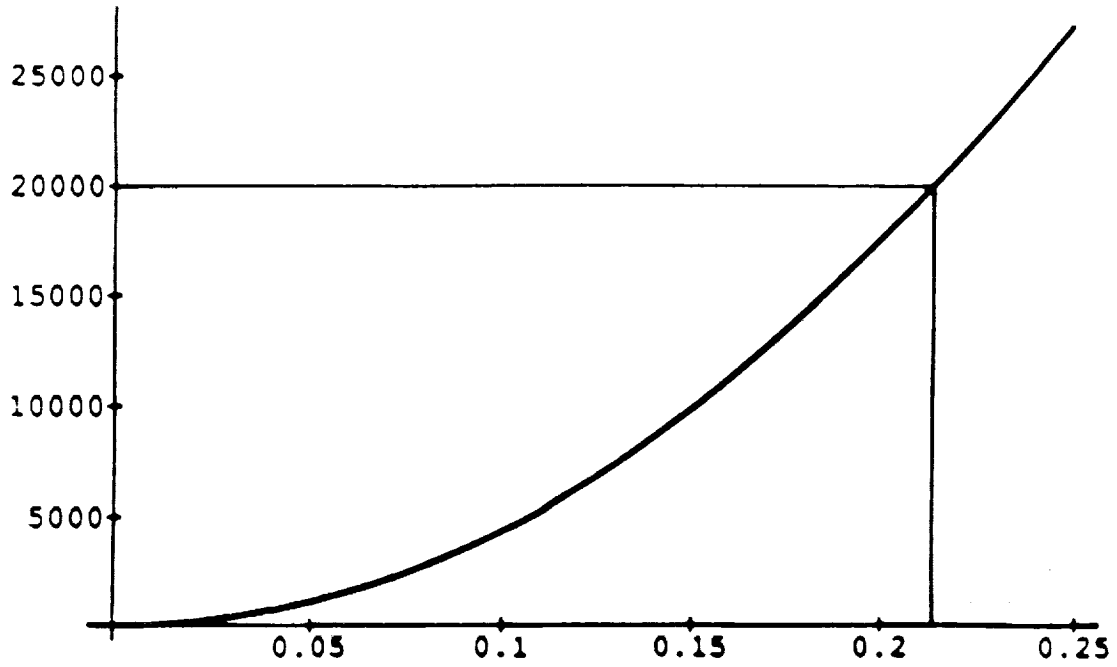


Figure 1. Stress (KSI) vs radius (inches) for 0.005" thickness.

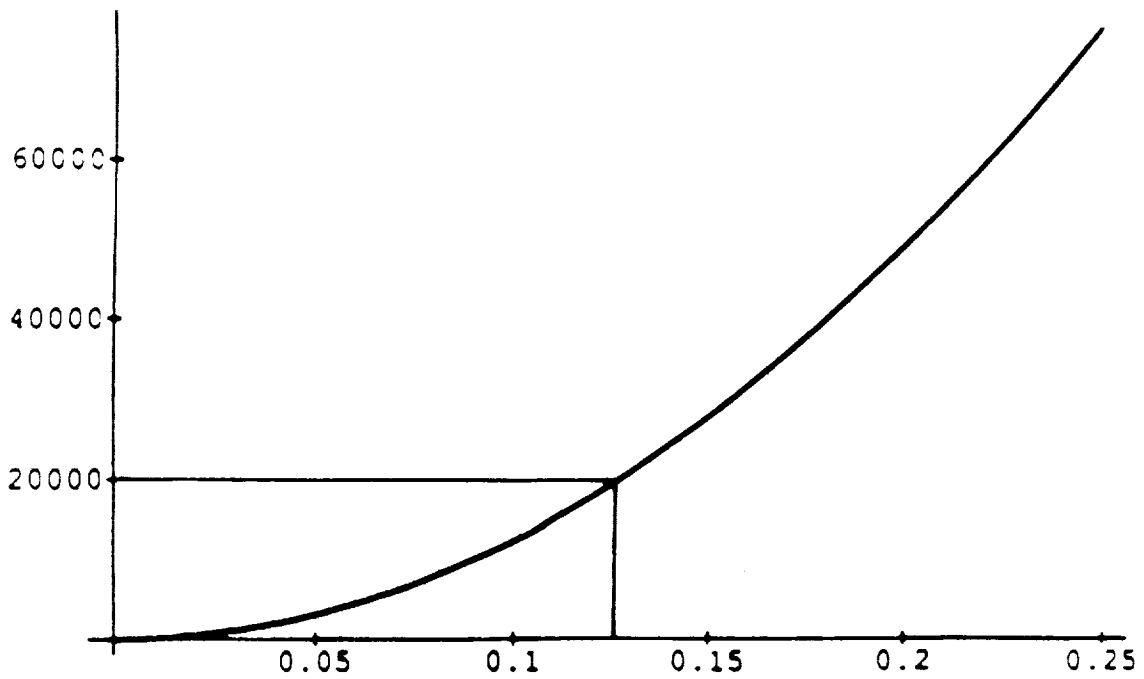


Figure 2. Stress (KSI) vs radius (inches) for 0.003" thickness.



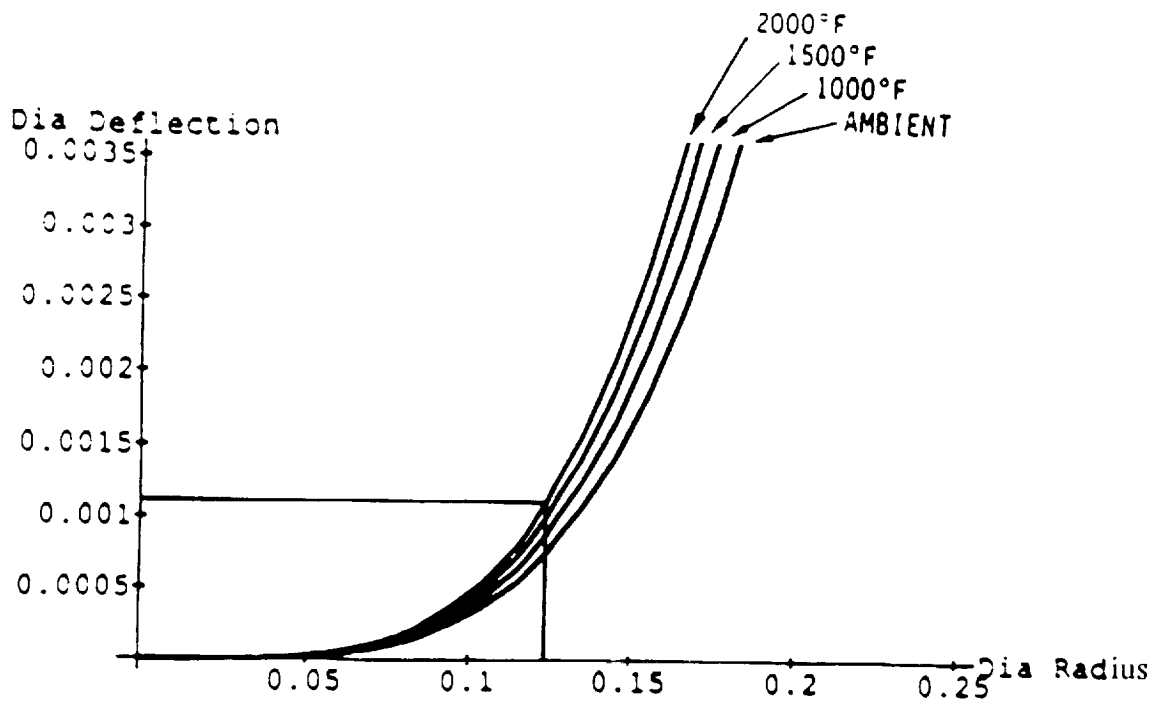


Figure 3. MA 6000 for 0.003" thickness.

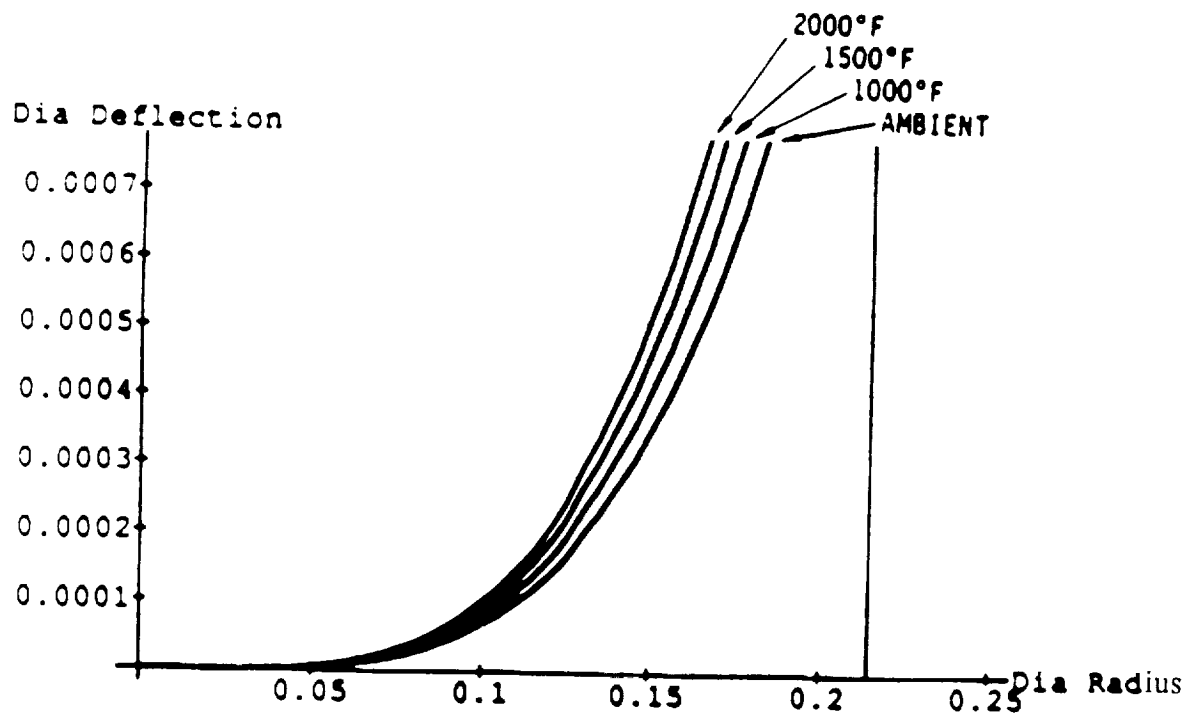


Figure 4. MA 6000 for 0.005" thickness.

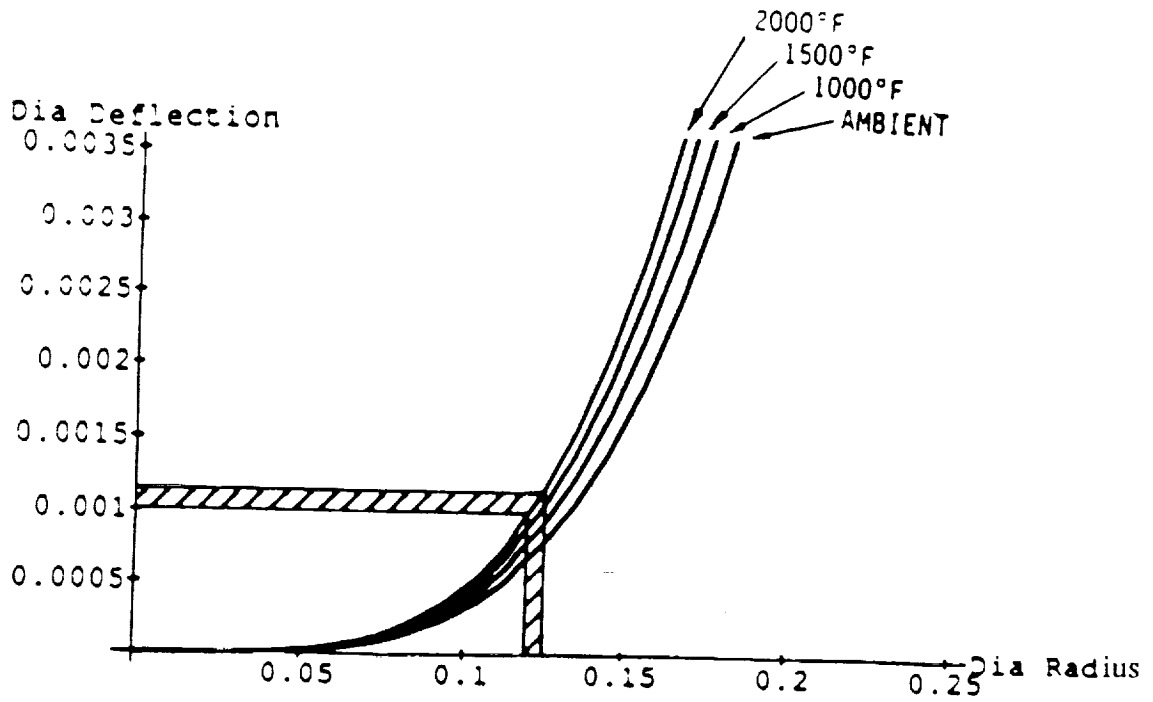


Figure 5. Eddy current feasible region.

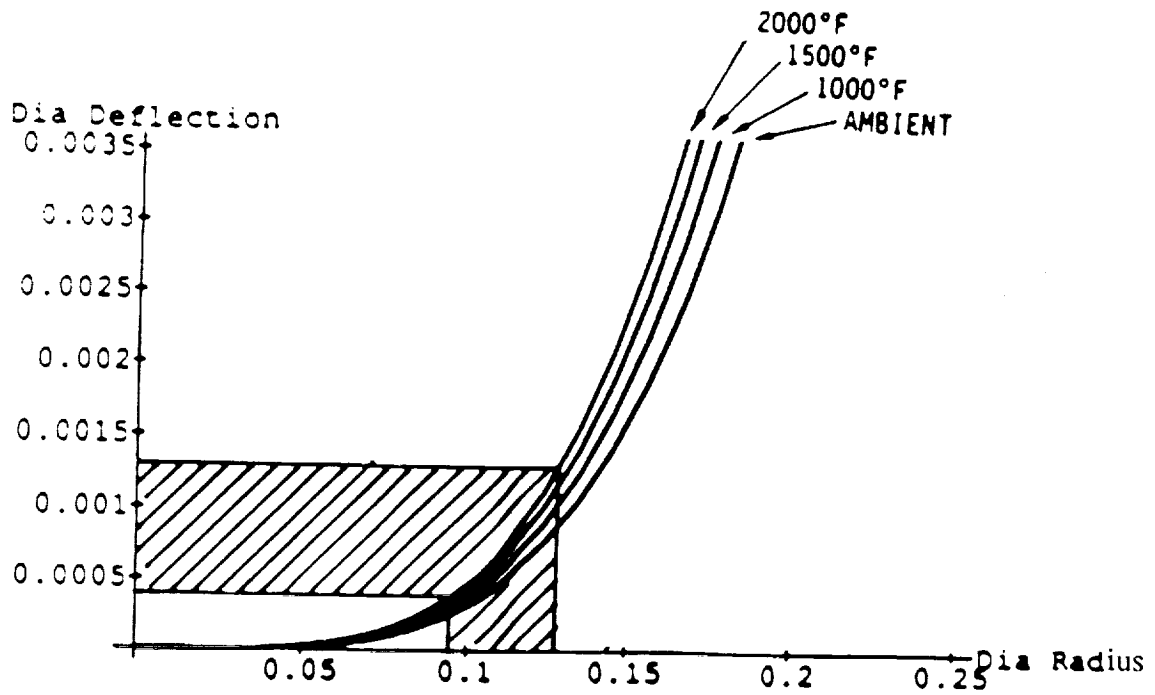


Figure 6. Fiber optic feasibility region.

Fiber optic sensors usually are divided into intrinsic, where the sensing occurs in the optical fiber, or extrinsic, where the sensing is external to the fiber and the fiber serves only to transport the light from the source to the sensor and then to the detector. Amplitude, phase, wavelength, and polarization are parameters that are affected by external stimuli and have been used as the basis for optical sensors. Pressure and acoustic sensors generally utilize amplitude, phase, or wavelength changes. Polarization generally is not used for these types of sensors and will not be discussed.

In amplitude sensors, the intensity of the light is modulated by the variable being measured. Amplitude sensors tend to be relatively simple, inexpensive, and easy to apply. Amplitude sensors include those that modulate the transmission of light across a gap (extrinsic) and microbend sensors (intrinsic). In gap sensors, the light exits a fiber, travels through a gap, may be reflected, and is received by the same fiber or a different one. The intensity of the light received is modulated by the size, or some other parameter, of the gap which varies with the quantity being measured. Microbend sensors make use of the fact that light is lost from an optical fiber when it is bent in a particular fashion. In this sensor, the fiber is placed between two ridged plates. When squeezed in response to some external variable, the fiber exhibits losses in a predictable manner. Microbend sensors tend to be much more sensitive than gap sensors, but have the disadvantage of being fairly large in order to accommodate the ridged plates.

Phase (or interferometric) sensors rely on a shift in phase of the optical signal relative to a reference signal and measure the interference that occurs when these signals combine. Phase sensors are more complicated than amplitude sensors, but usually offer greater sensitivity. Phase sensors have been built utilizing Mach-Zehnder, Fabry-Perot, Michelson, and Sagnac interferometers. These interferometers have many similarities. Generally, a source of coherent light is coupled into an optical fiber (usually single-mode) split into two paths (one a reference and the other the sensor), recombined such that interference occurs, and detected.

In a Mach-Zehnder interferometer, changes in characteristics of the sensor fiber (i.e., length or index of refraction) result in a change in phase relative to the reference path which is detected by the interferometer. Fabry-Perot interferometers generally consist of a single fiber with a sensor cavity at the end which has partially reflective surfaces at both ends. The amount of interference depends on the length of the cavity relative to the wavelength of the light. This type of sensor is generally insensitive to changes in the fiber characteristics. Michelson interferometers can be built similar to the Mach-Zehnder with a reference fiber and a sensor fiber. Displacements of a reflective mirror at the end of the sensor fiber cause phase differences relative to the signal reflected from a mirror at the end of the reference fiber. Michelson interferometers can also be constructed similar to Fabry-Perot interferometers utilizing only one fiber. In this case, half of the end of the fiber is coated with a reflective surface. The reference signal reflects off this surface, while the sensor signal exits the fiber and reflects off the sensor surface. The interference in the cable depends on the length from the end of the cable to the sensor surface relative to the wavelength of the light. As with the Fabry-Perot, this type of Michelson interferometer is generally insensitive to changes in the fiber characteristics. Sagnac interferometers inject light into both ends of a fiber coil and are sensitive to rotations about the axis of the coil. They are not generally used to sense pressure or acoustic signals.

Wavelength sensitive transducers tend to be the most complex, but can offer advantages in multiplexing more than one sensor on a single fiber. Sensors that make use of changes in wavelength include Bragg gratings and wavelength division multiplexing. Bragg grating sensors can be made by producing periodic variations in the index of refraction along a

short section in the core of an optical fiber. These gratings cause light corresponding to a wavelength of double the spacing of the index variations to be reflected. Spectrum analysis can be performed on the reflected or transmitted signal to determine the spacing of the index variations. In a sensor, the spacing of the index variations is made to vary as a function of the measured variable. Bragg gratings can easily be multiplexed by placing many sensors along one fiber, each sensitive to a different wavelength. Wavelength division multiplexing (WDM) sensors chromatically disperse the light from a broadband source and focus it on reflective/nonreflective code tracks. The presence or absence of reflection at different wavelengths is sensed by the detector and a digital output is formed which corresponds to the reflective code illuminated. The reflective code that is illuminated is made to vary as a function of the variable being sensed.

Due to the flexibility of fiber optics, there seems to be an infinite variety of fiber optic sensors. Those listed above are some of the more common types. Many others do exist, however, and could be the basis for an extreme environment sensor.

### Survey of Fiber Optic Capabilities

Numerous organizations have developed or are developing pressure and/or acoustic sensors using fiber optic techniques. It isn't possible within the constraints of this project to contact each of these organizations to ascertain their capabilities. A literature survey was conducted in order to identify those organizations most likely to be involved in the development of extreme environment pressure and acoustic sensors. These and several other companies were contacted. In addition to determining present capabilities, an attempt was made to determine what the possibilities and limitations are.

The survey indicated the following:

- 1) Presently available commercial fiber optic pressure and/or acoustic sensors are limited to approximately 450°C (840°F).
- 2) Silica optical fiber sensors have been developed in a research environment for temperatures of 900-1000°C (1650-1800°F). This appears to be the upper limit for silica sensors.
- 3) Several fiber optic manufacturers are willing to develop fiber optic sensors rated to approximately 1000°C (1800°F) on a "best effort" basis.
- 4) One researcher reports success measuring displacement using a sapphire sensor attached to a silica optical fiber up to 1600°C (2900°F). This technique could possibly be applied to pressure and/or acoustic sensors.
- 5) Interferometric methods are the most favored for small high temperature fiber optic pressure and/or acoustic sensors.

### Fiber Optic Sensor Considerations

In considering fiber optic sensors for the NASP application, it must be determined whether or not an accurate measurement can be made consistently with a sensor meeting the physical constraints over the range of environments expected. Of the common fiber optic sensor types, the size constraints and accuracy requirements appear to limit the choice to interferometers, especially Fabry-Perot or Michelson types, measuring displacement to a diaphragm. These provide the greatest accuracy with the smallest size. They also provide

relative immunity to changes in fiber characteristics with changes in temperature. Typically with interferometers, fringes are counted and interpolation is performed between fringes to increase resolution. Difficulties exist in determining diaphragm displacements using this technique due to ambiguities. Peaks in the output signal can be due to fringes or peaks in displacement. Usually a second sensor operating in quadrature and some sort of signal processing are required in order to remove the ambiguities. Also, determining absolute displacement can be a problem if the signal is temporarily lost or the sensor turned off. Changes in optical attenuation, due to changes in temperature, may cause intensity variations that could be interpreted as displacements.

Researchers at one organization report success measuring displacement with an unclad sapphire rod attached to a silica single-mode optical fiber up to approximately 1600°C (2900°F). They believe this to be the first successful silica to sapphire splice. The sensor is an interferometer which counts fringes and interpolates between them. A signal-to-noise ratio of 20 (13 dB) was achieved. This technique possibly could be applied to pressure and/or acoustic sensors measuring displacement to a diaphragm. No other researchers have been identified that have progressed this far in the development of high temperature fiber optic pressure and/or acoustic sensors.

Questions that must be asked when considering an extreme environment pressure and/or acoustic sensor include:

- Can adequate range and sensitivity be achieved?
- Can adequate resolution be achieved?
- Can changes in diaphragm characteristics over the temperature range be compensated?
- What is the frequency response?
- Can a sensor be built to withstand the expected environment?
- What is the minimum size?

The answers we can give to some of these questions will be more vague for fiber optic sensors than for capacitive or eddy current sensors due to the experimental nature of high temperature fiber optic sensors.

### Range and Sensitivity

Excellent range and sensitivity are characteristics of fiber optic interferometers. Because of the excellent sensitivity, the diaphragm can be designed for a smaller displacement, which leads directly to a smaller diameter sensor. Fiber optic interferometers may be the only way to achieve the NASP requirements for small size and high sensitivity. The maximum range is limited by how much light is captured by the sapphire rod after reflecting from the diaphragm. Because of the relatively large size of the sapphire, it appears that for the diaphragm diameters and displacements of interest, the range is more than adequate.

### Resolution

Experimental high temperature sapphire displacement sensors have not exhibited good resolution due to poor signal-to-noise ratio. There are several possible explanations for

this. It appears that these sapphire sensors may not be limited by the same factors that limit typical lower temperature fiber optic sensors. Instead, they appear to be limited by factors related to the high temperature and the need to attach a sapphire rod on the end of a silica fiber.

Figure 7 shows a typical sapphire fiber optic interferometer. Interference occurs between the light that is reflected from the end of the sapphire and that which exits the sapphire, reflects from the diaphragm, and re-enters the sapphire. The intensity of the light in the sapphire after the interference occurs is dependent on the distance from the end of the sapphire to the diaphragm relative to the wavelength of the light.

Resolution is determined by noise and error levels compared to signal level. Normal low temperature sensors are limited by spectral purity of the light source, detector dark current, and detector and amplifier noise. High temperature sapphire sensors have additional noise and errors due to optical noise caused by the glowing diaphragm, reflections at the silica-to-sapphire transition, and loss of light at the sapphire-to-silica transition due to the large difference in diameters.

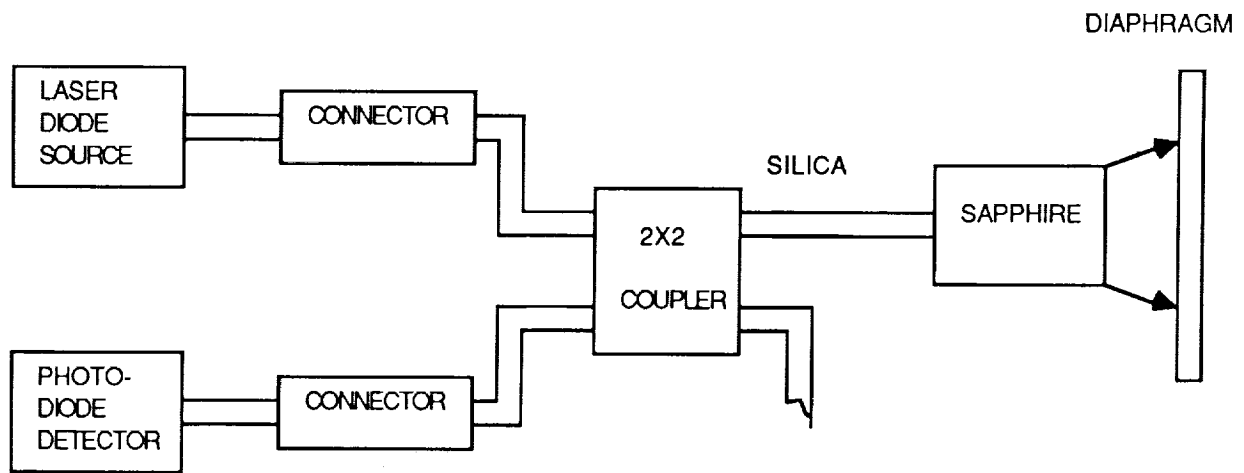


FIGURE 7. TYPICAL HIGH TEMPERATURE FIBER OPTIC PRESSURE/ACOUSTIC SENSOR

### Signal Level

Signal level at any point in the system is estimated by first estimating the power level coupled into the silica fiber by the laser diode source and then calculating the loss budget due to the various connectors, couplers, and the sensor. The electrical signal in the detector/amplifier is estimated by assuming a value for its responsivity at the wavelength of the source. Loss values for commercial connectors and couplers are specified by the manufacturer. A loss value due to reflection at the silica-to-sapphire transition can be calculated using the Fresnel reflectance coefficient (later we will discuss the unwanted interference that occurs here). Losses incurred at the end of the sapphire and the diaphragm can be estimated if some simplifying assumptions are made. Coupling loss at the sapphire-to-silica transition depends highly on the nature of the splice. Due to the large difference in diameter of the two fibers, considerable light loss is possible. Also, some light will be

reflected. Instead of estimating a value for this loss, calculations have been performed assuming 100 percent coupling efficiency and assuming a minimum efficiency determined by the ratio of the fiber diameters.

Typical laser diode modules will couple 2 mW of optical power into the source fiber. This value will be assumed in the following calculations. Loss values assumed for various components and associated power levels are given in Table 3. The sapphire-to-silica losses are based on a 50 micron sapphire fiber (which is the smallest available and results in the lowest losses). Because the sapphire is so much larger than the silica fiber, it is

<u>Table 3. Optical Signal Levels</u>		
<u>COMPONENT</u>	<u>LOSS</u> <u>dB</u>	<u>MAX. SIGNAL</u> <u>LEVEL (uW)</u>
Laser Diode Module	----	2000
Connector	0.5	1780
2X2 Coupler	3.5	801
Silica Fiber	1.0	633
Silica/Sapphire	.04	626
Sensor	2.4	363
Sapphire/Silica	.04-15.9	9-360
2X2 Coupler	3.5	4-162
Connector	0.5	4-144

difficult to couple all of the light in the sapphire into the silica, and also difficult to estimate what efficiency is possible. Therefore, a range of losses is given for this transition.

If perfect reflection from the diaphragm is assumed, and the maximum possible angle of the light exiting the sapphire is assumed to be dependent on the numerical aperture of the silica fiber, and the exit angle is assumed to be uniformly distributed, calculations indicate that more light is coupled back into the sapphire than what is reflected from the sapphire/air interface (for distances of 17.5 to 32.5 microns). This is not ideal for a good interferometer. For these calculations, it is assumed that the sapphire can be coated to increase the reflection and create an ideal interferometer (even though this may be very difficult in practice). If this is not the case, losses will be higher, resulting in lower signal levels.

Table 3 indicates that the power level in the fiber just prior to the detector is estimated to be between 4 and 144 microwatts, depending on the efficiency of the sapphire-to-silica splice. This table points out the importance of achieving an efficient splice. Please note that these calculations are meant to be rough estimates in order to identify general trends and not to be accurate design calculations.

#### Noise Levels

One of the advantages of using silica single-mode fiber to transport the light signal is the low loss of this fiber. Because the loss is low and an interferometer is insensitive to

changes in characteristics of the silica fiber, the sensor can be located a significant distance from the support electronics, allowing the electronics to be located in a controlled environment. This permits the use of standard laser diode sources and photodetectors. It is assumed since standard sources can be used that spectral purity of the light source is not a limit to the resolution of a sapphire interferometric sensor. This source of noise will be ignored in the following calculations.

Detector and amplifier noise can be estimated from the specifications of typical commercial hardware. A typical value for the noise equivalent power of a detector and amplifier is 0.044 microwatts. The noise equivalent power is the optical power in the fiber just prior to the detector that would result in equivalent electrical noise. This number allows comparison of the electrical noise of the detector and amplifier with the optical signal level. Compared to a signal level of 4 to 144 microwatts, we see that this noise can be quite significant (1%) if a poor sapphire-to-silica splice is made. Of course, if a lower noise detector/amplifier can be used, these numbers can be reduced.

A unique problem associated with high temperature fiber optic pressure/acoustic sensors is optical noise caused by glowing of the pressure diaphragm. The radiation from the diaphragm can be estimated using Planck's Radiation Law. Figure 8 shows the spectral exitance calculated for 1370°C (2500°F) for a black body. As can be seen from this figure, most of the energy is above 1000 nm in wavelength. Using typical responsivity curves for silicon and germanium detectors and assuming a spectral emittance for the diaphragm, the noise can be estimated. If the spectral responsivity curves are normalized to the signal wavelength (assumed to be 850 nm for silicon and 1330 nm for germanium), multiplied by the spectral exitance at 2500°F, integrated over wavelength and multiplied by the assumed spectral emittance of 0.65, the equivalent noise power can be calculated and compared to the signal power. Using this method, the noise in the sapphire is estimated to be 5 microwatts for the silicon detector and 90 microwatts for the germanium detector compared to an estimated signal level of 363 microwatts. This rough calculation indicates that the noise from the glowing diaphragm is significant, and from this standpoint it is better to use a shorter wavelength for the source and detector. A modulator/demodulator scheme may be necessary to minimize the effects of this noise.

### Error Sources

Typical photodiode dark currents are on the order of a few nanoamps. When compared to other error and noise sources, this is insignificant.

Less than 1% of the optical power is reflected at the silica-to-sapphire transition. This would appear to be insignificant. However, the electric field of the reflected signal is approximately 9% of the incident field. This reflected signal will interfere with the signal returning from the diaphragm after it has passed through the sapphire-to-silica transition. Even if no light is lost at the sapphire-to-silica transition, with the losses at the diaphragm, this interference will be significant. With significant losses at the sapphire-to-silica transition, this interference will swamp the sensor signal. The actual interference that occurs will depend on the relative phases of the two signals, which among other things depends on the length of the sapphire, which depends on temperature (a 1 cm piece of sapphire changes by over 100 wavelengths from 0 to 1370°C).



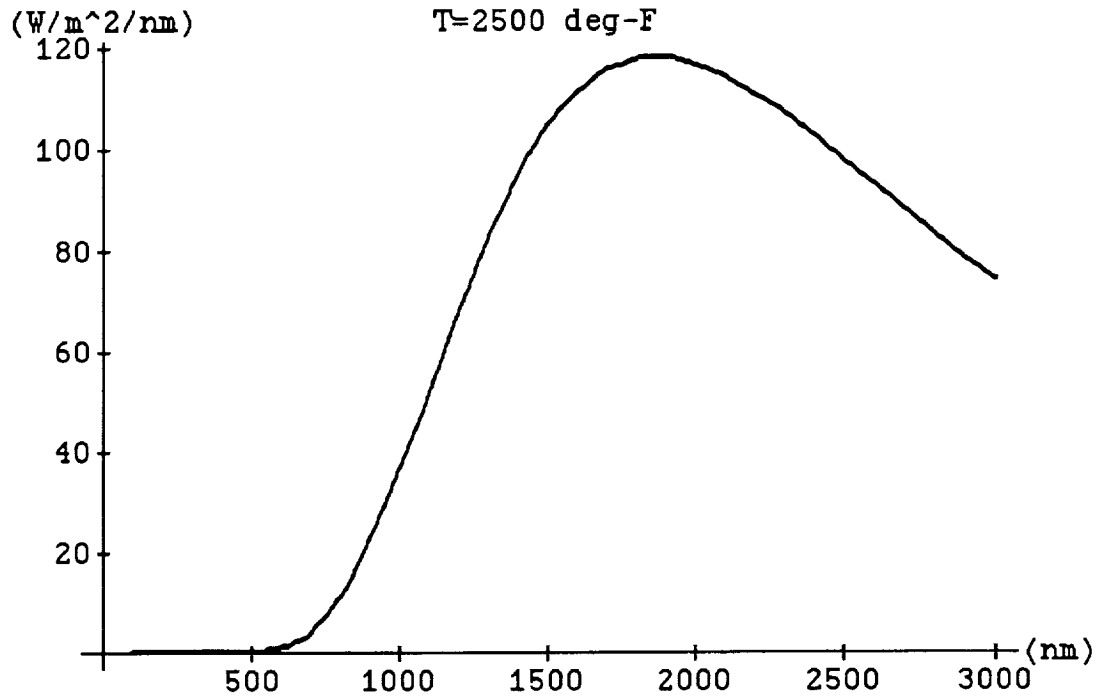


FIGURE 8. SPECTRAL EXITANCE FOR 2500°F

In summary, several noise and error sources limit resolution. Significant error can result when the reflected signal from the silica-to-sapphire transition interferes with the returning light, particularly if losses are high at the sapphire-to-silica transition. Also, optical noise due to the glowing diaphragm and detector/amplifier noise may possibly be significant.

#### Temperature Compensation

A concept has been developed using a reference sensor near the edge of the diaphragm to compensate for temperature induced variations in displacement. This appears to be a viable approach and may provide other advantages, including compensation for changes in intensity due to temperature changes and a measurement of noise due to radiation.

It most likely will be necessary to measure temperature in order to compensate for changes in diaphragm characteristics. This possibly can be done with a fiber optic sensor.

#### Frequency Response

Frequency response of fiber optic systems generally is well beyond that required for NASP. Frequency response in a high temperature sensor will be determined by diaphragm characteristics (see section on diaphragms).

#### Environmental/Materials

Sapphire is an excellent high temperature material. It is mechanically strong and hard and can withstand high temperature gradients. A disadvantage is that it is difficult to bond to other materials, such as silica fibers, claddings, and other sensor parts. Also, it is

produced using single crystal growth, a process that is slow and expensive. Impurities can be a problem. Presently, only rods and large diameter fibers (minimum size is 50 microns) are available for sensors. No single-mode fiber is produced. Because of this, high temperature sapphire interferometric sensors normally use silica single-mode fiber to transport the light signal from the source to the sensor and from the sensor to the detector. A splice is required to connect the silica fiber to the sapphire. Sapphire can easily withstand the temperatures required for NASP. Whether or not a practical sensor can be constructed using sapphire combined with other materials which can survive the expected environment is the question that is yet to be answered.

### Size

Present experimental high temperature fiber optic displacement sensors do not exhibit the small size required by NASP. However, the potential exists for a probe using fiber optic techniques to be smaller than those using other techniques if resolution can be improved so that a smaller diaphragm can be used.

### Other

As stated earlier, due to the low losses of silica optical fiber, the sensors most likely can be located a significant distance from the support electronics.

## Capacitive Sensors

### Transduction Techniques

Capacitive sensors have been used for many years to measure displacement in a non-contact manner. Pressure and acoustic sensors are constructed by measuring displacement to a pressure diaphragm, which deflects in a known manner as a function of pressure. Capacitive sensors can be divided into those that use parallel plate capacitors as sensing elements and those that depend on fringing capacitance. Measurement techniques vary widely. Most use a high frequency carrier to drive the sensor and demodulate the output.

The capacitance of an ideal parallel plate capacitor is equal to a constant times the area of the plates divided by the distance between the plates ( $C = kA/d$ ). This is the basis for most capacitive sensors. As the distance between the plates varies, the capacitance changes in an inverse relationship. Some capacitance sensors make use of the changing effective area of the plates as they move relative to each other in a transverse manner (not usually done in pressure/acoustic sensors). Generally in a parallel plate sensor, one plate is grounded and the other driven by an AC excitation signal.

Capacitances of actual sensors typically are 1 pF or less. Because of this, these sensors are sensitive to other capacitances between the sensor electrode (and anything connected to it) and ground. These include cable capacitances, capacitances in the electronics, and other stray capacitances. In order to minimize the effect of these capacitances, many sensors make use of a guard electrode. The guard electrode surrounds the sensor electrode and shields it from any grounds except the "target". The guard electrode is connected to the shield of a coax cable (near 100% shielding is necessary) and driven at the same potential as the sensor electrode, which is connected to the cable center conductor. The effect of the guard is to minimize currents flowing in the sensor circuit to charge and discharge extraneous capacitances. The guard also has the effect of reducing nonlinearities introduced by fringing fields at the edges of the sensor electrode.

Some capacitive sensors make use of fringe fields to sense displacement. These sensors typically use side by side plates and can measure the effect of grounded or ungrounded metal targets or even dielectrics introduced into the fringing field. In some cases, neither capacitor plate is grounded and a three terminal arrangement is used. In this arrangement, cable effects often can be minimized or eliminated.

Many different techniques are used to convert changes in capacitance to an electrical signal. These include bridge circuits, transformer ratio bridges, resonant circuits, and constant current sources used to measure capacitive reactance.

Bridge circuits use the sensor capacitance as one arm of a bridge. Changes in capacitance from a null position generate an output. Frequently, two sensor capacitors are used in a differential mode to improve linearity and provide some temperature compensation, at the expense of increased complexity.

Transformer ratio bridges use a transformer with multiple taps controlled by a microprocessor to balance the unknown sensor capacitance with a known reference capacitance. Three terminal techniques minimize the effects of cable capacitances. This method can provide very accurate results, but tends to be slow.

In a resonant circuit, the sensor capacitance is combined with an inductor to create a high Q resonance. The response at the carrier frequency varies as the frequency of resonance varies due to capacitance changes. Either amplitude or phase changes can be detected. This method tends to be very sensitive, but is also sensitive to changes in parameters of other circuit elements.

One method measures capacitive reactance ( $X_C$ ) instead of capacitance. Because reactance is inversely related to capacitance and capacitance is inversely related to displacement, capacitive reactance is directly related to displacement. This method uses an AC constant current source to drive the sensor, and the output voltage is directly related to displacement. Synchronous detection removes out of phase components due to resistive losses. A guard is required to minimize cable effects.

### Survey of Capacitive Sensor Capabilities

Many companies have developed and market capacitive based sensors. Because this is a more mature market than fiber optics, the tendency is for fewer organizations to be involved. Several were contacted in order to ascertain the state-of-the-art and to determine what might be possible. The survey indicated:

- 1) The highest temperature rating identified for a capacitive displacement sensor is 1000°C (1800°F). This sensor was operated accidentally to 1100°C (2000°F), but not in a calibrated fashion.
- 2) Other capacitive displacement sensors have been operated to 650-750°C (1200-1400°F).
- 3) Two manufacturers believe a 1200°C (2200°F) sensor is feasible, but would require a development effort.
- 4) One organization is presently working on a program to develop a 1650°C (3000°F) sensor.

- 5) A capacitive reactance type sensor driven by a constant current source and using a guard electrode appears to be the favored technology for a small, high temperature pressure and/or acoustic sensor.

### Capacitive Sensor Considerations

The technique using a constant current source to measure capacitive reactance is what has been used to construct the highest temperature capacitive sensors to date. Since this technique has resulted in the best results, appears to have many advantages, and is the most promising to extend to higher temperatures, it will be considered here. One of the advantages of this technique is that as the capacitance is reduced the signal level is increased. This supports the use of smaller electrodes with greater separation to some extent. However, as the capacitance is reduced, the necessary output impedance for a constant current source and the input impedance for the amplifier both increase. Also, as the distance from the sensor to the diaphragm increases, so do thermal variations.

### Range and Sensitivity

Range and sensitivity estimates are based on information obtained from a leading supplier of capacitive measurement systems. In the past, the highest temperature displacement systems have used a transducer with a sensor electrode of 0.060 inch. Transducers with electrodes as small as 0.040 inch are available but not for high temperature applications. The 0.060 inch electrode is what is recommended for an extended temperature range sensor. The maximum range for this electrode is approximately 0.030 inch, which is much larger than the diaphragm design will allow. Therefore, the range of this sensor is more than adequate.

In order to achieve adequate sensitivity, the supplier mentioned above estimates a full scale diaphragm deflection of at least 0.003 to 0.004 inch.

### Resolution

Resolution in capacitive sensors is generally limited by noise. Because of this, there is a trade-off between resolution and frequency response. Noise sources include thermal (Johnson) noise, amplifier voltage and current noises, cable noise and carrier noise. The impedance of a capacitive sensor tends to be very high due to the low value of capacitance. This reduces the current drive necessary to provide a reasonable output voltage, but adversely affects noise. The high impedance of the sensor necessitates a constant current source with an extremely high output impedance and an amplifier with an extremely high input impedance (to the extent that manufacturers patent their particular circuit). These extremely high impedances can result in high noise levels.

Typical resolution for a capacitive sensor of this type is 3 mVrms for a 5V maximum output and a frequency response of 200 Hz (at room temperature). With a frequency response of 3500 Hz, the resolution increases to 25 mVrms (at room temperature). Some of this is due to the carrier, which typically is at 15 KHz. The maximum carrier frequency is limited by available drive amplifier technology. With new driver technology and a new demodulation scheme, it is estimated that a 2000 Hz bandwidth can be achieved with a resolution of 10 mVrms (at room temperature).

Noise in high fidelity systems is usually a function of temperature. If it is assumed, due to the high impedance of the circuit, that the dominant noise is resistor thermal (Johnson) noise, the noise at high temperature can be estimated by multiplying the room temperature noise by the square root of the ratio of the absolute temperatures. This results

in a multiplier of 2.3 which leads us to estimate the noise at 2500°F to be 23 mVrms for a bandwidth of 2000 Hz and a maximum output of 2000 Hz and a maximum output of 5V. This is 0.7% of full scale.

### Temperature Compensation

Changes in the capacitive sensor output will occur due to changes in dielectric properties with temperatures even though every effort is made to eliminate this effect. If the temperature effects are repeatable and of the right polarity and magnitude, it may be possible to compensate changes in diaphragm characteristics as a function of temperature. The possibility for this type of compensation is not considered very likely.

For temperature compensation of diaphragm characteristics, a leading capacitive supplier believes a second capacitive sensor and/or temperature transducer will be required in each probe.

### Frequency Response

See discussion on resolution.

### Environmental/Materials

Capacitive sensors require conductive materials for the various electrodes and connections, insulating materials to separate the conductors, and materials to hold things together.

Because of the high impedance of the capacitive reactance, series impedances tend to be insignificant. These include conductor and electrode resistances and inductances. No special requirements are placed on the conductive materials, and any somewhat conductive material that meets the environmental and other requirements will do.

Also, because of the high impedance of the capacitive reactance, parallel impedances tend to be significant. These include cable and extraneous sensor capacitances and leakage in dielectric materials. In particular, in the constant current source system being discussed, whereas the impedance between the sensor electrode and guard can be quite low, the impedance between the guard and ground must be kept above one megohm. Several good high temperature ceramic materials are available. Unfortunately, due to the high capacitive reactance at the high temperatures to be encountered, even those have non-negligible conductances. To some degree, synchronous detection can eliminate the effects of leakage, but large leakage currents can load drivers and swamp the output signal. The design of a capacitive sensor will require careful attention to the selection of the dielectric material and the design of the insulators.

The selection of materials to hold things together possibly will be simplified by the lack of constraint on the conductive materials and complicated by the limited choice of dielectric materials.

### Size

The use of a 0.060 inch sensor electrode, as discussed in the section on range and sensitivity, and the need for a second sensor and/or temperature transducer result in a minimum probe size of approximately 1/4 inch. This does not include any additional room which may be required to increase the thickness of dielectrics in order to increase their electrical resistance at temperature.

The requirement to have a diaphragm displacement of 0.003 to 0.004 inch results in a minimum diaphragm diameter of approximately 3/4 inch (see the section on diaphragms for further discussion of this requirement). This requirement then is the driving one.

#### Other

Capacitive based sensors are sensitive to cable length. Most systems (including the one discussed here) are limited to cable lengths of 20 feet, with 5 to 10 feet being the preferred maximum length.

### Eddy Current Sensors

#### Eddy Current Transduction Techniques

Eddy current techniques have been used for non-contact displacement sensors for quite some time and the basic principles are well understood. This transduction technique can be used in pressure and/or acoustic sensors in a similar fashion to the other techniques discussed - measuring displacement to a pressure diaphragm.

In an eddy current sensor, an AC current flowing in a coil generates a magnetic field in the area near the coil. Placing the coil near a metal target induces a current flow in the target. Because the current flows in a circular pattern, it is called an "eddy current". The induced current produces a secondary magnetic field that opposes and reduces the intensity of the original field. This changes the effective impedance of the exciting coil. The impedance change depends on the distance of the target from the coil. It can be detected and provides the basis for a non-contact displacement sensor.

Typically, a balanced bridge network is used to detect impedance changes in the sensor coil. The bridge is driven by a high frequency (approximately 1 Mhz) carrier, and its output is amplified, demodulated, and converted to a linear output proportional to the target displacement.

#### Survey of Eddy Current Capabilities

The highest temperature eddy current sensor developed to date is an 1100°C (2000°F) microphone developed for the Air Force Dynamics Laboratory. This sensor had a dynamic range from less than 90 dB SPL to greater than 190 dB SPL (relative to 20 micropascals). Resolution was limited by noise, which was measured to be 0.195 mVrms with full scale (the worst case) output and a 10 KHz bandwidth (at room temperature).

#### Eddy Current Sensor Considerations

Eddy current sensors differ from capacitive sensors in that they are low impedance devices and they use magnetic fields versus electric fields. While some of the same considerations must be made, for the most part, they tend to be quite different.

#### Range & Sensitivity

Range of the sensor is limited by the size and inductance of the coil. For coils that can be built with available materials, more than adequate range is available for practical diaphragm displacements. Sensitivity of the eddy current sensor is determined by a number of factors, including the coil inductance and target resistivity. Sensitivity is an

important factor in determining necessary diaphragm displacement, which determines diameter. See the discussions on diaphragm design.

### Resolution

As with capacitive sensors, resolution is limited by noise. However, eddy current sensors have two properties which tend to greatly reduce noise levels. First, a much higher carrier frequency is used - about 1 MHz versus 15 KHz. This allows much higher bandwidths without introducing carrier noise. Also, any carrier present is usually beyond the frequency range of interest. Second, the low impedance of eddy current sensors results in much less noise being generated and greater attenuation of noise from other sources. The impedance of eddy current sensors is measured in hundreds of ohms versus tens or hundreds of megohms (or greater) for capacitive sensors. Signals from eddy current sensors do require higher levels of amplification, so some of the advantage is lost. Noise in eddy current systems mainly is generated in the amplifier and other electronics and, therefore, is not dependent on the sensor temperature. A noise level of 0.195 mVrms has been measured for a 1/2 inch diameter high temperature microphone with a bandwidth of 10 KHz and maximum signal level of 2.5V. This noise level is 0.01% of full scale. It is expected that the resolution of a 0.3 inch sensor will not be this good. Resolution of better than 1 part in 1000 is expected.

### Temperature Compensation

Due to the fact that eddy current sensors are low impedance devices, they are sensitive to changes in conductivity of the sensor coil and, to a lesser extent, target materials. Also, they are sensitive to inductance changes caused by thermal expansion (or contraction) of the sensor coils. Because changes in conductivity and thermal expansion are well behaved physical properties, in the past it has been possible to use these changes to compensate for changes in diaphragm characteristics with temperature. The ability to do this depends on the particular materials and geometry used.

In extreme environment applications, generally two coils are used in opposite legs of the bridge to provide a signal that is much less sensitive to extraneous environmental factors (such as temperature). Stimuli that act on both coils equally are effectively cancelled out.

### Frequency Response

As stated in the section on resolution, good resolution has been achieved in systems with 10 KHz bandwidth. Higher bandwidths are possible with lower resolution. However, it is likely that for an eddy current sensor, diaphragm characteristics will be the limit on frequency response (see the discussion on diaphragms).

### Environmental/Materials

The requirements for materials are quite different for eddy current sensors when compared to capacitive sensors, mainly due to the difference in impedance of the sensors. With eddy current sensors, the impedances of the conductors are significant and careful attention must be paid to the selection of conductor materials, including the diaphragm (which is the target). The properties of these materials must be well understood over the operating temperature range. As discussed in the section on temperature compensation, temperature-induced changes in different properties are often used to compensate each other. Dominant effects are due to changes in mechanical properties of the diaphragm, such as thermal expansion and change in modulus.

Due to the low impedance of the sensor, dielectric properties of the insulators are relatively unimportant and almost any good high temperature insulating material will do.

The selection of materials to hold things together possibly will be simplified by the lack of constraint on the dielectric materials and complicated by the choice of conductive materials.

#### Size

The minimum size for an eddy current sensor is determined by the smallest coil that can be wound with high temperature wire and have adequate inductance, coil side clearances, minimum diaphragm deflection, and sensor side wall thickness. See the section on diaphragms for further discussion. The minimum outside diameter for an eddy current sensor is estimated to be 0.3 inch.

#### Other

Maximum cable length is determined by the cable capacitance. The amount of cable capacitance that can be tolerated depends on the characteristics of a particular sensor. With extreme environment sensors built in the past, cable lengths have been limited to approximately 42 feet. This is likely to be different for a new sensor, and could be longer or shorter. If lower capacitance cable were used, it may be possible to extend this range.

### Summary Of Transduction Techniques

No transduction technique is available to meet the NASP requirements with existing technology.

Capacitive sensors are large relative to the NASP requirement and suffer from poor resolution and frequency response and the need for the sensor to be within 20 feet of the electronics. The poor resolution and frequency response are fundamental problems due to noise caused by the high impedance of the capacitive sensors. With further development, it might be possible to reduce the size or increase cable length, but not without adversely affecting resolution and frequency response.

Eddy current sensors are also large relative to the NASP requirement and also have limited cable lengths (typically 42 feet in the past). Although eddy current sensors have proven performance in extreme environments, due to the constraints in designing them, it is believed the size of an extreme environment sensor could be no smaller than 0.3 inch in diameter. With some work, cable lengths possibly could be extended.

Fiber optic sensors provide the possibility for a small sensor to meet the NASP requirement, even though present developments don't exhibit this characteristic. The need to use sapphire at high temperature complicates the design and introduces errors and uncertainties not present in low temperature silica sensors. Present research sensors suffer from poor resolution. A significant development effort will be required to realize the potential of fiber optic sensors.

Short-term development seems to favor eddy current techniques with the penalty of larger size. Long-term development may favor fiber optics with the penalties of cost, schedule and uncertainty.



## MATERIALS

For the development of an acoustic/pressure sensor that operates from -460 to 2000°F (and possibly higher) materials are the key limitation to performance. For the three sensor types considered in this development (capacitance, eddy-current, fiber optic), some of the basic material requirements are shown in Table 4.

Numerous materials are available in the above categories that will maintain useful properties up to 1500°F and some even up to 1800°F. However, very few choices remain when the requirement goes up to 2000°F. Platinum, molybdenum and rhodium are some of the choices for the conductors and magnet wire. Alumina, magnesia, hafnia, berylia and boron nitride are available as insulators. Cotronics and other manufacturers make ceramic cements with a range of properties that are useable to 3000°F and higher.

But when it comes to choosing a material for mechanical support and specifically the diaphragm, few materials have anything left to offer. For this study, the materials shown in Table 5 were reviewed for the diaphragm application.

The most promising material for use as a diaphragm at 2000°F and higher is the mechanically alloyed nickel base oxide dispersion strengthened and precipitation hardened series of metals. Two of these alloys are Inco Alloy's MA 6000 and MA 754. Samples of both these materials have been purchased for this study.

Both these alloys are machinable to the requirements of this study. Weldability has yet to be fully characterized but appears promising so far (two samples have been machined and hermetically welded). Compatibility with other materials has yet to be tested. High temperature properties have yet to be verified. Investigation of other materials necessary for these sensors is continuing.

Table 4. Types Of Materials Required

- Electrical Insulators - To isolate conductors
- Electrical Conductors - To transmit signals
- Mechanical Support - For insulators, conductors, and other components
- Diaphragm - To transduce pressure into displacement
- Hermetic Seal - To isolate sensor components from environment
- Magnet Wire - To make an efficient inductor (eddy current only)
- Sapphire and Silica Fiber - To transmit optical signals (fiber optic only)
- Silica or Sapphire to Metal or Ceramic Seal - To isolate components from environment (fiber optic only)
- Reflective Coatings - To improve signal to noise ratio (fiber optic only)
- Ceramic Cements - To assemble components
- Springs - To accommodate differential expansion of various materials
- Ceramic Fibers or Wool - To use as electrical insulators
- Transition Materials - For spanning different material properties

Table 5. Diaphragm Material Candidates

- Titanium Silicon Carbide Composite - SiC fibers 3 to 5 mils, too large for a 3 mil diaphragm
- Titanium Aluminide Composites - Same as Ti-SiC, fibers too large
- Nickel Aluminide - Shows promise
- Iron Aluminide - Shows promise
- Niobium Beryllides - Still under consideration
- Ceramic Matrix Composites - Non-conductive, may be suitable for fiber optic sensor
- Carbon-Carbon Composites - Non-conductive, may be suitable for fiber optic sensor
- INCO 718 - Insufficient strength at 2000 deg-F, useable to 1500 to 1800 deg-F.
- INCO MA 6000 - Shows promise, oxidizes rapidly above 2000 deg-F.

## CONCLUSIONS

- Diaphragm materials limit minimum size and maximum frequency responsible attainable.
- No transduction is available to meet all the NASP requirements with existing technology.
- Capacitive sensors are large relative to the requirement, have limited resolution and frequency response due to noise, and cable length is limited to approximately 20 feet.
- Eddy current sensors are large relative to the requirement and have limited cable lengths (typically 42 feet in the past).
- Fiber optic sensors provide the possibility for a small sensor, even though present developments don't exhibit that characteristic. The need to use sapphire at high temperature complicates the design. Present high temperature research sensors suffer from poor resolution. A significant development effort will be required to realize the potential of fiber optics.
- Short-term development seems to favor eddy current techniques with the penalty of larger size, and reduced dynamic range for acoustic sensors.
- Long-term development may favor fiber optics with the penalties of cost, schedule, and uncertainty.



## VERY HIGH TEMPERATURE SILICON ON SILICON PRESSURE TRANSDUCERS

Anthony D. Kurtz  
Timothy A. Nunn  
Stephen A. Briggs  
Alexander Ned  
Kulite Semiconductor Products, Inc.  
Leonia, NJ

### SUMMARY

A silicon on silicon pressure sensor has been developed for use at very high temperatures (1000°F). The design principles used to fabricate the pressure sensor are outlined and results are presented of its high temperature performance.

### INTRODUCTION

The small size and wide frequency response of piezoresistive silicon pressure sensors has made them the first choice for wind tunnel and aerospace development programs. Most of the silicon pressure sensors are fabricated by diffusing the strain gage pattern into a silicon diaphragm. Such a construction relies on the reversed biased P/N junction for its electrical isolation. The strong temperature dependence of the P/N junction leakage currents has limited the maximum temperature to about 400°F. Piezoresistive silicon strain gages are capable of operating to a considerably higher temperature than 400°F. In order, therefore, to realize the full high temperature potential of silicon pressure sensors, it is necessary to use a fabrication process that did not rely on P/N junctions for isolation.

### MECHANICAL PROPERTIES OF SILICON

To be useful at high temperatures, a piezoresistive silicon strain gage should have the following properties:

- 1) It must have good stable mechanical properties at the maximum operating temperature.
- 2) The piezoresistive coefficient should be sufficiently high that signal conditioning does not become a problem. If the strain gage is to be used over a wide temperature range, then the temperature coefficient of the gage factor should be such that it can be temperature compensated.
- 3) It must be possible to bond the strain gage to the structural member. In the case of a pressure transducer, this will usually be a diaphragm.

The mechanical properties of silicon have been fairly well studied at moderate temperatures. The published data at high temperatures is not extensive. The most often quoted is due to Pearson, Read and Feldmann (reference 1). The three authors showed that at a high enough temperature silicon no longer behaves like a brittle material. They showed that above 1000°F (approximately) silicon was able to yield and that the yield stress fell rapidly with increasing temperature. For the purpose of this paper, the interesting results from the paper of Pearson et al is the relative useful strength of silicon at high temperature. This is shown on Figure 1 as the percentage decrease in the strength of silicon as a function of temperature. (This figure is taken from the results plotted in Figure 5 of Reference 1). The change of ordinate from absolute to relative values was done because Reference 1 was concerned with whiskers of silicon which are known to have a higher strength than bulk silicon.

To use Figure 1 to determine the potential maximum working temperature for a silicon strain gage mainly involves a judgement as to the maximum "safe" operating stress. For pressure transducer manufacturers this basically involves determining proof pressure and burst pressure. In both cases, manufacturers are usually conservative so that a reduction in the strength of the silicon of 30% is probably acceptable. In which case, from mechanical considerations, silicon can be assumed to be usable up to 1100°F.

Perhaps the second most important mechanical property of a strain gage is its Young's modulus. Data are available on the room temperature stiffness coefficients (Reference 2) but not much data are available on the temperature dependence. Based on comparative studies a "best guess" for the reduction in Young's modulus at 1100°F from its room temperature value is of the order of 5%. This figure, if correct, is an acceptable reduction for a silicon strain gage.

#### PIEZORESISTIVE PROPERTIES OF SILICON

Having acceptable mechanical properties at high temperatures does not, of course, make a material a useful strain gage. It must also have an acceptable gage factor (GF). Potentially this should not be a problem with a silicon strain gage. By the proper choice of doping levels gage factors of >100 can be achieved at room temperature. Even if this were to be reduced by 80% at high temperatures it would still leave a very workable GF of 20. As is well known in the strain gage field, a high piezoresistive coefficient (high GF) is accompanied by a high (negative) temperature coefficient of GF (TCGF) and vice versa (References 3 and 4). As a consequence of this (crude) correlation between GF and TCGF it follows that two silicon strain gages which had different GF at room temperature could have the same GF at some higher temperature. If the two gages were to be used only at this higher temperature, then as far as the GF is concerned, it would not matter what the doping levels were. Pressure transducer users are rarely so easily satisfied. They invariably require the transducer to operate over a range

of temperatures; usually the higher the permitted maximum temperature the wider the temperature range requested. In which case the choice of doping levels and hence GF and TCGF becomes more important.

It is generally true that the higher the doping level, the more linear the temperature effects on the strain gage parameters. This allows the strain gage parameters to be easily temperature compensated. If the quest is for high GF, then the non-linear temperature characteristics can be accommodated over a moderate temperature range. This is invariably done by the use of non-linear temperature sensitive components which must experience the same temperature as the strain gages. This is acceptable so long as the non-linear temperature sensitive component can operate over the required temperature range. This use of non-linear strain gage components becomes a major problem as the upper temperature limit is increased.

Kulite has always used degenerate doping levels so as to ensure the optimum linear temperature characteristics. Over even moderate temperature ranges, this has the advantage that passive temperature compensation techniques could be used where the temperature compensation components (resistors) need not be at the same temperature as the piezoresistive strain gages. Over moderate temperature ranges (300°F) the merits of high or low doping levels are debatable. This is not the case as the temperature range is extended upwards. A limit will be reached where it is no longer possible to obtain non-linear temperature compensation components. At this upper temperature limit degenerate doping offers significant advantages.

#### SILICON ON SILICON SENSOR

So far the discussion has been concerned with the mechanical and electrical properties of silicon strain gages for use at high temperatures. For pressure transducer applications the chosen strain gages must be fixed to some structural member, the strain of which varies with pressure. The most popular structure used for pressure transducers is some form of rigidly clamped thin section plate. At high temperatures bonding of the strain gages to the pressure diaphragm is a problem.

This is not an easy problem to solve. First, there is the difficulty of achieving good adhesive strength at high temperatures. Secondly, there is the potential problem in the mismatch of the thermal expansion coefficients between the strain gages, adhesive and diaphragm. The most appealing way to overcome the above problems would be to use silicon as the diaphragm and diffuse the gage pattern into the diaphragm. This naturally is the now standard method of manufacturing piezoresistive pressure sensors. This approach overcomes all of the problems due to bonding and mismatch of thermal expansion. Unfortunately, the gages are isolated from the silicon diaphragm (and each other) by the P/N junction formed during the doping process. Although great improvements have been made in the leakage currents

of reverse biased P/N junctions, they all ultimately fail at high temperature because of the intrinsic exponential temperature relationship. The maximum working temperature, while still retaining adequate isolation, is around 400°F.

The Kulite approach to the high temperature problem was to stay as close as possible to the ideal design. That is of using silicon gages bonded to a silicon diaphragm but without the inherent problems of adhesives. Figure 2 shows a section through a Kulite silicon on silicon pressure sensor (Reference 5). The pressure sensitive diaphragm is formed by etching mono crystal silicon. The built in edges of the silicon diaphragm are anodically bonded to a relatively massive piece of glass. The thermal expansion coefficient of this glass base matches that of silicon. The anodic bond is a molecular bond so that the structure is mechanically stable over a very wide temperature range. The top surface of the silicon diaphragm is coated with a thin insulating layer of glass and the piezoresistive strain gages are anodically bonded to the thin glass layer. Four gages are bonded so as to form a fully active Wheatstone bridge. The silicon strain gages are thus isolated from the silicon diaphragm by the glass layer. The anodic bond between the strain gages and the glass results in the whole structure being held together by molecular bonds. This structure approaches the optimum that can be achieved for a high temperature piezoresistive silicon pressure sensor.

For the silicon pressure sensor described above to be useful as a pressure transducer, it must be housed in some suitable pressure fixture with some means of making electrical connections. The transducer housing need not be large because all that it will contain is the silicon sensor (size approximately .05 inch cube) and the electrical connections. There will not be any compensation components as none are suitable for operation at very high temperatures. The size of the transducer is, therefore, determined solely by the pressure and electrical connections. For very high temperature operation the most suitable electrical cable is the metal clad mineral insulated type, so this was the type chosen. One style of the Kulite very high temperature pressure transducer is shown in Figure 3.

## TEST RESULTS

This section presents results obtained from tests on about 200 very high temperature transducers employing the silicon pressure sensor described above. These covered full scale pressure ranges of 40 to 100 psia. The results are presented in terms of the most important pressure transducer parameters. These are the temperature induced changes in the sensitivity, offset and resistance of the strain gage bridge.



The overall nominal span (sensitivity) shift with temperature (Figure 4) was  $-3.8\%/100^{\circ}\text{F}$  referred to room temperature (RT). The nominal RT spans were 20mV/volt so that at  $1000^{\circ}\text{F}$  the outputs were 13mV/volt. Even with degenerate doping levels the span shifts over a  $920^{\circ}\text{F}$  temperature range had significant non-linearity. The same is true of the zero shifts (Figure 5) but the overall zero shift of just 5% up to  $1000^{\circ}\text{F}$  is an excellent achievement. Such a relatively low zero shift is a good demonstration of the high temperature stability of the silicon on silicon pressure sensor. The temperature coefficient of resistance (TCR) of the silicon on silicon sensors was approximately  $10.8\%/100^{\circ}\text{F}$  and is reasonably constant up to  $1000^{\circ}\text{F}$  (Figure 6).

Temperature compensation using a remote resistor network is nominally a linear temperature correction. It does, however, introduce its own (positive) non-linearity the size of which increases with increasing temperature range. The slight increase in TCR with temperature shown by Figure 6 does compensate for this to some extent; but then the (negative) increase in the TCGF (Figure 4) is detrimental. The performance that can be obtained with the silicon on silicon pressure sensors using passive temperature compensation is shown by Figure 7. Although perfect temperature compensation can be achieved at the temperature extremes, the span has a +6% error at mid temperature and the offset has an error of -1%. By choosing to compensate at two intermediate temperatures, the errors can obviously be halved to give  $\pm 3\%$  span error and  $\pm 0.5\%$  offset errors. It is possible to eliminate the above non-linear temperature error by using computer correction techniques. This involves the usual approach of storing the calibration constants of the pressure sensor at various temperatures and, by measuring the sensor temperature, applying the appropriate correction. This is made easier for a piezoresistive pressure sensor because the high TCR enables the strain gages to be used to measure temperature as well as pressure.

## CONCLUSIONS

From the tests which have been performed and reported upon here, there is no doubt that silicon on silicon pressure sensors are capable of a remarkably good performance up to very high temperatures. Silicon on silicon pressure sensors should considerably extend the upper temperature range for making both static and wide bandwidth dynamic measurements. Having extended the temperature range for piezoresistive pressure transducers up to  $1000^{\circ}\text{F}$  using silicon, work is already being done to extend the upper limit by using silicon carbide (Reference 6). A note of caution must, however, be sounded. The objective of developing miniature pressure sensors for very high temperature operation is to supply a tool for aerospace test engineers. Although the life at  $1000^{\circ}\text{F}$  of silicon on silicon pressure sensors is being extended, it is not intended for production use at  $1000^{\circ}\text{F}$ . Even the most optimistic models would predict a very low reliability at  $1000^{\circ}\text{F}$ .

## References

1. G.L. Pearson, W.T. Read Jr., and W.L. Feldmann, "Deformation and Fracture of Small Silicon Crystals", Acta Metallurgica, Vol. 5, p. 181, 1957.
2. J.J. Wortmann and R.A. Evans, "Young's Modulus, Shear Modulus and Poisson's Ratio in Silicon and Germanium", Journal of Applied Physics, Vol. 36, Number 1, Jan. 1965.
3. O.N. Tufte and E.L. Stelzer, "Piezoresistive Properties of Silicon Diffused Layers", Journal of Applied Physics, Vol. 34, Number 2, Feb. 1963.
4. J.S. Sanchez, "Semiconductor Strain Gage Evaluation at Extreme Temperatures", 19th Annual ISA Conference, New York, Oct. 1964.
5. United States Patent Numbers 4,672,354 and 4,739,298, Assignee Kulite Semiconductor Products, Inc., Ridgefield, NJ.
6. J.S. Shor, D. Goldstein and A.D. Kurtz, "Evaluation of B-SiC for Sensors" in Proceedings of the 1991 International Conference on Solid State Sensors and Actuators, June 22-26, 1991, p. 912-915.

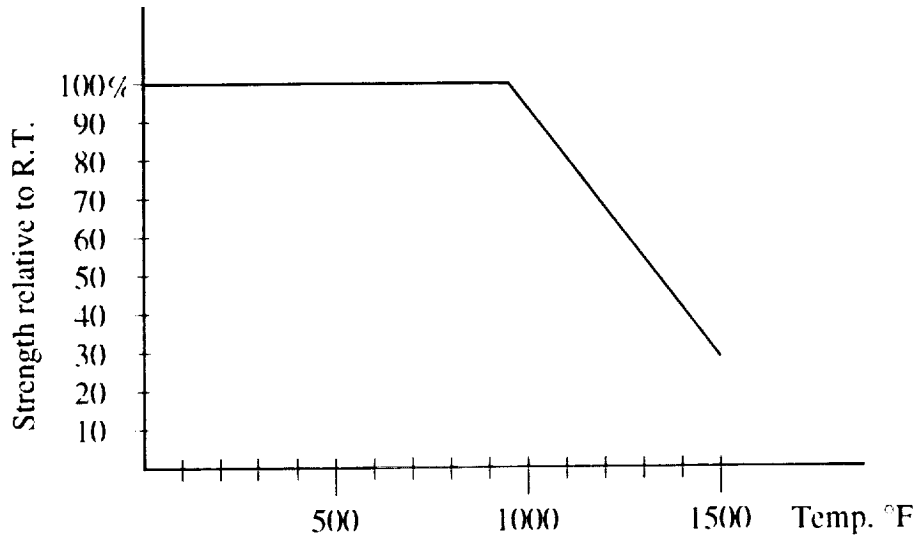


Figure 1. Temperature dependence of the strength of silicon. (Adapted from Fig. 5 of Ref. 1).

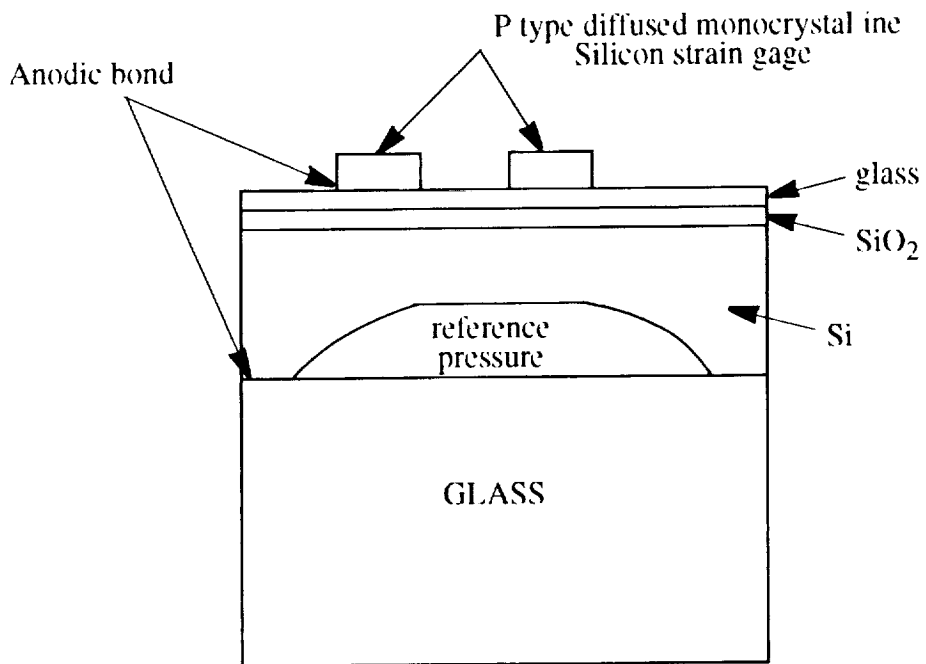


Figure 2. Schematic section of a Kulite silicon on silicon pressure sensor.

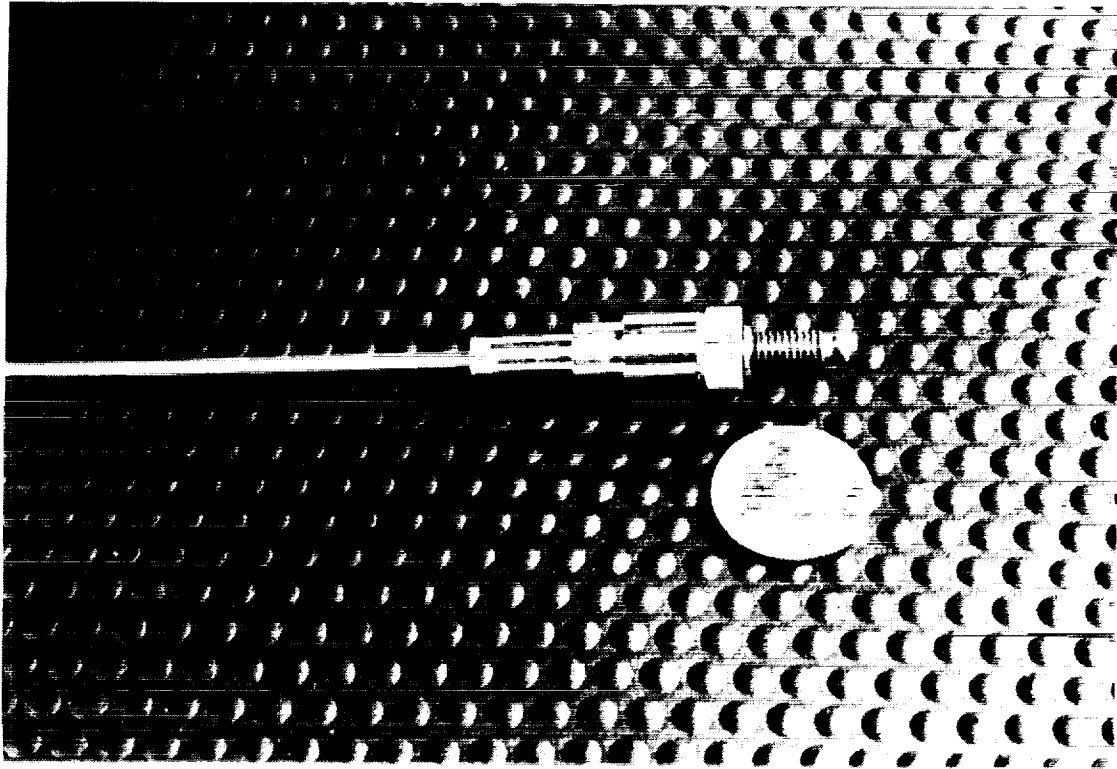


Figure 3. Photograph of one style of Kulite very high temperature pressure transducer.

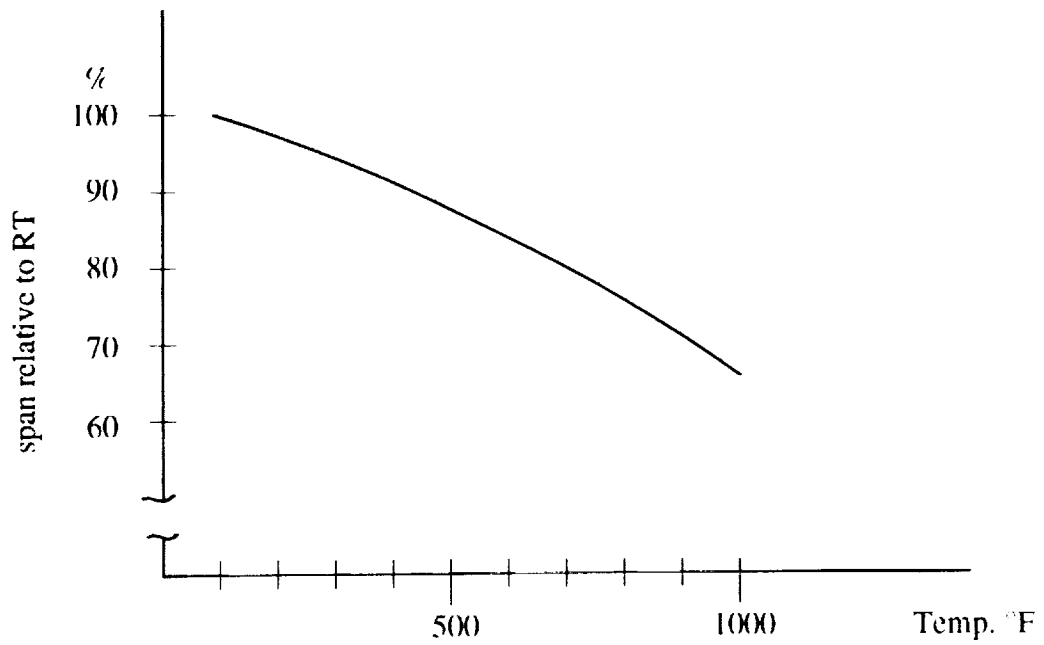


Figure 4. Temperature dependence of span output for a silicon on silicon pressure sensor.

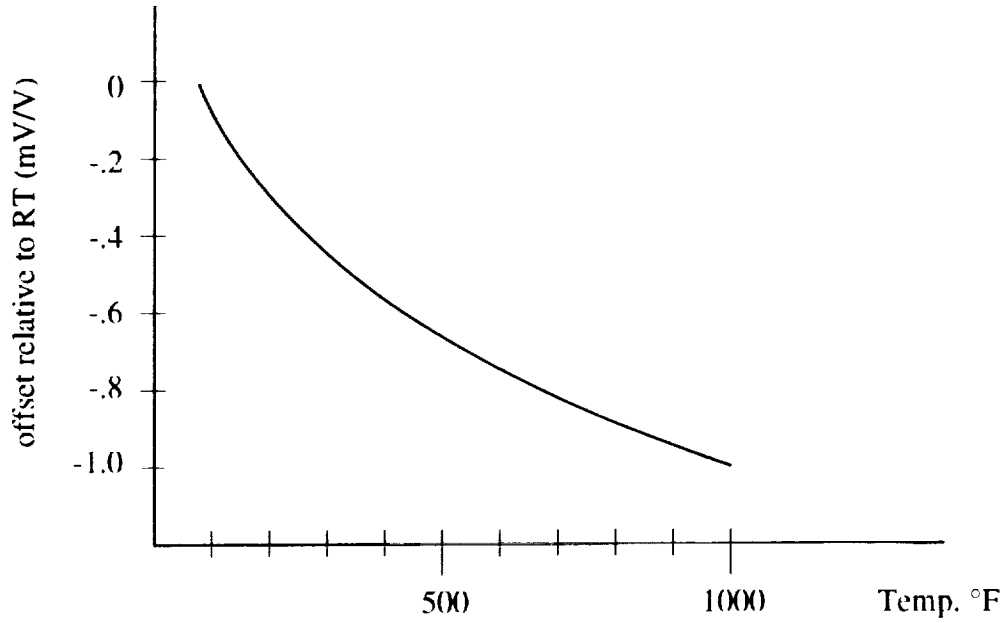


Figure 5. Temperature dependence of zero output for a silicon on silicon pressure sensor.

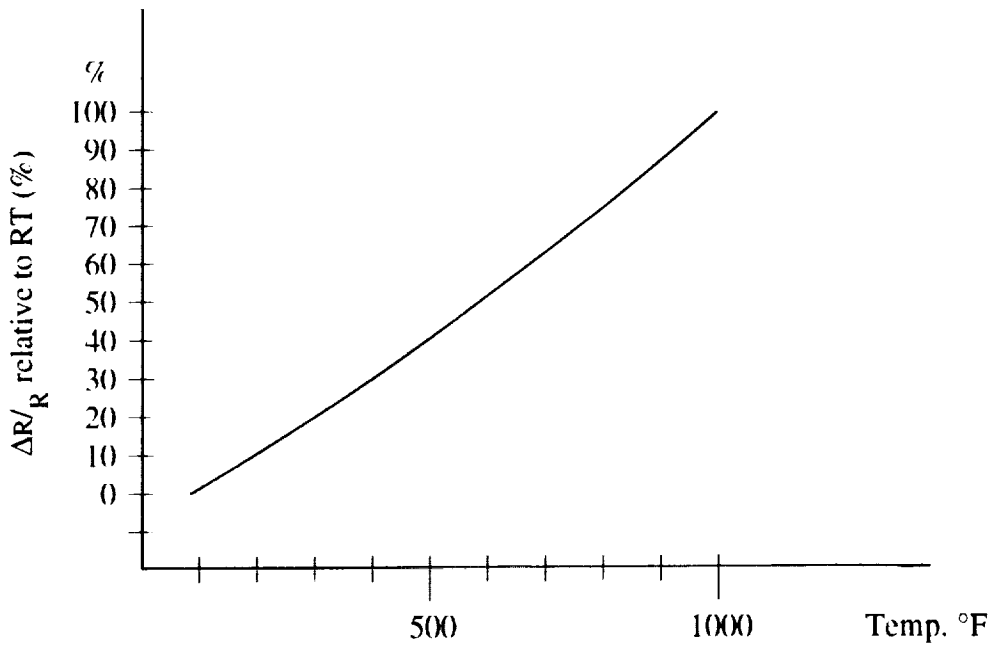


Figure 6. Temperature dependence of resistance for a silicon on silicon pressure sensor.

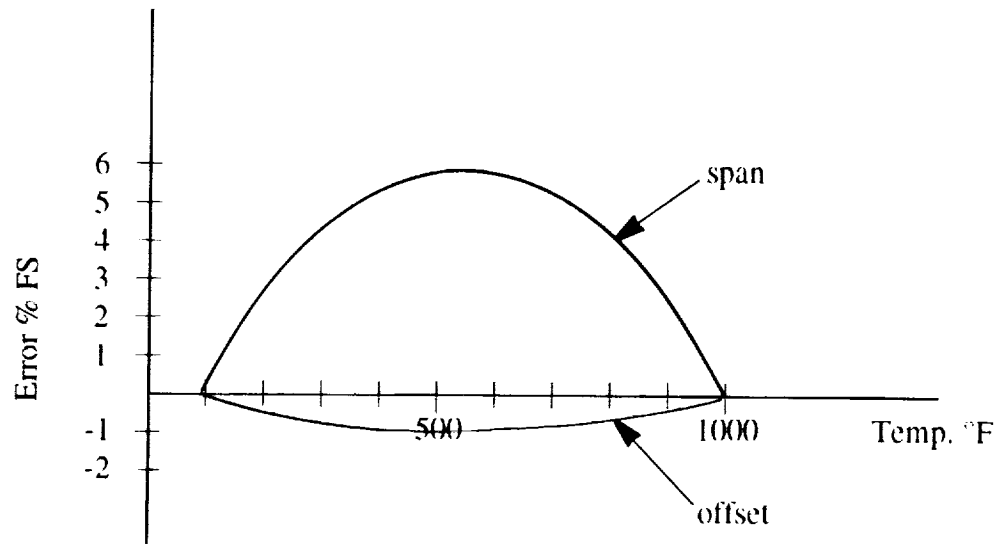


Figure 7. Span and offset errors for a passive temperature compensated silicon on silicon pressure transducer.

## DEVELOPMENTS ON HIGH TEMPERATURE FIBER OPTIC MICROPHONE

Kenneth D. Wright, II  
Allan J. Zuckerwar  
NASA Langley Research Center  
Hampton, VA

## SUMMARY

A fiber optic microphone, based on the principle of the fiber optic lever, features small size, extended bandwidth, and capability to operate at high temperatures. These are requirements for measurements in hypersonic flow. This paper describes the principles of operation of fiber optic sensors, a discussion of the design of a fiber optic microphone, the functional elements and packaging techniques of the optoelectronic circuitry, and the calibration techniques used in the development of the high temperature fiber optic microphone.

## Principles of Operation

The fiber optic microphones that are initially being developed are intensity-modulated (fiber optic lever) microphones. The fiber optic lever responds to changes in light reflected from a vibrating surface. Light from a light-emitting diode is directed through a transmitting fiber, reflected from a mirror on the bottom side of a stretched membrane, collected by a bundle of receiving fibers, and detected by a photodiode. When the membrane vibrates, it modulates the intensity of the received light [1]. The fiber optic lever microphone has three primary advantages over the condenser microphone. First, because acoustical signals are transmitted optically rather than electrically, there is no loading by cable capacitance or 60 Hz noise due to capacitive pickup. The usual practice of locating the condenser microphone preamplifier as closely as possible to the microphone cartridge is not viable at high temperatures. Secondly, the same loading effect limits the minimum practical size of a condenser microphone to about 1/8"; but the minimum size of a fiber optic microphone is limited by the size of the optical fibers. These fibers are currently available in diameters as small as 0.0039". Finally, the fiber optic microphone has an inherent advantage in bandwidth. The reason for this stems from the fact that the condenser microphone responds to the mean displacement of the membrane, while the fiber optic microphone responds to the displacement at the center.

## Microphone Design

A bundle of optical fibers, containing a central transmitting fiber and several peripheral receiving fibers, are pressed into a hypodermic needle. After the latter is inserted into the microphone body, the assembled cartridge is placed into a fixture, where the membrane is excited acoustically. The hypodermic needle is positioned until the microphone output is maximum, then locked in place by means of a pen vise at the bottom end of the cartridge.

The active diameter of the membrane is not the outside diameter of the cartridge, rather the diameter of the inside hole in the tension ring. In this manner microphones of very small active diameter can be constructed.

## Microphone Calibration

Most conventional methods of microphone calibration are not capable of being used in high temperature environments. The electrostatic actuator method was used because of its ability to withstand high temperatures. Figure 1 shows the electrostatic actuator setup. Three quartz pins are used to support the actuator electrode directly above the microphone. The quartz pins maintain a constant distance between the microphone and the actuator as temperature increases. This is an important property to preserve the integrity of the calibration at high temperature. The primary disadvantage of this method of calibration is that the sound pressure levels generated by the electrostatic actuator are low. As a result of this fact, the noise level of the system has to be minimized to allow for the calibration signal to be distinguished from the system noise.

## Optoelectronics

The optoelectronics primarily consists of the light-emitting diode (LED) which outputs light to a single transmitting fiber, and the photo detector-amplifier which amplifies the modulated light gathered from an array of six receiving fibers. Figure 2 is a block diagram of the optoelectronics. Several techniques are used to achieve the lowest system noise level possible. First, the power supply is wrapped in a shield to reduce the effects of electromagnetic interference. In addition, regulators are used to supply power to optoelectronic components because of their excellent noise suppression characteristics. Other noise reduction techniques such as braiding all wires to switches and connectors provided additional noise immunity. The result of these noise reduction techniques was a system noise level at the photodetector input of less than 10 nV. This level is 10 dB below the initial version of the optoelectronics that did not stress noise reduction. Another design goal for the optoelectronics is to get maximum power into the receiving fibers and to the photodetector because the signal-to-noise ratio increases in proportion to the square root of the power. To achieve this goal, great care is taken to assure that the photo diode and the photodetector are properly aligned with the fiber optic cable through the use of SMA connectors. Also incorporated into the optoelectronic design is an automatic zeroing circuit to compensate for any DC drift due to temperature changes. The electronics are housed in a portable shielded instrumentation enclosure.

## CONCLUSIONS

The fiber optic microphone was successfully tested in a laboratory setup. The microphone was operational at temperatures up to 1000 °F, it had a frequency response of 100 kHz, and dynamic range calculated to be 190 dB. Figure 3 shows the results obtained during a typical calibration. The successful implementation of the fiberoptic microphone is expected to lead to the development of a higher temperature microphone as materials are developed that can withstand the temperature goal of 2000 °F.

## REFERENCES

- [1] F.W. Cuomo "Pressure and Pressure Gradient Fiber-Optic Lever Hydrophones," J. Acoust. Soc. Am. 73, 1848-1857 (1983).



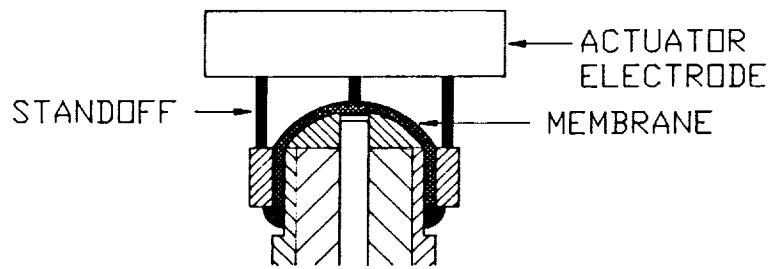


FIGURE 1. ELECTROSTATIC ACTUATOR FOR HIGH TEMPERATURE MICROPHONE CALIBRATION.

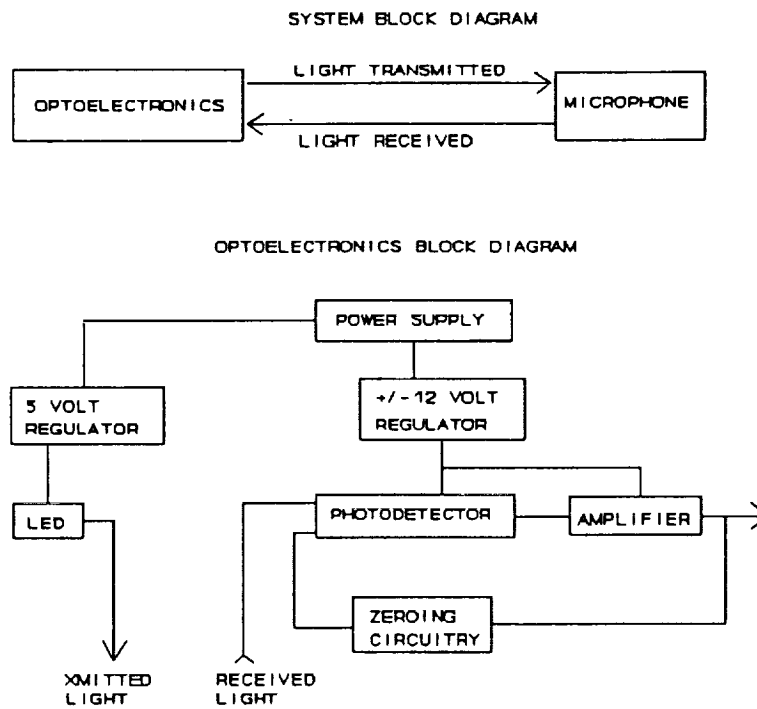
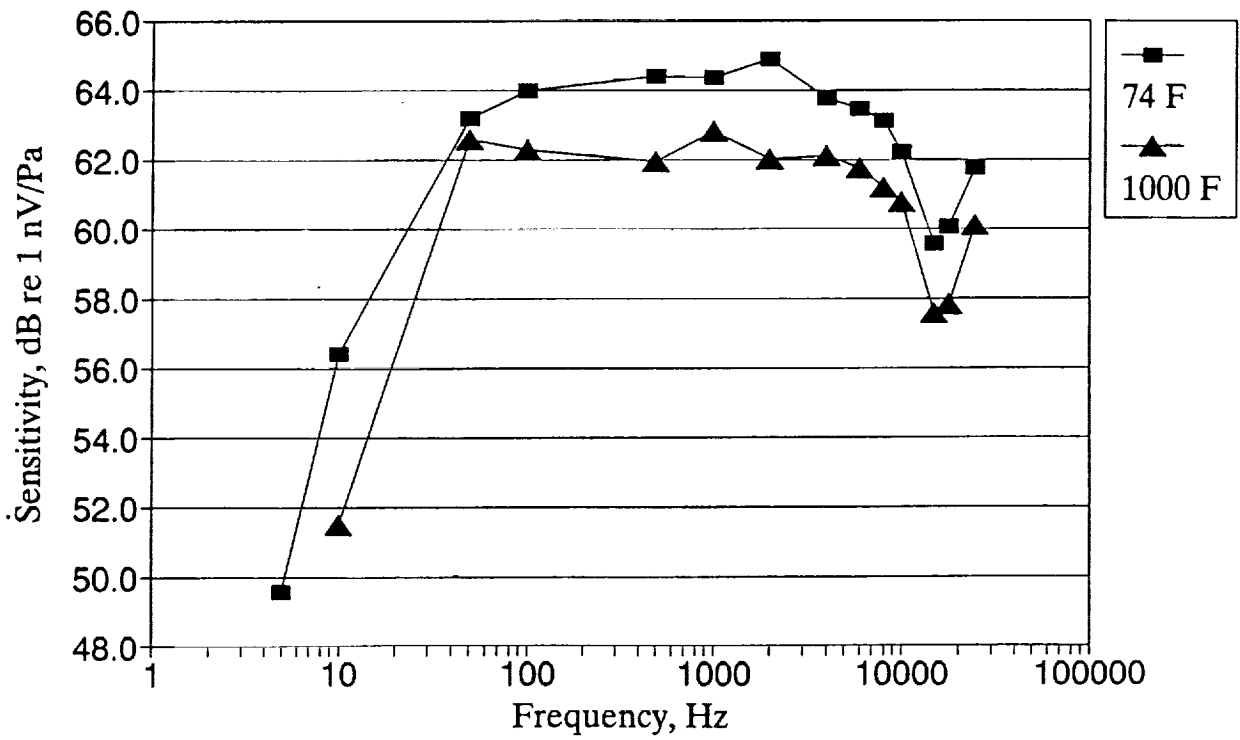


FIGURE 2



**FIGURE 3: TYPICAL MICROPHONE CALIBRATION**

# ELECTRON BEAM FLUORESCENCE MEASUREMENTS IN THE BOEING HYPERSONIC SHOCK TUNNEL\*

L. L. Price and W. D. Williams  
Calspan Corporation, AEDC Operations  
Arnold Engineering Development Center  
Arnold Air Force Base, Tennessee 37389

H. M. Powell, Consultant  
Professor, Dept. of Electrical Engineering  
Tennessee Technological University  
Cookeville, Tennessee 38505

## INTRODUCTION

A program entitled "Reacting Gas Experimental Data in Low Density Flow," which is funded by the Wright Laboratory/Flight Dynamics Directorate, is underway with the overall purpose of defining a set of standard experimental data against which the results of real gas computational codes can be evaluated. The goal of the particular task under which the present work was performed is to provide a complete characterization of the Boeing 30-in. Hypersonic Shock Tunnel (B30HST) at a selected test condition.

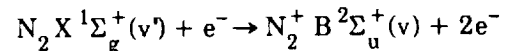
Initial experimental results for the flow characterization have been reported in Refs. 1-3. The measurement techniques utilized in these studies consisted of the usual (or classical) physical probes for determination of incident shock velocity, reflected shock pressure, nozzle wall static pressure, test section pitot and static pressure, and test section model heating rate. In addition, a direct measurement of free-stream velocity was made using a time-of-flight vaporizing wire technique. Nonintrusive techniques such as Rayleigh scattering for free-stream density determination and laser-induced fluorescence (LIF) for determination of nitric oxide concentration and vibrational temperature were also used. A general conclusion from these measurements was that additional nonintrusive measurements were required. Other measurements identified for these additional nonintrusive techniques were static density and temperature.

At the request of Wright Laboratory, the Calspan/AEDC electron beam fluorescence (EBF) technique was used to measure nitrogen density, nitrogen vibrational temperature, and the arrival time of the helium component of the driver gas. Determination of helium arrival time was needed to help define the usable flow duration. This paper describes the Calspan EBF measurement system, data reduc-

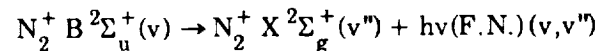
tion methods, and the results of the measurements which were performed under Task VI of the program, "Electron Beam Density Measurement in Hypersonic Flow." An analysis of these results are to be reported by Boeing (Ref.4).

The EBF technique uses a narrow beam of high energy (50 keV) electrons to ionize and excite all species of gas atoms and molecules within the path of the beam. As the gas atoms and molecules lose the energy gained from their collisions with the beam electrons, they emit radiation which is characteristic of their particular species. From the intensity and spectral distribution of the fluorescence, species concentration and temperature(s) can be determined, respectively. An overview of the EBF technique is given in Ref. 5.

Molecular nitrogen ( $N_2$ ) is directly excited by electron impact to the  $N_2^+ B^2\Sigma_u^+$  electronic state:

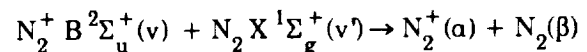


from which spontaneous radiation occurs by



where  $v$ ,  $v'$ , and  $v''$  denote different vibrational levels,  $X$  are ground electronic states, and  $h\nu(F.N.)$  denotes radiation from the  $N_2^+$  First Negative System.

The collisional de-excitation (quenching) process deactivates excited state molecules before spontaneous emission can occur; its process is:



in which the final states  $\alpha$  and  $\beta$  are unknown. As the number density of the gas increases, this effect becomes more pronounced.

\*The research reported herein was performed by the Arnold Engineering Development Center (AEDC), Air Force Systems Command. Work and analysis for this research were done by personnel of Calspan Corporation/AEDC Operations, operating contractor for the AEDC aerospace flight dynamics facilities. Further reproduction is authorized to satisfy needs of the U. S. Government.

In general, observation of an electron beam in a gas with a detection system of efficiency  $s(\lambda)$  and solid angle  $w$  results in a detector photon rate of

$$S = (\omega/4\pi)s(\lambda)(I/e)\sigma_{gi}n_gLA_{ij}\tau_i/(1 + k_i\tau_in_g) \quad (1)$$

where  $I$  is the beam current,  $e$  the electronic charge,  $\sigma_{gi}$  the excitation cross section for the ground state level  $g$  to  $i$  transition,  $n_g$  the ground state number density,  $L$  the observed length of beam,  $A_{ij}$  the Einstein spontaneous transition probability for the  $i$  to  $j$  transition,  $\tau_i$  the radiative lifetime of state  $i$ , and  $k_i$  the quenching rate constant for level  $i$ . The photon rate is directly proportional to the beam current and the ground state number density, but modified by the quenching term in the denominator, whose magnitude depends on the ground state number density. Rather than assigning values to each of these parameters, density calibrations are usually accomplished by using the detection system to measure the photon rate in a gas of known density, while keeping the same optical configuration, transition, etc., for the calibration and test.

The excitation and emission of nitrogen's  $N_2^+$  First Negative System bands are modeled in AEDC's EBFN2 computer program. Results from spectral band measurements are compared to program predictions to obtain rotational or vibrational temperatures. The fluorescent intensity distribution within a rotational band is a function of rotational temperature. The relative fluorescent intensities of two vibrational bands whose upper vibrational levels are different is a function of the vibrational temperature.

Small angle scattering collisions between primary electrons and gas molecules result in gradual spreading of the beam as it traverses the gas. The magnitude of beam spreading is primarily a function of the gas species, the beam energy, the density of the gas, and the distance from the exit orifice. Beam spreading equations (Ref. 6) were invoked for the B30HST setup and conditions; for a 50-keV beam a maximum beam spread of 8 mm at the observation volume was expected. Fields of view of the optical detection systems were designed to encompass this beam width and more.

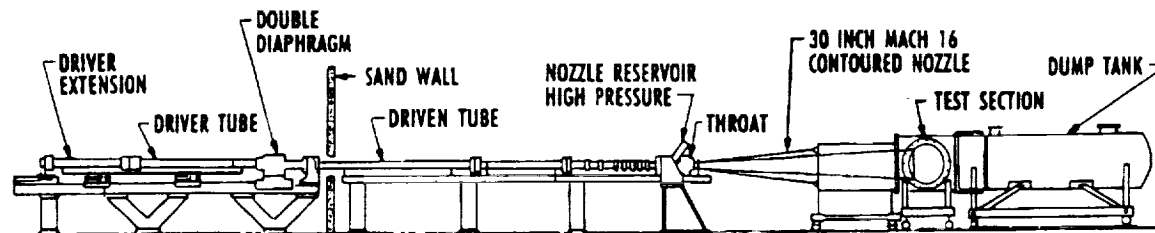


Fig. 1. Boeing 30-in. hypersonic shock tunnel.

† Figures 1-31 are cited in the text.

## THE BOEING 30-INCH HYPERSONIC SHOCK TUNNEL (B30HST)

Principal elements of the B30HST are presented in Fig. 1.<sup>†</sup> It consists of a 160-in.-long, 3-in.-diam combustion driver, a 299-in.-long, 3-in.-diam driven tube, a 175-in.-long, 30-in. exit diameter contoured nozzle, a 40-in.-diam open jet test section, and a vacuum dump tank. The driver is a combustible mixture of nominally 75 percent helium (He), 16.7 percent hydrogen (H<sub>2</sub>), and 8.3 percent oxygen (O<sub>2</sub>); this mixture is ignited by the simultaneous firing of 21 spark plugs. At a time slightly after peak pressure in the driver, a double diaphragm assembly which separates the driver and driven sections is ruptured by means of an electrical discharge in the argon gas between the two diaphragms. After release of the driver gas, an incident shock wave is formed which travels down the air-filled driven tube and reflects off the nozzle entrance to create the tunnel reservoir conditions. A Mylar® diaphragm which separates the air in the driven tube from the evacuated nozzle, test section, and dump tank is easily ruptured to allow the flow to begin. The nozzle was designed for nominal operation at Mach 16 and a range of operational Mach numbers from 8.5 to 20; for this program a 0.601-in.-diam throat insert was selected to provide a Mach 10 flow in the test section.

A program operational test point was chosen having the following characteristics: stagnation conditions of 5,130 psia pressure (measured) and 6,490 K temperature (calculated from driven tube incident shock speed measurements), free-stream static pressure of 0.034 psia (measured) and 450 K temperature (calculated), free-stream density of  $75 \times 10^{-6}$  lbm/ft<sup>3</sup> ( $3 \times 10^{16}$  molecules/cm<sup>3</sup>), and a 6.5-in.-thick boundary layer at the exit. The exit plane species mole fractions were calculated to be 0.698 N<sub>2</sub>, 0.147 O<sub>2</sub>, 0.065 NO (nitric oxide), 0.090 O,  $5 \times 10^{-10}$  N, and  $8 \times 10^{-8}$  NO<sup>+</sup> and e<sup>-</sup> (free electrons). The mole fraction of Ar (argon) was not modeled.

Numerous pressure transducers are located along the driver and driven tubes, the throat region, and the nozzle, and are used for evaluation of tunnel performance, nozzle flow-field characteristics and

test section conditions. The signal from a transducer located one inch upstream of the nozzle throat is used to provide a trigger pulse for critically timed events occurring in the test section. To monitor the test section pitot pressure, a two-transducer probe was positioned at the nozzle exit plane such that no interference with the electron beam would occur.

Forty transient data recorders (TDRs) are used for the acquisition of pressure transducer and diagnostic instrumentation outputs at sample rates of up to 500 kHz per channel. For time correlation during a run, all the TDR channels are triggered simultaneously. Data are stored on the TDRs until they are transferred to a PDP-11 hard disk. The data system is capable of manipulating and reducing raw data to standard engineering units. A moving average routine can be applied to the data to filter out any high frequency noise components. Any test specific data reduction routines, such as heat transfer calculations, can readily be included in the system. Reduced parameters can be printed or plotted on a laser printer. Files of raw and reduced data are stored on magnetic tape.

### ELECTRON GUN

The AEDC electron gun system was manufactured by Kimball Physics, Inc. The model EMG-22B electron gun has an accelerating potential variable up to 50 kV and delivers up to 10-mA current. It is capable of being modulated at pulse rates from 10 Hz to 10 kHz with pulse widths from 1 to 20  $\mu$ sec. The gun section, which must be maintained at a pressure of less than 0.1 mtorr, is pumped by a 56- $\ell$ /sec turbomolecular pump and has deflection and focusing coils that allow the beam to be precisely directed through a 1.0-mm-diam orifice. The base pressure is  $1 \times 10^{-7}$  torr. The original thin-walled copper orifice plate was replaced by a 4.8-mm-thick copper plate having a 1.0-mm-diam orifice, allowing a greater pressure differential and permitting operation in chamber pressures up to about 10 mtorr. The small, retractable, internal Faraday cup was removed from its position near the back side of the orifice. To enable evaluation of the gun performance, the orifice plate was electrically insulated and a lead was attached between it and the former cup's electrical feedthrough to allow external measurement of any orifice plate current. Orifice currents of less than 1  $\mu$ A can be detected. A pneumatic gate valve is located near the back side of the orifice. After passing through the orifice, another set of deflection and focusing coils provides a steerable beam diameter of 1 to 2 mm at a distance of approximately 0.6 m. A 30-

ft-long cable assembly connects the gun with the power supply.

The electron gun installation is illustrated in Fig. 2. An additional orifice and pumping section was required to maintain the gun at an acceptably low pressure (2 torr) during the flow duration of the B30HST. Stainless steel pipe of 2.0-in. inside diameter was used to construct this section. The water-cooled copper orifice plate of this differential pumping system was 2.9 mm thick, had a 2.0-mm-diam orifice, and was located 34 in. from the first orifice and 8 in. above the nozzle centerline. Electrical insulation of the orifice was necessary to enable measurement of orifice plate current. This was accomplished by using a micarta flange and other insulating components between the gate valve and orifice assembly. All the gun system parts within the test section were designed to prevent significant misalignment of the electron beam as the impact of the run occurred. A 50- $\ell$ /sec turbomolecular pump located outside the test cell pumped this section. To protect the gun and pumping system from the post-flow test section high pressure, an electro-pneumatic gate valve was positioned 4 in. above the second orifice. Immediately following each run, the operator manually closed this valve, closing the system in 1 sec, and turned off the power to the electron gun. A sharp-edged aluminum flow fairing was affixed to the pipe section between the gate valve and orifice to reduce the chance of tunnel blockage and minimize disturbance of the beam alignment by dynamic flow-field loads. To reduce flow distortions and pressure at the orifice exit, a 6.0-in.-wide, 5.2-in.-long, sharp-

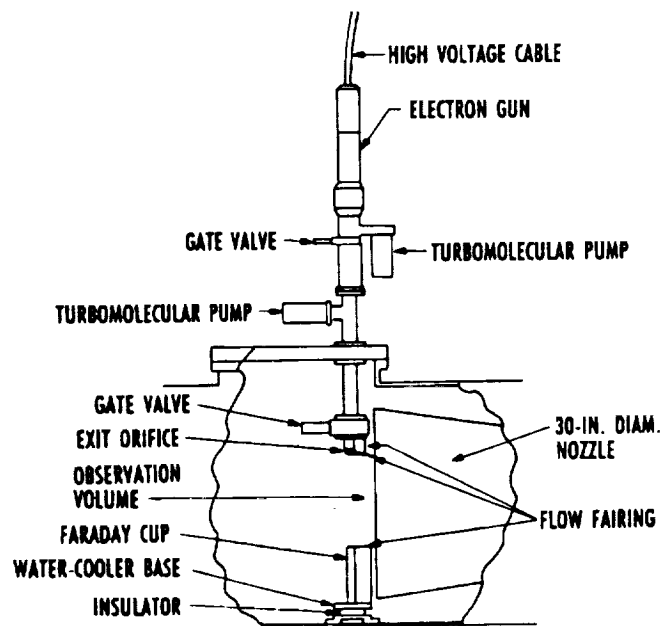


Fig. 2. Side view of B30HST with electron gun installation.

edged flat plate was bolted to the bottom of the orifice assembly.

Electron beam current was collected by a 2.25-in. inside diameter, 9.5-in.-long, copper Faraday cup whose entrance was 7 in. below nozzle centerline. The cup was attached to a water-cooled copper base which was firmly bolted to and insulated from the bottom of the test section. A flow fairing was placed upstream of the cup to reduce interactions with the flow field.

### OPTICAL INSTRUMENTATION

A plan view of the optical instrumentation layout is given in Fig. 3. Molecular nitrogen number density was measured by two identical AEDC systems. Fused silica lenses were used in both assemblies to reduce transmission losses. The north side system was tilted at a 10-deg angle, to observe the nozzle centerline downward through a window. This window was located directly above the window which accommodated the Boeing photomultiplier tube (PMT) detector system. Fluorescence at 391 nm was collected by a 7.38-in. focal length, 3.0-in.-diam lens at an object distance of 26.75 in. Before coming to a focus, the light was collimated to a 0.55-in.-diam by a -1.92-in.-focal length, 1.0-in.-diam, plano-concave lens. The collimated light passed through an interference filter before being focused onto the aperture of the PMT by a 3.83-in. focal length, 1.0-in.-diam plano-convex lens. Vignetting was minimized by reducing the separation of the two small lenses as much as possible. These optics projected the PMT aperture

dimensions onto the nozzle centerline by a magnification factor of 1.31, giving a resultant field of view of 30 mm horizontal and 10 mm vertical. Collection of fluorescence from the total width of the beam was assured by this arrangement. The south side PMT system was centrally located and was level. The north and south side AEDC nitrogen PMT systems were designated AEDC N<sub>2</sub> (North) and AEDC N<sub>2</sub> (South), respectively, in Fig. 3 and in following figures. Each 1.0-in.-diam nitrogen optical interference filter has a 39-percent transmission at the peak wavelength of 390.8 nm, a full-width half-maximum (FWHM) bandpass of 3.85 nm, and an optical density of four for blocking from 200 to 950 nm.

Similar optics were assembled for the AEDC helium PMT detector system, located adjacent to the south side nitrogen system. A 5.88-in. focal length, 3.0-in.-diam fused silica lens collected the light. A glass plano-convex lens of -1.96-in. focal length and 1.6-in. diam was placed before the focus to collimate the light to a diameter of 0.8 in., thus accommodating the 1.0-in.-diam helium interference filter. A glass plano-concave lens of 4.0-in. focal length and 1.25-in. diam focused the collimated light onto the PMT aperture, which was rotated 90 deg with respect to both nitrogen system apertures, allowing collection of light from a longer length of beam. This optical system provided a magnification factor of 1.74 of the PMT aperture dimensions onto the nozzle centerline, for a resultant field of view of 13 mm horizontal and 40 mm vertical. The helium optical interference filter had 50-percent transmission at the peak wavelength of 501.6 nm, a FWHM of 0.84 nm, and the same blocking characteristics as the nitrogen filters.

For noise reduction, the RCA C31034A PMTs were contained within thermoelectric coolers held at a temperature of -20°C. These PMTs feature high quantum efficiency and sensitivity, spectral response from 200 to 930 nm, extremely low dark noise, and fast time response characteristics. Each PMT required a separate high-voltage power supply.

An Acton Research Corporation SpectraPro-275 spectrometer coupled with a linear diode array detector was set up to measure nitrogen vibrational temperature. The spectrometer has a 0.275-m focal length, an f/3.8 aperture ratio, adjustable slits, and a 25-mm-wide focal plane. The three gratings which were mounted on the triple indexable turret had the following characteristics: 1,200 lines/mm holographic, 2,400 lines/mm holographic, and 3,600 lines/mm blazed at 240 nm. The 3,600 lines/mm grating was not used because its efficiency at 425 nm wavelength was determined at AEDC to be too low. A reciprocal linear dispersion of 3.0 nm/mm occurs for the 1,200 lines/mm grating.

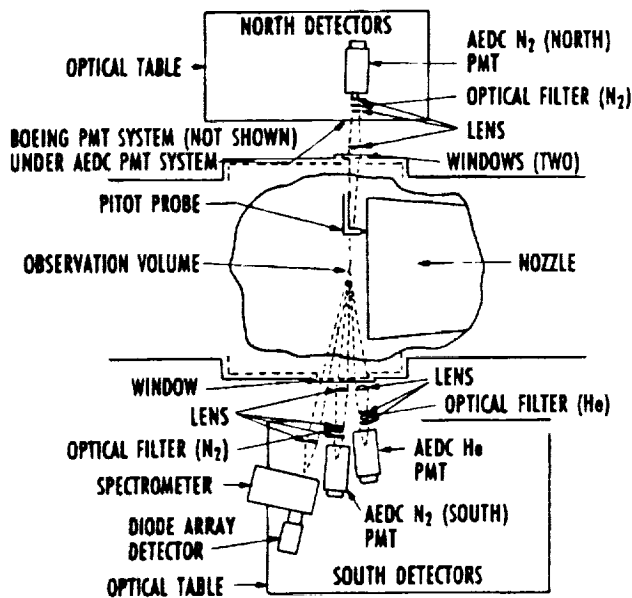


Fig. 3. Plan view of B30HST and Boeing/AEDC optical diagnostics installation.

Dispersed spectra were detected and processed by an Optical Spectrometric Multichannel Analyzer (OSMA) system. The detector was a Princeton Instruments, Inc. proximity focused MCP image intensified detector, model IRY-1024 S/RB. It is a gatatable detector with extended coverage in the UV and red wavelength regions. There are 1,000 active 25- $\mu\text{m}$ -wide by 2.5-mm-high diodes. The total array width of 25 mm matches the spectrometer's focal plane width. The detector yields 0.13 counts/photon at 425 nm wavelength, and its gain is not adjustable. Allowable gate widths range from 200  $\mu\text{sec}$  to 6 msec. Control of the detector was by means of Princeton Instruments model PG-10 Pulse Generator and model ST-100 Detector Controller. Tap water was circulated through the detector's thermoelectric cooler to reduce the temperature to  $-20^\circ\text{C}$ , thereby reducing the noise level. A desktop computer running Princeton Instruments software was used for data recording and processing.

A plano-convex fused silica lens collected the fluorescence and focused it onto the spectrometer slit. This 3.0-in.-diam lens had a 5.91-in. focal length at the nitrogen First Negative System (0,1) band's wavelength of 427 nm. The object and image distances were 39.0 and 7.0 in., resulting in a projection of the slit dimensions onto the observation volume with a magnification of 5.6.

### BOXCAR SYSTEM

Figure 4 shows a simplified block diagram of a typical boxcar integrator channel which was used for the basic data acquisition subsystem. The input to the boxcar integrator was the signal from a single PMT, and its output was passed to a single TDR channel. The basic function of the integrator channel

was to sample the PMT signal and hold it for output to the TDR. A single sample was obtained for each trigger of the boxcar channel.

The signals from the PMTs were anode currents whose amplitudes were representative of the signals observed from the sample volume. These currents were of sufficient magnitude that preconditioning was not required before input to the boxcar integrator. Because no external amplifier was used, sensitivity was controlled by adjustments in PMT high voltage and in the integrator time constant and gain. Settings were made according to the anticipated PMT signal levels and were manually recorded for use in posttest calibration and data reduction.

Four boxcar channels were required for the four PMT inputs. A fifth channel was used to obtain a second, time-delayed sample of the He PMT signal during a given data cycle. Dual sampling of the He PMT signal was possible because each boxcar channel gate could be independently triggered and optionally delayed with respect to the trigger. The delay capability was also used to obtain the gate for the AEDC  $\text{N}_2$ (North) PMT signal, coincident with the second He PMT signal sample. Gating circuits and timing diagrams are shown in Figures 5a and 5b.

During each data cycle the integrator circuit sampled the PMT output. Concurrently the integrator sample/hold circuit provided data read during the previous cycle to the TDR. Thus, while the system was recording a previously obtained sample, a new data sample was being generated.

The system of five boxcar channels was paced by the internal oscillator of the first channel [AEDC

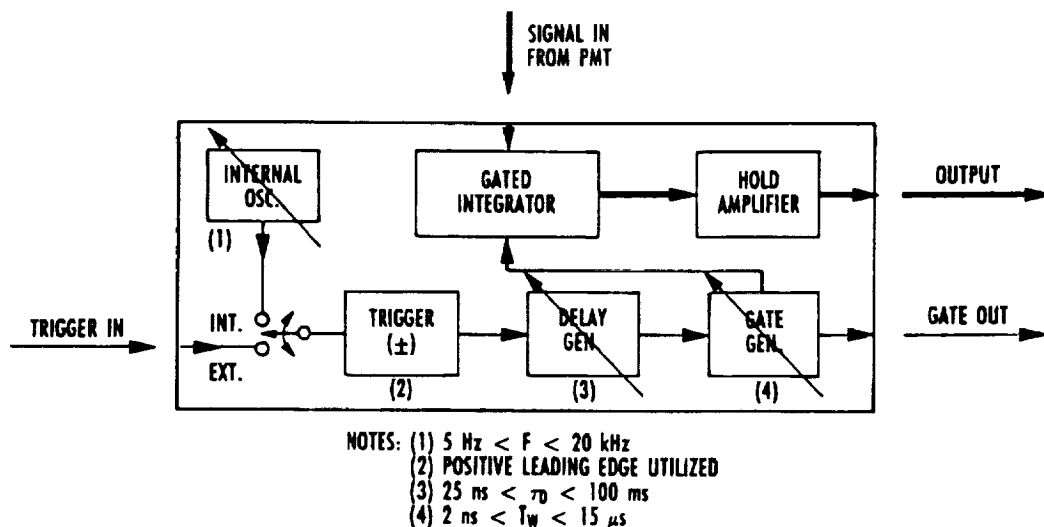
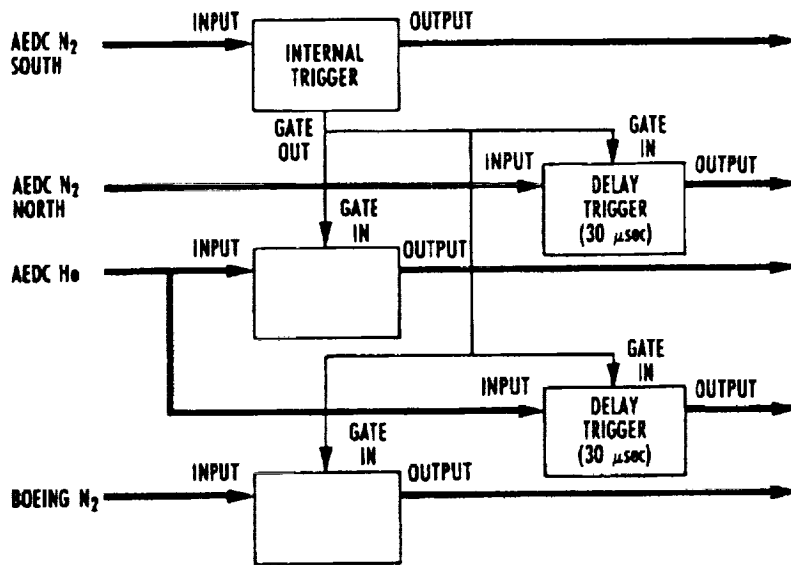
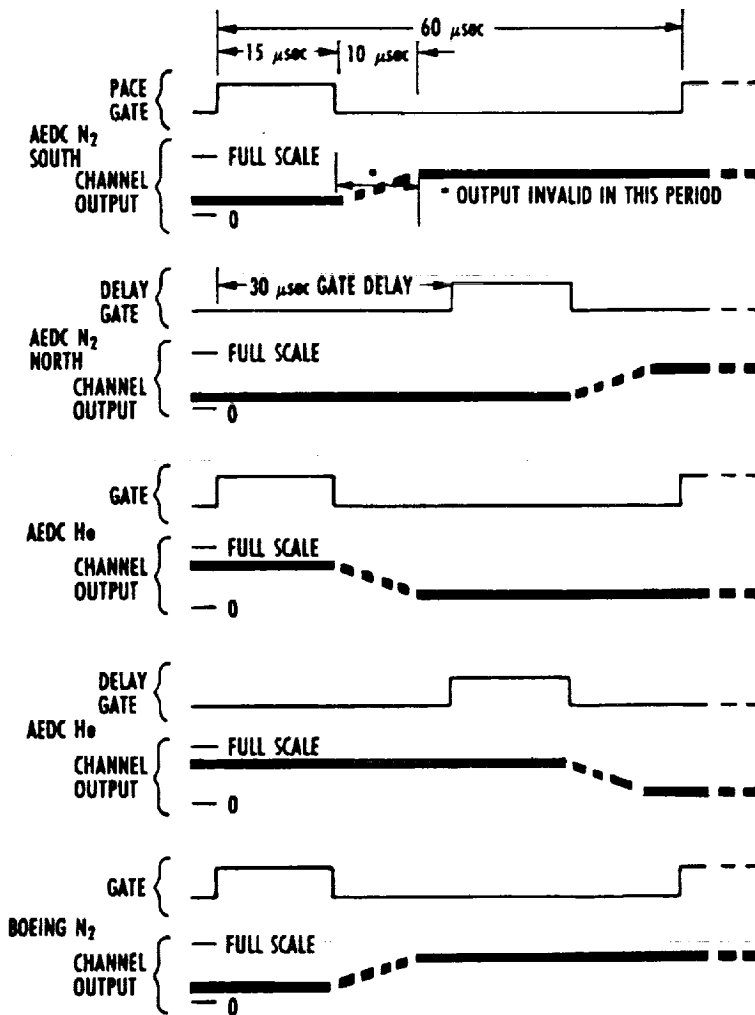


Fig. 4. Simplified block diagram for single gated integrator channel.



a. Interconnection of integrators



b. Timing diagram

Fig. 5. Block diagram and timing diagram for PMT gated integrators.

N<sub>2</sub>(South)] running at near-maximum rate (16.7 kHz). The leading edge of the pace integrator gate simultaneously triggered the other four channels. The integrator gates for the He and Boeing N<sub>2</sub> channels occurred simultaneously with that of the pace channel. The integrator gates for the AEDC N<sub>2</sub>(North) and He<sup>del</sup> channels were delayed by 30 μsec. All gate durations were set at 15 μsec. Following each integrator gate, a period of 10 μsec was required to perform the integration and sample/hold operations, during which the output was invalid (Fig. 5b). The data cycle time was set at 60 μsec. This yielded a 16.7-kHz sampling rate for all channels. Because of dual sampling, an effective rate of 33.3 kHz was achieved for the helium PMT. Each integrator channel output was sampled several times during each data cycle as a result of the significantly higher sampling rate (500 kHz) of the TDR data recording system.

## DATA

### RADIATIVE SPECIES

Spectra obtained by the spectrometer/array detector system during 14 of the runs listed in Table 1 are shown in Figs. 6-19. A variety of atomic lines and molecular bands were recorded and identified; they are listed by occurrence in Table 1 and by wavelength in Table 2, and their time history is plotted in Fig. 20. Data were acquired using three combinations of spectrometer gratings and central wavelength settings. The spectra include spurious positive and negative pulses and flat regions which are artifacts of the detector operation and should be ignored.

Wavelength scales were based on calibrations obtained from both Hg lamp spectra and other spectral features that were subsequently identified. Numbers on the ordinates correspond to detector output counts. Intensity scales, expressed in detector counts, were selected for optimum viewing.



Table 1. Spectrometer/Array Detector Results

RUN	BEAM	TRIG	EXP	GRAT	WAVE	SPECTRA
8001						BOMB SHOT; DETECTOR NOT IN SERVICE.
8002	ON	+0.3	2.0	2400	425	Cr I - THREE LINES. Fe I - ABOUT EIGHT LINES.
8003	OFF	0.0	2.0	1200	413	Cr I. Al I - TWO LINES. Mn I. MANY Fe LINES.
8004	OFF	0.0	1.0	1200	413	LIKE RUN 8003.
8005	ON	NO	RECORD	1200	413	SOME SATURATION; SOME DIFFERENCE FROM RUNS 8003 AND 8004.
8006	ON	0.0	1.0	1200	413	NO SPECTRUM; MISTRIGGERED.
8007	OFF	-0.5	1.0	1200	413	LIKE RUNS 8003 AND 8004 BUT VERY WEAK.
8008	OFF	+0.1	0.5	1200	413	LIKE RUN 8007.
8009	ON	+0.3	0.5	1200	413	STRONG N <sub>2</sub> <sup>+</sup> FIRST NEG. (0,0) AND (0,1) BANDS.
8010	ON	0.0	1.0	2400	425	N <sub>2</sub> <sup>+</sup> (0,0) AND (0,2) OVERLAID BY Cr I AND Fe I.
8011	ON	-0.5	0.5	2400	500	NO He I 501.6 NM LINE. CU 510.6 NM LINE. NITRIC OXIDE (0,2) BANDS.
8012	OFF	+0.2	1.0	2400	425	LIKE RUN 8002.
8013	ON	0.0	1.0	2400	425	LIKE RUN 8010.
8014	ON	0.0	0.5	2400	500	Cu 510.6 NM.
8015	ON	+4.0	1.0	2400	500	STRONG He I. AIO GREEN (0,1), (1,2), AND TAIL OF DELTA V = 0 BANDS. NO NITRIC OXIDE BANDS.
8016	ON	0.0?	1.0	2400	500	STRONG Cu I. MANY Fe I LINES IN ORDER II. NO He I. NO NITRIC OXIDE BANDS.
						TRIG = TRIGGER TIME RELATIVE TO PEAK PRESSURE AT NOZZLE EXIT, IN MSEC. EXP = EXPOSURE TIME IN MSEC. GRAT = GRATING LINES/MM (2400 IS HIGH RESOLUTION). WAVE = SPECTROMETER CENTER WAVELENGTH, NM.

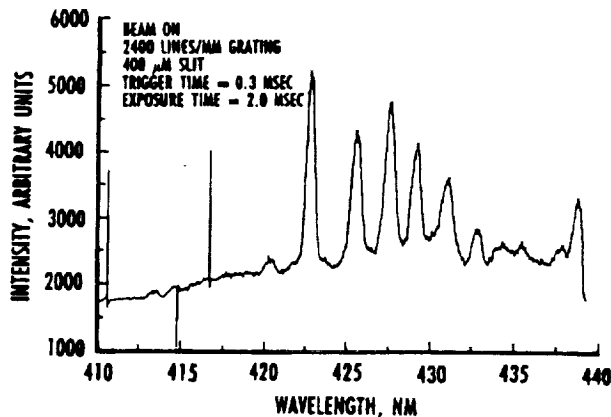


Fig. 6. Spectrometer/array detector spectrum for Run 8002.

The higher resolution of the 2,400 lines/mm grating with respect to the 1,200 lines/mm grating is evident, for example, upon comparison of the three chromium lines in Runs 8002 and 8003 (Figs. 6 and 7). To reduce scattered light, portions of the test section were spray painted flat black. Residual airborne particles from the paint apparently caused a large increase in scattered light, resulting in saturation

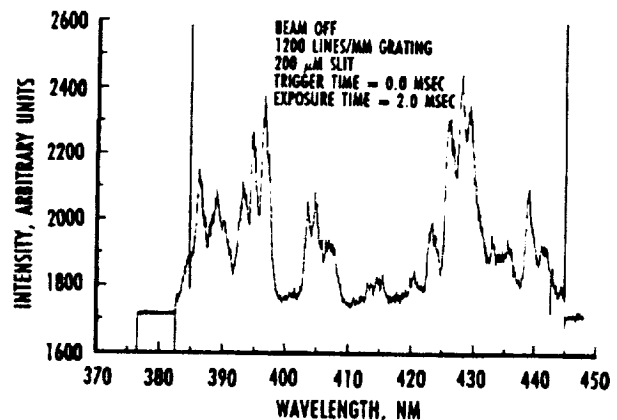


Fig. 7. Spectrometer/array detector spectrum for Run 8003.

of the spectra in Run 8005 (Fig. 9). Later, the blackening seemed to be effective, as indicated by the reduced background spectra of Runs 8007 and 8008 (Figs. 10 and 11). The effectiveness of the blackening is also indicated in Run 8009 (Fig. 12) by the strength of the electron beam-excited (0,0), (1,2), and (0,1) nitrogen First Negative System bands with respect to the background metal lines. Inexplicably,

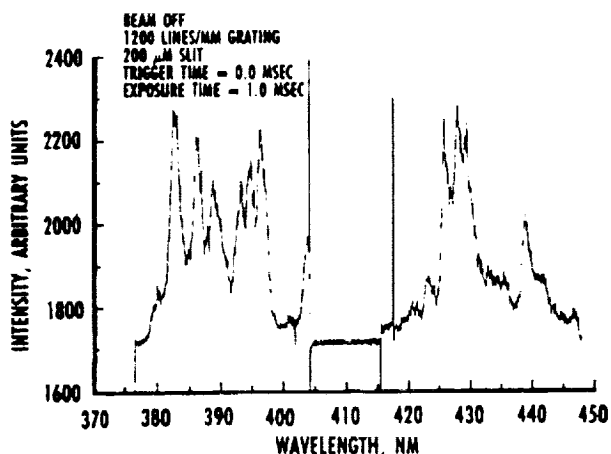


Fig. 8. Spectrometer/array detector spectrum for Run 8004.

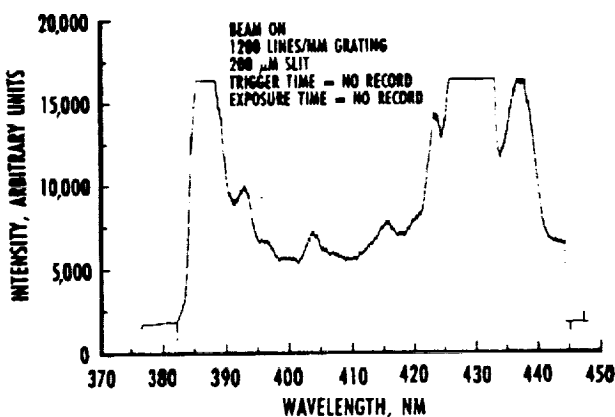


Fig. 9. Spectrometer/array detector spectrum for Run 8005.

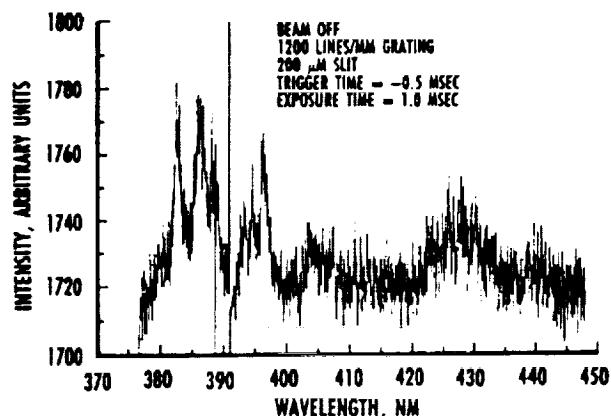


Fig. 10. Spectrometer/array detector spectrum for Run 8007.

spectra from the remaining runs with the center wavelength set at 425 nm were again dominated by the metal lines. For Runs 8010 and 8013 (Figs. 13 and 16), the (1,2) and (0,1) bands, which appear at

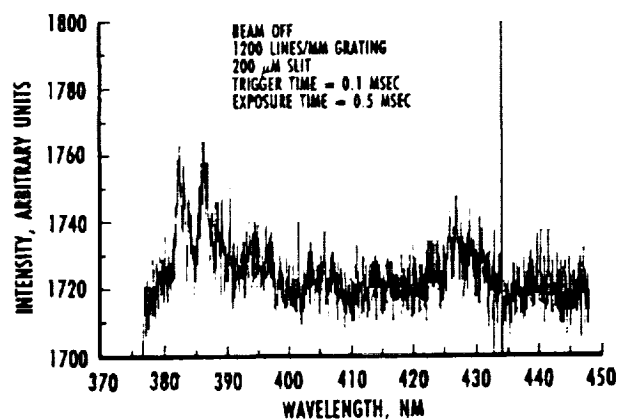


Fig. 11. Spectrometer/array detector spectrum for Run 8008.

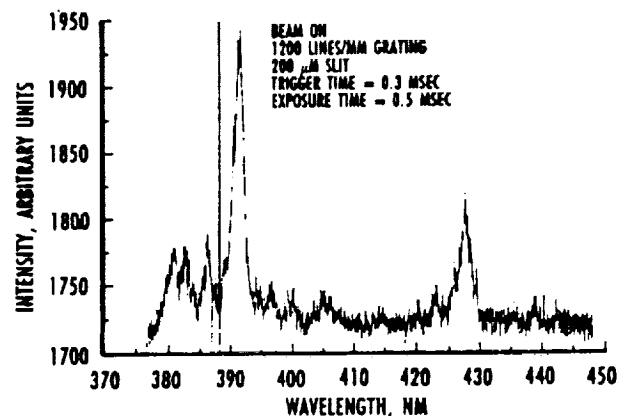


Fig. 12. Spectrometer/array detector spectrum for Run 8009.

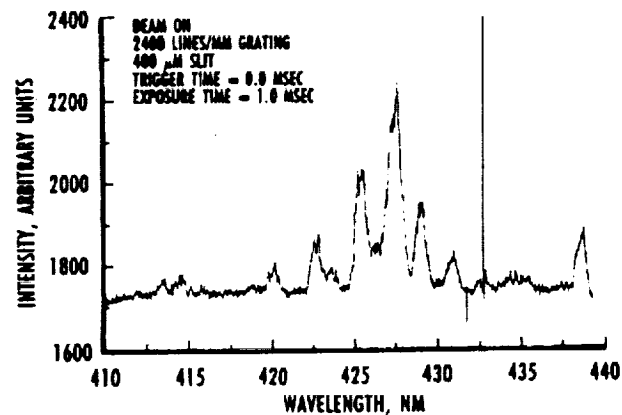


Fig. 13. Spectrometer/array detector spectrum for Run 8010.

423 nm and 427 nm, respectively, are weak with respect to the strong metal lines. Electron beam-excited NO bands were recorded in the early part of Run 8011 (Fig. 14), and AIO bands were recorded in the latter part of Run 8015 (Fig. 18).

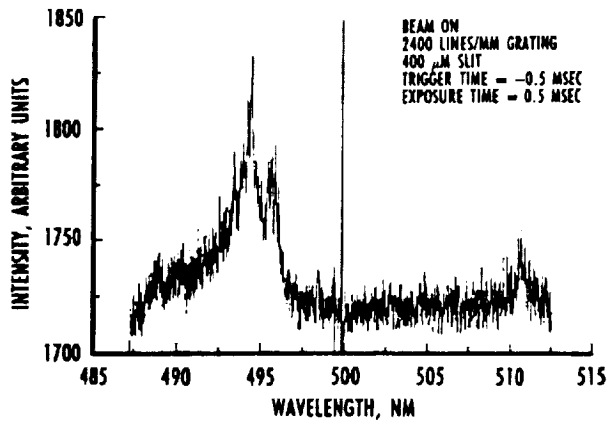


Fig. 14. Spectrometer/array detector spectrum for Run 8011.

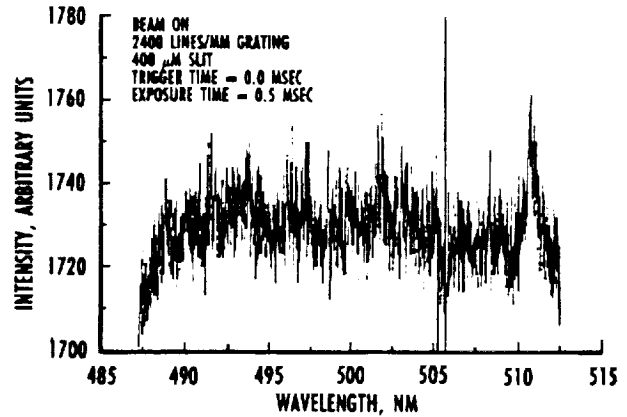


Fig. 17. Spectrometer/array detector spectrum for Run 8014.

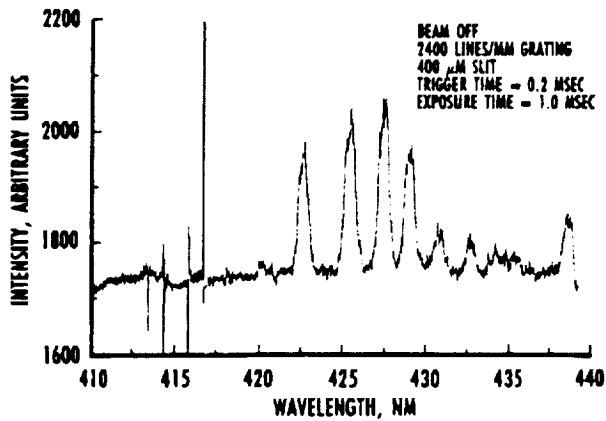


Fig. 15. Spectrometer/array detector spectrum for Run 8012.

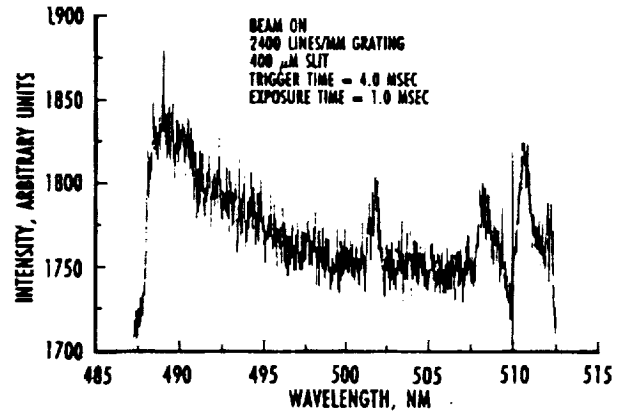


Fig. 18. Spectrometer/array detector spectrum for Run 8015.

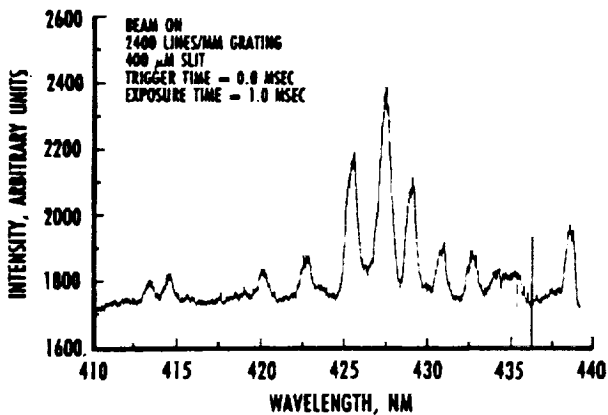


Fig. 16. Spectrometer/array detector spectrum for Run 8013.

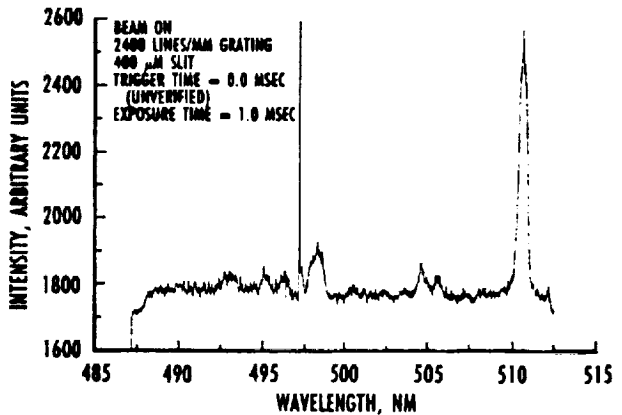


Fig. 19. Spectrometer/array detector spectrum for Run 8016.

#### HELIUM ARRIVAL TIME

The spectrometer/array detector system was set to record the helium 501.6-nm line in four of the last six runs. With respect to the peak pressure at the

nozzle exit, the trigger time of the detector was shifted as shown in Table 1. These data (see Fig. 20), in conjunction with other evidence, indicate that the chemically pure test time of the B30HST lies between 1.0 and 2.4 msec.

Table 2. Spectral Features

WAVELENGTH, NM	SPECIES	WAVELENGTH, NM	SPECIES
382.6	Fe I 382.588	427.5	Cr I 427.480
386.0	Fe I 385.991	427.8	N <sub>2</sub> <sup>+</sup> FIRST NEG. (0,1) BH
388.6	Fe I 388.628	429.0	Cr I 428.972
391.4	N <sub>2</sub> <sup>+</sup> FIRST NEG. (0,0) BH	430.8	Fe I 430.791
392.8	Fe I 392.792	432.6	Fe I 432.576
393.0	393.030	435.3	Fe I 435.274
394.4	Al I 394.403	437.6	Fe I 437.593
396.2	Al I 396.153	438.4	Fe I 438.355
403.1	Mn I 403.075	494.2	NO GAMMA (0,2) BH, ORDER II
404.6	Fe I 404.581	495.7	
406.4	Fe I 406.360	501.6	He I 501.567
420.2	Fe I 420.203	507.9	AIO GREEN (0,1) BH
422.7	Fe I 422.743	510.2	AIO GREEN (1,2) BH
423.7	N <sub>2</sub> <sup>+</sup> FIRST NEG. (1,2) BH	510.6	CU I 510.554
425.4	Cr I 425.435		

BH = BANDHEAD

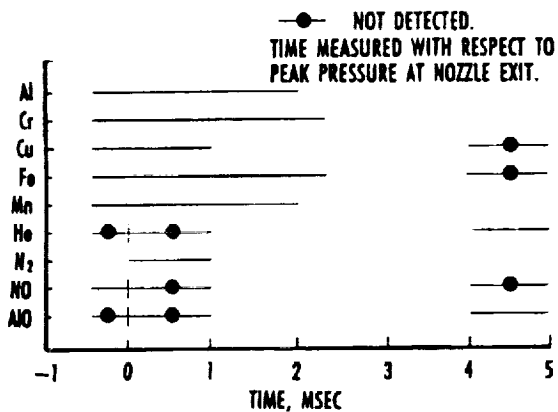


Fig. 20. B30HST species time history.

### DENSITY

Before each run, the PMT detection systems for the nitrogen number density measurements were calibrated using a gas of known density. This was accomplished by evacuating the test chamber, readmitting air to a measured level of temperature and pressure, and measuring the fluorescence collected by the actual PMT optical systems, signal conditioning, and data recording equipment. The detector collection optics were configured to ensure complete collection of the electron beam width. The electron beam current was manually recorded. Recorded fluorescent signals were normalized with the Faraday cup current values. Calibrations at pressures greater than 800

mtorr at 300 K ( $2.6 \times 10^{16} \text{ cm}^{-3}$  or  $77 \times 10^{-6} \text{ lbm/ft}^3$ ) could not be obtained because of poor gun performance at higher pressure levels.

For each calibration pressure, the density calibration factor  $A_{N_2}$  is defined by

$$A_{N_2} = n_{N_2}^{\text{cal,q}} / (S^{\text{cal,q}} / i^{\text{cal}}), \quad (2)$$

where  $S^{\text{cal}}$  is the detector's calibration signal,  $i^{\text{cal}}$  is the beam current at calibration, and  $n_{N_2}^{\text{cal,q}}$  is a modified nitrogen calibration density  $n_{N_2}^{\text{cal}}$  defined by

$$n_{N_2}^{\text{cal,q}} = n_{N_2}^{\text{cal}} / (1 + n_{\text{Air}}^{\text{cal}} k\tau), \quad (3)$$

where the quenching constant  $k\tau = 1.6 \times 10^{-17} \text{ cm}^3/\text{molecule}$  (obtained from prior AEDC studies). The quenched calibration signal is, therefore, coupled with an equivalently reduced value of the nitrogen calibration density. Application of the quenching factor requires the product of  $k\tau$  and the air density, not the nitrogen density. In air, it is assumed that the oxygen and nitrogen quenching constants are equal.

For a given test, the modified nitrogen test density is defined by

$$n_{N_2}^{\text{test,q}} = A_{N_2} S^{\text{test,q}} / i^{\text{test}}, \quad (4)$$

and the actual nitrogen number density is

$$n_{N_2}^{test} = n_{N_2}^{test,q} \left[ 1 - \left( n_{N_2}^{test,q} / M_{N_2}^{test} \right) k\tau \right], \quad (5)$$

where  $M_{N_2}^{test}$  is the nitrogen mole fraction in the test gas.

All density data were corrected for the difference in vibrational temperature between the calibration and test conditions. The fraction of nitrogen molecules in the lowest vibrational level ( $v = 0$ ), which is the level of the measured First Negative System (0,0) band, decreases with increasing vibrational temperature as higher vibrational levels ( $v = 1, 2, \dots$ ) become more populated. This fraction is given by:

$$n(v=0)/n = 1 - \exp(-3390/T_v), \quad (6)$$

where  $T_v$  is the vibrational temperature. The measured value of  $T_v$ , 1,240 K (see next section), yields a fraction of 0.935. Therefore, to correct for the difference in vibrational temperature, the measured densities were divided by this factor.

Reduction of the PMT detector system density data required subtraction of background light. The magnitude of the background light was assumed equal to the magnitude of the light recorded during a run having similar combustion characteristics and with the electron beam off. Data for Run 8010 were reduced using background light from Run 8008. Similarly, background light from Run 8012 was used to reduce the Run 8014 data. Runs 8012 and 8014 were classified as detonations (the diaphragms broke because of high pressure instead of the electrical discharge) as opposed to the preferred combustions, but their stagnation and pitot pressure traces were representative of the desired conditions. It was necessary to use the value of beam current existing just before each run, as the current data obtained during each run were noisy (large harmonics with a prominent superimposed beat structure). Among the causes for this were electrical signals generated by varying capacitance to ground, induced by shock and vibration of the Faraday cup during the run.

No quantitative information was extracted from either of the two south side AEDC PMT detectors. Signals from these detectors were never above background levels. For each run, a strong, spurious burst of signal was detected by both south side PMTs beginning approximately 1 msec before any indication of flow by the pitot probe. These bursts lasted for about 1 msec, ending at nearly the same time that flow was detected. The bursts could have been caused by light originating in the high-temperature

stagnation region near the nozzle throat at the driven tube end wall, then reflected by surfaces into the test section. Another possibility was that the south side signal cables were exposed to electrical interference as a result of their particular routing.

Through Run 8012, no useful He PMT data had been acquired. To obtain another time-resolved helium data channel, the AEDC  $N_2$ (South) PMT was converted to a helium detector after Run 8012. Neither He PMT detector system ever recorded an identifiable signal above background.

The respective calibration constants for Runs 8010 and 8014 were  $2.43 \times 10^{14}$  and  $2.23 \times 10^{14}$  molecules/cm<sup>3</sup>/(mV/mA) (average of two calibrations for each run). Runs 8010 and 8014 were reduced using, respectively, Runs 8008 and 8012 for the background, and the vibrational temperature correction was applied. These results are presented in Figs. 21 and 22. Theoretical frozen densities shown in the figures were calculated under the assumption of fully frozen flow in the nozzle expansion, while the theoretical equilibrium densities assume full chemical equilibrium during the nozzle expansion. The PMT system results are presented in two ways: (1) using the quenching constant  $k\tau = 0$  (no quenching in the flow), and (2)  $k\tau = 1.6 \times 10^{-17}$  cm<sup>3</sup>/molecule. For Run 8010 most of the PMT system values using  $k\tau = 1.6 \times 10^{-17}$  cm<sup>3</sup>/molecule are greater than the frozen flow values. For Run 8014 more of the PMT system values using  $k\tau = 1.6 \times 10^{-17}$  cm<sup>3</sup>/molecule are less than the frozen flow values. It should be noted that, at these high densities, even a slightly smaller quenching constant would substantially

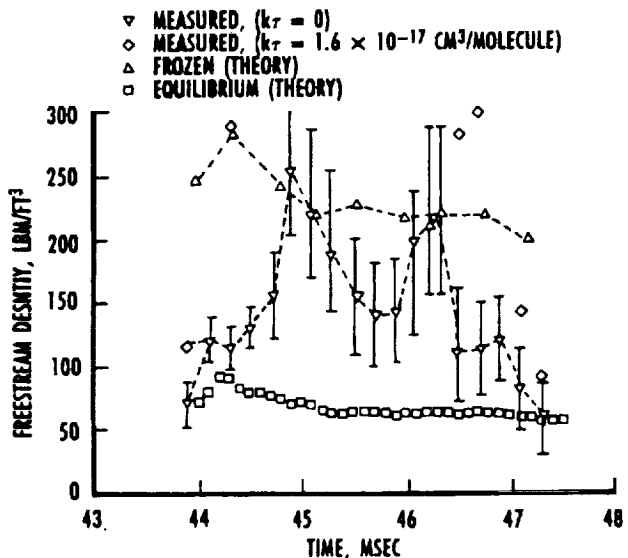


Fig. 21. Measured and theoretical flow densities for Run 8010.

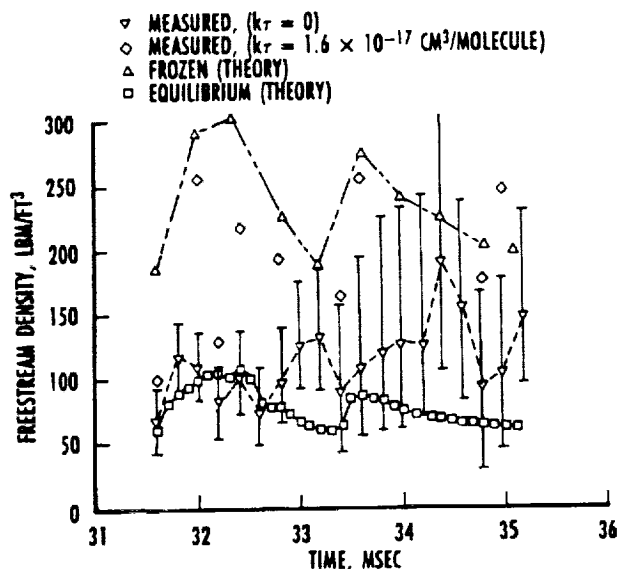


Fig. 22. Measured and theoretical flow densities for Run 8014.

reduce the PMT system values. It is certainly possible that, given the species content ( $N_2$ ,  $O_2$ ,  $NO$ ,  $O$ ) and higher temperatures of the flow, a quite different value of the quenching constant occurs. Uncertainty bars on the PMT system results derived from variations of background light levels.

Meaningful density results using the AEDC  $N_2$ (North) PMT were obtained only for Runs 8010 and 8014. The reduced data for Runs 8013 and 8015 were well above the upper bounds set by theoretical predictions. No PMT system data was obtained for Run 8009 because of misalignment of the AEDC  $N_2$ (North) detector.

### NITROGEN VIBRATIONAL TEMPERATURE

A vibrational temperature can only be extracted from two spectral bands having different upper vibrational energy levels. It is advantageous to select two bands of close proximity in wavelength. The (0,0) band is the strongest feature of the nitrogen First Negative System, but its accompanying (1,1) band is too weak at low vibrational temperatures. For this application, the optimum pair of bands was (0,1) and (1,2). They appeared in the array detector spectra of Runs 8009, 8010, and 8013 at their wavelengths of 427 nm and 423 nm, respectively.

Figure 23 shows a magnified spectrum obtained during Run 8009. Although the spectrum was recorded with the low-resolution grating, the (1,2) and (0,1) bands were separated sufficiently. The background level was chosen as shown, tails were faired in to the zero level by hand at both ends of each

band, and the band areas were measured using a polar planimeter. The ratio of these areas, 6.27, was the ratio of total band intensities. This ratio must be corrected for spectral sensitivity of the spectrometer/array detector system. A spectral sensitivity calibration using a standard tungsten strip lamp determined that the sensitivity at 423.5 nm was 1.8 percent greater than that at 427.8 nm when using the 1,200 lines/mm grating. Accounting for this higher sensitivity, the area ratio became 6.38. Considering possible errors in ascribing the tails and background to the bands, a standard deviation of 0.53 (8.5 percent) was estimated for the area ratio.

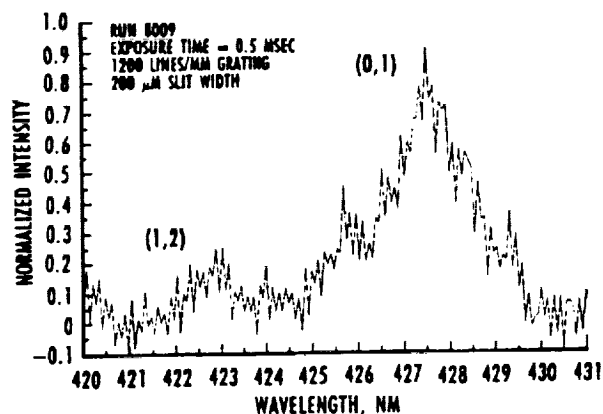


Fig. 23. Nitrogen (0,1) and (1,2) bands for Run 8009.

The 425.4- and 427.5-nm chromium lines occur within the wavelength range of the (0,1) band. The band can be observed convolved with these two lines in the spectra of Runs 8010 and 8013 (Figs. 13 and 16, beam on), when compared with Run 8012 (Fig. 15, beam off). The relative intensities of the three chromium lines remained reasonably constant in Runs 8002, 8003, 8004, and 8012 (Figs 6, 7, 8, and 15). The 429.0-nm chromium line was used as a reference line, since it does not fall within the (0,1) band. After background correction the magnitude of the 429.0-nm line of Run 8012 (Fig. 15, beam off) was adjusted to match the magnitude of that line in Run 8010 (Fig 13, beam on). Results are presented in Fig. 24. The difference in area of the two spectra between 424.8 and 428.4 nm represents the area of the Run 8010 (0,1) band.

To obtain the area of the (1,2) band, a different procedure was necessary because the (1,2) band was convolved with the 422.7-nm iron line. The intensity of the iron line was observed to be independent of the intensities of the chromium lines from run to run. The magnitude of the 422.7-nm line of Run 8012 (Fig 15, beam off) was adjusted to become only slightly smaller than the same line of Run 8010 (Fig. 12, beam on), especially on the low-wavelength

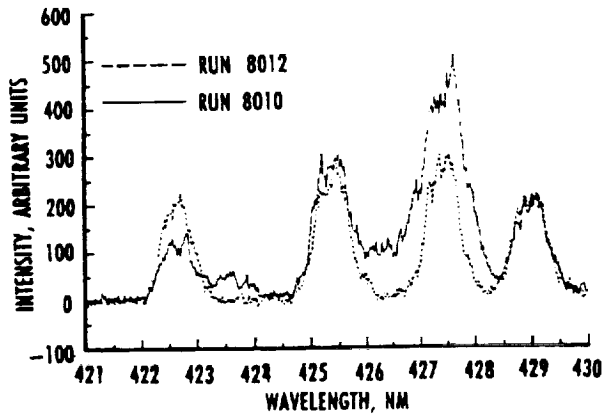


Fig. 24. Matched spectrum for Run 8010 (0,1) band.

side of the line where the weak tail of the R branch of the (1,2) band should be. This result is shown in Fig. 25. The difference in area of the two spectra between 422.0 nm and 424.3 nm represents the area of the Run 8010 (1,2) band.

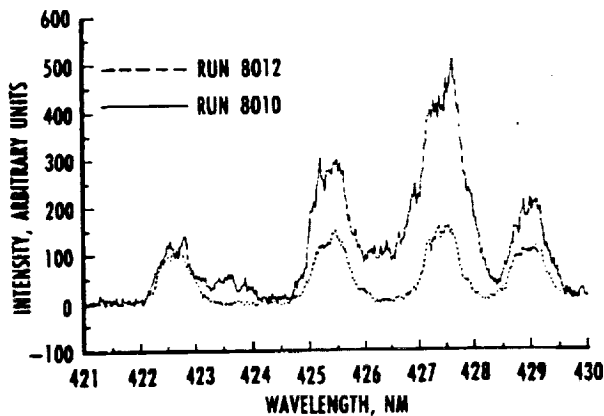


Fig. 25. Matched spectrum for Run 8010 (1,2) band.

The final deconvolved Run 8010 nitrogen band spectrum is presented in Fig. 26. The (0,1) band portion of the spectrum was obtained by subtracting the spectra in Fig. 24. Similarly, the (1,2) band portion is the difference between the Fig. 25 spectra. The two portions were joined at 424.45 nm.

Areas of the (0,1) and (1,2) bands were measured between their respective wavelength limits. The (0,1) to (1,2) area ratio was found to be 5.81 with an estimated standard deviation of 0.63 (10.8 percent), mainly attributed to uncertainty in establishing the relative magnitudes of the 422.7-nm iron line. Based on a tungsten strip lamp calibration, no spectral sensitivity correction was needed when the 2,400 lines/mm grating was used at these wavelengths.

The same matching procedure was carried out for Run 8013 (Fig. 16, beam on) in conjunction with

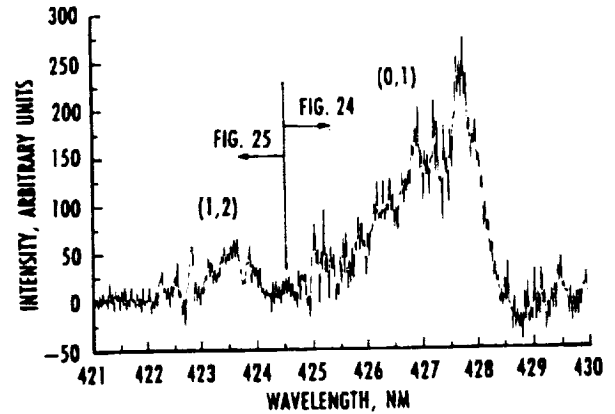


Fig. 26. Nitrogen (0,1) and (1,2) bands for Run 8010.

Run 8012 (Fig. 15, beam off). These results are given in Figs. 27-29. The resultant area ratio was 6.27, with an estimated standard deviation of 0.82 (13.0 percent).

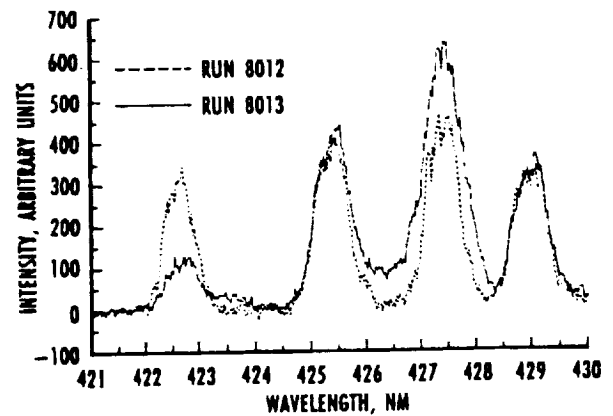


Fig. 27. Matched spectrum for Run 8013 (0,1) band.

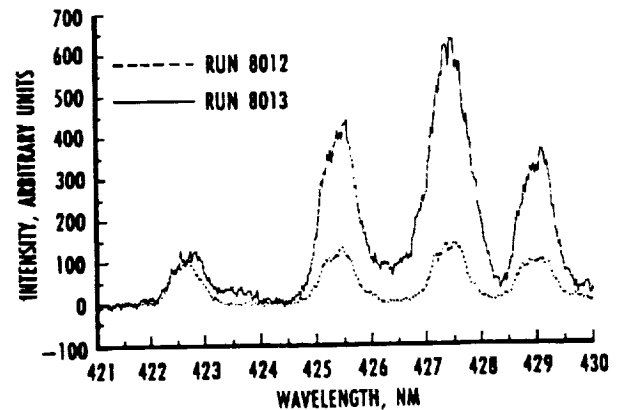


Fig. 28. Matched spectrum for Run 8013 (1,2) band.

Theoretical calculations of electron beam fluorescence for nitrogen are performed by an AEDC computer program designated EBFN2. Although quite comprehensive, the program does not include second-

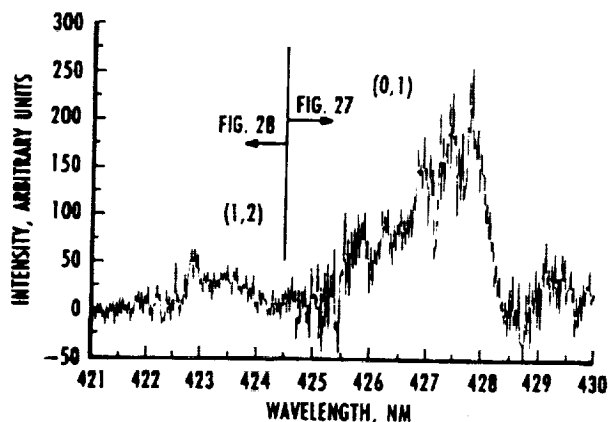


Fig. 29. Nitrogen (0,1) and (1,2) bands for Run 8013.

any electron effects, collisional and resonant photon excitations, convective and diffusion populating/depopulating mechanisms, and variations in quenching rate with rotational-vibrational level. The program was used to predict the ratio of the (0,1) and (1,2) band intensities as a function of vibrational temperature. The result of the prediction is given in Fig. 30, with the ratios normalized to 1.0 at a vibrational temperature of 300 K. For the reported measurements, the tails of each band were faired in before integration of the areas with the polar planimeter. For comparison with Fig. 30, the experimental area ratios were divided by 8.5, the value of the (0,1) to (1,2) area ratio measured in static conditions in the B30HST at 300 K.

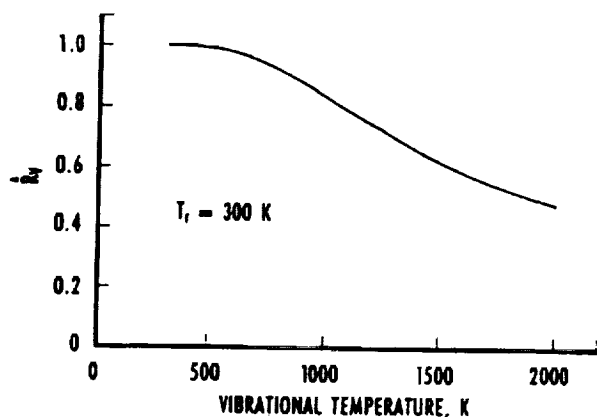


Fig. 30. Normalized intensity ratio of the (0,1) and (1,2) bands as a function of vibrational temperature.

Using the curve in Fig. 30, the measured band area ratios for the three runs converted into vibrational temperatures of 1,180 K, 1,330 K and 1,210 K, giving an average value of 1,240 K. Upon consideration of measurement uncertainty and uncertainties of parameter values used in the calculation by program EBFN2, a standard deviation of 100 K (8.1 percent) was estimated.

## NITRIC OXIDE ROTATIONAL TEMPERATURE

A spectrum of the NO Gamma System's (0,2) band was recorded by the spectrometer/array detector system in Run 8011 (Fig. 14). Although both tunnel diaphragms broke prematurely in this run, resulting in unusable flow conditions, it was of interest to determine the NO rotational temperature from the band profile. To determine a free-stream rotational temperature, an AEDC program designated EBFNO was developed for predicting the electron beam excitation and spontaneous emission process. This new computational model assumed that the excitation process was by primary beam electrons and that optical excitation rules applied. Collisional quenching was accounted for in the model, but variation in quenching rate with individual rotational levels was not included. Self-absorption of the electron beam-excited fluorescence was neglected; it is believed that this was a reasonable assumption because of the relatively low population of the third vibrational level of the ground electronic state. It is almost certain that the neglect of the influence of the beam's secondary electrons was not a good assumption, but fiscal limitations prevented development of a more complex model. The spectral relations and parameters in the model were taken from an existing program (LIFNO) developed at AEDC for modeling the laser-induced fluorescence process of NO Gamma, Beta, and Epsilon bands.

Run 8011's order II spectrum of the NO Gamma System's (0,2) band was fit with an order I wavelength scale and a normalized and background-corrected signal strength scale. Figure 31 shows an overlay of the EBFNO prediction with the spectrometer/array detector spectrum. The rotational and vibrational temperatures used in this prediction were 400 K and 1,200 K, respectively. The shape of the spectrum was relatively insensitive to the value of vibrational temperature over the range of values

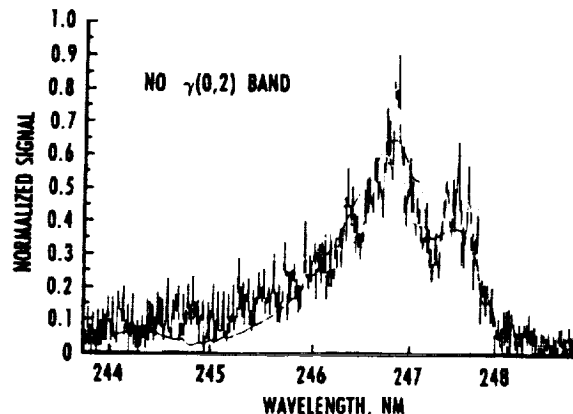


Fig. 31. NO experimental and model spectra for Run 8011.



possible for the tunnel conditions. The shape was, however, rather sensitive to the rotational temperature value. Overall, the 400 K value provided the best fit to the spectrum. It is believed that a much better fit could be achieved if time were available to fine tune spectrometer/array detector parameters and to account for spectral sensitivity variation over the wavelength and physical pixel region utilized. This measurement's uncertainty is a standard deviation of 50 K.

### SUMMARY

The measurements obtained are summarized in Table 3. Numerous self-emitting metallic species were identified, many of which may be associated with an aging/erosion process within the B30HST. Because there were only 16 tunnel runs, it was only possible to obtain spectral measurements over a limited range of wavelengths and time sampling periods. Many spectral features of the flow remain uninvestigated. Because flow self-emission is important to all optical diagnostic techniques, it is recommended that additional spectral studies be performed.

The three electron beam-excited species that were identified are nitrogen, helium, and nitric oxide. The high metallic radiation background interfered with attempts to obtain the time-wise variation of  $N_2$  density and He radiation with the optical filter/PMT channels. In the case of the  $N_2$  density measurements the result of interference was increased uncertainty. Unfortunately, the interference caused the time-wise He measurement to fail completely. It is recommended that the electron beam be modulated to provide discrimination against the background radiation in future  $N_2$  density measurements. Careful

data reduction produced useful measurements of  $N_2$  vibrational temperature, even though the high background from metallic species significantly increased measurement uncertainty. Perhaps the recommended additional spectral studies would reveal  $N_2^+$  First Negative System band-pair regions having less background. Detection of the He arrival (see Fig. 20) was easily accomplished with the spectrometer/array detector system. Because of this, it is recommended that this means of detecting He arrival be used in the future. With proper calibrations of the system an He number density could be obtained. Although the flow conditions were out of limits for the run in which the NO spectrum was recorded, the usefulness of the NO spectrum for determination of free-stream rotational temperature was demonstrated and should be exploited in future experiments. Indeed, based on the strong NO signals, it is recommended that lower resolution NO spectra be obtained to provide a measure of NO vibrational temperature in the same manner that the  $N_2$  vibrational temperature was obtained.

### REFERENCES

1. Neumann, R. D. "Requirements in the 1990's for High Enthalpy Ground Test Facilities for CFD Validation." 16th Aerodynamic Ground Testing Conference, Seattle, WA, June 18-20, 1990, AIAA Paper 90-1401.
2. Boeing Defense & Space Group, Military Airplanes Division. "Reacting Gas Experimental Data in Low Density Flow. Task I. Boeing 30 Inch Hypersonic Shock Tunnel Nozzle Experimental Survey." WRDC-TR-90-3010, May, 1990.

Table 3. Results

MEASUREMENT	RESULTS
SELF-EMITTING RADIATIVE SPECIES	ALUMINUM, CHROMIUM, COPPER, IRON, MANGANESE AND ALUMINUM OXIDE WERE DETECTED. LIGHT FROM THESE METALLIC SPECIES WAS GENERATED AT HIGH TEMPERATURE UPSTREAM OF THE NOZZLE THROAT, AND WAS PROBABLY REFLECTED BY SURFACES DOWNSTREAM OF THE THROAT INTO THE DETECTORS.
ELECTRON BEAM-EXCITED RADIATIVE SPECIES	NITROGEN, HELIUM, AND NITRIC OXIDE SPECTRA WERE RECORDED. NO APPEARED AT THE BEGINNING OF THE USABLE FLOW PERIOD, $N_2$ DURING THE PERIOD, AND $He$ AFTER THE PERIOD.
NITROGEN DENSITY	AIR DENSITY VALUES FELL BETWEEN FROZEN AND EQUILIBRIUM PREDICTIONS, AS EXPECTED (SEE FIGS. 21 AND 22). STRONG BACKGROUND LIGHT FROM METALLIC SPECIES AFFECTED THE MEASUREMENTS.
NITROGEN VIBRATIONAL TEMPERATURE	THREE MEASUREMENTS WERE ACQUIRED. THE $N_2^+$ FIRST NEGATIVE SYSTEM (0,1) AND (1,2) BANDS WERE USED. METALLIC BACKGROUND LIGHT CAUSED LOW SIGNAL TO NOISE CONDITIONS. THE AVERAGE VIBRATIONAL TEMPERATURE WAS 1240K WITH A STANDARD DEVIATION UNCERTAINTY OF 50K.
HELIUM (DRIVER GAS) ARRIVAL TIME	SPECTROMETER/ARRAY DETECTOR MEASUREMENTS OF THE $He$ ARRIVAL TIME INDICATED THE CHEMICALLY PURE TEST TIME RANGED BETWEEN 1.0 AND 2.4 MSEC. STRONG METALLIC LIGHT PREVENTED MEASUREMENT BY OPTICAL FILTER/PMT CHANNELS.
NITRIC OXIDE FREE-STREAM ROTATIONAL TEMPERATURE	THE NO ROTATIONAL TEMPERATURE WAS 400K WITH A STANDARD DEVIATION UNCERTAINTY OF 50K. THIS RUN'S FLOW CONDITIONS WERE OUT OF LIMITS BECAUSE OF PREMATURE DIAPHRAGM RUPTURE.

3. Cassady, P. E. and Lieberg, S. F. "Planar Laser Induced Fluorescence Measurements in Hypersonic Shock Tunnel Flow." 21st Fluid Dynamics, Plasma Dynamics and Lasers Conference, Seattle, WA, June 18-20, 1990, AIAA Paper 90-1549.

4. Shelton, D. P. and Cassady, P. E. "Electron Beam Density Measurement in a Hypersonic Shock Tunnel Flowfield." 17th Aerospace Ground Testing Conference, Nashville, TN, July 6-8, 1992, AIAA Paper 92-3933.

5. Muntz, E. P. "The Electron Beam Fluorescence Technique." AGARDograph 132, December 1968.

6. Center, R. E. "Plural and Multiple Scattering of Fast Electrons in Gases." *Physics of Fluids*, Vol. 13, No. 1, January 1970, p. 79.

**RESONANCE LAMP ABSORPTION MEASUREMENT OF OH NUMBER DENSITY  
AND TEMPERATURE IN EXPANSION TUBE SCRAMJET ENGINE TESTS\***

**Walter R. Lempert**  
Dept. of Mechanical & Aerospace Engineering  
Princeton University  
Princeton, New Jersey

**Richard E. Trucco**  
General Applied Science Laboratories  
Ronkonkoma, New York

**Robert D. Bittner**  
Analytical Services and Materials, Inc.  
Hampton, Virginia

**INTRODUCTION**

Optical absorption techniques have been used to obtain quantitative flow field and species data in a variety of combustion environments. Hanson and his co-workers (1) have developed an ultraviolet rapid (KHz) scanning method employing the second harmonic from a modified commercial ring dye laser which has been used to measure hydroxyl radical (OH) and nitric oxide (NO) (2) concentrations, as well as static temperature, density, and flow velocity. Recently, Cavolowsky, et al., (3) have applied this approach to the NASA-Ames 16-inch hypersonic shock tunnel, obtaining hydroxyl number density and static temperature. Frequency Modulation (FM) techniques have also been demonstrated for water vapor (4) and oxygen (5).

In this paper, we report results of hydroxyl radical and static temperature measurements performed in the General Applied Science Laboratories-NASA HYPULSE expansion tube facility using the microwave resonance lamp absorption technique (6,7,8). Data were obtained as part of a series of hydrogen/air and hydrogen/oxygen combustion tests at stagnation enthalpies corresponding to Mach 17 flight speeds. Data from a representative injector configuration is compared to a full Navier-Stokes CFD solution.

**TEST FACILITY**

Testing for this study was conducted in the GASL/NASA HYPULSE facility, isometrically portrayed in Fig. 1. HYPULSE, a 6-inch diameter, 115-ft long expansion tube, was built by NASA-Langley Research Center in the late 1960's, and decommissioned in 1983. In October 1987, the facility was transferred to GASL, and by May 1989, the full NASA operating capability was recovered. The operation of the expansion tube is similar to that of two shock tubes in series.

---

\* Work done on contract at General Applied Sciences Laboratories, NAS1-18450.

The driver section initiates the test flow in the first (intermediate) tube, which in turn starts the flow in the second (acceleration) tube, accelerating the flow to velocities necessary for hypersonic flight simulation by means of an unsteady expansion. These two sections are separated by a thin mylar diaphragm. The distance-time (x,t) diagram of Fig. 2 illustrates ideal expansion tube flow, where the shaded region represents the test gas. A complete description of the operation of the expansion tube is given in References 9-11. The critical feature of this facility is the ability to generate high enthalpy flow without stagnation. This results in low levels of dissociated nonequilibrium species, and, therefore, more closely resembles real free stream flight conditions. The tradeoff for this benefit is the brevity of the test time, nominally 250 to 400 microseconds.

The facility test conditions, derived from a combination of measured in-stream pitot and static pressures, wall static pressure and shock arrival speed, are shown in Table I. From these measurements, the quantities of Table II are calculated applying the numerical procedures described in Reference 12. A full description of the experimental efforts to calibrate the HYPULSE facility is detailed in Reference 13.

### COMBUSTOR MODEL

Figure 3 shows a schematic of the combustor model utilized for the test series, configured with a 15° flush wall fuel injector. The constant area model is 2" x 1" in cross section, 28" long and located so that its inlet is 1" from the exit of the acceleration tube. The leading edges are sharp wedges with a nominal tip bluntness of 0.020" diameter. Flow visualization of the near-field fuel injection region is afforded by 12" side windows (either BK-7 or fused silica glass). One-inch diameter UV windows, located at 17" and 26" from the inlet provide line-of-sight visibility for the OH absorption measurements. Access for planar laser fluorescence imaging, described in a separate paper (14), was achieved through a 6.25" x 1.125" fused silica window on the upper wall. The assembled model is shown in Fig. 4.

Interchangeable fuel injection manifold plates, located on the upper and lower walls at 6" from the inlet, are fed by the injector plenum. The injectors used during these tests were: A 15° flush wall injector, a single-hole 10° dual-swept ramp injector, and a 10° single unswept ramp injector. Hydrogen fuel was supplied to the unswept plenum by a Ludwig tube mechanism opened to synchronize with the test flow by fast acting valves as described in Reference 15.

The model was fitted with an array of piezoelectric pressure transducers and specially designed thin-film heat flux gauges, located throughout the upper and lower walls.

### OH RESONANCE ABSORPTION METHOD

The resonance lamp absorption technique, illustrated schematically in Fig. 5, is described in detail in References 6-8 and will only be summarized here. A low pressure water vapor microwave discharge provides a source of narrow bandwidth, ultraviolet emission lines from the hydroxyl radical X-A band near 309 nm. In the current experiments, the lamp output was amplitude modulated at 23 KHz using a 150 sector chopper wheel and coupled into UV transmitting optical fiber which "pipes" the light to the expansion tube. A lens is used to collimate the light through the combustor in an approximately 1/2" diameter beam. A second lens couples the partially transmitted beam into a receiving fiber to a custom polychrometer. The polychrometer consists of a fiber optic bundle placed in the exit plane of a 0.25 m spectrometer which disperses the OH A-X emission into eight spectral channels of approximately 1.50 nm width.

Individual phototubes are used to obtain the absorption in each spectral channel as a function of time. The analogue bandwidth was adjusted to approximately 100 KHz with a 5 Kohm parallel load resistor. Each channel was digitized with a LeCroy model 6810 A/D converter. The experimental absorption in each channel was averaged over the approximately 200 microsecond steady-state run time, yielding a single set of temporally and spatially averaged absorption values which is inverted to yield OH number density and static temperature.

As described in References 6-8, the lamp emission consists of approximately 100 discrete rotational transitions from both the (0,0) and (1,1) vibrational bands, resulting in a hybrid rotational/vibrational temperature determination.

## FACILITY INTERFACE

Figure 6 shows the resonance lamp absorption apparatus, as assembled for the HYPULSE combustion tests. The lamp, chopper wheel, polychromator, and associated power supplies and gauges were mounted on a 2' x 4' optical breadboard, located in a room adjacent to the expansion tube. The lamp output was transmitted to the facility with a 5 meter length of 1100 micron core silica fiber. The feed-thru to the test chamber was accomplished with a 1.5" length of 0.3125" OD x 0.047" ID tubing in the following manner: First the protective jacket was spliced and removed over half the length of the fiber. The bare core and cladding were then slid through the 0.047" ID tube, and sealed on both ends with silicon adhesive. This resulted in a leak proof feed-thru, without requiring a break in the fiber. The protective jacket was then replaced. The portion of the fiber inside the test chamber was threaded through rubber hoses to the collimating lens assembly to provide additional protection from post-test stresses. Threaded tubing, secured to the model side wall, fixed the optics and provided a pressure seal. The windows were 1" diameter with an additional 0.25" lip for flush mounting with the model inside surface. Despite these precautions, facility stresses did cause occasional damage to the windows, requiring replacement. Post-flow contamination from the secondary mylar diaphragm attenuated the transmission by approximately 30%, necessitating periodic cleaning. Figure 7 shows a schematic of the optical fiber/model interface, and Fig. 8 shows the assembly inside the test section.

## ONE-DIMENSIONAL ABSORPTION MODELING

The inversion of the experimental data is performed by means of a discrete least-squares fit to a surface of transmission values generated using a standard spectral model which is described in detail in Reference 8. The surface consists of 8 transmission values for each point in a 49 x 31 grid of OH number density-path length product, NI, and static temperature. The NI grid runs from  $1.0 \times 10^{15} \text{ cm}^{-2}$  to  $1.0 \times 10^{18} \text{ cm}^{-2}$  in factors of  $10^{0.625} = (1.15)$ , and the temperature grid runs from 1000 to 4000 K in 100 K increments. The result of the inversion procedure is a one-dimensional value of OH number density and static temperature, averaged spatially over the beam path and beam dimensions.

## RESULTS

The application of the technique to the HYPULSE expansion tube presented a significant challenge due to the severe environment and short (<300 microsecond) run times. Despite the fact that the measurements were performed 26" downstream from the model leading edge, where,

presumably, combustion was no longer occurring, the signal due to spontaneous combustor luminosity was as large, or larger, than that from the lamp itself. This, coupled with the high analogue bandwidth required to perform the measurement, resulted in lower signal-to-noise than obtained in previous experiments (7,8). In addition, for some tests the OH number density and static temperature were sufficiently high to cause virtually complete absorption, resulting in data which could not be inverted. Nonetheless, useful data was obtained for a  $\phi = 1$  (based on air), 15° flush wall injector H<sub>2</sub>/O<sub>2</sub> test, and a  $\phi = 3$ , 10° dual-swept ramp injector H<sub>2</sub>/air test. Figure 9 shows the experimental time trace from spectral channels 2 and 7 for a 15° flush wall injector  $\phi = 1$ --H<sub>2</sub>/O<sub>2</sub> combustion run. The run starts at approximately 5.18 msec. The stable run time, for which the data was averaged, is from 5.40 to 5.55 msec. The experimental transmission values are  $0.16 \pm 0.02$ , and  $0.68 \pm 0.05$  for channels 2 and 7, respectively.

Table III shows the experimental transmission values for the two tests described below. Also shown is the corresponding one-dimensional values for OH number density and static temperature, and an estimate of their uncertainty. (Due to limitations on the available number of facility A/D channels, spectral channels which had the lowest signal-to-noise ratio were not recorded.) The mean values and uncertainty estimates are obtained by performing the data inversion for all 729 (3<sup>6</sup>) possible combinations of measured transmission values  $\pm$  the uncertainty in the measured transmission. The results represent the mean and RMS deviation from the procedure. (It should be stressed that these are statistical uncertainties based upon the observed signal-to-noise ratio in the experimental data.) While it is difficult to compare these two tests due to differences in injectors, equivalence ratio, and mixture, it is not unrealistic to conclude that the H<sub>2</sub>/O<sub>2</sub> test would be expected to result in higher OH number density than the H<sub>2</sub>/air test.

### COMPARISON TO CFD

A full Navier-Stokes CFD solution was performed for the 15 degree flush wall injection,  $\phi = 1.0$  test described above. Figures 10 and 11 show contour plots of average OH number density and static temperatures as a function of height above the bottom wall (Z-axis), integrated in the lateral dimension (Y-axis). Also shown is the lamp output beam dimension and position. The variation with respect to the flow direction (X-axis) is considerably less. While there is no direct way to compare the experimental 1D absorption data with the CFD prediction, an analysis was performed as follows: First, a computer code was written to simulate the experimental absorption expected from a flow described by the CFD grid. This required spatial integration of the absorption in both the Z and Y dimensions. This integration was performed differently in the two dimensions. In Z (vertical), the CFD values for both OH number density and temperature were averaged over the beam height. This average was weighted to reflect the circular cross section of the beam, assuming negligible X (flow axis) dependence over the diameter of the beam (1/2"). This weighted averaging resulted in a single value of OH and T for each Y grid point. The absorption coefficients,  $K_y(N)$ , for each of the N spectral channels were then calculated using these OH and T values for each of the Y grid points. The simulated transmission in each channel is given by:

$$\tau_N = \sum_y \exp [-(K_y(N) l_y)] \quad (1)$$

where  $l_y$  is the length in the y direction of the "yth" grid element. (Note that the CFD grid is not equally spaced.) The final result of this procedure is a set of eight transmission values which are listed in Table IV. Comparison of Tables III and IV shows that the results of this

simulation predict transmission values which are on the order of 30 to 40% lower than the experimental data.

In order to attempt a more tangible assessment of the comparison between the CFD prediction and the experimental data, a sensitivity analysis was performed. This was done by repeating the above simulation procedure for all 9 combinations of CFD grid values  $\pm 40\%$  for OH and  $\pm 10\%$  for temperature. Table V shows the resulting 9 sets of simulated transmission values. Comparison of Tables III and V indicates that modification of the CFD predictions for OH by  $\pm 40\%$  and T by  $\pm 10\%$  result in a range of transmission values which bracket the experimental data to within the estimated statistical uncertainty.

As a final comparison, the simulated transmission values from the CFD grid were "inverted" with the ID software to obtain ID equivalent OH density and temperature. The resulting OH number density is  $4.27 \times 10^{16} \text{ cm}^{-3}$  and resulting static temperature is 2606 K. Comparison with the data of Table III indicates a discrepancy of approximately 40% in OH number density, and 10% in static temperature. There are several possible sources of error. First, a detailed measurement of the size of the beam as a function of lateral position (Y) was not performed. In general, the collimation of the 1100 micron core fiber is far from perfect, resulting in a beam size which varies with position. Second, the beam is assumed to have a uniformly intense circular cross section, which is clearly not the case. Finally, it is difficult to accurately predict the free stream inlet conditions produced by the expansion tubes. Calibrations performed just prior to the test sequence resulted in a measured static pressure and temperature of 14,478 Pa and 2237 K, respectively. The nominal values assumed for the CFD calculation were 16,478 Pa and 2089 K, respectively.

In attempting to assess the significance of the resonance absorption results with respect to CFD validation, it is useful to compare the above ID equivalent results for OH and T with spatial averages of the CFD grid itself. A simple linear averaging of the contours of Figs. 10 and 11 over the beam profile results in  $OH_{\text{ave}} = 4.26 \times 10^{16} \text{ cm}^{-3}$  and  $T_{\text{ave}} = 3037 \text{ K}$ . The level of agreement between average OH and equivalent ID OH is actually surprising considering the highly two-dimensional character of the flow field and the nonlinear nature of the absorption process. The discrepancy in temperature is most likely due to the inverse correlation of OH density and static temperature. From Figs. 10 and 11 it can be seen that the CFD predicts relatively low temperatures in regions of relatively high OH. Since the integral transmission is weighted by the regions of high OH Density, the result is a low value for ID equivalent temperature.

From the above it is fair to conclude that, for this case, the experimental resonance absorption OH concentration and static temperature are expected to agree within the order of 10% with the spatially averaged results of the CFD calculation, in the absence of any additional systematic error. Additional sets of data and calculations will be required in order to determine the generality of this statement for three-dimensional reacting flow fields.

## CONCLUSIONS

The resonance lamp absorption method has been used to obtain temporally averaged line-of-sight static temperature and OH concentrations in the HYPULSE hypersonic expansion tube facility. A comparison of the experimental data with a full CFD solution has been performed for a  $15^\circ$  flush wall injector,  $\text{H}_2/\text{O}_2$  combustion configuration. The experimentally determined OH number density was approximately 40% below the simulated prediction using the CFD grid, while experimental static temperature was approximately 10% low. It is likely that some of this discrepancy is due to the nominal combustor inlet density used for the CFD, which was

approximately 20% higher than that actually produced by the facility. Comparison of simulated temperature and OH number density, with simple spatial averaging of the CFD grid, resulted in agreement to within approximately 10%.

### ACKNOWLEDGEMENTS

The authors wish to acknowledge R. Gregory for providing the resonance lamp absorption instrumentation, and C. Rogers, R. McClinton, and J. Erdos for useful discussions.

### REFERENCES

1. Davidson, D.F., Chang, A.Y., DiRosa, M.D., and Hanson, R.K., "Continuous Wave Laser Absorption Techniques for Gasdynamic Measurements in Supersonic Flows," *Appl. Opt.* **30**, p. 2598 (1991).
2. Chang, A.Y., DiRosa, M.D., Davidson, D.F., and Hanson, R.K., "Rapid Tuning cw Laser Technique for Measurements of Gas Velocity, Temperature, Pressure, Density, and Mass Flux Using NO," *Appl. Opt.* **30**, p. 3011 (1991).
3. Cavolowsky, J. and Newfield, M., "Laser Absorption Measurements of OH Concentration and Temperature in Pulsed Facilities," AIAA 92-0142, 30th Aerospace Sciences Meeting, Reno, NV, January 6-9, (1992).
4. Wang, L-Q, Riris, H., Carlisle, C.B., and Gallagher, T.F., "Comparison of Approaches to Modulation Spectroscopy with GaAlAs Semiconductor Lasers: Application to Water Vapor," *Appl. Opt.* **27**, p. 2071 (1988).
5. Philippe, L. and Hanson, R., AIAA-92-0139, "Sensitive Diode Laser Absorption Technique for Aerodynamic Measurements," 30th Aerospace Sciences Meeting, Reno, NV, January 6-9 (1992).
6. Lempert, W.R., "Microwave Resonance Lamp Absorption Technique for Measuring Temperature and OH Number Density in Combustion Environments," *Combustion and Flame* **73**, p. 89 (1988).
7. McCullough, R.W. and Northam, G.B., in "Temperature, Its Measurement and Control in Science and Industry," J.F. Schooley, Editor, American Institute of Physics, New York, p. 665, Vol. 5, Pt. 1 (1982).
8. Northam, G.B., Lempert, W.R., Diskin, G.S., Gregory, R.W., and Bell, R.A., "Supersonic Combustion Performance of Hydrogen/Hydrocarbon Mixtures as Determined by a Nonintrusive Temperature Monitor," AIAA-88-3293, AIAA/SAE/ASME/ASEE 24th Joint Propulsion Conference, Boston, MA, July 11-13 (1988).
9. Miller, C.G., and Jones, J.J., "Development and Performance of the NASA-Langley Research Center Expansion Tube/Tunnel, a Hypersonic-Hypervelocity Real Gas Facility," 14th International Symposium on Shock Tubes and Waves, Sydney, Australia, August 15-18, 1983.
10. Tamagno, J., Bakos, R.J., and Pulsenetti, M.V., "Results of Preliminary Calibration Test in the GASL HYPULSE facility," NASP Contractor Report 1071, Ref. WBS 2.2.21, November 1983.



11. Tamagno, J., Bakos, R.J. Pulsenetti, M.V., and Erdos, J., "Hypervelocity Real Gas Capabilities of GASL's Expansion Tube (HYPULSE) Facility," AIAA Paper No. 90-1390, June 1990.
12. Mirels, H., "Test Time in Low-Pressure Shock Tubes," *Physics of Fluid* 6 (9), September 1963.
13. Calleja, J., and Tamagno, J., "Calibration of HYPULSE for Hypervelocity Air Flows Corresponding to Flight Mach Numbers 13.5, 15, and 17," GASL TR 335, February 1992.
14. Rubin, L.F., Swain, D.M., and Trucco, R.E., "Visualization of Hydrogen Injection in a Scramjet Engine by Simultaneous Planar Laser-Induced Fluorescence Imaging and Laser Holographic Interferometry," Proceedings of the NASA Langley Measurement Technology Conference, Hampton, VA, NASA CP-3161, 1992.
15. Trucco, R., and Danziger, L., "Performance of a Fast-Acting Valve for Hydrogen Injection into a SCRAMJET Engine Model," GASL TM 232, September 1989.

TABLE I. HYPULSE Calibration Data--Measured Quantities

<u>Nominal Conditions</u>	<u>M13.5 LP</u>	<u>M13.5 HP</u>	<u>M15</u>	<u>M17</u>	<u>M17 with Diffuser Air</u>	<u>M17 with Diffuser Oxygen</u>
Driver Pressure (MPa)	37.9	51.7	37.9	37.9	37.9	37.9
Static Pressure (KPa)	18.0 ± 0.3	23 ± 1	1.52 ± .07	2.00 ± 0.07	16 ± 2	14.5 ± 2
Core Pitot Pressure (KPa)	386 ± 32	510 ± 47	105 ± 6	156 ± 9	663 ± 90	602 ± 85
Secondary Shock Speed (M/S)	4169 ± 24	4176 ± 30	4707 ± 19	5176 ± 42	5244 ± 42	5189 ± 40
Useful Test Time (Microseconds)	450	450	400	350	350	350

TABLE II. HYPULSE Calibration Data--Calculated Quantities

<u>Nominal Conditions</u>	<u>M13.5 LP</u>	<u>M13.5 HP</u>	<u>M15</u>	<u>M17</u>	<u>M17 with Diffuser Air</u>	<u>M17 with Diffuser Oxygen</u>
Total Enthalpy (MJoule/kg)	9.89	9.84	11.14	14.05	15.07	16.16
Total Pressure (MPa)	10.3	14.7	59.8	153.1	138.0	258.0
Total Temperature (°K)	5780	5830	6870	8070	8370	6980
Static Temperature (°K)	2350	2280	1050	1140	2100	2240
Velocity (M/S)	3840	3840	4630	5120	5090	4960
Mach Number	4.10	4.19	7.31	7.77	5.75	5.75

TABLE III. Experimental Results from OH Resonance Absorption Measurements in HYPULSE Combustion Experiments

15 Degree Flush Wall Injector --  $\phi = 1.0$ , H<sub>2</sub>/O<sub>2</sub>

	1	2	3	4	5	6	7	8
Tau	0.18	0.16	0.16	0.26	--	0.59	0.68	--
Sig Tau	0.03	0.02	0.03	0.05	--	0.08	0.05	--

Mean OH Number Density:  $2.7 \times 10^{16} \text{ cm}^{-3}$   
 Statistical Uncertainty:  $2.7 \times 10^{15} \text{ cm}^{-3}$   
 Mean Static Temperature: 2320 K  
 Statistical Uncertainty: 204 K

10 Degree Dual-Swept Ramp Injector --  $\phi = 3.0$ , H<sub>2</sub>/air

	1	2	3	4	5	6	7	8
Tau	0.39	0.27	0.36	0.52	--	--	0.7	--
Sig Tau	0.05	0.03	0.04	0.04	--	--	0.04	--

Mean OH Number Density:  $1.2 \times 10^{16} \text{ cm}^{-3}$   
 Statistical Uncertainty:  $9.9 \times 10^{14} \text{ cm}^{-3}$   
 Mean Static Temperature: 2320 K  
 Statistical Uncertainty: 322 K

TABLE IV. Simulation of 1D OH Transmission from CFD Grid

15 Degree Flush Wall Injection --  $\phi = 1.0$

H<sub>2</sub>/O<sub>2</sub>

26" Downstream from Leading Edge

	1	2	3	4	5	6	7	8
Tau	0.146	0.094	0.096	0.143	0.323	0.439	0.535	0.618

TABLE V. Sensitivity Analysis Results from CFD Solution

TAU VALUES

OH/<OH>	T/<T>	1	2	3	4	5	6	7	8
0.60	0.90	.25	.13	.15	.22	.46	.60	.70	.77
0.60	1.00	.27	.15	.17	.23	.44	.57	.66	.74
0.60	1.10	.29	.16	.19	.23	.43	.56	.65	.72
1.00	0.90	.13	.08	.08	.14	.35	.48	.58	.66
1.00	1.00	.15	.09	.10	.14	.32	.44	.53	.62
1.00	1.10	.16	.10	.11	.14	.31	.42	.51	.59
1.4	0.90	.08	.06	.06	.11	.28	.39	.49	.58
1.4	1.00	.09	.07	.07	.11	.26	.35	.44	.53
1.4	1.10	.10	.07	.07	.11	.25	.33	.42	.50

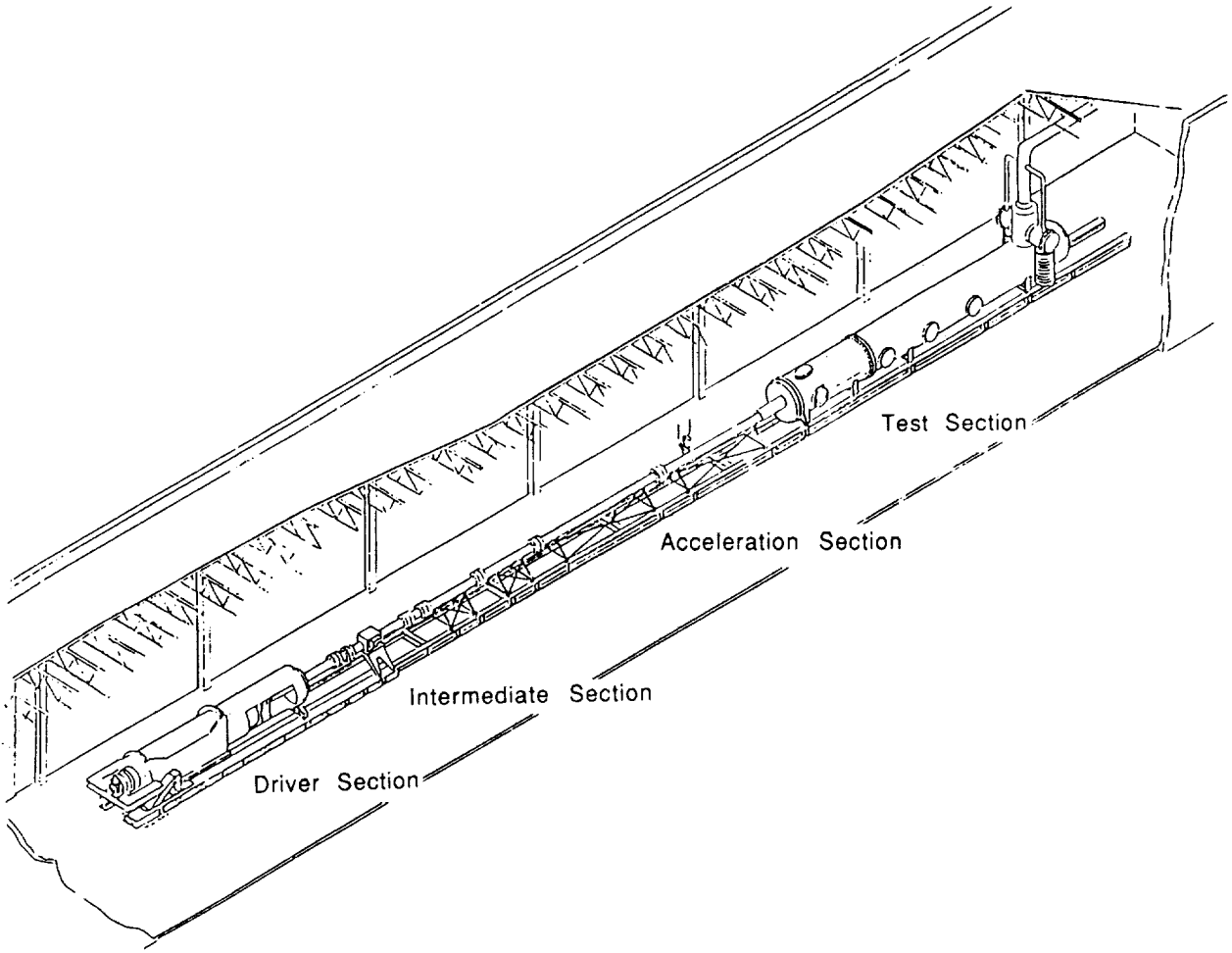


Figure 1. Isometric view of HYPULSE expansion tube.

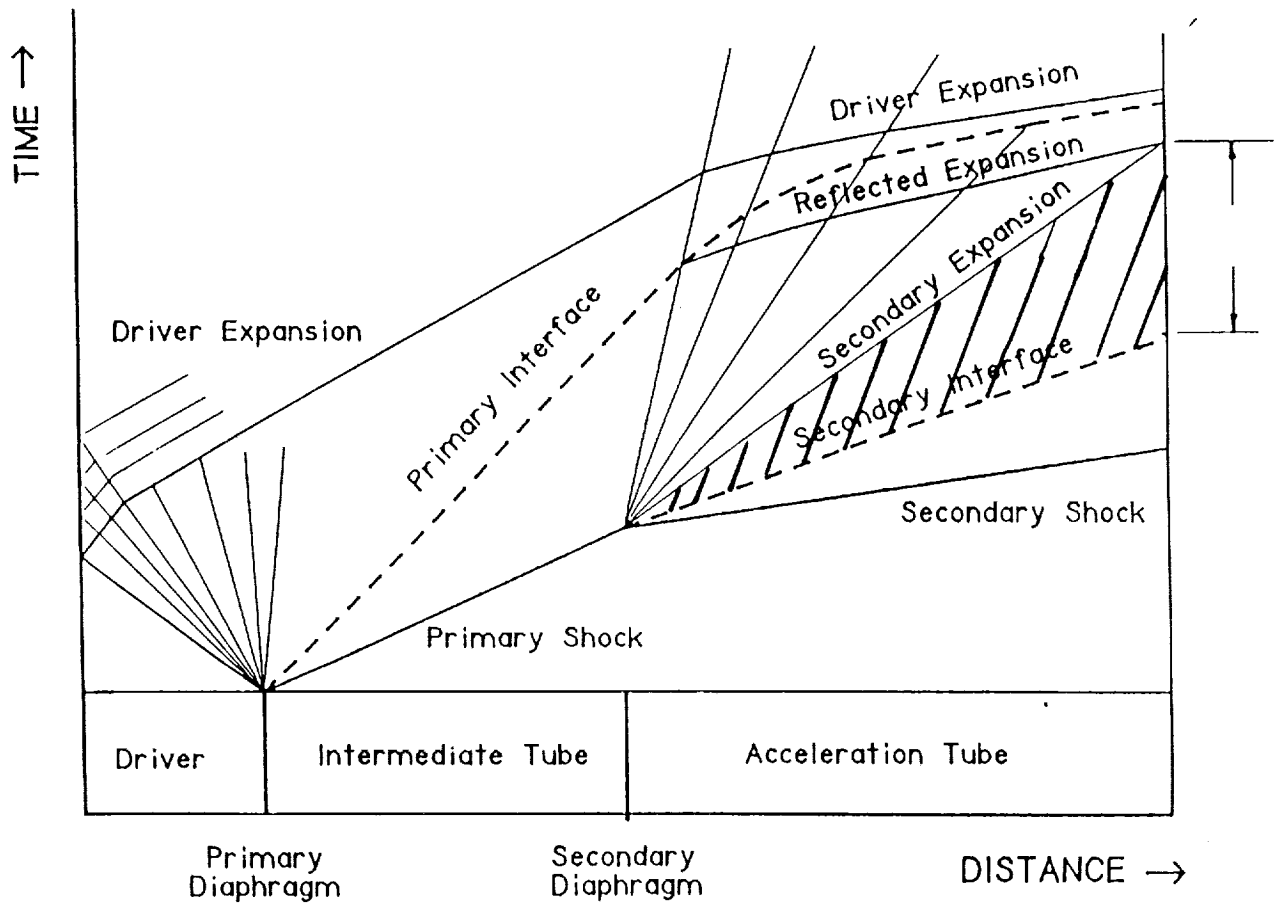


Figure 2. Time-distance for ideal expansion tube. Shaded region represents test gas.

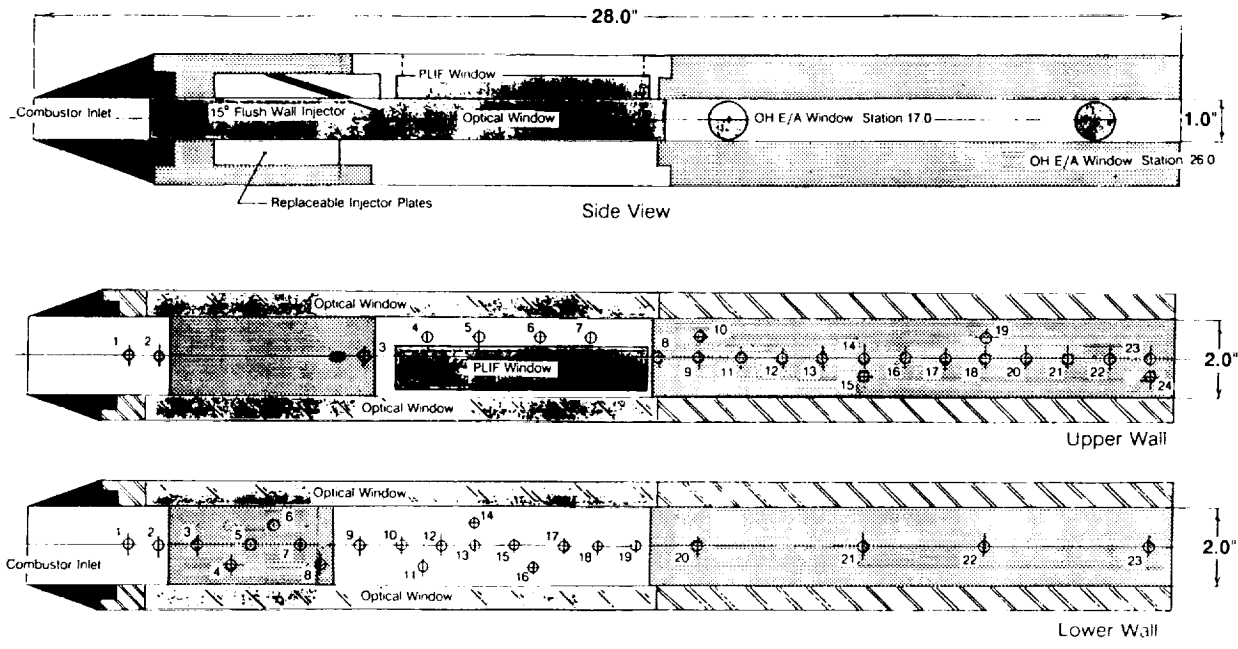


Figure 3. Schematic of combustor model.

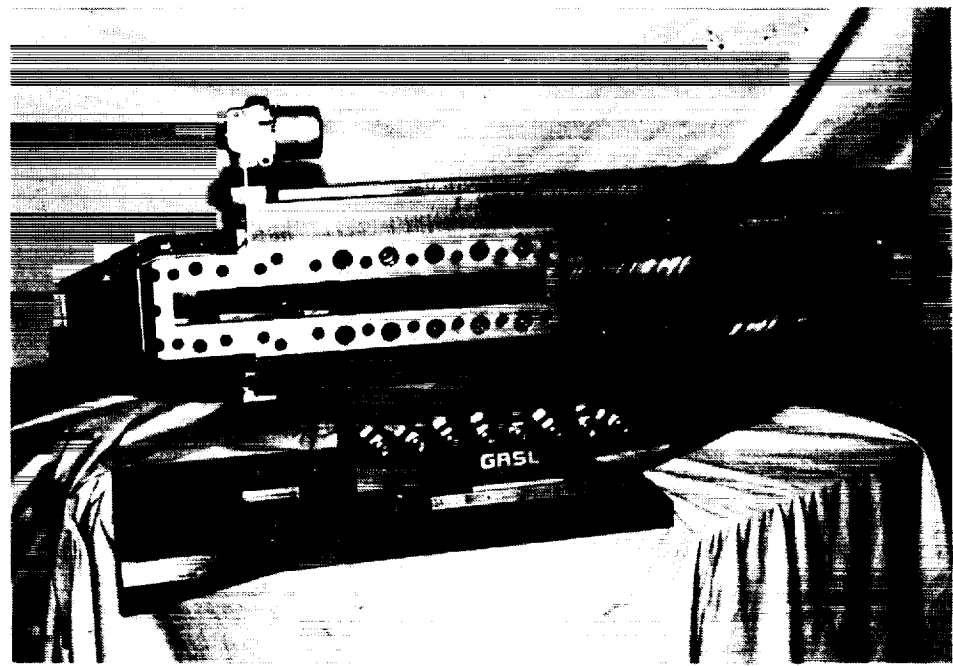


Figure 4. Assembled combustor model.

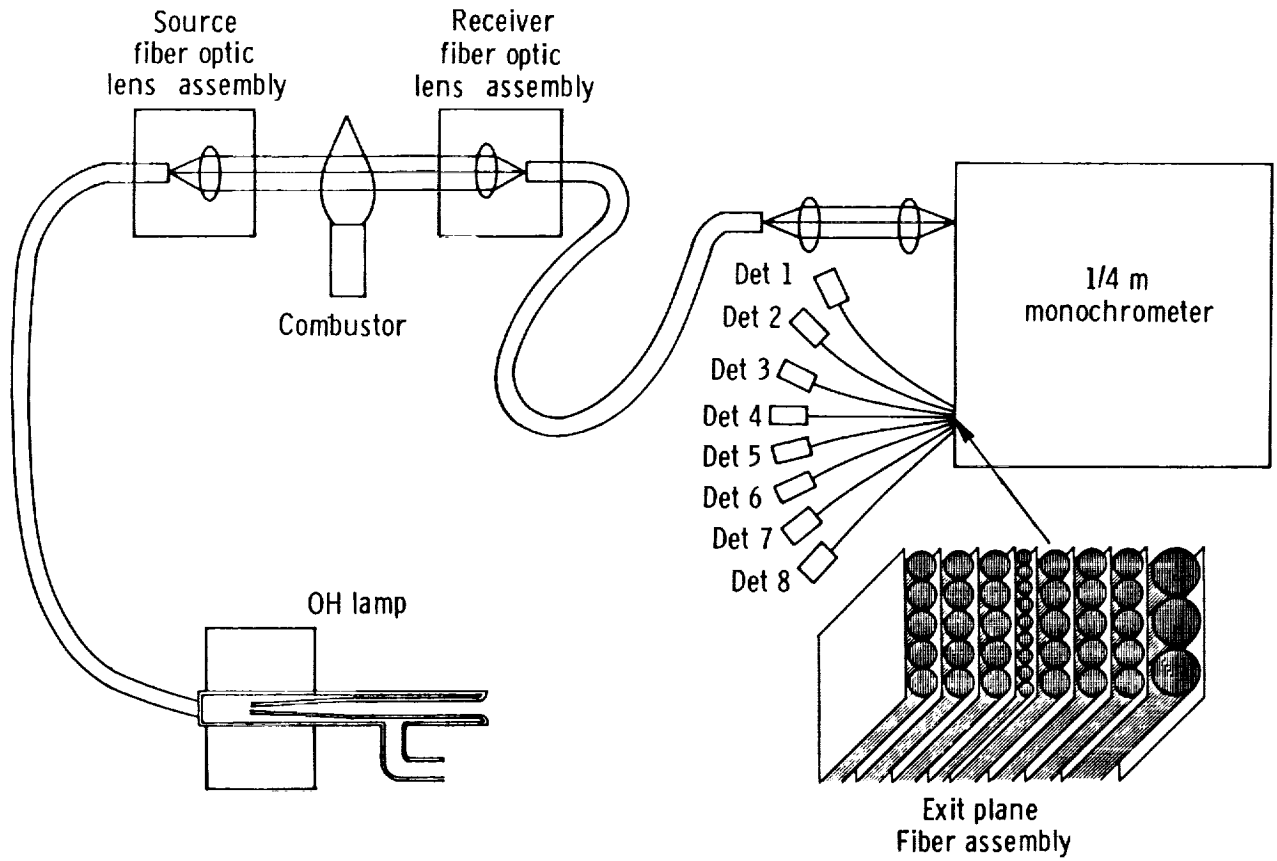


Figure 5. Schematic of resonance lamp absorption apparatus.



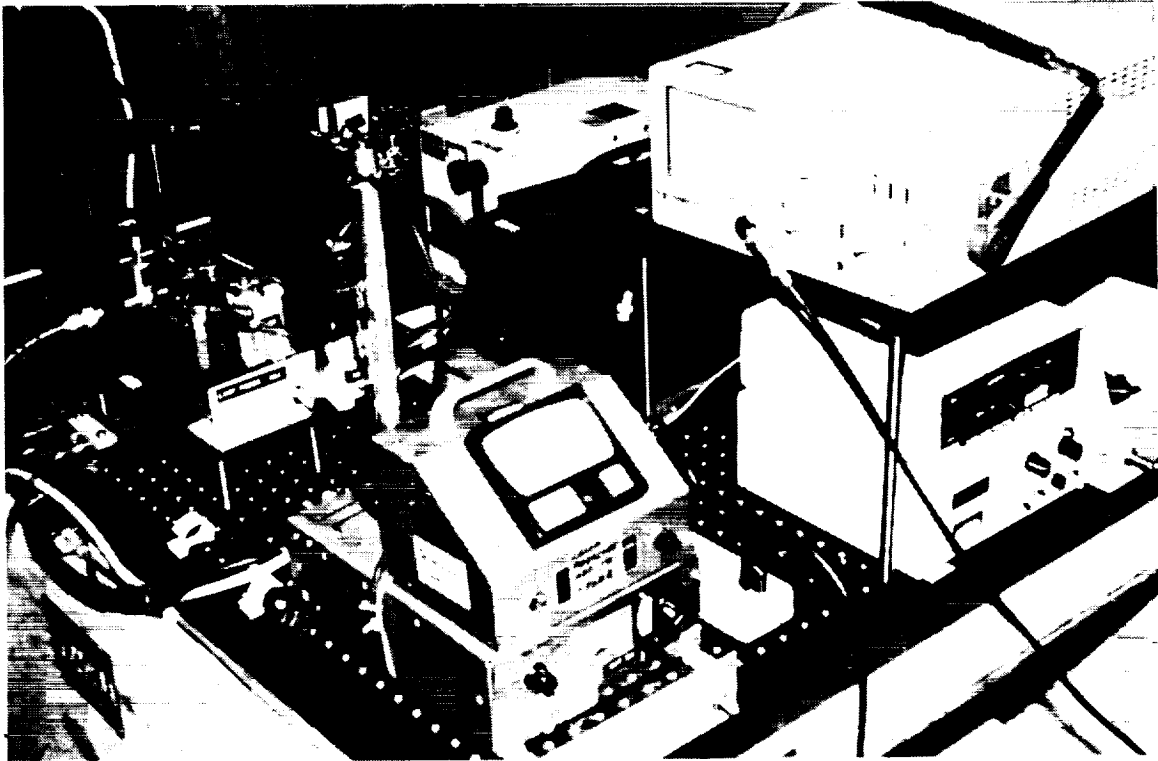


Figure 6. Assembled resonance lamp absorption apparatus.

### Model Side Wall

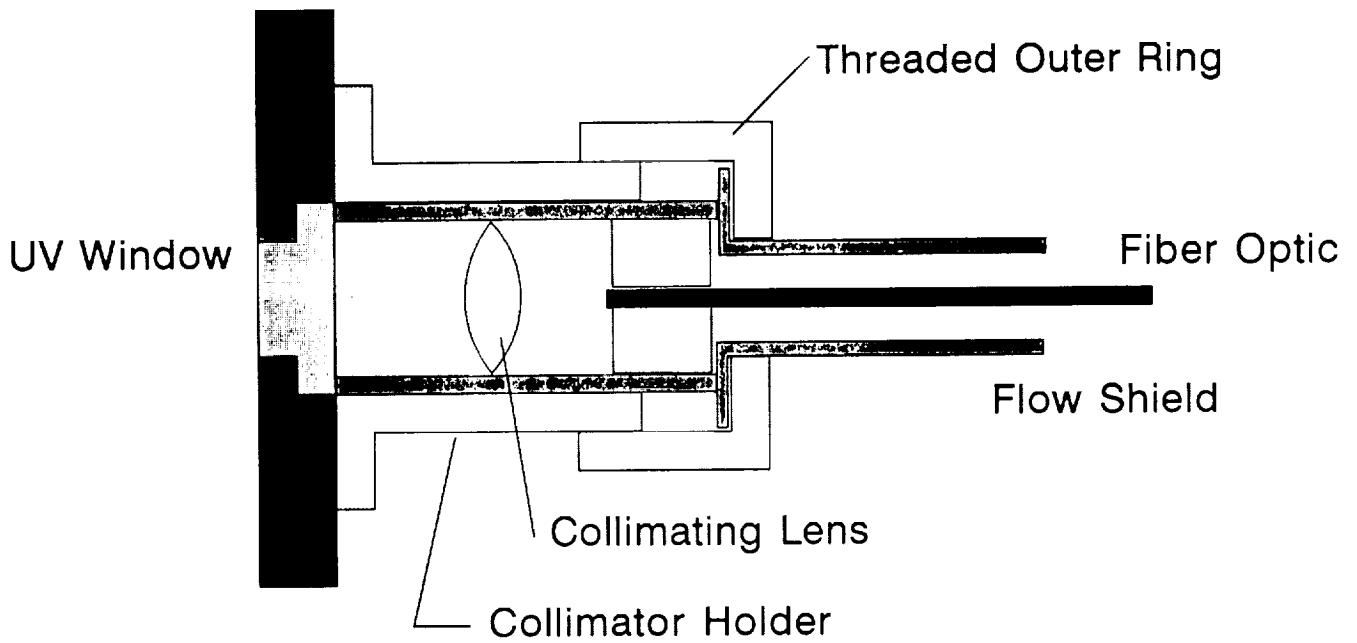


Figure 7. Schematic of optical fiber/model interface.

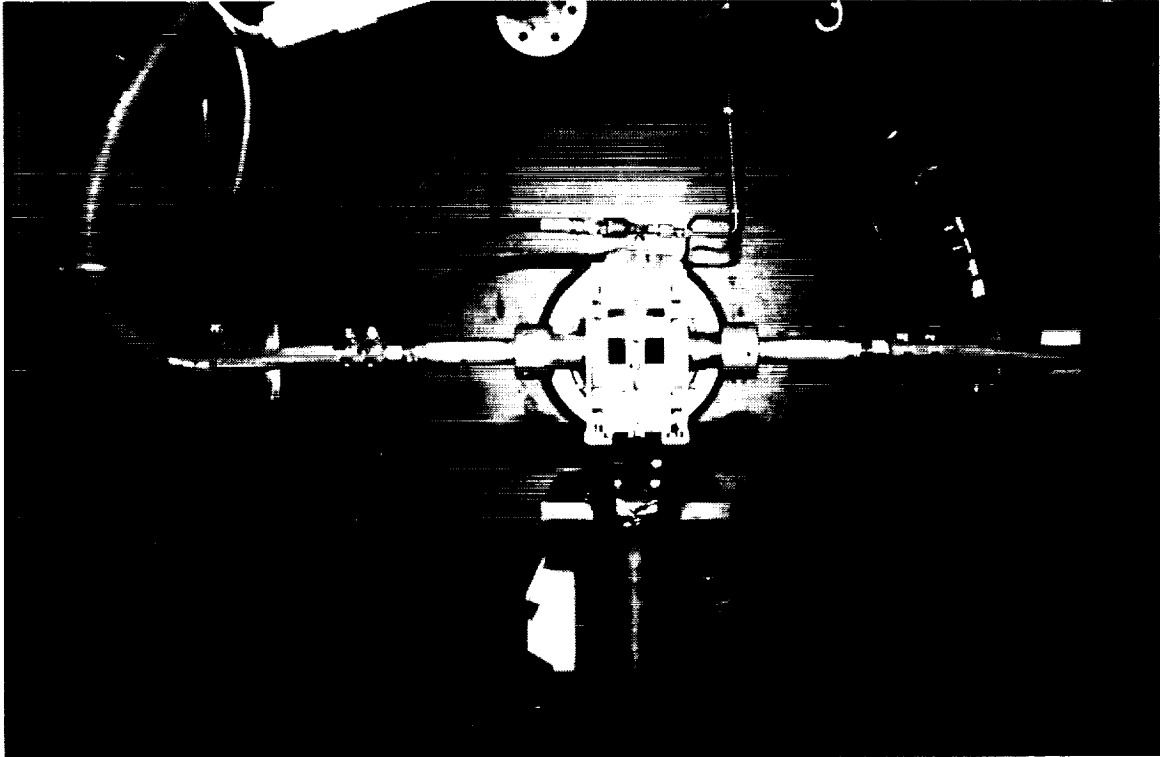


Figure 8. Optical fiber/model assembled inside facility test chamber.

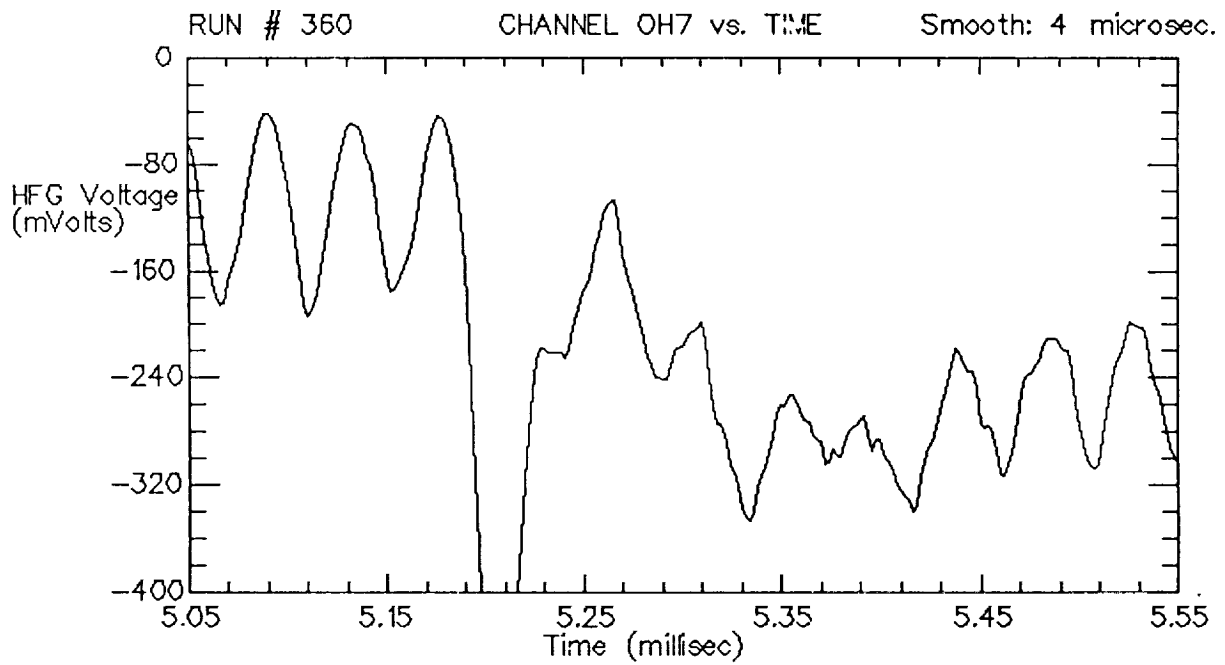
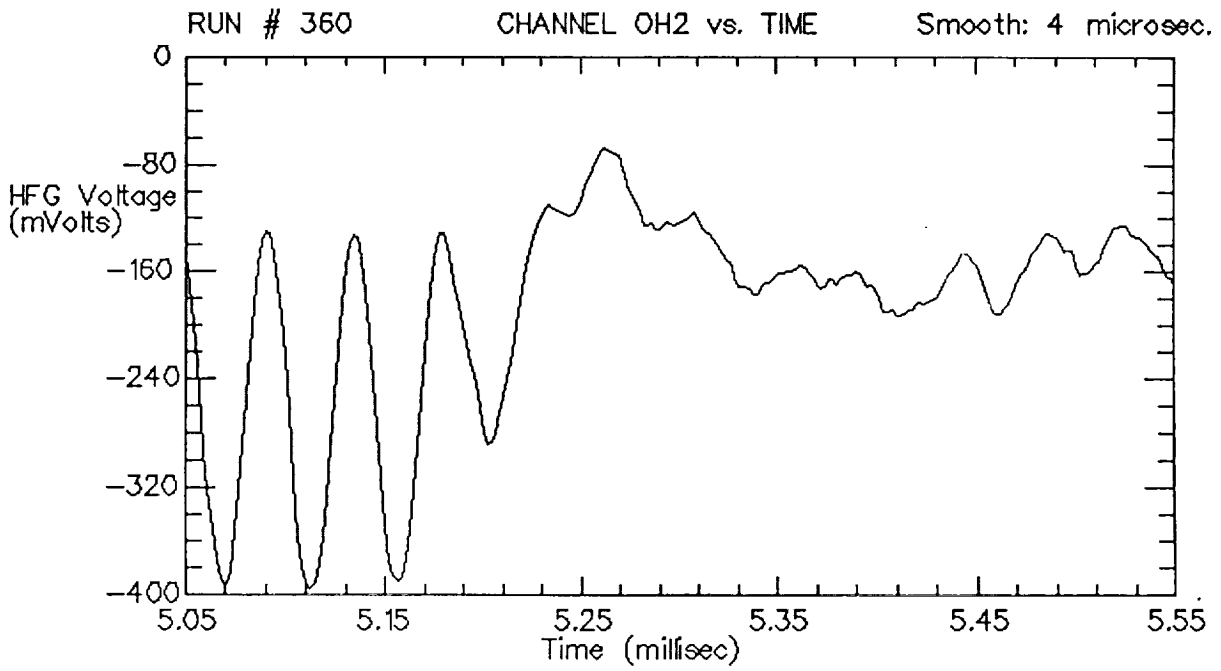


Figure 9. Experimental time traces for OH spectral Channels 2 and 7.  $\phi = \text{H}_2/\text{O}_2$  15° flush wall injector test.

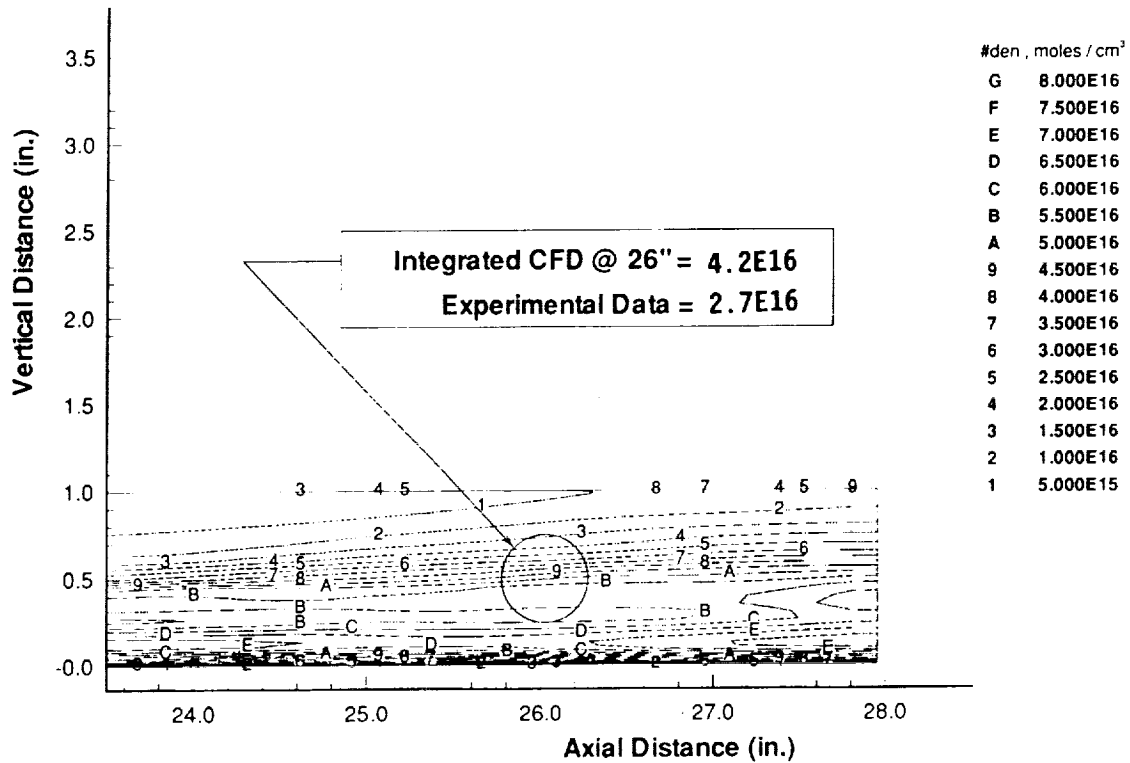


Figure 10. Laterally (Y) averaged contours of OH number density from CFD prediction.

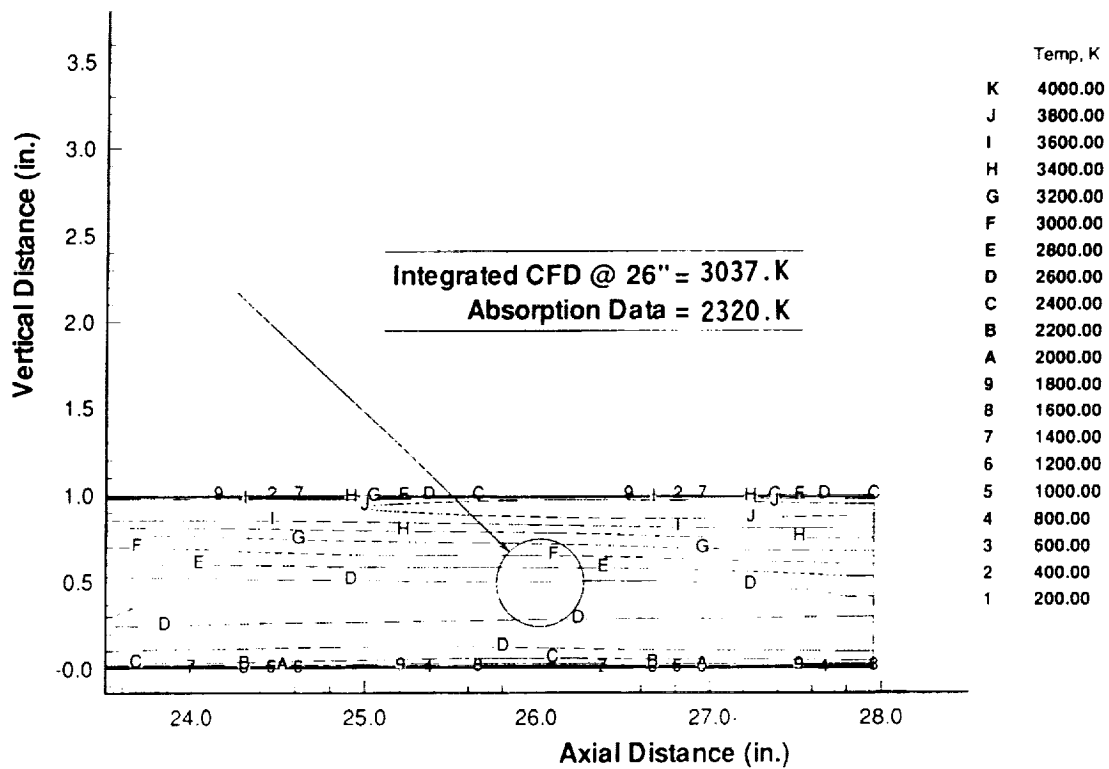


Figure 11. Laterally (Y) averaged contours of static temperature from CFD prediction.

VISUALIZATION OF HYDROGEN INJECTION IN A SCRAMJET ENGINE  
BY SIMULTANEOUS PLIF IMAGING AND LASER HOLOGRAPHIC IMAGING

R.C. Anderson  
National Aeronautics and Space Administration  
Lewis Research Center  
Cleveland, Ohio

R.E. Trucco  
General Applied Science Laboratories  
Ronkonkoma, New York

L.F. Rubin and D.M. Swain  
Rocketdyne, Rockwell International  
Canoga Park, California

## SUMMARY

Flowfield characterization has been accomplished for several fuel injector configurations using simultaneous Planar Laser Induced Fluorescence (PLIF) and Laser Holographic Imaging (LHI). The experiments were carried out in the GASL-NASA HYPULSE real gas expansion tube facility, a pulsed facility with steady test times of about 350 $\mu$ sec. The tests were done at simulated Mach numbers 13.5 and 17.

The 2" x 1" rectangular cross-section scramjet model was tested with no fuel injection (a "tare" run), with hydrogen injection into N<sub>2</sub> (a "mixing" run) and with fuel injection into air or oxygen (a "combustion" run). These fuel injection experiments were done at fuel flow rates corresponding to equivalence ratios of 1, 2, and 3 in air. Three injector configurations were used: a 15° flush wall injector, a 10° wedge injector, and a 10° swept wedge injector. The model offered side-view flow visualization access through 1" x 12" fused silica side windows. The PLIF laser sheet was admitted through a 1" x 6" window in the top of the model. The facility test section windows used were 9" in diameter allowing a perpendicular view of the flow over a 9" length. A window in the top of the facility test section allowed optical access to the top window of the model.

Both single-shot PLIF images of hydroxyl radicals (OH) and LHI measurements were obtained during the combustion tests, with approximately 50 $\mu$ sec between the PLIF and LHI. Only the LHI techniques were applied to the mixing and tare experiments (no OH present). The OH PLIF images were produced by illuminating the flow with either a laser sheet parallel to the flow or with the sheet

cutting the flow at an angle to the direction of the freestream. The side-view LHI was used in the double-exposure infinite-fringe and finite-fringe interferometry mode. The resulting holograms are instantaneous snapshots of the flow integrated along the line of sight. The LHI system was also used in the 5  $\mu$ sec separation double-pulse interferometry mode in an attempt to reveal high frequency transient phenomena.

The PLIF system used a doubled Nd:YAG pumped dye laser tuned to 283 nm to excite the OH  $Q_1(7)$  line of the A-X(1,0) transition. The images from the 512x240 pixel CCD camera were spectrally filtered to avoid contamination from background emission and scattering. The 6" fused silica top window enabled the UV light sheet to probe the same region of the flow being simultaneously interrogated by the holographic imaging system.

The holographic recording system employed a 30 nsec. pulsed ruby laser. Reconstruction of the holograms was accomplished with a CW helium-neon laser after the tests.

Wall pressure and thin film heat flux gages and exit plane pitot pressure probes were used in addition to the PLIF and LHI measurements for all the scramjet tests. An OH emission/absorption apparatus based on an OH resonant lamp was also used during the combustion tests. These measurements were useful for comparing with quantified OH PLIF images and with CFD calculations. The OH measurement volume was located at the downstream end of the model. The OH emission/absorption apparatus and results are discussed in another paper.

The PLIF images reveal large-scale turbulence which is not readily seen in the line-of-sight integrated holographic interferograms, although the general flow field structures observed with the two techniques are quite consistent. In addition, wall heat flux measurements appear to correlate with the features evident in the holographic images.

## INTRODUCTION

Pulsed gas dynamic test facilities (e.g. shock and expansion tubes and tunnels) provide the only means for ground simulation of high Mach number flows. These tunnels typically have steady flow times measured in fractions of a millisecond<sup>1</sup>. The short test time presents unique measurement problems and it also motivates the researcher to use techniques providing as much information as possible from every test.

In addition the environment in the flowfield is usually hostile to intruding probes, and the small duct dimensions of typical test articles mean that intruding probes have an unacceptably large effect on the flow. Wall pressure and temperature measurements are nonintrusive but give little information about phenomena in the main flowfield. This main flowfield data is required to characterize boundary layer flow and to fully evaluate the fuel mixing processes.

Two and three dimensional optical measurement techniques are not intrusive and provide simultaneous measurement at many points within the flow. The information content of optical measurements is potentially extremely large. Furthermore, multiple and simultaneous multidimensional diagnostic measurements complement one another and provide better insight into flow phenomena than single measurements, especially for pulsed flow facilities.

Pulsed laser-based optical measurement techniques are particularly attractive for use in pulsed flow facilities, providing instantaneous snapshots of flowfield properties. Optical measurement techniques such as schlieren, shadowgraph, and holographic interferometry (LHI) yield visualization of density gradients in the flow. When, as in the present case, a combustor system is under investigation, measurement techniques which depend on species present in combustion can be used such as Planar Laser-Induced Fluorescence (PLIF) and OH emission/absorption.

The work reported herein marks the first time that several multidimensional measurements have been made simultaneously in a pulsed facility simulating Mach 13 and 17 flows with a test time between 300 and 400  $\mu$ sec. Several examples exist where a single multidimensional optical technique has been used in a shock tunnel. However, Mach numbers were generally lower and available test times were longer than those in the present work. Henckels et. al.<sup>2</sup> used infra-red scanning to measure the temperature field around a model in a shock tunnel at Mach 7.6 with a 5 ms test duration. Cassady and Lieberg<sup>3</sup> performed Planar Laser-Induced Fluorescence Temperature Measurements in a shock tunnel at Mach 9 with a 2 millisecond test time.

The focus of this paper is on the measurement technologies used and their application in a research facility. The following text briefly describes the HYPULSE facility, the models used for the experiments, and the setup for the LHI and PLIF measurements. Measurement challenges and solutions are discussed. Results are presented for experiments with several fuel injector configurations and several equivalence ratios. OH absorption measurements made during the same test series are discussed in another paper<sup>4</sup>.

## TEST FACILITY

The experiments described herein were carried out in NASA's HYPULSE facility at GASL. This is an expansion tube (6-inch tube diameter, 120ft overall length) which was originally constructed at NASA Langley Research Center in the 1960's for real gas aerothermal studies<sup>5</sup>. The tunnel was decommissioned in 1983, and eventually recommissioned as the NASA HYPULSE facility operated by General Applied Science Laboratories (GASL)<sup>6</sup>. The facility is presently located at GASL.

The expansion tube enjoys several advantages compared to other hypersonic test facilities. These are described in reference 7. One trade-off for these advantages is the test duration. HYPULSE

steady test time is typically in the 300 to 400 microsecond range, limiting the maximum allowable model length to about 3 ft (1 m).

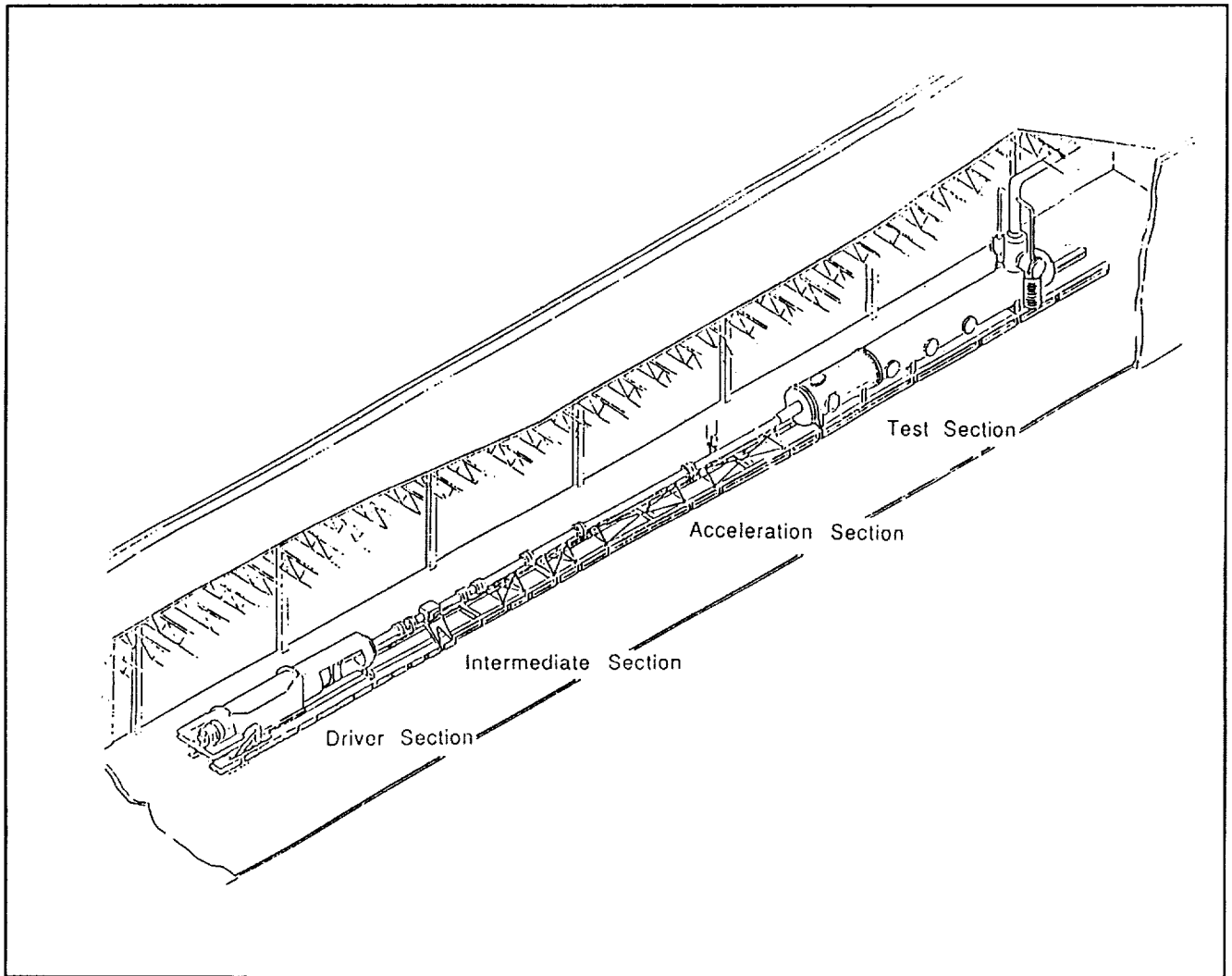


**Figure 1 - Isometric View of NASA HYPULSE Facility**

A schematic of the facility is shown in Figure 1. The facility consists of four sections: the driver section, the intermediate section, the acceleration section, and the test section/dump tank. The driver and intermediate sections are separated by a double metal diaphragm; and a mylar diaphragm separates the intermediate section and the acceleration/Test sections. The driver section is pressurized with helium and the short section between the metal diaphragms is pressurized to about half the pressure of the driver section. To start the flow the double diaphragm section is suddenly vented, bursting the diaphragms.

Facility transient data is acquired with a system composed of 80 transient waveform digitizers. Each digitizer can sample at a maximum rate of 1MHz with 12-bit voltage resolution and has on-board memory to store 512K samples. The data acquisition is controlled by a 386-based PC. This system is used to monitor facility operation and acquire pressure and heat flux data.



Piezoelectric pressure transducers provide pressure data and GASL-designed and manufactured heat flux gages provide heat flux data.

A Ludweig tube connected to a fast-acting valve (Trucco et al.<sup>8</sup>) was used to provide a gaseous hydrogen fuel supply for these experiments. The Ludweig tube fed a manifold connected to the injectors and was synchronized provide fuel before the test gas arrived at the test section.

Timing and triggering control were extremely important for the reasons detailed below. The sequence of events for a HYPULSE test run is given below in Table I.

TABLE I - TIMING OF HYPULSE FACILITY OPERATION EVENTS

Event	$t_{\text{test}} - t_{\text{event}}$	Event Duration
Evacuate Intermediate Section and Test Section/Dump Tank	- (1 hour)	45 min
Fill driver and between-diaphragms section; Fill Intermediate section to 28 mm Hg with Test GAS ( $N_2$ , Air, or $O_2$ ); Fill Test Section to 600 $\mu\text{m}$ Hg with helium.	- (45 min)	15 min
Begin vent of between-diaphragm section.	- (1-2 sec)	1-2 sec
Double diaphragm burst Mylar diaphragm burst	- 5 msec	
Fuel flow start	-2 msec	-

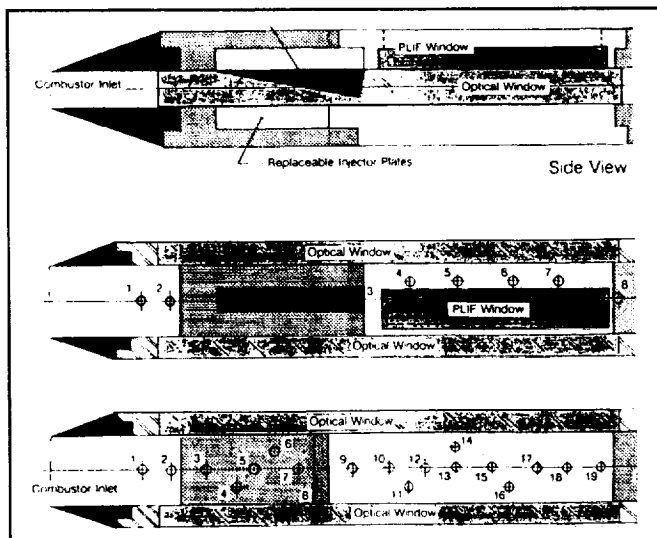


Figure 2 - Schematic of Unswept Ramp Injector Model.

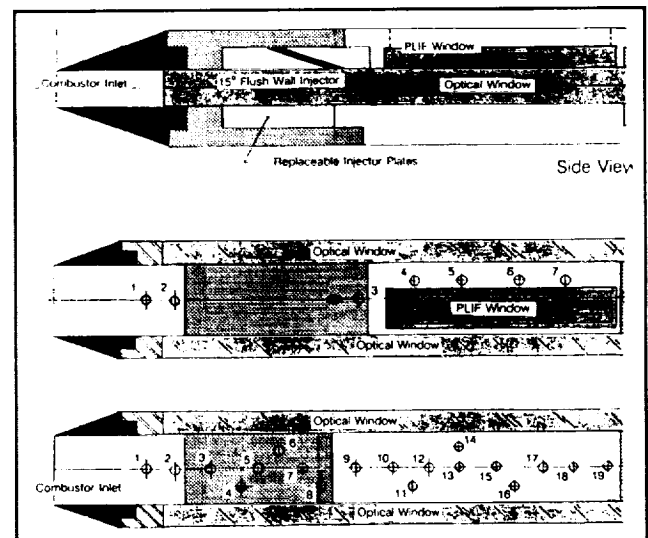


Figure 3 - Schematic of Flush Wall Injector Model

## TEST HARDWARE AND INSTRUMENTATION

### Model Hardware

Three injector configurations were tested during this program. Figures 2 through 4 show these configurations schematically. Figures 2-4 (top) show side views with the location and geometry of the injectors and optical windows. Figures 2-4 (middle) and (bottom) show the top and bottom views. Numbered holes shown in these views could be used for either pressure transducers or heat flux gages. The flow duct was rectangular in cross section with dimensions of 2 inches wide by 1 inch high. Optical access to the flow was available through three windows (top and both sides) in the Test Section/Dump Tank and three windows (also top and both sides) in the model. Window material was fused silica chosen for adequate transmission of wavelengths throughout the UV and visible spectrum. Since the test duration is so short heat transfer to the windows was low. Most of the diagnostic instrumentation components were housed in an air-conditioned enclosure just outside the Test Section/Dump Tank. Data acquisition equipment for other instrumentation was located in the facility control room.

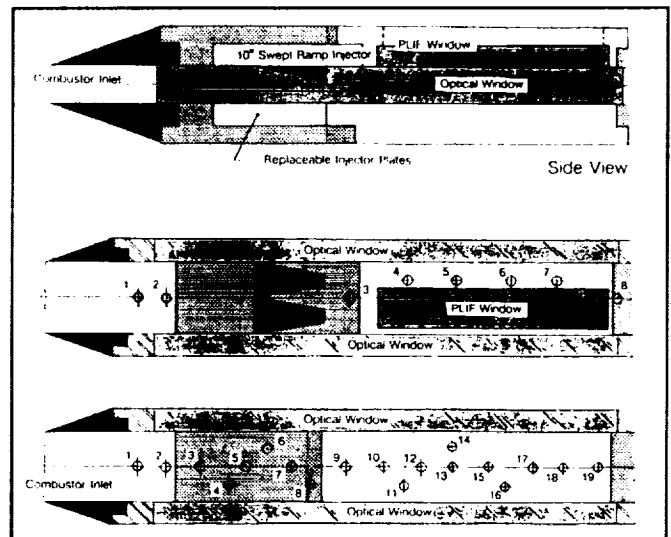
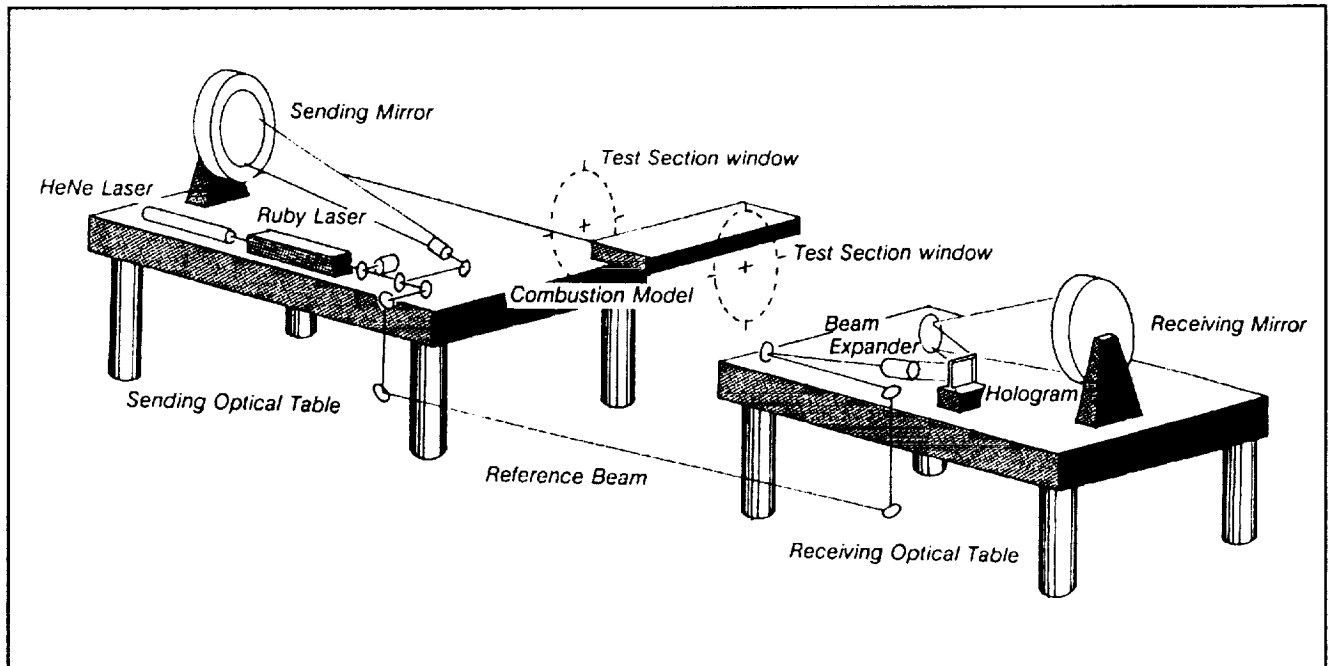


Figure 4 - Schematic of Swept Ramp Injector Model.

### Laser Holographic Interferometer

The Laser Holographic Imaging (LHI) system is shown in Figure 5. The system is mounted on two 4 x 10 foot vibration isolated tables (one on each side of the Test section) which were located in the enclosure mentioned above. For these tests some of the components for the PLIF and LHI systems occupied the same table. The test section is connected to the enclosure by 16 inch diameter rubber bellows which provide a light-tight environment.

A Q-switched ruby laser was used as the primary recording light source for the LHI system. Laser energy output was 30 milliJoules per 30 nsec pulse. A helium-neon laser was used for pre-test



**Figure 5 -** Diagram of Holographic Imaging System for HYPULSE.

alignment. A photodiode was used to confirm laser firing and synchronization. The main beam is split to form the object beam and the reference beam, at a 1 to 4 object to reference intensity ratio.

The reference beam is directed using several mirrors to pass around and outside the test section through a beam expander to the center of a photographic plate. The object beam is directed using parabolic mirrors through the test section to the center of the photographic plate. A shear-plate interferometer<sup>9</sup> is used to ensure that the reference beam and reconstruction beam are parallel. The reconstructed image was recorded on film. A helium-neon laser was used for hologram reconstruction.

### Planar Laser-Induced Fluorescence Measurement

A schematic of the PLIF system used is shown in figure 6. Not all of the system components shown were needed for the HYPULSE tests. The equipment used for these tests included the Neodymium:YAG-pumped dye laser system, two image detector systems, and the PC-based image acquisition and processing system. One detector is an intensified gated 512x240 pixel CCD camera; the other is an intensified 128 x 128 pixel diode array camera.

The YAG/dye laser beam was tuned to an electronic transition of the OH molecule near 283 nm using a propane torch to generate OH and a photomultiplier tube to monitor LIF. The beam was then directed to sheet-forming optics outside and above the Test section. The beam was formed into a sheet and split. Part of the beam was directed down through the Test section window through the

# MULTI-POINT, MULTI-PARAMETER DIAGNOSTIC SYSTEM

T-3366

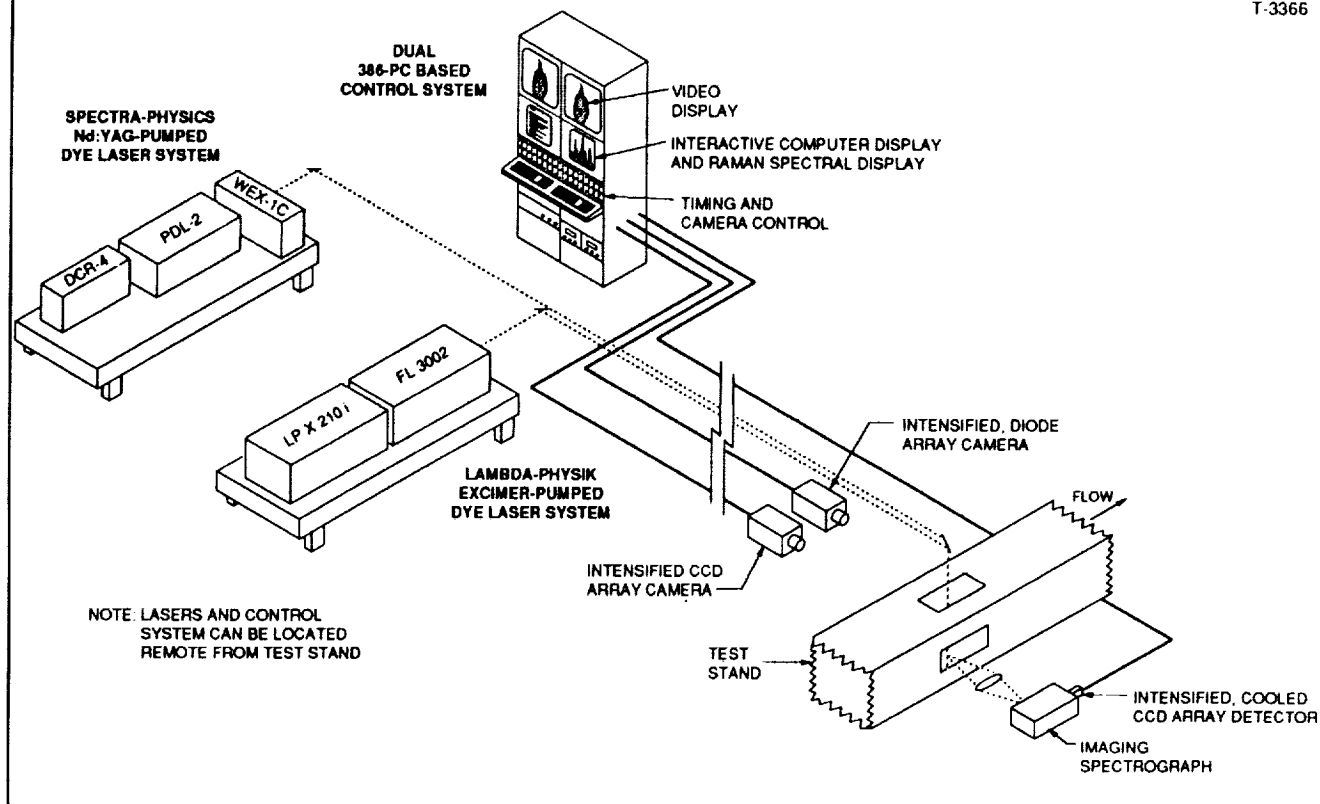


Figure 6 - Schematic of Multipoint Multiparameter Diagnostic System.

window on top of the model. The other part of the beam was directed to a fluorescent card. The beam image from the card was acquired by the 128x128 diode array camera system in real time during the test as a beam profile measurement. The effective beam profile was a weak but relatively significant function of the distance from the sheet-forming optics to the test article. To minimize any difference between the card-measured profile and the actual profile, the card was mounted the same distance from the sheet-forming optics as the test article probe volume.

The CCD camera was mounted at the side of the test section and was aimed through the Test section window to image the laser-induced fluorescence near 310 nm as viewed through the model window. Initially, a color filter was used to discriminate between the 283 nm laser wavelength and the OH fluorescence at 310 nm. In these tests, the color filter with its relatively broad passband did not sufficiently filter out the high background luminosity. To increase the spectral discrimination, an interference filter was installed with a much narrower passband centered on the OH emission wavelengths at 310 nm. This provided the necessary rejection characteristics.

As part of the pre-test activity, a fluorescent card was placed inside the model flow duct to assist in beam alignment. The 2D beam profile was acquired from the card using the 512 x 240 CCD camera system. Columns were summed and normalized in the two dimensional beamprofile images to yield the one dimensional beam profile used when available to correct PLIF images.

The PLIF system used was part of a larger Multiparameter Multipoint (MPMP) flow diagnostic system developed under a Rocketdyne contract with the NASA Lewis Research Center. The complete system includes an excimer-pumped dye laser system in addition to the components used for this test. To maximize fluorescence signal strength against the intense background emission expected, the Nd:YAG laser system was selected because of its higher pulse energy.

Use of the YAG-pumped dye laser presented severe timing and triggering challenges. This laser system requires a steady 10Hz pulse rate to maintain thermal stability and constant power supply charge per pulse. The laser pulse had to be timed to occur within the 350  $\mu$ sec test duration. This meant interrupting the laser for a period, and recharging and firing the laser in synchronization with the test period event.

Specialized circuitry was built to accomplish these timing requirements. If the delay was too long the pulse energy of the laser would decrease. A storage oscilloscope measuring the output of a photomultiplier was used to store the pulse shape during the test along with a typical undelayed pulse shape so that pulse decay could be measured. It was determined that a delay of 1 second or less was necessary to keep pulse strength at an acceptable level.

From the times in table 1 it can be seen that the double diaphragm venting occurs about 1-2 seconds before the test. This event was used to interrupt the laser. It was subsequently determined that interrupting the laser at vent start caused a delay that was too long and too variable. This resulted in laser pulse energy droop and jitter. An acceptable delay was created by interrupting the laser when the pressure in the between-diaphragm section fell below a pre-determined threshold rather than at vent start.

For both the LHI and PLIF laser systems the final trigger was derived from the output of pressure transducers sensing shock passage just upstream of the model. The LHI ruby laser was triggered at a slightly different time within the steady flow period to ensure that the PLIF camera intensifier was not gated ON during the ruby laser pulse.

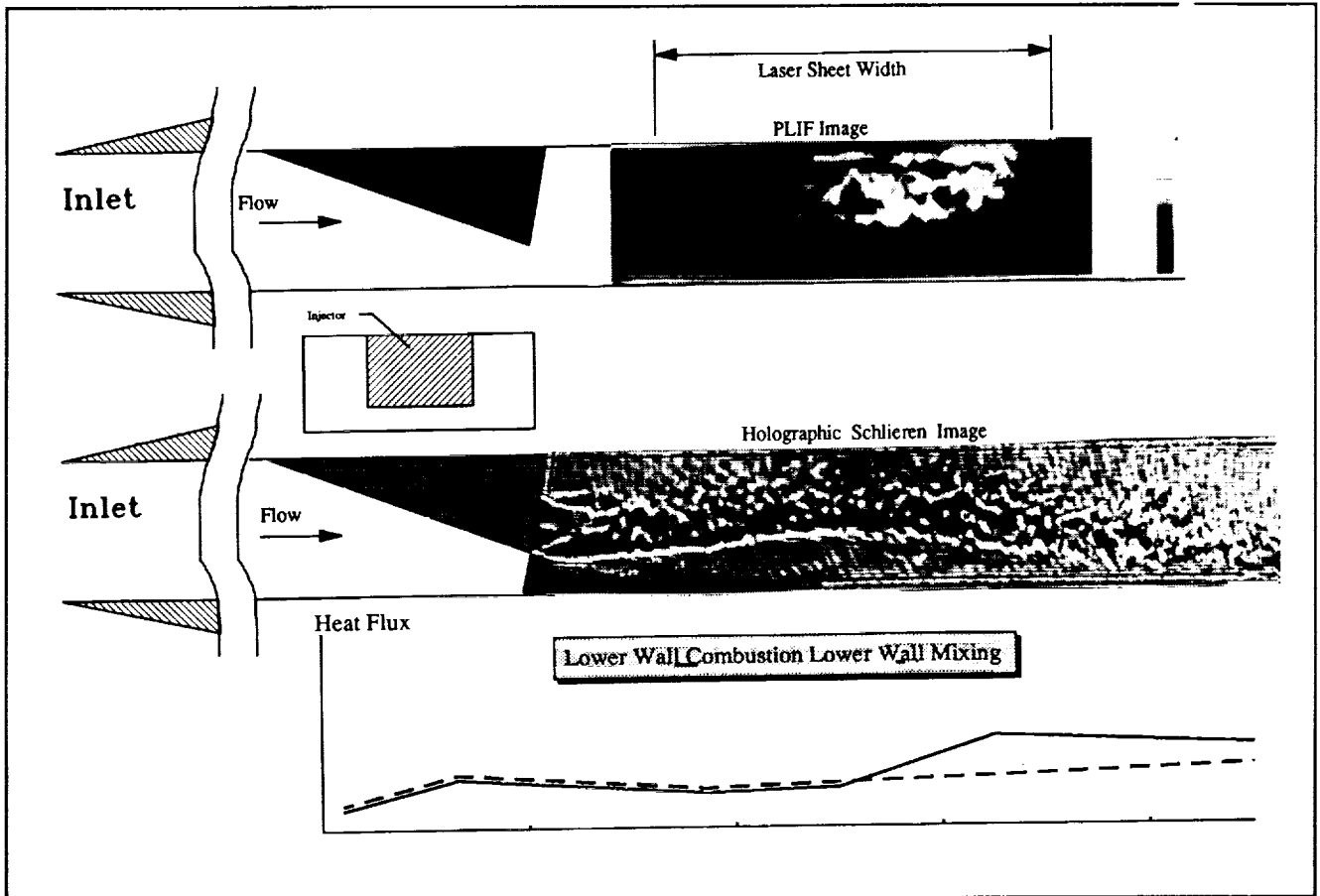


Figure 7 - HYPULSE Results For Unswept Ramp Injector Model  
Oxygen test gas;  $\Phi = 1.0$

## TEST RESULTS

### Unswept Ramp Injector

Figure 7 shows results from the PLIF, LHI and heat flux sensor measurements taken during tests using the unswept  $10^\circ$  ramp injector configuration. The PLIF laser sheet indicated at the top of figure 7 was directed through the top of the model to cut the flow in a plane in the center of the duct parallel to the flow. Two or three distinct flow structures are evident in the PLIF image which appear to correlate with the fuel streams evident in the hologram.

The holographic image shown in the middle of figure 7 was reconstructed as a schlieren image using a graded filter. The streams of gas leaving the injector ports are evident in the holographic image entering at the injector face and flowing from left to right. This hologram was not made at the same time as the PLIF image. It was made during a mixing experiment using nitrogen as the test gas.

The lower wall heat flux data plotted at the bottom of figure 7 compares the combustion test with a mixing test and appears to correlate with the PLIF and LHI data showing lower heat flux near the wall where there appears to be an expansion. Where the flow in the hologram appears to strike the wall the heat flux increases.

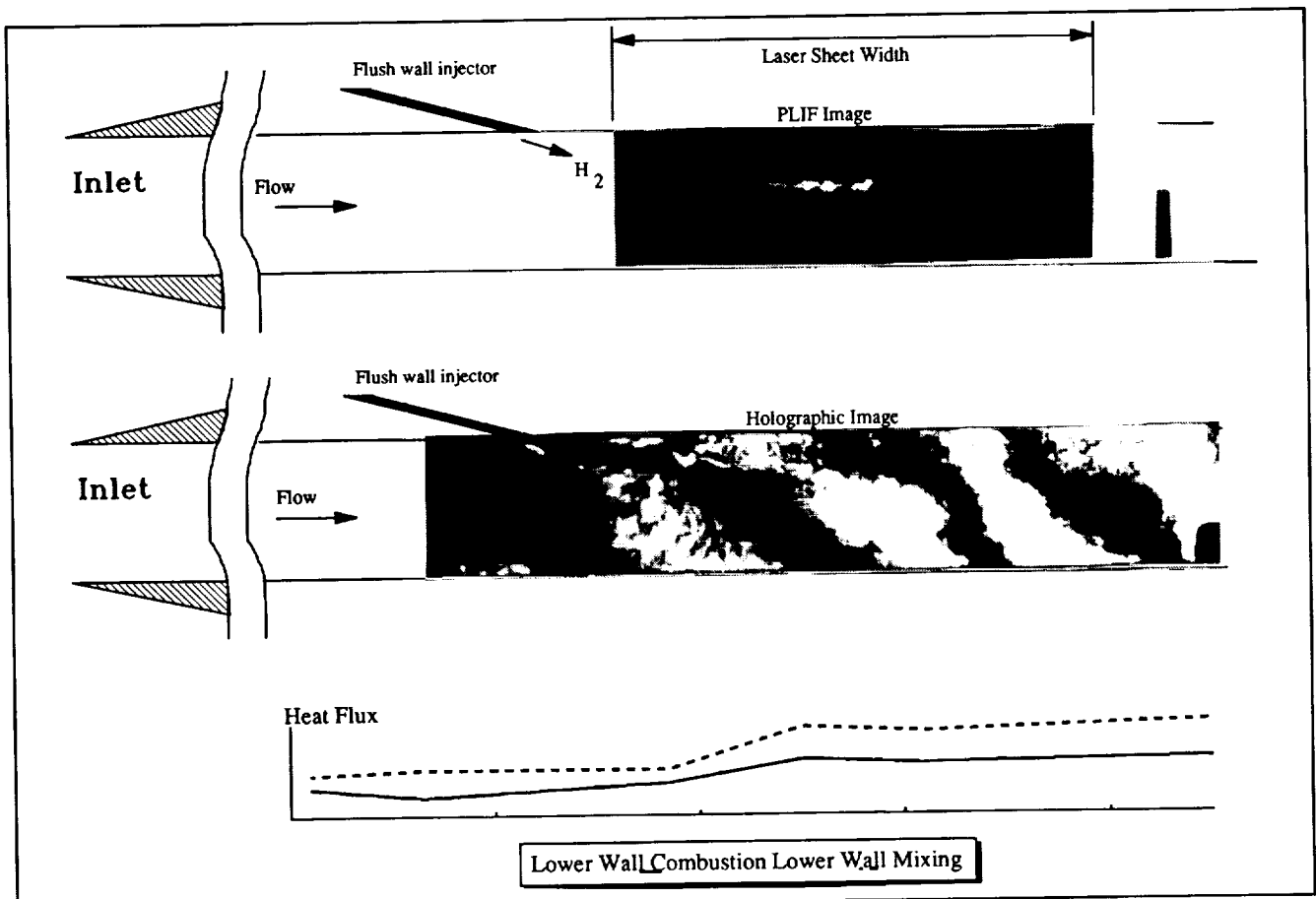


**Figure 8 - HYPULSE Results For Flush Wall Injector Model**  
Oxygen test gas;  $\Phi = 1.0$

### Flush Wall Injector

Figures 8 and 9 show results from PLIF, LHI, and heat flux sensor measurements obtained during testing of the 15° flush wall injector model. The PLIF laser sheet shown at the top of figures 8 was

again directed through the top of the model to cut the flow in a plane in the center of the duct parallel to the flow. The holographic image shown in the middle of figure 8 has been reconstructed as an infinite fringe interferogram. The stream of fuel leaving the injector port is evident in the holographic image as it enters at the injector and flows from left to right. One straight and narrow reaction zone is evident in the PLIF image which appears to correlate with the fuel stream seen in the holographic image. The heat flux data seems to correlate with the other data showing a rise in the heat flux where the bow shock from the injected fuel hits the lower wall. The apparent increase in fluorescence along the lower wall in the PLIF image was determined to be emission.

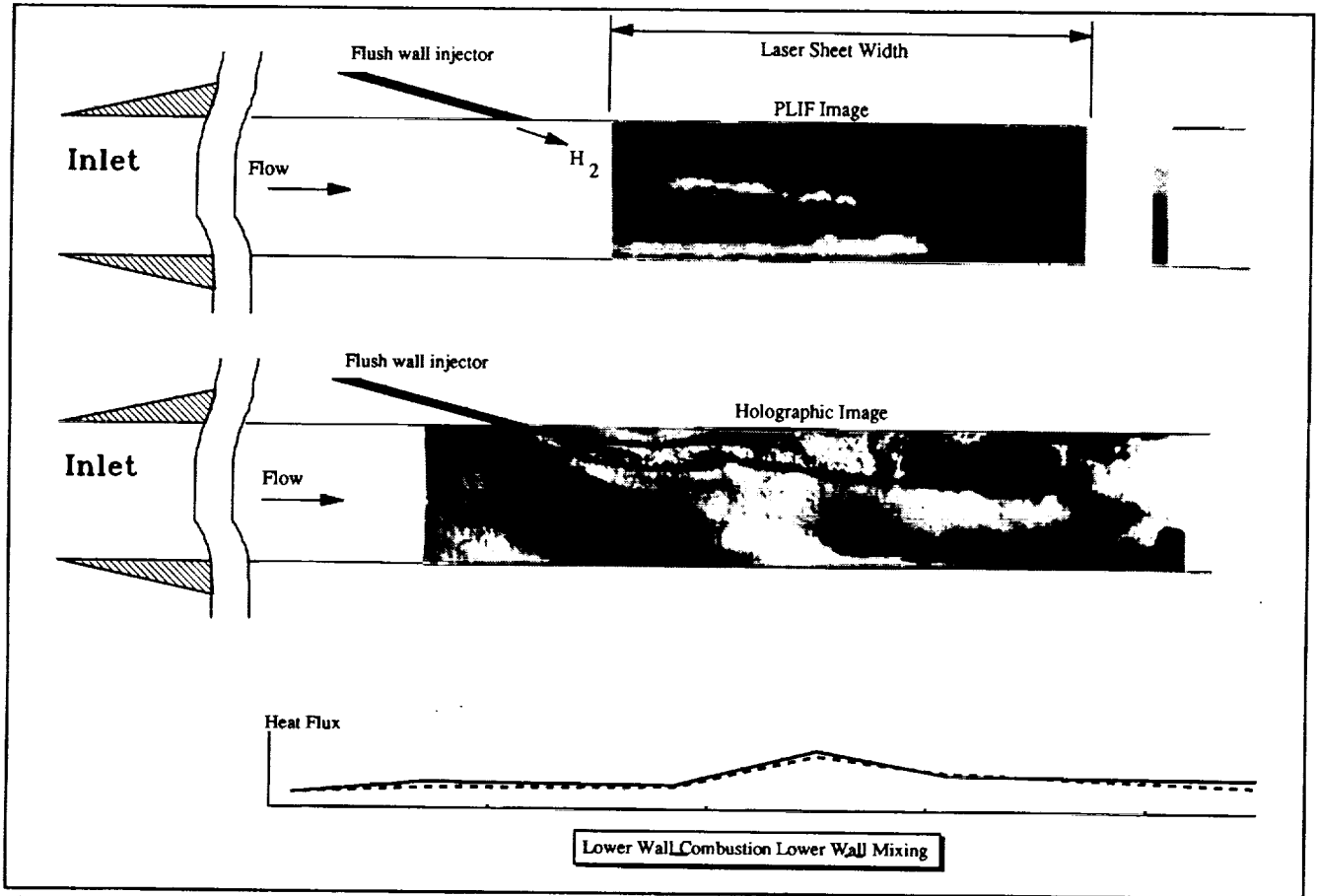


**Figure 9 - HYPULSE Results For Flush Wall Injector Model**  
Oxygen test gas;  $\Phi = 1.8$

Figure 9 shows flush wall injector results with a slightly higher equivalence ratio than that of figure 8. All other conditions are the same. The figure 9 PLIF image shows a structure similar to that of figure 8, but with the lower wall emission zone somewhat more evident.

The flush wall injector results are consistent with expectations. For low angle injection ( $15^\circ$ ), jet-induced longitudinal vortices are expected to be weak and self-entrainment small resulting in very limited spreading of the reaction zone. Furthermore, no significant distortion or enlargement of the mixing interface occurs.



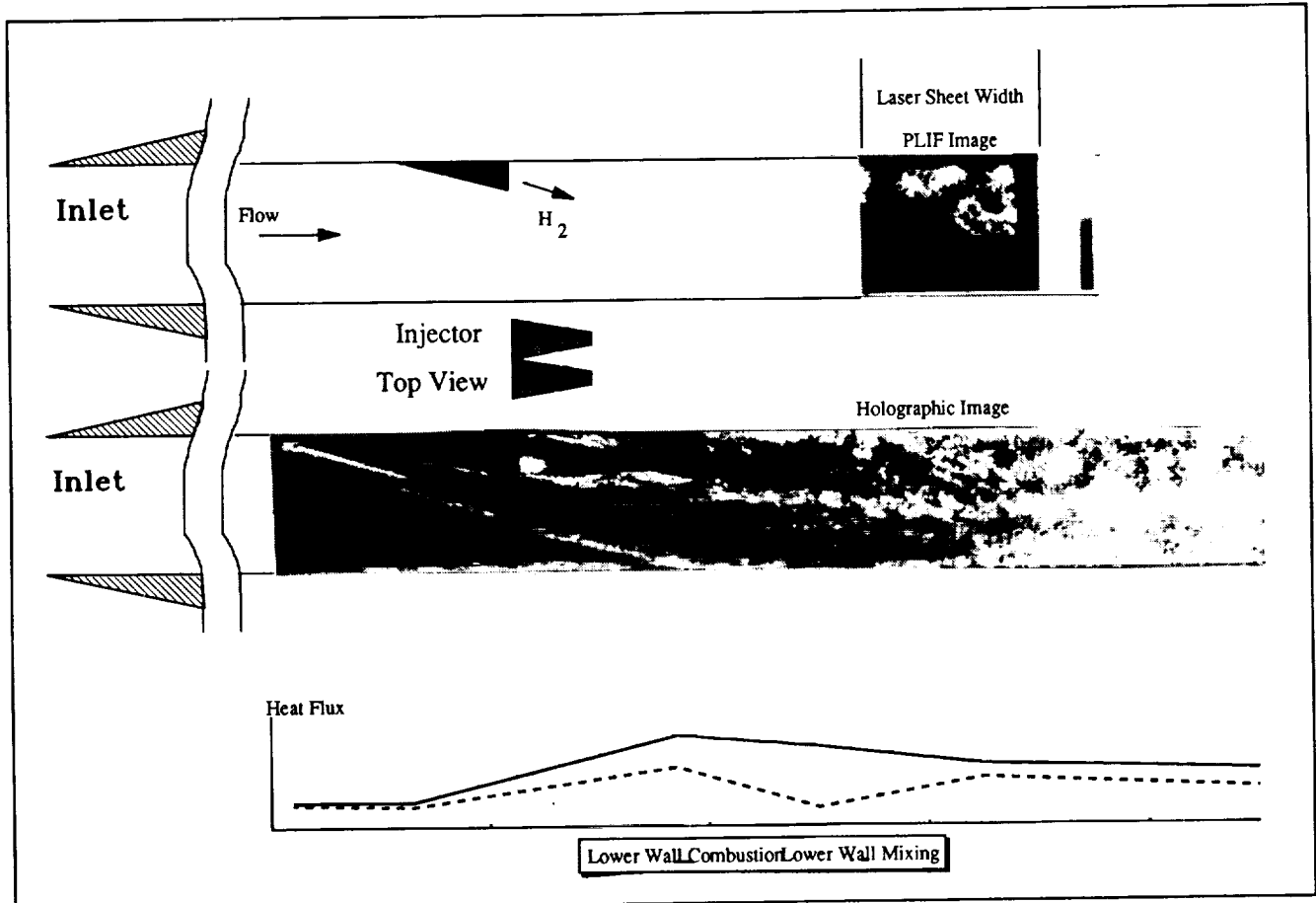


**Figure 10 - HYPULSE Results For Swept Ramp Injector Model**  
Oxygen test gas;  $\Phi = 1.0$

### Swept Ramp Injector

Figures 10 and 11 shows results from PLIF, LHI, and heat flux sensor measurements obtained during testing of a dual  $10^\circ$  swept ramp injector model. For these tests the PLIF laser sheet again passed down through the flow but at a  $39^\circ$  angle to the flow direction rather than parallel. This was done to image OH distributions across the flow instead of along the flow. As a result the left side of the PLIF images in figures 10 and 11 corresponds to flow near the centerline of the duct; and the right side corresponds to flow near the far wall.

The holographic image shown in the middle of figure 10 has been reconstructed as an infinite fringe interferogram. The injector shadow and its bow shock are evident in the holographic image. The density perturbations caused by the stream of fuel leaving the injectors can be seen exiting the injector and flowing from left to right. The PLIF image indicates a reaction zone along the upper

wall. The interaction of the injectant stream with the ramp generated vortex pairs and the boundary layer appears to enhance the flow entrainment and small scale turbulence development.

The PLIF laser sheet was first sent through the model upstream of the location shown in Figure 10. Little or no signal was detected at that station. It was only when the laser sheet was moved downstream to the location shown that OH was detected. This indicates a significant delay in combustion onset.

The lower wall heat flux data in figure 10 again shows the expected increase due to the injector bow shock striking the wall.

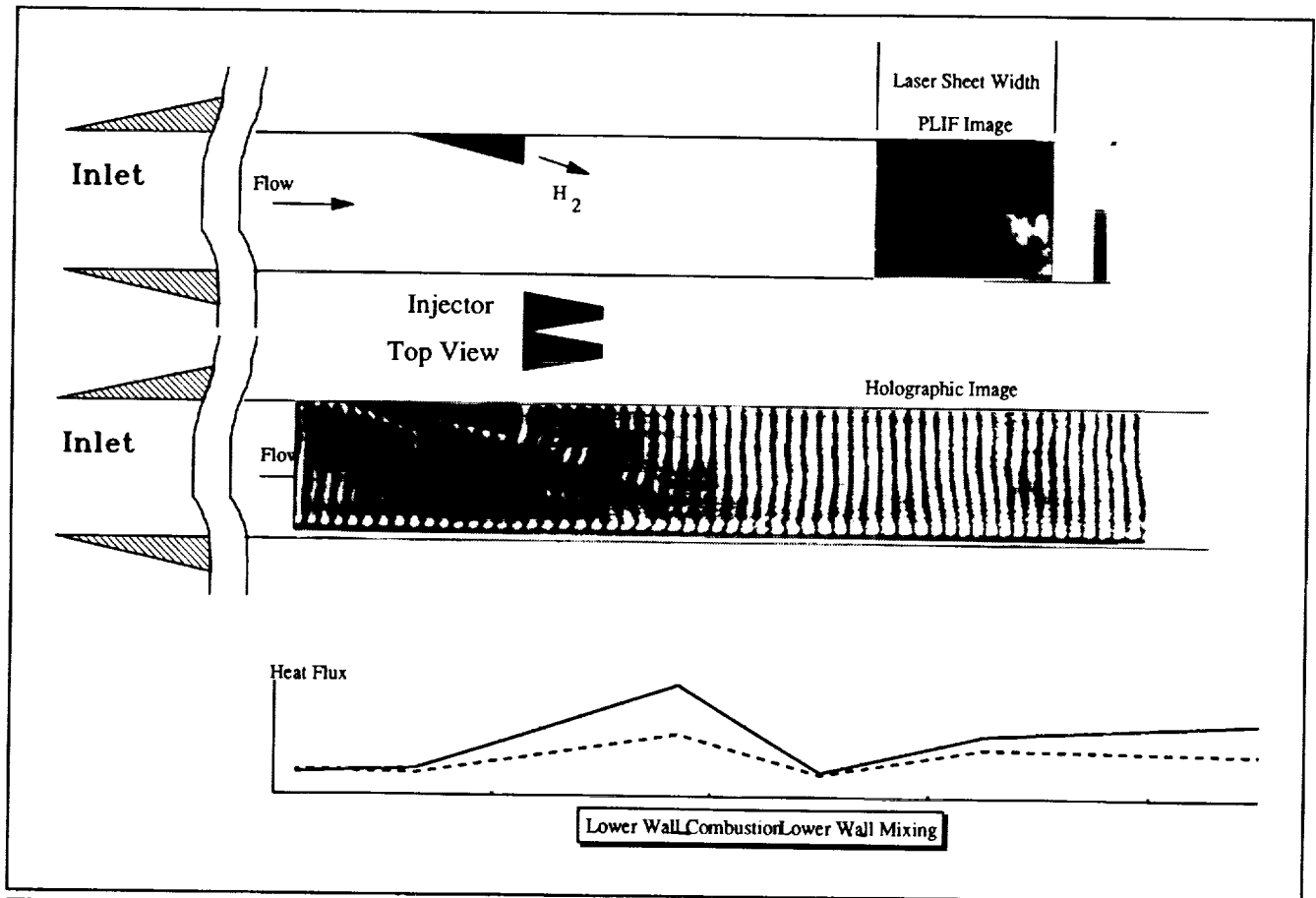


Figure 11 - HYPULSE Results For Swept Ramp Injector Model  
Oxygen test gas;  $\Phi = 3$ .

Figure 11 shows swept ramp data for an equivalence ratio of 3. The hologram image in this case is a finite fringe interferogram. Fringes are created by displacement of the holographic plate after the first exposure and variations in the flow density manifest themselves as perturbations of the fringes.

The reaction zone for the figure 11 test has clearly shifted toward the lower wall. Since the equivalence ratio is proportional to injectant dynamic pressure this shifting of reaction zone may be interpreted as the effect of increased jet penetration. It is also possible that the reaction zone could

have shifted downstream. There is some indication that at this high equivalence ratio, excess hydrogen fuel may have a reaction quenching effect which would increase ignition delay.

### Data Processing

Visual representation of the holographic images is relatively straightforward simply involving photographing the reconstructed image. PLIF image processing is more complex. In addition to the qualitative information presented in figures 7-11 estimates were made of the OH concentration for each of the PLIF images. These estimates were determined by a two step process. First the absolute fluorescence intensity was determined and then this intensity was related to the absolute number density of OH.

The absolute fluorescence intensity for each image was determined using camera calibration factors. The absolute photon count in the image in a given pixel may be written as a function of the total probed species number density and spectroscopic and geometric parameters. Detailed analysis of flowfield properties was beyond the scope of the work given resource constraints so rough estimates of fluorescence yield were made based on estimates of spatially averaged flowfield conditions in the locations probed by the PLIF sheet. The number density estimates for maximum OH concentration fell generally within the low to mid  $10^{15} \text{ cm}^{-3}$  range.

### CONCLUDING REMARKS

Simultaneous use of PLIF and LHI techniques has been demonstrated for several hypersonic injector configurations in the NASA HYPULSE facility. Unique challenges presented by the extremely short test duration and the required simultaneous operation of two pulsed laser systems were met successfully.

The combination of gated intensified cameras and narrow spectral filtering provided the capability for PLIF imaging of low OH concentrations in the flow. PLIF Data was acquired in both longitudinal and crossflow planes.

Simultaneous use of the LHI and PLIF systems was advantageous and permitted correlations to be made between density gradients and combustion zones.

## REFERENCES

1. Harsha, P.; Waldman, B.: "The NASP Challenge: Testing for Validation," First National Aero-Space Plane Conference, AIAA 89-5005, 1989.
2. Henckels, A.; Maurer, F.; Olivier, H.; Gronig, H.: "Fast Temperature Measurement by Infra-red Line Scanning in a Hypersonic Shock Tunnel", *Experiments in Fluids*, vol. 9, pp 298-300, 1990.
3. Cassady, P.E.; Lieberg, S.F.: "Planar Laser Induced Fluorescence Measurements in Hypersonic Air Flowfields", AIAA 91-1492, 1991.
4. Lempert, W.R.; Trucco, R.E.: "Resonance Lamp Absorption Measurement of OH Number Density and Temperature In Expansion Tube Scramjet Engine Tests", *NASA Langley Measurement Technology Conference*, NASA CP-3161, 1992.
5. Miller, C.G.; Jones, J.J.: "Development and Performance of the NASA Langley Research Center Expansion Tube/Tunnel, A Hypersonic Hypervelocity Real Gas Facility", *Proc. 14th Int'l. Symp. Shock Tubes and Waves*, Sydney, Australia, 1983.
6. Tamagno, J.; Bakos, R.; Pulsonetti, M.; Erdos, J.: "Hypervelocity Real Gas Capabilities of GASL's Expansion Tube (HYPULSE) Facility," AIAA 90-1390, 1990.
7. Erdos, J.; Tamagno, J.; R. Bakos, R.; Trucco, R.: "Experiments on Shear Layer Mixing at Hypervelocity Conditions", *30th Aerospace Sciences Meeting*, AIAA 92-0628, 1992.
8. Trucco, R.; Danziger L.: "Performance of a Fast Acting Valve for Hydrogen Injection into a Scramjet Engine Model", GASL TM 232, 1989.
9. Steel, W.H.: *Interferometry*, Cambridge University Press, London, 1967.

GAS TEMPERATURE AND DENSITY MEASUREMENTS  
BASED ON SPECTRALLY RESOLVED RAYLEIGH-BRILLOUIN SCATTERING

Richard G. Seasholtz  
NASA Lewis Research Center  
Cleveland, OH 44135

James A. Lock  
Physics Dept., Cleveland State University  
Cleveland, OH 44115

## SUMMARY

The use of molecular Rayleigh scattering for measurements of gas density and temperature is evaluated. The technique used is based on the measurement of the spectrum of the scattered light, where both temperature and density are determined from the spectral shape. Planar imaging of Rayleigh scattering from air using a laser light sheet is evaluated for ambient conditions. The Cramer-Rao lower bounds for the shot-noise limited density and temperature measurement uncertainties are calculated for an ideal optical spectrum analyzer and for a planar mirror Fabry-Perot interferometer used in a static, imaging mode. With this technique, a single image of the Rayleigh scattered light can be analyzed to obtain density (or pressure) and temperature. Experimental results are presented for planar measurements taken in a heated air stream.

## INTRODUCTION

Laser diagnostics based on molecular scattering are receiving increased attention for use in aerospace test facilities. These methods can provide information directly related to the parameters of the molecular state of the gas including temperature, density, and bulk velocity. Of the various molecular scattering techniques, Rayleigh scattering is the simplest and least expensive to implement. Rayleigh scattering has typically been used to obtain gas density by measuring the total Rayleigh scattered power. More information, however, is available from the spectrum of the Rayleigh scattered light.

The Rayleigh scattering spectrum is directly related to the molecular velocity distribution function, which is a function of the thermodynamic parameters (temperature, density, pressure), composition, mean velocity, and turbulence parameters. Light scattered at a single scattering angle provides information related to one component of the molecular velocities. Thus one

component of the mean velocity can be determined (from the shift of the spectral peak), and temperature and density can be determined from the spectral shape (for a low turbulence flow).

Extraction of the parameters of interest (temperature and density) from the spectrum can be accomplished by measuring the spectrum with a high resolution spectrometer, such as a Fabry-Perot or Michelson interferometer. Sharp cutoff atomic or molecular absorption filters<sup>1,2</sup> have also been used to measure gas temperature. Point measurements of Rayleigh scattering spectra with scanning Fabry-Perot interferometers have been used to measure temperature in a hydrogen-air flame<sup>3,4</sup> and velocity, density, and temperature in the exhaust of a small hydrogen-oxygen rocket<sup>5</sup>. Rayleigh scattering has been proposed for atmospheric temperature measurements<sup>6,7</sup>. In this paper we examine an imaging technique to measure density and temperature using a planar mirror Fabry-Perot interferometer. It is an extension of a 1D technique used to measure temperature and number density in a heated nitrogen jet<sup>8</sup> and is similar to Fabry-Perot imaging techniques for measurement of instantaneous velocity of solid surfaces<sup>9</sup>, temperature and velocity in the upper atmosphere<sup>10</sup>, and solar corona measurements<sup>11</sup>.

We first analyze a hypothetical planar imaging experiment where the measurement region is illuminated with a laser light sheet, and the Rayleigh scattered light is detected with a 2D array detector. It is assumed that the medium under study is particle-free, zero-turbulence air. Cramer-Rao lower bounds are calculated for the shot-noise limited uncertainty in density and temperature measurements based on the shape of the spectrum of the Rayleigh-Brillouin scattered light.

The use of 2D spectrally resolved Rayleigh imaging is demonstrated with an experiment to map temperature and pressure in a heated air stream.

## THEORY

In this section we obtain theoretical lower bounds for the uncertainty in velocity and temperature measurements for two cases where the scattered light is detected with a 2D array detector. The first case assumes that an ideal instrument is used to measure the spectrum. The second case assumes that the spectrum is measured with a Fabry-Perot interferometer operated in a static, imaging mode (this is the technique described in the Experiment section). Only errors resulting from the Poisson statistics of the detected light are considered. Thus these results represent lower bounds for measurement errors.

### 2D Rayleigh Scattering Diagnostic

Consider a planar imaging experiment where a laser sheet uniformly illuminates a region in the object plane corresponding to the image of an array detector having  $N_r$  rows (measured perpendicular to the beam propagation direction) and  $N_c$  columns of pixels. Let the detector pixel size be  $L_x \times L_x$  (square pixels) and let the system have a magnification  $M$  (i.e., the measurement plane has dimensions  $(N_c L_x \times N_r L_x)/M$ ). The expected number of detected photons per pixel can be written<sup>12</sup>

$$\langle NPP \rangle = \frac{E_1}{N_r} \frac{\epsilon n L_x \lambda_o \Omega}{hcM} \left[ \frac{d\sigma}{d\Omega} \right] \quad (1)$$

where  $E_1$  is the laser energy,  $\lambda_o$  is the laser wavelength,  $(d\sigma/d\Omega)$  is the differential Rayleigh

scattering cross section,  $n$  is the molecular number density,  $\Omega$  is the solid angle of the collected light,  $h$  is Planck's constant,  $c$  is the velocity of light, and  $\epsilon$  is the overall detection efficiency (including detector quantum efficiency and system losses).

As an example, consider air at NTP ( $T = 293\text{K}$ ,  $P = 1\text{atm}$ ,  $N = 2.5 \times 10^{25} \text{ m}^{-3}$ ),  $\lambda_0 = 488\text{nm}$ ,  $E_l = 1\text{J}$ ,  $L_x = 23\mu\text{m}$ ,  $N_r = 384$ ,  $M = 0.5$  (measurement plane =  $6.6\text{mm} \times 4.4\text{mm}$ ),  $\Omega = 0.05$  ( $f/4$ ),  $\epsilon = 0.025$ , and  $(d\sigma/d\Omega) = 8.4 \times 10^{-32} \text{ m}^2/\text{sr}$ . For this case, equation 1 gives  $\langle \text{NPP} \rangle = 770$  detected photons per pixel.

## Spectrum of Rayleigh Scattered Light

Quasi-elastic scattering of light by gas molecules is known as Rayleigh-Brillouin scattering<sup>13,14</sup>. In this scattering process, the internal energy of the scattering molecules is unchanged and the frequency of the scattered light differs only slightly from the frequency of the incident light; the frequency shifts are due to the Doppler effect on the light scattered from molecules in random thermal or collective motion. The Doppler shift for elastic scattering from a single molecule with velocity  $\mathbf{v}$  is given by

$$f = \mathbf{K} \cdot \mathbf{v} / 2\pi \quad (2)$$

where  $\mathbf{K} = \mathbf{k}_s - \mathbf{k}_o$  with  $\mathbf{k}_s$  and  $\mathbf{k}_o$  being the wave vectors of the scattered and incident light, respectively. The magnitude of  $\mathbf{K}$  is a function of the scattering angle  $\theta_s$  and the wavelength  $\lambda$

$$K = |\mathbf{K}| = (4\pi/\lambda)\sin(\theta_s/2) \quad (3)$$

The corresponding wavelength

$$\Lambda = \frac{2\pi}{K} \quad (4)$$

is the wavelength of the scattering process, or interaction wavelength.

The spectrum of the Rayleigh scattered light from a gas is a composite of the light scattered from the individual molecules in the gas. For a low density gas, the molecules can be considered as independent scatterers. And, for a single component gas with a Maxwellian velocity distribution, the normalized spectrum of the scattered light is a simple Gaussian<sup>14</sup>

$$S(f) df = \frac{2\sqrt{\pi}}{aK} e^{-[2\pi(f-f_0) - \mathbf{K} \cdot \mathbf{V}]^2 / a^2 K^2} df \quad (5)$$

where  $a = (2\kappa T/m)^{1/2}$  ( $m$  = molecular mass;  $\kappa$  = Boltzman's constant) is the most probable molecular speed. The spectral peak is shifted from the laser frequency  $f_0 = c/\lambda_0$  by  $\mathbf{K} \cdot \mathbf{V} / 2\pi$ , where  $\mathbf{V}$  is the bulk velocity of the gas. Here, the spectrum is normalized so that

$$\int S(f) df = 1 \quad (6)$$

(Note that all integrations over frequency have limits  $[-\infty, +\infty]$ .)

For higher density gases, the molecular velocities become correlated and the spectrum deviates from the Gaussian form given by equation 5. At high densities, the scattering can be treated as scattering from thermally induced density fluctuations (Brillouin scattering), and the

spectrum can be calculated using relatively simple continuum (hydrodynamic) theory<sup>15</sup>. In this regime the spectrum is characterized by three peaks: the central peak results from scattering from non-propagating entropy fluctuations; and the side peaks result from propagating pressure fluctuations (i.e., acoustic waves). For intermediate densities the spectrum makes a transition from the Gaussian to the Brillouin spectrum. Here, the spectrum has been calculated using various kinetic theory models<sup>16-19</sup>, with the 6-moment model of reference 18 being the best model presently available for a single species gas<sup>20,21</sup>.

The Rayleigh-Brillouin spectrum is generally parameterized by a non-dimensional frequency shift

$$x = \frac{2\pi f'}{Ka} \quad (7)$$

and a non-dimensional quantity

$$y = \frac{p}{\mu Ka} \quad (8)$$

where  $p$  is the gas pressure and  $\mu$  is the shear viscosity. The  $x$  parameter is the ratio of the frequency shift  $f' = f - f_0$  to the acoustic frequency, and the  $y$  parameter is the ratio of the molecular collision frequency to the acoustic frequency (or, equivalently, the ratio of the interaction wavelength  $\Lambda$  to the molecular mean-free-path). For single component gases, the normalized spectrum is, in general, a function of  $x$  and  $y$  alone<sup>22</sup>. For low density gases,  $y \rightarrow 0$ ; and the spectrum is the Gaussian given by equation 5, which can be written

$$S(x) dx = \pi^{-1/2} e^{-x^2} dx \quad (9)$$

where the bulk velocity is assumed to be zero.

Typical spectra calculated using the S6 model of reference 18 are shown in figure 1.\* These examples are for air with a laser wavelength  $\lambda = 488\text{nm}$  and a scattering angle  $\theta_s = 90^\circ$ . The viscosity and thermal conductivity are calculated using the program described in reference 23. The transition between the Gaussian spectrum and the hydrodynamic spectrum occurs for  $y \approx 1$ . Note that  $y = 0.75$  for air at ambient temperature and pressure, which means the simple Gaussian spectrum is not appropriate.

### Cramer-Rao Lower Bounds

As we are interested in applying Rayleigh-Brillouin scattering as a diagnostic for measuring the thermodynamic parameters of a gas, we find it useful to establish the theoretical lower bounds for accuracy of estimates of temperature and density based on the measurement of Rayleigh-Brillouin spectra. The lower bounds are a result of the Poisson statistics of the photon arrival rates (shot-noise limit).

The observed Rayleigh scattering spectrum can be expressed as a set of counts

$$\langle n_j \rangle = G_R S(f_j) \Delta f \quad (10)$$

which are the expected number of counts in frequency interval  $f_j$  to  $f_j + \Delta f$  where  $G_R$  is the total



number of detected photons in the spectrum. The spectrum is thus a function of a set of three unknown parameters that can be expressed as the vector

$$\alpha = [G_R, \rho, T] \quad (11)$$

where  $\rho$  is the gas density, and  $T$  is the gas temperature. Assuming that the parameters are uncorrelated, the estimate of the variance of  $\alpha_i$  (Cramer-Rao lower bound)<sup>24</sup> is given by

$$V(\hat{\alpha}_i) = \frac{1}{\Gamma_{ii}} \quad (12)$$

where  $\Gamma$  is the Fisher information matrix given (for Poisson statistics) by<sup>25</sup>

$$\Gamma_{ij} = \sum_q \frac{1}{\langle n_q \rangle} \frac{\partial \langle n_q \rangle}{\partial \alpha_i} \frac{\partial \langle n_q \rangle}{\partial \alpha_j} \quad (13)$$

For this work, we want to obtain the temperature and density from the shape of the spectrum. (i.e., the total scattered power is not used). (We could just as well have selected pressure and temperature as the independent thermodynamic parameters.) Expressed as standard deviations  $\sigma(\alpha_i) = [V(\alpha_i)]^{1/2}$ , the lower bounds for measurement uncertainties for density and temperature are

$$\sigma(\rho) = \left[ G_R \left[ \frac{\partial y}{\partial \rho} \right]^{1/2} \int \frac{1}{S} \left[ \frac{\partial S}{\partial y} \right] dx \right]^{-1/2} \quad (14)$$

$$\sigma(T) = \left[ G_R \int \frac{1}{S} \left[ \frac{\partial y}{\partial T} \frac{\partial S}{\partial y} - \frac{1}{2T} \left[ S + x \frac{\partial S}{\partial y} \right] \right]^2 dx \right]^{-1/2} \quad (15)$$

For the low density limit  $y \rightarrow 0$ , and the Gaussian spectrum given by equation 9 can be used in equation 15 to find

$$\sigma(T)_{y=0} = (2/G_R)^{1/2} T \quad (16)$$

For higher densities where the spectrum is not Gaussian, the integrals in equations 14 and 15 can be numerically evaluated. Using the spectrum calculated from the 6-moment model<sup>18</sup> and the gas properties calculated using the FLUID program<sup>23</sup>, the relative uncertainties for temperature and density as a function of the parameter  $y$  are shown on figure 2. Note that the temperature uncertainty decreases slowly from the low density limit with increasing  $y$ , reaching 1/2 of the low density value at  $y=5$ . The uncertainty in the density decreases with increasing  $y$  from very large values at low density. Also, note that the uncertainty in the density measurement determined from the spectral shape is at least a factor of  $2^{1/2}$  larger than the uncertainty based on measurements of the total scattered light. (The relative density uncertainty based on the total scattered light is  $G_R^{-1/2}$ .)

## Numerical Example

Consider the 2D imaging example discussed above for air at NTP, where the detected photons/pixel was  $\langle NPP \rangle = 770$ . For  $\theta_s = 90^\circ$  and  $\lambda = 488\text{nm}$ ,  $K = 1.821 \times 10^7 \text{m}^{-1}$ ,  $a = 410\text{m/sec}$ , and  $y = 0.75$ . Based on the light detected at a single pixel ( $G_R = 770$ ), figure 2 gives the lower bound for density uncertainty  $\sigma(\rho)/\rho = 27\%$ , and the lower bound for temperature  $\sigma(T)/T = 5\%$ . Note that both uncertainties are inversely proportional to the square root of the number of pixels; e.g., for the light collected from 100 pixels, the uncertainties would decrease by a factor of 10 (and the spatial resolution would decrease by a factor of 10). Finally, it must be emphasized that these uncertainties are lower bounds based on spectral measurements with an ideal spectrum analyzer. Actual measurements using non-ideal spectrum analyzers will always give larger uncertainties.

### Fabry-Perot Interferometer

The above error estimates were based on the use of an ideal instrument to measure the spectrum. In this section we perform the error estimation based on measurement of the intensity distribution of light imaged through a planar mirror Fabry-Perot interferometer (fig. 3). The expected number of detected photoelectrons  $\langle NDP \rangle$  for the  $q$ th pixel is

$$\langle NDP_q \rangle = \langle NPP_q \rangle \iint S(f) I_t(f, \theta_r) df dA_{\text{pixel}} \quad (17)$$

where the Fabry-Perot transmission function<sup>26</sup>

$$I_t(\psi) = \frac{1}{1 + F \sin^2(\psi/2)} \quad (18)$$

with  $\psi$  being the phase delay of the light for one pass through the interferometer given by

$$\psi = \frac{4\pi\mu df \cos\theta_r}{c} \quad (19)$$

and  $F = (2N_R/\pi)^2$ , where  $N_R$  is the reflective finesse. In this equation,  $f$  is the frequency of the light,  $\mu$  is the refractive index of the medium in the Fabry-Perot cavity (taken as unity here),  $d$  is the Fabry-Perot mirror spacing, and  $\theta_r$  is the angle between the ray and the optic axis. For simplicity, we neglect spectral broadening due to the finite size of the aperture of the collection optics.

We now select, for this example, a particular Fabry-Perot configuration (mirror spacing  $d = 15\text{mm}$ ; finesse  $N_R = 20$ ) and numerically evaluate the Fisher matrix elements

$$\Gamma_{ij} = \sum_q \frac{1}{\langle NDP_q \rangle} \frac{\partial \langle NDP_q \rangle}{\partial \alpha_i} \frac{\partial \langle NDP_q \rangle}{\partial \alpha_j} \quad (20)$$

where the sum is over a  $50 \times 50$  pixel subregion, giving a spatial resolution of about  $0.6\text{mm}$ . This relatively large subregion was chosen so that it would encompass the entire width of the first (largest width) fringe. Use of subregions smaller than the fringe width result in larger

uncertainties, even for the same number of total counts in the subregion. The results of this calculation are given in Table 1 for several locations of the subregion (denoted by fringe radii). The density uncertainty is about 5% (10 times that achievable with an ideal spectrum analyzer) and the temperature uncertainty, except for the first fringe, is about 0.3% (3 times that of ideal). The larger temperature uncertainty at the first fringe is probably caused by the relatively large fringe width relative to the subregion size.

### Other Error Sources

The above calculations for lower bounds of measurement uncertainties using a Fabry-Perot interferometer represent an idealized measurement process. In practice, a variety of factors will increase these calculated uncertainties. One factor is the assumption of constant finesse. The effective finesse will not be constant; vignetting reduces the effective number of reflections in the interferometer cavity, thereby decreasing the finesse at larger fringe radii. This means that the finesse must be measured, as is done in the experiment described later in this paper. Another factor is the stability of the laser frequency and Fabry-Perot interferometer alignment, which will also decrease measurement accuracy. A third factor is the assumption of a known gas composition; if the gas is made up of an unknown mixture of component gases, the spectrum cannot be uniquely related to the temperature. Also, if the flow is highly turbulent, and the measurement is obtained over a duration much greater than the turbulence time scale, the spectrum is broadened with both temperature and turbulence contributing to the spectral width. Thus, if one of these is known, the other can be determined from the spectral width, but both cannot be simultaneously determined. Finally, contaminant particles in the flow will strongly scatter. In some cases where the particle number density is low, the images can be processed to remove the obvious particles. If the particle number density is so large that the particles images overlap and cannot be removed, the spectral shape is changed from that of pure molecular scattering and density and temperature measurements cannot be obtained.

## EXPERIMENT

### Apparatus

An experiment (fig. 4) was conducted to demonstrate the technique discussed above to measure gas temperature and density based on the measurement of the spectrum of Rayleigh-Brillouin scattering. A commercial electric torch (9mm dia.) was used to generate the low velocity hot air stream. A co-flow arrangement, where the electric torch was located in a larger (53 mm dia.) flow of particle-free, ambient temperature air was used to eliminate particles from the measurement region. The temperature of the hot stream was measured with a thermocouple located at the center of the measurement region. As no correction was made for conduction losses, it was expected that the thermocouple temperature would be less than the actual air temperature. The beam from an argon-ion laser (2.5W, 488nm) was formed into a sheet (about 10mm high by 0.2mm thick) using a combination of cylindrical and spherical lenses. The light sheet passed through the center of the hot air stream about 17mm above the exit plane of the

torch. A 250mm focal length  $f/3.6$  lens was used to collect and collimate the light scattered at  $90^\circ$ . The collimated light was passed through a planar mirror Fabry-Perot interferometer (70mm diameter aperture and 14.96mm mirror spacing) and focused onto the CCD array with a 500mm focal length lens. The CCD array had 384 rows by 576 columns of  $23\mu\text{m} \times 23\mu\text{m}$  square pixels (giving a field size in the flow of  $4.4\text{mm} \times 6.6\text{mm}$ ) and was cooled to about  $-50^\circ\text{C}$  to reduce dark current. The CCD pixel data was digitized with 12 bit resolution and transferred to an 80386 PC via an IEEE-488 interface for storage and analysis.

The initial step in the measurement process was to measure the instrument function  $[I_t(\psi), \text{ for } f=f_0]$ . A diffusely scattering target was placed in the field of view and illuminated with laser light scattered from a rotating diffuse target (the rotating target was used to reduce speckle in the recorded image). The Rayleigh scattered light from the flow was then recorded. Exposure times were 0.1s for the instrument function and 10s for the Rayleigh scattering. Two images of the Rayleigh scattered light were taken, so the technique described in reference 27 could be used to reduce the effect of any residual particles.

### Data Reduction

The data reduction was done in two steps. First, the instrument function image (such as figure 5a) was analyzed to determine the center of the circular fringe pattern, the finesse, and the phase corresponding to the laser frequency. Because the effective finesse and phase varied over the image plane, it was necessary to determine them as a function of location in the image (typically, the finesse varied from about 20 at the center to about 4 at the edges of the image). Seventy-seven  $50 \times 50$  pixel subregions were used. The subregions were positioned evenly spaced around the fringes. A typical pattern of subregions is shown in figure 6. A 4<sup>th</sup> degree, 2D polynomial (15 parameters) was then fit to these values of phase and finesse. The coefficients for the polynomial fits were saved for the second step (analyzing the image of the Rayleigh scattered light).

In the second step, the image of the Rayleigh scattered light (fig. 5b) in each subregion was fit to a model function given by equation 10 using the 6-moment model of reference 18 with the gas properties of air. The temperature and pressure values obtained at each subregion were fit to 2D 4<sup>th</sup> degree polynomials, which were used to generate contour plots.

### Results

Data were taken at ambient conditions and for two different temperatures of heated air. The centers of the 77  $50 \times 50$  pixel subregions are shown in figure 6. Temperature and pressure were determined at each of the 77 subregions. (Pressure was obtained instead of density to facilitate comparison with the measured ambient static pressure.).

#### Ambient Condition Measurement

The measured ambient temperature and pressure were 296K and 14.35 psia. The mean temperature based on the 77 individual subregion measurements was 302K with standard

deviation 7K. The mean pressure was 14.4psia with standard deviation 0.7psia. The contour plots of temperature and pressure obtained from the 77 subregions are shown in figures 7a and 8a. As the contours are based on this set of measurements, the contours outside the region where measurements were taken should be disregarded (i.e., at the corners). Both the temperature and pressure results agree well with the actual conditions.

## Heated Air Measurements

Figures 7b,c and 8b,c show contour plots for temperature and pressure taken at measured (thermocouple) air temperatures of 471K and 677K. For the higher temperature measurement, the first ring was not included in the data reduction because its width was too large relative to the subregion size, which results in decreased accuracy. The maximum temperatures shown on the contour plots are 510K and 750K. As expected, these are somewhat higher than the temperatures measured with the thermocouple. The pressure measurements, except for the inner fringe subregions, do not show the same level of agreement with the actual pressure as did the ambient temperature measurements. For the 471K flow, the mean pressure and standard deviation were 12.1psia and 1.4psia. For the 750K flow, the mean pressure and standard deviation were 9.2psia and 2.6psia. The poor results for pressure at the elevated temperatures may be explained by the smaller  $y$  parameter values corresponding to the lower densities at the higher temperatures (the  $y$  parameters were 0.72 (296K), 0.37 (510K), and 0.24 (750K)). (As discussed above, the uncertainty in density, or pressure, measurements rapidly increases as  $y$  decreases.)

The observed standard deviations in the measurements are larger than the uncertainties based only on the shot-noise limits. This indicates that for the relatively high signal levels, other sources outweigh these statistical errors. One potential error source is the drift in the Fabry-Perot mirror spacing between recording the instrument function and the Rayleigh data.

The data reduction requires rather lengthy processing, chiefly because of the numerical integration in equation 17. The time per iteration for each  $50 \times 50$  pixel subregion is about 45s using a 80486/33MHz/Weitek 4167. Thus an image with 77 subregions and an average of 6 iterations requires about 6 hr to process. No attempt was made to optimize the code at this time, so it should be possible to substantially reduce the data reduction time.

## CONCLUDING REMARKS

The results of this work show the feasibility of using measurements of the spectrum of molecular Rayleigh scattering as a diagnostic for measurement of both density and temperature based solely on the shape of the spectrum of the scattered light. The determination of temperature can be made at any density (provided, of course, that adequate scattered light is collected). For the same amount of collected scattered light, the temperature measurement uncertainty decreases for  $y$  on the order of or larger than unity. The density determination, however, is only feasible for higher densities, where the  $y$  parameter is on the order or larger than unity. The use of the spectral shape for density measurements offers the advantage compared to the measurement of the total scattered light in that no calibration is required. (The calibration constant, as seen in eq. 1, is a function of incident irradiance, optical collection angle and system losses.) This could be particularly significant in measurement situations where the calibration constant changes due to window contamination, laser beam wander, etc.

Although not discussed in this paper, bulk velocity is also measurable based on the shift of the peak of the Rayleigh scattered light (or on the frequency shift of Mie scattered light from particles).

The experimental results for temperature are consistent with temperature measured with a thermocouple. The pressure measurements presented agree with the actual pressure with the unheated flow, but show significant deviation with the heated flow. This is attributed to the reduced sensitivity of the technique at reduced densities. It is important to note that the results for temperature and pressure given involve no calibration or adjustable parameters. Only the gas parameters (molecular weight, viscosity), laser wavelength, and geometrical quantities (Fabry-Perot mirror spacing, scattering angle) are required.

The experimental work reported here used a CW argon-ion laser, which results in time-averaged measurements. Use of a pulsed laser and gated detection would offer several advantages. Measurements based on an image from a single laser pulse would give 2D maps of the gas parameters at an instant of time. The effect of background light, such as flame luminosity, could be greatly reduced. And particle images, if not too dense, should be easier to identify and remove from the flow field image. (A large number density of particles in the flow generally will prevent temperature and density measurements.)

Finally, care should be taken to prevent spurious laser light from reaching the receiving optics. Even though this light can be accounted for in the data reduction, it will degrade the signal-to-noise ratio and measurement accuracy. This problem is particularly severe in internal flows where it is very difficult to eliminate all spuriously scattered light. The technique described by Miles et al.<sup>2</sup> for blocking light at the laser frequency should be useful for high velocity flows where the frequency of the Rayleigh scattered light is shifted well away from the laser frequency.

## ACKNOWLEDGEMENTS

We would like to acknowledge the efforts of Mr. Andrew Kremer, who was responsible for setting up and aligning the optical system used for the measurements. We also wish to thank Prof. G. Tenti for kindly providing us with the computer code for the 6-moment model.

## REFERENCES

1. Shimizu, H.; Lee, S.A.; and She, C.Y.: High spectral resolution lidar system with atomic blocking filters for measuring atmospheric parameters, *Appl. Opt.*, vol. 22, 1983, pp. 1373-1381.
2. Miles, R.B.; Lempert, W.R.; and Forkey, J.: Instantaneous velocity fields and background suppression by filtered Rayleigh scattering, *AIAA 29th Aerospace Sciences Meeting, Reno, 1991*, AIAA paper 91-0357.
3. Cattolica, R.; Robben, F.; and Talbot, L.: (1976) The interpretation of the spectral structure of Rayleigh scattered light from combustion gases, *AIAA 14th Aerospace Sciences Meeting, Washington, 1976*, AIAA paper 76-31.

4. Pitz, R.W.; et al.: Temperature and density in a hydrogen-air flame from Rayleigh scattering, *Comb. and Flame*, vol. 27, 1976, pp. 313-320.
5. Seasholtz, R.G.; Zupanc, F.J.; and Schneider, S.J.: Spectrally resolved Rayleigh scattering diagnostic for hydrogen-oxygen rocket plume studies, *AIAA 29th Aerospace Sciences Meeting, Reno*, 1991, AIAA paper 91-0462.
6. Schwiesow, R.L.; and Lading, L. : Temperature profiling by Rayleigh-scattering lidar, *Appl. Opt.* vol. 20, 1981, pp. 1972-1979.
7. Rees, D.; et al.: The Doppler imaging system: initial observations of the auroral thermosphere, *Planet. Space Sci.*, vol. 32, ,1984, pp. 273-285.
8. Lock, J.A.; Seasholtz, R.G.; and John, W.T.: Using Rayleigh-Brillouin scattering to determine one-dimensional temperature and number density profiles of a gas flow field, *Appl. Opt.*, vol. 31, 1992.
9. Gidon, S.; and Behar G.: Instantaneous velocity field measurements: application to shock wave studies, *Appl. Opt.*, vol. 25, 1986, pp. 1429-1433.
10. Sivjee, G.G.; Hallinan, T.J.; and Swenson, G.R.: Fabry-Perot interferometer imaging system for thermospheric temperature and wind measurements, *Appl. Opt.*, vol. 19, ,1980, pp. 2206-2209.
11. Chandrasekhar, T.; Desai, J.N.; and Angreji, P.D.: Temperatures and differential line-of-sight velocities observed in the solar corona during a total solar eclipse , *Appl. Opt.*, vol. 20, 1981, pp. 2172-2173.
12. Eckbreth, A.C.: *Laser Diagnostics for Combustion, Temperature, and Species*, Abacus Press, Tunbridge Wells, Kent, 1988, p. 367.
13. Young, A.T.: Rayleigh scattering, *Physics Today*, Jan. 19, 1982, pp. 42-48.
14. Fabelinskii, I.L.: *Molecular scattering of light*, Plenum Press, New York, 1968, p. 263.
15. Clark, N.A.: Inelastic light scattering from density fluctuations in dilute gases. The kinetic-hydrodynamic transition in monoatomic gas, *Phys. Rev.*,vol. A12, 1975, pp. 232-244.
16. Sugawara, A.; and Yip: Kinetic model analysis of light scattering by molecular gases, *Phys. Fluids*, vol. 10, 1967, pp. 1911-1921.
17. Boley, C.D.; Desai, R.C.; and Tenti, G.: Kinetic models and Brillouin scattering in a molecular gas, *Can J. Phys.*, vol. 50, 1972, pp. 2158-2173.
18. Tenti, G.; Boley, C.D.; and Desai, R.C.: On the kinetic model description of Rayleigh-Brillouin scattering from molecular gases, *Can. J. Phys.*,vol. 52, 1974 ,pp. 285-290.
19. Hubert, M.; and May A.D.: The Rayleigh-Brillouin spectrum of normal and parahydrogen: A test of model solutions of the Wang-Chang Uhlenbeck equation, *Can. J. Phys.*, vol. 53, 1974, pp. 343-350.

20. Young, A.T.; and Kattawar, G.W.: Rayleigh-scattering line profiles, *Appl. Opt.*, vol. 22, 1983, pp. 3668-3670.
21. She, C.Y.; et al.: Stimulated Rayleigh-Brillouin gain spectroscopy, *Phys. Rev.*, vol. A31, 1985, pp. 3733-3740.
22. Nelkin, M.; and Ghatak, A.: Simple binary collision model for Van Hove's  $G_s(r,t)$ , *Phys. Rev.*, vol. 135A, 1964, pp. 4-9.
23. Fessler, T.E.: *FLUID: A numerical interpolation procedure for obtaining thermodynamic and transport properties of fluids*, NASA TM X-3572, 1977.
24. Whalen, A.D.: *Detection of signals in noise*, Academic Press, New York, 1971, pp. 324-331.
25. Lading, L.; and Jensen, A.S.: Estimating the spectral width of a narrowband optical signal, *Appl. Opt.* vol. 19, 1980, pp. 2750-2756.
26. Vaughan, J.M.: *The Fabry-Perot Interferometer, History, Theory, Practice and Applications*, Adam Hilger, Bristol, 1989, Chapter 3.
27. Kay, L.; and Sadler, D.A.: A method for processing CCD images to remove cosmic rays and other randomly positioned spurious events - theory and experiment , *Measurement Science and Technology*, vol. 2, 1991, pp. 532-535.



Fringe number	Fringe radius	$\sigma(T)/T$	$\sigma(\rho)/\rho$
1	64 pixels	0.46%	3.10%
2	136	0.24	4.56
3	181	0.26	5.34
4	217	0.26	5.86
5	248	0.25	5.75
ideal		0.09	0.53

TABLE 1. Lower bounds for uncertainty in density and temperature measurements in air.  $\langle NPP \rangle = 770$ ;  $50 \times 50$  pixel area;  $T = 300\text{K}$ ;  $p = 1\text{atm}$ .

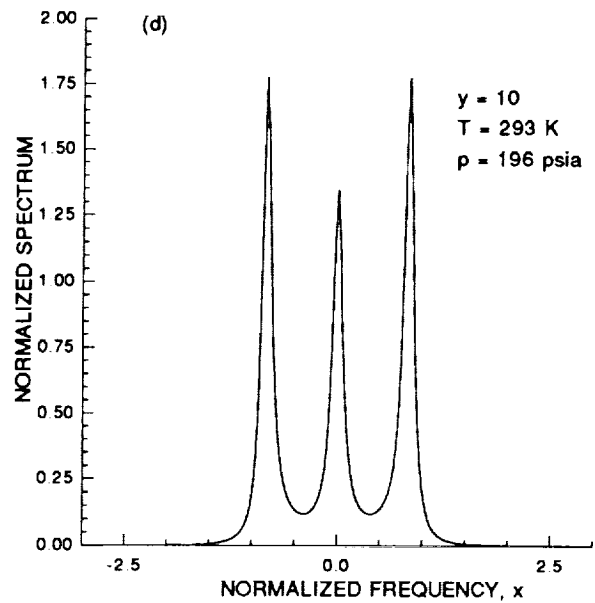
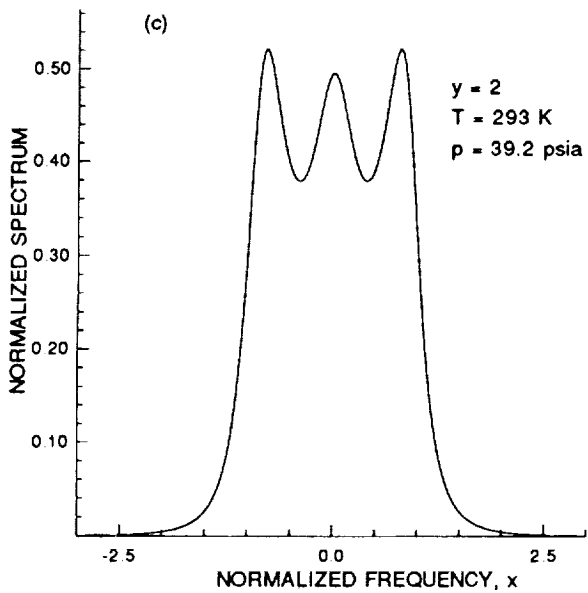
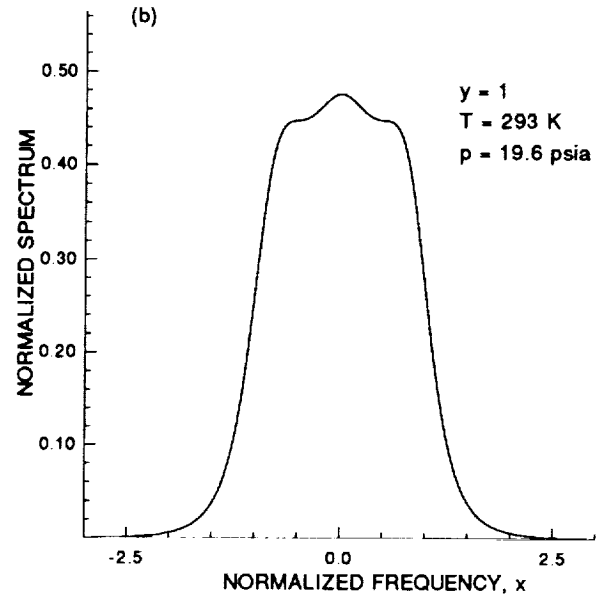
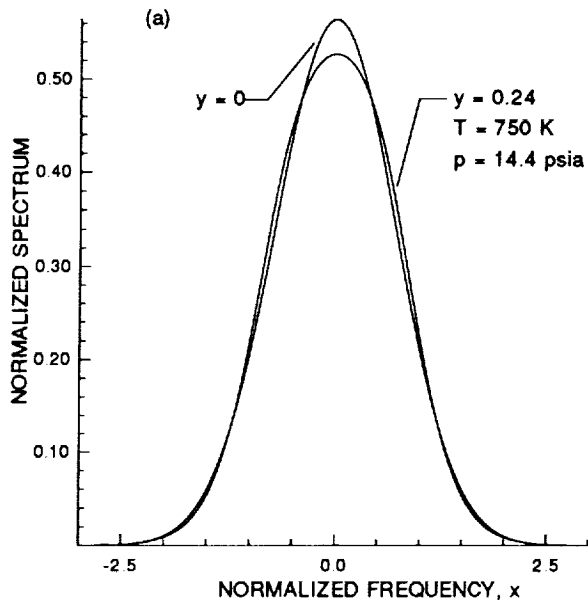


Figure 1. Calculated Rayleigh-Brillouin spectra for air K: (a)  $y=0,0.24$ , (b)  $y=1$ , (c)  $y=2$ , (d)  $y=10$ .

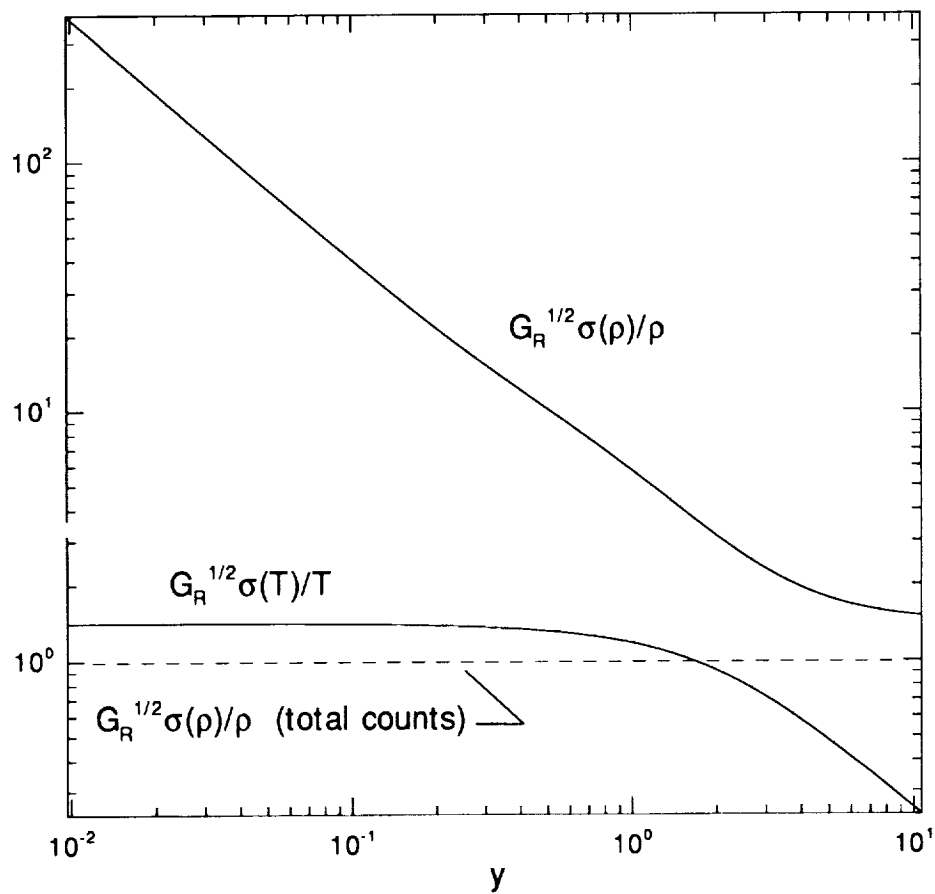


Figure 2. Cramer-Rao lower bounds for density and temperature measurement uncertainties.  $G_R$  is total number of detected photons. Dashed line is lower bound for density based on total scattered light.

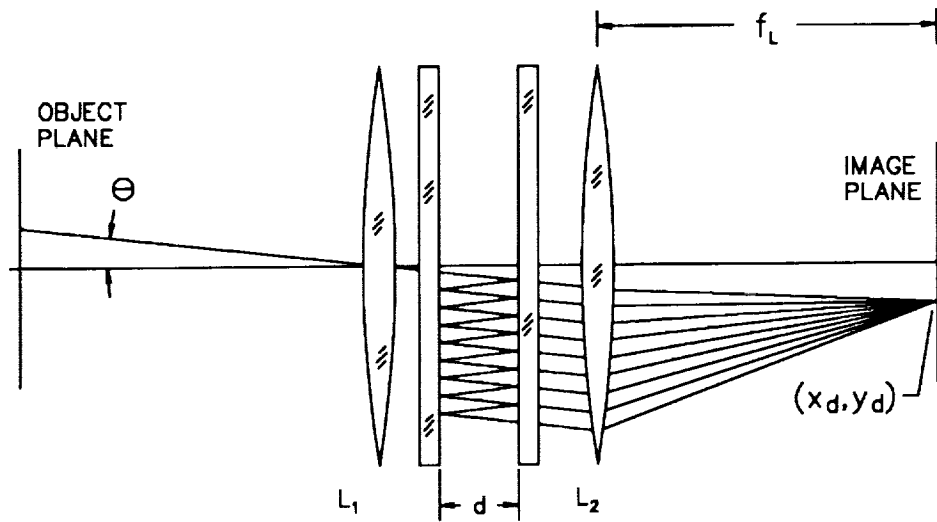


Figure 3. Fabry-Perot interferometer.

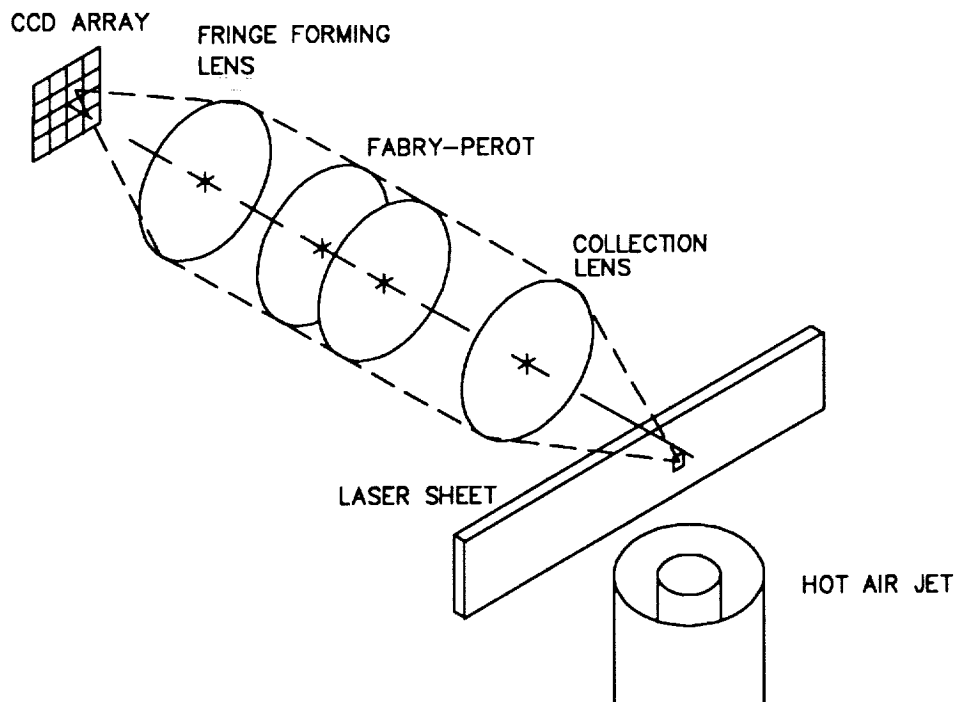


Figure 4. Experiment to map temperature and pressure in hot air stream.

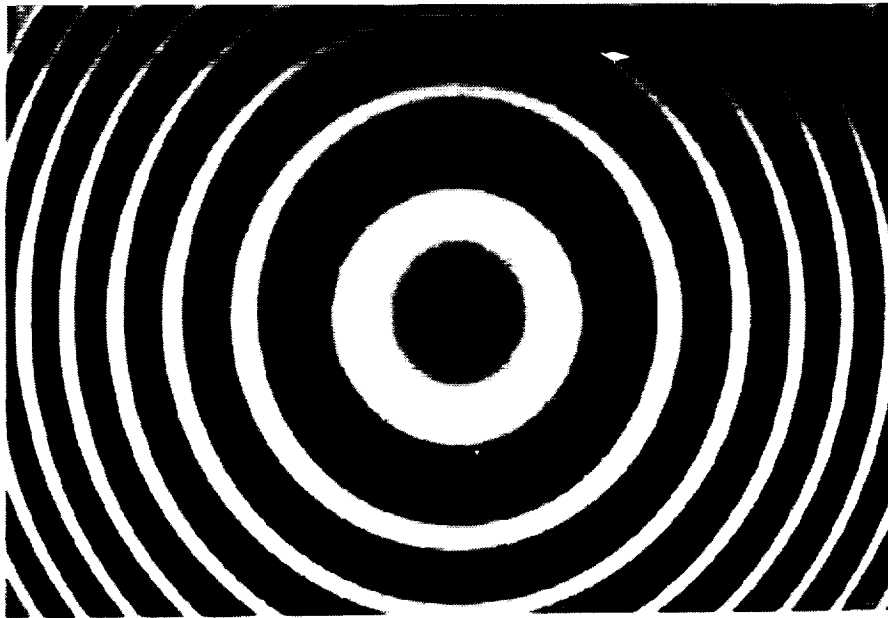
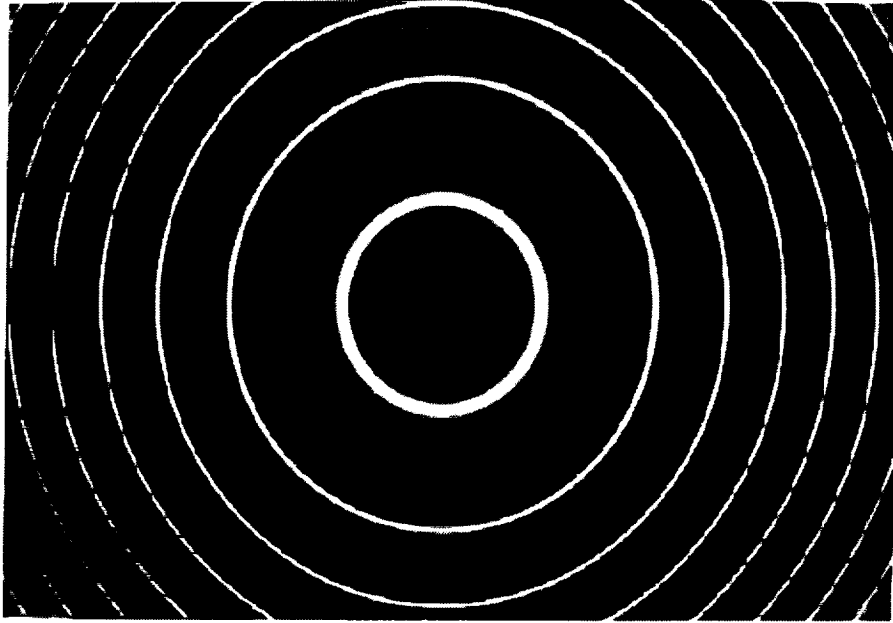


Figure 5. Fabry-Perot fringe patterns recorded with CCD camera: (a) instrument function, (b) Rayleigh scattered light.

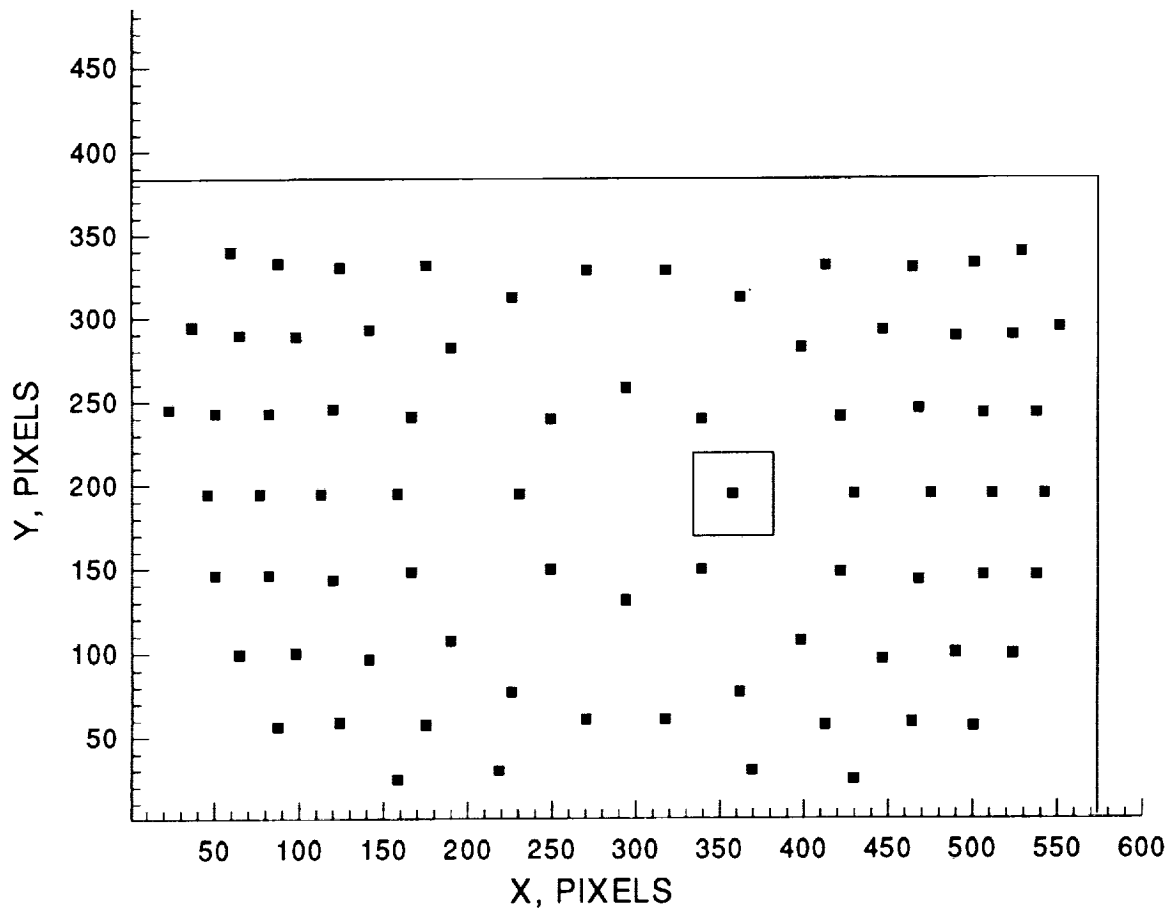


Figure 6. Pattern of subregions used for data analysis. Open box shows size of 50x50 pixel subregion.

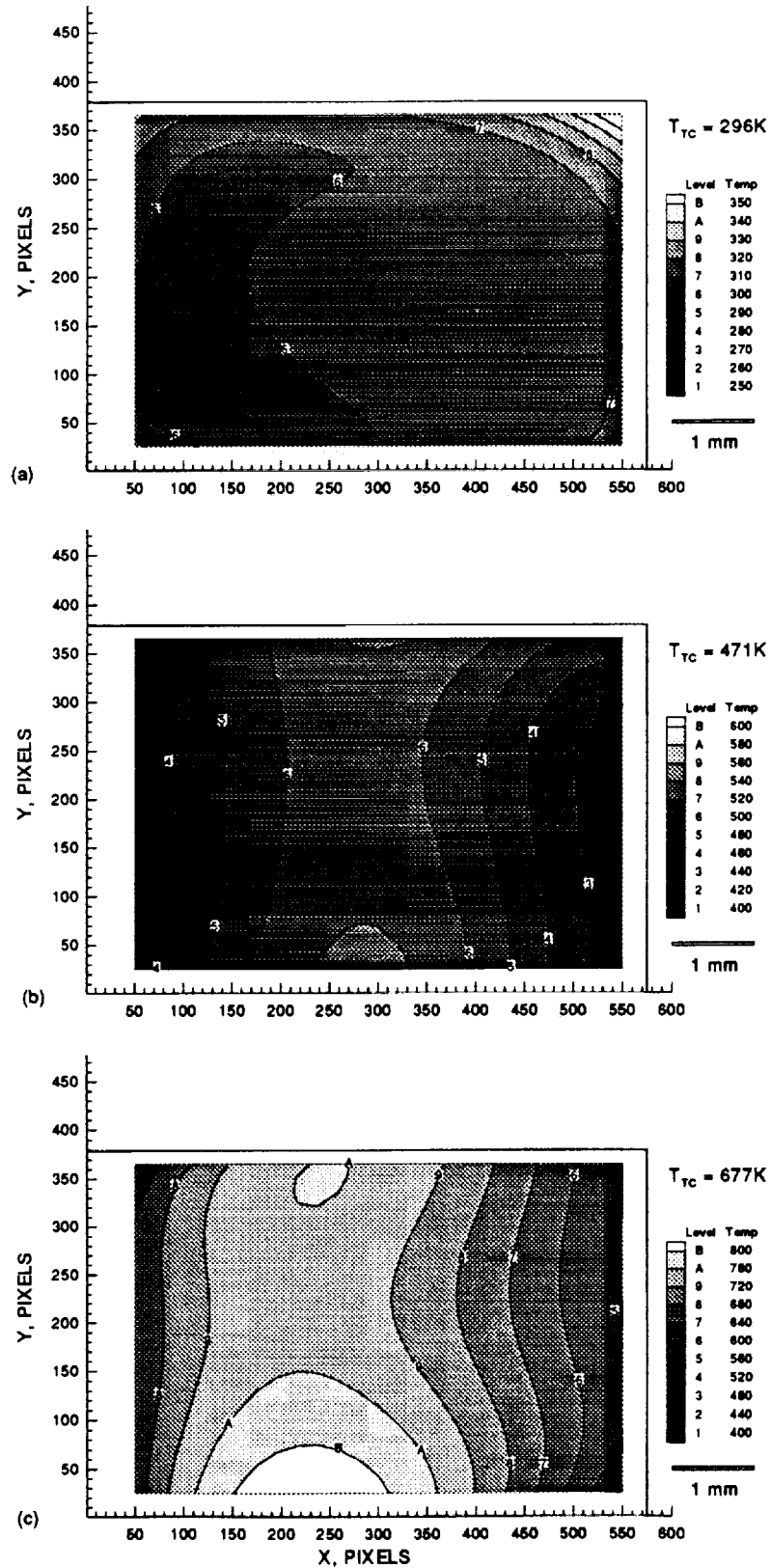


Figure 7. Contour plots of measured temperature: (a) ambient condition,  $T=296K$ ,  $p=14.35psia$  (b) heated air flow, thermocouple temperature =  $471K$  (c) heated air flow, thermocouple temperature =  $677K$ .

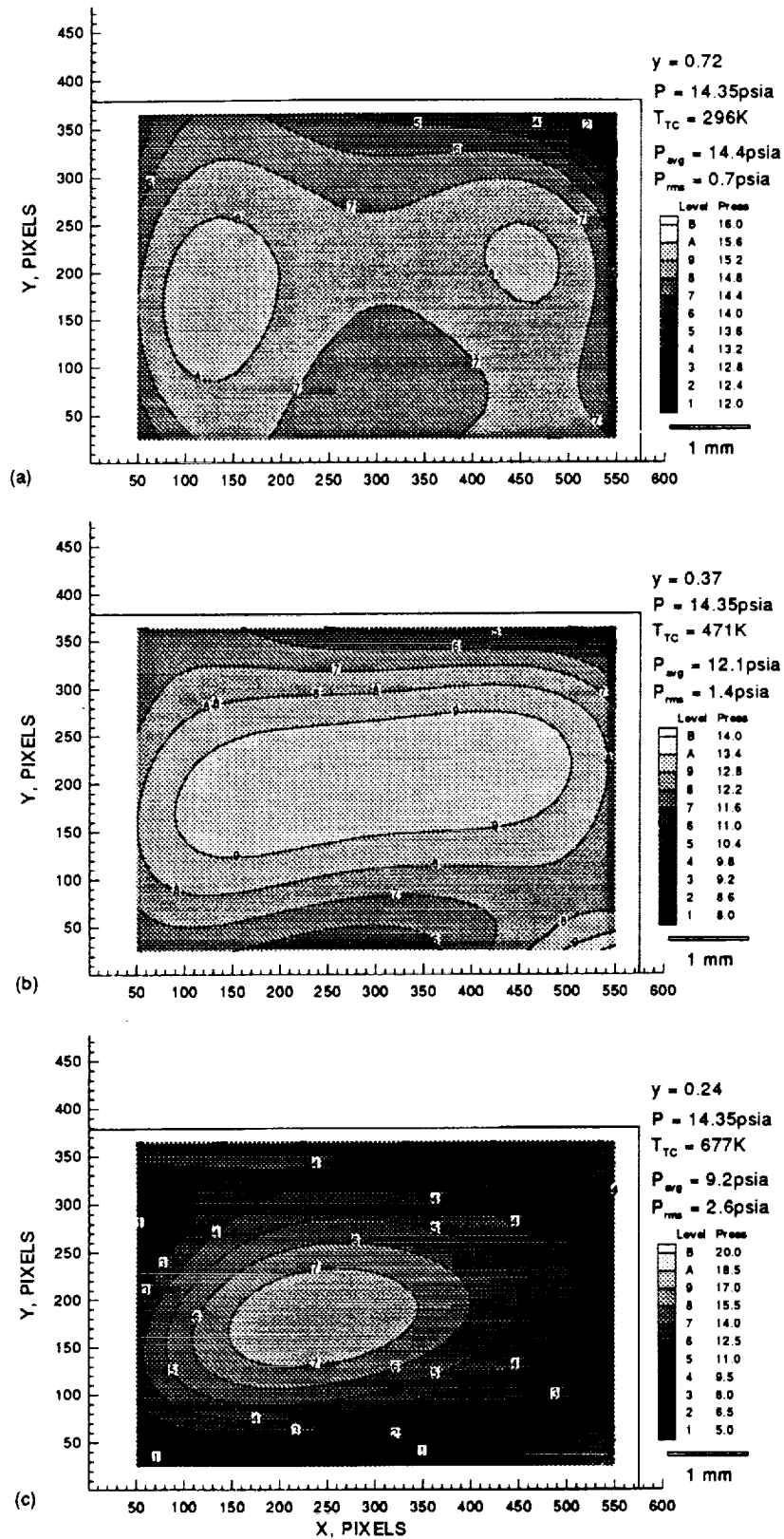


Figure 8. Contour plots of measured pressure: (a) ambient condition,  $T=296\text{K}$ ,  $p=14.35\text{psia}$  (b) heated air flow, thermocouple temperature =  $471\text{K}$  (c) heated air flow, thermocouple temperature =  $677\text{K}$ .



PLANAR LASER-INDUCED FLUORESCENCE MEASUREMENTS  
OF HIGH-ENTHALPY FREE JET FLOW WITH NITRIC OXIDE\*

Jennifer L. Palmer, Brian K. McMillin, and Ronald K. Hanson  
High Temperature Gasdynamics Laboratory  
Department of Mechanical Engineering  
Stanford University, Stanford, CA 94305-3032

SUMMARY

Planar laser-induced fluorescence (PLIF) measurements of property fields in a high-enthalpy, supersonic, underexpanded free jet generated in a reflection-type shock tunnel are reported. PLIF images showing velocity and temperature sensitivity are presented. The inferred radial velocity and relative rotational temperature fields are found to be in agreement with those predicted by a numerical simulation of the flowfield using the method of characteristics.

INTRODUCTION

Planar laser-induced fluorescence (PLIF) has been used in a variety of experiments to visualize gas flows and to give limited information about their aero-thermochemical properties. Recently, interest has shifted towards variations of PLIF which allow quantitative velocity and temperature measurements. The goal of the present work is to develop experimental methods for making quantitative, single-shot measurements of several properties in a high-stagnation condition supersonic flowfield using PLIF of nitric oxide (NO) <sup>1,2</sup>, a species naturally present in many flowfields of practical importance. Extension of PLIF techniques to truly quantitative measurements will provide the capability for detailed analysis of flowfields of interest to the aeronautics and propulsion communities and will allow improved experimental validation of computational fluid dynamics models.

Several velocimetry studies have been performed previously using time- or frame-averaged PLIF imaging of NO <sup>3,4</sup> and molecular iodine (I<sub>2</sub>) <sup>5</sup>. In the present work, single-shot PLIF images have been used to provide an instantaneous measurement of the radial velocity field in a high-stagnation temperature, high-speed free jet under the assumption that the flowfield is axisymmetric.

---

\*Work sponsored by AFOSR, Aerospace Sciences Directorate.

One- and two-line PLIF thermometry techniques have been applied in a variety of flowfields using several fluorescent species, including NO,<sup>6-8</sup> I<sub>2</sub>,<sup>5,9</sup> molecular oxygen (O<sub>2</sub>),<sup>7,10</sup> and the hydroxyl radical (OH).<sup>7,11-13</sup> Time- or frame-averaged images have been obtained with I<sub>2</sub> and NO,<sup>5,7</sup> while instantaneous PLIF temperature measurements have been limited to NO<sup>6,8</sup> or O<sub>2</sub> in isobaric, constant mole-fraction flows<sup>7</sup> or to OH in reacting flows.<sup>11-13</sup> Here, single-shot images obtained by exciting transitions from different rotational levels have been used in measuring the temperature field throughout the free jet.

The experiments to be discussed here were performed in a reflection-type shock tunnel facility in which a high-enthalpy, underexpanded free jet is created. The test gas was argon seeded with a small amount of NO. A schematic of a high-pressure ratio free jet is shown in figure 1 with its primary features labelled. This flowfield exhibits extreme variations in pressure and temperature, as well as high speed, which make it a challenging and appropriate environment in which to pursue the development of PLIF for more complex supersonic/hypersonic flows.

In the following sections, a brief description of the PLIF method is given and requirements for quantitative measurements in the shock tunnel free jet flow are discussed. The experimental facility and techniques are described, and PLIF images of the velocity and temperature fields are presented. The experimental results are compared with predictions made using a method of characteristics (MOC) simulation to assess their accuracy and to identify areas where improvement is needed.

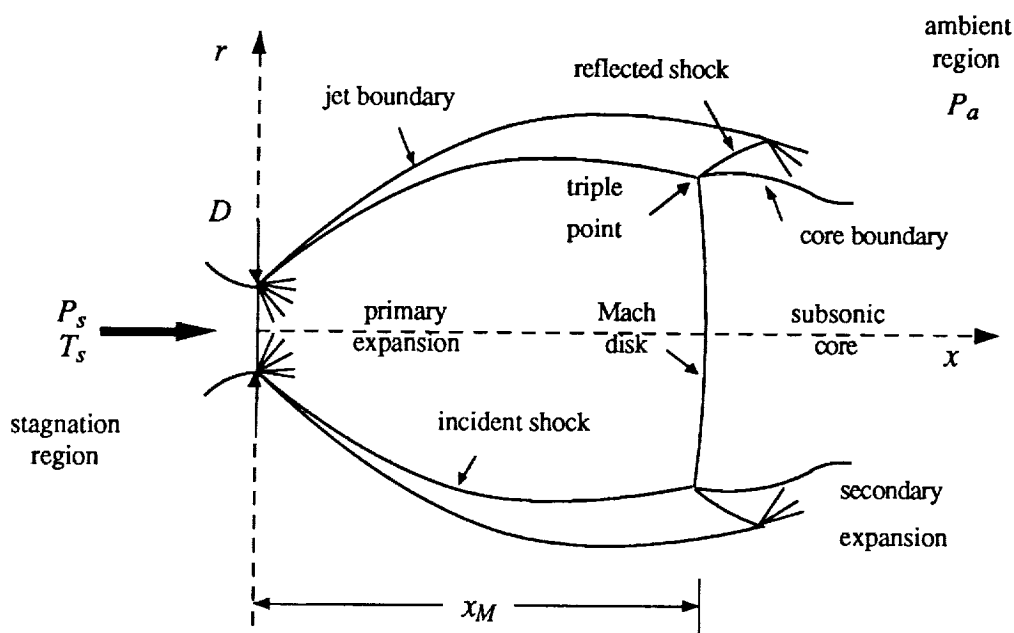


Figure 1. Schematic of underexpanded, supersonic free jet flowfield.

## PLIF TECHNIQUES

PLIF experiments utilize a thin sheet of laser light, directed through the flowfield in the desired plane of observation. The laser is tuned to resonantly excite a particular electronic transition of a molecular species present in the flow; pulsed lasers are used to provide an essentially instantaneous view of the flowfield. A portion of the fluorescent radiation is collected perpendicular to the observation plane by an optical system and imaged onto a two-dimensional solid-state array. The resultant temporally integrated signal is then analyzed to extract a spatially resolved property field. In this experiment, excitation of several electronic transitions in the  $A^2\Sigma^+ \leftarrow X^2\Pi(0,0)$  band of NO at  $\sim 226$  nm is used with broadband fluorescence detection.

The total fluorescence signal for weak excitation of an isolated absorption line is given by:

$$S_f = E_p g B N_a f_{v''j''}(T) \left( \frac{A}{A+Q} \right) C_{opt}, \quad (1)$$

where  $E_p$  is the laser pulse energy;  $g$  is the spectral convolution of the laser and absorption lineshapes;  $A$  and  $B$  are Einstein coefficients;  $N_a$  is the mole fraction of the absorbing species;  $T$  is the temperature;  $f_{v''j''}(T)$  is the Boltzmann fraction of the absorbing state;  $Q$  is the electronic quenching rate of the excited state;  $C_{opt}$  is a constant dependent upon the optical arrangement, collection efficiency, etc.

$S_f$  is also sensitive to the Doppler shift of the absorption induced by the bulk motion of the flow in the direction of laser propagation. In the experimental arrangement used here, laser light propagates perpendicularly through the jet axis. The Doppler shift is thus proportional to the radial component of the velocity,  $V_r$ . Since the flowfield is symmetric, the signals  $S_f(x,r)$  and  $S_f(x,-r)$  result from identical thermodynamic conditions and equal-but-opposite Doppler shifts. For a Gaussian laser lineshape significantly broader than the absorption line, the following expression may be used to obtain  $V_r$  from the fluorescence signal:<sup>1</sup>

$$\frac{S_f(x,r) - S_f(x,-r)}{S_f(x,r) + S_f(x,-r)} = \tanh \left\{ 8 \ln 2 \ v_a \frac{V_r}{c} \frac{v_a - v_l}{\Delta v_l^2} \right\}, \quad (2)$$

where  $v_a$  and  $v_l$  are the center frequencies of the absorption and laser lines, respectively;  $\Delta v_l$  is the FWHM of the laser lineshape; and  $c$  is the speed of light. The right-hand-side of this equation may be simplified for small values of the argument, yielding a linear relationship between the processed signal and the radial velocity. Use of the linearized form can be the source of substantial systematic error in velocity measurements.<sup>3</sup>

Another excitation and processing technique is used to measure the rotational temperature field.<sup>8</sup> A ratio of signals  $S_{j1}(x,r)$  and  $S_{j2}(x,r)$  obtained with the laser tuned first to excite one transition and then another from a different rotational state, but the same lower vibrational level gives the result:

$$R(x,r,T) = \frac{S_{j1}(x,r)}{S_{j2}(x,r)} = C_{12} \exp\left\{-\frac{[F(J''_1)-F(J''_2)]}{kT}\right\}. \quad (3)$$

Here  $C_{12}$  is a constant dependent on the ratio of the laser energies, spectral convolutions, Hönl-London factors (the rotationally-dependent part of  $B$ ), lower state population degeneracies, collection efficiencies, etc. To avoid amplification of existing random error in the inferred temperature,  $F(J''_1)-F(J''_2) \geq kT$  is required. Note that throughout the temperature measurements to be discussed here, the laser was tuned to line center and passed perpendicularly through the jet axis. The images are thus symmetric, i.e.,  $S_j(x,r) = S_j(x,-r)$ .

Because a single excitation/collection system is used at present, temperature-sensitive images with different  $J''$  must be acquired individually. Reproducibility when combining temperature-sensitive images and a symmetric flowfield for velocity extraction from a single image are required. Fortunately, the inviscid core of the free jet flowfield is extremely symmetric and repeatable, except for some slight shot-to-shot variation in the shock position. Instantaneous velocity and temperature fields in the turbulent portions of the flowfield, such as in the shear layer where jet fluid meets the ambient, are not captured with this method, however.

## EXPERIMENTAL FACILITY

### Shock Tunnel System

The facility in which these experiments were performed may be operated either as a shock tube or as a shock tunnel. The performance characteristics of the shock tube are well known, as it has been used previously in several gasdynamic studies.<sup>8</sup> Shock tunnel characterization has also been carried out.<sup>1,2</sup> Figure 2 shows a schematic of the facility, along with the optical and electronic components required for PLIF imaging of the flowfield.

A large range of stagnation conditions,  $P_s$  and  $T_s$ , are available for experiments in the shock tunnel with an initial loading of Ar (or 2% NO in Ar) at room temperature.<sup>2</sup> In all of the experiments, a test gas mixture of 2% NO in Ar initially at 20 torr was loaded into the shock tube, which yielded an incident shock with average Mach number  $M_s = 4.20 \pm 0.05$ . Calculations<sup>14</sup>

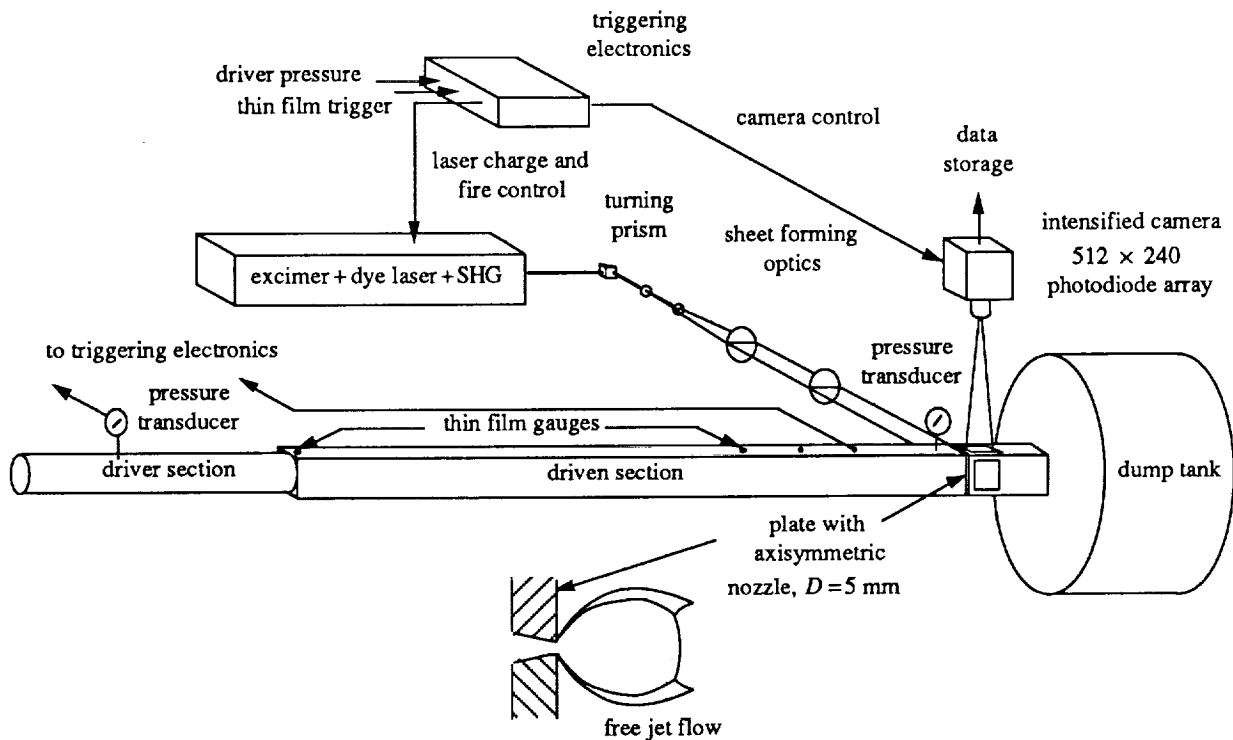


Figure 2. Schematic of experimental facility with associated optical and electronic components for PLIF imaging.

based on the actual shock tube performance indicate that the reservoir conditions were  $T_s = 4200 \pm 200$  K and  $P_s = 3.00 \pm 0.10$  atm. Since the ambient region of the flowfield was decoupled from the initial loading of the shock tube by the presence of a diaphragm at the nozzle,  $P_s/P_a$  may be adjusted independently for a given set of stagnation conditions. Pure Ar at 10 torr formed the ambient of the free jet flowfield, yielding  $P_s/P_a \approx 230$ . PLIF images were acquired shortly after the jet became fully developed.

### PLIF Imaging System

Frequency-doubled light from a broadband, tunable XeCl-pumped dye laser with Coumarin 450 dye was used to excite several transitions in the  $A^2\Sigma^+ \leftarrow X^2\Pi(0,0)$  band of NO. The frequency-doubled output of the laser was  $\sim 0.5$  mJ/pulse with a spot size  $\sim 2$  mm in diameter. A combination of cylindrical lenses was used to form a thin, collimated sheet of laser light. The sheet propagated through the axis of the free jet, where it was  $\sim 5$  cm wide and  $\sim 0.4$  mm thick. The laser detuning ( $\sim 0.13$   $\text{cm}^{-1}$ ) and Gaussian linewidth ( $\sim 0.36$   $\text{cm}^{-1}$ ) were measured just prior to each velocity experiment with an etalon for use in equation 2.

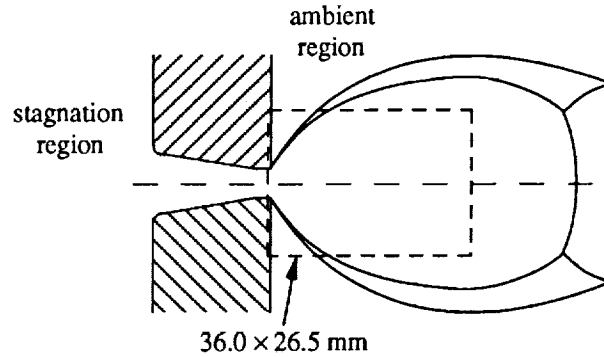


Figure 3. Imaging geometry for PLIF experiments.

An electronic delay sequence initiated firing of the laser/intensifier/camera system to allow observation of the jet flowfield at the proper time during the shock tunnel transient. The broadband fluorescence resulting from excitation of the test gas by a single laser pulse was collected normal to the direction of laser propagation, as shown in figure 2. A Cassegrainian reflecting lens imaged the fluorescence onto a single microchannel plate-intensified CCD array sampled to  $512 \times 240$ . The region of the flowfield imaged in the PLIF experiments is shown in figure 3. A 2 mm thick UG-5 Schott glass filter was used to block elastically scattered light. PLIF data images were corrected for background and laser sheet variations on a pixel-by-pixel basis.

## RESULTS AND DISCUSSION

### Velocity Imaging

The single-shot and 5-frame average radial velocity images shown in figure 4 were obtained by exciting the overlapping transitions  $P_1(5)$  and  $P_1(12)$  of NO. The predicted radial velocity field from the MOC calculation is shown for comparison. The signal level displayed is proportional to  $V_r$ , as indicated by the grey-scale bar.

The measured velocity profiles at  $x/D = 1, 2,$  and  $3$  obtained from the image shown in figure 4(b) are shown in figure 5, along with those from the MOC. The effect of using the nonlinear velocity algorithm (equation 2), rather than its simplified, linear version is illustrated by the departure of the two inferred profiles at high values of  $V_r$ . The linear calculation systematically under-predicts  $V_r$ ; although the noise in the data is amplified by the nonlinear velocity conversion algorithm. In this case, the error resulting from the use of the linear conversion algorithm is as much as 30%. For moderate  $V_r$  (up to  $\sim 1$  km/s) the measured profiles follow the MOC predictions.

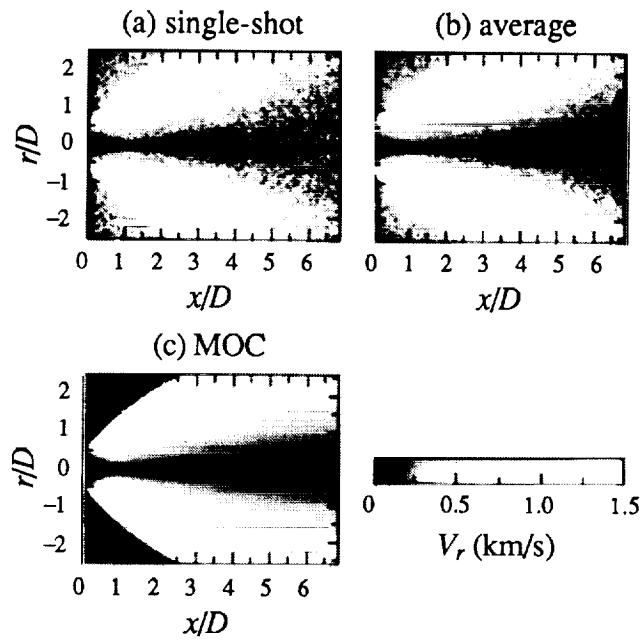


Figure 4. Radial velocity images: (a) single-shot, (b) 5-frame average, and (c) simulated by the MOC. The jet stagnation conditions were:  $P_a = 3.00$  atm,  $T_a = 4200$  K,  $P_j/P_a = 230$  in a test gas of 2% NO in Ar.

Random error in the single-shot velocity data is a consequence of the relatively small NO concentration in the test gas and the limited dynamic range of the data collected. The unprocessed PLIF images had signal-to-noise ratios of 10:1 for small  $x/D$  ( $\leq 2$ ), with minimum levels of  $\sim 5:1$  at large  $x/D$  ( $\geq 5$ ). Random fluctuations of  $\pm 50$ -100 m/s occur in the velocity data obtained from an average image at small  $x/D$ , as shown in figure 5.

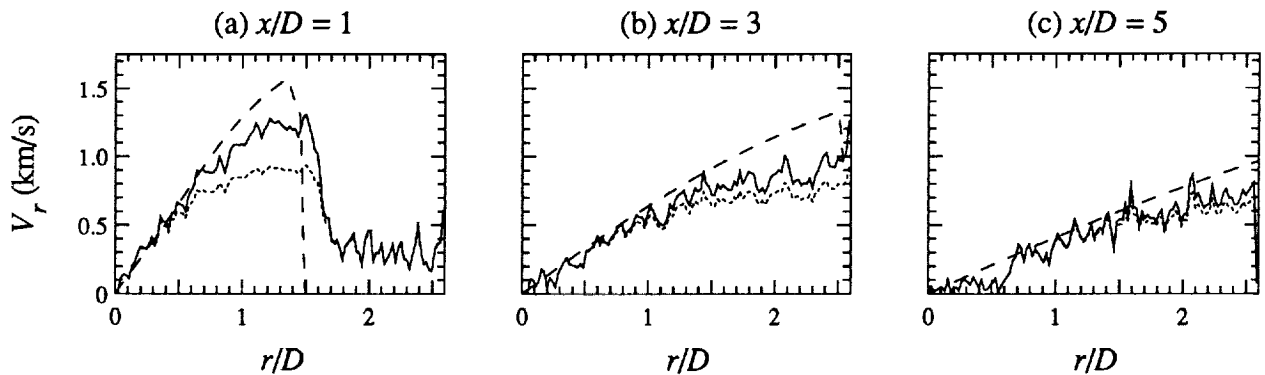


Figure 5. Average measured and calculated radial velocity distributions as a function of normalized radial distance from the jet axis at several axial locations at (a)  $x/D = 1$ , (b)  $x/D = 3$ , and (c)  $x/D = 5$ . The velocity inferred with the nonlinear algorithm is shown with a solid line and the linear result with a dotted one. MOC results are shown with a dashed line.

The systematic error present mainly at large  $V_r$ , probably results from laser lineshape uncertainties and from the insensitivity of the measurement to velocity when  $\Delta v_D \geq v_a - v_l$ , as well.<sup>3</sup> Saturation of the absorption is another source of error which would result in an inferred  $V_r$  lower than expected, particularly at large  $x/D$ , where saturation is most likely to occur.

### Temperature Imaging

Four ro-vibronic transitions from different  $J''$  states were used in measuring the rotational temperature field of the free jet. The limited dynamic range of the data, coupled with the requirement for  $F(J''_1) - F(J''_2) \geq kT$  necessitates the use of more than two transitions to obtain a temperature field with acceptable signal-to-noise throughout. The raw single-shot images exhibit signal-to-noise of 10:1 or better. Images obtained from ratios of individual single-shots as well as from 5-frame average images for two of the six possible line pair combinations are displayed in figure 6. Simulated temperature-dependent fields are shown for comparison. The relative logarithmic conversion from  $R(x,r,T)$  to  $T$  is illustrated by the grey-scale bar labels for each set.

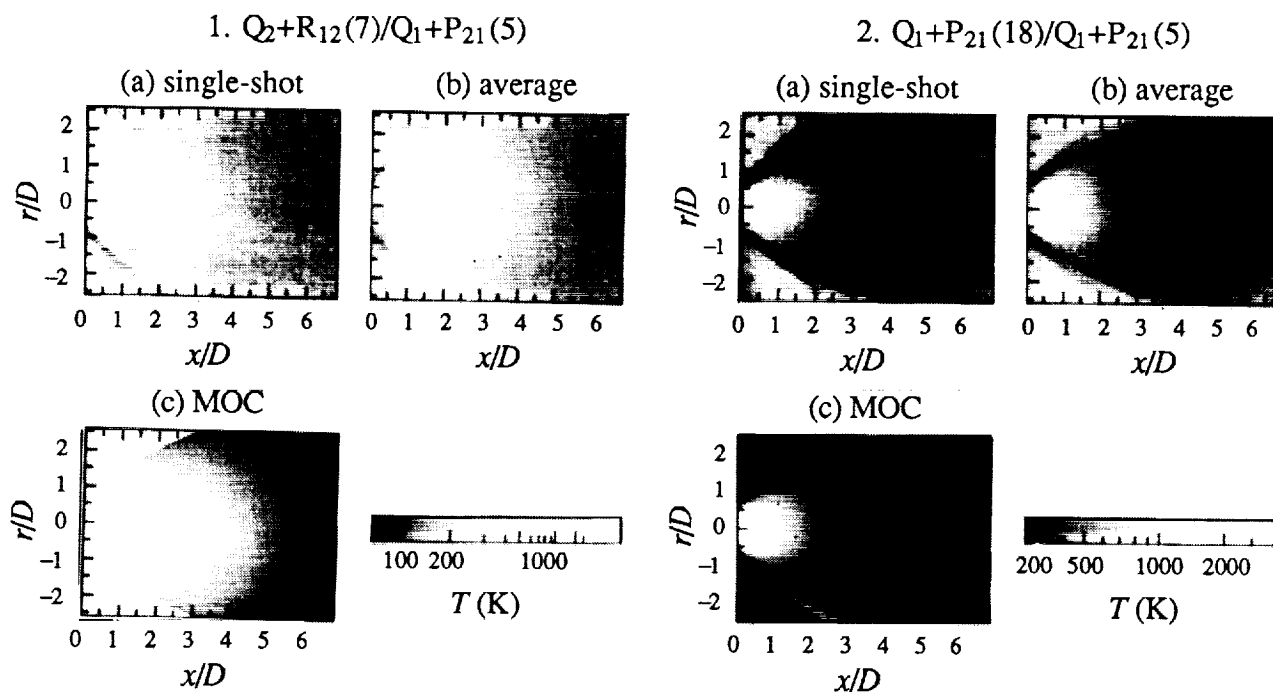


Figure 6. Temperature images: (a) single-shot, (b) 5-frame average, and (c) simulated using the MOC for two line pair ratios: 1.  $Q_2+R_{12}(7)/Q_1+P_{21}(5)$  and 2.  $Q_1+P_{21}(18)/Q_1+P_{21}(5)$ . The jet stagnation conditions were:  $P_a = 3.00$  atm,  $T_a = 4200$  K,  $P_j/P_a = 230$  in a test gas of 2% NO in Ar.



The images of figures 6.1(a) and (b) for the line pair ratio  $Q_2+R_{12}(7)/Q_1+P_{21}(5)$  show a slowly decreasing signal ratio with increasing  $x/D$ , as would be expected with falling temperature. The increasing signal in the PLIF images for  $Q_1+P_{21}(18)/Q_1+P_{21}(5)$  at large  $x/D$  resulted from noise present in that portion of the individual images making up the ratio, exacerbated by the limited dynamic range of the data. For this reason, only the temperature measured in the region  $x/D \leq 5$  is valid using the line pair combination  $Q_1+P_{21}(18)/Q_1+P_{21}(5)$ . Also, very near the nozzle exit, the temperature inferred from any of the line pair combinations may be flawed due to emission and/or to the larger absorption linewidth there. Each line pair ratio has for similar reasons, a limited range of validity.

Figure 7 shows the temperature variation along the jet axis inferred from several line pair combinations. The data for each ratio was obtained using average images for the individual line pairs and is displayed only within the limits discussed above. The axial temperature distribution from the MOC simulation is found to be very well reproduced by the data for  $0.2 \leq x/D \leq 6.8$ . The radial temperature distribution at any given axial location has also been found to be accurately measured using a combination of several line pairs. A uniformly valid average rotational temperature field was obtained with a signal-to-noise ratio of  $\geq 20:1$  throughout the region  $0.2 \leq x/D \leq 6.8$  from single-shot raw data images with signal-to-noise of 10:1 or better.

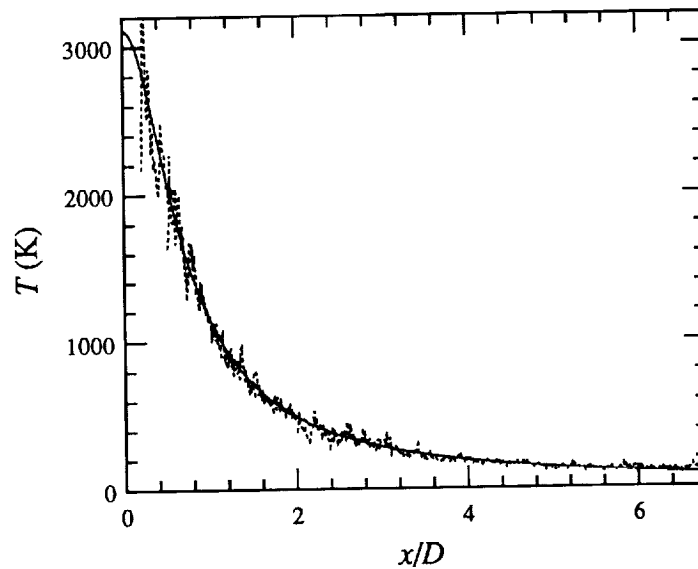


Figure 7. Relative measured and calculated rotational temperature as a function of distance along the jet axis. The temperatures inferred from several average PLIF image ratios are shown with dotted lines. The results shown are from line pair ratios:  $Q_1+P_{21}(28)/Q_2+R_{12}(7)$  ( $0.2 \leq x/D \leq 2.0$ ),  $Q_1+P_{21}(28)/Q_1+P_{21}(5)$  ( $0.5 \leq x/D \leq 2.0$ ),  $Q_1+P_{21}(18)/Q_1+P_{21}(5)$  ( $1.0 \leq x/D \leq 3.0$ ), and  $Q_2+R_{12}(7)/Q_1+P_{21}(5)$  ( $2.0 \leq x/D \leq 6.8$ ). MOC results are shown with a solid line.

## CONCLUSIONS

PLIF imaging of NO has been used in the measurement of velocity and temperature fields in a supersonic, high-stagnation condition, free jet flowfield. Experimental techniques for obtaining quantitative measures of the radial velocity and the rotational temperature were discussed. Application of these methods yielded velocity and temperature fields in good agreement with predictions made using the MOC.

The radial component of velocity was obtained from single-shot PLIF images to give an instantaneous field in the core of the jet. Accurate values of the laser parameters upon which the spectral convolution and, hence, the processed signal depend were used in converting the PLIF signal to velocity. The full, nonlinear form of the velocity conversion algorithm was used in processing the data; and the results compared well with those from the MOC calculation of the flowfield, up to  $\sim 1$  km/s. Substantial deviation from the nonlinear result was found to occur from use of the linear velocity conversion in regions of the jet with large velocities. Single-shot and average radial velocity images were found to have random fluctuations of  $\pm 100$ - $200$  m/s and  $\pm 50$ - $100$  m/s, respectively, having been calculated from PLIF images with maximum signal-to-noise ratios of 10:1 and 20:1.

The strategy implemented for temperature imaging involved the use of several different transitions to obtain a valid measurement with acceptable random fluctuations throughout the free jet flowfield. Single-shot images for each of the four line pairs used had signal-to-noise ratios greater than 10:1. Correspondingly, average images showed random fluctuations of less than  $\pm 5\%$ . Different line pair combinations were found to be of use in calculating the temperature field in different portions of the jet. The range of validity for each ratio of average images was limited to the overlap of the areas in the raw images where adequate signal above background was recorded. Another limit on the use of a given line pair combination arose from the undesirable amplification of noise in areas with large temperature relative to the energy spacing of the two line pairs.

The conversion from signal ratio to temperature was performed in each case by normalizing the measured ratio along a portion of the jet axis to that predicted by the MOC. Generally, excellent agreement was found between the measured and calculated temperature fields in the inviscid core of the jet for  $0.2 \leq x/D \leq 6.8$ . The temperature field resulting from an amalgamation of several line pair ratios typically showed random fluctuations of  $\pm 5\%$ . Maximum random error of  $\pm 10$ - $15\%$  was observed close to the nozzle exit, where the temperature was significantly higher than the equivalent energy spacing for the line pair combination used.

The shock tunnel facility has proven useful as a ground test facility, as it provides dependable high-enthalpy supersonic flow conditions at low cost. Successful measurement of some of the flowfield parameters of interest has been carried out using PLIF of NO and reported here. In the future, development of quantitative PLIF techniques will continue, with extension planned to axial velocity and vibrational temperature field measurements, for example.

#### ACKNOWLEDGEMENT

The authors gratefully acknowledge the contributions of Mr. Frank Levy and Drs. M.P. Lee and J.M. Seitzman.

#### REFERENCES

1. J.L. Palmer, B.K. McMillin, and R.K. Hanson, "Planar-Laser Induced Fluorescence Imaging of Underexpanded Free Jet Flow in a Shock Tunnel Facility," AIAA-91-1687, Jun., 1991.
2. J.L. Palmer, B.K. McMillin, and R.K. Hanson, "Planar-Laser Induced Fluorescence Imaging of Velocity and Temperature in Shock Tunnel Free Jet Flow," AIAA-92-0762, Jan., 1992.
3. P.H. Paul, J.M. Seitzman, M.P. Lee, J.L. Palmer, and R.K. Hanson, "Planar Laser-Induced Fluorescence Imaging in Supersonic Flows," AIAA-89-2912, Jul., 1989.
4. P.H. Paul, M.P. Lee, R.K. Hanson, "Molecular Velocimetry Imaging of Supersonic Flows Using Planar Laser-Induced Fluorescence of NO," *Optics Letters*, Vol. 14, 1989, pp. 417-421.
5. R.J. Hartfield, Jr., S.D. Hollo, and J.C. McDaniel, "A Unified Planar Measurement Technique for Compressible Flows Using Laser-Induced Iodine Fluorescence," AIAA-92-0141, Jan., 1992.
6. J.M. Seitzman, G. Kychakoff, and R.K. Hanson, "Instantaneous Temperature Field Measurements Using Planar-Laser Induced Fluorescence," *Optics Letters*, Vol. 10, 1985, pp. 439-441.
7. R.K. Hanson, J.M. Seitzman, and P.H. Paul, "Planar Laser-Induced Fluorescence Imaging of Combustion Gases," *Applied Physics B*, Vol. 50, 1989, pp. 441-454.

8. B.K. McMillin, J.L. Palmer, and R.K. Hanson, "Two-Dimensional Temperature Measurements of Nonequilibrium Supersonic Flows Using Planar Laser-Induced Fluorescence of Nitric Oxide," AIAA-91-1670, Jun., 1991.
9. T. Ni-Imi, T. Fujimoto, and N. Shimizu, "Method for Planar Measurement of Temperature in Compressible Flow Using Two-Line Laser-Induced Iodine Fluorescence," *Optics Letters*, Vol. 15, 1990, pp. 918-920.
10. M.P. Lee, P.H. Paul, and R.K. Hanson, "Quantitative Imaging of Temperature Fields in Air Using Planar Laser-Induced Fluorescence of O<sub>2</sub>," *Optics Letters*, Vol. 12, 1987, pp. 75-77.
11. P.H. Paul and R.K. Hanson, "Applications of Planar Laser-Induced Fluorescence Imaging Diagnostics to Reacting Flows," AIAA-90-1844, Jul., 1990.
12. M.G. Allen, S.J. Davis, and K. Donohue, "Planar Measurements of Instantaneous Species and Temperature Distributions in Reacting Flows: A Novel Approach to Ground Testing Instrumentation," AIAA-90-2383, Jul., 1990.
13. P.H. Paul, U.E. Meier, and R.K. Hanson, "Single-Shot, Multiple-Camera Planar Laser-Induced Fluorescence Imaging in Gaseous Flows," AIAA-91-0459, Jan., 1991.
14. A.G. Gaydon and I.R. Hurle, *The Shock Tube in High-Temperature Chemical Physics*, Reinhold, NY, 1963.

**PLANAR LASER-INDUCED FLUORESCENCE IMAGING  
OF OH IN THE EXHAUST OF A BI-PROPELLANT THRUSTER**

P. H. Paul and N. T. Clemens  
Combustion Research Facility  
Sandia National Laboratories  
Livermore, CA 94550

D. B. Makel  
Aerojet Propulsion Division  
Gencorp Aerojet  
Sacramento, CA 95813

**SUMMARY**

Planar laser-induced fluorescence imaging of the hydroxyl radical has been performed on the flow produced by the exhaust of a subscale  $H_2/O_2$  fueled bi-propellant rocket engine. Measurements were made to test the feasibility of OH (0,0) and (3,0) excitation strategies by using injection seeded XeCl and KrF excimer lasers, respectively. The flow is produced with hydrogen and oxygen reacting at a combustor chamber pressure of 5 atm which then exhausts to the ambient. The hydroxyl concentration in the exhaust flow is approximately 8%. Fluorescence images obtained by pumping the  $Q_1(3)$  transition in the (0,0) band exhibited very high signals but also showed the effect of laser beam absorption. To obtain images when pumping the  $P_1(8)$  transition in the (3,0) band it was necessary to use exceptionally fast imaging optics and unacceptably high intensifier gains. The result was single-shot images which displayed a signal-to-noise ratio of order unity or less when measured on a per pixel basis.

**INTRODUCTION**

Measurement techniques based on planar laser-induced fluorescence (PLIF) imaging provide a powerful tool for the study of complex reacting gaseous flows. In addition to the wide use of PLIF for flow visualization, there is also a growing body of work which has concentrated on developing PLIF spectroscopic strategies to measure species concentration, temperature, pressure and velocity<sup>1</sup>. The present effort is directed towards the evaluation of these techniques for application to flows produced by hydrogen-fueled rocket engines. Poor injector mixing, flow stratification, and excess fuel film cooling in these engines represent a performance loss which reduces the engine specific impulse. High oxidizer concentrations near the thrust chamber wall and in the nozzle, which result from poor mixing or injector maldistribution, can result in reduced engine life.

Cold flow imaging studies have been performed using particulates\* or molecular tracers (e.g. iodine or NO). However, for actual engine evaluation, a nascent molecular species is required. Of particular interest is the hydroxyl radical; the concentration distribution of OH may be viewed as a zero'th order indicator of mixture fraction in the high temperature gases. Further, OH is an excellent candidate for PLIF temperature and velocity imaging<sup>2</sup>. In the following we describe the results of OH imaging experiments using (0,0) and (3,0) excitation performed with injection seeded XeCL and KrF excimer lasers, respectively. The measurements were made in the exit plane of a subscale O<sub>2</sub>/H<sub>2</sub> engine. The high temperature, supersonic flow studied here is similar to the conditions encountered in large scale engines.

For an optically thin medium, the fluorescence signal on a per laser pulse basis may be written as,

$$S_f = C_{opt} f_B(T) E_p B g_{al} \chi_a n_0 g_D A/(A+Q+V+P) (1 - H(E_p B)) \quad (1)$$

Here  $C_{opt}$  is a collection of constants which describe the optical system,  $f_B$  is the Boltzman fraction in the ground ro-vib state,  $E_p$  is the laser energy,  $B$  is the Einstein coefficient for absorption,  $\chi_a n_0$  is the number density of the absorbing species,  $g_D$  is the detector spectral response fraction, and  $P$  is the excited state predissociation rate. The other terms in equation 1 must be thought of as functions of field variables  $\mathbf{E}$ ; that is they depend on the local distribution of temperature, pressure and perturbing species mixture fraction. Thus  $g_{al}(\mathbf{E})$  is the convolution of the absorption and laser spectral profiles which also depends on velocity through the molecular Doppler-shift,  $A(\mathbf{E})$  is the effective spontaneous emission rate,  $Q(\mathbf{E})$  is the collisional quenching rate,  $V(\mathbf{E})$  is the excited state vibrational transfer rate and  $H(E_p B, \mathbf{E}, \tau_{las})$  is a correction which goes to zero in the limit of weak pumping.

By using various pump/detection strategies, different terms in equation 1 can be made dominant. Here the cases of particular interest are termed 'predissociation' and 'quenching' dominated. These are to first order

$$\begin{aligned} S_f &\propto f_B(T) \chi_a n_0 & ; & & P \gg A+Q+V \\ S_f &\propto f_B(T) T^{-\alpha} \chi_a & ; & & P = 0, Q+V \gg A \end{aligned} \quad (2)$$

In both cases, careful selection of the ro-vib transition can be used to minimize the stray temperature dependence giving images that primarily represent OH number density or mixture fraction, respectively. The predissociation limit is attractive since the influence of collisional effects can be removed<sup>3</sup>. For flow visualization studies, these are adequate descriptions of how the signal depends on field variables. Even when the image has a secondary dependence on temperature or mixture fraction such data can still be used effectively to study flowfield topology<sup>4</sup>. To extend the technique to a 'quantitative' measurement requires a much more detailed approach to both the

\* D. B. Makel and I. M. Kennedy, 'Cold flow mixing measurements for a swirl triplet liquid rocket gas generator system,' (submitted to AIAA Journal of Propulsion and Power, 1992).

fluorescence model and to imaging system performance<sup>5</sup>. We will address some of these issues in the discussion below.

## EXPERIMENTAL APPARATUS

Sets of images using single laser shot PLIF of OH were obtained using two different excitation strategies. The first scheme uses the injection seeded XeCl excimer (Lambda Physik, EMG 150 T MSc) to excite the  $Q_1(3)$  transition in the OH  $A^2\Sigma \leftarrow X^2\Pi(0,0)$  band. Broadband detection was employed and the images were recorded with an f/4.5 lens (Nikon, UV-Nikor) on a custom-built gated intensified CCD array operating in an RS-170 format. Images were digitized to 8-bits with a Data Translation DT2851 frame grabber in an PC/AT computer. This technique has been used before for reacting flow studies<sup>4</sup> and for PLIF velocity imaging<sup>2</sup>. The second scheme uses the same laser operated on KrF to excite the  $P_1(8)$  transition in the OH  $A^2\Sigma \leftarrow X^2\Pi(3,0)$  band. These measurements were made with the same camera now equipped with a long pass filter (1 mm Schott WG-280) which was required to reject Rayleigh scattering and a custom built f/1.2 imaging lens. PLIF measurements of OH using this later method have been reported by Andresen et al.<sup>6</sup> and single point LIF measurements have been reported by Pitz et al.<sup>7</sup>

The experimental setup is shown in figure 1. The laser and camera were operated in a 60 Hz mode. The laser beam was expanded into a 10 cm high sheet which was positioned to bisect the engine exhaust plume. The sheet thickness was estimated to be 0.4 mm full-width at  $1/e^2$ . Line tuning was optimized using a propane torch during pretest and checked post-test. A schematic of the subscale engine (5 lbf motor with an expansion ratio of 1.8:1) is shown in figure 2. The engine consists of an integral spark ignitor/injector, a water cooled combustion section, and a water-cooled nozzle. The oxidizer is injected on the centerline through the gap formed by the ignitor electrode and the engine body. The fuel is injected radially into the oxidizer flow and downstream of the spark gap. The combustion chamber is designed with a turbulence ring to promote mixing. The nozzle used for the present study has a 5 mm throat made of a ZrCu alloy and the external nozzle body is tapered to minimize interference to the laser sheet and imaging optics. The combustion chamber can be operated at pressures up to 10 atm producing flow Mach numbers in excess of 2 in the exit plane.

The flow conditions used for the present study were:  $P_0 = 72$  psia,  $f(O_2) = 182$  SLPM,  $f(H_2) = 182$  SLPM. These give a mixture ratio of 8.0 and exit plane conditions calculated to be:  $T_{static} = 2670$  K,  $P_{static} = 8$  psia,  $v = 2560$  m/s and  $M = 1.95$ . Species mole fractions in the exit plane were calculated from equilibrium to be: 0.08, 0.70, 0.03, 0.11, 0.04, and 0.02 for OH, H<sub>2</sub>O, O<sub>2</sub>, H<sub>2</sub>, H and O, respectively. During the runs the oxygen flowrate was metered using a mass flow controller and the hydrogen flowrate was controlled with a sonic orifice. Engine temperatures and pressures were digitized and stored on a computer. Chamber ignition was performed with an oxygen lead to minimize the exhaust of unreacted hydrogen. Nitrogen flows controlled by check valves were used to automatically purge the engine at start-up and shut-down.

## EXPERIMENTAL RESULTS

Figure 3 is a conventional time-exposure photograph of the exhaust plume which shows the diamond shock structure characteristic of an over-expanded jet. The luminosity of the plume is apparent to the eye for over 25 cm downstream of the nozzle, although the last visible shock diamond is seen at approximately 7.5 cm downstream. Figure 4 shows two representative single-shot PLIF images obtained by using (0,0) excitation. The signal levels are very high and required the use of a low intensifier gain to prevent saturation of the CCD camera. The high signal level becomes apparent when one considers that resonant detection is being used thus: the bright spots which turn to black at their center are the result of scattering from water droplets which are regularly ejected by the engine; while the faint blur seen at the bottom of the images is the nozzle body which scatters some stray laser light (the laser sheet being cut-off at approximately 0.5 cm above the engine). One may also notice a systematic left-to-right attenuation in the signal, the result of a large absorption coefficient for the  $Q_1(3)$  line (of order  $100 \text{ cm}^{-1} \text{ atm}^{-1}$ ). These images are quite similar to that which would be obtained in a simple zero-heat-release reactive mixing experiment. Downstream of the potential core, intrusions of ambient air are seen to cut completely across the jet which often exhibit behavior similar to 'flame-tip' burnout or separation. No evidence of the diamond shock pattern is seen in these images since the primary signal dependence is on OH mole fraction and temperature, the latter being only slightly modulated in the weak shocks present in this flow.

Figure 5 shows two representative single-shot PLIF images obtained by using (3,0) excitation. The difference from the previous data set is dramatic. The recorded signal levels are exceptionally low and as a result are subject to strong signal shot noise. This is apparent when one considers that these images were obtained using a microchannel plate (MCP) gain in excess of  $1500 \text{ e}^-/\text{e}^-$ , thus the pattern in the background is likely the result of thermal emission from the MCP. Further it is possible to again see evidence of the engine nozzle, this being the result of secondary scattering of the OH emission or scattered laser light as collected through a filter attenuation of order  $10^{-5}$ . A 15-frame average of images taken with (3,0) excitation, given in figure 6, shows some evidence of the diamond shock structures as the signal is now directly dependent on total density. However the noise level in this averaged image is still of order 20% peak-to-peak of the total signal variation seen across the first diamond shock (see figure 7). It is also of note that when the long-pass filter was removed the Rayleigh scattering from the ambient room air overwhelmed the OH PLIF signal, and it was possible to readily observe the drop in Rayleigh signal in the low density engine exhaust gases.

## DISCUSSION

For the (0,0) pumping case, an  $f/4.5$  lens was used and the intensifier MCP gain was approximately  $50 \text{ e}^-/\text{e}^-$ . While for the (3,0) pumping case an  $f/1.2$  lens was used and the intensifier gain was approximately  $1500 \text{ e}^-/\text{e}^-$ . The fraction of the  $v'=3$  emission collected through the



longpass filter was estimated by a weighted sum of the product of filter spectral transmission and band lifetimes and found to be 78%. We find the ratio of the measured signals on an equal imaging system basis to be  $S_{f(0,0)}/S_{f(3,0)} \approx 350$ . Using the predictions given by Seitzman<sup>8</sup> and adjusting the (0,0) quenching rate to reflect the conditions studied here ( $Q(\text{H}_2\text{O}) \approx 1.68/\text{ns}$  and  $Q(\text{H}) \approx 0.19/\text{ns}$ ; see Appendix A) we find a value of  $S_{f(0,0)}/S_{f(3,0)} \approx 524$  which is in reasonable agreement with the experimental observation. We expect the measured value to be somewhat lower than the prediction since some degree of depopulation of the ground-state with (0,0) pumping should occur in the experiment.

The quality, that is the spatial resolution and signal-to-noise performance, of the images obtained in these experiments has a direct impact on the ability to use such data for quantitative measurements. In both of the cases described above the image data is in the signal-shot-noise limit. Thus the signal-to-noise ratio on a per-pixel basis is given by  $S/N = \sqrt{(\eta S_f / \kappa(G))}$ , where  $\eta$  is the detector quantum efficiency and  $\kappa$  is the intensifier noise factor<sup>5</sup>. The useful signal dynamic range,  $D_s$ , is defined to be the ratio of that signal which produces a non-recoverable saturation to that signal which gives an S/N of unity,  $D_s \approx C_s S(G) / (G \kappa(G))$ <sup>5</sup>. Here  $C_s$  is a constant which depends on the details of the camera system,  $S$  is an MCP saturation function and  $G$  is the MCP electron gain. Values for the conditions used in the present experiment were evaluated using a model for the image and signal transfer function of intensified cameras<sup>5</sup>. For the (0,0) pumping experiment we find  $\kappa \approx 3.7$  and  $D_s \approx 114$ . In this case the S/N could have actually been improved by a slight increase in lens f-number with a commensurate increase in MCP gain. For the case of (3,0) pumping we find  $\kappa \approx 2.2$  and  $D_s \approx 4$ . For this later case the severe compression in dynamic range would preclude a quantitative measurement even if the S/N were improved. The modulation transfer function, which quantifies the ability of the imaging system to transfer object contrast to the image, for the fast lens used for the (3,0) experiment is calculated to be significantly worse than that obtained in the (0,0) experiment. This observation is with regard to both the blur spot radius and to the shape of the function at intermediate spatial frequencies. Even if the S/N were improved in the (3,0) experiment, significant systematic errors would occur in taking gradients to obtain scalar dissipation or using radiometric image processing to obtain temperature as a direct result of the contrast reduction.

In the present experiment, the OH is found in a bath composed mostly of water vapor, however the effect of collisions with the radicals cannot be disregarded. For the conditions at the nozzle exit the predominant electronic quencher is water followed by atomic hydrogen and the conventional view would be that vibrational energy transfer (VET) could be neglected. However, OH is present at 8% and both OH-A and OH-X states have large dipole moments; thus a noticeable VET rate is expected as a result of 'near-resonant' electronic energy transfer (e.g.  $\text{OH}^{**} + \text{OH} \rightarrow \text{OH}^\dagger + \text{OH}^*$  where the asterisk denotes electronic excitation and the dagger denotes vibrational excitation)<sup>9</sup>. This process can be quite effective and has been observed in NO<sup>10</sup>. Using the model of Cross and Gordon<sup>11</sup> we estimate a contribution to the total VET rate of

$V_3 = V_{32} + V_{31} + V_{30} \approx 0.12/\text{ns}$  due to collisions with OH  $X^2\Pi$  at the engine nozzle exit conditions. Upon mixing with the ambient air the temperature and radical population in the exhaust products will drop and  $N_2$  and  $O_2$  will be introduced as collision partners. For  $v'=3$  and conditions found in  $H_2/\text{air}$  post flame products at atmospheric pressure, we estimate that the total VET rate due to  $N_2$  to be near equal to the electronic quenching rate due to  $H_2O$ . Evidence for effective VET from  $v'=3$  can be seen in OH fluorescence dispersion spectra obtained in laminar  $H_2/O_2$  and butane/air flames<sup>†</sup>. For the butane flame, emission in the (0,0) band is larger than emission in the (1,1) band which is noticeably larger than emission from  $R_2(6) (3,3)$ . This result is likely due to the presence of  $CO_2$  and suggests that multiple VET steps are occurring. In the  $H_2/O_2$  flame, emission in the (0,0) and (1,1) bands is near equal and both are smaller than emission from  $R_2(6) (3,3)$ . The later result is consistent with the measurement having been made in a laminar flame with near equilibrium OH concentrations and without the presence of  $N_2$ .

For the range of 1400 K to 2700 K we do not expect a strong variation in the  $v'=0$  quenching rate for the ambient air or the engine exhaust products except as occurs due to the loss of the atomic hydrogen as a collision partner. We estimate that the effective quenching cross-section will decrease by no more than 10% from conditions at the nozzle exit plane to conditions of an equal mixture of frozen exhaust products with room air. Thus the variation in signal using (0,0) pumping depends directly on OH mole fraction and on  $f_B(T)/\sqrt{T}$ . This latter function goes approximately as  $T^{-1.4}$  and will increase nearly three-fold in going from 2700 K to 1400 K. A much better choice for the study would have been a value of  $N'' \approx 10$  which would have flattened out this temperature dependence. However this is not possible using the XeCl excimer laser. An alternative approach would be to use a doubled dye laser to pump the (1,0) band or to use the KrF excimer as Raman shifted in  $D_2$  to pump the (2,0) band. The later approach should provide approximately 25 mJ of useable energy from 267.7 to 268.9 nm thus access to strong transitions with near optimal values for  $N''$  in the (2,0) band as well as freedom from radiation trapping effects.

Collisional effects play an important role in the description of the dependence of the fluorescence signal on the distribution of flow scalars. Pumping to predissociated states of OH does yield a reasonably well-defined dependence, however, the signal levels are too low for single-shot PLIF imaging. When this technique is applied to flows that produce a noticeable VET rate (e.g. vitiated air) the signal will be further reduced by the need to reject emission from  $v' \neq 3$ . Predissociated techniques can be successful for single-shot imaging and for relatively small flows when the target molecule is a major species and exhibits a large absorption cross-section (e.g.  $NO D^2\Sigma-X^2\Pi$  as a flow tracer or  $O_2 B^3\Sigma-X^3\Sigma$ ). Since OH is generally a minor species and the predissociated states exhibit a relatively small absorption cross-section, PLIF using predissociated states of OH is probably relegated to time-averaged imaging. In many cases, the total cross-section for electronic quenching of OH  $A^2\Sigma(v' < 3)$  will contribute a relatively weak dependence on flow scalars, although a reasonably well-defined dependence can be elucidated. In either case,

<sup>†</sup> (private communication: Dr. P. Andresen, Max-Planck Inst, Göttingen, 1989)

quantitative measurements will need to be based on ratiometric image processing, which to a large extent can cancel-out these collisional effects<sup>2</sup>.

## CONCLUSIONS

Planar laser-induced fluorescence imaging of OH has been conducted in the exhaust of an H<sub>2</sub>/O<sub>2</sub> fueled rocket engine. Tests have been made using both OH (0,0) and (3,0) excitation, the former being collisional quenching and the latter predissociation dominated. The measurements support a view that single-shot PLIF measurements of OH using predissociated excited states will not yield sufficient signal for flow visualization studies much less quantitative imaging. As expected Q<sub>1</sub>(3) (0,0) excitation was found to be subject to beam attenuation and presumably radiation trapping. For flow studies of small engines use of the weaker R<sub>2</sub>(3) (0,0) transition will provide a convenient means to reduce laser beam attenuation to acceptable levels. For the conditions expected in engine exhausts radical species have been identified as having a significant role in collisional deexcitation; specifically OH as a VET partner via 'near-resonant' exchange and atomic hydrogen as a quenching partner. To avoid beam attenuation, to minimize the effect of radiation trapping and to reduce the dependence on temperature, a scheme based on pumping the (2,0) band has been proposed. This may be conveniently performed by using D<sub>2</sub> Raman shifted radiation from the injection seeded KrF excimer laser.

## ACKNOWLEDGEMENTS

The authors would like to acknowledge Mr. J. Muss and Ms. J. Griggs of Gencorp Aerojet for assistance with the experimental setup and for the thermal analysis and instrumentation of the engine. Dr. Paul and Dr. Clemens are supported by the Department of Energy, Office of Basic Energy Sciences, Division of Chemical Sciences.

## APPENDIX A

Collisional effects in OH A<sup>2</sup>Σ have been studied in some detail<sup>12</sup>. However, there is only limited experimental data for temperatures above 1200 K and little or no data for v' > 1. Thus we resort to a model of the process to extrapolate the experimental data base to the conditions of interest. This model is based on the assumption that the gross behavior of quenching and vibrational relaxation in OH A<sup>2</sup>Σ is described by long lived collision-complexes<sup>13</sup>. The rate for process W (electronic quenching or vibrational relaxation), due to collision partners p, is given by

$$W = n_0 \langle v_{OH} \rangle \sum_p \chi_p \sigma_{w,p}(T, N') \sqrt{(1+m_{OH}/m_p)} \quad (A.1)$$

Here σ is the species and process specific thermally averaged cross-section, which is a function of temperature and rotational level. Taking a classical approach, the cross-section is given by

$$\sigma_W = \pi \int_{\mathbf{v}} \int_{\Theta} v f_B(v, \Theta) \int_b P_W(b, v, \Theta) db^2 d\Theta dv / \langle v \rangle \quad (\text{A.2})$$

Here  $P_W$  is the probability of process  $W$  occurring upon collision as a function of the collision impact parameter  $b$ , the relative velocity  $v$ , and relative molecular orientation  $\Theta$ . In the model we take  $P_W$  to be a product of the probability for capture within a barrier formed by centripetal repulsion and molecular attraction, and a constant probability for the specific process,  $P_Q$  or  $P_V$ . We take the attractive forces to be given by point multipole expansions. With these assumptions equation (A.2) reduces to a 6-fold nested integral which contains a set of transcendental equations. Previous approaches to a solution have taken the collision partners to be in the orientation most favorable for dipole-dipole interactions; this reduces the problem to a single integral over a transcendental equation<sup>14</sup>. We find that by neglecting the quadrupole-quadrupole and higher multipole terms and by transforming to a radial integral metric the problem reduces to a three-fold integral over an explicit function and can be easily evaluated.

The present formulation does not introduce a direct dependence on rotational level and the model does not provide an absolute value for the cross-section. Thus we assume that: solutions for OH in the most attractive orientation correspond to the case of  $N'' = 0$ ; and solutions for OH with a geometrically averaged potential correspond to the case of  $N'' \gg 1$ . Analytical perturbation solutions in these limits suggest the functional form,

$$\sigma(T, N') \approx \sigma(T_r, 0) y^{-p_1} ((B_{N'} + b y)/(1 + b))^{p_2} \quad (\text{A.3})$$

where  $y \equiv T/T_r$  and  $B_{N'}=1$  for  $N'=0$  and goes to zero for large  $N'$ . The coefficients  $p_1$ ,  $p_2$  and  $b$  are collision partner specific and are determined from fits to the results of the full simulation, where the inputs are molecular electrical properties. Using the suggestion of Crosley<sup>12</sup> we take  $B_{N'} = \exp(-aN'(N'+1))$ . Experimental data at  $T_r = 300$  K are used to provide the coefficients  $\sigma(T_r, 0)$  and  $a$ , which are collision partner and process specific.

Simulations have been evaluated for all of the major collision partners present in the  $H_2$ /air combustion system. Comparisons to the available experimental data are favorable for all species except for electronic quenching by  $N_2$  although VET by  $N_2$  is well described. One possible explanation is that the necessary mixing of internal states required for quenching by  $N_2$  introduces a strong orientation dependence. In the present model this detail has been relegated to the constant  $P_Q$ . By using  $N_2$  quenching data for  $N' \geq 3$  to provide the fit we find a significantly better match to measurements at 1200 K. Compared to the use of the 'optimum dipole' result<sup>15</sup>, this formulation provides a significant improvement in the prediction of high temperature behavior for all of the species. Full tabulation of these results is beyond the scope of the present paper but we give as example the terms for quenching OH  $A^2\Sigma(v'=0)$  by  $H_2O$ :  $\sigma_0 = 94.1$ ,  $p_1 = 0.667$ ,  $a = 0.019$ ,  $b = 0.21$ , and  $p_2 = 0.33$ .

## REFERENCES

- 1 R. K. Hanson, J. M. Seitzman and P. H. Paul, 'Planar laser-induced fluorescence imaging in combustion gases,' *Appl. Phys.* **B 40**, pp 441 (1990). R. K. Hanson 'Combustion diagnostics: planar imaging techniques,' in *Proc. 21<sup>st</sup> Symposium (international) on Combustion*, (The Combustion Inst., 1986), pp 1677.
- 2 P. H. Paul, U. E. Meier, and R. K. Hanson, 'Single-shot, multiple-camera planar laser-induced fluorescence imaging in gaseous flows,' *AIAA 29<sup>th</sup> Aerospace Sciences Conf.* (1991), AIAA-91-0459.
- 3 P. H. Paul, M. P. Lee and R. K. Hanson, 'Quantitative imaging of temperature fields in air using planar laser-induced fluorescence imaging of O<sub>2</sub>,' *Opt. Letts.* **12**, pp 75, (1987).
- 4 J. M. Seitzman, A. Üngüt, P. H. Paul and R. K. Hanson, 'Imaging and characterization of OH structures in a turbulent nonpremixed flame,' in *Proc. 23<sup>rd</sup> Symposium (international) on Combustion*, (The Combustion Inst., 1991), pp 637.
- 5 P. H. Paul, 'The application of intensified array detectors to quantitative planar laser-induced fluorescence imaging,' *AIAA 27<sup>th</sup> Joint Prop. Conf.* (1991), AIAA 91-2315.
- 6 P. Andresen, A. Bath, W. Gröger, H. W. Lulf, G. Meijer and J. J. ter Meulen, 'Laser-induced fluorescence with tuneable excimer lasers as a possible method for instantaneous temperature field measurements at high pressures: check with an atmospheric flame,' *Appl. Opt.* **27**, pp 365, (1988).
- 7 R. W. Pitz, T. S. Cheng, S. R. March and J. A. Wehrmeyer, 'Effects of swirl on finite-rate chemistry in lifted jet diffusion flames,' *AIAA 27<sup>th</sup> Joint Propulsion Conf.* (1991), AIAA 91-2319.
- 8 J. M. Seitzman, *Quantitative applications of fluorescence imaging in combustion*, ' Doctoral Dissertation, (Stanford Univ. 1991), HTGL report T-275.
- 9 J. T. Yardley, *Introduction to molecular energy transfer*, (Academic, 1980).
- 10 L. A. Melton and W. Klemperer, *JCP* **55**, pp 1468, (1971). R. G. Gordon and Y-N. Chiu 'On a first-order electronic dipole-dipole mechanism for energy transfer in molecular collisions,' *JCP* **55**, pp 1469, (1971).

- 11 R. J. Cross and R. G. Gordon, 'Long-range scattering from anisotropic potentials: dipole-dipole scattering,' *JCP* **45**, pp 3571 (1966).
- 12 D. R. Crosley, 'Rotational and translational effects in collisions of electronically excited diatomic hydrides,' *JPC* **93**, pp 6273 (1989).
- 13 R. K. Lengal and D. R. Crosley, 'Rotational dependence of vibrational relaxation in  $A^2\Sigma^+$  OH,' *Chem. Phys. Letts.* **32**, pp 261 (1975).
- 14 P. W. Fairchild, G. P. Smith and D. R. Crosley 'Collisional quenching of  $A^2\Sigma^+$  OH at elevated temperatures,' *JCP* **79**, pp 1795 (1983).
- 15 R. A. Copeland and D. R. Crosley, 'Temperature dependent electronic quenching of  $OH(A^2\Sigma^+, v'=0)$  between 230 and 310 K,' *JCP* **84**, pp 3099 (1986). N. L. Garland and D. R. Crosley, 'On the collisional quenching of electronically excited OH, NH and CH in flames,' in *Proc. 21<sup>st</sup> Symposium (international) on Combustion*, (The Combustion Inst., 1986), pp 1693.

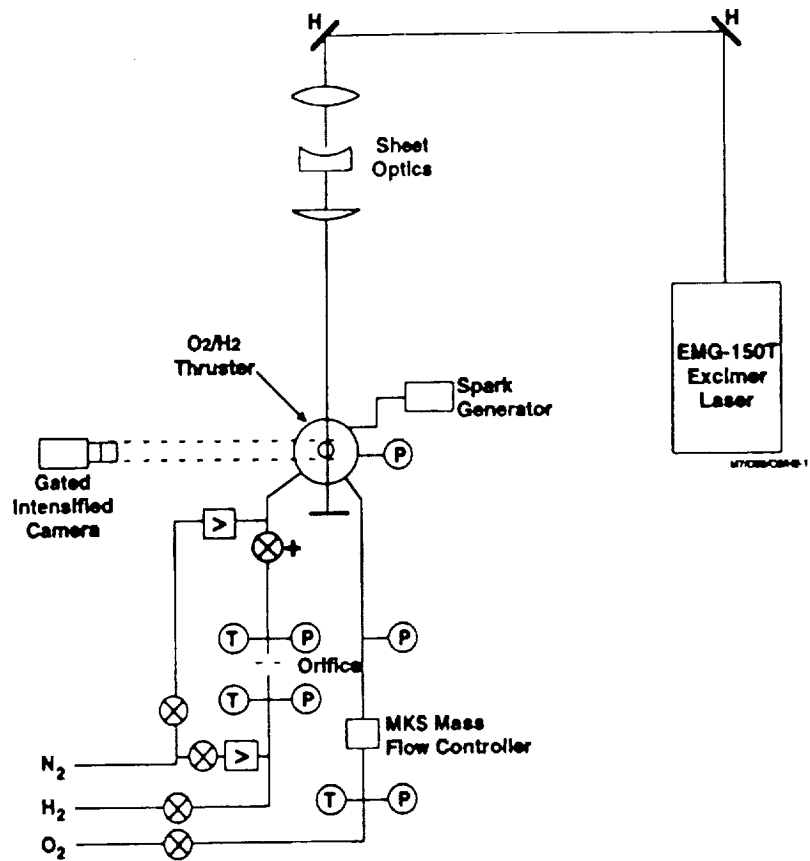


Figure 1. Schematic of the experimental setup.

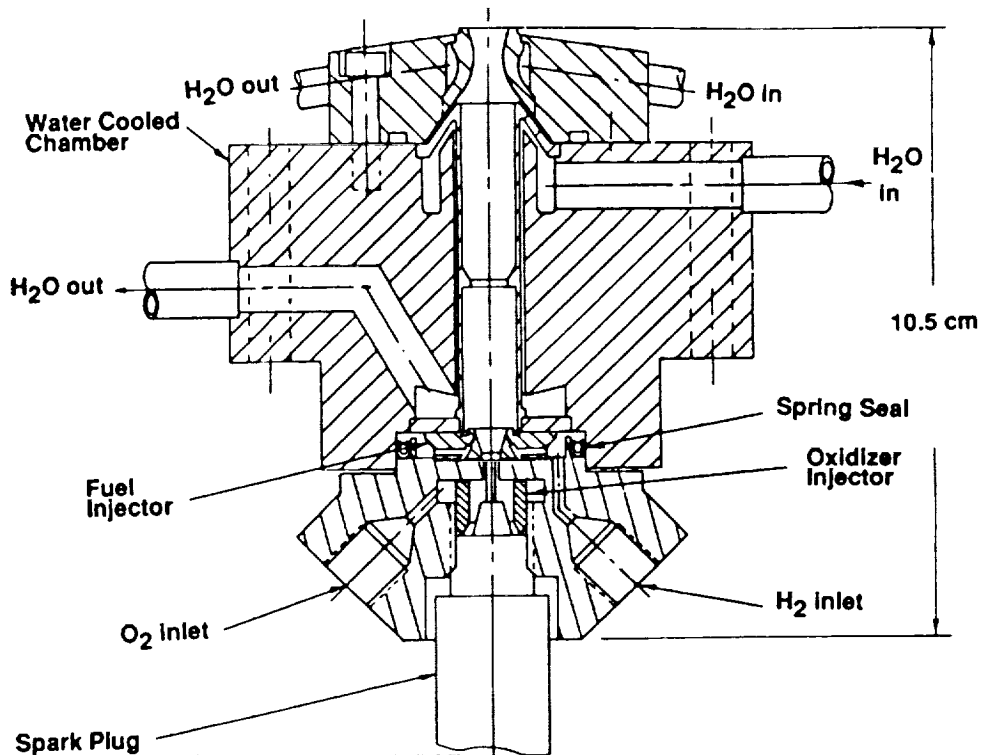


Figure 2. Schematic of the subscale 5 lbf thrust rocket engine.

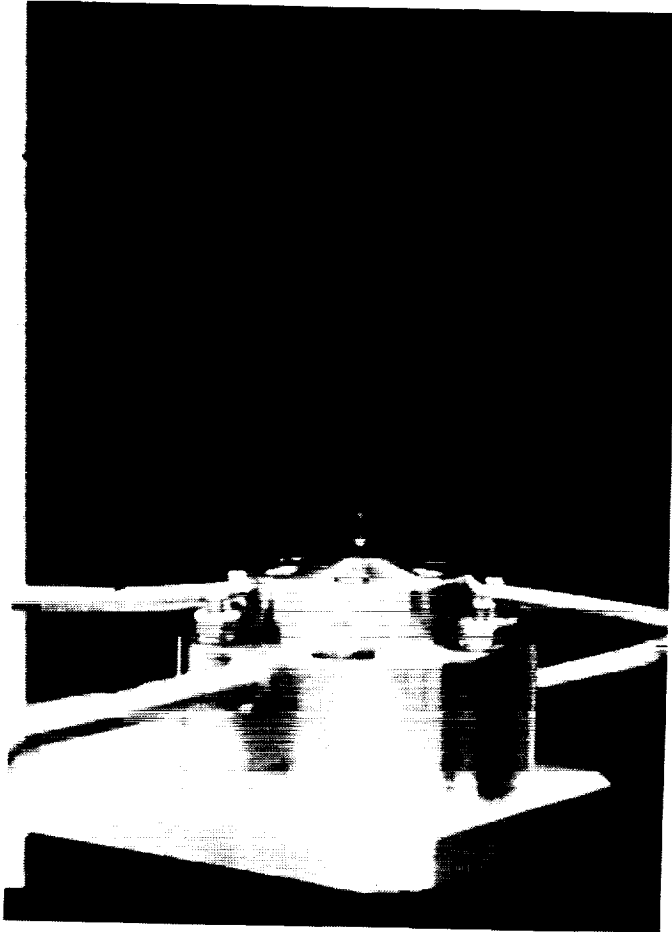


Figure 3. Conventional time-exposure photograph of the natural emission from the engine exhaust plume.

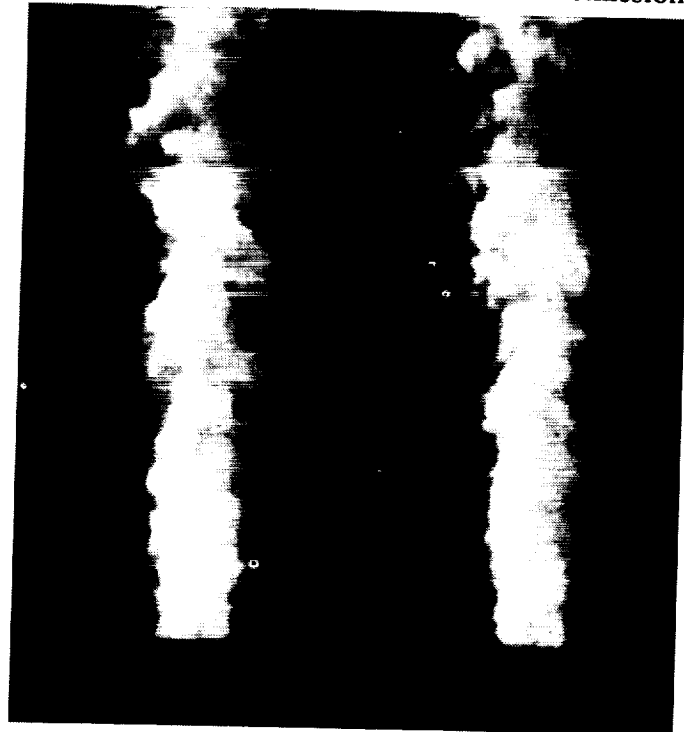


Figure 4. Two single-shot PLIF images of OH in the engine exhaust plume, obtained by pumping the (0,0) band.



ORIGINAL PAGE  
BLACK AND WHITE PHOTOGRAPH



Figure 5. Two single-shot PLIF images of OH in the engine exhaust plume, obtained by pumping the (3,0) band.

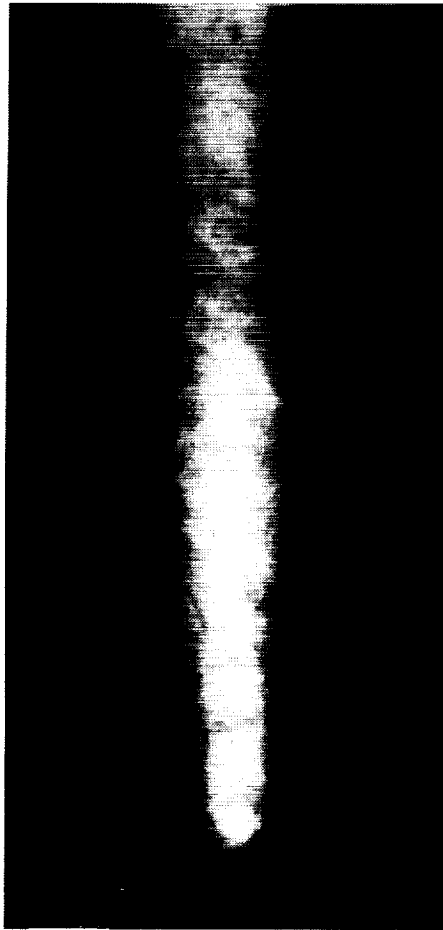


Figure 6. Fifteen frame average image of OH in the engine exhaust plume, obtained by pumping the (3,0) band.

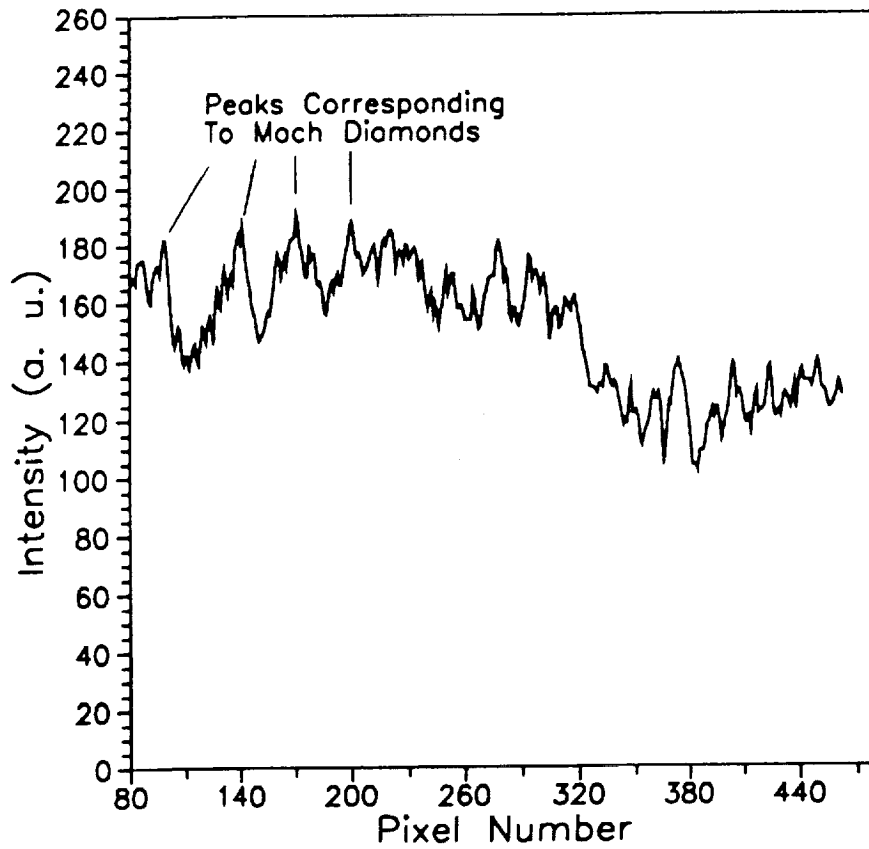


Figure 7. Pixel intensity variation taken from figure 6 and along the axis of the engine exhaust plume. The positions of the shock diamonds have been indicated.



EXIT PLANE H<sub>2</sub>O CONCENTRATION MEASUREMENTS CORRELATED WITH OH  
PLIF NEAR-INJECTOR MIXING MEASUREMENTS FOR SCRAMJET FLOWS

T.E. Parker, M.G. Allen, R.R. Foutter, D.M. Sonnenfroh, and W.T. Rawlins  
Physical Sciences Inc.  
Andover, MA 01810

## ABSTRACT

Mixing and combusting high enthalpy flows, similar to those encountered in scramjet engines, were investigated using a shock tunnel to produce the flow in conjunction with non-intrusive optical diagnostics which monitored the performance of two injector configurations. The shock tunnel is configured to produce Mach 3 flow and stagnation enthalpies corresponding to flight equivalent Mach numbers between 7 and 11. A pulsed hydrogen injection capability and interchangeable injector blocks provide a means of examining high speed, high enthalpy reacting flows. Planar Laser Induced Fluorescence (PLIF) of OH molecules in the near injector region produced images which show the combusting and mixing zones for the reacting flow. Line-of-sight exit plane measurement of water concentration and temperature were used to provide a unique method of monitoring exit plane products. These results demonstrated that a velocity matched axial injection system produced a fuel jet that lifted off the floor of the duct. Mixing was observed to increase for this system as a velocity mismatch was introduced. Comparison of exit plane water concentrations for a wall jet injection system and a velocity matched injection system indicated similar mixing performance but an accurate pressure measurement is necessary to further validate the result. In addition, exit plane measurements indicated an approximate steady-state condition was achieved during the 1 to 2 ms test times.

## INTRODUCTION

The development of supersonic combusting ram jet (SCRAMJET) engines requires testing using new, non-intrusive methods in high speed, high enthalpy flow facilities. A critical factor for effective thrust production in a scramjet is the efficient mixing of fuel with air and the subsequent chemical reactions which produce water. This paper describes an experimental effort which measured the concentration of water at the exit plane of a simulated scramjet in addition to using Planar Laser Induced Fluorescence (PLIF) of OH to visualize the mixing zone where hydrogen is injected into the Mach 3.0 flow. These results allow direct comparison of the degree of mixing near the hydrogen injector, as determined by the production of OH, with temperatures and concentration values for water 20 duct heights downstream of the injection station.

Results in this paper are for the initial development of a non-intrusive diagnostic for line-integrated temperature and concentration measurements of water. The observed quantity is infrared emission from the  $\nu_2$  vibrational band centered at  $6.27 \mu\text{m}$ , coupled with OH PLIF measurements in the near injector zone of a high enthalpy reacting flow. The flows were produced using a shock

tunnel which generates Mach 3.0 flow with stagnation conditions ranging from 2500 to 3800 K. Two hydrogen injector configurations were employed: a dual hole sonic wall injection system, and a swept ramp injector which was specifically designed to be nearly velocity matched with the mainstream flow. In addition to the water and OH PLIF measurements, exit plane emission from OH and entrance plane emission from NO were monitored. In the following sections we describe the shock tunnel and its operating characteristics, the injection system and its operating parameters, the OH PLIF measurements and methodology, the development of the water temperature and concentration measurement, and, finally, results from an initial test series with the two different injection geometries.

## SHOCK TUNNEL DESCRIPTION

A full description of the shock tunnel and its operation has been previously published.<sup>1</sup> Briefly, the high speed, high enthalpy flows for these tests were produced using a shock tunnel which is capable of generating stagnation temperatures far greater than those available using a conventional furnace or vitiated combustion methods. The facility also includes a hydrogen injection capability which makes combustion tests possible for these flows. This system was carefully designed to provide on-demand injection and can be configured to test a variety of injector geometries. The shock tunnel is configured to operate at Mach 3.0 with a two dimensional half-nozzle expanding to a square cross section. The nozzle is followed by a rearward facing step in the floor of the tunnel. A replaceable injector block lies immediately downstream of the isolation step. Five orthogonal optical access stations are included along the shock tunnel so that both line-of-sight and PLIF imaging measurements can be made. The first optical port is immediately after the full expansion point for the nozzle and includes three windows. The first three windows are shown schematically in Figure 1 along with the interchangeable injector block. The region immediately after the rearward facing step includes two side windows that give full height optical access for a 14 cm flow length, along with full laser access at the top of the tunnel.

Figure 2 illustrates the shock tunnel and diagnostics as configured for this test series. Four distinct optical measurements were included. In addition to OH PLIF and water vapor emission measurements, a radiometer centered at  $4.95 \mu\text{m}$  was included at the nozzle exit and a gated intensified camera filtered to monitor the OH chemiluminescent emission was included at the exit plane. The upstream radiometer was used to monitor the flow in the tunnel via emission from the NO fundamental vibrational band as described in a separate publication<sup>2</sup>. This measurement is critical in determining the test conditions for the shock tunnel since it provides a signal from the thermal emission from NO generated in the plenum. Measurable emission signals are only present when the flow in the tunnel is at the elevated temperatures produced by the reflected shock zone. This measurement is therefore much more specific in determining the tunnel test times than conventional pressure measurements. A critical performance parameter for impulse test facilities, such as a shock tunnel, is the time duration of the high enthalpy flow. Test times determined using the previously described radiometer were typically between 1 and 2 ms.

The shock tunnel is used to produce the very high stagnation conditions associated with supersonic/hypersonic flight. Figure 3 illustrates the flight simulation capabilities for the shock tunnel compared with a flight corridor adopted by Billig<sup>3</sup>. Clearly the shock tunnel is capable of

simulating flight speeds below 3 km/s in the lower pressure regions of the flight corridor. Also included in this figure is the testing region examined in this work. Flight equivalent Mach numbers ranged from 7 to 11.

## HYDROGEN INJECTION SYSTEM AND INJECTOR CONFIGURATIONS

To produce reacting flows similar to those in a scramjet, hydrogen must be injected into the shock tunnel flow. The requirements for this are pulsed operation with a fast response time, near constant injection flow rates during the shock tunnel run time, and a reliable method of limiting the quantity of hydrogen injected into the system. We have addressed these requirements using a 1 gal, 3000 psi rated bladder accumulator with a custom manufactured, explosive burst diaphragm and manifold system. A dual diaphragm system separates the nitrogen pressurized hydrogen from the delivery system for the injector block. Injection is possible on demand by simply igniting a hydrogen/oxygen mixture contained between the diaphragms with a spark plug. Testing of this system revealed that initiation times of 800  $\mu$ s were routinely produced. The injection system can therefore be triggered using one of the pressure transducer signals from the shock tube.

The overall stoichiometry for the combustor system can be easily described since the injectors in the combustion zone are configured to produce sonic flow at a known area. Using standard gasdynamic relationships, the product of injection pressure and injector exit hole area can be shown to be a function of system stoichiometry and reflected shock temperatures and pressures, Eq. (1).

$$P_{O,H_2} A_{inj} = \phi \frac{P_5}{\sqrt{T_5}} K_1 \quad (1)$$

where

- $P_{O,H_2}$  - stagnation injection pressure
- $A_{inj}$  - injector sonic area
- $\phi$  - fuel equivalence ratio
- $P_5, T_5$  - reflected shock plenum pressure and temperature
- $K_1$  - system constant,  $2.12 \times 10^{-3} \text{ m}^2\text{-K}^{1/2}$ .

This equation was derived by considering the ratio of mass flows through the shock tunnel nozzle throat and the mass flow at the sonic exit point of the fuel injection system. Using this equation, a specific heat ratio of 1.3 for the air flow, and recognizing that an equivalence ratio of 1.0 corresponds to a mass ratio, hydrogen to air, of 0.029, Eq. (1) may be constructed. The system constant,  $K_1$ , includes the area of the shock tunnel throat as well as the various constants used to relate one-dimensional sonic flow to the zero velocity plenum conditions.

The two injector configurations used in this work are illustrated in Figures 4 and 5. The wall injection system consists of two ports located in the tunnel floor after the rearward facing step,

along the tunnel centerline, at 2.3 and 8.4 step heights downstream. The equal area inlets are directed at 30 and 60 deg angles with respect to the tunnel flow. The axial injection system was implemented by lengthening the step across the full tunnel width. This addition was sectorized into three equal widths with the outer sectors machined to produce a 13.2 deg ramp between the step and the tunnel floor. The center sector consists of a backward facing step with a nozzle in the downstream face. This nozzle was a simple 7 deg taper with a throat area of  $0.317 \text{ cm}^2$  and an exit area ratio of 3.2. This system was specifically designed to produce bulk and injection flow velocities of approximately equal magnitude. Table 1 lists relevant velocities and stoichiometries for four of the conditions examined in this work.

## OH PLIF MEASUREMENTS

The OH PLIF measurements were made using a Spectra-Physics Nd:YAG-pumped dye laser with frequency-doubling to 283 nm. The dye laser was modified for a larger spectral bandwidth by operating the grating in third order rather than fifth and adding a pre-amplifier cell. Using this approach, the frequency-doubled output of the dye laser was in excess of  $0.6 \text{ cm}^{-1}$ , more than twice that of the OH absorption linewidth. Between 6 and 10 mJ of laser energy was delivered to the test plane of the shock tunnel in sheets of 4.5 to 10.5 cm. The laser sheet thickness was on the order of 0.05 cm. Fluorescence was imaged using an intensified camera system, consisting of an image-intensified full-frame transfer array. The fluorescence was collected at right angles using a 105 mm UV lens operated at f/4.5 and filtered with carefully selected UV filter glasses. The filter glasses provided a long-pass cut-off near 310 nm which rejected the laser elastic scattering from the tunnel floor. The total transmission at the fluorescence wavelengths was about 25%. The intensifier was gated to  $\sim 20 \text{ ns}$  around the  $\sim 10 \text{ ns}$  laser pulse. This narrow gate width eliminated any chemiluminescent or thermal emission from the PLIF images.

The laser and PLIF data acquisition system were remotely sited from the tunnel in an adjacent laboratory. The laser beam was transported to the tunnel using a series of prisms and expanded into a thin sheet which was oriented along the flow axis and focussed along the centerline of the tunnel at each of the imaging stations. The intensified camera system and the high-speed gate generator were located immediately adjacent to the tunnel test section. The laser and camera system were triggered from a pressure transducer in the reflected-shock plenum so that the measurement time could be adjusted throughout the nominally 2 ms test time. OH PLIF measurements were made in the near field of both injector configurations, spanning the first region of the test section downstream of the rear-facing step or the ramp injector, as well as at a second imaging station located downstream of the test section entrance.

In addition to the OH PLIF measurements, a second, PSI-designed, intensified CCD camera was used to image the OH chemiluminescence from a 10 cm diameter window located near the exit of the tunnel test section. For the emission measurements, the second camera was filtered with 3 mm of UG-5 glass to isolate the OH A-state emission, and a  $1 \mu\text{s}$  gate was used. This longer gate time integrated the emission signal which was eliminated from the PLIF images by the much shorter gate time. The depth-of-focus of the emission-imaging camera was sufficient to span the 7.62 cm tunnel width, providing a line-of-sight averaged view of the spreading of the flame plume at the test section exit.



The OH PLIF measurements were obtained by exciting the isolated  $Q_1(7)$  transition at 283.29 nm. This transition was chosen because of its strength at the expected  $H_2$ -air combustion temperatures and our desire to have maximum sensitivity for these experiments. For the conditions of these tests, we may express the fluorescence signal obtained from each pixel on the detector array as

$$S_F = (I_\nu B) \cdot (F_y) \cdot (f_B N_t V_c) \cdot \left[ \eta \frac{\Omega}{4\pi} \right] \cdot \tau_p \quad (2)$$

where

$I_\nu$	=	laser spectral intensity
$B$	=	Einstein B coefficient for absorption
$F_y$	=	fluorescence yield
$f_B$	=	Boltzmann population fraction
$N_t$	=	species number density
$V_c$	=	collection volume
$\eta$	=	filter transmission, detector responsivity, etc.
$\Omega$	=	collection solid angle of imaging system
$\tau_p$	=	pulse duration.

The form of the fluorescence yield,  $F_y$ , appropriate for this excitation strategy in OH is given by<sup>4</sup>

$$F_y = \frac{A_{eff}}{Q} \quad (3)$$

where  $Q$  is the total rate of removal of the laser-excited vibrational level,  $A_{eff}$  is the total collected photon rate and the sum of the product of the filter transmission and the individual spontaneous radiative transition rates for the detected transitions.

In general, many of the terms in Eq. (2) have temperature, pressure, or gas compositional dependencies. For OH in most flame environments, it is reasonable to assume that the quenching term can be expressed as

$$Q = (8 \times 10^8) (P/P_{ref})^{5-8} \quad (4)$$

where  $P_{ref}$  is 1 atm and the constant is recommended for flame values from previous studies.<sup>5-8</sup> Hence, in regions of the flow with little pressure variation across the measurement plane, as in the downstream PLIF imaging station, the quenching term is essentially constant and the PLIF image is a relative measure of the product of the OH number density and the temperature-dependent Boltzmann population term. For  $J'' = 7.5$ , the population term is only weakly sensitive to temperature over the range of temperatures where OH is likely to be found, as shown in Figure 6. The quenching term may vary as much as a factor of two from the nominal value of Eq. (4) in extremely fuel rich portions of the flow. However, most of the measurable OH will only be found in stoichiometric or fuel-lean regions of the flow, so that we can assume the relative uncertainty in number density across a nearly constant pressure image is about  $\pm 10\%$  due to the Boltzmann temperature variations.

In strongly pressure variant flows, however, the fluorescence signal is better viewed as the ratio of the pressure-dependent OH number density and the pressure-dependent quenching term. Expressing  $N_{OH}$  as

$$N_{OH} = \chi_{OH} P/RT \quad (5)$$

where  $\chi_{OH}$  is the volumetric mole-fraction of OH, the overall pressure-dependence of Eq. (2) vanishes, and the fluorescence signal is given by

$$S_F = \text{constant} \cdot f_B/T \cdot \chi_{OH} \quad (6)$$

Since the Boltzmann term at low  $J''$  values is nearly temperature-independent, the ratio  $f_B/T$  is an inverse function of temperature and is also plotted in Figure 6. Hence, the fluorescence signal is proportional to the local mole-fraction of OH with a factor of four variation from 1500 to 3000 K. It is possible to choose another transition so that the ratio  $f_B/T$  is essentially constant over some temperature range of interest so that, in strongly pressure varying flows, the fluorescence signal is directly proportional to species mole-fraction. For the range of 1500 to 3000 K, exciting transitions originating from higher  $J''$  values results in about  $\pm 5\%$  variation in fluorescence at constant mole-fraction with only a factor of two loss in sensitivity at 2000 K due to the relatively lower total population. For these initial measurements, the increased sensitivity was deemed more important and we chose to accept the temperature variations in the strongly pressure-variant region of the flow in the vicinity of the dual wall injectors.

## MEASUREMENTS OF H<sub>2</sub>O CONCENTRATION AND TEMPERATURE

A major thrust for this work was to develop a non-intrusive diagnostic suitable for monitoring the temperature and concentration of water in the exit plane of a high enthalpy reacting flow system. The motivation for this measurement technique is quite clear; it will provide a direct measure of a combustion product and its temperature along a line-of-sight at the combustor exit and will therefore provide a measure of combustor performance. The measurement relies on radiation from the  $\nu_2$  band centered at 6.27  $\mu\text{m}$  and uses a custom-designed infrared spectrometer system capable of acquiring synchronous spectra at a 125 kHz rate. This device consists of a liquid-nitrogen-cooled HgCdTe linear detector array (Infrared Associates) interfaced to a 0.3m,  $f/6.2$  monochromator. The resulting spectral resolution is 0.19  $\mu\text{m}/\text{pixel}$ . Each pixel in the array has a dedicated amplifier and digitizer providing synchronous collection of spectra at data rates of 125 kHz. The data were acquired and processed through a multichannel data acquisition system interfaced to an PC/AT computer. Absolute responsivity calibrations were performed with a temperature-controlled blackbody source. For the present measurements, the instrument was configured to obtain time-resolved, first-order spectra over the wavelength range 6.5 to 8.55. The field of view of the instrument was controlled using a folded imaging system consisting of a gold spherical mirror (focal length 10 cm) and a gold planar mirror. This optical system defined a collection area in the tunnel of 3.1 by 3.1 mm at the tunnel centerline and 6.6 by 6.6 mm at the near and far edges. In addition, due to the strong absorption strength of atmospheric water in this spectral region, the spectrometer and imaging optics assembly were purged with dry nitrogen. The unpurged path length in the atmosphere was 7 cm and this length was shown to produce insignificant

absorption for wavelengths greater than 6.5  $\mu\text{m}$ . This conclusion is supported by a comparison of the spectrometer calibrations performed in high and low relative humidity environments.

Prior to implementation of the system on the shock tunnel, the observed radiances and bandshapes were calibrated for  $\text{H}_2\text{O}$  concentration and temperature by recording emission spectra from an incident shock heated mixture of argon, hydrogen, and oxygen (85%, 10%, 5%). The measurements were performed at near 1 atm pressures in a 10.4 cm diameter shock tube using previously prepared gas mixtures of UHP argon, hydrogen, and oxygen. The reacting system is modeled using an incident shock chemical kinetics package produced by Sandia (DSHOCK), and calibration temperatures and concentrations are carefully extracted from the pseudo-steady state region following an initially reactive period. A typical calibration shock is shown in Figure 7.

Relative calibration spectra are shown in Figure 8 and these spectra show the increased radiance for long wavelengths at elevated temperatures that is typical of increased populations in upper vibrational states. The vibrational temperature for the water can therefore be determined by monitoring the relative shape of the emission spectra while the concentration is determined by monitoring the absolute radiance in one of the bandpasses. In order to produce a systematic temperature and concentration measurement methodology we have assumed that the radiance in each bandpass follows the functional form given in Eq. (7).

$$\frac{N_\lambda}{[\text{H}_2\text{O}]\ell} = \alpha_\lambda e^{\beta_\lambda/T} \quad (7)$$

where

- $N_\lambda$  - system radiance at wavelength  $\lambda$
- $[\text{H}_2\text{O}]$  - concentration of water molecules
- $\ell$  - path length
- $T$  - temperature
- $\alpha_\lambda, \beta_\lambda$  - empirically determined constants.

The characteristic exponential slope  $\beta_\lambda$  increases with wavelength as would be expected from the spectra shown in Figure 8. Inspection of Eq. (7) reveals that ratios of radiances at two wavelengths are sensitive to temperature only and are independent of concentration. Equation (8) formalizes this relationship and provides a direct means of calculating temperature. The values of  $\alpha_\lambda$  and  $\beta_\lambda$  are determined using a least squares fit of the calibration observations to Eq. (7). Therefore, observed radiance ratios can be used to determine the temperature via Eq. (8) and column density ( $[\text{H}_2\text{O}]\ell$ ) using Eq. (7).

$$T = \frac{\beta_{\lambda_1} - \beta_{\lambda_2}}{\ln \left[ \frac{N_{\lambda_1} \alpha_{\lambda_2}}{N_{\lambda_2} \alpha_{\lambda_1}} \right]} \quad (8)$$

The specific bandpass wavelengths which are used for temperature and concentration determination is important for the shock tunnel data. Figure 9 illustrates sample spectra at the exit

plane of the shock tunnel for a combusting flow. These spectra include a feature centered at 8.25  $\mu\text{m}$  which was not apparent in the shock tube calibrations. This feature is either due to a molecular radiator that was not present in the shock tube calibrations (which included no nitrogen) or is indicative of vibrational non-equilibrium for the radiating water. Although we cannot rule out vibrational non-equilibrium, vibrational relaxation rates from  $\nu_2 = 1$  to  $\nu_2 = 0$  are relatively fast.<sup>9</sup> For 2500 K, 0.3 atm conditions in the tunnel, the half-life of the  $\nu_2 = 1$  state is approximately 7 ns. This indicates that our system should be in vibrational equilibrium. In either case, we have chosen to determine temperature using the bandpasses centered at 6.68 and 7.43  $\mu\text{m}$ . Concentration is determined using this temperature and the radiance from 6.68  $\mu\text{m}$  bandpass. These bandpasses were selected to provide the highest sensitivity in the temperature calculation while the concentration calculation was specifically chosen to be insensitive to temperature.

Finally, a note on the accuracy of the temperature and concentration measurement is in order. This diagnostic is currently being developed and the calibration data set is not large enough to produce system constants that are highly specified. The absolute accuracy for the current data set is approximately 30%. However, careful implementation of a comprehensive calibration matrix and carefully executed chemical kinetic modeling would bring the absolute accuracy to better than 10%. Once these calibration constants are accurately specified, the limiting accuracy for the temperature measurement is simply the signal-to-noise ratio in the radiance measurements. The direct implication is that temperature *comparisons* within this data set are limited only by the noise in the radiometric signals. In all cases, the signal levels used in this work had signal-to-noise ratios of between 10 and 50. The relative uncertainty in temperature is therefore between 14 and 3%, while the relative uncertainty in concentration for a 3000 K system also ranges from 14% for signal to noise ratios of 10 to 3% and for signal-to-noise ratios of 50.

## RESULTS AND DISCUSSION

The data acquired as a part of this test series includes four basic flow conditions as described in Table 1 and we will present results from each of these conditions. However, before discussing these images and the exit plane water measurements, a brief discussion of the flow and timing in the shock tunnel is necessary. Figure 10 illustrates the signals from a reacting flow test and shows the pressure in the injector plenum, the signal from the radiometer at the nozzle exit, and the pressure on the top wall immediately following the injector station. Also included in this figure are the injector times and PLIF laser pulse. Features to note in this figure are the clear demarcation of the flow test time by the radiometer, the relatively stable pressure trace following the injector station, and the constant pressure in the injector plenum during the flow time. In addition, note that tunnel pressure and radiance signals are not coincident in space (separation is 0.30m) and therefore sample, at a given instant, different portions of the flow.

Figure 11 is an image of the OH distribution in the immediate vicinity of the first injector of the dual injector system. In this and all other images, the flow is from left to right and the relative fluorescence signal levels are false-color-encoded according to the lookup table at the left side of the image. Also in each image, the bottom of the PLIF image corresponds to the bottom wall of the tunnel. The field of view in Figure 11 is 80 mm (H) by 60 mm (V) and the left side of the image is just upstream of the first injector. A low, fairly uniform level of OH in the recirculation

zone/boundary layer upstream of the injector is visible in the lower left hand corner of the image. A thin filament of OH, on the order of 1 mm thick, attaches very near the recirculation zone and extends away from the wall along an irregular line, indicative of the shear-generated turbulence between the high-speed injectant flow and the free-stream flow. From earlier studies<sup>4</sup>, we know that just upstream of this OH zone lies the bow shock generated by the interaction of the injectant plume and the free stream flow. The dark regions above this thin filament, of course, correspond to the free-stream flowfield where no hydrogen and air mixing has occurred. The center of the fuel plume itself is also dark, indicating no mixing and OH formation. Downstream and underneath the fuel plume, between the two injectors along the tunnel floor, significant amounts of OH are observed in a spatially extended, reasonably well-mixed zone.

Figure 12 is a similar image from another test, now taken with a larger field of view, observing a region 105 by 79 mm. Again, the left side of the image is just upstream of the first injector position. This image also clearly shows the thin OH filament between the first injector and the free stream flow. The large field of view, however, encompasses the second injector station and more clearly shows the large, well-mixed levels of high OH concentration between the two injectors. The right side of this image corresponds to the second injector station and shows an abrupt disappearance of the OH at the second H<sub>2</sub> plume, although a second thin filament is observable at a larger angle to the wall than the first filament due to the higher angle of the second injector. Both images indicate that the thin OH filament is typically on the order of 1 mm thick, although it fluctuates spatially with the turbulence motion in observable scales up to about 7 mm in diameter. The first jet penetrates to an average height of 16 mm (defined by the edge of the OH filament) before fully aligning with the free stream flow.

Using the fluorescence model presented above and assuming nominal conditions of 0.5 atm and 2000 K, the peak OH fluorescence signal in the thin filament between the fuel jet and the free-stream corresponds to an OH number density of about  $1 \times 10^{15} \text{ cm}^{-3}$ , or about 500 ppm. The pressure and temperature field in this portion of the flowfield is very complex. The nominal conditions are reasonable for the OH in the filament above the fuel jet. Below the fuel jet and between the two injectors, however, the flow expands from a stagnation point upstream of the first injector and then stagnates again upstream of the second injector. Since we have not yet measured the pressure or temperature variations in this flow, we can only bound the uncertainty in quantitatively interpreting the relative fluorescence signals in this image in terms of the relative OH number density or mole-fraction. The pressure in this region may vary from near the free stream value to near the post-bow shock pressure, or from about 0.5 to about 4 atm. The temperature in which OH is likely to be found was discussed in the previous section and we observe that, in the stagnation region upstream of the second injector station, the bulk gas temperature may approach the stagnation temperature of  $\sim 3500 \text{ K}$ .

The highest fluorescence signals originate in the large, well-mixed portion of the flow where the flow temperatures and pressures are substantially higher than the nominal conditions used to estimate the OH concentration in the flame filament. The peak signal levels here are two to three times higher than in the filament. Considering the mole-fraction sensitivity of the fluorescence signal (which is independent of pressure), we expect the fluorescence signal at constant mole-fraction to decrease by about a factor of two from the nominal filament temperature to the stagnation temperature. Combining the increased signal levels and the decreased absorption strength at higher temperature, we estimate that the peak mole-fractions obtained in the region between the two

injectors is on the order of 2,000 to 3,000 ppm, or 0.2 to 0.3% of the total number density. These numbers are reasonable for hydrogen/air combustion at these temperatures, particularly considering the relatively long residence time for the fuel and air to molecularly mix in the slow flow between the injectors.

The flame zone in the upper filament, as viewed by the OH fluorescence, is intermittent. Our detection limit for the nominal conditions is about  $1 \times 10^{13} \text{ cm}^{-3}$ , or about 5 ppm. Hence, intermittency is determined in this case by the OH concentration falling below this level. This type of non-equilibrium flame extinction has been observed in turbulent hydrogen/air jet diffusion flames and is reasonably expected in the highly turbulent flow in the injector vicinity. The PLIF images of Figures 11 and 12 indicate the importance of time-resolved spatial measurements and suggest that accurate predictions of ignition and near-injector behavior will require multi-step chemical kinetic and accurate turbulence modeling.

The remaining PLIF images all correspond to the axial injector and were obtained 29 cm downstream of the injector exit plane. Figure 13 is a PLIF image at the similar flow condition to Figures 11 and 12 and corresponds to a field of view of 45 by 34 cm. In these images, the injectant hydrogen velocity was nearly matched to the free stream centerline velocity above the injector. The OH filament separating the fuel jet from the free stream is typically on the order of  $500 \mu\text{m}$  thick, although it fluctuates spatially due to the turbulence in the shear layer. This turbulence level is relatively low, however, as evidenced by the thin, probably diffusion limited flame sheet and the relatively large scale associated with the typical filament fluctuations. It is also notable that no extinction of the flame sheet is observed. The dark region below the flame sheet corresponds to the fuel jet itself, which measures approximately 12 mm in diameter, essentially the same as the injector jet diameter. The position of this jet above the tunnel flow, however, fluctuates with downstream distance. The mean position of the jet centerline is about 20 mm.

In marked contrast to the interface between the fuel jet and the free stream, the region between the fuel jet and the wall shows a much thicker mixing layer. Significant free stream air entrainment and mixing is evidenced by the large, relatively uniform [OH] in this region. The picture that emerges from this image is of a fuel jet lifting away from the wall and vigorously mixing underneath. The peak OH levels in these images are again on the order of  $2\text{-}3 \times 10^{15} \text{ cm}^{-3}$ . Since the pressure across this image is reasonably constant, we can more accurately relate the fluorescence signal variations to number density variations than in the images above the side wall injectors. Interestingly, the OH formation per unit volume is similar everywhere in this image to the thin filaments above the side wall injectors, although the total OH produced in the image (proportional to the total hydrogen conversion) is much greater due to the vigorous mixing below the jet.

Figure 14 is an OH PLIF image at the same station with a different field of view and flow conditions as given in Table 1. In Figure 14 the field of view was increased to 60 x 45 cm and the velocity difference between the fuel jet and free stream was nearly 300 m/s (the fuel jet velocity is greater than that of the free stream). This image reveals a very different mixing pattern for the fuel jet. Instead of a clearly defined fuel jet with a thin filament separating the jet from the free stream, vigorous mixing has occurred on both sides of the jet. Indeed, the jet itself is almost indistinguishable, with measurable OH throughout its diameter. The penetration of the fuel jet into the free stream is slightly diminished although the mixing and total OH formed within the image is substantially higher. The sensitivity in these images is the same as in Figures 12 and 13 indicating

peak concentrations on the order of  $10^{15} \text{ cm}^{-3}$ . It is interesting to note that the increased turbulence intensity of the fuel jet/free stream shear layer now results in intermittency of the flame sheet.

A last PLIF image was obtained at the same location, now with the free-stream gas temperature over 1500 K and a velocity over 2000 m/s. In this case, the free-stream velocity slightly exceeds the expected fuel jet velocity, though the total velocity mismatch is comparable to that in Figure 14. The OH PLIF image in Figure 15 reveals a mixing pattern very similar to that of Figure 13, although the highest signal levels are now in the thin filament between the fuel and the free stream rather than between the fuel and the wall. The penetration of the jet into the free stream is noticeably improved, with the outer OH boundary extending 34 mm above the tunnel floor.

Figures 16 and 17 show the results from the time resolved,  $\text{H}_2\text{O}$  temperature and concentration measurements. These results are for the wall injection system and swept ramp injector at similar flow conditions as listed in Table 1. Figure 16 illustrates the temperature and column density profiles for the two hole wall injection system. This plot uses the 125 khz spectral data which was previously described with a three point running average to remove spurious noise. Several features are prominent in this figure. First, the end of the test time is clearly shown by a steep drop in the temperature of the water. The length of the test time, as defined by the infrared radiometer at the nozzle exit, is used to identify the beginning of the flow time at this optical station. This time is consistent with the expected arrival time of the hot gas slug based on the distance between the measurement stations and convective velocity in the tunnel. This figure is also marked to note the region where the signal-to-noise ratios rise above the 10:1 level. Both temperature and column density start at relatively low values and after approximately 1 ms asymptote to relatively steady conditions. This is an important observation since it supports the hypothesis that pulsed, short duration flow facilities can be used to study the steady state properties of these high temperature reacting flows. The observed exit plane temperature is approximately 2700 K with a column density of  $4\text{-}5 \times 10^{18} \text{ molec/cm}^2$ .

Figure 16 also includes idealized temperature and column density predictions. These predictions are based on a simplified model which creates an initial, fully mixed starting condition based on the air and hydrogen injection flows and then allows this system to react as it flows down the duct. This prediction follows the temperature, pressure, species concentrations, and velocity as the system proceeds down the duct. The starting condition for this calculation is determined by specifying a completely homogeneous system with the pressure, temperature, and velocity imposed by conserving mass, momentum, and enthalpy from the inlet air and hydrogen flows (note that the momentum of the hydrogen for the wall injection system was neglected since it was not oriented in the downstream direction). The initial chemical composition is chosen to reflect the exit composition of the air and hydrogen flows. Results from these calculations provide a relevant comparison for the exit temperature and column density measurements. In all of the experimental cases, the agreement between predicted and observed temperatures was excellent. However, the agreement in predicted and measured column densities is less consistent.

The column density observed in Figure 16 was approximately 60% of the idealized value. This discrepancy could be due to either incomplete mixing and therefore incomplete product formation, finite rate chemistry which would slow the rate of product formation, variations in the composition of the exit plane, or heat transfer losses in the system which will act to decrease the

density and therefore the water concentration. Unfortunately, our measurements for this effort did not include reliable pressure measurements at the exit plane. In all cases, pressure measurements are clearly biased by a heating of the piezo electric transducer which produces a continuous drift in the pressure signal during the experiment. In the future, this problem will be corrected by recessing the transducer from the flow so that it will not be directly subjected to the high temperatures and velocities of the exit plane.

Figure 17 illustrates the results for an axial injection system operated at conditions identical to that for Figure 16 (wall injection system). The observed column density for this system is very similar to that observed for the wall injector. In each of the two cases the observed column density was approximately 60% of their observed idealized values which preliminary indicates that the mixing of the velocity matched swept ramp system was equivalent to that of the wall injection system. If the mixing for one of the systems was exceptionally poor, the result would be decreased water in the exit plane of the combustor. Unfortunately this conclusion must be tempered by the absence of a pressure measurement which would allow a complete comparison between the two data sets. However, it is encouraging that the results for the velocity matched axial system and the wall injection system are similar.

## CONCLUSIONS

Complementary non-intrusive diagnostic measurements have been used to study the operation and performance of two different types of injection systems in high enthalpy flows. Planar Laser Induced Fluorescence of OH was used to image the regions near the injectors and a line-of-sight emission measurement in the infrared was used to quantify the temperature and the column density of water at the exit plane centerline. A fast gating, intensified camera system was shown to effectively eliminate emission from the fluorescence images. The exit plane emission measurement monitored the radiance from the  $\nu_2$  band for water. Relative band shape was used as a measure of temperature and the absolute intensity as a measure of the column density. PLIF images of OH for a wall injection system indicated prompt ignition at the hydrogen outlet with a flame sheet which attaches to the recirculation zone and extends away from the wall along an irregular line. An intense reaction zone was clearly shown to exist between the first and second fuel jet. For the axial injection system, OH was not observable immediately downstream of the injector outlet. However, further downstream, the fuel jet was shown to be reacting vigorously with the free stream flow. The axial injector was tested in both a velocity matched and mismatched mode. In all cases the jet was observed to lift off the tunnel floor with a reaction zone forming between the jet and the tunnel floor. In addition, the character of the mixing zone for the swept ramp systems was shown to change dramatically between velocity matched and mismatched systems. Exit plane measurements of the temperature were in excellent agreement with the values predicted for these flows. In addition, exit plane measurements indicated an approximate steady-state condition was achieved during the 1 to 2 ms test times.



## ACKNOWLEDGEMENTS

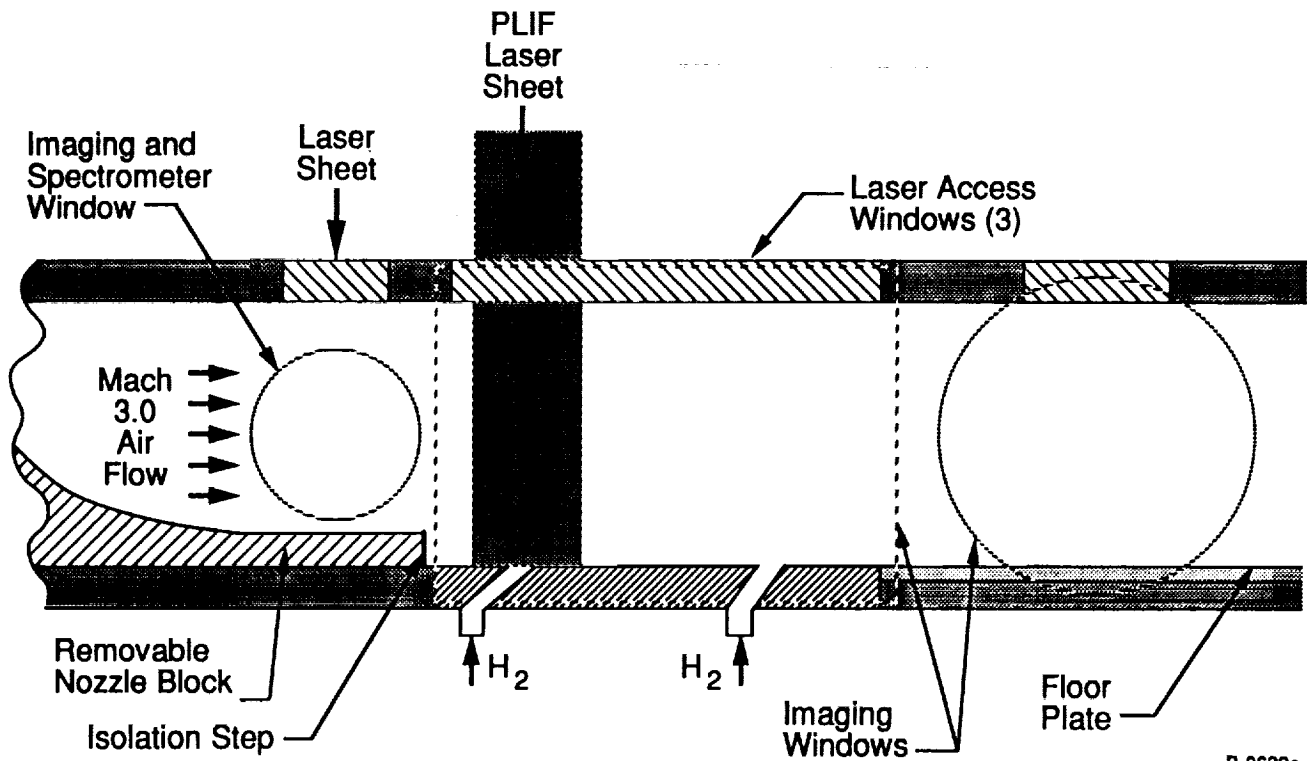
This work was supported by the Air Force under Contract F33615-91-C-2204, Dr. Kervyn Mach, monitor. We also appreciate our discussions with Dr. G. Burt Northam of NASA Langley on fuel injection geometries.

## REFERENCES

1. T.E. Parker, M.G. Allen, W.G. Reinecke, H.H. Legner, R.R. Foutter, and W.T. Rawlins, Paper No. 92-0761, AIAA 30th Aerospace Sciences Meeting and Exhibit, January 1992.
2. W.T. Rawlins, T.E. Parker, R.R. Foutter, and M.G. Allen, "Path Averaged Number Density and Temperature in High Enthalpy, Supersonic Air Flows by Time-Resolved Infrared Emission Spectroscopy," Paper No. 92-0140, AIAA 30th Aerospace Sciences Meeting, January 1992.
3. F.S. Billig, "Current Problems in Non-Equilibrium Gas Dynamics SCRAMJET Engines," presented at AIAA Professional Study Seminar on Gas Dynamics, Buffalo, NY, June 1989.
4. M.G. Allen, T.E. Parker, W.G. Reinecke, H.H. Legner, R.R. Foutter, W.T. Rawlins, and S.J. Davis, "Instantaneous Temperature and Concentration Imaging in Supersonic Air Flow Behind a Rear-Facing Step with Hydrogen Injection," Paper No. 92-0137, AIAA 30th Aerospace Sciences Meeting, January (1992).
5. G.P. Smith and D.R. Crosley, "Vibrational Energy Transfer in  $A^2\Sigma^+$  OH in Flames," *App. Opt.* **22**(10), 1428 (1983).
6. N.L. Garland and D.R. Crosley, "On the Collisional Quenching of Electronically Excited OH, NH, and CH in Flames," *21st Symposium (Int.) on Combustion* (Pittsburgh: The Combustion Institute), 1693 (1986).
7. M.C. Drake and R.W. Pitz, "Comparison of Turbulent Diffusion Flame Measurements of OH by Planar Fluorescence and Saturated Fluorescence," *Experiments in Fluids* **3**, 283 (1985).
8. R.S. Barlow and A. Collignon, "Linear LIF Measurements of OH in Non-Premixed Methane-Air Flames: When Are Quenching Corrections Unnecessary," Paper no. 91-0179, AIAA 29th Aerospace Sciences Meeting, January (1991).
9. P.F. Lewis and D.W. Trainor, "Survey of Vibrational Relaxation Data for  $O_2$ ,  $N_2$ , NO,  $H_2$ , CO, HF, HCL,  $CO_2$ , and  $H_2O$ ," Advanced Research Projects Agency Report No. 1092 (1974).

Table 1. Injection and Flow Parameters

Injector	Tunnel Flow			Fuel Equivalence Ratio	Injector Velocity (m/s)	OH PLIF Image Figure #	H <sub>2</sub> O Exit Plane Figure #
	Velocity (m/s)	Pressure (atm)	Temperature (K)				
Wall	2120	0.27	1310	2.1	-	11	-
Wall	2170	0.29	1360	2.1	-	12	16
Axial	1930	0.68	1100	0.64	2270	14	0
Axial	2184	0.30	1375	1.82	2270	13	17
Axial	2330	0.40	1530	1.35	2270	15	-



B-9622a

Figure 1. Schematic diagram of optical access for the shock tunnel test section

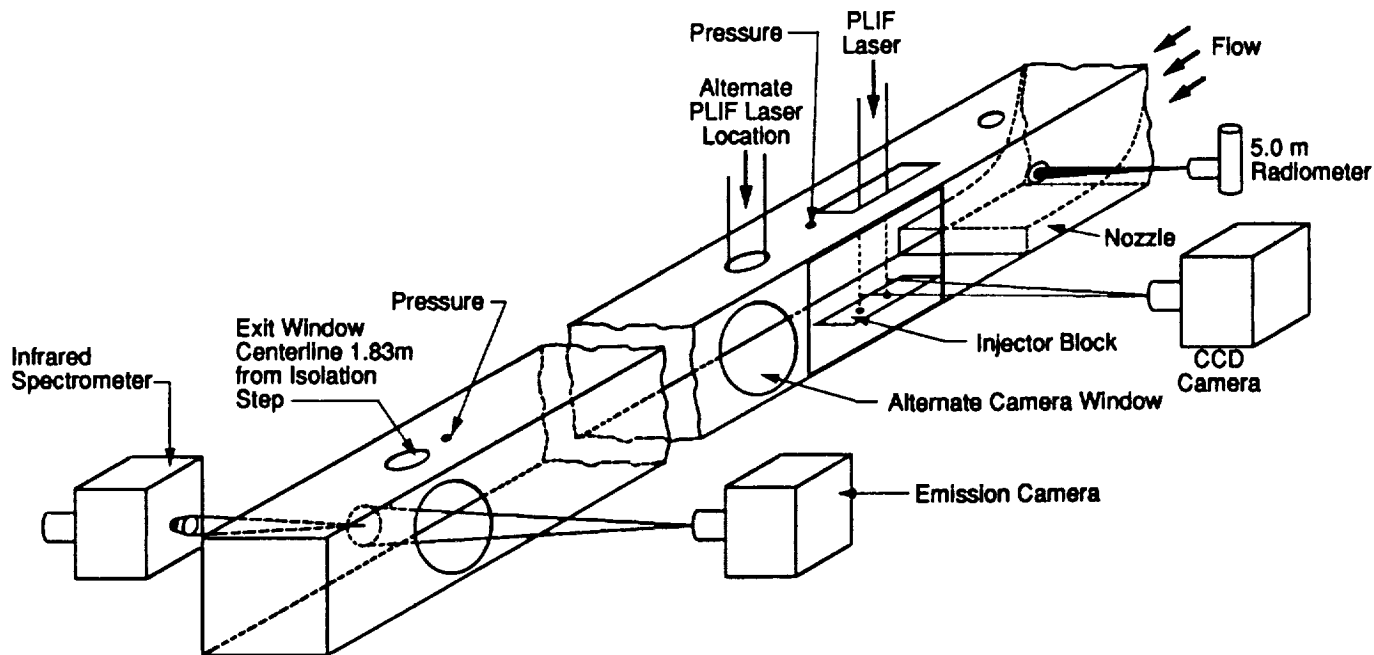


Figure 2. Diagnostic setup for reacting flow tests

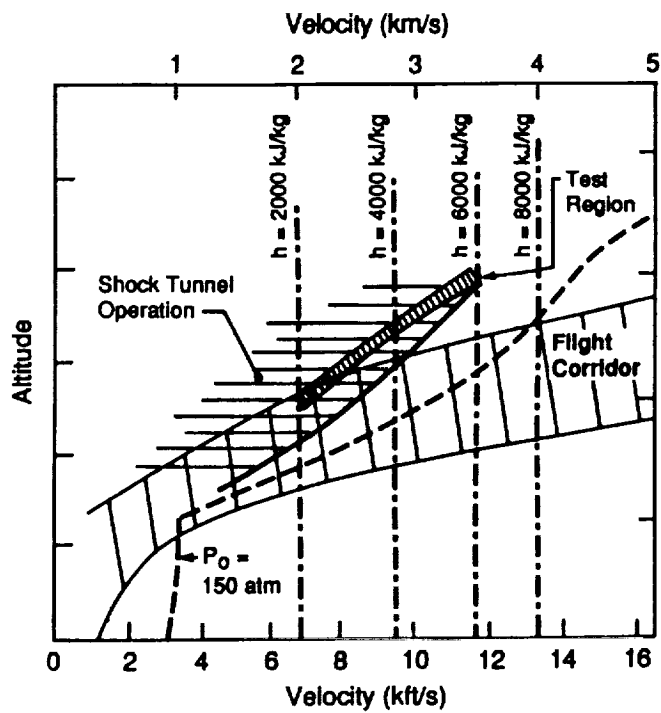


Figure 3. Shock tunnel operating conditions in terms of altitude and velocity simulation

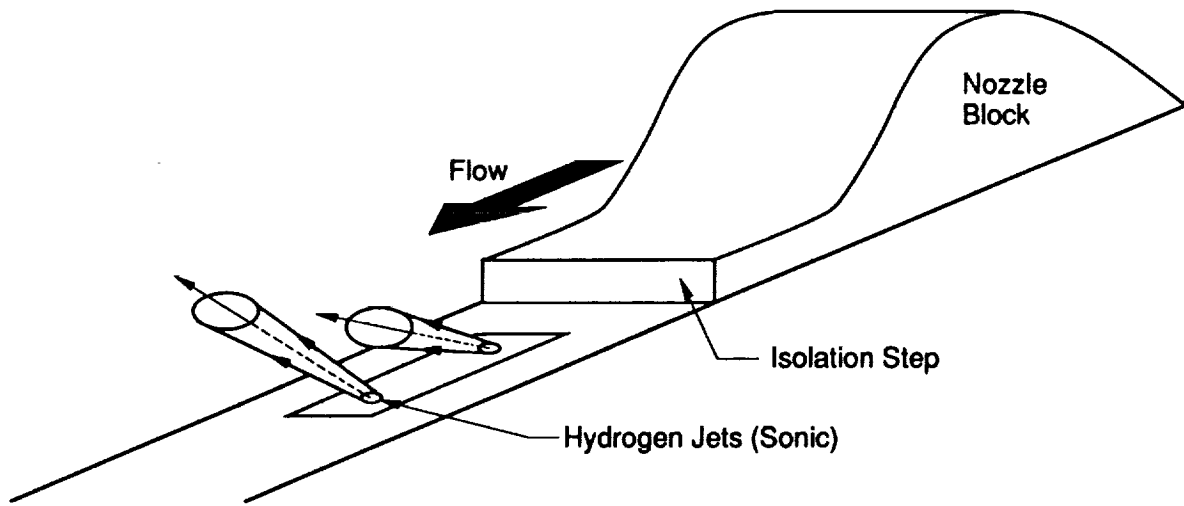


Figure 4. Wall injection system

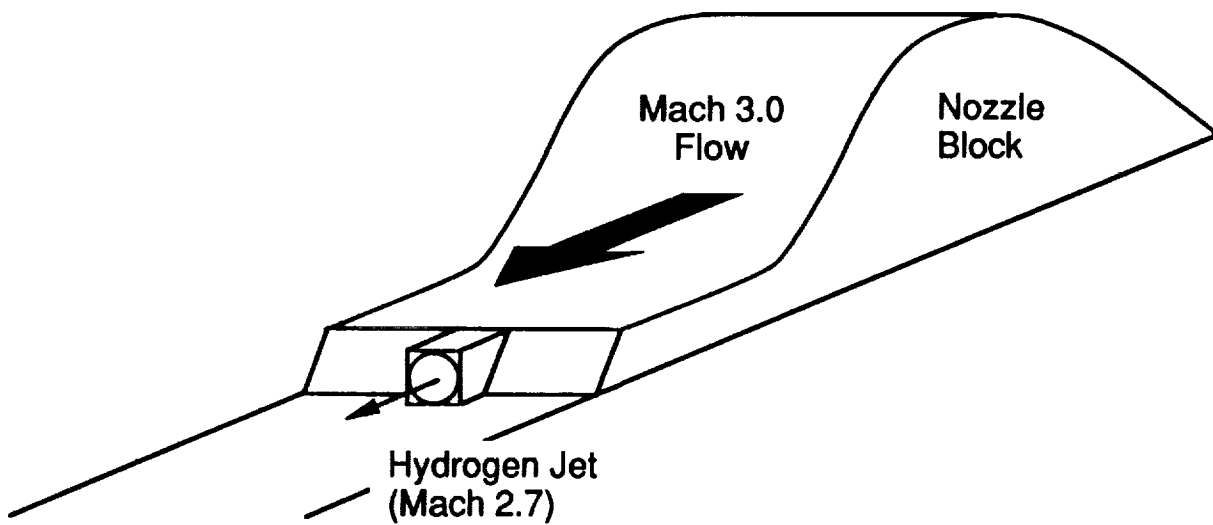


Figure 5. Swept ramp injection system

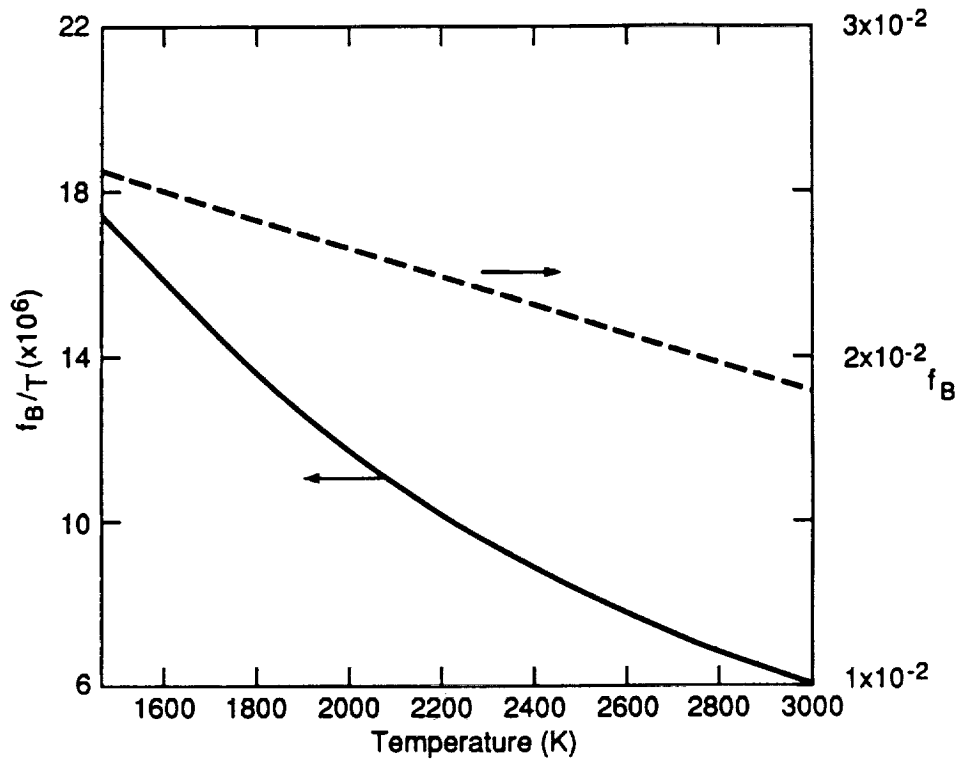


Figure 6. Temperature dependence of the Boltzmann population fraction,  $F_B$ , and the ratio  $f_B/T$  for  $J'' = 7.5$  in OH

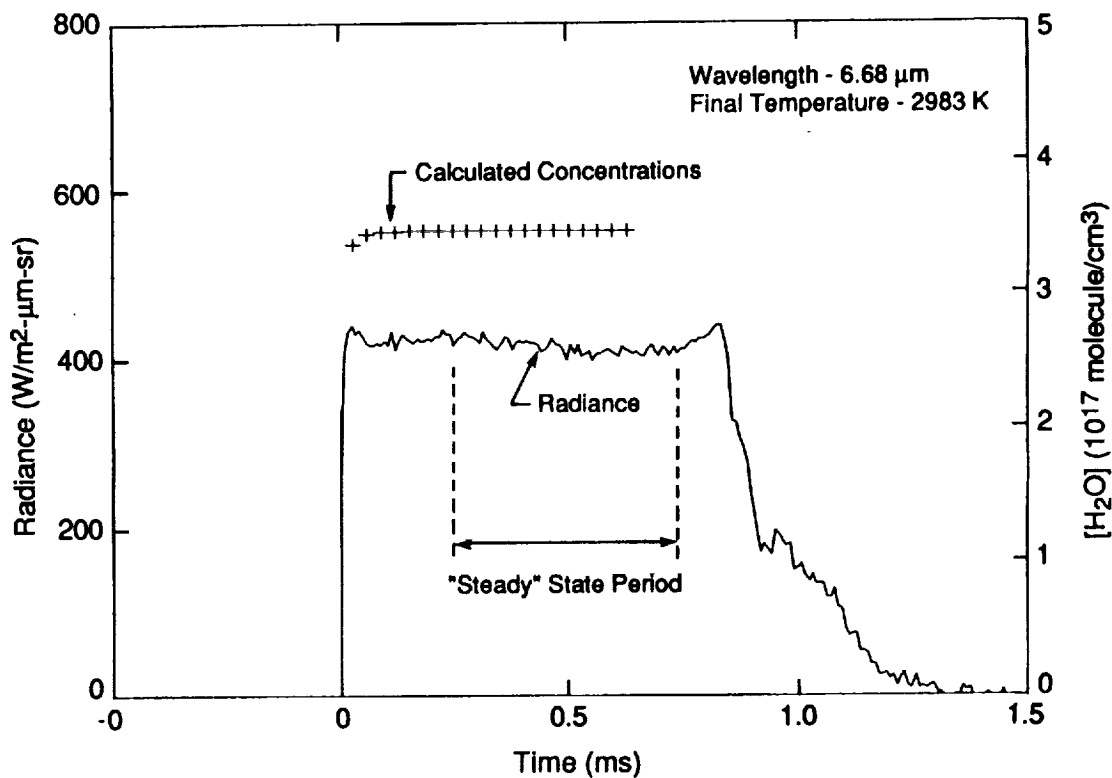


Figure 7. Incident shock tube calibration results and kinetic calculations of  $[H_2O]$

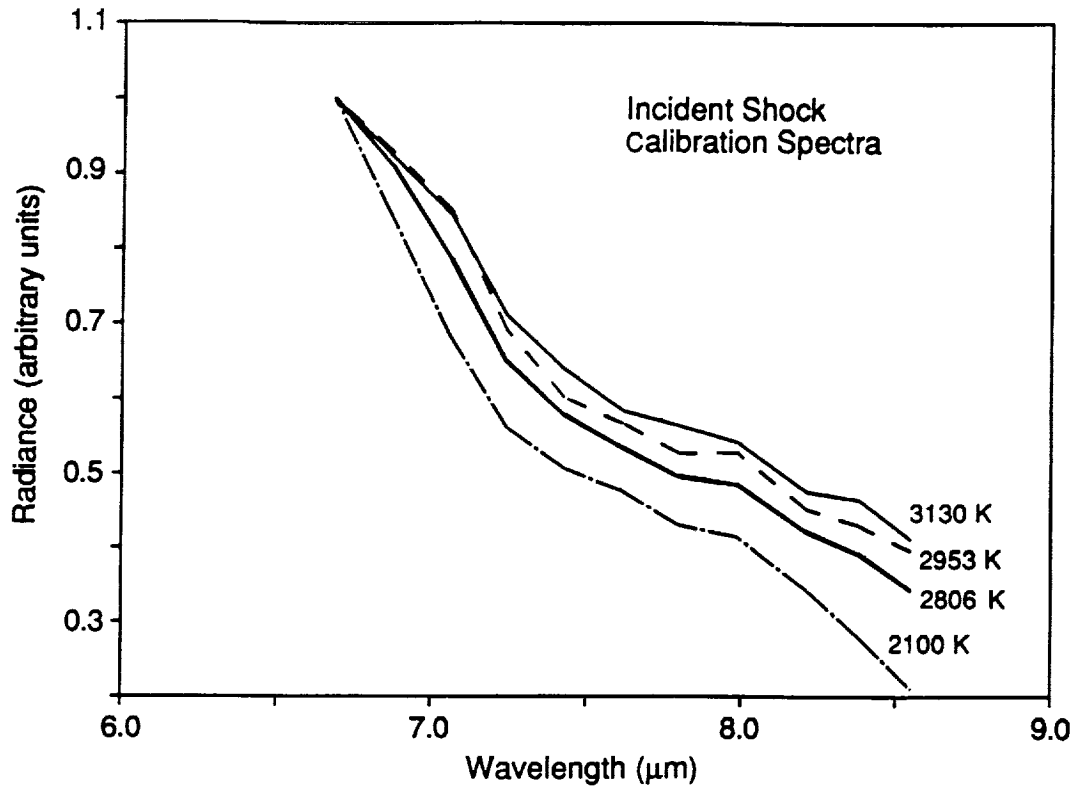


Figure 8. Normalized calibration spectra for water

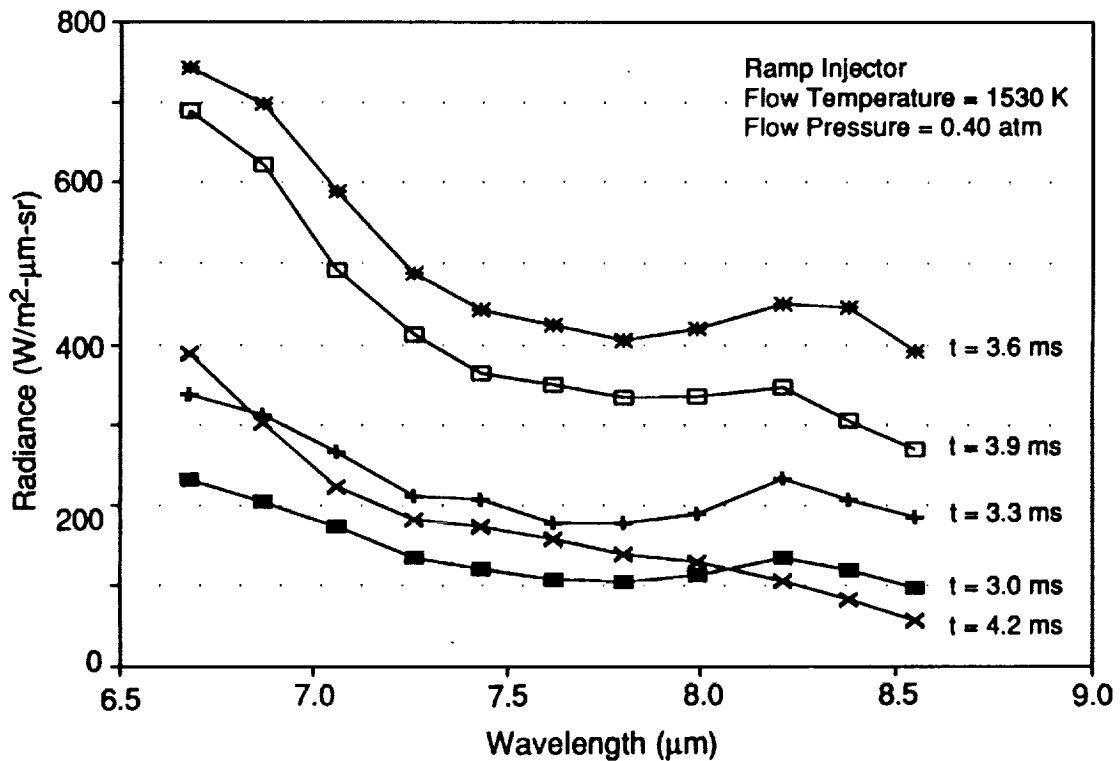


Figure 9. Time resolved spectra from the shock tunnel exit plane

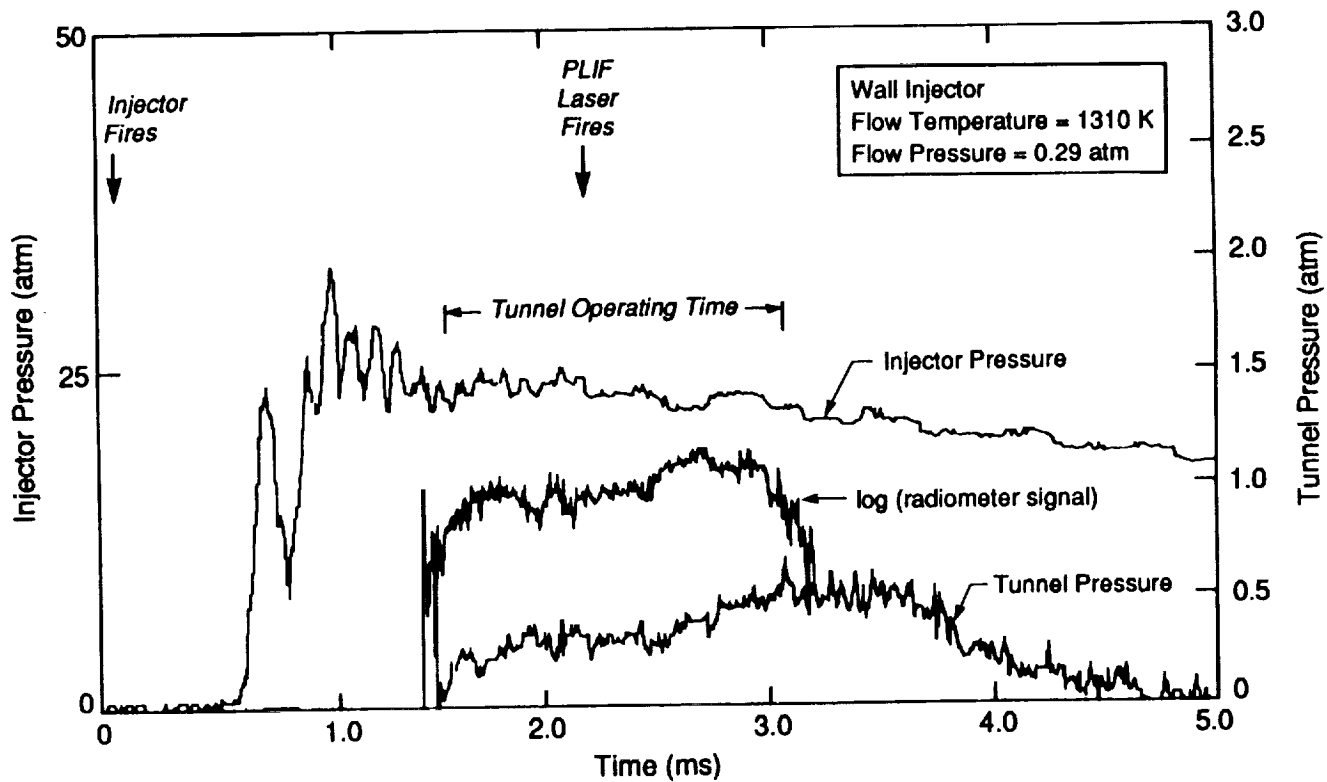


Figure 10. Injection pressure, tunnel pressure, and radiometer signal for a reacting flow measurement

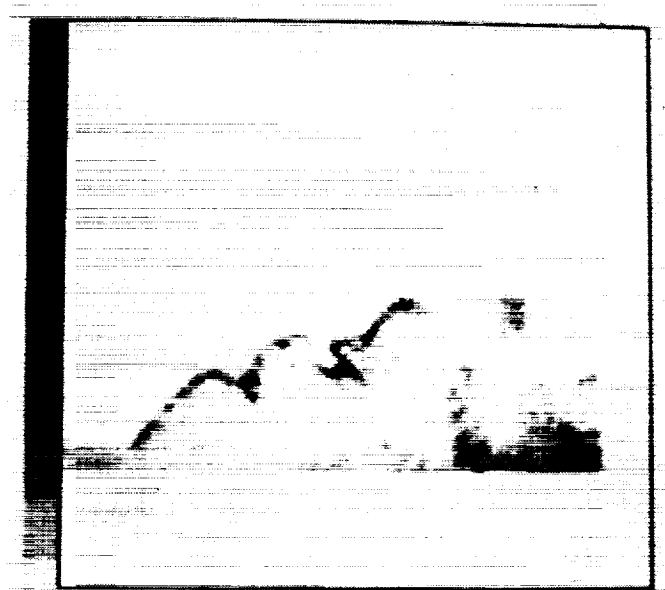


Figure 11. OH PLIF image above the first side wall injector, flow temperature = 1310 K

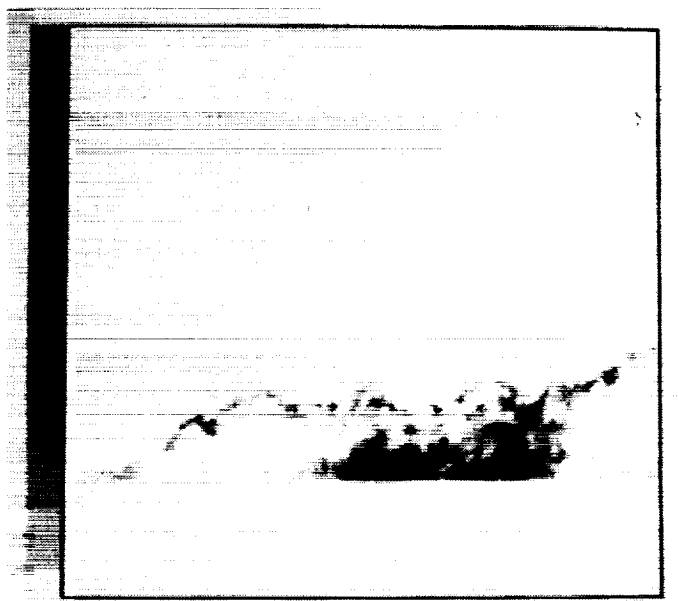


Figure 12. OH PLIF image above both side wall injectors, flow temperature = 1360 K



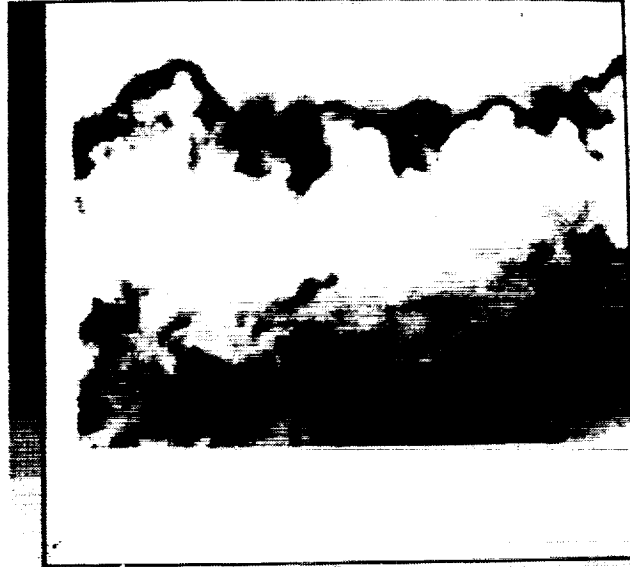


Figure 13. OH PLIF image downstream of axial injector, flow temperature = 1375 K

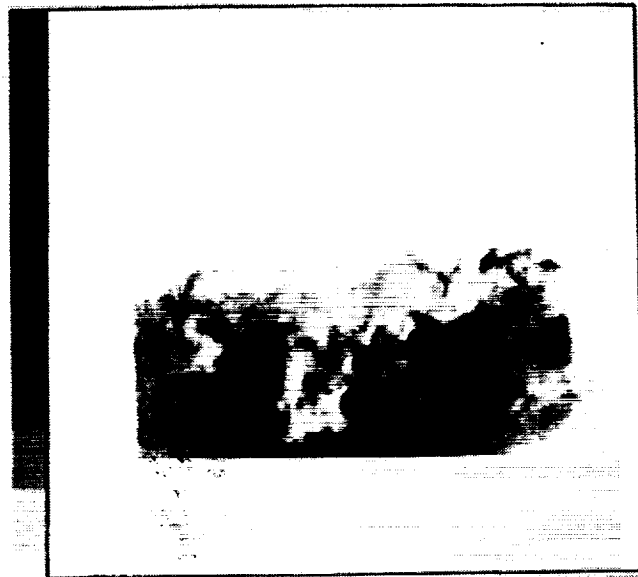


Figure 14. OH PLIF downstream of swept ramp injector with velocity mismatch, flow temperature = 1100 K

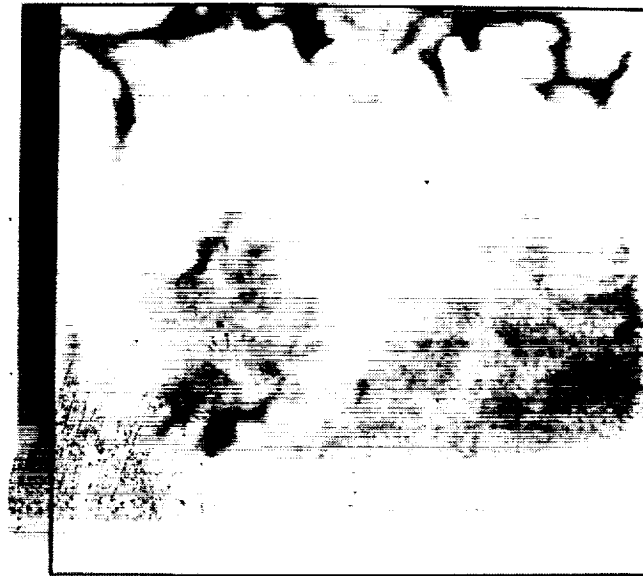
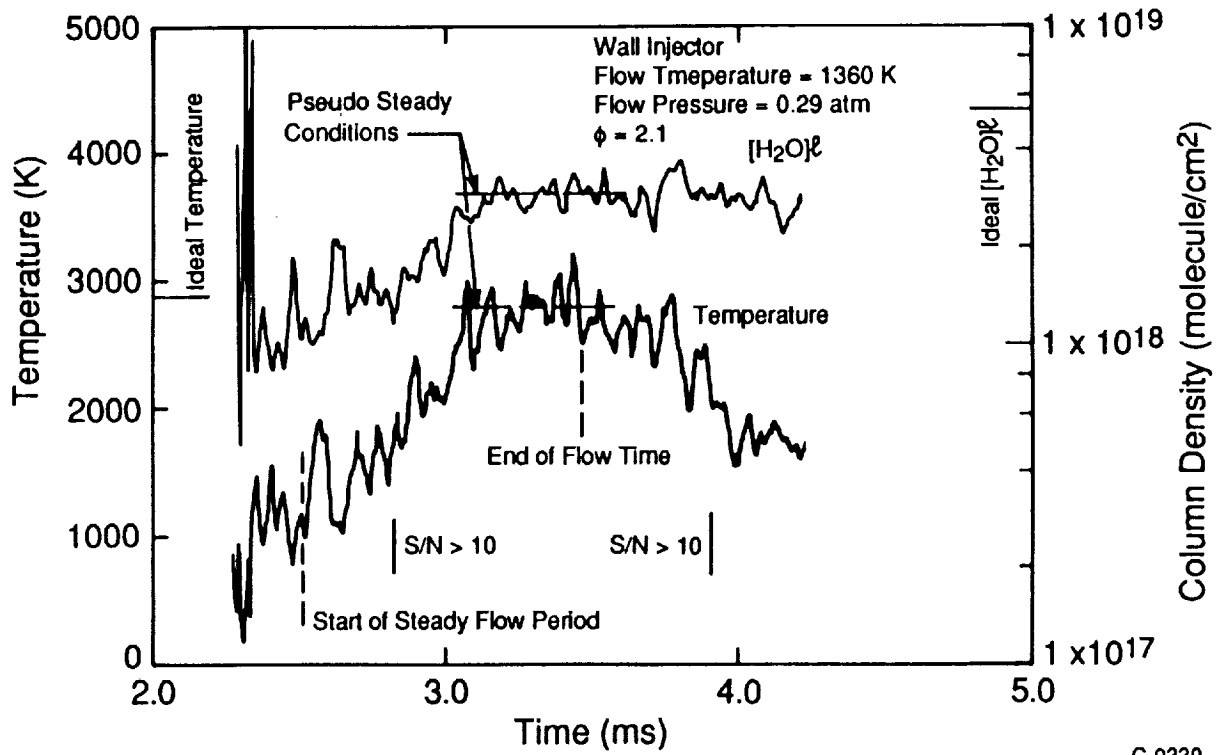
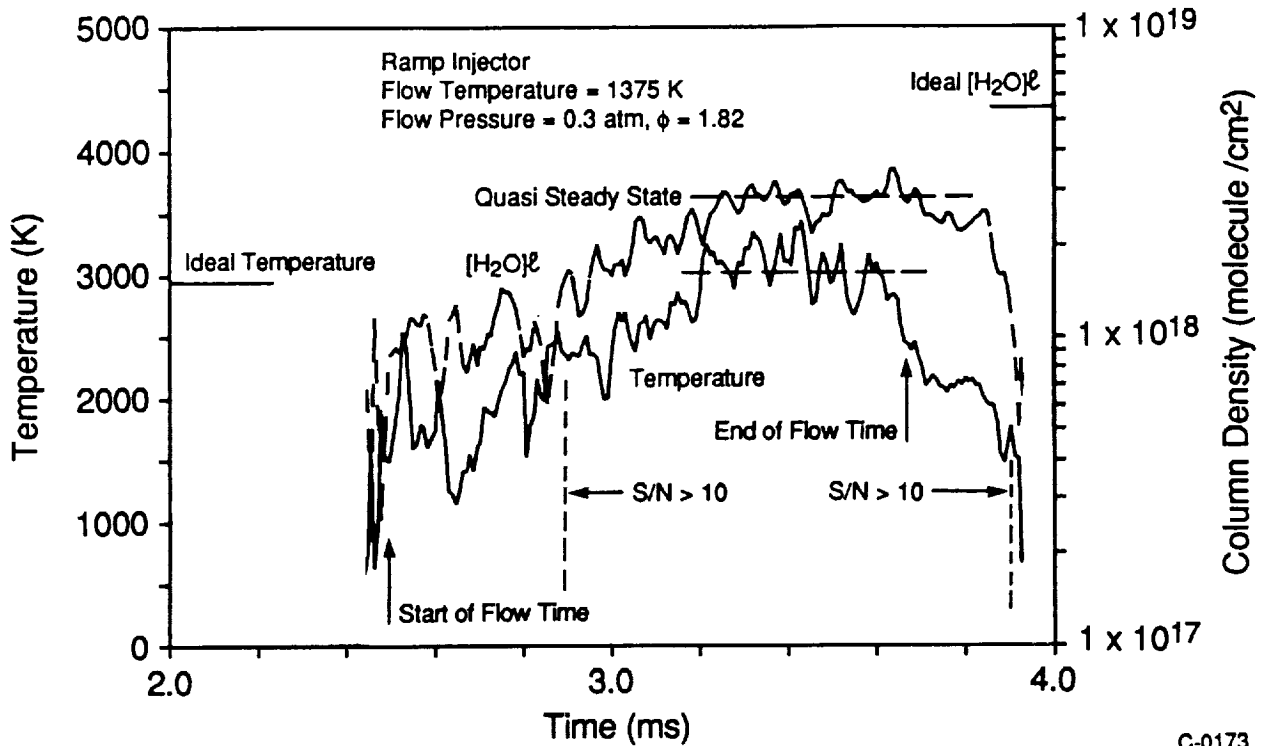


Figure 15. OH PLIF image downstream of swept ramp injector with high speed free stream, flow temperature = 1530 K



C-0339

Figure 16. Wall injection exit plane results



C-0173

Figure 17. Axial injection (with velocity matching) exit plane results





REPORT DOCUMENTATION PAGE			Form Approved OMB No. 0704-0188	
Public reporting burden for this collection of information is estimated to average 1 hour per response, including the time for reviewing instructions, searching existing data sources, gathering and maintaining the data needed, and completing and reviewing the collection of information. Send comments regarding this burden estimate or any other aspect of this collection of information, including suggestions for reducing this burden, to Washington Headquarters Services, Directorate for Information Operations and Reports, 1215 Jefferson Davis Highway, Suite 1204, Arlington, VA 22202-4302, and to the Office of Management and Budget, Paperwork Reduction Project (0704-0188), Washington, DC 20503.				
1. AGENCY USE ONLY (Leave blank)	2. REPORT DATE September 1992	3. REPORT TYPE AND DATES COVERED Conference Proceedings		
4. TITLE AND SUBTITLE The 1992 NASA Langley Measurement Technology Conference: Measurement Technology for Aerospace Applications in High-Temperature Environments			5. FUNDING NUMBERS WU 505-59-54-02	
6. AUTHOR(S) Jag J. Singh and Richard R. Antcliff (Editors)				
7. PERFORMING ORGANIZATION NAME(S) AND ADDRESS(ES) NASA Langley Research Center Hampton, VA 23681-0001			8. PERFORMING ORGANIZATION REPORT NUMBER L-17127	
9. SPONSORING/MONITORING AGENCY NAME(S) AND ADDRESS(ES) National Aeronautics and Space Administration Washington, DC 20546-0001			10. SPONSORING/MONITORING AGENCY REPORT NUMBER NASA CP-3161	
11. SUPPLEMENTARY NOTES Co-sponsors: American Institute for Astronautics and Aeronautics, Washington, DC; The Test Measurement Division and the Aerospace Industries Division of the Instrument Society of America, Research Triangle Park, Raleigh, NC.				
12a. DISTRIBUTION/AVAILABILITY STATEMENT Unclassified-Unlimited Subject Category 35			12b. DISTRIBUTION CODE	
13. ABSTRACT (Maximum 200 words) An intensive 2-day Conference to discuss the current status of measurement technology in the areas of temperature/heat flux, stress/strain, pressure, and flowfield diagnostics for high temperature aerospace applications was held at Langley Research Center, Hampton, Virginia, on April 22 and 23, 1992. Complete texts of the papers presented at the Conference are included in these proceedings.				
14. SUBJECT TERMS Thermocouples; Heat flux sensors; Strain gauges; Rayleigh scattering; Laser speckle; Flowfield diagnostics; Laser-induced fluorescence			15. NUMBER OF PAGES 444	
			16. PRICE CODE A19	
17. SECURITY CLASSIFICATION OF REPORT Unclassified	18. SECURITY CLASSIFICATION OF THIS PAGE Unclassified	19. SECURITY CLASSIFICATION OF ABSTRACT Unclassified	20. LIMITATION OF ABSTRACT	

National Aeronautics and  
Space Administration  
Code JTT  
Washington, D.C.  
20546-0001

Official Business  
Penalty for Private Use, \$300

SPECIAL FOURTH-CLASS RATE  
POSTAGE & FEES PAID  
NASA  
PERMIT No. G27



POSTMASTER: If Undeliverable (Section 158  
Postal Manual) Do Not Return

